

Subhas Chandra Mukhopadhyay
Boby George
Joyanta Kumar Roy
Tarikul Islam *Editors*

Interdigital Sensors

Progress over the Last Two Decades

Smart Sensors, Measurement and Instrumentation

Volume 36

Series Editor

Subhas Chandra Mukhopadhyay
School of Engineering
Macquarie University
Sydney, NSW
Australia

More information about this series at <http://www.springer.com/series/10617>


Subhas Chandra Mukhopadhyay ·
Boby George · Joyanta Kumar Roy ·
Tarikul Islam
Editors

Interdigital Sensors

Progress over the Last Two Decades

 Springer

Editors

Subhas Chandra Mukhopadhyay 
School of Engineering
Macquarie University
Sydney, NSW, Australia

Boby George
Department of Electrical Engineering
Indian Institute of Technology Madras
Chennai, Tamil Nadu, India

Joyanta Kumar Roy
Department of Electronics
and Communications Engineering
MCKV Institute of Engineering
Howrah, West Bengal, India

Tarikul Islam
Department of Electrical Engineering
Jamia Millia Islamia (Central University)
New Delhi, Delhi, India

Eureka Sciencetech Research Foundation
Kolkata, West Bengal, India

ISSN 2194-8402

ISSN 2194-8410 (electronic)

Smart Sensors, Measurement and Instrumentation

ISBN 978-3-030-62683-9

ISBN 978-3-030-62684-6 (eBook)

<https://doi.org/10.1007/978-3-030-62684-6>

© The Editor(s) (if applicable) and The Author(s), under exclusive license to Springer Nature Switzerland AG 2021

This work is subject to copyright. All rights are solely and exclusively licensed by the Publisher, whether the whole or part of the material is concerned, specifically the rights of translation, reprinting, reuse of illustrations, recitation, broadcasting, reproduction on microfilms or in any other physical way, and transmission or information storage and retrieval, electronic adaptation, computer software, or by similar or dissimilar methodology now known or hereafter developed.

The use of general descriptive names, registered names, trademarks, service marks, etc. in this publication does not imply, even in the absence of a specific statement, that such names are exempt from the relevant protective laws and regulations and therefore free for general use.

The publisher, the authors and the editors are safe to assume that the advice and information in this book are believed to be true and accurate at the date of publication. Neither the publisher nor the authors or the editors give a warranty, expressed or implied, with respect to the material contained herein or for any errors or omissions that may have been made. The publisher remains neutral with regard to jurisdictional claims in published maps and institutional affiliations.

This Springer imprint is published by the registered company Springer Nature Switzerland AG
The registered company address is: Gewerbestrasse 11, 6330 Cham, Switzerland

Preface

Sensors to information systems are not very different from what senses are to human beings. Just like our brains rely on the feedback from the senses to make hundreds of decisions every day, the systems need sensors to function properly, and achieve their intended objectives. The indispensability of sensors becomes even more evident when we imagine the consequences of a sensor malfunctioning, or worse yet stops working, while being part of a control system in the industry, regulators in a powerhouse, fuel flow regulation systems, or speed control module in a vehicle or autonomous vehicle, to name a few examples. And if these examples are not impactful enough, we could always imagine the smartphone without a functioning touchpad on a working day! Essentially, as we progressed through industrialization, to automation, and information-based systems, sensors for monitoring numerous parameters became inevitable. Due to the market demand, and advancements in science and technology, today, we have very high-quality sensors available for most of these applications; thanks to the great contributions of the sensor community across the world and the industry that manufactures them. The demand for miniaturized, easy to manufacture sensors that can be produced at a large scale, retaining, if not improving, the performance factors such as high sensitivity, selectivity and reliability, low cost and power consumption, and large life cycles, is very high. While this demand for perfecting the existing sensors is present, there is an ever-increasing need for new sensing functionalities, which will continue as long as the humankind exists!

There are certain types of sensors, and associated sensor structures that can be used to address sensing solutions in several fields, while the manufacturing process required is simple, the power needed for sensing very low, the space required for installation minimal, and the demand for maintenance pretty much nonexistent. Interdigital sensors, the sensors utilizing the planar interdigitated electrode structures, constitute an important category among such sensors. The dimensions and the materials that make up the interdigitated electrode structure can be selected suitably, to form specific electric field patterns which help to gather information that is otherwise not feasible using the existing sensors. While this is more about the structure of the sensing element and the material employed, realizing a sensor

system needs other equally important units such as interfacing circuits, digitizers, processors enabling edge computing, and low power yet reliable wireless communication modules. It has also been noticed that when such sensor systems are available, our smart engineers invariably come up with novel and useful applications have not been thought of before!

This book is a well thought out collation of developments in interdigital sensor structures, fabrication processes, interfacing circuits, and applications from the past two decades. It contains invited chapters from experts in the field, presenting the latest interdigital sensors, the science behind the sensing function, and captivating applications. This will help the reader to not only get updated on the latest trends and applications in this field, but also gain sufficient information and maybe even spark the curiosity to learn more and develop their very own smart interdigital sensors to serve the needs of the industry and the society better. To serve this purpose, this book has been carefully organized as detailed below.

An overview of the progress of interdigital sensors, touching upon their design, fabrication, flexibility, and applications is presented in chapter “[Progress of Interdigital Sensors Over Last Two Decades: A researcher’s Perspective](#)”. This is followed by a chapter “[Interdigital Proximity Sensor: Electrode Configuration, Interfacing, and An Application](#)” on a specially designed interdigital proximity sensor to help to solve the problem of child-left behind in the car. Chapter “[Fabrication of Interdigitated Sensors: Issues and Resolution](#)” focuses on the design and fabrication aspects of the various interdigital sensors. The process has been illustrated, in detail, with the help of intriguing examples.

Chapter “[Design and Fabrication of Fringing Field Interdigital Sensors for Physical Parameters Measurement](#)” presents a specially designed interdigital sensor for humidity sensing. The entire cycle of electrode design, using analytical expressions to compute the capacitance, fabrication procedures, and evaluation of the complete system is discussed in this chapter. One can always come up with an electrode design, but the important question is whether it is the best choice for a certain application. This aspect is illustrated in chapter “[Optimization of Interdigitated Sensor Characteristics](#)” through an optimal design presented to characterize a bio-sample. This chapter also discusses how in some cases, finite element analysis is helpful for the functionality test and optimization.

Chapter “[Epsilon-Near-Zero Microwave Sensors](#)” discusses the possibilities of utilizing the epsilon-near-zero effect in waveguides as a sensing technology. The sensor is realized using the multilayer planar technology that enables multi-frequency measurements. Chapter “[An Overview of Interdigitated Microwave Resonance Sensors for Liquid Samples Permittivity Detection](#)” specializes further on interdigitated microwave sensors for permittivity measurements. Some of the applications presented are quite fascinating, like the one for smart health system development. In the chapter “[IDC Planar RF Sensors for Dielectric Testing and Applications](#)”, some of the theoretical aspects of interdigital microwave sensors employed in permittivity measurements are discussed. Glucose measurement is presented as a potential application. The readers from the biomedical domain will find chapters “[An Overview of Interdigitated Microwave Resonance Sensors for](#)

Liquid Samples Permittivity Detection”, “IDC Planar RF Sensors for Dielectric Testing and Applications”, and “Biomedical Application of Interdigital Sensors” compelling. In fact, chapter “Biomedical Application of Interdigital Sensors” is based on an interdigital impedance sensor, unlike the microwave presented in chapters “Epsilon-Near-Zero Microwave Sensors” to “IDC Planar RF Sensors for Dielectric Testing and Applications”. Multiple interdigital sensors at different frequencies are employed to characterize the sample under test. The benefit of the array-based approach is exemplified through engaging examples, in chapter “Biomedical Application of Interdigital Sensors”.

The applications of interdigital sensors and sensor electrode structures in biomedical sensing are continued in chapter “Fabrication of Interdigital Electrodes for Monolithic Biosensing”. Here, the fabrication of an organic field-effect transistor with interdigital contacts in the channel for monolithic biosensing is detailed. This chapter also talks about the use of finite element analysis in the sensor design and optimization. Chapter “Interdigital Sensing System for Kidney Health Monitoring” is a very interesting one. It presents an interdigital sensor to measure the Creatinine level, which is a key indicator of kidney functioning. Details of a proof-of-concept device developed, tested, and compared with a suitable reference are presented in this chapter.

Chapters “Recent Advancement of Interdigital Sensor for Nitrate Monitoring in Water” and “Temperature and Humidity Compensated Graphene Oxide (GO) Coated Interdigital Sensor for Carbon Dioxide (CO₂) Gas Sensing” deal with environmental monitoring. Chapter “Recent Advancement of Interdigital Sensor for Nitrate Monitoring in Water” presents the need to detect and monitor nitrates in water. This is a difficult task as multiple similar ions are present in the water. A specially designed interdigital sensor is presented for this purpose in this chapter. Its design, fabrication, characterization, and the test results are presented. Chapter “Temperature and Humidity Compensated Graphene Oxide (GO) Coated Interdigital Sensor for Carbon Dioxide (CO₂) Gas Sensing” discusses an interdigital CO₂ sensor designed to operate in both outdoor and indoor conditions. This offers a low-cost solution for this application. The performance of the sensor for different temperatures, humidity, and CO₂ concentrations is tested, and the results are provided. Also presented are the detailed repeatability studies conducted.

Surface acoustic wave (SAW) based sensors give smart ways to realize non-intrusive sensing. The interdigital electrode pattern is very common in SAW sensors. Chapter “Development of Dual-Friction Drive Based Piezoelectric Surface Acoustic Wave Actuator” talks about the integration of a piezoelectric actuator together with two interdigital stators on opposite sides. The design of the SAW motor presented is interesting. Chapters “Interdigital Sensor for IoT Applications” and “Some Applications of Interdigital Sensor for Future Technologies” give ideas on how to develop sensor systems using interdigital sensors. What are the important sub-blocks in a sensor system? How can these be optimally integrated to achieve certain goals? These are important points to know for a system building engineer. These are detailed in chapter “Interdigital Sensor for IoT Applications”. In continuation of this chapter, a brief review of the current trends, new possible

applications of interdigital sensors and future directions are discussed in chapter “[Some Applications of Interdigital Sensor for Future Technologies](#)”.

The authors have taken a special interest, in preparing their chapters, in such a way that it conveys complex ideas in a simple manner. Their valuable time and effort spent in writing the chapters based on the latest work in the research laboratories and industry have helped very much to realize a high-quality book uncovering a wide spectrum of technology and applications of interdigital sensors. We are extremely thankful to the authors for their valuable contributions and readiness to take part in this endeavor, thus leading to this very interesting and useful book for the readers.

Sydney, Australia

Subhas Chandra Mukhopadhyay
Guest Editor
Subhas.Mukhopadhyay@mq.edu.au

Chennai, India

Boby George
boby@ee.iitm.ac.in

Kolkata, India

Joyanta Kumar Roy
jkroy.cal51@gmail.com

New Delhi, India

Tarikul Islam
tislam@jmi.ac.in

Contents

Progress of Interdigital Sensors Over Last Two Decades: A researcher’s Perspective	1
S. C. Mukhopadhyay, C. P. Gooneratne, and J. K. Roy	
Interdigital Proximity Sensor: Electrode Configuration, Interfacing, and An Application	23
Abhishek Ranjan, Bobby George, and S. C. Mukhopadhyay	
Fabrication of Interdigitated Sensors: Issues and Resolution	35
Anindya Nag, S. C. Mukhopadhyay, and C. P. Gooneratne	
Design and Fabrication of Fringing Field Interdigital Sensors for Physical Parameters Measurement	71
Tarikul Islam	
Optimization of Interdigitated Sensor Characteristics	91
J. Claudel, A. L. Alves de Araujo, D. Kourtiche, M. Nadi, and A. Bourjilat	
Epsilon-Near-Zero Microwave Sensors	123
Abhishek Kumar Jha	
An Overview of Interdigitated Microwave Resonance Sensors for Liquid Samples Permittivity Detection	153
S. Kiani, P. Rezaei, and M. Fakhr	
IDC Planar RF Sensors for Dielectric Testing and Applications	199
M Jaleel Akhtar, Nilesh K Tiwari, and Greeshmaja Govind	
Biomedical Application of Interdigital Sensors	231
Nasrin Afsarimanesh, Ghobad Shafiei Sabet, and S. C. Mukhopadhyay	
Fabrication of Interdigital Electrodes for Monolithic Biosensing	247
Nireekshan Kumar Sodavaram and S. C. Mukhopadhyay	

Interdigital Sensing System for Kidney Health Monitoring	267
S. N. Prabhu, C. P. Gooneratne, K. A. Hoang, S. C. Mukhopadhyay, A. S. Davidson, and G. Liu	
Recent Advancement of Interdigital Sensor for Nitrate Monitoring in Water	311
Md. Eshrat E. Alahi, Yun Hui, Fahmida Wazed Tina, Fowzia Akhter, Anindya Nag, Tianzhun Wu, and S. C. Mukhopadhyay	
Temperature and Humidity Compensated Graphene Oxide (GO) Coated Interdigital Sensor for Carbon Dioxide (CO₂) Gas Sensing	329
Fowzia Akhter, Saima Hasan, Md. Eshrat E. Alahi, and S. C. Mukhopadhyay	
Development of Dual-Friction Drive Based Piezoelectric Surface Acoustic Wave Actuator	351
Basudeba Behera	
Interdigital Sensor for IoT Applications	369
M. Adhikary	
Some Applications of Interdigital Sensor for Future Technologies	383
J. K. Roy and S. C. Mukhopadhyay	

About the Editors



Dr. Subhas Chandra Mukhopadhyay (M'97, SM'02, F'11) graduated from the Department of Electrical Engineering, Jadavpur University, Calcutta, India with a gold medal and received Master of Electrical Engineering from Indian Institute of Science, Bengaluru, India. He obtained Ph.D. (Eng.) from Jadavpur University, India and Doctor of Engineering from Kanazawa University, Japan.

Currently, he is working as a Professor of Mechanical/Electronics Engineering and Discipline Leader of the Mechatronics Degree Programme of the School of Engineering, Macquarie University, Sydney, Australia. He has over 30 years of teaching and research experience.

His fields of interest include Smart Sensors and Sensing Technology, Wireless Sensor Networks, Internet of Things, Electromagnetics, Control Engineering, Magnetic Bearing, Fault Current Limiter, Electrical Machines, Numerical Field Calculation, etc.

He has authored/co-authored over 500 papers in different international journals, conferences, and book chapters. He has edited 18 conference proceedings. He has also edited 25 special issues of international journals as lead guest editor and 35 books with Springer-Verlag.

He was awarded numerous awards throughout his career and attracted over AUD 6.2 M on different research projects.

He has delivered 359 seminars including keynote, tutorial, invited, and special seminars.

He is a Fellow of IEEE (USA), a Fellow of IET (UK), and a Fellow of IETE (India). He is a Topical Editor of IEEE

Sensors Journal and an Associate Editor IEEE Transactions on Instrumentation. He has organized many international conferences either as General Chair or Technical Programme Chair. He is the Founding Chair of the IEEE Sensors Council New South Wales Chapter.



Dr. Bobby George received M.Tech. and Ph.D. in Electrical Engineering from the Indian Institute of Technology (IIT) Madras, Chennai, India, in 2003 and 2007, respectively. He was a Postdoctoral Fellow with the Institute of Electrical Measurement and Measurement Signal Processing, Technical University of Graz, Graz, Austria, from 2007 to 2010. He joined the faculty of the Department of Electrical Engineering, IIT Madras in 2010. Currently, he is working as a Professor there. He serves as one of the Associate Editors of the IEEE Sensors Journal, IEEE Transactions on Instrumentation and Measurements and IEEE Transactions on Industrial Electronics. His areas of interests include measurements, sensors, and instrumentation.



Prof. Joyanta Kumar Roy has been working in electronics and automation engineering since 1984 as Company Director, Consulting Engineering, Developer, Researcher, and Educationist. He graduated from the Department of Physics from the University of Calcutta, India, and received Master of Science in Physics in 1977. He started his career as an entrepreneur in the year 1984 and founded a small manufacturing enterprise named System Advance Technologies Pvt. Ltd., dealing with turnkey execution of SCADA, automation, and industrial instrumentation system. In 2004, he obtained Ph.D. (Technology) in Applied Physics from University of Calcutta, India, and executed a number of projects related to control, automation, and instrumentation in several engineering sectors. After a long association with industry, he started his academic career from 2005. He worked with many educational institutes as principal, dean, and professor. His research group developed low-cost non-contact liquid-level transmitter, temperature transmitter, pressure transmitter, vortex flow transmitter, mass flow meter, etc. He has contributed more than 150 scientific and technical publications in the form of books, book chapters, journal papers, conference papers, manuals, and engineering design of industrial

project. He is a technical speaker and has given invited talks in a number of international and national-level conferences. He organized many technical events, national and international events and worked as TPC member. He is the Founder Chairman of Eureka Scientech Research Foundation. He is a senior member IEEE and chapter chair IEEE Circuits & Systems, Region-10, India, Kolkata Section, Chairman and EC member IET (UK) Kolkata Network, Fellow of IWWWA, and Fellow of IETE. Presently, he is working as Editor of S2IS and a regular reviewer of research articles. His present research interest includes development of smart measurement and control system for water production and distribution, multifunction sensor, IoT-based m-health, technology-assisted living, smart home and city.



Tarikul Islam (M'16-SM'20) was born in Murshidabad, West Bengal, India. He received M.Sc. Engineering in Instrumentation and Control System from A. M. U. Aligarh, U.P. in 1997 and Ph.D. (Engineering) from Jadavpur University, Kolkata, India, in 2007. From 1997 to 2006, he was Assistant Professor and from 2006 to 2012, he was Associate Professor with the Electrical Engineering Department, Jamia Millia Islamia (A Central University), New Delhi. Since 2012, he is working as Professor at the same University. He has over 20 years of teaching and research experience. He has authored/co-authored 5 book chapters, 1 edited book, filed 2 Indian patents and published more than 160 papers in peer-reviewed journals and conferences. He received research grants from government agencies like DST, DRDO, MHRD, CPRI, DAE of more than 260,000 (US\$). His research interests include sensors and sensing technologies, electronic instrumentation. He is a life member of IETE (India), ISTE (India) and a senior member of IEEE. He is a topical editor for IEEE Sensors Journal. He is an Associate Editor for IEEE Transactions on Instrumentation and Measurement, and International Journal on Smart Sensing and Intelligent Systems. He is a Co-Editor of a special issue of an International Journal of Electronics, MDPI.

Progress of Interdigital Sensors Over Last Two Decades: A researcher's Perspective



S. C. Mukhopadhyay, C. P. Gooneratne, and J. K. Roy

Abstract Interdigital sensors are being used in many different applications around us to help human beings to live a safe, sound and healthy life. The transition has taken place due to significant changes in terms of material, manufacturing, signal processing, and applications and so on. The current chapter will describe a few applications in which the author is involved over the last two decades to show the gradual changes taken place during the time.

1 Introduction

Planar sensors are very popular and useful in the field of science and engineering, to detect different parameters of interest. Over the years there has been a growing interest to develop different types of planar structured sensors, namely meander, mesh, interdigital types as well as circular, spiral and many other types to cater many different applications due to the advantage of one-side access.

2 Early Applications of Planar Sensors

Planar meander type of sensors have been used to determine the quality of printed circuit board during the nineties [1]. The meander patterned conductor carry a high frequency current to generate the magnetic field is usually kept on top of the PCB.

S. C. Mukhopadhyay (✉)

School of Engineering, Macquarie University, North Ryde, NSW 2109, Australia

e-mail: Subhas.Mukhopadhyay@mq.edu.au

C. P. Gooneratne

Saudi Aramco, Dhahran 31311, Saudi Arabia

J. K. Roy

Eureka Sciencetech Research Foundation, Kolkata, West Bengal, India

© The Editor(s) (if applicable) and The Author(s), under exclusive license to Springer Nature Switzerland AG 2021

S. C. Mukhopadhyay et al. (eds.), *Interdigital Sensors*, Smart Sensors, Measurement and Instrumentation 36, https://doi.org/10.1007/978-3-030-62684-6_1

It is possible to determine the quality of the PCB tracks such as non-uniformity, discontinuity, short-circuit for single-layer as well as multi-layer PCBs. Planar mesh type coils have been used for the estimation of surface properties [2] as well determination of the quality of electroplated materials [3, 4]. The size of the track-width especially pitch of the mesh type of coil is very important for accurate determination of properties [5]. The detailed model and its formulation for analytical determination of impedance of the sensor as well as estimation of properties has been reported [6, 7]. The comparison of performance of planar sensors has been conducted [8, 9]. Most of the activities on planar type sensors mainly meander and mesh type were conducted at Kanazawa University, Japan. Relatively high end equipment and instrumentation is essential for this type of research activity.

3 Research on Interdigital Sensors

In the last few decades there has been a significant improvement on the performance of interdigital sensors. In country like New Zealand where agriculture is extremely important, capacitive sensor plays an important role for inspection of quality of water, food, beverages, meat etc. Interdigital sensor is the planar form of capacitive sensor with one side access. Figure 1 shows the transformation process of a conventional three dimensional capacitive sensor to a 2-D planar interdigital sensor. The first prototype as shows in Fig. 1e was fabricated from conventional printed circuit board design technique [10–12]. The sensor is very cheap to fabricate as it uses the simple PCB fabrication technology which is usually available in most of the universities. The necessary electronic circuits cum instrumentation are simple as the sensor usually operates at relatively low frequency, up to a few kHz. In universities without a dedicated research facilities, the interdigital sensors based research is feasible and possible using the available teaching facilities.

3.1 *Inspection of Meat Quality*

The first application of the fabricated interdigital sensor was determination of fat and protein content in meat [10]. Usually piece of meat are cut into rectangular shape of around 120 mm × 100 mm X 30 mm dimensions and weighing around 1.5 kgs. To be able to measure the piece of meat in one measurement, the interdigital sensors using the PCB technique was fabricated in the similar shape and sizes. The pictorial representation of measurement along with sensors are shown in Fig. 2. Three different pitch lengths of interdigital sensors were fabricated to see the effectiveness and accuracy of measurement. The detailed results are presented in [10].

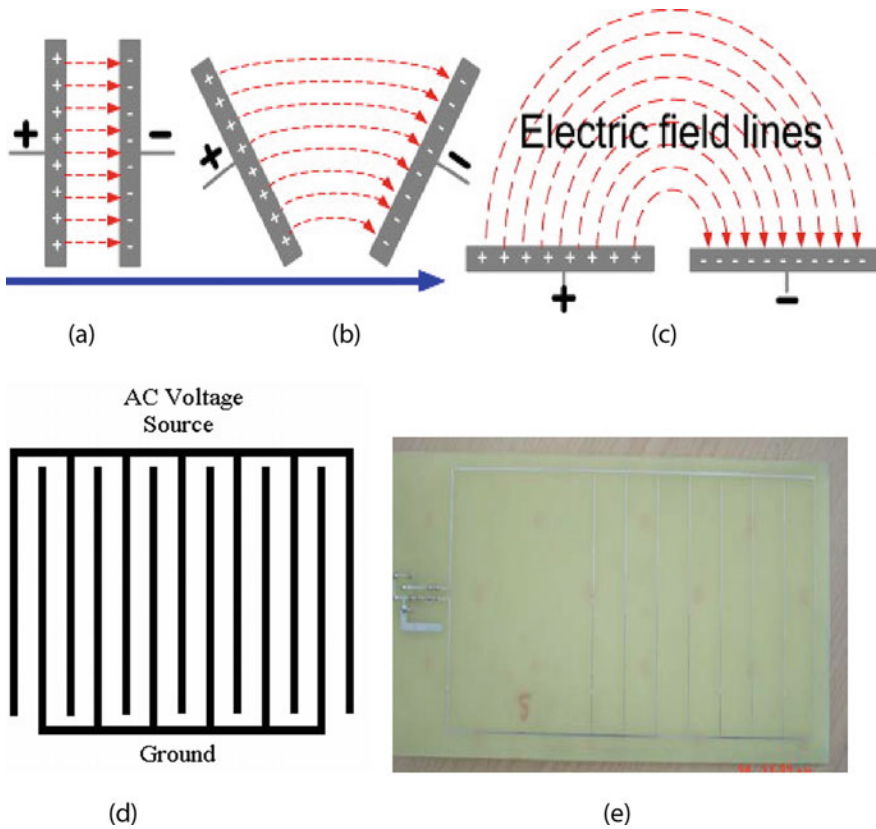


Fig. 1 Interdigital sensors; **a** 3-D conventional capacitive sensor; **b** converting 3-D capacitor to a 2-D planar interdigital sensor; **c** electric field lines of interdigital sensor; **d** enhancement of sensitivity by multiple electrodes; **e** first prototype from conventional printed circuit board technique. Courtesy Refs. [10–12]

3.2 Determination of Looseness of Leather

The next application of interdigital sensor was conducted to inspect the looseness of leather [11]. The traditional method of determination of looseness is based on mechanical force measurement and can be subjective. The planar sensor based measurement will be able to eliminate the error. The methodology has been shown in Fig. 3 and the details are available in [11].



Fig. 2 Inspection of quality of meat [10]

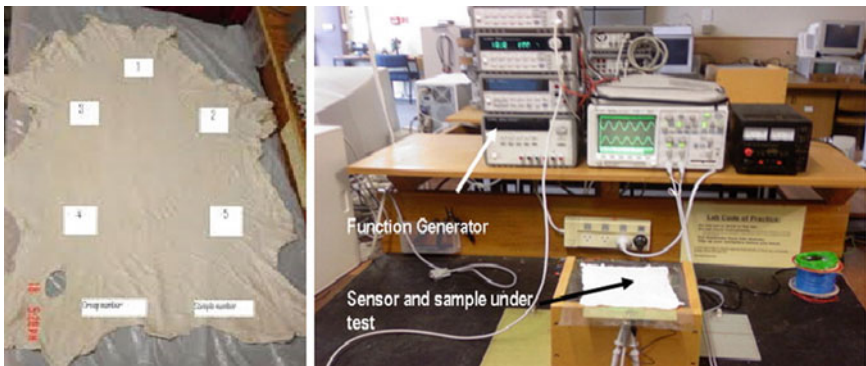


Fig. 3 Inspection of quality of leather [11]

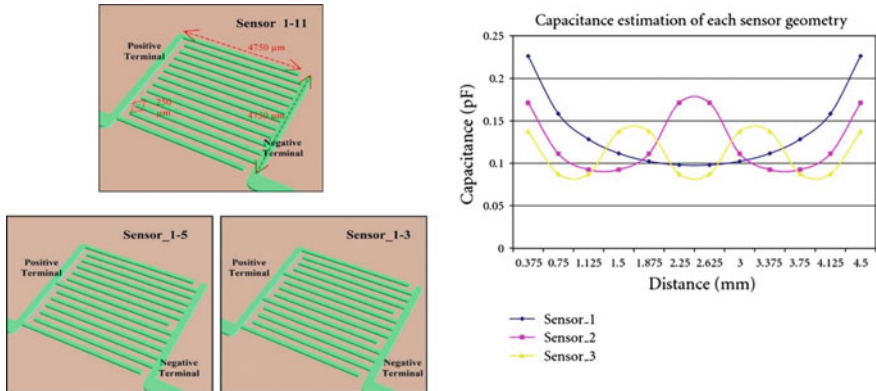


Fig. 4 Fabrication of new structure of interdigital sensors [14]

4 New Structure of Interdigital Sensors

The size of the interdigital sensors as reported before was large, more than 100 mm in length and the structure was of conventional type, the +ve and -ve electrodes are one after another and separated by a distance. In order to explore different structures and their effectiveness, we fabricated small size sensors of a few mm length and width. The small sensors have been used to inspect quality of seafood especially whether the seafood is contaminated with natural biotoxins [12, 13]. The structure has been changed so that the field distribution is uniform through the sensing region. Figure 4 shows the arrangement in which 1-11-1, meaning 1 exciting electrode (positive), 11 sensing (negative) electrodes with same pitch gap between consecutive electrodes. The detailed analysis has been reported in [14]. The developed seafood inspection tool has been shown in Fig. 5.

5 Planar Electromagnetic Sensors

Planar electromagnetic sensors consist of planar meander and interdigital sensor working together. The magnetic field is created by the current flowing through the meander coil and the electric field is generated by the interdigital structure. The meander coil and the interdigital coil may be connected in series and parallel form depending on applications. The frequency of operation is very important to measure properties of materials under test. A schematic diagram and the equivalent circuit to measure the impedances to determine the measured parameters are shown in Fig. 6 [16–19]. The planar electromagnetic sensor has been used to detect nitrate contamination in water and results have been reported in [16–19]. The electrochemical impedance spectroscopy based method is used to determine the impedances of the

Sample Thickness	No. of Samples	Threshold Sensitivity	Sensor Detection
1.3 mm – 1.9 mm	23	12.6	Yes
2.0 mm – 2.8 mm	17	17.0	Yes
2.9 mm – 3.4 mm	13	24.3	Yes

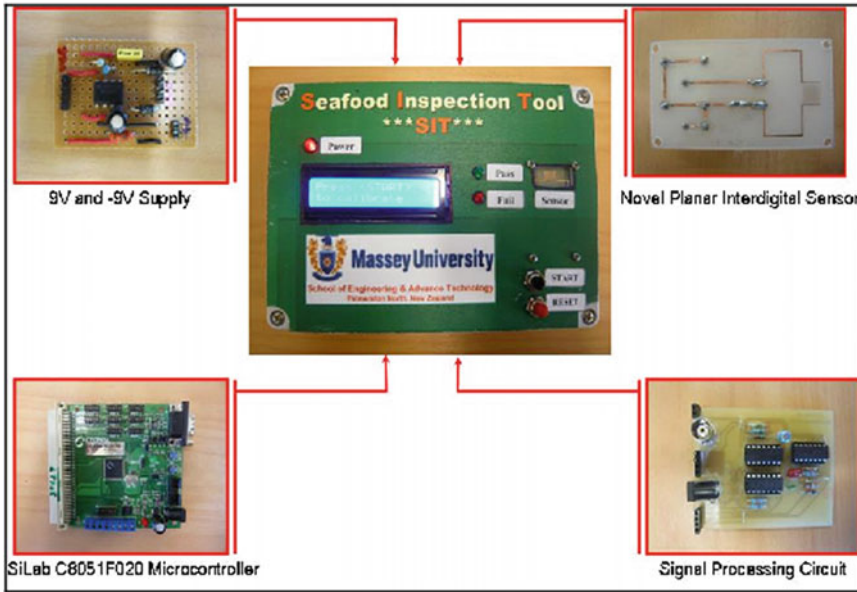


Fig. 5 Inspection of seafood (seafood inspection tool) [14, 15]

coil and from which the materials properties are determined. The measured properties are not based on selective detection but based on experimental evaluation.

6 MEMS Based Interdigital Sensor

So far the sensors described in earlier sections are of large sizes varying between a cm to tens of cms. The pitch length of the sensor was a few millimetres and more. In order to detect something of very small sizes, it is important to have the sensors of very small pitch lengths. It is difficult to fabricate sensors of pitch lengths of a few tens of micrometres using conventional PCB fabrication technology. With the collaboration of King Abdullah University of Science and Technology (KAUST), Saudi Arabia, smart sensors have been fabricated using Micro Electro-Mechanical Systems (MEMS) technology. Figure 7 shows picture of the fabricated sensors where

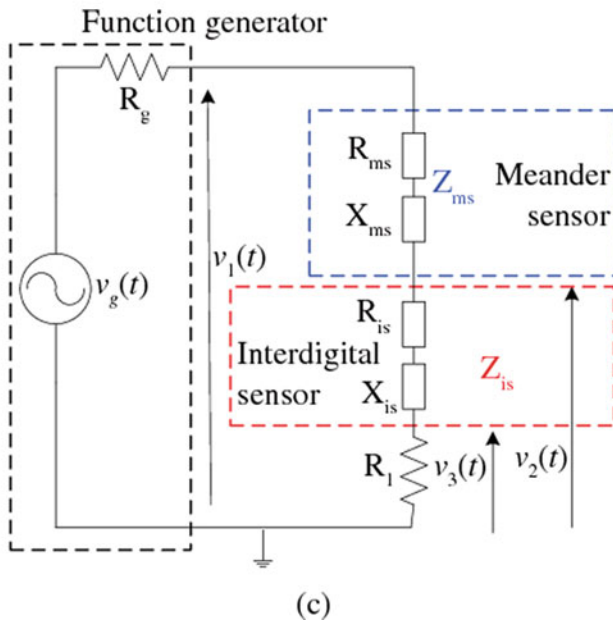
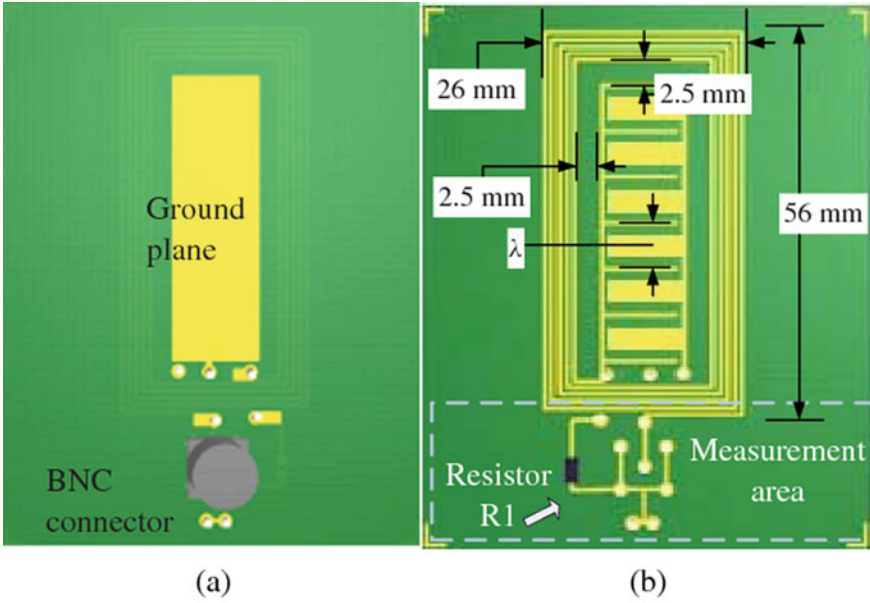


Fig. 6 Planar electromagnetic sensor for detection of nitrate contamination in water [16–19]

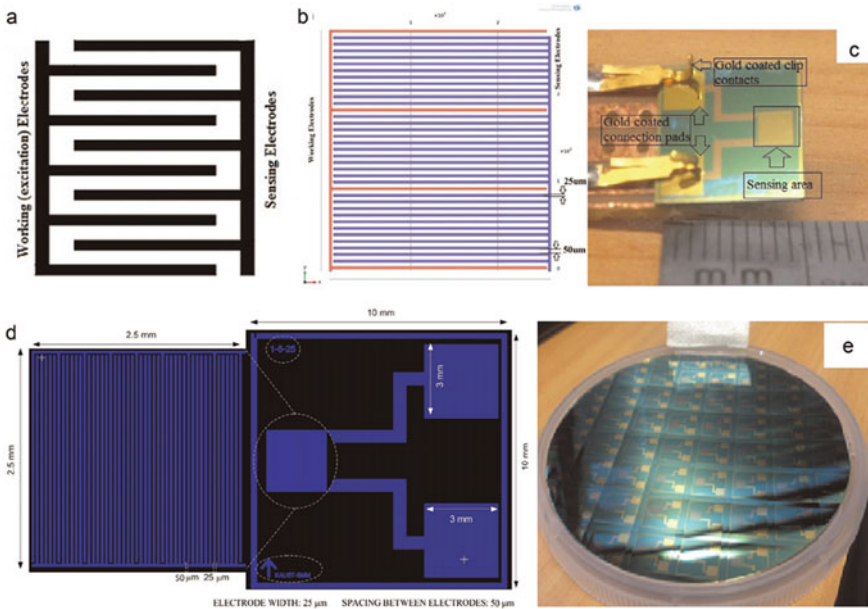


Fig. 7 MEMS based interdigital sensor design [20, 21]

the conventional sensors of pitch length of 25 micro-meters as well as new structure of 1-11-1 and other configurations have been fabricated. The sensors have been used to determine contamination of E-coli bacteria in meat [20] and detection of phthalate contamination in water coming from plastic [21].

7 Introducing Selectivity

The interdigital sensors are used in many applications as the sensor is very sensitive to any kind of dielectric materials. The sensitivity is one of the most important features of any sensor and high value of it is very desirable but it is not everything. When the sensor is used to determine a specific parameter which is mixed within many items, it is extremely important that the sensor should respond to the parameter of interest. In other words the sensor should be selective to the parameter of measurement. In order to make the sensor to be selective to a particular chemical or biological parameter, the surface of the sensor to be functionalized so that the sensor surface is selective to measured parameters. There are many ways the functionalization of sensor surface can be done but there are still some challenges remain. One of the biggest challenge is the re-usability of the sensor as the sensor surface reacts with the sample for test, the sensitivity of measurement gets reduced. Moreover, the surface gets contaminated to the sample of measurement so may not be useful for future use. One of the option

will be to have only one time use of the sensor electrode and throw the sensor after measurement like diabetic measurement. In the following section some projects will be explained briefly.

7.1 Meat Quality Inspection

In one project MEMS based interdigital sensor was used to detect E-coli bacterial infection in food especially in meat [20]. Food poisoning are usually caused by endotoxins or Lipopolysaccharide (LPS) are associated with Gram-negative bacteria. Major food-borne pathogens such as Escherichia coli (E-coli) and Salmonella are Gram-negative bacteria cause a large number of outbreaks of food poisoning. Interdigital sensors have been functionalized with carboxyl functional polymer, APTES (3 Aminopropyltriethoxysilane) and then the coated sensors were immobilized with PmB (Polymyxin B) which has specific binding properties to LPS. Figure 8 shows SEM images of the sensor surface at different operating conditions. The procedure of the functionalization as well as immobilization to be followed a certain rules, the details of the procedures along with results have been described in [20]. The functionalized material, in this case APTES is extremely important and to be selected for different applications very carefully.

7.2 Detection of Phthalate Contaminated in Water

In another project the phthalate contaminated in water leaching out of plastic bottle has been detected by MEMS based interdigital sensor. In this case the coating materials is a polymer which is produced by a method known as Molecular Imprinted Polymer (MIP) and the polymer is selective to any molecules to be detected. The MIP method is very useful to detect at molecular level though the shortcoming of the method is the sensor cannot be used for many times. The method of preparation of polymer is shown in Fig. 9 and the details of the system along with experimental results are available in [21–23].

The interdigital sensor along with the electrochemical impedance spectroscopy method was also used to detect liquefied petroleum gas (LPG) with and without coated particles of tin oxide (SnO_2) in the form of a thin layer. A thin film of SnO_2 was spin-coated on the sensing surface of the interdigital sensor to induce selectivity to LPG that consists of a 60/40 mixture of propane and butane, respectively. The research outcomes have reported a novel strategy for gas detection under ambient temperature and humidity conditions. The response time of the coated sensor was encouraging and own a promising potential to the development of a complete efficient gas sensing system [24, 25].

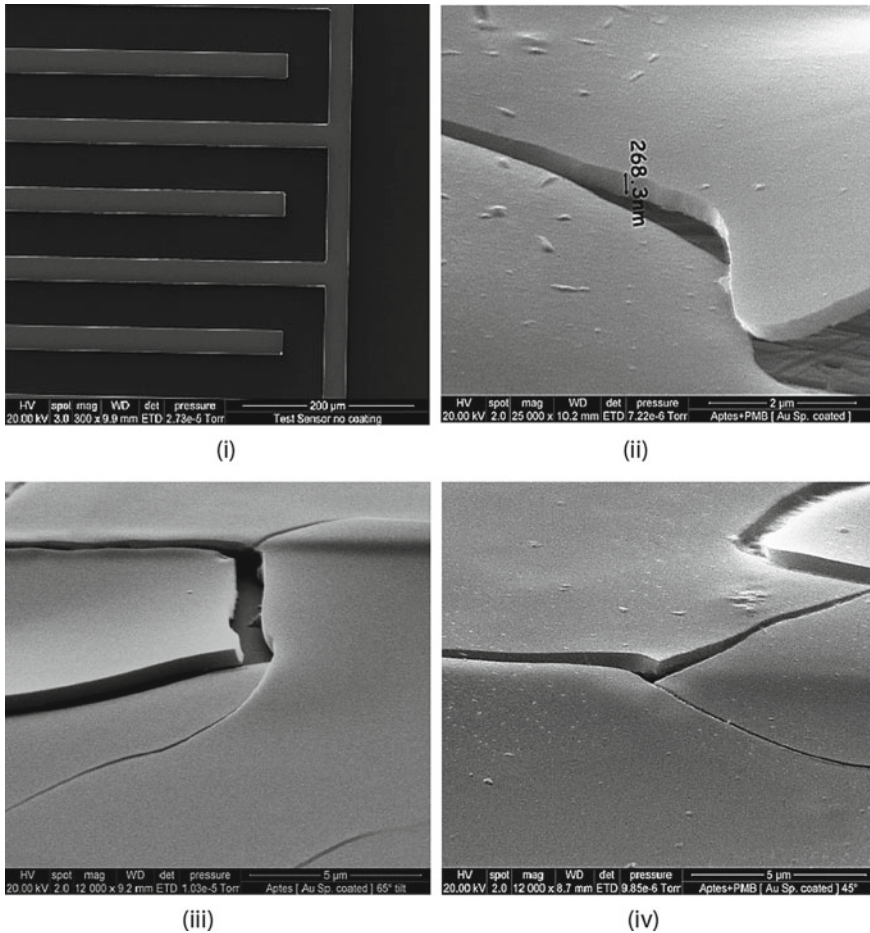


Fig. 8 SEM images of bare and coated MEMS based sensor; **a** bare sensor; **b** sensor coated with one time dipping in APTES; (iii) sensor before PmB immobilization; (iv) Sensor after PmB immobilization

7.3 Biomedical Applications

The interdigital based sensor can be used as a smart sensing system for biomedical and healthcare applications. The interdental sensor based system has been designed and developed as a point-of-care device to detect at the early stage of disease which is essential for an efficient treatment. Bone loss can be detected and monitored by regular measurement of serum or urine C-terminal telopeptide of type 1 collagen (CTx-1). An Internet of Things (IoT)-based selective, sensitive, quick, and inexpensive device for the quantification of CTx-1 levels in serum has been reported [26–30]. A planar interdigital sensor was coated with artificial antibodies, prepared

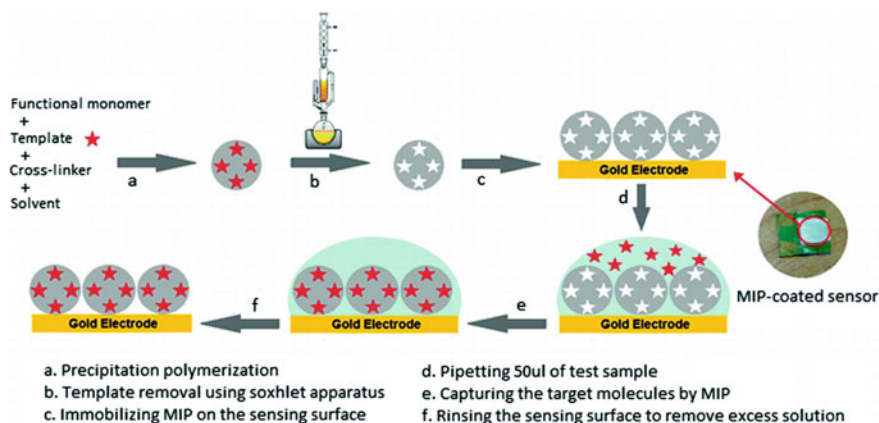


Fig. 9 Preparation of molecular imprinted polymer [21–23]

by molecular imprinting technology. Electrochemical impedance spectroscopy was used to evaluate the resistive and capacitive properties of the sample solutions. A microcontroller-based system was developed for the measurement of the level of CTx-1 in serum and for data transmission to an IoT-based cloud server. The data can be provided to the medical practitioner and a detailed investigation can start for early detection and treatment. The developed sensing system responded linearly in a range of 0.1–2.5 ppb, which covers the normal reference range of CTx-1 in serum, with a limit of detection of 0.09 ppb. The results demonstrated that the proposed portable bio sensing system could provide a rapid, simple, and selective approach for CTx-1 measurement in serum. Sheep serum samples were tested using the proposed system and the validation of the results was done using an enzyme-linked immunosorbent assay kit.

Figure 10 shows the results of the response of the sensor with NIP (Non-imprinted polymer) as well as with MIP coated sensor. It clearly shows that MIP coated sensor has more ability to detect the sample with CTX-I compared to NIP coated sensor. Figure 11 shows the complete block diagram of the IoT enabled smart sensing system and the Fig. 12 shows the microcontroller based prototype developed in the laboratory.

7.4 Detection of Nitrate Contamination

MEMS based interdigital sensor has been developed as a smart sensing system to detect and measure the level of nitrate contamination in water as shown in Fig. 13. The results have been shared in [31–34]. The uncoated sensor can be used to measure the response of the sensor with different known concentration and the calibration curve can be made. Using the calibration curve, the unknown level of nitrate can be

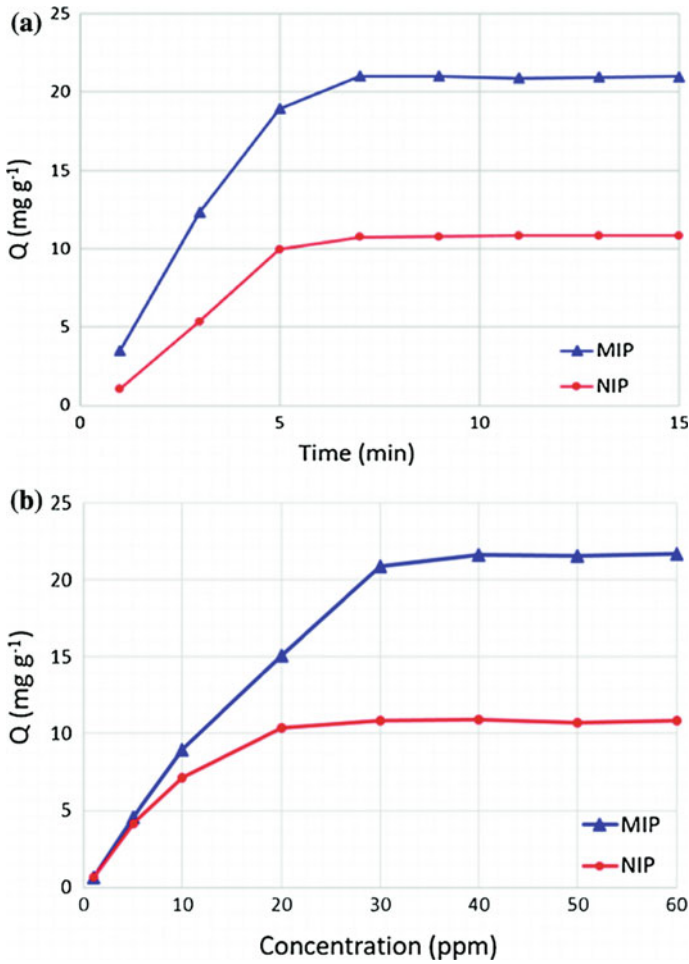


Fig. 10 Response of the sensor to CTX-I with both NIP and MIP [26]

measured. The interdigital sensor being a capacitive in nature is usually influenced by temperature and humidity. Since the sensor is dipped in water the effect of humidity is absent. To overcome the effect of temperature on the accuracy of measurement, a compensation circuit has been developed and is reported in [32]. To detect only nitrate the selective property has been achieved by developing a MIP based polymer and has been reported in [33]. A graphene based sensor of interdigital structure as well as temperature compensation has been reported in [34].

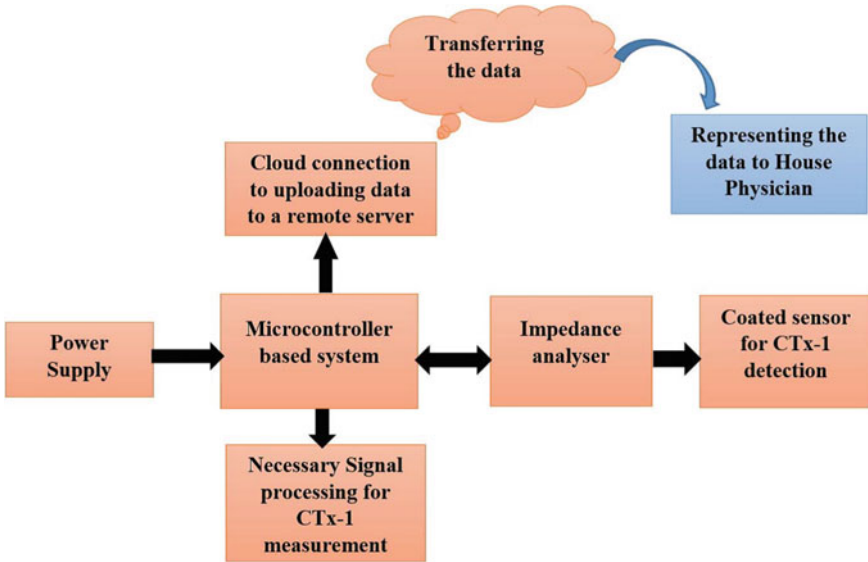


Fig. 11 The block diagram of the IoT enabled smart sensing system [27]

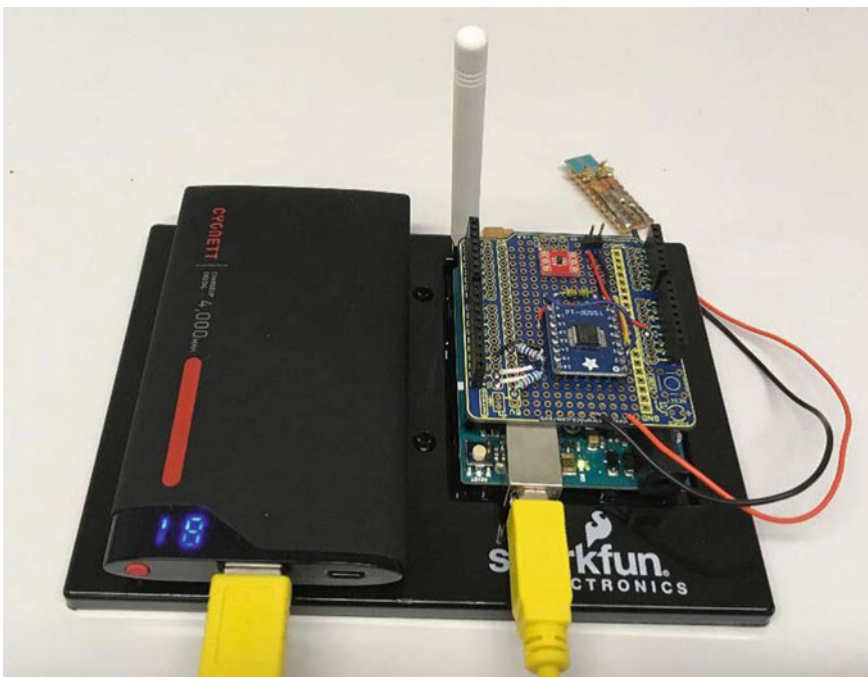


Fig. 12 A microcontroller based developed point-of-care device to detect early stage of osteoporosis [28]



Fig. 13 IoT enabled interdigital sensor based nitrate monitoring; (i) the complete system; (ii) inside electronic components [31]

8 Interdigital Sensors Based on Flexible Materials

In recent times, the research and developmental activities on flexible sensors are happening at very high pace and a lot of systems are reported. Of course, it does not mean that MEMS based sensors will be obsolete but in many applications the flexible sensors offer more advantages. A few of them are listed here.

- Difficult to attach sensors with rigid substrates.
- The cost of fabrication of sensors with rigid substrates is high.
- Difficulty in fabrication process.
- Electrode material comes off on attachment of the chips.
- Difficult to work with liquids due to hydrophilicity.

The design, development, and fabrication of a flexible and wearable sensor based on carbon nanotube nanocomposite for monitoring specific physiological parameters has been presented in [35]. Polydimethylsiloxane (PDMS) was used as the substrate with a thin layer of a nanocomposite comprising functionalized multi-walled carbon nanotubes (MWCNTs) and PDMS as electrodes. The sensor patch functionalized on strain-sensitive capacitive sensing from interdigitated electrodes which were patterned with a laser on the nanocomposite layer. The thickness of the electrode layer was optimized regarding strain and conductivity. Traditionally MEMB based interdigital sensor senses parameters which is reflected by changes of resistance and capacitances without changing its dimensional properties. But with reference to Fig. 14, the interdigital sensor based on flexible materials can measure force, pressure as is shown as the physical dimension changes leading to change of resistance and capacitance. The sensor patch was connected to a monitoring device from one end and attached to the body on the other for examining purposes. Experimental results show the capability of the sensor patch used to detect respiration and limb movements. This work is a stepping stone of the sensing system to be developed

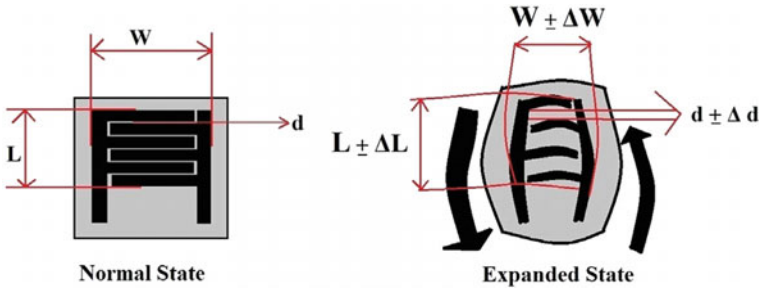


Fig. 14 Interdigital sensor based on flexible material [35]

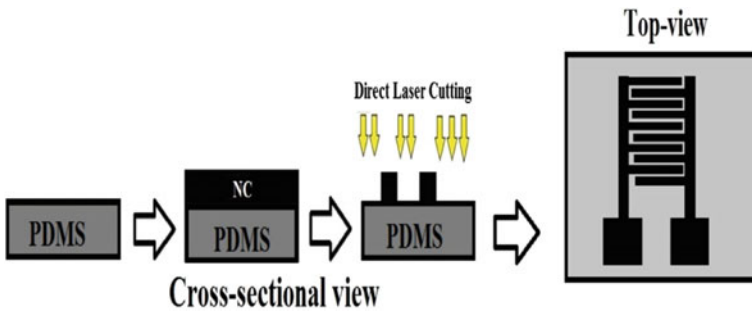


Fig. 15 Schematic diagram of the fabrication steps. PDMS: Polydimethylsiloxane. NC: Nanocomposite [35]

for multiple physiological parameters. Figure 15 shows the steps of fabrication of PDMS-NC based flexible interdigital sensor.

Design, fabrication, and implementation of a novel sensor patch developed from commercial polyethylene terephthalate films metallized with aluminium on one side has been reported [36]. The aluminium was ablated with laser to form interdigitated electrodes to make sensor prototypes. The interdigitated electrodes were patterned on the substrate with a laser cutter. The steps of fabrication are shown in Fig. 16. The prototypes have been used as a tactile sensor showing promising results for using these patches in applications with contact pressures considerably lesser than normal human contact pressure.

The flexible sensors are made up of different materials, the base materials can be either PDMS, PET or Polyimide films. The materials for electrode can be made of CNT, graphene or Aluminium. The relative advantages and disadvantages of different materials are described in Table 1.

Over the last few years, different types of sensors based on flexible materials have been designed and fabricated. Laser induced graphene sensor for salinity measurement utilizing strain effect based on graphene/PDMS has been presented in [37, 38]. The Ref. [39] is a review article on graphene based sensors and different applications. Flexible sensor for determination of taste has been presented in [40]. Wearable

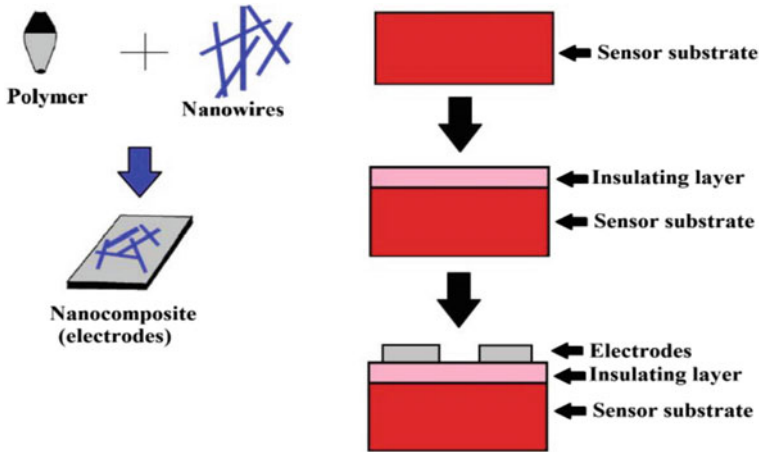


Fig. 16 Fabrication of a nanocomposite based sensor [36]

Table 1 Materials for flexible sensors

	PDM5 (Polydimethylsiloxane)	PET (Polyethylene terephthalate)	Polyimide
• Advantages	<ul style="list-style-type: none"> • Inert • Non-toxic • Non-flammable • Hydrophobic in nature 	<ul style="list-style-type: none"> • Cheap • Good chemical resistance • High resistance to temperature • High flexibility 	<ul style="list-style-type: none"> • High flexibility • Good chemical and thermal resistance • High mechanical toughness
• Disadvantages	<ul style="list-style-type: none"> • Difficult to integrate electrodes • Carry out deposition directly on its surface 	<ul style="list-style-type: none"> • Very susceptible to heat degradation • Poor impact strength 	<ul style="list-style-type: none"> • Expensive • Poor resistance to alkalis • Low impact strength
	CNTs	Graphene	Aluminum
• Advantages	<ul style="list-style-type: none"> • Better dispersion with the mixed polymer • Better compatibility • Higher flexibility 	<ul style="list-style-type: none"> • High surface-to-volume ratio • Excellent electrical conductivity • High carrier mobility and density • High thermal conductivity 	<ul style="list-style-type: none"> • Corrosion resistance • Strong at low temperatures
• Disadvantages	<ul style="list-style-type: none"> • Low purity • Low lifeline • Expensive growth process 	<ul style="list-style-type: none"> • Does not have a band gap • High quality graphene is expensive and complex process • Graphene exhibits some toxic qualities 	<ul style="list-style-type: none"> • Growth of oxide layer • More expensive than steel • Abrasive to tooling

sensor based on PDMS-embedded conductive fabric has also been investigated and are available in [41]. Flexible sensors can be fabricated for application in low-force environment as reported in [42]. The developed sensors is of tactile in nature and can be used in the robotic arms in an industrial environment [43]. Graphite and PDMS based Interdigital sensor to detect phosphate level in water has been reported in [44] where the measured data is uploaded in cloud. Laser induced flexible graphene sensor with interdigital pattern has been reported in [45]. Interdigital sensors for biomedical, environmental and industrial applications have been reviewed in [46], fabrication and characterization has been described in [47] and applications have been presented in [48] respectively.

9 Measurement System

The interdigital sensor is predominantly a capacitive sensor which is measured with the help of a simple circuit as shown in Fig. 17. An alternating excitation is applied across the sensor and the capacitance is measured with the help of voltage and current measurement. To measure the current flowing through the sensor a series resistance is connected. The resistance value should be very low with respect to the capacitive impedance of the sensor so that the effect of the series resistance is negligible. With the help of a microcontroller programming a desired frequency alternating signal can be generated. The applied voltage across the sensor as well as the voltage across the sensing resistance can be measured with the help of the same microcontroller. Both the magnitude and phase of the capacitive impedance are measured to determine the real and imaginary part of the impedance. The details of the circuit and measurement has been explained in step by step in [49] and some more information are available in [50–54]

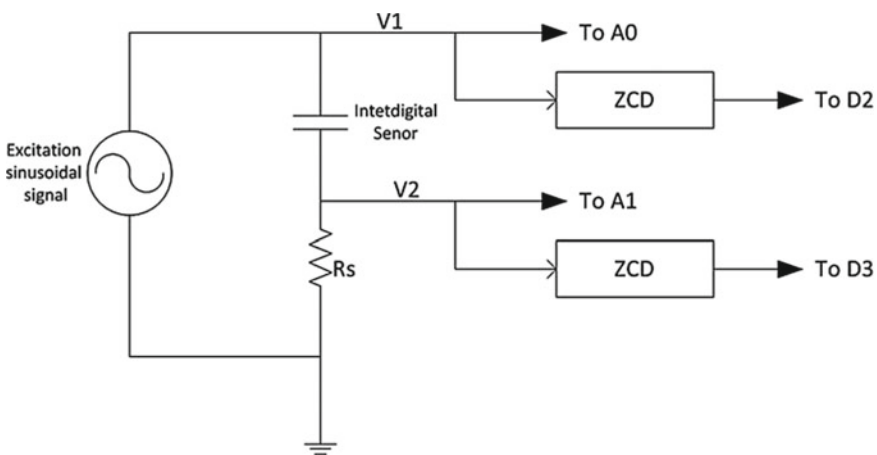


Fig. 17 Measurement circuit for interdigital sensor

10 Conclusions and Future Possibilities

Interdigital sensors are with us over a few decades and there are numerous applications of making use of it. The chapter has described a few applications over the last decade starting from a simple printed circuit based design to recent flexible materials based design. The sensitivity is enhanced by choice of design, materials, configurations, number of layers etc. The selectivity is entirely depended on the applications and can be achieved by providing a suitable layer on top of the sensor surface. Though molecular imprinted polymer based selective detection is very popular in recent times but there are challenges on functionalization, repeatability and re-usability as well as usage in portable applications. In recent times, there is an effort made to make use of it in implanted conditions and it is expected that it will deliver good results [55, 56].

References

1. S. Yamada, H. Fujiki, M. Iwahara, S.C. Mukhopadhyay, F.P. Dawson, Investigation of printed wiring board testing by using planar coil type ECT probe. *IEEE Trans. Magnet.* **33**(5), 3376–3378 (1997)
2. S.C. Mukhopadhyay, S. Yamada, M. Iwahara, Evaluation of near-surface material properties using planar type mesh coils with post-processing from neural network model. *Int. J. Stud. Appl. Electromag. Mech.* IOS Press **23**, 181–189 (2002)
3. S.C. Mukhopadhyay, S. Yamada, M. Iwahara, Inspection of electroplated materials—performance comparison with planar meander and mesh type magnetic sensor. *Int. J. Appl. Electromag. Mech.* **15**, 323–329 (2002)
4. S.C. Mukhopadhyay, Quality inspection of electroplated materials using planar type micro-magnetic sensors with post processing from neural network model. *IEE Proc.—Sci. Measure. Tech.* **149**(4), 165–171 (2002)
5. S.C. Mukhopadhyay, S. Yamada, M. Iwahara, Experimental determination of optimum coil pitch for a planar mesh type micro-magnetic sensor. *IEEE Trans. Mag.* **38**(5), 3380–3382 (2002)
6. S.C. Mukhopadhyay, A novel planar mesh type micro-electromagnetic sensor: part I—model formulation. *IEEE Sens. J.* **4**(3), 301–307 (2004)
7. S.C. Mukhopadhyay, A novel planar mesh type micro-electromagnetic sensor: part II—estimation of system properties. *IEEE Sens. J.* **4**(3), 308–312 (2004)
8. S.C. Mukhopadhyay, C.P. Gooneratne, G.S. Gupta, S. Yamada, Characterization and comparative evaluation of novel planar electromagnetic sensors. *IEEE Trans. Magnet.* **41**(10), 3658–3660 (2005)
9. S.C. Mukhopadhyay, Novel planar electromagnetic sensors: modeling and performance evaluation. *Sensors* **5**, 546–579. ISSN 1424-8220 ©2005 by MDPI <https://www.mdpi.org/sensors> (2005)
10. S.C. Mukhopadhyay, C.P. Gooneratne, A novel planar-type biosensor for noninvasive meat inspection. *IEEE Sens. J.* **7**(9), 1340–1346 (2007)
11. S.C. Mukhopadhyay, S.D. Choudhury, T. Allsop, V. Kasturi, G.E. Norris, Assessment of pelt quality in leather making using a novel non-invasive sensing approach. *J. Biochem. Biophys. Methods*, Elsevier, **JBBM70**, 809–815 (2008)
12. M.A.R. Syaifudin, K.P. Jayasundera, S.C. Mukhopadhyay, Initial investigation of using planar interdigital sensors for assessment of quality in seafood. *J. Sens.*, **9**. Article ID 150874 (2008).

- <https://doi.org/10.1155/2008/150874>, <https://www.hindawi.com/getarticle.aspx?doi=10.1155/2008/150874>
13. A.R.M. Syaifudin, K.P. Jayasundera, S.C. Mukhopadhyay, A low cost novel sensing system for detection of dangerous marine biotoxins in seafood. *Sens. Actuat. B Chem.* **137**, 67–75 (2009). <https://doi.org/10.1016/j.snb.2008.12.053>
 14. A.R.M. Syaifudin, S.C. Mukhopadhyay, P.L. Yu, Modelling and fabrication of optimum structure of novel interdigital sensors for food inspection. *Int. J. Numer. Model. Electron. Netw. Devices Fields* **25**(1), 64–81 (2012). Article first published online: 25 Apr 2011. <https://doi.org/10.1002/jnm.813>
 15. M.S.A. Rahman, S.C. Mukhopadhyay, P.L. Yu, C.H. Chuang, M. Haji-Sheikh, Measurements and performance evaluation of novel interdigital sensors for different chemicals related to food poisoning. *IEEE Sens. J.* **11**(11), 2957–2965 (2011)
 16. M.A. Yunus, S.C. Mukhopadhyay, Development of planar electromagnetic sensors for measurement and monitoring of environmental parameters. *Meas. Sci. Technol.* **22**, 025107 (9 pp.) (2011). <https://doi.org/10.1088/0957-0233/22/2/025107>
 17. M.A. Yunus, S.C. Mukhopadhyay, Novel planar electromagnetic sensors for detection of nitrates and contamination in natural water sources. *IEEE Sens. J.* **11**(6), 1440–1447 (2011)
 18. M.A. Yunus, S.C. Mukhopadhyay, S. Ibrahim, Planar electromagnetic sensors based estimation of nitrates contamination in water sources using independent component analysis. *IEEE Sens. J.* **12**(6), 2024–2033 (2012)
 19. A. Azmi, A.A. Azman, K.K. Kaman, S. Ibrahim, S.C. Mukhopadhyay, S.W. Nawawi, M.A.M. Yunus, Electromagnetic sensing array to detect water contamination. *IEEE Sens. J.* **17**(16), 5244–5251 (2017)
 20. M.S.A. Rahman, S.C. Mukhopadhyay, P.L. Yu, J. Goicoechea, I.R. Matias, C.P. Gooneratne, J. Kosel (2013) Detection of bacterial endotoxin in food: new planar interdigital sensors based approach. *J. Food Eng.* **114**, 346–360 (2013). <https://doi.org/10.1016/j.jfoodeng.2012.08.026>
 21. A.I. Zia, M.S.A. Rahman, S.C. Mukhopadhyay, P.-L. Yu, I.H. Al-Bahadly, C.P. Gooneratne, J. Kosel, T.-S. Liao, Technique for rapid detection of phthalates in water and beverages. *J. Food Eng.* **116**, 515–523 (2013)
 22. A.I. Zia, M.S.A. Rahman, S.C. Mukhopadhyay, P.-L. Yu, I.H. Al-Bahadly, C.P. Gooneratne, J. Kosel, Post annealing performance evaluation of printable interdigital capacitive sensors by principal component analysis. *IEEE Sens. J.* (2014) <https://doi.org/10.1109/JSEN.2014.2355224>
 23. A.I. Zia, S.C. Mukhopadhyay, P.-L. Yu, I.H. Al-Bahadly, C.P. Gooneratne, J. Kosel, Rapid and molecular selective electrochemical sensing of phthalates in aqueous solution. *Biosens. Bioelectron.* **67**, 342–349 (2015). <https://doi.org/10.1016/j.bios.2014.08.050>
 24. A. Nag, A.I. Zia, L. Xie, S.C. Mukhopadhyay, K. Jürgen, Novel sensing approach for LPG leakage detection: part I: operating mechanism and preliminary results. *IEEE Sens. J.* **16**(2), 996–1003 (2016)
 25. A. Nag, A.I. Zia, L. Xie, S.C. Mukhopadhyay, K. Jürgen, Novel sensing approach for LPG leakage detection: part II: effects of particle size, composition and coating layer thickness. *IEEE Sens. J.* **16**(2), 1088–1094 (2016)
 26. N. Afsarimanesh, A.I. Zia, S.C. Mukhopadhyay, M. Kruger, P.-L. Yu, J. Kosel, Z. Kovacs, Smart sensing system for the prognostic monitoring of bone health. *Sensors*, **MDPI****16**, 976 (2016) <https://doi.org/10.3390/s16070976>
 27. N. Afsarimanesh, S.C. Mukhopadhyay, M. Kruger, Biosensors for the measurement of C-terminal telopeptide of type I collagen (CTX-I). *J. Osteopor. Phys. Act.* **5**, 199 (2017). <https://doi.org/10.4172/2329-9509.1000199>
 28. N. Afsarimanesh, S.C. Mukhopadhyay, M. Kruger, Performance assessment of interdigital sensor for varied coating thicknesses to detect CTX-I. *IEEE Sens. J.* **18**(10), 3524–3531 (2018)
 29. N. Afsarimanesh, M.E.E. Alahi, S.C. Mukhopadhyay, M. Kruger, Development of IoT-based impedimetric biosensor for point-of-care monitoring of bone loss. *IEEE J. Emerg. Select. Topics Circuits Syst.* **8**(2), 211–220 (2018)

30. N. Afsarimanesh, S.C. Mukhopadhyay, M. Kruger, Molecularly imprinted polymer-based electrochemical biosensor for bone loss detection. *IEEE Trans. Biomed. Eng.* **65**(6), 1264–1271
31. M.E.E. Alahi, N. Pereira-Ishak, S.C. Mukhopadhyay, L. Burkitt, An internet-of-things enabled smart sensing system for nitrate monitoring. *IEEE Internet Things J.* **5**(6), 4409–4417 (2018)
32. M.E.E. Alahi, L. Xie, S. Mukhopadhyay, L. Burkitt, A temperature compensated smart nitrate-sensor for agricultural industry. *IEEE Trans. Ind. Electron.* **64**(9), 7333–7341 (2017)
33. M.E.E. Alahi, S.C. Mukhopadhyay, L. Burkitt, Imprinted polymer coated impedimetric nitrate sensor for real-time water quality monitoring. *Sens. Actuat. B* **259**, 753–761
34. M.E.E. Alahi, A. Nag, S.C. Mukhopadhyay, L. Burkitt, A temperature-compensated graphene sensor for nitrate monitoring in real-time application. *Sens. Actuat. A* **269**, 79–90 (2018)
35. A. Nag, S.C. Mukhopadhyay, K. Jürgen, Flexible carbon nanotube nanocomposite sensor for multiple physiological parameter monitoring. *Sens. Actuat. A* **251**, 148–155 (2016)
36. A. Nag, S.C. Mukhopadhyay, K. Jürgen, Tactile sensing from laser-ablated metallized PET films. *IEEE Sens. J.* **17**(1), 7–13 (2017)
37. A. Nag, N. Afsarimanesh, S. Feng, S.C. Mukhopadhyay, Strain induced graphite/PDMS sensors for biomedical applications. *Sens. Actuat. A* **271**, 257–269 (2018)
38. A. Nag, N. Afsarimanesh, S.C. Mukhopadhyay, Impedimetric microsensors for biomedical applications. *Curr Opin Biomed Eng* **9**, 1–7
39. A. Nag, A. Mitra, S.C. Mukhopadhyay, Graphene and its sensor-based applications: a review. *Sens. Actuat. A* **270**, 177–194 (2018)
40. A. Nag, S. Mukhopadhyay, Fabrication and implementation of printed sensors for taste sensing applications. *Sens. Actuat. A* **269**(1), 53–61 (2018)
41. A. Nag, B.V.B.R. Simorangkir, E. Valentin, T. Bjorninen, L. Ukkonen, M.R. Hashmi, S.C. Mukhopadhyay, A transparent strain sensor based on PDMS-embedded conductive fabric for wearable sensing applications. *IEEE Access* **6**, 71020–71027 (2018)
42. A. Nag, S. Feng, S.C. Mukhopadhyay, J. Kosel, D. Inglis, 3-D printed mould-based graphite/PDMS sensor for low force applications. *Sens. Actuat. A* **280**, 525–534 (2018)
43. A. Nag, B. Menzies, S.C. Mukhopadhyay, Performance analysis of flexible printed sensors for robotic arm applications. *Sens. Actuat. A* **276**, 226–236 (2018)
44. A. Nag, M.E.E. Alahi, S. Feng, S.C. Mukhopadhyay, IoT-based sensing system for phosphate detection using graphite/PDMS sensors. *Sens. Actuat. A* **286**, 43–50 (2019)
45. T. Han, A. Nag, R.B.V.B. Simorangkir, N. Afsarimanesh, H. Liu, S.C. Mukhopadhyay, Y. Xu, M. Zhadobov, R. Sauleau, Multifunctional flexible sensor based on laser-induced grapheme. *Sensors* **19**, 3477. <https://doi.org/10.3390/s19163477>
46. N. Afsarimanesh, A. Nag, E.E. Alahi, T. Han, S.C. Mukhopadhyay, Interdigital sensors: biomedical, environmental and industrial applications. *Sens. Actuat. A Phys.* **305**, 18 (2020). <https://doi.org/10.1016/j.sna.2020.111923>
47. A. Nag, S.C. Mukhopadhyay, Wearable flexible sensors: fabrication and characterization. <https://doi.org/10.1088/978-0-7503-1505-0ch1>, pp. 2-1 to 2-27, in *Wearable Sensors Applications, Design and Implementation*, ed. by S.C. Mukhopadhyay, T. Islam. ISBN 978-0-7503-1505-0 (ebook), ISBN 978-0-7503-1503-6 (print), ISBN 978-0-7503-1504-3 (mobi). <https://doi.org/10.1088/978-0-7503-1505-0> (2017)
48. T. Islam, S.C. Mukhopadhyay, Wearable sensors for physiological parameters measurement: physics, characteristics, design and applications, <https://doi.org/10.1088/978-0-7503-1505-0ch1>, pp. 1-1 to 1-31, in *Wearable Sensors Applications, Design and Implementation*, ed. by S.C. Mukhopadhyay, T. Islam. ISBN 978-0-7503-1505-0 (ebook), ISBN 978-0-7503-1503-6 (print), ISBN 978-0-7503-1504-3 (mobi). <https://doi.org/10.1088/978-0-7503-1505-0> (2017)
49. M.E.E. Alahi, A. Nag, N. Afsarimanesh, S.C. Mukhopadhyay J.K. Roy, “A simple embedded sensor: excitation and interfacing”, smart sensors, measurement and instrumentation, in *Advanced Interfacing Techniques for Sensors*, vol. 25, ed. B. George, J.K. Roy, V.J. Kumar, S.C. Mukhopadhyay (Springer, 2017), pp. 111–138. ISBN 978-3-319-55368-9
50. M.E.E. Alahi, X. Li, S.C. Mukhopadhyay, L. Burkitt, Application of practical nitrate sensor based on electrochemical impedance spectroscopy”, smart sensors, measurement and instrumentation, in *Sensors for Everyday Life: Environmental and Food Engineering*, vol. 23, ed. by

- S.C. Mukhopadhyay, O. Postolache, K.P. Jayasudnera, A. Swain (Springer, 2016), pp. 109–136. ISBN 978-3-319-47321-5
51. A. Nag, S.C. Mukhopadhyay, J. Kosel, Flexible printed sensors for ubiquitous human monitoring”, smart sensors, measurement and instrumentation, in *Sensors for Everyday Life: Healthcare Settings*, vol. 22, ed. by O. Postolache, S.C. Mukhopadhyay, K.P. Jayasudnera, A. Swain (Springer, 2016), pp. 135–158. ISBN 978-3-319-47318-5
 52. N. Afsarimanesh, S.C. Mukhopadhyay, M. Kruger, P. Yu, Sensing system for bone health monitoring, smart sensors, measurement and instrumentation, in *Sensors for Everyday Life: Healthcare Settings*, vol. 22 ed. by O. Postolache, S.C. Mukhopadhyay, K.P. Jayasudnera, A. Swain (Springer, 2016), pp. 23–44. ISBN 978-3-319-47318-5
 53. A.I. Zia, A.R.M. Syaifudin, S.C. Mukhopadhyay, P.L. Yu, I.H.A. Bahadly, C.P. Gooneratne, J. Kosel, T.-S. Liao, Electrochemical impedance spectroscopy based MEMS sensors for phthalates detection in water and juices, in *Proceedings of the 6th Vacuum and Surface Sciences Conference of Asia and Australia (VASSCAA-6) IOP Publishing, Journal of Physics: Conference Series*, vol. 439, pp. 012026 (12 pp.) (2013). <https://doi.org/10.1088/1742-6596/439/1/012026>
 54. X. Wang, Y. Wang, H. Leung, S.C. Mukhopadhyay, S. Chen, Y. Cui, A self-adaptive and wide-range conductivity measurement method based on planar interdigital electrode array. *IEEE Access* 173159–173165 (2019)
 55. V.A.S. Ramakrishna, U. Chamoli, G. Rajan, S.C. Mukhopadhyay, B.G. Prusty, A.D. Diwan, Smart orthopaedic implants: a targeted approach for continuous postoperative evaluation in the spine. *J. Biomech.*, Elsevier 109690 (7 pp) (2020)
 56. A. Nag, S.C. Mukhopadhyay, J. Kosel, Sensing system for salinity testing using laser-induced graphene sensor. *Sens. Actuat. A* **264**, 107–116 (2017)

Interdigital Proximity Sensor: Electrode Configuration, Interfacing, and An Application



Abhishek Ranjan, Bobby George, and S. C. Mukhopadhyay

Abstract Capacitive sensors are widely used for proximity applications ranging from touch-sensitive screens to sensors for classifying human proximity. It is a well-established field with contributions from many researchers. In this chapter, an interdigitated capacitive proximity sensor to address an unsolved problem of children from being left behind in hot cars. The sensor presented is integrated into the infant seat. It works by utilizing the large relative permittivity of the human body. The existing mechanisms utilize the weight of the child/infant or a mechanical switch under the seat to detect the presence and fail to meet the functionality requirements sufficiently. As the presented one is not relying on such parameters and it only requires the proximity, the overall reliability that can be achieved is high. The electrode structure, together with the measurement scheme utilizes the coupling and shielding effects of the electric field. The electrode structure is a combination of a planar two-electrode scheme and interdigitated electrodes. The chapter presents a brief note on the state of the art, a potential solution, and test results from a prototype developed and evaluated in a car.

1 Introduction

Sensors, although not explicitly seen, play important roles in our day-to-day lives. They help to improve our comfort and safety and have become an integral part of our lives. Examples include a simple temperature sensor for air-conditioned room to a

A. Ranjan
OLA Electric, Bangalore, India
e-mail: abhi.ranjan03@gmail.com

A. Ranjan · B. George (✉)
Department of Electrical Engineering, Indian Institute of Technology Madras, Chennai, India
e-mail: boby@ee.iitm.ac.in

S. C. Mukhopadhyay
School of Engineering and Advanced Technology, Macquarie University, Sydney, Australia
e-mail: S.C.Mukhopadhyay@massey.ac.nz

© The Editor(s) (if applicable) and The Author(s), under exclusive license to Springer Nature Switzerland AG 2021

S. C. Mukhopadhyay et al. (eds.), *Interdigital Sensors*, Smart Sensors, Measurement and Instrumentation 36, https://doi.org/10.1007/978-3-030-62684-6_2

car crash sensor initiating the deployment of airbags within a critical time frame. The sensors act as an extension of our five senses, playing important roles in improving the safety of various systems, e.g. fire detectors and alarms, rollover sensors and crash sensors in automotive systems, etc. In applications involving human safety, the reliability of the sensors cannot be compromised. Hence selection of the right sensing technique and the correct measurement approach is needed to design suitable sensors meeting the functionality, and reliability standards keeping the cost minimum. The focus of this chapter is on human proximity sensing for safety applications.

Capacitive sensors have their inherent advantages over other types of sensors like optical, inductive, or mechanical methods when it comes to human proximity [1, 2]. Most of the optical sensors are not well suited for the harsh environment. Inductive sensors are a good option but work only for objects that are either metallic (eddy current sensor) or magnetic (utilizing the permeability) in nature. On the other hand, if we use mechanical switches, they simply get activated with any force or pressure above a threshold and thus cannot be used to differentiate between humans and other objects. Moreover, mechanical switches require physical contact for activation, and the lifetime of such devices is limited to a certain number of cycles. For sensing human proximity, the relative permittivity or dielectric constant (≈ 80 , considering the water content) of the human body and the presence of distributed capacitance between the human body and ground can be exploited.

There are many sensors reported, to improve human safety, that work based on the relative permittivity. In [3], a capacitive seat occupancy system is discussed. Multiple capacitive electrodes are employed in the seat of a car to determine occupancy based on the change in the dielectric constant of the medium. This is used to enable or disable air-bag or deploy at lower power when an accident occurs. Force or weight-based sensors fail to work satisfactorily in such situations. A capacitive sensor to detect floating targets like humans close to the rear end of a truck is discussed in [4]. Capacitive sensors have also been used in conjunction with ultrasound sensors to extend range and reliability for assisted parking in cars [5]. A capacitive sensor reported in [6] is used to switch off a chain saw automatically, if a human body is detected close to the chain. Capacitive sensing approaches are also used to realize non-contact control of switches, by utilizing the proximity of the hand of the user [7]. The capacitive proximity sensing approach has also been utilized to determine three-dimension (3D) position sensing of object [8, 9].

Typical capacitive proximity sensors have two electrodes. The electrodes could be a planar arrangement of parallel plates as in Fig. 1a. It could also be circular with a center electrode surrounded by a planar ring. The value of the electric field lines will be relatively large close to the inner facing nearby edge regions of the electrodes A and B, in Fig. 1a. The values will be maximum when the electrodes are kept as close as possible without touching each other. The electric field with similar values can be made available almost throughout the sensor area if the interdigitated electrode structure is given in Fig. 1b can be employed. This is an advantage compared to the two-plate structure. As can be seen, the comb structure given in Fig. 1b ensures that the gap between the electrodes is small. This helps to get a large electric field across the sensor area. The width of the electrodes and the gap between them can be

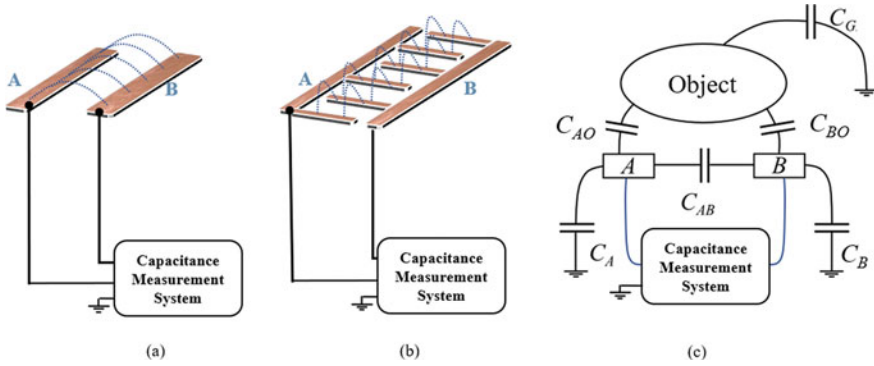


Fig. 1 Capacitive proximity sensors. A pictorial view of the electric field lines is shown for illustration purposes. (a) planar parallel plate arrangement, and (b) Interdigitated electrode structure. The electrical equivalent circuit, considering the lumped model, in the presence of an object, is shown in (c)

designed as per the need. This kind of structure is particularly useful if the object to be sensed is expected to be close to the electrodes in comparison with the distance between outer edges of A and B. These are not only used for proximity sensing but also used for insulation testing [10], and several other applications [11–14]. There is also a single electrode-based capacitive proximity sensor, suitable for grounded objects or objects capacitively coupled to the ground [15]. This is not illustrated here.

An electrical equivalent circuit of the capacitive proximity sensor, in the presence of an object, is shown in Fig. 1c. In this diagram, the object is considered to have much less impedance compared to the impedance of the capacitances shown. From the electrode A, there is a capacitance C_{AB} to electrode B, capacitance C_A to ground, and capacitance C_{AO} to the object. The object has a capacitance C_G to ground. Similar to the A, the electrode B has capacitance C_B to ground and C_{BO} to the object. A suitable measurement system can be used to measure the capacitance of interest [3, 16–19].

In this chapter, the application of an interdigitated capacitive proximity sensor is presented. It is about sensing of a child in the child/baby seat in a car. The details are presented below.

2 Child Left Behind the Problem and Reminder Technologies

There have been more than 700 incidents of child death (from 1998 to 2016) [20], reported in the U.S alone because they were left behind alone in parked cars during the daytime. An event that seems so not alarming to many people can prove to be fatal. Even on a normal day when the temperature is around 21 °C, the temperature

inside a parked car shoots up rapidly within a few minutes [21]. This has been rechecked by us monitoring change in temperature inside a car and comparing it with ambient temperature. To do this, two temperature sensors (IC LM35 from Texas Instruments [22]) were employed, one kept inside a car and another outside the car. The outputs from these were recorded using a data acquisition system (from Measurement Computing Corporation) and a computer. The car was initially brought from the shade and then parked in sunlight. The windows were kept closed for the first 20 min and then lowered down by 5 cm for the next 20 min (approx.). Later, all the windows were opened fully and the car was brought back to shade after 5 min. The outputs from both the temperature sensors were recorded throughout the whole period. The plot of the same given in Fig. 2 shows a steep rise in temperature. In the first 20 min, the temperature inside reached to about 50 °C from 34 °C ambient temperature.

Since the thermo-regulatory system of infants is underdeveloped, their body temperature rises three to five times faster compared to an adult [23]. This leads to hyperthermia, known as ‘heatstroke’ which proves to be fatal in many cases [24]. Parents usually forget their children in the car unintentionally. Sometimes it is merely because they want to let the child have an undisturbed sleep or just leave the child with an intent to come back within a few minutes. Unexpected changes in the daily routine of stressed-out parents can easily result in such situations. Analyzing the incidents and reasons behind shows that a large percentage of such cases occurred due to the negligence of parents/guardian leaving or forgetting their child in the car. Study shows that the reasons behind such circumstances are usually because parents/guardians tend to forget their children or left unattended inside the car [25].

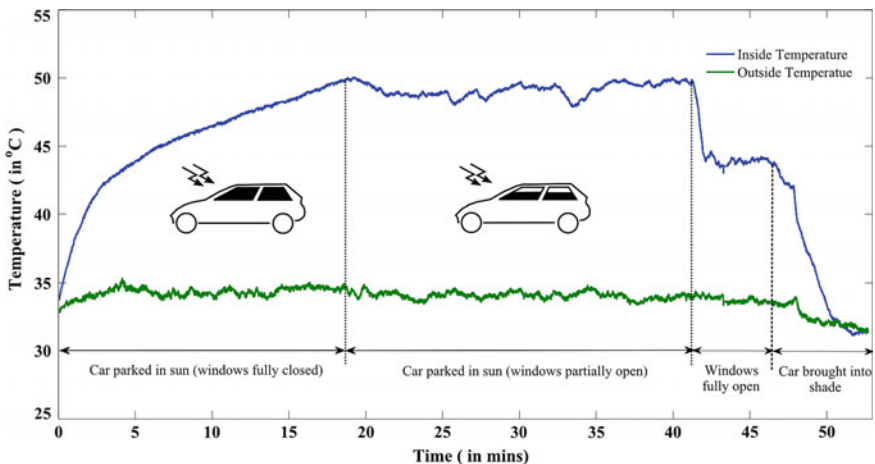


Fig. 2 Rise in temperature inside a car with respect to outside when parked in the sun. The variations in the measured temperature seen during the windows partially open are due to the breeze present during the test. This shows that partially lowering the windows will not help much in reducing the temperature inside

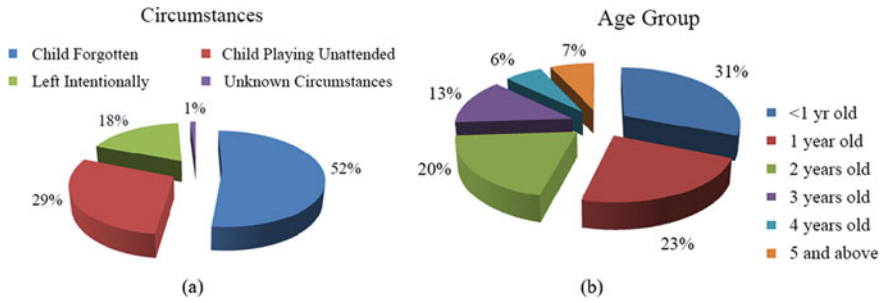


Fig. 3 **a** A pie chart showing reasons for children's death inside a parked car. **b** Age-wise distribution of incidents

Figure 3a [20] shows that around 81% of the incidents reported are due to the reasons mentioned above. In terms of the age group, children below 2 years old are most vulnerable to such mishaps, as seen clearly in Fig. 3b [7].

A study conducted by the National Highway Traffic Safety Administration (N.H.T.S.A) [26], U.S. Department of Transportation, assessed the performance of all the products designed to prevent children from being left behind in parked cars. A total of 18 different technologies were identified for child reminder. Out of these, seven were based on pressure or force sensors, four were mechanical switch-based (on buckle or door) detectors, while five others didn't have any sensing capabilities. The remaining two devices were integrated with the vehicle. A mechanical switch on the child seat buckle does not guarantee a child's presence and thus may initiate a false alarm. While the vehicle integrated system is possible only if the particular car models having the system installed are bought. Pressure or force-based technologies reviewed by NHTSA also proved inconsistent and unreliable performance. The devices required frequent adjustment of child/dummy in the seat for activation.

A system to detect the presence of a child based on a combination of an optical detector, mechanical switch and temperature sensor has been reported in [27]. Optical or thermal sensors are not well suited for this as it may not detect when a child is wrapped in a blanket or clothes. An electric field sensor to detect infants sitting in a rearward position in an infant seat in a car has been reported in [28]. A capacitive seat occupancy detection system (for adult passengers) that provides occupancy information to an airbag control unit has been reported in [3]. In these schemes, sensing electrodes are placed in the car seat as it is to detect adult occupancy. The thickness of the infant seat available in the market is not fixed. Thus, the distance between the child and electrodes in a car seat can be between 5 and 12 cm (depending on the manufacturer). Thus, it is difficult to sense the presence of a child using these sensors, reliably. Also, such capacitive/electric field systems are not available in all the cars and usually, if available, it is not installed in back seats of cars where the child seat is placed, and the probability of forgetting a child is high. A weighing-based child detector has been developed by NASA's Langley Research Center [29]. Such weight-based sensors may detect water or milk bottles, filled thermo-flask or bag,

toy, etc. (or any combination of such items) as a child and activate an (unwanted) alarm. There is news, reported recently that Tesla is planning to develop a suitable sensor using millimeter wave technology [30]. It will require special approval from regulatory agencies to use this technology inside the car.

Timely detection of a child left behind in a car (child seat) can help to initiate immediate action and avoid a tragedy. As per the study conducted by NHTSA, the existing sensors in the market fail to meet multiple criteria required for a child occupant sensor. In this chapter, a capacitive proximity sensing scheme that uses variation in distributed capacitance and permittivity of the human (child) body is presented. Special electrode structures and measurement techniques are required to achieve reliable functionality. Sensing the presence along with position and hence the active state of the occupant is some of the desirable features of the sensor.

3 Interdigitated Capacitive Proximity Sensor for Occupancy Detection in Child Seat

A capacitive proximity-based child presence detection system is illustrated in Fig. 4. As can be seen, the capacitive sensor employs an interdigitated structure. Additionally, it has two outer electrodes to capture more information. It has a child presence detector and a warning system [31]. The sensor and the measurement and control unit (MCU) can be together in the final packaging. The MCU has a Capacitance-to-Digital Converter (CDC) whose input terminals p, q, r, and s are connected to the capacitive sensor. The output of the CDC is given to a controller in the MCU. The MCU also has a temperature sensor, and it takes input from the engine control unit about the ON or OFF status of the vehicle. As soon as the MCU notes that the engine is turned off from a turned-on condition, it instructs the CDC to measure the capacitance. If the controller finds, using an algorithm, that a child is present in the infant seat, it makes an audible alarm without any delay. This process repeats for every 1 min, and the volume of the alarm increases every min until the child is removed from the infant seat by the parents or other responsible people. If the child is not taken from the infant seat even 7 min (a time that can be preset) after the engine has been turned off, the controller turns ON the GSM modem and dials to the pre-entered phone number of the driver. In case of no response from the driver, it will dial to the parents. And, if still no response it will dial to a help/emergency number (say 911) and pass a preloaded message. This message will contain the vehicle number, address and phone number of the immediate person to be contacted, the temperature inside the car, etc. to take appropriate action by the authorities. The system could be equipped with a GPS unit if required to provide the location information. The system is programmed in such a way that the phone numbers can be easily loaded into the unit and can be modified. Similarly, the time at which the unit initiates an audible alarm and dialing a phone number can be adjusted depending on the preference of the users. Test results from this system, for different scenarios, are presented in [31]. Test

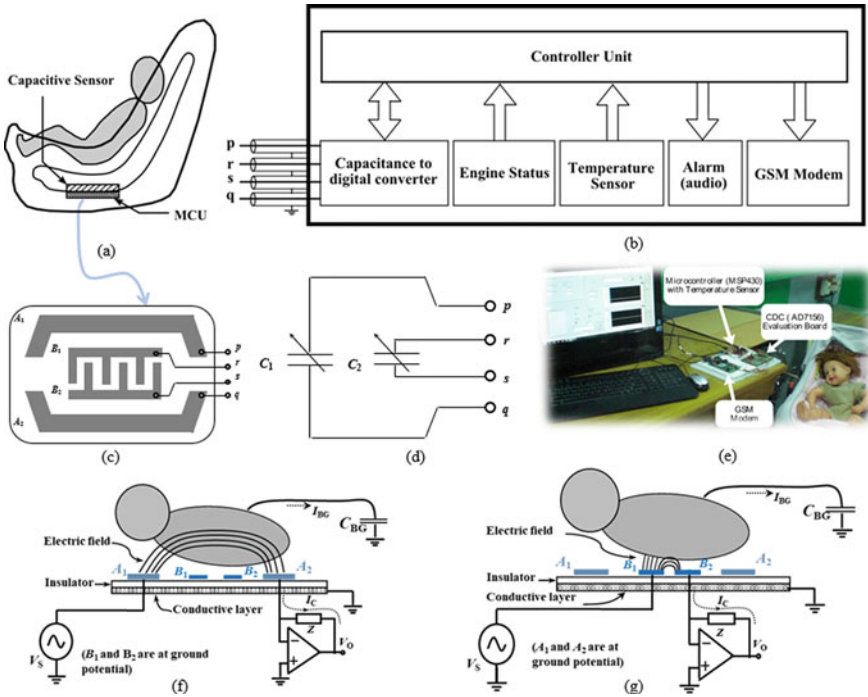


Fig. 4 Interdigitated capacitive proximity sensor for a child seat. **a** Diagram of the seat with a sensor. **b** The measurement and control unit, **c** sensor electrode structure, **d** Simplified electrical equivalent circuit, **e** photograph of the experimental set-up with a dummy baby filled with water. The prototype sensor is integrated into the seat. Measurements using electrodes A_1 – A_2 and B_1 – B_2 are illustrated in **f** and **g** respectively. More details are available in [31]

results showed that the presence of a child in an infant seat can be reliably detected and suitable warning signal can be generated to save the child.

4 Modified System

Although the above-mentioned system serves the required functionality, it is beneficial to get an idea about the position and change in the positions or activeness and if possible, even the respiration rate of the child. To sense position along with occupancy, the electrode pattern adopted earlier was altered. The two outer electrodes p and q were split into two each. Electrode p was split into p and p' while q formed q and q' . The new electrode configuration as shown in Fig. 5 gives more sensing capacitors which can be measured to determine occupancy as well as position (like left, right, center, backward or forward) of the child. The sensing capacitances can be measured using a synchronous demodulation technique [16] as indicated in Fig. 6.

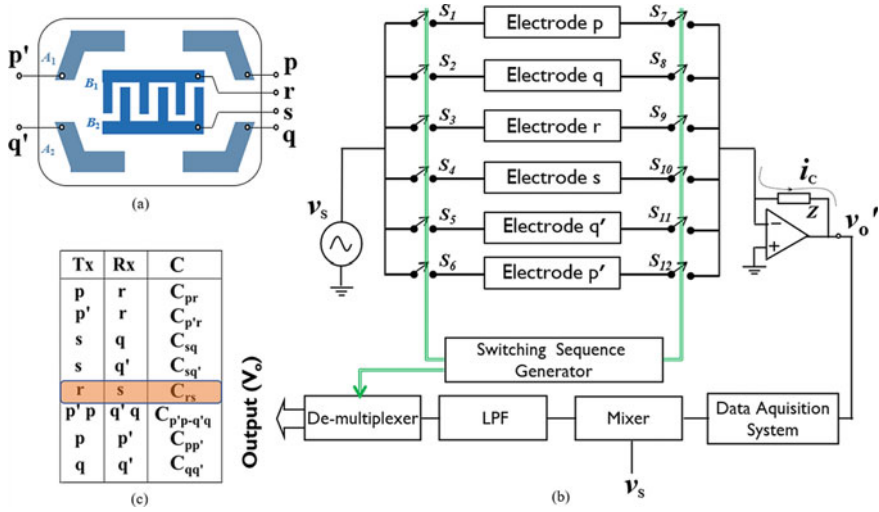


Fig. 5 Interdigitated capacitive proximity sensor with additional outer electrodes. **a** Electrode structure, **b** Measurement circuit, **c** Nodes connected to the measurement system through the switches, and the corresponding capacitance being measured

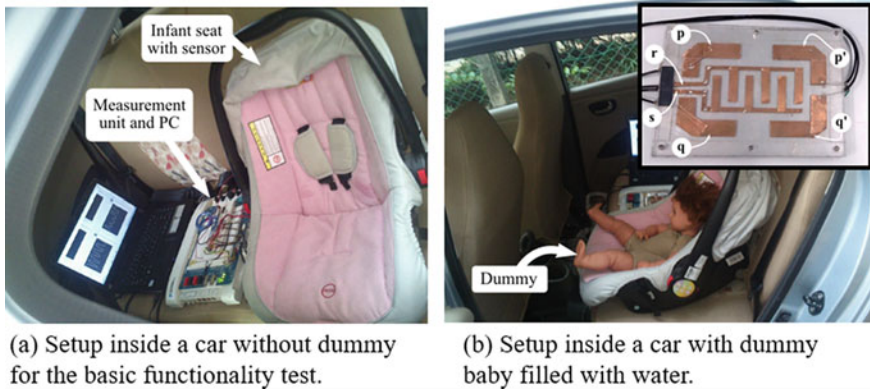


Fig. 6 Testing the system inside a car with the dummy baby. The fabricated and packaged sensor structure is visible in the inset of (b)

In this scheme, multiple switches are employed to measure one sensing capacitor at a time. Switches S_1 to S_6 connects electrode terminals to the source thereby act as a transmitter electrode (T_x). While S_7 to S_{12} connects electrode terminals to a current-to-voltage converter and works as a receiver (R_x). For instance, if we need to measure the value of capacitor C_{rs} between electrodes r and s, only the switch S_3 and S_{10} will be closed. By closing switch S_3 , electrode r is connected to excitation source V_S whereas S_{10} makes s electrode to serve as receiver node. The current I_C reaching

terminal s flows through the feedback impedance (Z) connected between the output and inverting terminal of the op-amp. The op-amp output voltage v_o' , being directly proportional to C_{rs} can be used to measure the change in this capacitance. Similarly, by controlling the switches in a fixed sequence repetitively, all the fifteen possible capacitors (between any two electrodes) can be measured. The signal acquired, first goes through a Phase Sensitive Detector (PSD) and then averaged using a moving average filter with a window size of 16 samples. The purpose of using a PSD was to correctly retrieve the amplitude of the signal of interest (i. e. 10 kHz sinusoidal wave) at the output, even in the presence of noise.

The modified version of the sensor configuration and measurement system was tested using a dummy, which is filled with water to emulate a baby, in various positions. Though there are fifteen combinations possible with the new electrode pattern, this study was restricted to eight of them. This selection was determined based on initial tests conducted in the laboratory with the sensor unit. The sensing capacitors which showed very low relative change with the dummy child were discarded in further study. Finally, only eight out of fifteen were considered. These capacitances are C_{pr} , $C_{p'r}$, C_{sq} , $C_{sq'}$, C_{rs} , $C_{p'p-q'q}$, $C_{pp'}$, and $C_{qq'}$ as marked in the table in Fig. 5.

Figure 6 shows the test setup inside a car. The changes in output obtained due to change in the eight capacitors when the dummy was placed in different positions in the car seat are given in Fig. 7. Further tests were carried out in three phases. At first, the system was tested in a car with a dummy for special conditions like (a) the engine turned ON and then OFF, (b) when an adult touches the dummy. As expected, changes were observed in all the eight sensing capacitors when the dummy was placed in the child car seat. Some of them showed an increase while in the case of others there was decrease in output voltage due to the reasons discussed. This shielding and coupling effects are expected as per the electrode geometry [3, 31]. When the dummy was touched, by an adult, the output for each capacitor showed a dip in their values due to a decrease in the current received by the electrode (Rx). When an adult touches, the

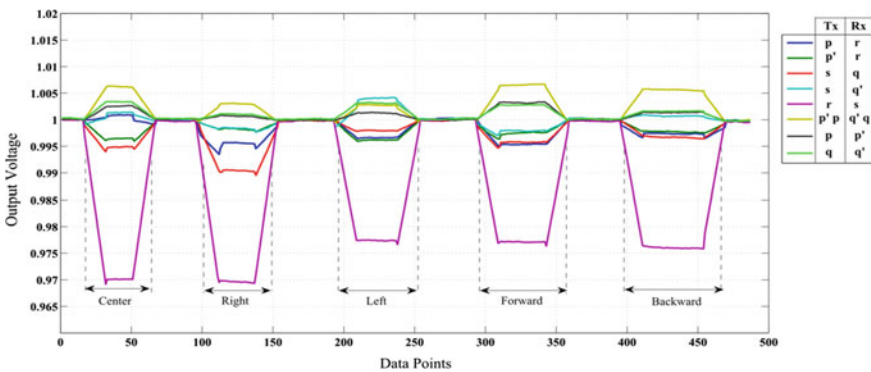


Fig. 7 Test results using the prototype sensor in different positions of the dummy baby in the infant seat. Output in a vacant case is taken as unity. T_x and R_x represent the transmitter and receiver electrodes involved in the particular set of measurements

capacitance between the body of the child and ground increases providing increases in shielding effect. The change while touching was noted to be approximately the same whether being touched from inside or outside the car. Turning the car ON or OFF did not reflect any change in any of the capacitance values.

Figure 7 shows the output in different positions of the dummy such as center, left, right, forward, and backward. Changes in sensing capacitors C_{rs} and $C_{p'p-q'q}$ were found to be sufficient to detect the presence of a child using a simple threshold-based algorithm. There were significant changes in the other six capacitors values C_{pr} , $C_{p'r}$, C_{sq} , $C_{sq'}$, $C_{pp'}$, and $C_{qq'}$. The change in these capacitors was observed to be sensitive to even slight displacement in position. To quantify the activity (change in position), from the data observed, a more complex algorithm than a threshold based one is required. Based on the studies, it is observed that the breathing rate of the child cannot be sensed reliably using the system developed. This is because the change in distributed capacitance and hence the change in shielding is very small when a child inhales or exhales air. This in combination with other movements of the baby, makes it difficult to sense the breath rate. It could be possible by improving the sensitivity of the system, further, and by developing efficient algorithms. As mentioned above, the results from the developed system clearly showed that the detection of the presence of the baby in the infant seat and activities (change in position) are possible with high reliability, aiding to solve the 'child-left-behind' problem in a car.

5 Conclusions

A simple, effective, and low-cost solution for the 'child-left-behind' problem in a car is presented in this chapter. The system is built around a capacitive proximity sensor using an interdigitated electrode structure, to detect the presence of a child in an infant seat. It was found based on the tests conducted using the prototype system that the presence of a child and an active or non-active status of the child can be detected. Interdigitated capacitive sensors are used in several applications, and this is one of such applications. The system required to measure from the sensor could be any typical capacitance measurement system for the specified range, sensitivity, and signal to noise ratio. In certain applications, the frequency of excitation needs to be carefully selected depending on the properties of the dielectric medium and required bandwidth of the measurement system.

References

1. J. Lenz, A review of magnetic sensors. *Proc. IEEE* **78**(6), 973–989 (1990)
2. S. Tumanski, Induction coil sensors—a review. *Meas. Sci. Technol.* **18**(3), R31 (2007)
3. B. George, H. Zangl, T. Bretterkieber, G. Brasseur, A Novel Seat Occupancy Detection System Based on Capacitive Sensing. 2008 IEEE Instrumentation and Measurement Technology Conference, British Columbia, Canada, 1515–1519 (2008)
4. S. Nihtianov, G. Meijer, Application challenges of capacitive sensors with floating targets, in *AFRICON* (2011), pp. 1–6
5. T. Schlegl, T. Bretterkieber, M. Neumayer, H. Zangl, Combined capacitive and ultrasonic distance measurement for automotive applications. *Sens. J., IEEE* **11**(11), 2636–2642 (2011)
6. B. George, H. Zangl, T. Bretterkieber, A warning system for chainsaw personal safety based on capacitive sensing, in *Sensors* (IEEE, 2008), pp. 419–422
7. P. Buttolo, S.C. Salter, M.S. Dassanayake, I.J.S. Rankin, D. Ghosh, Ford global technologies LLC (2017). Proximity sensor assembly having interleaved electrode configuration. U.S. Patent 9,548,733
8. J. Ferri, R. Llinares Llopis, G. Martinez, J.V. Lidon Roger, E. Garcia-Breijo, Comparison of E-textile techniques and materials for 3D gesture sensor with boosted electrode design. *Sensors* **20**(8), 2369 (2020)
9. R. Aubauer, A. Dorfner, Microchip technology Germany GmbH, 2020. Electrode arrangement for gesture detection and tracking. U.S. Patent 10,649,488
10. R.H. Bhuiyan, R.A. Dougal, M. Ali, Proximity coupled interdigitated sensors to detect insulation damage in power system cables. *IEEE Sens. J.* **7**(12), 1589–1596 (2007)
11. P. Chen, Q. Yu, Proximity capacitance array sensor based on data aggregation strategy for rainfall detection. *Sens. Mater.* **30**(5), 957–977
12. J. Döring, L. Tharmakularajah, J. Happel, K.L. Krieger, A novel approach for road surface wetness detection with planar capacitive sensors. *J. Sens. Sens. Syst.* **8**(1), 57–66
13. V. Kasturi, S.C. Mukhopadhyay, Planar interdigital sensors based looseness estimation of leather, in *2008 3rd International Conference on Sensing Technology* (2008), pp. 462–466
14. A. Nag, S.C. Mukhopadhyay, J. Kosel, Sensing system for salinity testing using laser-induced graphene sensors. *Sens. Actuators A: Phys.* **264**, 107–116 (2017)
15. C. Baby, B. George, A simple analog front-end circuit for grounded capacitive sensors with offset capacitance, in *2013 IEEE International Instrumentation and Measurement Technology Conference (I2MTC)* (2013), pp. 1372–1375
16. R. Pallas-Areny, J. G. Webster, “Sensors and signal conditioning”, John Wiley & Sons; Nov. 2012.
17. R. Abhishek, B. George, A new capacitance-to-digital convertor suitable for human proximity sensing, in *Proceedings of 19th IMEKO TC-4 Symposium Measurements of Electrical Quantities* (Barcelona, Spain, 2013), pp. 250–254. Accessed 16–18 July 2013
18. V. Prashanth, B. George, A direct digital readout circuit for impedance sensors. *IEEE Trans. Instrum. Meas.* **64**(4), 902–912 (2015)
19. L. Areekath, B. George, F. Reverter, An extended study on an interference-insensitive switched capacitor CDC. *IEEE Sens. J.* **19**(18), 8283–8292. Accessed 15 Sept 2019
20. Pediatric Vehicular Heatstroke Fact Sheet [online]. https://www.noheatstroke.org/fact_sheet.pdf. Accessed 06 Sept 2020
21. C. McLaren, J. Null, J. Quinn, Heat stress from enclosed vehicles: moderate ambient temperatures cause a significant temperature rise in enclosed vehicles. *Pediatrics* **116**(1), 109–112 (2005)
22. Datasheet, LM35 precision centigrade temperature sensors, Texas Instruments (1999) [Online]. <https://www.ti.com/lit/ds/symlink/lm35.pdf>. Accessed 06 Sept 2020
23. K. Tsuzuki-Hayakawa, Y. Tochihara, T. Ohnaka, Thermoregulation during heat exposure of young children compared to their mothers. *Eur. J. Appl. Physiol.* **72**(1–2), 12–17 (1995)

24. J. Booth, G. Davis, J. Waterbor, G. McGwin, Hyperthermia deaths among children in parked vehicles: an analysis of 231 fatalities in the united states, 1999 to 2007. *Forensic Sci., Med., Pathol.* **6**, 99–105 (2010). [Online]. <https://doi.org/10.1007/s12024-010-9149-x>. Accessed 06 Sept 2020
25. A. Guard, S.S. Gallagher, Heat related deaths to young children in parked cars: an analysis of 171 fatalities in the united states, 1995–2002. *Inj. Prev.* **11**(1), 33–37 (2005)
26. N.H.T.S.A., Reducing the potential for heatstroke to children in parked motor vehicles: Evaluation of reminder technology. [Online]. www.nhtsa.gov/DOT/NHTSA/NVS/811632.pdf. Accessed 06 Sept 2020
27. M. Rossi, Warning system for detecting presence of a child in an infant seat. US Patent 5 949 340. Accessed 7 Sept 1999
28. J. Smith, Electric field imaging. Ph.D. Dissertation, Massachusetts Institute of Technology (1998)
29. C. Rink, M. Braukus, Nasa develops child car seat safety device. Internet. <https://www.nasa.gov/centers/langley/news/releases/2002/02-008.html>. 5 Feb 2002. Accessed 06 Sept 2020
30. News, Tesla is working on a sensor that can detect a child left behind in a hot car. [online]. <https://www.theverge.com/2020/8/20/21377981/tesla-radar-sensor-child-hot-car-fcc>. Accessed 06 Sept 2020
31. R. Abhishek, B. George, A child-left-behind warning system based on capacitive sensing principle, in *2013 IEEE International Instrumentation and Measurement Technology Conference (I2MTC)*, pp. 702–706 (2013)

Fabrication of Interdigitated Sensors: Issues and Resolution



Anindya Nag, S. C. Mukhopadhyay, and C. P. Gooneratne

Abstract The design and implementation of interdigital sensors in the sensing world have been pivotal in the last few decades. Due to the advantages imparted by these designs, researchers all over the world have practiced developing prototypes based on them. The variation in the physical and material specificities of the interdigital sensors varies with their individual applications. In order to develop a range of sensing prototypes for biomedical, industrial and environmental applications, the optimization of the fabrication of these interdigitated electrodes has been done over the years. This chapter highlights some of the research works done on their design, development and implementation, based on a range of fabrication processes. Some of the issues faced by each of these fabrication techniques, as well as the formed prototypes, have also been discussed in the chapter. Finally, some of the possible remedies to address the existing issues have been elucidated, along with a brief market survey that has been mentioned at the end of the chapter.

1 Introduction

The exponential growth in the use of sensing technology for ubiquitous monitoring of daily activities has been state-of-the-art in recent years. Since the dawn of laboratory-developed sensors, scientists have frequently been trying to include new kinds of applications for the sensors. With this, the range of uses of the research-based sensors has been growing every day. The development parameters for a particular type of sensor is dependent on a lot of factors, including its application, the environment

A. Nag (✉)

Computer, Electrical and Mathematical Science and Engineering, King Abdullah University of Science and Technology, Thuwal, Saudi Arabia

e-mail: anindya1991@gmail.com

S. C. Mukhopadhyay

School of Engineering, Macquarie University, Sydney, Australia

C. P. Gooneratne

Saudi Aramco, Darham, Saudi Arabia

© The Editor(s) (if applicable) and The Author(s), under exclusive license to Springer Nature Switzerland AG 2021

S. C. Mukhopadhyay et al. (eds.), *Interdigital Sensors*, Smart Sensors, Measurement and Instrumentation 36, https://doi.org/10.1007/978-3-030-62684-6_3

it will be deployed in and the signal-conditioning circuit it will be embedded to [1, 2]. Among these factors, the application of sensors is the most important one as it decides the processed materials, structure, design and dimensions of the sensors and the fabrication technique. Keeping all these factors into consideration, the structural design has been one specification that the researchers did not focus much in the past years [3–5]. When the application of a sensor is chosen, its dimensions and fabrication technique are two things that get sorted out [6, 7]. Depending on the availability of the electrical support and facilities for the regulation of the generated heat, the decision for the designs of the electrodes is made.

Different kinds of microelectromechanical (MEMS)-based and flexible sensors are being developed every year, which are most suitable to be operated for the laboratory-controlled environment [8, 9]. Although the MEMS-based sensors imparted certain advantages like miniaturization, a quick multiplicity of the sensors, low power consumption, high sensitivity, concept of microelectronics and easy integration into systems, there were specific disadvantages associated to them which need an alternation. Some of the associated disadvantages are high production cost per unit, which requires upfront expensive cleanroom facilities, expensive equipment required for characterization and testing the performance. Another major factor leading to the formation of flexible sensors is the rigidity and intransigency shown by the MEMS sensors towards biomedical applications. The attributes for forming flexible sensors were more precise in comparison to the MEMS-based sensors due to their enhanced electrical, mechanical and thermal characteristics. Also, the wearable nature of the sensors has been a major attribute that approved the development and utilization of flexible sensors [10]. Figure 1 [11] shows some of the printing techniques that are

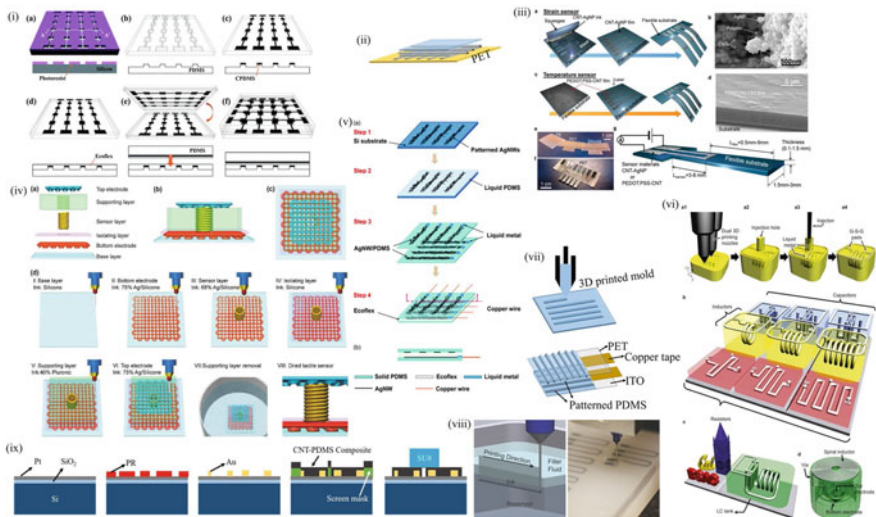


Fig. 1 Representation of some of the printing techniques that are used to develop flexible sensing prototypes [11]

Table 1 Comparison of some of the techniques that have been used to develop interdigital sensors in MEMS and flexible sensors

MEMS sensors	Flexible sensors
• Semiconductor device fabrication technique	• Laser-cutting
• Surface Micromachining	• Micro-contrast printing
• Bulk micromachining	• Ink-jet printing
• Deep reactive ion etching	• Nano-imprinting
• Laser micromachining	• Screen printings
• Electro-discharge micromachining	• Slot-die printing
• Hot embossing	• Dry transfer printing
• Micromachining	• Gravure printing
• XeF ₂ dry phase etching	• Offset printing
• LIGA	• Flexography printing

currently used for developing flexible sensors. The existing fabrication techniques had to be optimized, along with the origination of new fabrication techniques, to overcome the issues faced by the developed prototypes for a particular application. Table 1 shows a comparison of some of the popular techniques that have been utilized so far for developing MEMS and flexible sensors-based interdigitated electrodes. It is seen from the table that a lot of methods have been utilized so far, which have been far enough to develop prototypes with varied efficiency in terms of sensitivity, repeatability, specificity, stability, robustness and longevity [12]. The uses of each of these techniques were based on the application for which the fabricated interdigitated sensors were used.

Even though the methods mentioned in Table 1 had been enough, there are still changes need in them, especially in the current era of nanotechnology. With further miniaturization of the sensors to increase their sensitivity and specificity towards the target analyte, these existing techniques have to be improved. A thorough review has not yet been done on the existing techniques, their advantages and challenges. Each of the fabrication methodologies that have been used to develop interdigitated sensors has not analyzed based on the quality of the formed prototypes. This chapter deals with the issues faced by the fabrication techniques during the development and implementation of interdigital sensors for different applications. The work has been separately classified based on the techniques that have been used to form the MEMS and flexible sensors. This categorization would help the readers to understand the attributes imparted in each type of sensor when fabricated using a particular technique.

Resistive, capacitive and inductive are the three types in which the sensing prototypes can be operated. Nowadays, most of the academic and industry-based works are done with a combination of two or more ways [13–15]. The researchers and engineers are constantly trying to optimize the sensing systems based on the combination of these operating principles to decrease the fabrication cost while maintaining the

robustness and efficiency of their performances. In order to develop the sensors operating on these three types, the design of the electrodes has been largely varied [16–18]. The most popular of them being the interdigital electrodes, which operate on capacitive sensing. These types of electrodes have been formed since the 1970s [19–21] when the idea of capacitive sensing was getting popularized among the researchers who were working on a related field. In the 1990s, when the semiconductor sensors were being developed on an industrial scale [22–24], interdigital sensing faced its most popular phase due to the growing interest in capacitive sensing. As this gave rise to MEMS and flexible sensing systems, interdigitated capacitive sensors started to be used as point-of-care devices for a range of applications [25, 26]. Some of the specific advantages of using interdigitated sensing are:

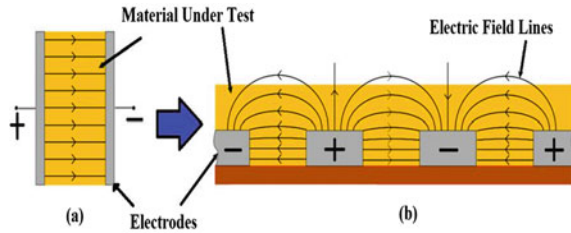
- They provide a non-invasive measurement technique to determine the dielectric properties of the insulating and semi-insulating materials.
- The prototypes are generally small in size and have a relatively low cost in nature.
- Due to the one-sided measurement, the fringing electric fields can be used to determine the characteristics of the material under test.
- The parameters of the interdigital sensors can be varied to optimize their performances and power density.
- These sensors can be operated at low frequencies, thus achieving lesser attenuations.

Interdigital sensors were then started to be operated alongside resistive and inductive sensing to have a combined effect on the detection of the target analyte. The design and development of these interdigital sensors using the above-mentioned techniques have been done substantially over these years [27–29]. But there are still some loopholes that can be addressed, analyzed and rectified for the formed interdigital sensors. This chapter deals with such bottlenecks related to each of the above-mentioned fabrication techniques. The explanation has been done in terms of some of the significant research works done by the researchers working in disparate sensing fields.

2 Working Mechanism of Interdigital Sensors

Before heading into the implementation of interdigital electrodes, it is important to understand their operating principle. Interdigital electrodes operate on the principle of the parallel-plate capacitor. Figure 2 [30] shows the schematic diagram of the modification of a parallel-plate capacitor to its co-planar form. The planar form of the electrodes assists in the non-invasive and one-sided measurements. The opposite side of the electrodes, known as the guard plane, is generally sputtered with an insulating material to restrict the direction of the generated electric field to one side. The two electrodes, in common nomenclature, are referred to as the excitation and sensing electrodes. When a time-dependent low amplitude voltage signal is given as an input, the electric field is generated between two electrode fingers of opposite

Fig. 2 Schematic diagram of the conversion of the parallel-plate capacitor to the co-planar interdigital sensor [30]



polarity. Since the intensity of the generated electric field is low due to the low voltage signal, the number of electrodes is generally repeated to have a stronger resultant electric field. The distance between two consecutive electrode fingers is known as the interdigital distance (d). Due to the planar structure of the electrodes, the electric field bulges between the electrodes. If any material with dielectric properties is kept in contact or in proximity to the generated electric field, the generated electric field penetrates the tested material while traveling between the electrodes. The height of the penetration depth of this generated electric field can be varied by varying the distance between the electrode fingers. This property is called in the pitch, which can be defined as the distance between two electrodes of similar polarity [31, 32].

The performance of the interdigital sensors depends on certain parameters, including fringing fields and their signal strength, interdigital distance, pitch and overall size of the sensing area. The optimization of these factors helps in the detection of the material properties of the sample with high sensitivity. Researchers have done simulations using 3D finite element models (FEM) [33, 34] to design the sensor geometry to obtain the required penetration depth of the electric field by studying the necessary passive electrical parameters. The resultant capacitances are calculated as a function of the number of electrode fingers and the ratio of the width and interdigital distance of the fingers [35, 36]. Parametric equations are formed to obtain the capacitance of the sensors as a function of the mentioned geometric parameters of the sensors. Figure 3 [35] shows the schematic diagram of the interdigital sensor that was used to perform the calculations related to the parametric equations. The calculations were done based on both the presence and absence of the metal as a backplane to the interdigitated electrodes.

The utilization of these sensors has been widely done for different healthcare [37, 38], industrial [39–41] and environmental [42–44] applications. For electrochemical sensing, the measurements have been done on the basis of the detection of the change in impedance and current using spectroscopic [45–47] and voltammetry [48–50] techniques. For strain and electrical sensing, the change in the conductance is mostly studied [51–53] with respect to the changes in the input conditions.

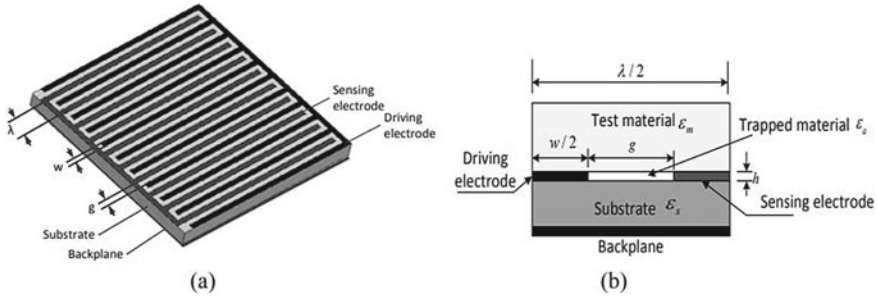


Fig. 3 Schematic representations of the **a** perspective and **b** cross-sectional views of the coplanar interdigital capacitive sensor [35]

3 Case Studies with Different Research Works

A lot of research work had been done regarding the fabrication and implementation of interdigital electrodes among MEMS and flexible sensors. The development of each of these prototypes has been done with a specific fabrication technique, which helps in achieving the physical attributes required for a specific application. Among the fabrication methodologies that been mentioned in Table 1, a few of the most significant ones have been chosen in the succeeding sub-sections. These techniques have been selected based on their significance in the field of microelectronics, where their frequent utilization has been done to develop MEMS and flexible sensors. These techniques have developed sensors with optimized physio-chemical properties. The explanation related to all of the techniques initially includes the development and implementation of the sensors, followed by the issues that need to be addressed.

3.1 MEMS Sensors with Interdigital Electrodes

With the initial growth of semiconductor sensors, MEMS has been a standardized technique for mass production of commercial sensors. Sensors with silicon substrates have been largely preferred due to their stability in the responses, high accuracy in the readings, low drift in the response due to ambient temperature and humidity, excellent signal-to-noise ratio, low hysteresis, high robustness and high repeatability in the responses [54, 55]. In order to process the raw silicon for using them as substrates in the MEMS-based sensors, scientists have chosen a few methods like surface micromachining, bulk micromachining and LIGA (lithography, electroplating and molding), due to their advantages like the formation of sensors with high aspect ratios, the formation of single-crystal devices with excellent mechanical properties and high reliability [56–58]. Among them, the most common one related to the fabrication of interdigital sensors is the semiconductor device fabrication technique.

The exponential growth related to its use is related to the highly efficient sensors developed by this process.

3.1.1 Semiconductor Device Fabrication Technique

Most of the silicon-based sensors that we use in today's sensing world has been developed using semiconductor device fabrication technique. This process is a combination of several sub-techniques which involves the alternation in the physiochemical nature of the processed materials. Some of the methods like photolithography, surface passivation, thermal oxidation, sputtering and sonication are used in specific order to design the substrates and electrodes of the sensors. Equipment used for these processes are placed in specialized rooms called clean-room facilities to protect them from dust particles and UV light. The quality of cleanrooms has been categorized based on the minimum size of the particles present in those rooms [59, 60].

One of the recent works related to the modeling and development of interdigital sensors was done by Yunos et al. [61]. The prototypes were formed on FR4 boards, having a copper layer being used as electrodes. These sensors were utilized for estimating the blood glucose levels via determining the changes in the capacitive values. The width of the electrodes was varied between 0.5 and 0.7 mm, followed by determining the resonant frequencies using a vector network analyzer. The characterization was done between 1 and 3 GHz to determine the S-parameters. The highest quality factor was obtained to be 11.72 at a frequency of 2.11 GHz, with the resonant frequencies being at 2.02, 2.11 and 2.14 GHz. Some of the issues related to these sensors are regarding the raw materials used in conjugation with the MEMS technique. With the sensors being developed on FR4 substrates, it is a highly expensive and labor-consuming process. Secondly, multi-layered sensors cannot be formed using these circuit boards. Thus, if the specificity of these glucose sensors needs to be increased, it will be difficult to exert a selective layer on top of these boards. Secondly, the association of high-frequency operation with interdigital sensors has demerits related to it. It not only requires higher input power but also the amount of information transmitted to the receiving unit is also limited. These FR4 boards should be replaced with single-crystal silicon substrates to perform experiments at lower frequencies. Also, with the amount of work done on glucose sensing, high sensitivities need to be obtained with the presence of a specific layer that would act as a template to the glucose molecules. The wearable nature is another point that needs to be noted for deploying these sensors for point-of-care performances.

Zhang et al. [62] showed the development and implementation of piezoelectric sensors via thin-film resonators on silicon substrates. This system-on-chip was formed using a fully-differential configuration to eliminate the negative effect of the feedthrough. The insertion loss and signal-to-background ratio obtained with these MEMS-based sensors were 4.27 and 42.47 dB, respectively. The developed sensors had a length of 300 microns and a width of 160 microns, which was supported by two pairs of tether beams. The piezoelectric layer was sandwiched between a metal layer and a single-crystal silicon layer. The operating mechanism of the sensors was

driven by this metal layer formed with aluminum nitride. This metal was a pattern on the layer having a thickness of 500 nm. The ground electrode of the sensor was formed with highly-doped silicon using phosphorous as a dopant. The responses of the sensors were obtained at the electrode, where the signal was generated due to the piezoelectric effect. Some of the issues related to the fabrication techniques are the intermediate steps followed to develop the sensors. Firstly, the deep-ion etching technique that was used to define the mechanical structure has certain disadvantages like the probability of surface damage, low level of selectivity and low etch rate. This degrades the quality of the sensors, and subsequently, their performances. Instead of reactive ion etching, alternative etching techniques such as wet etching should be used to have a better quality of the surface. Also, although the inert loss has been reduced in these sensors in comparison to other reported research, it is still large enough for systems operating for a long time. The formation of other substrates using as polyvinylidene fluoride (PVDF) can also be considered instead of silicon due to certain attributes like low acoustic impedance, low permittivity, high thermal and chemical stabilities.

Other than LPG sensing, the detection of benzene gas can also be emphasized upon using MEMS-based sensors, as shown by Ku et al. [63]. Platinum (Pt) metal was used to form interdigitated electrodes along with an integrated micro-heater in the sensing system. An additive layer of tungsten-oxide (WO_3) on top of the sensing surface to increase the sensitivity towards the benzene gas. Figure 4 [63] shows the schematic diagram of the fabrication process of the thin-film gas sensors. The deposition of

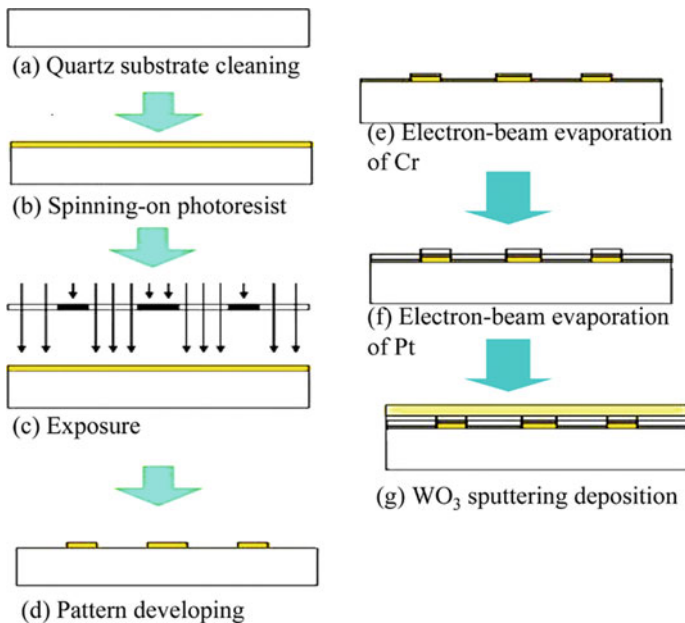


Fig. 4 Schematic diagram of the fabrication interdigitated sensors based on WO_3 thin-films [63]

chromium and platinum was done as the adhesive and conducting layers, respectively. The lift-off technique was used to pattern the micro-heater and interdigitated electrodes. Finally, RF-magnetron sputtering was done separately on the sensing surface using 99.99% purity of tungsten, followed by the oxide layer. The pressure was fixed at 10^{-6} Torr during the pre-sputtering and sputtering processes for 10 min and 50 min, respectively. Prior to the experiments, the sensor was annealed from 25 to 500 °C for over 60 min. Oxidization occurred on the heated WO_3 film when it got exposed to the benzene concentrations. This changed its electrical conductivity, and as a result, the resistance of the sensors. The sensors achieved an optimized working temperature of 300 °C, to obtain sensitivity, the limit of detection and response time of 1 k Ω /ppm, 0.2 ppm and 35 s, respectively. The limitations of these sensors are related to the additional need for a masked template to form the electrodes. Also, the use of SiO_2 serves as better substrates than WO_3 to form semiconductor sensors. This reason behind this could be attributed to the different forms of WO_3 that can be used to form the sensors. Since the stoichiometric form of WO_3 is an insulator, the use of the non-stoichiometric form is generally preferable to form the substrates which operate as n-type semiconductor [64]. There is no mention of the type of WO_3 here, which shows its arbitrary nature.

Zhou et al. [65] developed a reflector array that as used for the enhancement of the quality factor. The sensors were developed with aluminum nitride and silicon as electrodes and substrates, respectively. The sensing arrays were configured in the shape of fish scales, that were subsequently used for enhancement purposes by reducing the anchor loss. The arrays achieved a 3.5 folds' increase in the quality factor in comparison to the traditional design.

This was obtained by reducing the reflector array inside in the x-direction to integrate it inside the resonant body. The sensors in the array comprised of a thin-film piezoelectric layer that is composed of aluminum nitride between two electrodes. The thicknesses of aluminum electrodes were 1 micron, where the whole system was formed on substrates formed with anisotropic doped silicon. The thickness of the substrates was 10 microns, which had an additive layer of silicon-on-insulator. The disadvantages related to this work can be attributed to the electrodes developed with aluminum. Even though aluminum serves as lightweight and corrosion-resistant material, but the formation of a thin oxidative layer degrades its performances in comparison to other inert metals like gold. Another disadvantage that can be pointed out was the small thickness of the silicon substrates. If the thickness of the substrate is 10 microns with the presence of a one-micron thickness of the interdigitated electrodes, the resolution and performance would be poorer in comparison to their bulk counterparts [66].

One of the interesting works was shown by Wu et al. [67], where the design, fabrication and employment of piezoelectric MEMS generators were done for scavenging the mechanical energy of the ambient vibrations and converting them into electrical energy. These generators had the potential to be used as prototypes that consume and harvest low-intensity power from the environment. The sensors consisted of a beam-shaped structure that includes interdigital electrodes, silicon wafer and a piezoelectric (PZT) layer that laminated the substrate. The PZT layer that was formed with

lead zirconate was primarily responsible for the transformation of the mechanical strain into electrical charge. The piezoelectric material was poled in $\pm x$ directions with the help of the PZT deposition chamber. The vibrations of the micro-cantilever between the substrate and electrodes induced mechanical stress in the PZT layers, which was then subsequently converted into electrical energy. The charges generated with this generated were obtained as the output from the interdigitated electrodes. The interdigital distance between the electrodes correspondingly varied the obtained power and voltage. The experimental values of the interdigital distance consisted of 20, 30 and 40 μ , with 30 μ obtaining the maximum output power and voltage. The micro-cantilever structure had a dimension of $3000 \times 1500 \mu$, along with a PZT layer of 12 μ . The issues related to this structure was both the presence and dimensions of the proof mass, which assisted in the vibrations to the PZT layer. With the presence of the proof mass at the free end of the cantilever beam, the output voltage and power also varied as a function of the rate of acceleration of the movement due to the subsequent variation of the resonating frequency. Also, only three values of the interdigital distance were considered, where much better sensitivities were obtained with interdigital sensors having lesser distances between two consecutive electrodes. Optimization should have been done to detect till lowest interdigital distance till which the sensors obtained the highest sensitivities.

One of the significant research depicting the use of interdigitated electrodes in CMOS sensors was done by Zhao et al. [68]. These sensors, along with polysilicon heaters, were used for humidity sensing purposes. Industrial standard CMOS process and MEMS post-processing steps were used to process polyimide due to its wide range of linearity. Aluminum electrodes were employed to form the interdigital sensors, where the heater was placed under the electrodes. The reliability was improved by using the etching passivation layer between the electrodes. Silicon dioxide (SiO_2) and silicon nitride (Si_3N_4) were used as the substrates and passivation layer, respectively. The thicknesses of thermally-grown SiO_2 and passivation layers were 0.045 μ and 0.45 μ , respectively. Low-pressure Chemical Vapor Deposition was used to etch the SiO_2 by 0.35 μ for proper deposition of Aluminum electrodes. The packing of the sensors was done to improve the hysteresis and recovery time of the prototypes. High repeatability and good linearity were observed with the sensors for the entire testing range. After the fabrication of the sensors, a thin polyimide layer was heated at different temperatures of 80 $^\circ\text{C}$, 120 $^\circ\text{C}$ and 250 $^\circ\text{C}$ for different times of 30 min, 1 h and 2.5 h, respectively, and subsequently coated on the electrodes. The sensors were able to respond to a humidity ranging between 30% RH and 90% RH, having a response time of 32 s and a recovery time of 24 s. These sensors had a couple of issues related to the raw materials used during the fabrication process. Based on the provided Scanning Electron Microscopic (SEM) images, the coating of polyimide film was not uniform in nature. This definitely affected the responses of the sensors. Also, the comparative values of the R^2 values before and after the packaging did not have much difference. This could be attributed to the use of FR4 boards that were used for packaging purposes. These boards have uneven surfaces, which affects in maintaining the experimental conditions inside the chamber.

Mehran et al. [69] showed the use of interdigitated electrodes on silicon substrates via capacitive accelerometers for possible applications in earthquake sensing. The fabrication was based on the use of micromachining and deep reactive ion etching techniques on silicon to form the conjugation of anisotropic back-side and vertical front-side. Two sub-classes of passivation and etching were used through a hydrogen-assisted deep etching process. The substrates were formed with a p-type silicon wafer having a thermally-grown oxide layer of a thickness of 0.3μ on top of it. Chromium layers were deposited on the front and back sides of the prototypes as their back-plane and electrodes, respectively. The silicon from the bottom surface was etched a couple of microns extra to avoid the short-circuiting of the electrodes. The prototypes were made sensitive to inclinations and accelerations by incorporating silicon-based nanostructures. The sensors were tested by tilting them from 0 to 90° to detect the capacitive changes in terms of pF. Some of the loopholes related to the fabrication of these sensors can be related to the dimensions of the prototypes and synthesis of specific parts of the sensors. For example, the value of the vertical etching that was done to avoid the short-circuiting should be optimized to calculate the effect on the generated electric field. Also, if $1-2 \mu$ extra is done, how does it affect the uniformity in the fringing electric fields. Also, after the deformation of the interdigitated electrodes in the presence of water droplets, the intensity of the reformation of the fingers back to its real shape is also unknown. It is significant to know if there is any offset after the first primary reformation and then for the subsequent cycles. This would affect the effective interdigital distance between the electrodes and the generated electric field.

3.2 Flexible Sensors with Interdigital Electrodes

With the enhanced properties of flexible sensors, these prototypes have been utilized with interdigitated electrodes to a greater extent. Unlike MEMS-based sensors, the flexible sensors have deployed the interdigitated electrodes for both electrochemical and strain-sensing purposes. Among the several processes that have been utilized to form the flexible sensors, below are some of the popular ones that are considered by the researchers. Each of these techniques has its own advantages, which leads to the fabrication of sensors with unique physical properties.

3.2.1 Laser-Cutting Technique

With different kinds of laser systems getting commercialized, the researchers are opting for the laser systems that can generate ultra-flexible sensors with high sensitivity. Other advantages of these systems are a low cost of production, quick fabrication process, high accuracy and precision cuts, roll-to-roll production, sensors with low power consumption, lesser waste of processing materials and minimized damage to the prototypes during production process [70]. These systems are operated with

different kinds of parameters like power, frequency, speed, pulse per inch (PPI) and others. All these parameters are optimized to generate sensors specific to a particular application.

One of the works, as shown by Hao et al. [71], was related to the development of NO₂-based gas sensors using two-beam-laser interference (TBLI). The reduction of graphene oxide (GO) was made to form prototypes that can be used for sensing at room temperature. The dissociation energies provided by the two-beam laser reduced the GO into graphene nanostructures. The operating principle was based on splitting a laser beam having a wavelength of 355 nm into two branches. Interference occurred during the laser exposure, which was identifiable due to the reduction of the GO film through the transparency of the sinusoidal nature. These nanostructures for sensors using molecular adsorption techniques at acceleration response and recovery rates. The experiments were conducted at 20 ppm of the gas. The sensors obtain a response of 1.27 in terms of resistance, along with a response time of 10 s and a recovery time of 7 s. These values obtained with graphene nanostructures were higher than those obtained with thermally reduced graphene oxide. The resistive response, response time and recovery time of the thermally-reduced graphene oxide were 1.04, 34 s and 45 s, respectively. The issues related to the fabrication of these sensors can be specifically targeted to the further improvement that can be done to the two-beam laser interference. It is arbitrary if the splitting of the laser beam was done into two branches or not. Also, the choice of the wavelength of the laser beam was unknown. Optimization needed to be done on the splitting of the laser, which could have further improved the response and recovery times. The specifications of the formed graphene nanostructures were also unknown. Also, the power used for forming the interdigital electrodes on the ceramic substrates was 0.15 W. This value is very low as compared to the graphene nanostructures formed by the laser-ablation technique [72, 73].

Heng et al. [74] showed the implementation of flexible sensors that were developed using the laser-cutting process. The prototypes were used as insole sensors for the detection of gait analysis. Surface processing of a conductive rubber was done to form pressure-sensitive insoles for real-time pressure measurement. The sensors were formed using inkjet-printed electrodes on flexible substrates for pressure measurement with good sensing performance. Multi-Walled Carbon Nanotubes (MWCNTs) and Polydimethylsiloxane (PDMS) were used as electrodes and substrates, respectively, due to their individual advantages. Initially, a pressure-sensitive layer was formed by mixing MWCNTs, PDMS and n-hexane at a ratio of 20:40:1. After curing these samples, a polyimide layer was put on top of the substrate prior to the laser-cutting process. The laser cutting was done using a power of 15 W and a speed of 5% to form the pressure-sensitive units. At last, interdigital electrodes were formed on the polyimide layer during the packaging of the sensing unit. The interdigital electrodes were patterned with silver nanoparticles for conducting purpose. Figure 5 [74] shows the schematic diagram of the steps of the fabrication of the pressure sensors. The responses were analyzed in terms of resistive signals which were wirelessly transmitted to the monitoring unit. The analysis was done based on the 60-gait-cycle data that was selected from the walking experiment.

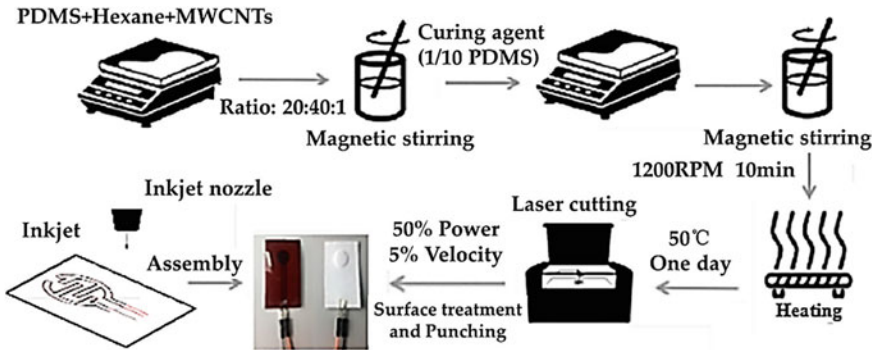


Fig. 5 Schematic diagram of the fabrication of laser-induced interdigital sensors [74]

The bottlenecks related to this work can be associated with the relation between the fabrication process and processed materials. The use of the polyimide layer on top of the pressure-sensitive layer is questionable, especially for the fact that Young’s Modulus for polyimide is very high [75]. The second loophole would be the amount of MWCNTs mixed with PDMS during the formation of a pressure-sensitive layer that needs optimization as the amount of nanotubes added is very high. Sensors have also been developed much lesser amount of MWCNTs have been added to PDMS to form nanocomposite-based sensors [76].

Nie et al. [77] showed the development of the graphene-based capacitive sensors for measuring the dew point via controlling the active temperature. Laser-induced graphene was developed from commercial polymer films and transferred on PDMS substrates to form interdigital electrodes. The humidity sensor was formed by using this laser-induced graphene oxide to form a thin-film layer via the electro-spray technique. Kapton tapes having a thickness of 50 μ were attached to the silicon substrates for the laser-ablation process. A CO₂-based laser with a wavelength of 10.6 μ was used to form graphene out of the Kapton tapes. Liquid PDMS was poured on the formed graphene and cured to use the laser-induced graphene as electrodes of the sensor. This was followed by diluting the graphene oxide solution before it was used for the electro-spraying process on the sensing area of the prototypes. A dew point temperature of 10.5 °C DP was set to test the sensors. The capacitive values of the sensors increase linearly with the decrease in temperature. After a certain value, the capacitive values saturate and become constant. The issues with these sensors can be particularly associated with the steps subsequent to the laser-ablation process. When the liquid PDMS was added to the induced graphene, the nanostructures and PDMS formed a composite subsequent to the curing process. This decreased the overall conductivity of the graphene. Also, the electro-spraying technique used to coat the sensing area with a graphene oxide solution is not reliable. The disadvantage is that this process cannot be used on templates with existing pores. The sensing area on which the electro-spinning of the graphene-oxide solution was done consisted of pores due to the presence of graphene nanostructures. Instead, other techniques

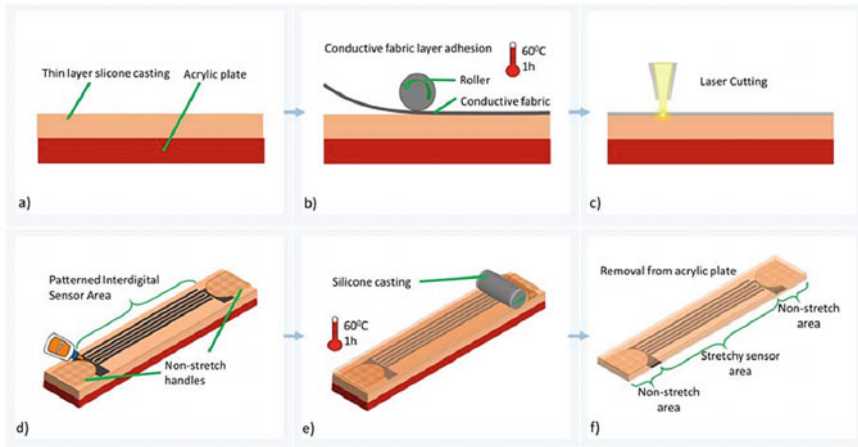


Fig. 6 Schematic diagram of the steps of fabrication of interdigital electrodes with laser-cutting on conductive fabrics [78]

like the dip-coating process can be used for a greater effect of the graphene-oxide solution.

Atalay et al. [78] showed an intriguing work on the use of interdigital electrodes with capacitive, textile-based sensors. These prototypes have been formed using conductive fabric that was knitted inside the silicone matrix to form interdigitated electrodes. Figure 6 [78] shows the schematic diagram of the steps of the fabrication of the conductive fabric-based sensors. Eco flex 30 was used as the substrates due to their high elongation limit and biocompatibility. The embedded samples were cured in the oven for an hour at 60 °C, followed by laser-cutting the samples to form the interdigitated electrodes. A power of 40 W and a speed of 5% was used to form the interdigitated electrodes, and the excess fabric parts were subsequently removed from the samples. The prototypes were used to determine the movement of the knee joints during different scenarios. The sensors showed a high linear output of $R^2 = 0.997$. The response time and resolution of the sensors were 50 ms and 1.36%, respectively. The issues related to these sensors can be associated with the embedding of the conductive fabric done within the silicone elastomers. The embedding of the fabric and the elastomer deters their combined stretchability, as well as changing the Young's Modulus. This would create problems to determine their individual effects when the sensors were used for monitoring of knee joint movements. Another issue is the combination of high power and low speed used for the laser-cutting technique to form the interdigital electrodes. Even though the electrodes might be formed, the amount of heat generation with this combination creates minor cracks on the conductive fabric. This reduces the sensitivity and robustness of the sensors.

Dupla et al. [79] showed the design and fabrication of high-temperature sensors based on the surface acoustic wave (SAW) generation and propagation. The operating principle of the sensors was based on the piezoelectric non-ferroelectric

glass–ceramics that contained fresnoite crystals. These sensors could operate up to 900 °C through the generation and reception of SAW using interdigital electrodes. The coupling of the alternative polarities of the fingers and piezoelectric effect on the input sinusoidal waves created Rayleigh waves. A binding layer consisting of 55% of copper (Cu), 45% of nickel (Ni) and platinum was sputtered with a thickness of 200 nm on the glass–ceramic surface prior to the laser-ablation process. An Nd:YVO₄ microsecond pulsed laser was used to form the interdigital electrodes and remove the residual layer. The issues related to these sensors can be attributed to the use of high frequency with interdigital sensors. Although these electrodes were used in conjugation with the piezoelectric effect to create SAW, the individualistic effects of these phenomena would have a greater effect. The interdigital distance of these sensors are also unknown, whose optimization would be needed to have a higher intensity of SAW. The value of the wavelength or pitch needs to be optimized using FEM to detect its value that would avoid the compensation of the polarization effect during its conjugation with the piezoelectric effect.

Hammarling et al. [80] depicted the development of pH sensors using laser-processed interdigitated sensors. The sensors had a broad range of operation that was formed with laser processing and blade coating techniques. A coating of hydrogel was used to depict the pH ranging between 2.94 and 11.80. The response time was around 3 min, with the stability of the responses being reached after 4 min. Polyethylene terephthalate (PET) films were used as substrates where a thin-film gold layer was used as the electrodes having a thickness of 105 μ and 30 nm, respectively. The laser patterning was done using a 355 nm nanosecond pulsed laser ablation system that had a spatial resolution of 10 microns. The width and interdigital distance of the electrodes were 120 μ and 40 μ , respectively. Two additional layers of SU8 and acryl terminated oligo beta-amino ester's (AOBAE) were used as insulating layers to avoid the contact of the pH solutions with the electrodes. The thickness of the SU8 layer was around 4 ± 1 μ , whereas the hydrogel (AOBEA) layer had variable thicknesses of 5.5 ± 3 μ , 18.5 ± 3.5 μ and 30.5 ± 7 μ . The standard deviations obtained at a time duration of 1200 s for a pH of 7.12 and 8.38 are 3.37 pF and 4.69 pF, respectively. The bottlenecks related to the fabrication part of these sensors can be related to the conjugative use of two additive layers on top of the sensing area. The primary motive of the use of interdigital electrodes is to determine the properties of the material under test via the penetration of the electric field through it. When the presence of the additive layers, even though the electrodes are getting protected from the tested solutions, the generated electric field also could not penetrate properly through the different pH solutions. Also, the range of the tested pH solutions was not capable of affecting the electrodes. Although the hydrogel layer added on top of the interdigital electrodes assists in the sensitivity of the prototypes towards the tested pH concentrations, certain advantages like weak bonding of hydrogels create an additive capacitive layer between the hydrogen and electrodes, which leads to erroneous results.

Bellan et al. [81] showed the manufacturing of ultrasonic interdigital transducers on piezo-polymer films that can be used as carbon epoxy composites in spacecraft, satellite and airplanes. Metalized polyvinylidene fluoride (PVDF) was used

as a singular processing material where laser ablation was done to form interdigital electrodes. A wavelength of 8 mm was used to operate with Lamb waves to form piezopolymer transducers. Migration of CAD drawing and Nd: YAG laser marking tools were used to form electrodes on the PVDF films. The thicknesses of the PVDF films and metalized gold nanoparticles were 100 and 10 μ , respectively. The processing time required to form each of the prototypes was around one minute. Optimization was done on the laser micromachining process to avoid mechanical damage due to overheating. After the interdigital electrodes were formed, the PVDF material in between the fingers was depolarized in order to decrease the cross-coupling between the fingers. But one of the disadvantages of this system can be realized through the use of lasers on the PVDF thin-films. Due to certain disadvantages like high melting viscosity and inferior scratching and marrying resistance, the use of the laser ablation on these thin-films can be degrading to the quality of the substrates [82]. Another issue can be related to the requirement of optimization of the width and interdigital distance of the electrodes that can generate an electric field with the highest penetration depth. Also, the lamination of the interdigital electrodes should be done on thinner carbon fiber reinforced plastic composites. This is because, with thicker composites, the overall flexibility and stretchability of the sensors gets reduced to a great extent. The optimal thickness of the plastic composites would be double of that of the metalized PVDF films.

3.2.2 Screen Printing

The next most popular technique used in fabricating flexible sensors with interdigital electrodes is the screen-printing process. This process has been used since the 1800s where a mask has been designed to form the electrodes. Different kinds of conductive inks depending on their electrical conductivity, surface tension, specific gravity, adhesion, viscosity and curing are being chosen for forming the electrodes by transferring the ink through a mask on the substrates. It has certain advantages like high-quality output, simplicity, affordability, speed, high durability of the sensors and versatility in the use of substrates [83, 84]. Here, some of the significant works has been explained along with the loopholes related to their fabrication technique.

Alsuradi et al. [85] explained the implementation of wearable biomedical sensors via screen-printed circuit boards on bio-degradable hydrocolloid dressings. Screen printing of passive elements was done along with the preparation and characterization of the surface of the hydrocolloid to connect the former using conductive silver paste. FEM simulations were done to show the appropriateness of the use of thick-film screen-printed passives for developing wireless prototypes. These sensors contained spiral inductors, serpentine resistors and interdigital electrodes that were subsequently used for humidity sensing applications. All these passive elements were designed using Computer-Aided Design (CAD) tool to form masks for printing purposes. The area limitation of the hydrocolloids was considered prior to the formation of the passive elements. These hydrocolloids were smoothened, applying an additive transparent layer of Polyvinyl Acetate (PVA) for filling the micro-features.

Finally, the screen-printing was done using a conductive silver paste to execute the designs. The issues related to the fabrication of these devices is the proximity of the three types of electrical elements present on the hydrocolloids. The presence of these three elements within a small area interference with each other's working phenomenon, especially with that of the spiral inductors and interdigital electrodes. Also, some of the disadvantages of flexible printed circuit boards like high cost, increased risk of damage during handling, more difficulty in assembly and difficulty to repair in case of faults or issues [86].

Interesting work was shown by Nomura et al. [87], where a wearable blood leakage sensor was developed using a screen-offset printing technique. Cotton textiles were used as substrates where interdigital electrodes were formed to test blood in sub-megahertz frequency ranges. The dispersion of blood was done at volumes of low concentrations of 15 μl . The novelty of this work includes two the conjugation of two techniques, namely screen-offset printing and specific dielectric dispersion processes. In order to avoid the permeation of the ink through the text in the conventional screen-printing technique, screen-offset printing was used, which used an initial silicon-based roll-blanket to print the patterns. Then, the conductive ink was transferred to the final substrates to transfer the patterns. The printing of the curable conductive ink was overprinted two to three times on a silicone blanket in order to avoid the possibility of disconnection of wiring. PDMS and a base film were used as silicone blankets where the initial printing of interdigital electrodes was done. The width and interdigital distance that was printed on the textile were 500 μ and 1000 μ , respectively. The detection was done using an impedance analyzer to determine the impedance and phase difference between two situations before and after dropping blood on the sensing area of the prototypes. The bottlenecks related to the fabrication process of these sensors can be associated with the parameters used for the screen-offset printing process. There is a high risk in the change in the properties of the conductive ink during the dual transfer of the conductive inks on the blanket and then the substrate. The use of conductive inks on the textile also depends on the porosity of the substrates. Another issue could be associated with the probability of a reduction in the quality of the electrodes on the final substrates. The edges of the electrode lines could be distorted due to the permeability of the textile-based substrates.

Soukup et al. [88] showed the development of novel organic sensors based on the deposition of layers using the screen-printing technique. Organic humidity sensors were formed with alumina substrates and a mixture of gold and resinate paste electrodes. Interdigital electrodes were formed with the width and interdigital distance being 50 μ . Additive protective and sensing films were provided by adding polymer and phthalocyanine layers, respectively. Optimization was done to achieve high reproducibility and high resolution of the printing lines. The electrodes were formed using an organometallic compound containing resinate paste and gold. The additive sensing film was formed using sulfonated nickel phthalocyanine ($\text{NiPc}(\text{SO}_3\text{Na})_4$) to add semiconducting properties to the sensor. Polystyrene was used as the passive protective layer to add stability and sensitivity to the prototypes. The coating of the screen was done using high definition photo-emulsion with a mesh of 3 μ . The

sensing layer was added using the spin-coating technique. The thickness of this layer was optimized to increase the sensitivity by minimizing the influence of the dynamic characteristics of the sensors by absorbing water molecules. These phthalocyanines imparted the electrons and ions to the sensing film to display the change in the electrical properties of these sensors. This is due to the existence of conjugated bonds in the molecular chains of the compound. The issues related to these sensors can be linked to the conjugative presence of two layers on top of the electrodes. Although the phthalocyanine imparted additive semiconducting properties to the interdigital electrodes, polystyrene being insulator in nature can interfere with the generated electric field. The ratio of gold and resinate that was used to form the electrodes was also unknown and required further optimization regarding the specific amount of the presence of metallic content.

Tan et al. [89] worked on an interesting area where low temperature co-fired ceramic technology was used to develop interdigital electrodes-based capacitive pressure sensors. The electrical circuit consists of an interdigital capacitor and a constant inductor. The inductors and capacitors were formed by screen-printing technique. The fabrication process was carried out in seven steps, namely cutting samples, pattern printing, stacking, lamination, slice, sintering and sealing. After the samples were cut using lasers, proper fill printing was carried out to avoid the disconnection of any of the formed sensor circuits. Then, sealing was done to fill the cavities with carbon film to avoid transmogrification. Then, the sensors were laminated by pressing them in water and subsequently cutting into square pieces of 40 mm. Finally, the sensors were sintered in a box and sealed to complete the process. A wireless mutual inductance coupling method was used to conduct pressure-sensing experiments. The sensitivity obtained with developed sensors was around 273.95 kHz/bar when the experiments were conducted at a pressure below 2 bar. The max readout distance operated with external antennas at around 600 °C was 3 cm. The potential applications of the developed sensors were the detection of gas pressure in harsh environments. The issues related to these sensors can be attributed to the association of the sintering process with the carbon-films. Due to the negative temperature coefficient of pure carbon films, the increase in the temperature in the sintering process leads to a corresponding increase in the resistance values. This destroys purity and degrades the performance of the sensors.

Qi et al. [90] examined the properties of the screen-printed zinc oxide-based sensors that were developed humidity sensing. Flower-like zinc oxide nanorods were used to form sensors that showed high sensitivity, fast response and recovery times, small hysteresis and high stability of the responses of the sensors. Figure 7 [90] shows the schematic diagram and optical image of the developed prototypes. ZnO nanorods were mixed with DI at a weight ratio of 100:25 to form a paste, which was subsequently used to screen-print on the substrates. The substrates of sensors were formed with ceramic, while interdigital electrodes were formed with silver and palladium. Five pairs of interdigital electrodes were formed with a thickness of 10 microns. The samples were finally heated at a temperature of 60 °C for 5 h. A protective layer was coated on the sensing area of the prototypes by using a solution formed with ethylcellulose solution and ethyl ester acetate. The change in impedance

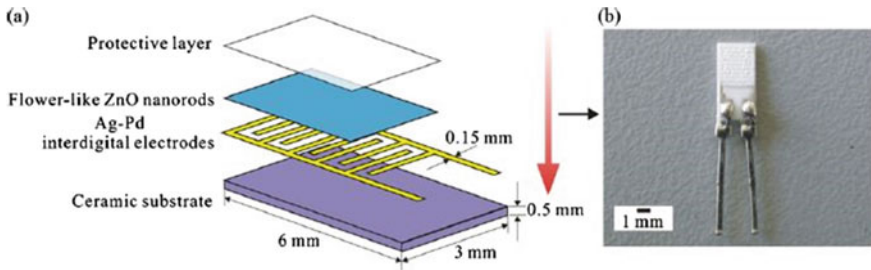


Fig. 7 a Schematic diagram of the structure of the developed prototypes. b Top-view of the optical image of the sensor [90]

was detected with respect to the corresponding change in the relative humidity (RH). An input voltage of 1 V and a frequency of 100 Hz were used as input parameters during the experimental process. A range of 11 to 95% of RH was tested to obtain a response and recovery times of 5 s and 10 s, respectively. The issues related to the fabrication technique of these sensors can be associated with the use of ceramics as substrates. Along with some of its disadvantages like easy damage and low impact strength, the biggest limitation would be the presence of cracks due to the highly fragile nature of these substrates. Also, the formation and employment of ZnO-based paste for formed, forming an additive layer for the formation of electrodes can be disadvantageous due to the weaker fabrication reproducibility and higher weakness in comparison to bare solid materials.

Kulha et al. [91] showed the development and deployment of low-cost capacitive systems where screen-printing and lamination techniques were used to form the electrodes. PET foils were used as substrates along the electrodes synthesized with a paste formed with silver and poly(3,4-ethylenedioxythiophene) polystyrene sulfonate (PEDOT: PSS). The silver paste was cured at 121 °C for 15 min, along with the curing of PEDOT: PSS at 110 for 5 °C minutes. The thicknesses of the silver layer and PEDOT: PSS layers were 10 μ and 300 μ, respectively. Microcontroller-based systems were formed with interdigital sensors which had a range of length of 10 mm and 15 mm and width/interdigital distance of 300–800 μ, respectively. The connections of the microcontroller with other passive components were made using silver conductive paste. The external terminal board was connected with the printed sensors using silver adhesive and thin copper wires. Finally, the entire structure was covered with a PET foil with a thickness of 80 μ. This layer served both as a protective and dielectric layer. Experiments were conducted with these sensors with varied conductivities and dielectric constants. The highest sensitivities of 0.7 pF/mm and 0.08 pF/mm were obtained for water and oil, respectively. The resolution of the sensors are 0.1 mm. The loopholes related to this work can be attributed to the additive layer that is added on top of the sensing area of the prototypes. The presence of the PET layer on top of the electrodes deters with the electric field generated from the interdigital sensor. This changes the overall permittivity of the sensors. Also, there

is a probability that the application of heat with the hot rollers on the lamination foil might change the properties of the foil [92].

Another interesting work done on the development of low-cost, flexible sensors using the screen-printing technique was shown in [93]. Pressure-sensitive ink was used for screen-printing purposes to develop prototypes that had an operating range of 0–2 MPa. The advantages of these sensors are their low-cost, high mechanical flexibility and non-invasive mode of measurement. Commercial polyimide films having a thickness of 5 μ were used as foils on which interdigital electrodes were formed using the screen-printing technique. The polyimide films were placed on substrate wafers prior to the screen-printing process. The conductive silver paste was used as the processing material for screen-printing of the electrodes of a thickness of around 3 μ . The printing purpose was done with a mesh having a mesh size of 180 meshes per centimeter. A two-component, intrinsically pressure-sensitive ink was deposited on top of the electrodes. The testing of the developed prototypes was done using a stamp having a dimension of 10 mm by 10 mm. The changes in the responses of the sensors were determined in terms of resistance with respect to pressure. The loopholes with this work can be related to the processing materials associated with the fabrication process. Firstly, the electrical conductivity and thickness of the pressure-sensitive ink should be optimized. The deposition of this layer on top of the electrodes is also not mentioned. Certain techniques like electrospinning and spin-coating can be used to coat the sensing area of the prototypes. Secondly, other polymers like PET or PDMS could have been used for developing the electrodes instead of polyimide, due to the low surface tension of the latter. Polymers like PDMS, when cured, have high durability to hold the screen-printed conductive ink.

3.2.3 Gravure Printing

This is the next most accepted type of printing process that has been used to develop interdigital electrodes-based flexible sensors. This process is similar to that of the screen-printing, with a difference of applying the conductive ink from the cylinder to the substrate. The advantages of this process include quick roll-to-roll production, high quality and consistent printing quality and relatively low labor costs. A few significant research works have been mentioned below, along with their loopholes.

Pudas et al. [94] showed the development of capacitive and inductive sensors based on high-resolution printing done on ceramic substrates. Hydrocarbon inks were used to form the electrodes to analyze certain attributes like ink flow, image distortions, ribbing, scooping, streaking and groove blocking. Grauel dry-offset printing machine was employed for the printing purpose that had a moving roller with a diameter of 60 mm. The substrate table was fixed along with adjustable gravure. The gravure was fixed in the horizontal direction while being adjustable in the vertical direction. A doctoring unit was designed consisting of two knives at fixed angles of 60°. Each of the knives was moved in opposite directions. When one knife was doctored, the other one was lifted off the gravure surface. The glass substrates that were considered for the experiments had a thickness and purity of 0.63 mm and 96%, respectively.

The printing as done using hydrocarbon binder ceramic inks that contained 72.5% inorganic solid load. The solids consisted of 70% silver and the rest of it was made of glass-frit that assisted adhesion to the alumina substrates. Some of the materials that consisted of organic components were non-polar resin, solvent compatible with the resin and thixotropic agent. The issues related to this work can be related to the conjugation of the processing materials with the fabrication technique. The concentration of the hydrocarbons needs to be optimized as the increase in the concentration limits the mechanical flexibility of the formed inks [95]. Another issue is the use of alumina substrates with this type of printing process. The disadvantage of alumina substrates is low toughness and poor thermal shock resistance that cannot withstand an increase in temperature during the printing process [96].

Reddy et al. [97] showed the development of interdigital electrodes-based electrochemical biosensors using a rotogravure printing technique. The substrates and electrodes of the sensors were formed using PET and silver nanoparticles, respectively. These silver nanoparticles having an average size between 20 and 30 nm were used for the metallization of the sensors. The fabricated sensors consisted of 8 pairs of electrode fingers, having a length, width and interdigital distance of the electrodes were 8600 μ , 200 μ and 200 μ , respectively. The bio-sensing experiments conducted with the formed sensors included electrochemical impedance spectroscopic (EIS) detection of cadmium sulfide, lead sulfide, D-proline and mouse I_gG. The sensors were tested with an input voltage of 100 mV and a frequency ranging from 1 Hz to 1 MHz. The responses were collected on a desktop using a customized LabVIEW program. The loopholes associated with this work can be related to the use of PET as substrates for the sensors. The increase in temperature for gravure printing can be disastrous for PET as exposure to excess heat creates deformation of the material [92]. Also, exposure to excess heat emits harmful gases.

Xiao et al. [98] described the fabrication and implementation of micro-supercapacitors (MSCs) based on electrodes formed with hybridized conductive materials. These hybrid materials were formed using sulfonated reduced graphene oxide (S-rGO) and molybdenum sulfide (MoS₂) nanoflowers. The interdigital electrodes were formed on flexible polyimide substrates. Figure 8 [98] shows the schematic diagram of the fabrication process of the hybrid sensors. After the formation of reduced graphene oxide (rGO) using Hummer's method, sulfonating was done by treating the rGO with aryl diazonium of sulfanilic acid. Then, S-rGO was mixed with sodium molybdate and sodium hydroxide to obtain a pH of 6.5. Finally, a solution was formed using L-cysteine and DI, and subsequently heated at 240 °C for 24 h. Then, centrifugation was done to collect black precipitate which were mixed with MoS₂@S-rGO to prepare the conductive material for gravure printing purposes.

Finally, polyimide was cleaned with DI water using ultra-sonication and reactive ion etching techniques for using it as substrates. After the gravure printing of the electrodes, a silver paste was printed on top of the MoS₂@S-rGO active materials. Finally, KOH-PVA gel was used to cover the channel area of the interdigital electrodes as a protective layer. The developed MSCs had a high specific capacitance, energy density and power density of 6.56 mF/cm², 0.58 mWh/cm³, 12.4 mW/cm³, respectively. The sensors achieved high stability with a loss of just 9% of the maximum

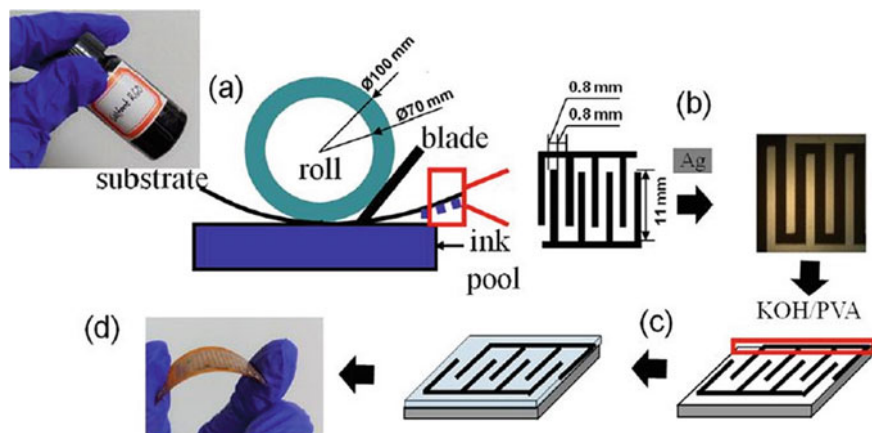


Fig. 8 Schematic diagram of the fabrication of interdigital electrodes formed with sulfonated reduced graphene oxide and molybdenum sulfide [98]

capacity after experimenting with them for over 1000 cycles. The bottlenecks related to this work can be related to the use of PVA as a composite as a protective layer. The composites formed with PVA has a high probability of being fragile when used as thin-film layers, so it should be avoided to be deployed as a protective layer on the sensing surface [99]. Also, the use of graphene for forming composites to develop the electrodes has certain disadvantages like non-uniform dispersion and the existence of a number of layers that affect the characteristics of the electrodes [100].

Another use in the employment of graphene for developing interdigital-based sensors with the help of gravure printing was shown by Zhang et al. [101]. Interdigital supercapacitors were formed with crumpled graphene ink on polyimide substrates, where magnesium hydroxide nano-sheets were inserted as nano-spacers into the layers of graphene oxide. This asserted oxygen-containing groups, which assisted in the ionic transport and exposure of the electrochemically active layer. The template-assisted graphene nano-sheets were optimized by mixing magnesium oxide and graphene oxide at different mass ratios of 15:1, 10:1 and 5:1, respectively. The optimal capacitive properties were achieved for the ratio of 10:1. Then, this mixture was milled with zirconia balls and poly (tetrafluoroethylene) vials. Finally, graphene powder was dispersed with the mixture along with ethanol and DI water. Finally, polyimide templates were cleaned with DI water and used as substrates for the reactive ion etching process. Some of the parameters of this ion etching process were 100 W, 80 sccm and 10 Pa for power, gas flow and gas pressure, respectively. Then, the printing of interdigital electrodes was done using silver and subsequently dried at 120 °C for ten minutes. The thickness of the graphene nano-sheet was fixed at 10 μ with a printing number of 20. The developed MSCs had high energy and power densities of 1.41 mWh/cm³ at 25 mW/cm³ and 0.35 mWh/cm³ at 300 mW/cm³, respectively. The application of these sensors was to drive a liquid crystal display via the connection of two serial and parallel supercapacitors. The loopholes related

to this work can be linked to the processing materials used for developing these prototypes. Even though crumpled graphene offers the highest surface area [102], the production parameters have still not been optimized. The second disadvantage would be the agglomeration of the crumpled graphene caused due to the sintering effect [103]. This causes a change in the color of the crumpled graphene as a result of the partial restoration of the π network.

The development and implementation of LC sensors were also done using gravure printing technology [104]. The work is related to the fabrication of a sensing system consisting of an inductor, detection coil and interdigitated electrodes using PET and silver ink as substrates and conductive ink, respectively. A conjugation of screen and gravure printing technologies were used to form the sensors. In gravure printing, the components were cylinder, ink fountain, doctor blade and impression cylinder. The impression cylinder assisted in the transfer of ink from the cells onto the substrate. The sensors consisted of 8 pairs of electrode lines, each one having a length and width of 8600 μ and 200 μ , respectively. The interdigital distance was fixed at 200 μ . These sensors were used for the detection of toxic heavy metals at low concentrations. The wireless operation was carried out to test the formed sensors for two metals of cadmium sulfide and lead sulfide. The sensors obtained high sensitivity with resonant frequencies obtained at 1.2, 2.5, 16.2 and 40 kHz. The drawbacks of this work can be related to the conductive silver epoxy that was used for connecting wires in the LC circuit. There is a high probability inconsistency as a result of formation air bubbles from batch to batch, which can eventually vary the resistivity of the connections.

Wang et al. [105] explain the fabrication and characterization of MSCs using a stamp-assisted gravure printing technique. The printing process was carried out on conductive polymer composites to form the sensors. The composites were developed using CNTs and PDMS, which were subsequently used as printing inks. Optimization was done on the values of CNTs that were mixed with PDMS to form conductive inks on paper substrates. 300 mg of CNTs was initially mixed with toluene, followed by mixing into 3 gm of PDMS. Magnetic stirring was done at room temperature for 4 h to form a homogeneous mixture. This was followed by pouring the mixture on a dish in order to evaporate toluene. Finally, a cross-linker was added to the mixture with further magnetic stirring for 30 min. The viscosity of the nanocomposites was matched with that of the commercial ink by optimizing the amount of residual toluene. A thin-film layer of release agent was sprayed on the surface of the stamp base in order to increase the integrity of the gravure transferring. Then, the stamp was dipped into the CNTs-PDMS ink and subsequently used for printing the interdigital electrodes on the flexible substrates. Then, the ink got transferred onto the substrate after removing the groove. Finally, a gel consisting of polyvinyl alcohol and phosphoric acid was sprayed on the interdigital electrodes. The areal capacitance obtained for the MSCs was 10.491 $\mu\text{F}/\text{cm}^2$. One of the loopholes related to this work was the use of toluene for the proper dispersion of CNTs. The use of toluene for the dispersion of CNTs in composites has a high probability of partially destroying the nanotubes [106]. Secondly, the mixing of cross-linker with the pre-polymer after it was mixed with CNTs is detrimental for the proper linkage of the PDMS. When the CNTs are mixed

with the pre-polymer, the silicone elastomers already get arbitrarily linked with the nanotubes, thus negating the effect of cross-linker.

Pavinatto et al. [107] show the synthesis of gravure printed flexible sensors consisting of interdigitated ink-jetted electrodes. The sensors consisted of flexible plastic substrates which had interdigital electrodes made of gold nanoparticles on them. Tyrosinase (Tyr) was used as an active layer on top of the sensing area of the electrodes, while the entire biosensors were encapsulated with cellulose acetate. The Tyr ink that was finally formed using shear stress in gravure printing contained 1% w/v of trehalose, 0.05% v/v of Triton X-100, 6 mg/mL of CMC and 68.5 of Tyr. This ink was printed on polyethylene terephthalate (PET) and polyethylene naphthalate (PEN) substrates with the gravure printing method. Two of the laser parameters, namely the printing speed and force of the gravure cylinder to compress the substrates, were optimized during the fabrication process. The sensors had an electrical conductivity of 5×10^6 S/m after they were sintered at 200 °C for 6 h. These prototypes were employed as biosensors, where the change in impedance was calculated with the corresponding change in the concentration of a model antioxidant. The sensors obtained sensitivity and limit of detection of 5.68 $\Omega/\mu\text{m}$ and 200 μm , respectively. The issues with this work can be highlighted with the relation of the sintering process with the PET and PEN substrates. One of the major issues of polyethylene substrates is their high susceptibility with increased heat. Since the optimal temperature of these substrates should be kept close to room temperature, the quality of these substrates degraded in this case.

3.2.4 Ink-Jet Printing

The next type of printing technique that has been largely used for developing interdigital electrodes-based flexible sensors has been inkjet printing. Although the concept of this printing technique evolved in the 1950s, it is during the late 1990s [108, 109] when this method has been used extensively for research purposes. This method has been largely used in bioprinting sectors, where thin-film organic sensors and solar cells have been developed for industrial and environmental applications. One of the works related to inkjet-printing can be shown in [110], where interdigital capacitors were formed for monitoring of liquid levels. Two sensors were formed, namely level and reference sensors, using flexible PET substrates and silver ink nanoparticles. Each of the sensors had 9 fingers, whose length and interdigital distance was 135 mm and 1.5 mm, respectively. The fabricated prototypes were connected to an impedance analyzer for the experimental purpose of testing three different types of liquids. The frequency range was swept between 1 and 9 MHz to determine the changes in the capacitive values. Finally, the changes in the capacitance values took place due to the differences in the permittivity of the respective liquids. The issues with this work can be linked to both the devices and their operating mechanism. Firstly, the use of two sensors for experimental purposes increases the equipment cost. Secondly, the differences in the capacitive values of the chosen liquids do not change symmetrically, which states that optimization needs to be done on the chosen frequency range.

Another issue can be related to the compatibility of the PET substrates with the silver ink. PET substrates are normally compatible with solvent, eco-solvent and UV inks [111].

The introduction of an additive dielectric interlayer in the interdigitated capacitive sensors was shown in [112]. Inkjet printing technique was employed to develop the sensors on flexible organic foils. A thin-film dielectric layer of Parylene C was formed on top of the electrodes prior to the second layer. This technique was employed to prevent the chances of short-circuits, which makes the devices non-functional. Before the silver ink was printed to form the first comb on flexible PET films, the substrates were treated with microwave oxygen plasma at a power of 400 W for 15 s. This step was performed to improve the wettability of the printed ink. Then, the organic residuals present in the ink of the electrode lines were removed using the sintering process for two hours at 150 °C. The deposition of Parylene C on the first electrodes comb was done using Chemical Vapor Deposition (CVD) technique. The thickness of the Parylene C layer was around 2 μ . The sensors were validated by functionalizing them with an additive humidity sensing layer and subsequently determining the changes in their responses against corresponding changes in the relative humidity. The changes were determined in terms of capacitive values at a frequency and time interval of 100 kHz and 5 s, respectively. The loophole of this work can be attributed to the presence of two interdigitated electrode combs in separate layers. The characteristics of the generated electric field between the electrodes of opposite polarity would change due to the presence of the dielectric layer. Also, the consistency in the uniformity of the two printed layers might also vary depending on the uniformity of the dielectric layer and bottom PET substrate.

Crowley et al. [113] show the fabrication and implementation of polyaniline (PANI)-based gas sensors for the detection of hydrogen sulfide at low concentrations. Flexible PET polymers were used as substrates where interdigitated electrodes were developed using printed layers of PANI and copper chloride. The sensors were used as chemiresistors where the change in current was determined corresponding to the change in the concentration of the target gas. The linear range and LOD of the sensors were 10–100 ppmv and 2.5 ppmv, respectively. Screen printing along inkjet printing was used as fabrication technology to form electrodes and prototypes. After the electrode designs were drawn using AutoCAD, commercial carbon paste and silver ink were used to form the electrodes. Optimization was done on the voltages of the piezoelectric nozzle prior to the printing process. The voltage range was set between 16 and 26 V before every round of printing. 16 nozzles having a space of 254 μ were used for developing printing purposes. The printing was done on PET substrates, followed by their heat treatment at 150 °C for 30 min. The copper chloride solutions were printed at a voltage of 16 V and a resolution of 40 μ . This was achieved by passing the solutions through the filter, having a spacing of 0.45 μ . The loopholes related to this work can be related to the experimental process followed to develop the sensors. The heat treatment of the printed inks creates a probability of increasing the surface cracks on the surface of the electrodes.

Yi et al. [114] showed the use of inkjet printing technique for the development of carbon and silver-based strain sensors. The fabrication of fully printed strain sensors

was done, which had the potential to be used as wearable sensors for structural health monitoring applications. Carbon and silver inks nanoparticles were employed to form the electrodes, whereas PI polymers were used to develop the substrates of the prototypes. The presence of carbon ink in the sensors assisted in increasing the resultant resistance of the sensors when they were bent to a certain degree. The printing of the silver ink was done using an inkjet printing technique on substrates having a thickness of 120 μ . After the formation of the designs, the samples were heated inside an oven at 100 °C for an hour, in order to dry the ink. The thickness of the formed electrodes was around 4 microns. Finally, the carbon ink was brushed on the electrodes and electrodes to form the additive layer, followed by drying the samples in the oven at 100 °C for 30 min. The sensors had a size of 2.25 cm² whose responses changed up to a maximum limit of 7.9% with a maximum bent in the sensors. The first loophole of this work is the presence of two layers, which form a capacitive layer between each other, and with the interdigitated electrodes. The second issue would be the irreversible cracks that are formed on the sensing surface due to the applied pressure. The presence of these cracks deters the quality of the prototypes, which considerably reduces their lifetime.

Fang et al. [115] showed the fabrication of flexible interdigitated gas sensors using an inkjet printing technique. Silver nanoparticles were printed on flexible Kapton substrates. The deposited silver nanoparticles were converted to highly porous gold counterparts by using a mild and facile two-step process in ambient temperature. Initially, a layer of functionalized Single-Walled Carbon Nanotubes (SWCNTs) was uniformly deposited on the sensing surface using a novel layer-by-layer method. This was followed by printing the silver nanoparticles on top of the sensing elements. The silver particles were spherical in shape, having a diameter of 150 nm. Finally, the wet chemical reaction technique was used where tetrachloroauric acid (HAuCl₄) was used for converting the silver nanoparticles into morphologically similar gold nanoparticles. The SWCNTs were present in a randomly and evenly distributed form between the interdigital electrodes. The sensors were operated as chemiresistors, where the Schottky contact between the porous gold electrodes and SWCNTs played a significant role in the responses of the sensors. The sensors showed high sensitivity towards the diethyl ethyl phosphonate (DEEP) gas, which is a stimulant for the nerve agent sarin. The responses of these sensors were around five times better than those performed with initially printed dense silver nanoparticles. The issues in this work can be questioned on the use of HAuCl₄ for the conversion of silver particles. The probability of complete conversion of the silver particles is very low. In addition to this, the presence of functionalized SWCNTs below the converted silver particles deters their characteristics.

Similar work can be seen in [116], where elucidation of the design and development of fully printed capacitive gas sensors were done, which were subsequently used for gas-sensing applications. The sensors were formed with silver electrodes on PET substrates. The characteristics of the prototypes were optimized using the sintering method, in addition to the electroplated passivation layers of Ni and Parylene-C. The width and interdigital distance of the electrode fingers were $95 \pm 3 \mu$ and $105 \pm 3 \mu$, respectively. A capacitive value of 5 pF was targeted. A drop-on-demand

printing technique was used to form the electrodes. The stability was improved by optimizing the sensor prototypes under high vacuum conditions. During the addition of the passivation layer, the monomers were used to coat the entire prototypes. This was done by cross-linking the polymers. The developed prototypes were used in experimental conditions having a maximum limit of 70% relative humidity. The operation of the sensors at higher relative humidity made the gaseous reactions irreversible. The output of the sensors was measured in terms of change in capacitance and conductance. The issue with this work can be related to the mechanism that needs to be followed to increase the operating range of relative humidity levels. In order to make the responses of the sensors reversible, the experiments need to be carried out at a wider range of temperatures. The increase in temperature values above the ambient level reduces their potential to be operated in dynamic conditions.

Rosati et al. [117] showcased the development of interdigitated biosensors for the study of detection of contamination of bacteriophage in milk products. Silver nanoparticles-based inks were used for forming interdigital electrodes on a range of flexible substrates such as PET, office and photo papers. Black and silver-colored nanoparticles were used for fabrication on transparent PET substrates. The designs of the electrodes were developed using AutoCAD software. Optimization was done on the conductivity and ratio between the real and nominal printed lines. The dimensions of the interdigital electrode fingers were also optimized with different values of electrode widths and the width of the passivation windows. The passivation layer was formed by patterning vinyl adhesive patches with RoboMaster CraftRobo CC330. The prototypes were used for monitoring bacterial cultures via the EIS technique. Phosphate buffered saline was used as the buffer solution. The frequency sweep was done between 100 and 1 MHz, along with the input DC bias and AC voltages of 0 V and 5 mV, respectively. The changes in capacitance and impedance values were studied with the help of a standard buffer solution to test *Lactococcus lactis* and bacteriophage infection. The loopholes related to this work can be focused on the material that was used as a passivation layer on the electrodes. The presence of tapes not only deters the stability of the responses of the prototypes but also increases the probability of damaging the shape and design of the electrode fingers.

4 Possible Resolutions to the Existing Challenges

Although a lot of work has been done on the fabrication of interdigital-based sensors, there are still some issues, as mentioned above, that need to be addressed. Each of the mentioned research has been based on the preliminary work done on the design, development and utilization of interdigitated sensors for different kinds of biomedical, industrial and environmental applications. Some of the advantages of these sensors include their single-side access, the formation of low-cost devices, equipment with faster ionic diffusion in case of electrochemical reactions, high power density and adjustable signal strength. For the issues that are pointed out in the preceding section, there are some possible remedies that can be carried out to improve the

quality of the prototypes. Firstly, the interdigital electrodes that were developed using printing techniques, compatible substrates should be selected that can withstand a high range of temperatures. It is better to print the nanoparticles-based electrodes on substrates that do not degrade its quality with a rise in temperature. A few of the options are PDMS and Polyimide, which can be considered for printed sensors. Secondly, the presence of an additional protective layer on top of the electrodes changes the overall permittivity of the sensors. This negates the characteristics of the conductive material that is used to form the electrodes. Instead of using an additive layer, nanocomposites can be formed by mixing all the elements, which can be subsequently used to form the electrodes. Also, the formation of nanocomposites in certain cases like graphene and CNTs where their dispersion does not happen homogeneously in aqueous media without the assistance of any surfactants, functionalized carbon allotropes are a better alternative than can be considered instead of pure elements. For example, instead of using MWCNTs, functionalized CNTs can be employed for forming nanocomposites due to certain advantages. Some of them are better interfacial bonding within the polymer matrix, biocompatibility, solubility, cellular interaction pathways and reduced cytotoxic effects [118].

Another issue to be rectified is the formation of a thin oxidative layer in the environment on top of some of the electrodes. There are two possible ways to deal with this problem. Firstly, the use of certain metallic and carbon-based elements should be done to form the electrodes. For example, among the nanomaterials, gold nanoparticles can be considered due to their high stability in the environment. Among the carbon-based materials, graphene and CNTs are favorable choices due to the low bandgap. One of the ways of dealing with the cracks that happen in the strain sensors due to constant bending is the use of nanofillers with the electrodes. The presence of additional nanofillers, along with the conductive material in the electrodes, can reconstruct their interconnections to maintain the overall integrity of the prototypes. Certain subsidiary nanomaterials can form a covalent bond with the primary conductive material and polymer matrix to form composites that can completely heal itself, even after repetitive tests. This would also help in maintaining the consistency of the responses of the sensors.

In order to deal with the drawbacks of the interdigitated electrodes, one of the possible opportunities is the use of certain non-finger-based ones, such as fractal shapes. The advantages of these types of electrodes have higher surface area that generates larger electric fields and higher energy density in comparison to interdigital electrodes. These types of electrodes have been used a lot to form biosensors [119, 120] and RF-based antennas [121, 122]. These types of electrodes have been largely developed using conventional MEMS techniques and having a working mechanism similar to parallel-plate capacitors. The operational capability in terms of frequency is also high as the antennas developed in these forms operation at frequencies as high as 10 GHz [123]. Resonating frequencies above 40 GHz have also been obtained [124] with these types of sensing prototypes that have been used as variable capacitors. The sensors have been formed with the backbone concept, which consists of a movable plate to obtain a specific fractal geometric shape. High-quality factors have also been obtained with the RF-based fractal sensors. One of the biggest

advantages of these designs is the elimination of parasitic capacitance, which helps in precise measurements. Researchers are constantly working on the modeling and fabrication of sensors based on these designs to increase the tuning range of the variable capacitors [125]. These sensors have high potential for other applications like energy harvesting [126] using a variety of fabrication techniques like 3D printing and screen printing. These sensors have been embedded with signal-conditioning circuits to operate them as IoT devices for harvesting energy from ambient sources. Real-time testing has been done with these devices where up to 500 mV have been harvested. The utilization of interdigital designs in conjugation with fractal shapes will be another intriguing sector that can be worked upon to improve the quality of the sensors in microelectronics industries.

5 Conclusion

This chapter explains some of the significant work done on the design, fabrication and implementation of interdigital-based sensors. These sensors have been formed using different kinds of MEMS and printing techniques, which altered the structure and dimension of the prototypes. The variation in the nature of the prototypes in terms of structure, size and shape, resulted in their use in different sectors. Some of the issues related to each of the above-mentioned works have been presented, along with possible remedies in the preceding section. Although the use of these designs has been done for quite some time, there are still some opportunities that can be harnessed in the future for further improvement. These electrode designs can be formed using nanomaterials [127, 128] to have enhanced electrochemical characteristics and high longevity. The rectifications of the existing issues, along with their further improvement, can increase the usage of interdigital designs for developing ubiquitous sensors to a great extent.

References

1. S. C. Mukhopadhyay, A. Lay-Ekuakille, A. Fuchs, *New Developments and Applications in Sensing Technology* (Springer, 2011)
2. S.C. Mukhopadhyay, *Interfacing of Sensors and Signal Conditioning, in Intelligent Sensing* (Springer, Instrumentation and Measurements, 2013), pp. 29–53
3. M. Kraft, N. M. White, *MEMS for Automotive and Aerospace Applications* (Elsevier, 2013)
4. M. Esashi, Revolution of sensors in micro-electromechanical systems. *Jpn. J. Appl. Phys.* **51**(8R), 080001 (2012)
5. J.C. Costa, F. Spina, P. Lugoda, L. Garcia-Garcia, D. Roggen, N. Münzenrieder, Flexible sensors—from materials to applications. *Technologies* **7**(2), 35 (2019)
6. A.C.R. Grayson et al., A BioMEMS review: MEMS technology for physiologically integrated devices. *Proc. IEEE* **92**(1), 6–21 (2004)
7. Y.-H. Wang et al., MEMS-based gas flow sensors. *Microfluid. Nanofluid.* **6**(3), 333 (2009)

8. M. Ahmed, I. E. Gonenli, G. S. Nadvi, R. Kilaru, D. P. Butler, Z. Celik-Butler, MEMS sensors on flexible substrates towards a smart skin, in *SENSORS, 2012 IEEE* (IEEE, 2012), pp. 1–4
9. F. Xu et al., Recent developments for flexible pressure sensors: A review. *Micromachines* **9**(11), 580 (2018)
10. A. Nag, S.C. Mukhopadhyay, J. Kosel, Wearable flexible sensors: A review. *IEEE Sens. J.* **17**(13), 3949–3960 (2017)
11. C. Parameswaran, D. Gupta, Large area flexible pressure/strain sensors and arrays using nanomaterials and printing techniques. *Nano Convergence* **6**(1), 1–23 (2019)
12. A. Nag, S. Mukhopadhyay, Wearable flexible sensors: fabrication and characterization
13. J. Yin, V.J. Santos, J.D. Posner, Bioinspired flexible microfluidic shear force sensor skin. *Sens. Actuators* **264**, 289–297 (2017)
14. X. Tang, Y. Miao, X. Chen, B. Nie, A flexible and highly sensitive inductive pressure sensor array based on ferrite films. *Sensors* **19**(10), 2406 (2019)
15. A. Nag, S.C. Mukhopadhyay, J. Kosel, *Sensing System for Salinity Testing Using Laser-Induced Graphene Sensors* (Physical, Sensors and Actuators A, 2017).
16. Y. Jiang, Q. Zhou, L. Lin, Planar MEMS supercapacitor using carbon nanotube forests, in *2009 IEEE 22nd International Conference on Micro Electro Mechanical Systems* (IEEE, 2009), pp. 587–590
17. T. Han, S. Kundu, A. Nag, Y. Xu, 3D printed sensors for biomedical applications: a review. *Sensors* **19**(7), 1706 (2019)
18. T. Han, A. Nag, N. Afsarimanesh, S.C. Mukhopadhyay, S. Kundu, Y. Xu, Laser-assisted printed flexible sensors: a review. *Sensors* **19**(6), 1462 (2019)
19. S.D. Senturia, N.F. Sheppard, S.Y. Poh, H.R. Appelman, The feasibility of electrical monitoring of resin cure with the charge-flow transistor. *Polym. Eng. Sci.* **21**(2), 113–118 (1981)
20. J. Temmyo, S. Yoshikawa, Aluminum evaporation conditions for SAW interdigital transducers. *IEEE Trans. Sonics Ultrasonics* **27**(4), 219–220 (1980)
21. T.M. Reeder, D.E. Cullen, Surface-acoustic-wave pressure and temperature sensors. *Proc. IEEE* **64**(5), 754–756 (1976)
22. N. Yamazoe, New approaches for improving semiconductor gas sensors. *Sens Actuators B Chem* **5**(1), 7–19 (1991)
23. S.M. Sze, *Semiconductor Sensors* (Wiley, New York, 1994).
24. N. Yamazoe, G. Sakai, K. Shimano, Oxide semiconductor gas sensors. *Catal. Surv. Asia* **7**(1), 63–75 (2003)
25. A. Nag et al., A transparent strain sensor based on PDMS-embedded conductive fabric for wearable sensing applications. *IEEE Access* **6**, 71020–71027 (2018)
26. A. Nag, A.I. Zia, X. Li, S.C. Mukhopadhyay, J. Kosel, Novel sensing approach for LPG leakage detection: part I—operating mechanism and preliminary results. *IEEE Sens. J.* **16**(4), 996–1003 (2016)
27. M.S.A. Rahman, S.C. Mukhopadhyay, P.-L. Yu, *Novel Planar Interdigital Sensors, in Novel Sensors for Food Inspection: Modelling* (Springer, Fabrication and Experimentation, 2014), pp. 11–35
28. A.I. Zia et al., Technique for rapid detection of phthalates in water and beverages. *J. Food Eng.* **116**(2), 515–523 (2013)
29. N. Thanh-Tuan, S. Hamidreza, K. Djilali, A planar interdigital sensor for bio-impedance measurement: theoretical analysis, optimization and simulation (2014)
30. A. Nag, S.C. Mukhopadhyay, Fabrication and implementation of printed sensors for taste sensing applications. *Sens. Actuators, A* **269**, 53–61 (2018)
31. A. Mohd Syaifudin, S. Mukhopadhyay, P. Yu, Electromagnetic field computation using COMSOL Multiphysics to evaluate the performance of novel interdigital sensors, in *Applied Electromagnetics Conference (AEMC)*, (IEEE, 2009), pp. 1–4
32. V. Kasturi, S. Mukhopadhyay, Estimation of property of sheep skin to modify the tanning process using interdigital sensors, in *Sensors* (Springer, 2008), pp. 91–110

33. J. Oberländer et al., Study of interdigitated electrode arrays using experiments and finite element models for the evaluation of sterilization processes. *Sensors* **15**(10), 26115–26127 (2015)
34. O. Tigli, M.E. Zaghoul, Finite element modeling and analysis of CMOS-SAW sensors,” in *Nanotechnology 2010: Electronics, Devices, Fabrication, MEMS, Fluidics and Computational-2010 NSTI Nanotechnology Conference and Expo*. NSTI-Nanotech **2010**, 601–604 (2010)
35. Y. Huang, Z. Zhan, N. Bowler, Optimization of the coplanar interdigital capacitive sensor, in *AIP Conference Proceedings*, vol. 1806, no. 1 (AIP Publishing LLC, 2017), p. 110017
36. A.V. Mamishev, K. Sundara-Rajan, F. Yang, Y. Du, M. Zahn, Interdigital sensors and transducers. *Proc. IEEE* **92**(5), 808–845 (2004)
37. A. Nag, N. Afsarimanesh, S. Feng, S.C. Mukhopadhyay, Strain induced graphite/PDMS sensors for biomedical applications. *Sens Actuators A* **271**(1), 257–269 (2018)
38. N. Afsarimanesh, M.E.E. Alahi, S.C. Mukhopadhyay, M. Kruger, Development of IoT-based impedometric biosensor for point-of-care monitoring of bone loss. *IEEE J Emerg Select Top Circ Syst* **8**(2), 211–220 (2018)
39. A. Nag, B. Menzies, S.C. Mukhopadhyay, *Performance Analysis of Flexible Printed Sensors for Robotic Arm Applications* (Physical, Sensors and Actuators A, 2018).
40. A. Nag, S. Feng, S. Mukhopadhyay, J. Kosel, D. Inglis, 3D printed mould-based graphite/PDMS sensor for low-force applications. *Sens. Actuators, A* **280**, 525–534 (2018)
41. A.I. Zia, S.C. Mukhopadhyay, P.-L. Yu, I.H. Al-Bahadly, C.P. Gooneratne, J. Kosel, Rapid and molecular selective electrochemical sensing of phthalates in aqueous solution. *Biosens. Bioelectron.* **67**, 342–349 (2015)
42. M.S.A. Rahman et al., Detection of bacterial endotoxin in food: New planar interdigital sensors based approach. *J. Food Eng.* **114**(3), 346–360 (2013)
43. M.E.E. Alahi, A. Nag, S.C. Mukhopadhyay, L. Burkitt, A temperature-compensated graphene sensor for nitrate monitoring in real-time application. *Sens. Actuators, A* **269**, 79–90 (2018)
44. M.E.E. Alahi, S.C. Mukhopadhyay, L. Burkitt, Imprinted polymer coated impedimetric nitrate sensor for real-time water quality monitoring. *Sens Actuators B: Chem* **259**, 753–761 (2018)
45. A. Nag, S.C. Mukhopadhyay, J. Kosel, Tactile sensing from laser-ablated metallized PET films. *IEEE Sens. J.* **17**(1), 7–13 (2016)
46. N. Afsarimanesh, S.C. Mukhopadhyay, M. Kruger, Performance assessment of interdigital sensor for varied coating thicknesses to detect CTX-I. *IEEE Sens. J.* **18**(10), 3924–3931 (2018)
47. A. I. Zia et al., Development of electrochemical impedance spectroscopy based sensing system for DEHP detection, in *Sensing Technology (ICST), 2011 Fifth International Conference on* (IEEE, 2011), pp. 666–674
48. P.-A. Gross, T. Jaramillo, B. Pruitt, Cyclic-voltammetry-based solid-state gas sensor for methane and other VOC detection. *Anal. Chem.* **90**(10), 6102–6108 (2018)
49. S. Zhao, J. Tong, Y. Li, J. Sun, C. Bian, S. Xia, Palladium-gold modified ultramicro interdigital array electrode chip for nitrate detection in neutral water. *Micromachines* **10**(4), 223 (2019)
50. H. C. Lai, S. F. Chin, S. C. Pang, H. Sum, M. Sia, D. Perera, Carbon nanoparticles based electrochemical biosensor strip for detection of Japanese Encephalitis Virus. *J. Nanomater.* 2017 (2017)
51. V. Markevicius, D. Navikas, A. Valinevicius, D. Andriukaitis, M. Cepenas, The soil moisture content determination using interdigital sensor. *Elektronika Ir Elektrotechnika* **18**(10), 25–28 (2012)
52. P. Songgrod, S. Worawat, Determination of water added in raw milk using interdigital capacitor sensor. *Przegląd Elektrotechniczny* **91**(9), 265–267 (2015)
53. G.J. Brom-Verheijden, M.H. Goedbloed, M.A. Zevenbergen, A microfabricated 4-electrode conductivity sensor with enhanced range. *Multi. Digital Publishing Inst. Proc.* **2**(13), 797 (2018)
54. Y. Xu et al., Silicon-based sensors for biomedical applications: a review. *Sensors* **19**(13), 2908 (2019)
55. P.M. Sarro, Sensor technology strategy in silicon. *Sens. Actuators, A* **31**(1–3), 138–143 (1992)

56. N. Nguyen, Micromachined flow sensors—a review. *Flow Meas. Instrum.* **8**(1), 7–16 (1997)
57. X.-M. Jing, D. Chen, D.-M. Fang, C. Huang, J.-Q. Liu, X. Chen, Multi-layer microstructure fabrication by combining bulk silicon micromachining and UV-LIGA technology. *Microelectron. J.* **38**(1), 120–124 (2007)
58. S.-H. Kim, S.-H. Lee, Y.-K. Kim, A high-aspect-ratio comb actuator using UV-LIGA surface micromachining and (110) silicon bulk micromachining. *J. Micromech. Microeng.* **12**(2), 128 (2002)
59. D. Ensor, R. Donovan, B. Locke, Particle size distributions in clean rooms. *J. Environ. Sci.* **30**(6), 44–49 (1987)
60. O. Hamberg, E. Shon, Particle size distribution on surfaces in clean rooms, in *Aerospace Corp El Segundo CA Vehicle Engineering Div* (1984)
61. M. F. A. Bin Yunus, A. N. Nordin, A. Zainuddin, S. Khan, Modeling and development of radio frequency planar interdigital electrode sensors. *Bull. Electr. Eng. Inform.* **8**(3), 978–984 (2019)
62. Y. Zhang, J.-F. Bao, X.-Y. Li, X. Zhou, Z.-H. Wu, X.-S. Zhang, Fully-differential TPOs resonators based on dual interdigital electrodes for feedthrough suppression. *Micromachines* **11**(2), 119 (2020)
63. M.-T. Ke, M.-T. Lee, C.-Y. Lee, L.-M. Fu, A MEMS-based benzene gas sensor with a self-heating WO₃ sensing layer. *Sensors* **9**(4), 2895–2906 (2009)
64. E. Çiftiyürek, K. Sabolsky, E.M. Sabolsky, Molybdenum and tungsten oxide based gas sensors for high temperature detection of environmentally hazardous sulfur species. *Sens. Actuators B: Chem.* **237**, 262–274 (2016)
65. X. Zhou, J. Liu, F. Bao, Y. Song, J. Bao, X. Zhang, Fish scale-shaped acoustic reflector array for quality factor enhancement of AlN-on-silicon MEMS resonator, in *2019 IEEE International Ultrasonics Symposium (IUS)*, (IEEE, 2019), pp. 1720–1723
66. S. Beeby, Printed thick-film mechanical microsystems (MEMS), in *Printed Films* (Elsevier, 2012), pp. 259–277
67. B.-S. Lee, W.-J. Wu, W.-P. Shih, D. Vasic, F. Costa, P2E-3 power harvesting using piezoelectric MEMS generator with interdigital electrodes, in *Ultrasonics Symposium, 2007* (IEEE, 2007), pp. 1598–1601
68. C.-L. Zhao, M. Qin, Q.-A. Huang, A fully packaged CMOS interdigital capacitive humidity sensor with polysilicon heaters. *IEEE Sens. J.* **11**(11), 2986–2992 (2011)
69. M. Mehran, S. Mohajerzadeh, High sensitivity nanostructure incorporated interdigital silicon based capacitive accelerometer. *Microelectron. J.* **46**(2), 166–173 (2015)
70. Laser Cutting: Advantages and Benefits. Available: <https://www.engineeredmechanicalsystems.com/laser-cutting-advantages-benefits/>
71. L. Guo et al., Improved NO₂ gas sensing properties of graphene oxide reduced by two-beam-laser interference. *Sci. Rep.* **8**(1), 1–7 (2018)
72. A. Nag, S. Mukhopadhyay, J. Kosel, Urinary incontinence monitoring system using laser-induced graphene sensors, in *Sensors, 2017* (IEEE, 2017), pp. 1–3
73. J. Lin et al., Laser-induced porous graphene films from commercial polymers. *Nat. Commun.* **5** (2014)
74. W. Heng, G. Pang, F. Xu, X. Huang, Z. Pang, G. Yang, Flexible insole sensors with stably connected electrodes for gait phase detection. *Sensors* **19**(23), 5197 (2019)
75. T. Han et al., Gold/polyimide-based resistive strain sensors. *Electronics* **8**(5), 565 (2019)
76. A. Nag, S.C. Mukhopadhyay, J. Kosel, Flexible carbon nanotube nanocomposite sensor for multiple physiological parameter monitoring. *Sens. Actuators, A* **251**, 148–155 (2016)
77. J. Nie et al., Dew point measurement using a carbon-based capacitive sensor with active temperature control. *ACS Appl. Mater. Interfaces.* **11**(1), 1699–1705 (2018)
78. O. Atalay, Textile-based, interdigital, capacitive, soft-strain sensor for wearable applications. *Materials* **11**(5), 768 (2018)
79. F. Dupla et al., Surface acoustic wave generation and propagation on polar glass-ceramic for high temperature sensors, in *2019 20th International Conference on Solid-State Sensors, Actuators and Microsystems & Eurosensors XXXIII (TRANSDUCERS & EUROSENSORS XXXIII)*, (IEEE, 2019), pp. 1921–1924

80. K. Hammarling, M. Engholm, H. Andersson, M. Sandberg, H.-E. Nilsson, Broad-range hydrogel-based pH sensor with capacitive readout manufactured on a flexible substrate. *Chemosensors* **6**(3), 30 (2018)
81. F. Bellan et al., A new design and manufacturing process for embedded Lamb waves interdigital transducers based on piezopolymer film. *Sens. Actuators, A* **123**, 379–387 (2005)
82. PVDF/Acrylic Blends characterization before and after UV exposure. Available: https://shodhanga.inflibnet.ac.in/bitstream/10603/85739/12/12_chapter%206.pdf
83. S. Khan, L. Lorenzelli, R.S. Dahiya, Technologies for printing sensors and electronics over large flexible substrates: a review. *IEEE Sens. J.* **15**(6), 3164–3185 (2015)
84. J. J. Licari, L. R. Enlow, *Hybrid Microcircuit Technology Handbook: Materials, Processes, Design, Testing and Production* (Elsevier, 1998)
85. H. Alsuradi, J. Yoo, Screen printed passives and interconnects on bio-degradable medical hydrocolloid dressing for wearable sensors. *Sci. Rep.* **9**(1), 1–12 (2019)
86. Benefits or Advantages of Flexible PCB. Available: <https://www.rfwireless-world.com/Terminology/Advantages-and-Disadvantages-of-Flexible-PCB.html>
87. K.-I. Nomura, Y. Horii, S. Kanazawa, Y. Kusaka, H. Ushijima, Fabrication of a textile-based wearable blood leakage sensor using screen-offset printing. *Sensors* **18**(1), 240 (2018)
88. R. Soukup, A. Hamáček, J. Řeboun, Organic based sensors: Novel screen printing technique for sensing layers deposition, in *2012 35th International Spring Seminar on Electronics Technology*, (IEEE, 2012), pp. 19–24
89. Q. Tan et al., A novel interdigital capacitor pressure sensor based on LTCC technology, *J. Sens.* **2014** (2014)
90. Q. Qi et al., Properties of humidity sensing ZnO nanorods-base sensor fabricated by screen-printing. *Sens. Actuators B: Chem.* **133**(2), 638–643 (2008)
91. P. Kulha, W. Hilber, A. Laposá, B. Jakoby, Screen printed and laminated electrodes for low-cost capacitive level measurement systems. *J. Electr. Eng.* **69**(2), 177–182 (2018)
92. Polyethylene Terephthalate—PET. Available: <https://www.azom.com/article.aspx?ArticleID=796>
93. D. Gräbner, M. Tintelott, G. Dumstorff, W. Lang, Low-cost thin and flexible screen-printed pressure sensor, in *Multidisciplinary Digital Publishing Institute Proceedings*, 2017, vol. 1, p. 616
94. M. Pudas*, J. Hagberg, S. Leppävuori, Roller-type gravure offset printing of conductive inks for high-resolution printing on ceramic substrates. *Int. J. Electron.* **92**(5), 251–269 (2005)
95. R. B. McKay, *Technological Applications of Dispersions* (CRC Press, 1994)
96. W. Weber, S. Luzi, M. Karlsson, M. Fussenegger, A novel hybrid dual-channel catalytic-biological sensor system for assessment of fruit quality. *J. Biotechnol.* **139**(4), 314–317 (2009)
97. A. Reddy, B. Narakathu, M. Atashbar, M. Rebros, E. Rebrosova, M. Joyce, Gravure printed electrochemical biosensor. *Procedia Eng.* **25**, 956–959 (2011)
98. Y. Xiao, L. Huang, Q. Zhang, S. Xu, Q. Chen, W. Shi, Gravure printing of hybrid MoS₂@S-rGO interdigitated electrodes for flexible microsupercapacitors. *Appl. Phys. Lett.* **107**(1), 013906 (2015)
99. I. Angelidaki et al., Biogas Upgrading: Current and Emerging Technologies, in *Biofuels: Alternative Feedstocks and Conversion Processes for the Production of Liquid and Gaseous Biofuels* (Elsevier, 2019), pp. 817–843
100. D. Verma, K. L. Goh, Functionalized graphene-based nanocomposites for energy applications, in *Functionalized Graphene Nanocomposites and their Derivatives* (Elsevier, 2019), pp. 219–243
101. Q. Zhang, L. Huang, Q. Chang, W. Shi, L. Shen, Q. Chen, Gravure-printed interdigital microsupercapacitors on a flexible polyimide substrate using crumpled graphene ink. *Nanotechnology* **27**(10), 105401 (2016)
102. J. Semat, W. Rashmi, V. Mahesh, M. Khalid, J. Priyanka, Synthesis of crumpled graphene by fast cooling method, in *AIP Conference Proceedings*, vol. 2137, no. 1 (AIP Publishing LLC, 2019), p. 020014

103. W.M. El Rouby, Crumpled graphene: preparation and applications. *RSC Adv.* **5**(82), 66767–66796 (2015)
104. A. S. Reddy et al., P1. 9.12 fully printed wireless LC sensor for heavy metal detection, *Tagungsband*, pp. 1191–1194 (2012)
105. H. Wang et al., Stamp-assisted gravure printing of micro-supercapacitors with general flexible substrates, in *2019 IEEE 32nd International Conference on Micro Electro Mechanical Systems (MEMS)* (IEEE, 2019), pp. 950–953
106. O. V. Kharissova, B. I. Kharisov, *Solubilization and Dispersion of Carbon Nanotubes* (Springer, 2017)
107. F.J. Pavinatto, C.W. Paschoal, A.C. Arias, Printed and flexible biosensor for antioxidants using interdigitated ink-jetted electrodes and gravure-deposited active layer. *Biosens. Bioelectron.* **67**, 553–559 (2015)
108. M. Singh, H.M. Haverinen, P. Dhagat, G.E. Jabbour, Inkjet printing—process and its applications. *Adv. Mater.* **22**(6), 673–685 (2010)
109. P. Calvert, Inkjet printing for materials and devices. *Chem. Mater.* **13**(10), 3299–3305 (2001)
110. M. Kisic, N. Blaz, C. Zlebic, L. Zivanov, M. Damnjanovic, Flexible inkjet printed sensor for liquid level monitoring, in *2015 38th International Spring Seminar on Electronics Technology (ISSE)*, (IEEE, 2015), pp. 472–476
111. The Pros & Cons of PET. Available: <https://www.ultraflexeuropa.com/news/the-pros-cons-of-pet/>
112. F. Molina-Lopez, D. Briand, N. de Rooij, Inkjet printing of interdigitated capacitive chemical sensors with reduced size by the introduction of a dielectric interlayer. *Procedia Eng.* **47**, 1173–1176 (2012)
113. K. Crowley et al., Fabrication of polyaniline-based gas sensors using piezoelectric inkjet and screen printing for the detection of hydrogen sulfide. *IEEE Sens. J.* **10**(9), 1419–1426 (2010)
114. Y. Yi, S. Ali, B. Wang, An inkjet-printed strain sensor with a carbon-silver/polyimide topology, in *2019 IEEE International Conference on Flexible and Printable Sensors and Systems (FLEPS)*, (IEEE, 2019), pp. 1–3
115. Y. Fang, M. Akbari, J.G. Hester, L. Sydänheimo, L. Ukkonen, M.M. Tentzeris, Sensitivity enhancement of flexible gas sensors via conversion of inkjet-printed silver electrodes into porous gold counterparts. *Sci. Rep.* **7**(1), 1–10 (2017)
116. U. Altenberend et al., Towards fully printed capacitive gas sensors on flexible PET substrates based on Ag interdigitated transducers with increased stability. *Sens. Actuators B: Chem.* **187**, 280–287 (2013)
117. G. Rosati et al., Inkjet printed interdigitated biosensor for easy and rapid detection of bacteriophage contamination: A preliminary study for milk processing control applications. *Chemosensors* **7**(1), 8 (2019)
118. S. Vardharajula et al., Functionalized carbon nanotubes: biomedical applications. *Int. J. Nanomed.* **7**, 5361 (2012)
119. Y. Mashraei, S. Sivashankar, U. Buttner, K.N. Salama, Integration of fractal biosensor in a digital microfluidic platform. *IEEE Sens. J.* **16**(24), 8775–8783 (2016)
120. M.K. Hota, Q. Jiang, Y. Mashraei, K.N. Salama, H.N. Alshareef, Fractal electrochemical microsupercapacitors. *Adv. Electron. Mater.* **3**(10), 1700185 (2017)
121. F.A. Ghaffar, M.U. Khalid, K.N. Salama, A. Shamim, 24-GHz LTCC fractal antenna array SoP with integrated Fresnel lens. *IEEE Antennas Wirel. Propag. Lett.* **10**, 705–708 (2011)
122. F. A. Ghaffar, A. Shamim, K. N. Salama, A miniaturized wide-band LTCC based fractal antenna
123. A.M. Elshurafa, K.N. Salama, Two-layer radio frequency MEMS fractal capacitors in PolyMUMPS for S-band applications. *Micro Nano Lett.* **7**(5), 419–421 (2012)
124. A.M. Elshurafa, P. Ho, A. Radwan, M. Ouda, K.N. Salama, Low-voltage puzzle-like fractal microelectromechanical system variable capacitor suppressing pull-in. *Micro Nano Lett.* **7**(9), 965–969 (2012)
125. A. M. Elshurafa, K. N. Salama, P. Ho, Modeling and fabrication of an RF MEMS variable capacitor with a fractal geometry, in *2013 IEEE International Symposium on Circuits and Systems (ISCAS)*, (IEEE, 2013), pp. 2711–2714

126. A. Bakytbekov, T.Q. Nguyen, C. Huynh, K.N. Salama, A. Shamim, Fully printed 3D cube-shaped multiband fractal rectenna for ambient RF energy harvesting. *Nano Energy* **53**, 587–595 (2018)
127. Y. Zhuang, S. Han, W. Liu, X. Wei, Z. Xu, An interdigital electrode type sensor based on P (VDF-TrFE) nanofibers, *J. Alloys Compounds*, 154657 (2020)
128. N. Afsarimanesh, A. Nag, M. E. E. Alahi, T. Han, S. C. Mukhopadhyay, Interdigital sensors: biomedical, environmental and industrial applications, *Sens. Actuators A: Phys.* 111923 (2020)

Design and Fabrication of Fringing Field Interdigital Sensors for Physical Parameters Measurement



Tarikul Islam

Abstract Fringing electric field, a notorious edging effect of a parallel plate capacitor causes error in the measurement of capacitance value of the capacitor. It requires a guard electrode to minimize the error due to the fringing field. However, today fringing field interdigital electrodes (IDT) capacitive sensors are playing an important role in the measurement of different types of physical and chemical parameters. The important advantages of the sensors are simple inexpensive fabrication, single side testing of the materials and suitability of nondestructive measurement. These sensors are widely used for different physical parameters measurement including humidity, soil moisture, corn/grain moisture, moisture in paper pulp, leather etc. With the passage of time, it is expected to explore many new wonderful applications of this IDT sensor in near future. In this chapter, design of fringing IDT capacitive sensor with the help of analytical expression to optimize the geometrical parameters for maximum field penetration depth is discussed. Two IDT sensors of different geometrical configurations are designed and fabricated to measure physical parameters such as humidity and liquid level.

1 Introduction

Interdigital electrodes fringing field sensors are extensively used for different sensing applications including moisture measurement in agricultural food products, soil [1, 2], detection of microdroplets [3, 4], water intrusion in composite structures [5], moisture measurement in printed circuit board [6], humidity measurement [7], rapid detection of phthalates in water and beverages [8], measurement of liquid level [9], C-terminal telopeptide of type-I collagen (CTX-I) detection [10], in smart agriculture for phosphate and nitrate monitoring [11, 12], low force sensing [13], flexible printed pressure sensing for robotic arm [14], for biomedical applications [15]. These IDT

T. Islam (✉)

Department of Electrical Engineering, Jamia Millia Islamia (Central University), New Delhi 110025, India

e-mail: tislam@jmi.ac.in

© The Editor(s) (if applicable) and The Author(s), under exclusive license to Springer Nature Switzerland AG 2021

S. C. Mukhopadhyay et al. (eds.), *Interdigital Sensors*, Smart Sensors, Measurement and Instrumentation 36, https://doi.org/10.1007/978-3-030-62684-6_4

sensors can be used for the destructive (invasive) and non-destructive measurement of samples. Invasive sensors when the test samples are in touch with samples suffer from electrode contamination/oxidation, contamination of samples, possibility of irreversible reaction and have short life time. However, the non-destructive sensors where the sample is not in touch with the sensors do not suffer from these disadvantages of the destructive sensor. In a normal parallel plate capacitor, the test medium should be placed within the electrodes and the fringing electric field causes error in the capacitance value. However, this fringing electric field is used in an IDT sensor, where the medium can be tested from a single side by passing the electric field through the sample under test (SUT). Although the IDT capacitive sensors look like a parallel plate capacitor and many times, the capacitance value is represented by the same expression like $C = \epsilon_0 \epsilon_r \frac{A}{l}$ but this is not truly the correct expression [16]. However, for coplanar fringing IDT capacitors, the capacitance value is represented by complex mathematical expressions. Purpose of this chapter is to highlight some design aspects of different configurations of the IDT sensors and to discuss some applications of the IDT sensors for physical parameters measurement [3, 17]. Two different IDT configurations such as (i) 1-1-1 configuration (equally spaced working and sensing electrodes) (ii) 1-n-1 configuration (n number of sensing electrodes between two working electrodes) are studied [18].

2 Fringing Field Interdigital Electrode Sensor

A. IDT Sensor with Equal Number of Working and Sensing Electrodes

Figure 1a shows the coplanar interdigital configuration of a sensor structure which can be used to test the sample. Here the coplanar and semi-infinite metal fingers separated by uniform gaps are placed within a dielectric medium of permittivity ϵ_r . It has an equal number of sensing and working electrodes. The test medium can directly be in touch with the sensor in case of destructive sensing or there will be an insulating barrier in between the test sample and the sensor for non-destructive sensing. The IDT has N number of fingers where the fingers in working electrodes (WE) and sensing electrodes (SE) are equally spaced. The gap between the electrodes is $2g$ and the length of the finger is l , the width of the electrode is w and the wavelength is λ (length between two fingers on same side of the IDT). The height of the SUT is T . The electrodes are excited by electric potential $\pm V$. Due to this electric potential, the electric field lines go from the positive electrodes to the negative electrodes penetrating the dielectric SUT. The maximum height of the electric field is h . Here, the width of the electrode is much higher than the gap between the electrodes ($W \gg 2g$). Expanded view of two coplanar semi-infinite parallel plate electrodes separated by gap $2g$ is shown in Fig. 1b. Two-dimensional electrode field distribution shown in Fig. 1b can be conveniently solved using conformal mapping technique with the help of inverse-cosine transform [3, 19]. The results of solution of conformal mapping can be used to find an approximate expression of capacitance [20].

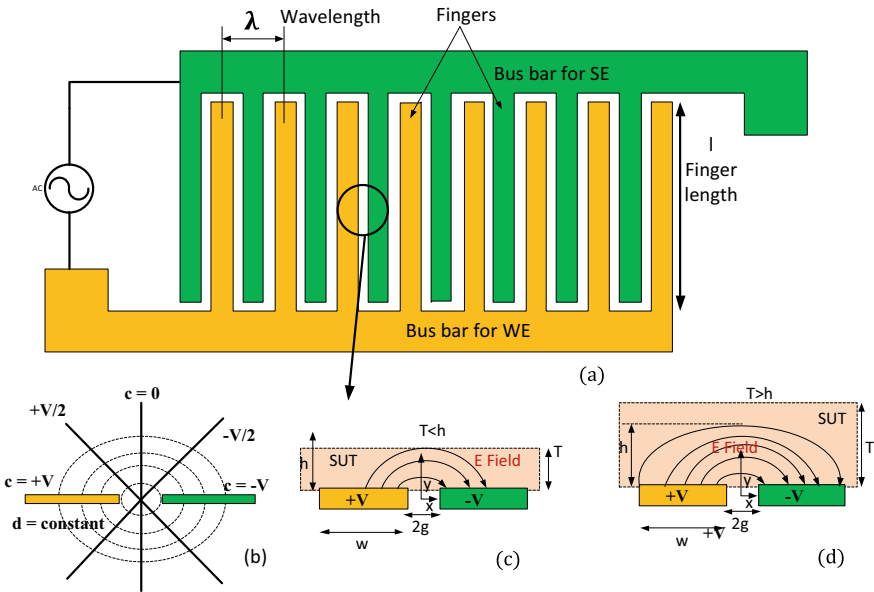


Fig. 1. **a** The schematic of the IDT structure showing details of configuration **b** electric field distribution due to applied potential difference between the WE and SE **c** electric field penetration when the sample thickness T is less than field penetration depth **d** electric field penetration when the sample thickness T is greater than field penetration depth

The inverse cosine transfer function is given by

$$A = V_0 - \frac{2V_0}{\pi} \cos^{-1} \frac{Z}{g} \tag{1}$$

Here, $A = c(x, y) + id(x, y)$, where c is the electric potential function and d is electric flux function, $2V_0$ represents potential difference between the two electrodes (WE and SE). The coordinate position (x, y) in the complex plane is represented by $Z = x + iy$.

The coordinates values can be represented in terms of c and d by

$$x = g \cos \left[\frac{\pi}{2V_0} (V_0 - c) \right] \cosh \left(\frac{\pi}{2V_0} d \right) \tag{2}$$

$$y = g \sin \left[\frac{\pi}{2V_0} (V_0 - c) \right] \sinh \left(\frac{\pi}{2V_0} d \right) \tag{3}$$

Equations (2) and (3) can be combined into elliptic or hyperbolic form to separately find the solutions of c and d .

$$\frac{x^2}{\cosh^2\left(\frac{\pi}{2V_0}d\right)} + \frac{y^2}{\sinh^2\left(\frac{\pi}{2V_0}d\right)} = g^2 \quad (4)$$

$$\frac{x^2}{\cos^2\left(\frac{\pi}{2V_0}(V_0 - c)\right)} - \frac{y^2}{\sin^2\left(\frac{\pi}{2V_0}(V_0 - c)\right)} = g^2 \quad (5)$$

Figure 1c represents the contour plot of electric potential $c(x, y)$ (solid line) and electric flux $d(x, y)$ (dotted lines).

Differentiating (3) with respect to y , one can get expression

$$\begin{aligned} \frac{1}{a} &= \frac{\pi}{2V_0} \frac{\partial c}{\partial y} \cos\left[\frac{\pi}{2V_0}(V_0 - c)\right] \sinh\left(\frac{\pi}{2V_0}d\right) \\ &+ \frac{\pi}{2V_0} \frac{\partial d}{\partial y} \sin\left[\frac{\pi}{2V_0}(V_0 - c)\right] \cosh\left(\frac{\pi}{2V_0}d\right) \end{aligned} \quad (6)$$

Along the surface of electrode defined by ($g \leq x \leq g + w$, $y = 0$), the electric potential $c = +V_0$ and the normal derivative of the electric flux ($\frac{\partial d}{\partial y}|_{y=0}$) is zero. Putting this condition in (6), it can be simplified as

$$\left(\frac{\delta c}{\delta y}\right)_{y=0} = -\frac{2V_0}{g\pi} \frac{1}{\sinh\left(\frac{\pi}{2V_0}d\right)} \quad (7)$$

Total surface charge on single electrode can be approximately given by surface integration of the electric displacement vector along the plane.

$$y = 0, \text{ where } D(y = 0) = \left(-\epsilon_r \epsilon_0 \left(\left(\frac{\partial c}{\partial y}\right)_{y=0}\right), 0\right)$$

Assuming all the charges are localized to the plane $y = 0$, and $l \gg g$

$$\begin{aligned} Q &= \iint D \cdot dA = 2l \int_g^{g+w} |D(y = 0)| dx \\ &= \frac{4\epsilon_r \epsilon_0 V_0 l}{g\pi} \int_g^{g+w} \frac{1}{\sinh\left(\frac{\pi}{2V_0}d\right)_{y=0}} dx \end{aligned} \quad (8)$$

At $y = 0$, $c = +V_0$, then putting this in (2),

$$x = g \cosh\left(\frac{\pi d}{2V_0}\right)_{y=0} \text{ and } \left(\cos h^2\left(\frac{\pi}{2V_0}d\right)_{y=0} - \sin h^2\left(\frac{\pi}{2V_0}d\right)_{y=0} = 1\right),$$

$$\text{So, } \sinh\left(\frac{\pi}{2V_0}d\right)_{y=0} = \sqrt{\left(\frac{x}{g}\right)^2 - 1},$$

Then expression (8) can be written as

$$Q = \frac{4\varepsilon_r\varepsilon_0V_0l}{g\pi} \int_g^{g+w} \frac{1}{\sqrt{\left(\frac{x}{g}\right)^2 - 1}} dx \quad (9)$$

Or

$$Q = \frac{4\varepsilon_r\varepsilon_0V_0l}{\pi} \ln \left[\left(1 + \frac{w}{g}\right) + \sqrt{\left(1 + \frac{w}{g}\right)^2 - 1} \right] \quad (10)$$

Then the capacitance value is given by

$$C = \frac{Q}{2V_0} = \frac{2\varepsilon_r\varepsilon_0l}{\pi} \ln \left[\left(1 + \frac{w}{g}\right) + \sqrt{\left(1 + \frac{w}{g}\right)^2 - 1} \right] \quad (11)$$

Equation (11) shows reliable expression of capacitance of two coplanar electrodes provided $l \gg w$ and $\frac{w}{g} \gg 1$.

For the interdigital capacitance having N number of fingers, the total capacitance can

be given by

$$C_T = \frac{2\varepsilon_r\varepsilon_0(N-1)l}{\pi} \ln \left[\left(1 + \frac{w}{g}\right) + \sqrt{\left(1 + \frac{w}{g}\right)^2 - 1} \right] \quad (12)$$

B. Determination of expression of electric field penetration depth

Case 1: When the SUT height $T > H_f$

The field penetration height H_f can be determined from the solution of (4) at $x = 0$ and the solution of (2) at $x = g + w$.

At $x = 0$, using (4), the field penetration depth H_f corresponding to the maximum vertical displacement of field line emanating from the outermost edge of the electrode pair is given by

$$H_f = g \sinh\left(\frac{\pi d}{2V_0}\right) \quad (13)$$

and at $x = g + w$, $c = +V_0$, $g + w = g \cosh\left(\frac{\pi}{2V_0}d\right)$, then

$$\left(\frac{\pi}{2V_0}d\right) = \cosh^{-1}\left(1 + \frac{w}{g}\right)$$

Equation (12) can be written as

$$H_f = g \sinh \left[\cosh^{-1} \left(1 + \frac{w}{g} \right) \right] = g \sqrt{\left(1 + \frac{w}{g} \right)^2 - 1} \quad (14)$$

Case 2: When the SUT height $T < H_f$.

The capacitance value can be determined by those electric field lines emanating from a portion of the electrode width represented by w_a in Fig 1d.

At $x = 0$, the field height H_f is given by.

$$H_f = g \sinh \left(\frac{\pi}{2V_0} d \right) \quad (15a)$$

$$\text{And at } x = g + w_a, c = V_0, \text{ then } g + w_a = g \cosh \left(\frac{\pi}{2v_0} d \right) \quad (15b)$$

Equation (15a, 15b) can be written as

$$\frac{w_a}{g} + 1 = \cosh \left(\sinh^{-1} \left(\frac{H_f}{g} \right) \right) = \sqrt{1 + \left(\frac{H_f}{g} \right)^2} \quad (16)$$

The value of ratio $\left(\frac{H_f}{T} \right)$ serves important purpose to obtain detectable sensitivity.

If this ratio $\left(\frac{H_f}{T} \right) \gg 1$ or $\left(\frac{H_f}{T} \right) \ll 1$, the capacitance value is greatly reduced. In the former case, the sample height (large sample) is so larger than the maximum field height, the field penetration through the sample is small. In the latter case, the liquid sample is very small.

For maximum capacitance value and better signal to noise ratio, H_f should be comparable to the electrode width w . Then the capacitance value for $H_f (=w)$ for N number of fingers can be

$$C_m = \frac{\epsilon_r \epsilon_0 l (N - 1)}{\pi} \ln \left[\sqrt{\left(1 + \frac{H_f}{g} \right)^2} + \frac{H_f}{g} \right] \quad (17)$$

This relation shows that for maximum capacitance, the gap between the electrodes will be minimum and the width of the electrode should be close to the height (breadth of the container) of the sample under test. The effectiveness of the expression is validated by simulation results for different values of w/g . There is a close agreement between the simulation and the analytical results. For $w/a = 1000$, the simulation result deviates from the analytical value by only 0.2% [3].

3 Interdigital Capacitive Sensor for Humidity Measurement

Humidity measurement using thin film sensors have gained increasing demand over the past decade for a wide range of applications in many automated industrial processes, food quality monitoring, air conditioning systems, meteorology, textile industry, smart irrigation and farming and so on. Humidity sensors also find their use in the medical field, pharmaceutical processing, rear-window defoggers in automobile industries, and health monitoring of electrical equipment. The quality of the finished products from many industrial processes prominently depends on the humidity of the surroundings. Due to advances in nanotechnology, the humidity sensors are also getting smaller in size, cheaper, and of better performance. The dynamic range of humidity measurement is wide. Various transduction principles are used in humidity sensors, such as optical, gravimetric, resistive and capacitive [21]. The capacitive humidity sensors are extensively used, owing to small size, temperature stability, easy adsorption and desorption, small power consumption, and relatively low cost.

On exposing the capacitive humidity sensor to ambient humidity, the effective dielectric constant of the sensing layer changes, accordingly, the capacitance value changes. The essential requirements for the humidity sensor are resolution in case of low ppm detection, stability, fast response, high sensitivity, negligible drift due to ageing, wide range and low cost [7, 22]. Porous forms of oxides are some finest materials for humidity measurement, it offers ample space for water vapour condensation and suitable pore morphology which leads to high sensitivity to the water vapour molecules. This nanostructure film offers a large surface-to-volume ratio, and the availability of a large number of voids. The oxide porous layer can be formed by anodic oxidation, sputtering, spray pyrolysis, chemical vapour deposition, and sol-gel technique etc. The sol-gel method provides a simple and low-cost way for the fabrication of highly pure porous Al_2O_3 thin film humidity sensors. The film is very hydrophilic to water molecules but not soluble in water, and is thermally and chemically very stable [7].

Most of the capacitive humidity sensors utilize the simple parallel plate or interdigitated design. The yield ratio of the parallel plate capacitive humidity sensors in case of hyper thin film is low due to shorting of the electrodes. But the interdigital fringing field type capacitive sensor there is no shorting problem, and the humidity can be measured by single side sensing film.

The capacitive structure shown in Fig. 1 which has an equal number of working and sensing electrodes can be used to measure humidity. Working and sensing electrodes are separated by identical gaps which are smaller than the width of the finger. To enhance sensitivity towards humidity, a hydrophilic film made of porous metal oxide/polymer can be deposited on the IDT electrodes.

Figure 2a shows the schematic diagram of the 1-1-1 structure capacitive humidity sensor. The sensor can be made on an inert substrate which may be made of the alumina substrate (alpha)/silicon, glass etc. In the present case, an alumina substrate

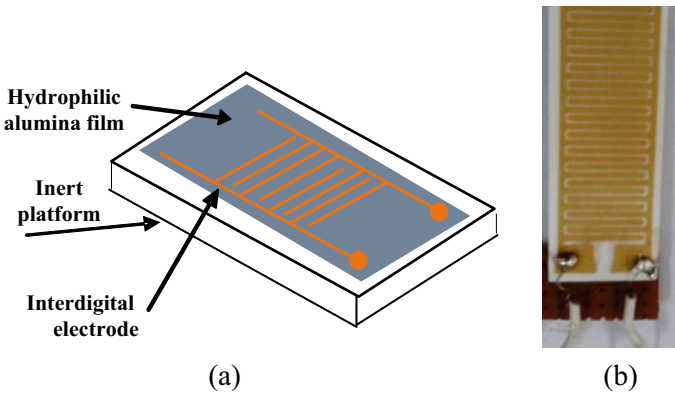


Fig. 2 a Schematic of the sol-gel thin film capacitive relative humidity sensor, b photograph [7]

of size $85 \text{ mm} \times 19 \text{ mm} \times 0.65 \text{ mm}$ was used. The IDT electrode of the sensor was fabricated by manual screen-printing technique. Prior to the fabrication of the IDT electrode, a mask was made using AutoCAD software. The electrodes were made of gold of size $70 \text{ mm} \times 16 \text{ mm}$. The gap between the two fingers of the interdigital electrode was 0.3 mm and the width of each finger was 0.5 mm . The electrode was sintered at $900 \text{ }^\circ\text{C}$ for 1 h. A sol solution of aluminum hydroxide ($\text{AlO}(\text{OH})$) was prepared by Yoldas method using aluminum sec butoxide precursor [23].

Then a thin film of $\gamma\text{-Al}_2\text{O}_3$ of thickness $\sim 6 \mu\text{m}$ was deposited on the IDT electrode from the sol solution by dip coating instrument. The film was initially heated at low temperature of nearly $80 \text{ }^\circ\text{C}$ for 5 m and then sintered at $450 \text{ }^\circ\text{C}$ for 3 h to make the stable Al_2O_3 thin film on the electrode.

To maintain the uniformity of the sensing film without cracking, the heating rate of the film was kept very small $\sim 10 \text{ }^\circ\text{C/h}$. Figure 2b is the photograph of the sensor. Pore morphology of the film was studied by BET surface area analyzer. The effective surface area of the film was around $200 \text{ m}^2/\text{gm}$. The average size of the pores was around 10 nm and the distribution of the pores in the film was in the range of ~ 1 to 30 nm [24].

To determine the response characteristics, the schematic experimental setup shown in Fig. 3 was used. The sensor was placed in a 100 cc sealed and properly grounded metallic chamber. The humidity in the sensor chamber varied from $0\% \text{RH}$ to $90\% \text{RH}$ by mixing water vapour to dry N_2 gas using control valves. The sensor chamber was connected in series with the commercial RH meter (2D/RH-100C) to measure the humidity exposed to the sensor. It is a relative humidity cum ambient temperature indicator.

The meter is made of Honeywell polymer capacitive humidity sensor. The meter has humidity measurement range of $0\text{--}100\% \text{RH}$ with an accuracy of $\pm 2\% \text{RH}$ and temperature range of $0\text{--}100 \text{ }^\circ\text{C}$, with a resolution of $0.1 \text{ }^\circ\text{C}$ and an accuracy of $\pm 0.5 \text{ }^\circ\text{C}$. Experiment was conducted to measure the capacitive response of the sensor with variation of humidity at two frequencies. Results of capacitance variation at 5

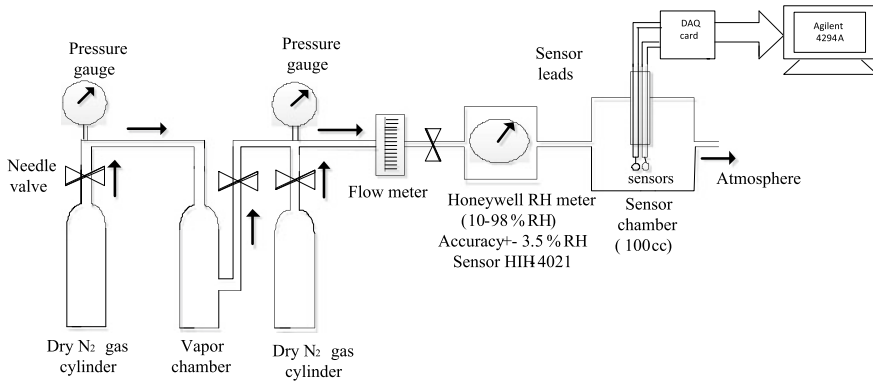


Fig. 3 Schematic of the experimental set up to determine the response of the IDT humidity sensor [7]

and 10 kHz are shown in Fig. 4a. It is observed that the capacitance value increases with increase in humidity at both frequencies, but the capacitance change at low frequency is significantly very high than the capacitance changes at 10 kHz.

It has been observed that the capacitance value decreases with increase in frequency. However, the nonlinearity of the sensor output decreases with increase in frequency. Figure 4b shows the variation of percentage nonlinearity with increase in frequency. At low frequency, although sensitivity is high but nonlinearity is also high. Selecting suitable signal frequency which is of the order of few tens of kHz is important for the optimum performance of the sensor.

Initially, water molecules are condensed on the surface and condensed in the pores through capillary condensation. Capillary condensation leads to the partial filling in the pores gradually. Therefore, the capacitance value increases due to gradual increase in dielectric constant of the sensor. It is seen in Eq. (17), that the capacitance value directly depends on the relative permittivity of the dielectric layer. When the water molecules are completely filled in the pores, there is no further increase in capacitance value. In addition to formation of dielectric capacitance due to condensation of water vapour, two more capacitances are formed at low frequency such as Stern layer capacitance and diffusion layer capacitance. These capacitances are formed when charges are accumulated at the electrode and water layer interface. Formation of these space charge layers thus results in the substantial increase in overall capacitance of the sensor but not the capacitance of the dielectric film. However, these Stern layer and diffusion capacitances are frequency dependent and decrease with increase in frequency till it reaches to a certain critical value [25]. In short, we can say that at low frequency, the capacitive response of the sensor has strong influence of double layer capacitance including the capacitance of the dielectric film which occurs due to water adsorption. The effective dielectric capacitance can be approximately given by Looyenga’s empirical equation as in (18).

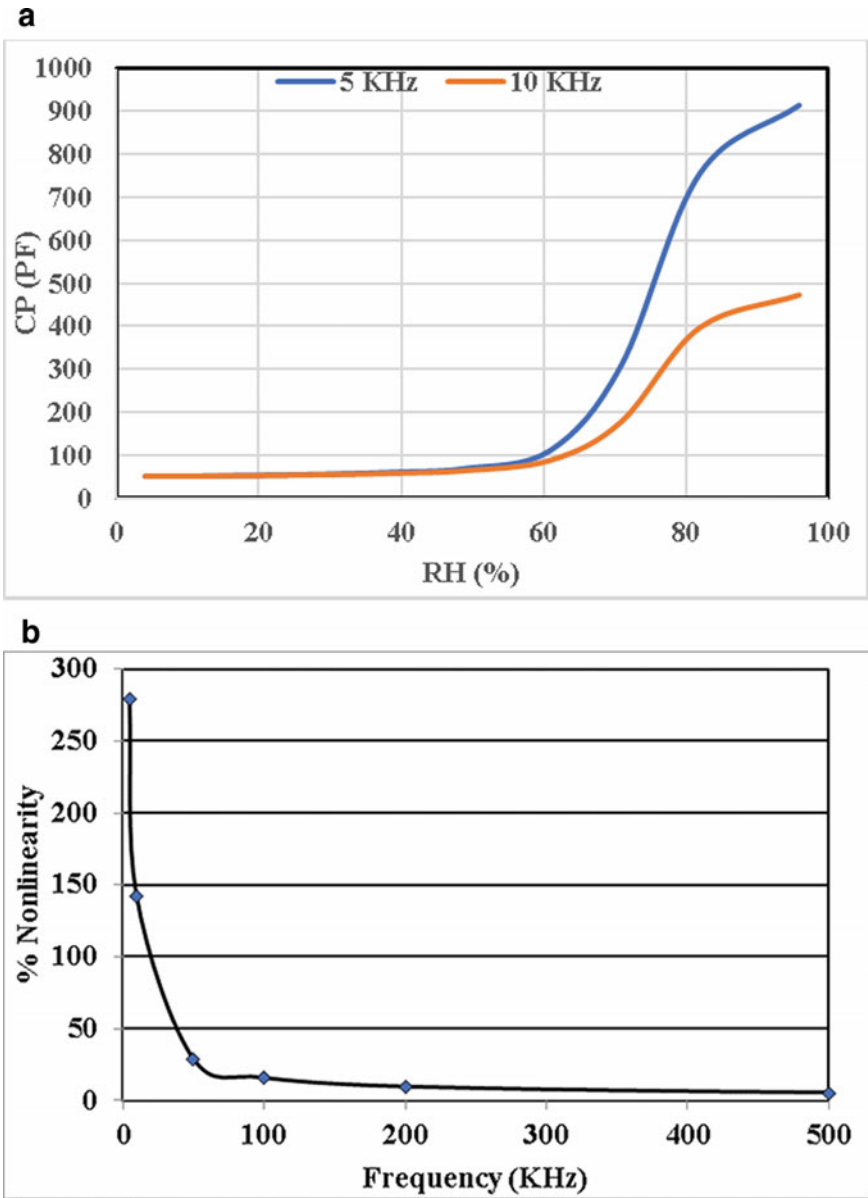


Fig. 4 **a** Variation of capacitance of the sensor with %RH at 5 and 10 kHz frequencies ($V_{ac} = 500$ mV) [7]. **b** Variation of sensor nonlinearity with signal frequency

$$\varepsilon_r = \{\gamma(\varepsilon_\omega^{1/3} - \varepsilon_p^{1/3}) + \varepsilon_p^{1/3}\}^3 \quad (18)$$

where ε_ω is dielectric constant of water and γ is the volume fraction of water condensed in the film.

However, the resistance value of the sensor also changes due to adsorption of water vapour molecules. The resistance R_p at any humidity (RH) can be approximately represented by another empirical relation of (19).

$$\log \frac{R_p}{R_0} = (\log a - \log \Phi) / \left(1 + \frac{b}{\Phi}\right) \quad (19)$$

where, R_0 is the resistance value at dry condition. The factor, n is the correction factor, a , b are the constants depending on the composition of the film and its structure. The resistance change is due to change in electronic and ionic conductivity of the film when water molecules are adsorbed on the surface [24].

The IDT sensor is simple to work with humidity sensing at a high level. However, this is not suitable for measurement of moisture in ppm level in gaseous environment. However, some work using a micrometre digital IDT sensor is reported to measure ppm moisture in the range of 175–625 ppm but not below 100 ppm [22]. Exploring the possibility of moisture sensing in ppm level in transformer oil using the IDT sensor is a scope of further work.

4 The Fringing Electric Field Coplanar IDT Structure for Liquid Level Measurement

Liquid level measurement is important for different industrial and home applications. Different techniques are used for level measurement including optical, ultrasonic, resistive and capacitive methods. The capacitive parallel plate/coaxial cylindrical are widely used for level measurement. However, most of them are contact types which require frequent maintenance, and the sensor output drifts with time because of contamination of electrodes with liquid samples. In this section, a simple noncontact interdigitated fringing field capacitance sensor for liquid level measurement is discussed. Two interdigital (IDT) sensors one having 1-3-1 coplanar electrodes and another one having 1-5-1 have been designed, simulated (finite element method) and then fabricated to measure water level from 0 to 30 mm. The capacitance value of both the sensors vary almost linearly with the variation of liquid level.

In the previous section we have discussed how to optimize the geometrical parameters of the IDT sensor to maximize the capacitance value between the working and sensing electrode. Figure 5a shows the schematic diagram of the proposed structure which consists of two coplanar electrodes separated by a small gap attached on the wall of a liquid container. Both the WE and SE are shielded to minimize error due

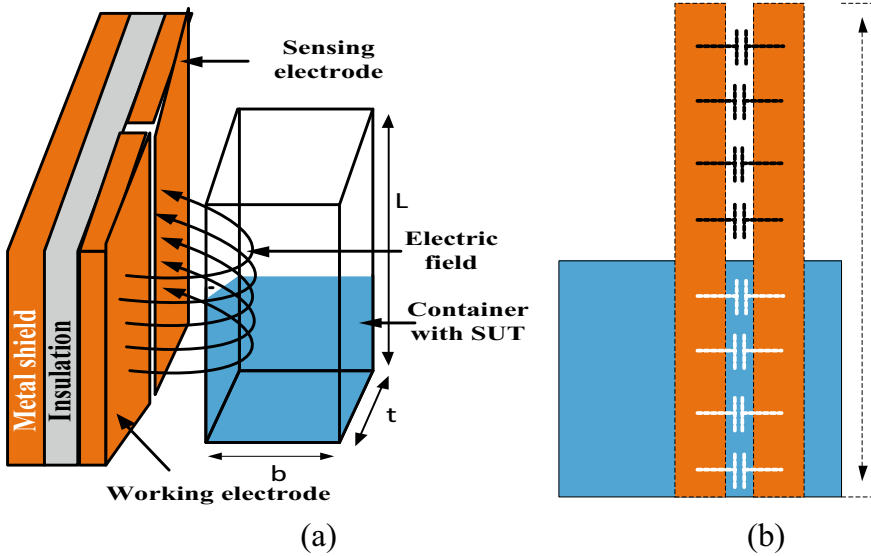


Fig. 5 a Coplanar electrodes separated by gap (g) is attached on the wall of the plastic fibre container with liquid sample, b equivalent capacitance formation

to external influence. For noncontact measurement, the coplanar sensor should be attached on the outer wall of the container but for the destructive measurement, it can be placed on the inner wall. The container is made of plastic fibre or Teflon. This structure can be easily fabricated using double sided copper clad FR4 substrate by electrochemical etching of undesired metal parts. Figure 5b shows the schematic view of pure dielectric liquid level measurement. The part of the electric field passes through the liquid sample and part of the field passes through the air. It is assumed that there is no air gap between the electrodes and the wall of the container. So, two capacitances are formed (i) the capacitance due to liquid level (C_l) and (ii) the capacitance due to air (C_a).

The capacitance value is given by

$$C_T = C_l + C_a, \tag{20}$$

where $C_l \propto H \times \epsilon_0 \epsilon_l$ and $C_a \propto (L - H) \epsilon_a$.

L is the maximum measurable height of the liquid column (electrode), H is the actual liquid height, ϵ_l is the dielectric constant of liquid and ϵ_a is the dielectric constant of air.

If the coplanar structure consists of two fingers as shown in Fig. 1, and the field penetration depth is close to the width of the liquid sample (b), then single capacitance between positive (WE) and negative electrode (SE) is given by (17).

This is to note that if the electrodes are placed on the outer wall of the container, additional capacitance will be formed due to the dielectric constant of the container.

This capacitance value depends on the dielectric constant and thickness of the container. This capacitance will be in series with the capacitance C_T , so efforts will be made to keep its capacitance high in comparison to the capacitance value of C_T . This can be ensured by taking a container with a thin wall.

The coplanar structure with metal guard on the opposite side can be represented by an equivalent circuit shown in Fig. 6. Here, the coplanar structure is made on coplanar cladded FR4 substrate. The IDT can be made on one side of the substrate and the opposite is the metal shield. The coplanar electrodes are exposed to the SUT. When the WE is excited by the electric potential, the electric field penetrates through the sample to the working electrode. If the metal shield is connected to the WE, the field will be directed to the sensing electrode only. The SUT can be approximately represented by an impedance having parallel form of capacitance and resistance. For pure dielectric samples, the impedance is predominantly capacitive. If the metal shield is grounded, then unwanted offset impedances shown in Fig. 6 will be formed at both the WE and SE. This is due to some electric field also penetrating to the back side grounded electrode. If the SE is connected to the inverting input of the Opamp, the offset impedance at the SE will be nullified due to virtual ground potential of the inverting input. The offset impedance at the working electrode is across the input excitation. If the excitation has low input impedance, then offset impedance has negligible effect on the output of the Opamp [26, 27].

If the sensor structure is IDT with N number of fingers with 1-1-1 structure and used for liquid level measurement, the capacitance value can be increased by $(N - 1)$ times of the capacitance having only two coplanar electrodes as shown in Fig. 5a.

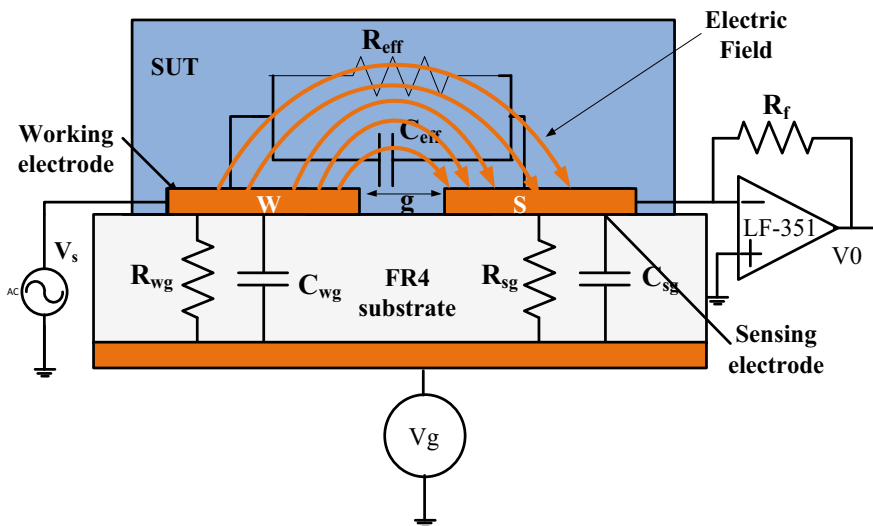
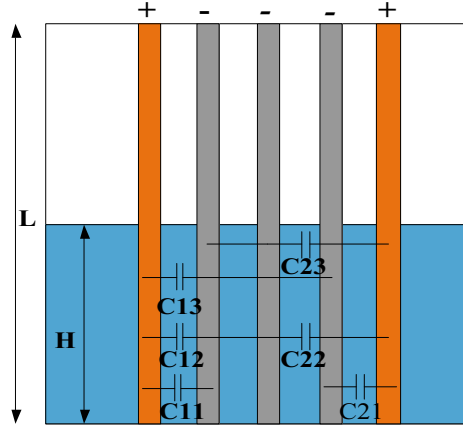


Fig. 6 Equivalent circuit of the coplanar structure with metal shield

Fig. 7 The schematic diagram of the 1-3-1 IDT sensor for liquid level measurement



A. Fringing field Interdigital electrode with unequal working and sending electrodes

Figure 7 shows the schematic diagram of the 1-3-1 IDT structure placed on the outer wall of a plastic container. It has three sensing electrodes (SE) between two working electrodes (WE). When the working electrode is connected to the high potential ac excitation with respect to sensing electrodes, the sensor forms different parallel plate capacitors as shown in the diagram. The fringing electric field is generated from the WE and goes to the SE. The field penetration and the capacitance formation depend on the geometrical configuration of the sensor, the sensing film deposited on the electrode and the strength of the excitation. Since, the geometrical configuration and ac signal do not vary, so the effective capacitance will vary due to the variation of the liquid level [27].

In Fig. 7, the capacitors between WE and SE are connected in parallel. Therefore, the capacitance is function of distance between positive electrode (WE) and negative electrode (SE).

$$C_{12} = \frac{1}{2} C_{11} : \text{-----} . C_{1n} = \frac{1}{n} C_{11} \quad (21)$$

and

$$C_{22} = \frac{1}{2} C_{21} : \text{-----} . C_{2n} = \frac{1}{n} C_{21} \quad (22)$$

where, $C_{11} = C_{21}$: C_{11} is the capacitance between the positive electrode and closest negative electrode.

Therefore, the total equivalent capacitance (C_{eq}) for each sensor's geometry is given by;

$$C_{eq1} = C_{11} + C_{12} + \dots + C_{1n} \quad (23)$$

$$C_{eq2} = C_{21} + C_{22} + \dots + C_{2n} \quad (24)$$

where, C_{eq1} is for equivalent capacitance in the first geometry of each sensor while (C_{2n}) is the equivalent capacitance in the second geometry of each sensor. Since, there may be several working electrodes, total capacitance within sensor geometry is given by;

$$C_{total} = C_{eq1} + C_{eq2} + \dots + C_{eqn} \quad (25)$$

B Design and simulation

The diagram of the interdigitated electrode structure shown in Fig. 7 was designed using finite element software. The simulation study was done using finite element software ANSYS Maxwell 15.0 and its electrostatic solver. The structure 1-5-1, had five sensing electrodes (fingers) between two working electrodes. The maximum length sensor was 35 mm. The width of each finger was 2 mm and the thickness was 25 μ m. The gap between two fingers was 1 mm. The structure was made using FR4 double sided copper clad substrate. The IDT sensor was placed on the outside wall of the acrylic container of 1.5 mm thickness. RO water was considered as a liquid sample for level measurement. Its conductivity was 0.01 siemens. Automatic adaptive mesh refinement technique with triangular mesh grid was used for modelling the structure for better accuracy. The potential difference between the WE and SE was 6.6 V. Figure 8 shows the electric field distribution with and without water in the Vessel. Figure 9 shows the variation of capacitance value with RO water level obtained through simulation results using 1-5-1 sensor. The capacitance values for this sensor increases almost linearly with increase in water level. Similarly, the capacitance value of 1-3-1 sensors increases with increase in water level. The sensors 1-3-1 and 1-5-1 have different slopes and also the initial offset capacitance values are different due to different electrode structure. The sensor 1-5-1 has better sensitivity than the 1-3-1 sensor. Simulation results clearly show that the structure can be useful to measure liquid level noninvasively with almost linear response. The average sensitivity of the level measurement of the 1-5-1 IDT sensor through simulation was 30 fF/mm.

C. Fabrication of the 1-3-1 and 1-5-1 IDT structures

The sensors were fabricated using double sided copper FR4 substrate (Roger) and copper etchant solutions. So, the sensor can be fabricated at low cost in bulk. The interdigitated sensor structure was designed by Auto CAD software. The IDT patterns of 1-3-1 and 1-5-1 were printed using an inkjet printer on the photo paper. The print was then transferred to the copper layer of the PCB using thermal heating press. The exposed part of the copper was then etched out with copper etching solution. The

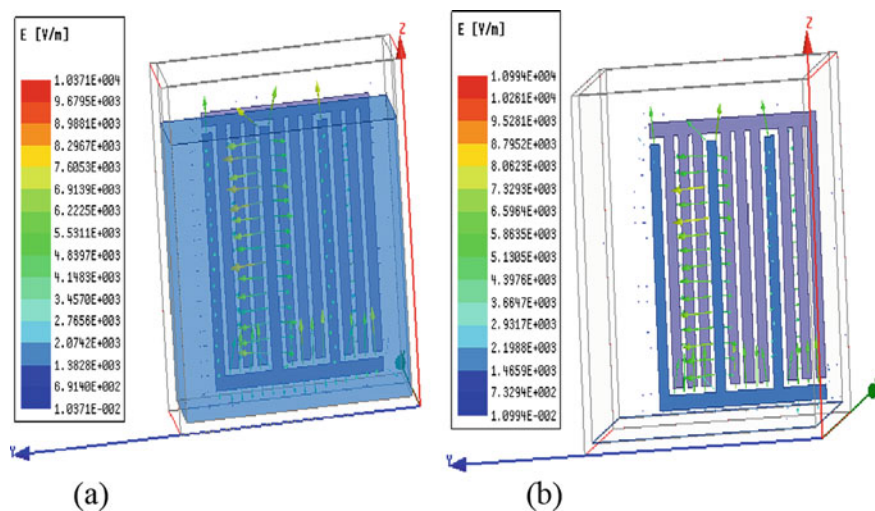


Fig. 8 Electrical field distribution of the sensor in the acrylic tank **a** with water level **b**, without water [27]

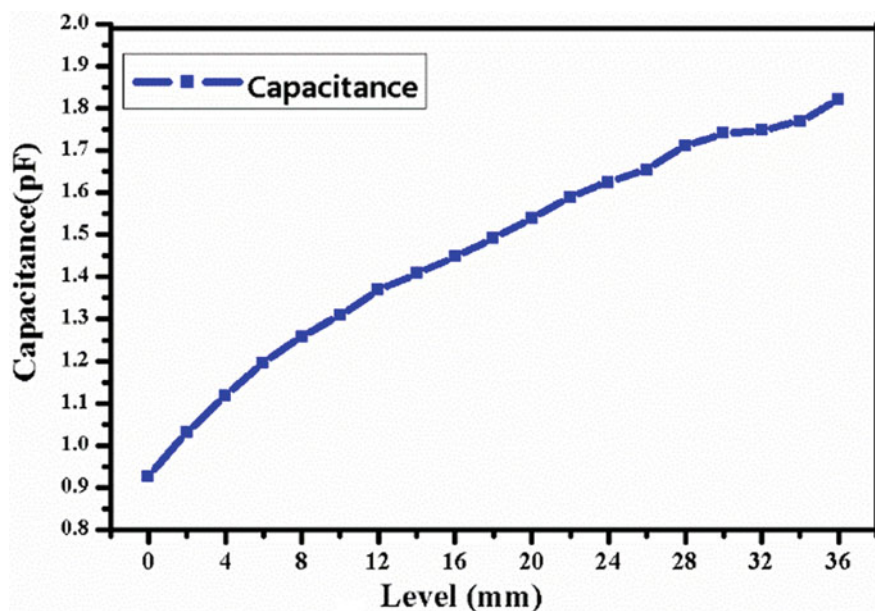


Fig. 9 Change in capacitance values with water level for 1-5-1 sensor

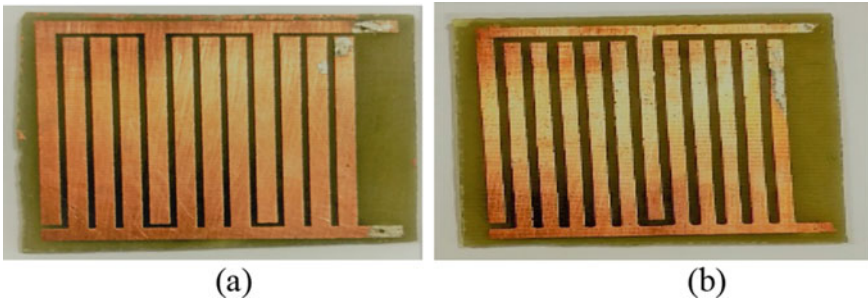


Fig. 10 Fabricated IDT sensors **a**1-3-1 **b** 1-5-1 [27]

substrates were then cleaned thoroughly using acetone, ethyl alcohol and distilled water. The sensors were then dried. Figure 10 shows the photographs of the sensors.

D. *Experimental methods and results*

The capacitance value of the sensor was measured by the capacitance to digital converter evaluation board (FDC1004, Texas Instrument). This board was procured by Texas Instruments. The board can be interfaced to the PC using I²C interfacing to measure the capacitance value digitally. The CDC board has resolution of 0.5 fF, the capacitance range of 0–400 pF. It operates with supply voltage 3.3 V and has operating temperature range of –40–125 °C. The board has the provision of active guarding. The IDT sensor was then pasted on the outer wall of a plastic container, the IDT pattern on the inner side and the copper metal shield on the outer side. The sensor was connected to the board with the help of shielded cable. The photograph of the set up for conducting the experiment is shown in Fig. 11. On another side of the container calibrated scale was fixed to measure the length of the water. The experiment was conducted with the variation of water level in the range of 0–25 mm. Water was poured into the vessel up to a certain height with level marked, the water was allowed to settle for some time to reduce the fluctuation of its level. The capacitance was then measured. Several capacitance values were measured at the same height, the average of the capacitances obtained at that level was noted. Experiments were then repeated for other levels in the range of 0–25 mm. The variation of the capacitance value of 1-5-1 sensor with water level is shown in Fig. 12. The capacitance value increases with increase in water level almost linearly. The sensitivity of the output response is ~40 fF/mm, and the resolution of the water level is ~0.1 mm. Similarly, the experiment was conducted with the 1-3-1 IDT sensor. Results are shown in Fig. 12. Experimental capacitance values of each sensor are linearly fitted. Experimental results show that the capacitance values of both the sensors increase almost linearly with increase in liquid level. However, the capacitance change for the 1-5-1 sensor is maximum. Some mismatch of the reading of the experimental results from simulation may be due to difference in the dielectric property of the water which was selected for simulation and experiential work. There may be some error due to the lead capacitance effect of the sensors which can be minimized by active guarding.

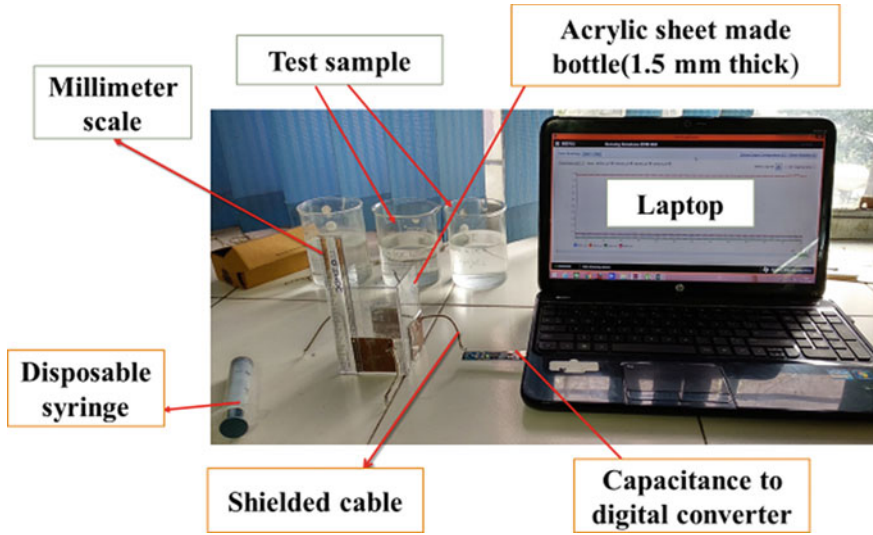


Fig. 11 Test setup for non-contact water level measurement [27]

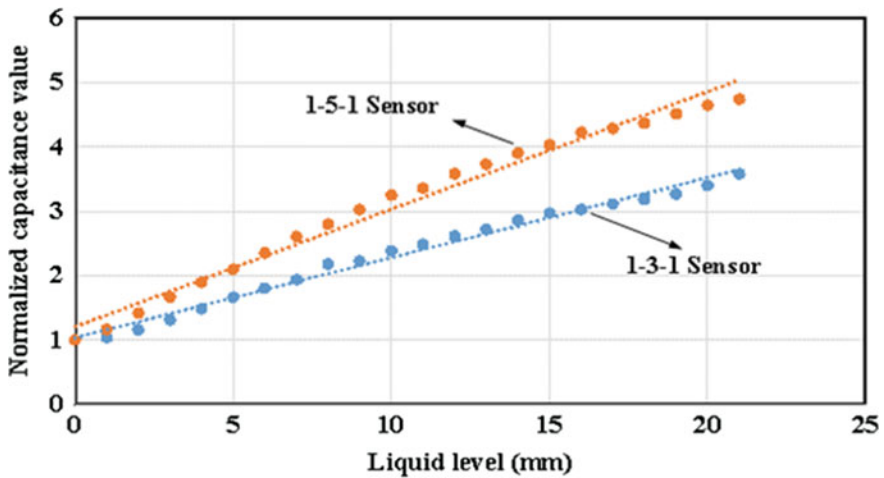


Fig. 12 Variation of the capacitance value with change in water level

5 Conclusions

In this chapter, design of the interdigital capacitive sensors for single side testing of test medium is discussed. Two different IDT structures are studied (i) one having 1-1-1 electrode structure and (ii) the other one is having 1-n-1 structure, where n is number of sensing electrodes between two working electrodes. The attractive features of the IDT sensors are simple fabrication, and suitability for non-destructive measurement

of physical or chemical parameters. However, finding the exact expression of capacitance value is difficult. Although the expression of parallel plate capacitor is used for the determination of the capacitance value of the IDT sensor, it is too simple to match the experimental results. Effort is made to find the expression of capacitance using conformal mapping technique. Two applications of physical parameters measurement of the IDT sensors are investigated in detail. Numerous applications of this sensor for pure and lossy dielectric are possible. The capacitive sensor needs extra precautions to avoid the errors due to stray effects, particularly for the low capacitance measurement. The sensor should be properly guarded to avoid the influence of external capacitance.

References

1. R.B. McIntosh, M.E. Casada, Fringing field capacitance sensor for measuring the moisture content of agricultural commodities. *IEEE Sens. J.* **8**(3), 240–247 (2008)
2. J. Mizuguchi, J.C. Piai, J.A. de França, M.B. de Moraes França, K. Yamashita, L. Carlos Mathias, Fringing field capacitive sensor for measuring soil water content: design, manufacture, and testing. *IEEE Trans. Instrum. Meas.* **64**(1), 212–219 (2014)
3. J.Z. Chen, A.A. Darhuber, S.M. Troain, S. Wagnern, *Lab on Chip*, vol. 4 (2004), pp. 473–480
4. C. Elbuken, T. Glawdel, D. Chan, C.L. Ren, Detection of microdroplet size and speed using capacitive sensors. *Sens. Actuators A: Phys.* **171**, 55–62 (2011)
5. A.A. Nassr, W.H. Ahmed, W.W. El-Dakhakhni, Coplanar capacitance sensors for detecting water intrusion in composite structures. *Meas. Sci. Technol.* **19**, 075702–075709 (2008)
6. R.N. Dean, A.K. Rane, M.E. Baginski, J. Richard, Z. Hartzog, D. Elton, A capacitive fringing field sensor design for moisture measurement based on printed circuit board technology. *IEEE Trans. Instrum. Meas.* **61**(4), 1105–1112 (2012)
7. T. Islam, M.Z. Rahman, Investigation of the electrical characteristics on measurement frequency of a thin-film ceramic humidity sensor. *IEEE Trans. Instrum. Meas.* **65**(3), 694–702 (2016)
8. A.I. Zia, M.S.A. Rahman, S.C. Mukhopadhyay et al., Technique for rapid detection of phthalates in water and beverages. *J. Food Eng.* **116**, 515–523 (2013)
9. K. Chetpattananondh, T. Tapoanoi, P. Phukpattaranont, N. Jindapetch, A self-calibration water level measurement using an interdigital capacitive sensor. *Sens. Actuators, A* **209**, 175–182 (2014)
10. N. Afsarimanesh, S.C. Mukhopadhyay, M. Kruger, Performance assessment of interdigital sensor for varied coating thicknesses to detect CTX-I. *IEEE Sens. J.* **18**(10), 3524–3531 (2018)
11. A. Nag, M.E. Alahi., S. Feng, S.C. Mukhopadhyay, IoT-based sensing system for phosphate detection using Graphite/PDMS sensors. *Sens. Actuators A: Phys.* **286**, 43–50 (2019)
12. Md.E. Alahi, N.P. Ishak, S.C. Mukhopadhyay, L. Burkitt, An internet-of-things enabled smart sensing system for nitrate monitoring. *IEEE Int. Things J.* **5**(6), 4409–4417 (2018). S. Nag, S. Feng, C. Mukhopadhyay, J. Kosel, D. Inglis, 3-D printed mould-based Graphite/PDMS sensor for low force applications. *Sens. Actuators A: Phys.* **280**, 525–534 (2018)
13. M.B. Nag, S.C. Mukhopadhyay, Performance analysis of flexible printed sensors for robotic arm applications. *Sens. Actuators A: Phys.* **276**, 226–236 (2018)
14. A. Nag, N. Afsarimanesh, S.C. Mukhopadhyay, Impedimetric microsensors for biomedical applications. *Curr. Opin. Biomed. Eng.* **9**, 1–7 (2019)
15. R. Mohd Syaifudin, S.C. Mukhopadhyay, P.L. Yu, Modelling and fabrication of optimum structure of novel interdigital sensors for food inspection. *Numer. Model.: Electr. Netw. Dev. Fields* **25**(1), 64–81 (2012)

16. T. Islam, S.C. Mukhopadhyay, N.K. Suryadevara, Smart sensors and internet of things: a postgraduate paper. *IEEE Sens. J.* **17**(3), 577–588 (IF:2.512) (2017)
17. R. Igreja, C.J. Dias, Analytical evaluation of the interdigital electrodes capacitance for a multi-layered structure. *Sens. Actuators A: Phys.* **112**(2–3), 291–301 (2004)
18. X.B. Li, S.D. Larson, A.S. Zyuzin, A.V. Mamishev, Design principles for multichannel fringing electric field sensors. *IEEE Sen. J.* **6**(2), 434–440 (2006)
19. S. Ramo, J.R. Whinnery, T. Van Duzer, *Fields and Waves in Communication Electronics* (J. Wiley & Sons, New York, 1994).
20. Z.M. Rittersma, Recent achievements in miniaturised humidity sensors—a review of transduction techniques. *Sens. Actuators, A* **96**, 196–210 (2002)
21. T. Islam, A.T. Nimal, U. Mittal, M.U. Sharma, A micro interdigitated thin film metal oxide capacitive sensor for measuring moisture in the range of 175–625 ppm. *Sens. Actuators B: Chem.* **221**, 357–364 (2015)
22. E. Yoldas, Design of sol-gel coating media for ink-jet printing. *J. Sol-Gel Sci. Technol.* **13**(1), 147–152 (1998)
23. Md.R. Mahboob, Z.H. Zargar, T. Islam, A sensitive and highly linear capacitive thin film sensor for trace moisture measurement in gases. *Sens. Actuators B: Chem.* **228**, 658–664 (2016)
24. H. Wang, L. Pilon, Intrinsic limitations of impedance measurements in determining electric double layer capacitances. *Electrochim. Acta* **63**, 55–63 (2012)
25. A.V. Mamishev, K.S. Rajan, F. Young, Y. Du, M Zahn. *Proc. IEEE* **92**(5), 808–845 (2004)
26. T. Islam, S.C. Mukhopadhyay, Wearable sensors for physiological parameters measurement: physics, characteristics, design and applications, in *Wearable Sensors: Applications, Design and Implementation*, ed. by S.C. Mukhopadhyay, T. Islam (Institute of Physics (IOP), Publishing, Bristol, UK, 2017), pp. 1–31
27. T. Islam, O.P. Maurya, Design and fabrication of non-contact fringing field capacitive sensor for liquid level measurement, in *2019 IEEE 16th India Council International Conference* (Marwadi University, Rajkot, IEEE Explore) 978–1–7281–2327–1/19/\$31.00 ©2019 IEEE

Optimization of Interdigitated Sensor Characteristics



J. Claudel, A. L. Alves de Araujo, D. Kourtiche, M. Nadi, and A. Bourjilat

Abstract Interdigitated sensors for bioimpedance analysis (BIA) are specially adapted for the characterization of low-volume (microliter scale) biological samples and the monitoring of a thin-film of biological cells for cell culture or cell settling and coagulation analysis. Impedance spectroscopy has the advantage of being a marker-free method (a combined impedance and marker is also possible), which considerably simplifies the preparation of samples. The geometry of the interdigitated sensor simultaneously represents microscopic sizes as the electrodes' width, gap, and millimetric surface, making the sample deposition easier. The microscopic size of the electrodes induces an increase in double-layer effects, which can completely occult interesting bandwidth of the impedance measurements. This effect, therefore, must be considered early in the sensor optimization design. In this work, we propose a complete approach to optimize interdigitated sensors according to targeted applications. A complete analytical model is proposed and validated with a finite element method simulation using COMSOL Multiphysics software. The model examines the influence of all geometrical parameters, such as number of electrodes, width, gap, and substrate material. A detailed methodology is proposed to choose the best compromise between sensitivity and useful bandwidth. To validate the proposed methodology, measurements were performed on biological samples (yeast cells) using five sensors with different optimized geometries. Results demonstrated the validity of the proposed methodology and the possibility to extract all the intrinsic electrical parameters of the biological samples using both optimized sensors and our models.

J. Claudel · A. L. Alves de Araujo · D. Kourtiche · M. Nadi (✉) · A. Bourjilat
Institut Jean Lamour, Lorraine University (CNRS—UMR 7198), 54011 Nancy, France
e-mail: mustapha.nadi@univ-lorraine.fr

J. Claudel
e-mail: julien.claudel@univ-lorraine.fr

© The Editor(s) (if applicable) and The Author(s), under exclusive license to Springer Nature Switzerland AG 2021

S. C. Mukhopadhyay et al. (eds.), *Interdigital Sensors*, Smart Sensors, Measurement and Instrumentation 36, https://doi.org/10.1007/978-3-030-62684-6_5

1 Introduction

Since the invention of Clark's electrode oxygen sensor (1956) [1], many improvements in the sensitivity, selectivity, and multiplexing of biosensors (Lab-on-chip) have emerged. Biosensors can be defined as a compact analytical device incorporating a biological detection element associated with a physicochemical transducer [2]. These methods are often based on charge transfer sensors, impedance-based sensors, and capacitance-based sensors. Impedance spectroscopy is now well known as a powerful technique for biological sensing characterization at both macroscopic and microscopic scales [3]. Electrodes serve for applying an electric field to the sample under test and for measuring the electrical detection signals. They also can provide information on relative permittivity and electrical conductivity of the biosamples, which correspond to intrinsic parameters [4]. At the macroscopic scale, impedance sensors are generally composed of two parallel plates where the sample is enclosed. They are easy to use but need a large quantity of biosamples (few to tens of mL). Moreover, electrodes only provide average information about the whole sample. On the contrary, the combination of impedance spectroscopy and microscopic electrodes, such as interdigitated sensors [5], provides more sensitive sensors that can analyze, at the microscopic scale, cell surface cultures [6], cell settling, and trapped bacteria, as well as detecting DNA oligonucleotides [7]. Beyond a simple interface, the geometrical properties of electrodes can have a significant impact on the efficiency of the biosensor [8, 9]. They need to be optimized a priori during the sensors' design step according to the targeted application and the nature of the cells to analyze [10, 11]. To achieve this optimization of the sensor design, we present a detailed methodology to define the best interdigitated structure according to the targeted application.

In the first section, a complete and detailed analytical model is presented. The model considers all the sensor's parameters, such as the electrode length, gap, width, and electrical properties of the medium. Moreover, it accounts for double-layer effects. The model is based on the impedance model of a pair of electrodes, extended to a succession of electrodes, and considering edge effects. The model was validated using simulation by the finite element method (FEM).

In the following section, "Interdigitated sensor optimization," the effects of all geometrical parameters were tested independently to determine their impact on bioimpedance measurements. One important purpose is to maintain a sufficiently wide bandwidth to characterize the biosample over many decades. To obtain the correct optimization, which consists of the best compromise between bandwidth and sensitivity, a detailed optimization methodology is presented. A step-by-step description appears at the end of this section.

The last section focuses on the experimental validation of the two previous sections. Five sensor designs with different degrees of optimization were fabricated using a classical microfabrication process. Characterizations were performed on calibrated electrolytic solutions and yeast cells samples by a conventional macroscopic probe and compared to the measurement performed with fabricated sensors.

2 Analytical Method

2.1 Coplanar Electrodes

Interdigitated electrodes are based on a succession of coplanar microelectrodes. The first step is to model the electrical response, which depends on the electric field distribution between a pair of coplanar electrodes. This pair of electrodes is assumed to be an electric capacitor. For standard parallel capacitors, electrodes are placed face-to-face with a uniform distribution of the electric field. When electrodes are gradually opened, the electric field extends in a wider space and generates a fringing field. However, if the electrodes open on a planar plane, the fringing field becomes heterogeneously allocated between the electrodes, and one obtains a coplanar electrode sensor [12]. Figure 1 illustrates the evolution from a parallel plate capacitor to a coplanar electrodes' sensor.

A simplified analysis for calculating the capacity of a pair of semi-infinite electrodes is first used to introduce two important design quantities, namely the penetration depth of the field \mathbf{T} and the effective width of electrodes \mathbf{W}_{eff} . The two-dimensional distribution of the electric field for this geometry can easily be solved with conformal mapping techniques using an inverse cosine transform [13]. For semi-finished electrodes, the capacity of a pair of finite-width electrodes w and gap g can be calculated as follows:

$$C = \frac{Q}{2V_0} = \frac{2\epsilon_0\epsilon_r L}{\pi} \ln \left[\sqrt{\left(1 + \frac{w}{a}\right)^2 - 1} + \left(1 + \frac{w}{a}\right) \right] \quad (1)$$

where \mathbf{Q} is the total charge of a single electrode, ϵ_0 the permittivity of the vacuum, \mathbf{L} is the length of the electrodes and $\mathbf{a} = \mathbf{g}/2$. For $\mathbf{L} \gg \mathbf{w}$, Eq. (1) provides a reliable estimation of the capacity for a pair of coplanar electrodes with finite width ($\mathbf{w}/\mathbf{g} \gg 1$). The electrode's width \mathbf{w} establishes a maximum field penetration depth \mathbf{T} in a medium whose thickness is labeled by \mathbf{h}_{med} . The penetration depth is calculated from the elliptic contours, which correspond to the intensity of the field at a fixed position $r = (x^2 + y^2)^{-1/2}$. \mathbf{T} corresponds to the vertical displacement of the electric

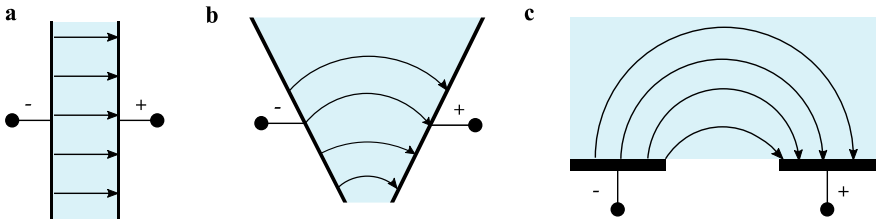


Fig. 1 Transition of a parallel to a coplanar electrode capacitor. **a** Parallel electrode sensor, **b** open transition, and **c** coplanar electrode capacitor

field line issued from the end of the electrode and can be calculated as follows:

$$T = a \sinh \left[\cosh^{-1} \left(1 + \frac{w}{a} \right) \right] = a \sqrt{\left(1 + \frac{w}{a} \right)^2 - 1} \quad (2)$$

For a medium whose thickness $\mathbf{h}_{\text{med}} < \mathbf{T}$, the capacitance is determined only by the electric field lines emanating from the effective width \mathbf{W}_{eff} , as shown in Eq. (3).

$$\frac{w_{\text{eff}}}{a} = a \sqrt{\left(1 + \frac{h_{\text{med}}}{a} \right)^2 - 1} \quad (3)$$

This concept of effective width is only applicable when the permittivity of the dielectric environment is higher than that of the air. This is the case for water-based solutions. The ratio $\mathbf{h}_{\text{med}}/\mathbf{T}$ can be used as an approximate indicator of the signal detection level for this electrode geometry. When $\mathbf{h}_{\text{med}} \gg \mathbf{T}$, the capacity does not depend on the sample thickness. This is confirmed by analytical simulations, as shown in Fig. 2, for coplanar electrodes with parameters $\mathbf{T} = 4.17 \mu\text{m}$. The impact of the distance between the electrode and the edge of the sample \mathbf{g}_h is also examined. For $\mathbf{g}_h \geq 0.5 \times \mathbf{h}_{\text{med}}$, we notice that the capacity is maximal with a constant value. Furthermore, when $\mathbf{g}_h > \mathbf{T}$, \mathbf{g}_h has no more impact on the electrodes' capacitance.

Simulations confirm that Eq. (3) can be used as an approximation for the capacitance and allow for determining an optimal thickness for the two electrodes.

The maximum capacitive signal can be obtained by minimizing the gap \mathbf{g} while modeling electrodes, the width of which is comparable to the thickness of the solution. In opposition to parallel plates capacitors, the capacitance does not increase in proportion to w/a , but proportionally to $\ln(w/a)$.

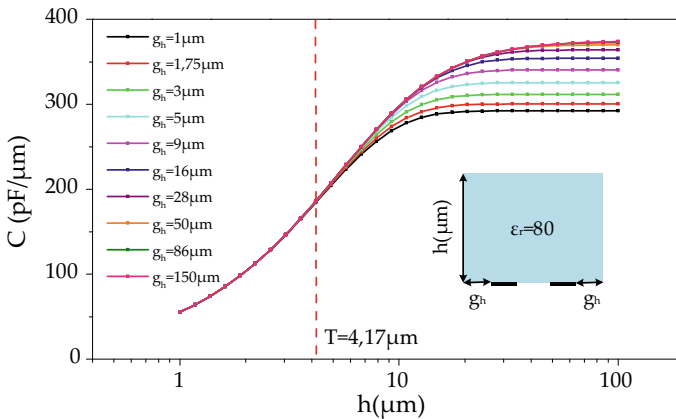


Fig. 2 Capacitance as a function of \mathbf{h}_{med} and \mathbf{g}_h

2.2 Interdigitated Electrode Modeling

2.2.1 Semi-layer Capacitance Calculation

The analytical study of interdigitated electrodes allows for determining the essential geometrical parameters for optimization and how they influence the response of the biosensor. The structure of coplanar interdigitated electrodes is given in Fig. 3a. It can be considered as the concatenation of unitary symmetric coplanar electrodes forming fingers. These fingers have the same width w and are separated by an interval g . The length L is generally large enough to neglect the side effect of the electric field.

The capacitance of unitary cells (C_I/C_E) can be expressed according to $k^{c_{cell}}$, the unit cell factor. $k^{c_{cell}}$ depends on three parameters: the metalization ratio η , the periodicity of electrodes λ [14], and the ratio of height/width r defined by Eqs. (4) and (5). The parameter λ depends on w and g .

$$\eta = \frac{w}{w + g} = \frac{2w}{\lambda} \tag{4}$$

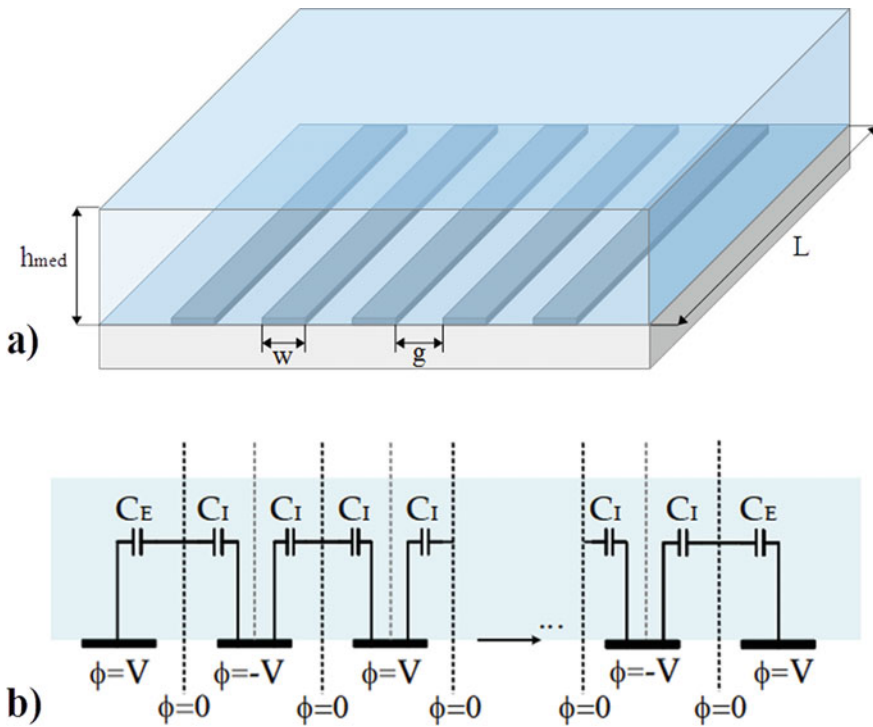


Fig. 3 Diagram of interdigitated electrodes

$$r = \frac{2h_{med}}{w + g} \quad (5)$$

Using corresponding techniques of a conformal map (or angle-preserving), one can determine the internal and external capacitances of coplanar electrodes [15]. The equivalent electrical circuit for a configuration of \mathbf{N} electrodes is shown in Fig. 3b. To simplify the model, we assume that the electrodes are sufficiently long to maintain a relatively constant electric field along the electrodes. Therefore, the capacitance of a single layer could be considered to be the association of two capacities: \mathbf{C}_I , which is the half-capacitance between the internal electrode and the reference ($\mathbf{V}_{ref} = 0$), and \mathbf{C}_E , which is the capacitance between an external electrode and the substrate. The total capacitance of a single layer is thus given by:

$$C = (N - 3) \frac{C_I}{2} + 2 \frac{C_I C_E}{C_I + C_E} \quad (6)$$

If $\mathbf{N} < 4$, the capacitance of a two-cell structure becomes $\mathbf{C} = \mathbf{C}_E/2$. \mathbf{C}_I and \mathbf{C}_E can be calculated as follows.

$$C/L = \varepsilon_0 \varepsilon_{r,med} K_{cell}(\eta, h_{med}) \quad (7)$$

where ε_0 is the vacuum permittivity, $\varepsilon_{r,med}$ the relative permittivity of the sample medium, and \mathbf{k}^c_{cell} is the geometric factor. \mathbf{k}^c_{cell} can be calculated in the case of coplanar electrode configuration using Jacobi's elliptic equations [12], as shown in Table 1. This technique uses the method of partial capacitances for a multilayer dielectric material with the calculation of partial parallel capacitance (PPC) and partial series capacitance (PSC) for each layer. In the case of a semi-infinite layer ($\mathbf{h}_{med} \gg \mathbf{T}$), as here, the model is simpler and consists of calculating only one capacitance.

To verify the analytical expression of the capacitance for interdigitated electrodes, simulations were performed using FEM with COMSOL Multiphysics software and AC/DC modules. The capacitance (\mathbf{C}) is determined as follows: $\mathbf{C} = \mathbf{Q}/\mathbf{V}$ (where \mathbf{Q} is the electric charge and \mathbf{V} the electric potential). Three sets of simulations were done, and results are given in Fig. 4a–c.

First, simulations were performed by varying $\varepsilon_{r,med}$ from 1 to 100, for two numbers of electrodes ($\mathbf{N} = 10$ and 20) by keeping η to 0.5. They were performed considering a semi-infinite layer: $\mathbf{h}_{med} \rightarrow \infty$ for analytical models and $\mathbf{h}_{med} \gg \mathbf{T}$ for FEM simulations.

Second, simulations were performed by varying the electrodes' periodicity λ for 8 layer heights by keeping η to 0.5, $\varepsilon_{r,med}$ to 80, and using the semi-finite \mathbf{k}^c_{cell} coefficient. These results demonstrate that the impact of the sample height can be neglected if it is at least two times higher than the electrodes' periodicity. Ninety-nine percent of the injected signal power is concentrated in the first 2λ depth. This property allows for controlling the penetration depth of the electric field of interdigitated electrodes by fixing λ .

Table 1 K_{cell}^c equations for a semi-infinite and semi-finite layer

	C_I	C_E
	PSC	PSC
	PPC	PPC
$h < \infty$	$k_{cell}^c = \frac{K(k_{I,CPS'})}{K(k_{I,CPS})}$ $k_{I,CPS} = t_2$	$k_{cell}^c = \frac{K(k_{E,CPS})}{K(k_{E,CPS'})}$ $k_{E,CPS} = \sqrt{\frac{(t_4 - t_3)}{(t_4 - 1)}}$
	$k_{cell}^c = \frac{K(k_{I,PPC'})}{K(k_{I,PPC})}$ $k_{I,PPC} = \sqrt{\frac{(t_2^2 - 1)}{(t_4^2 - t_2^2)}}$	$k_{cell}^c = \frac{K(k_{E,PPC'})}{K(k_{E,PPC})}$ $k_{E,PPC} = \frac{1}{t_3} \sqrt{\frac{(t_2^2 - t_3^2)}{(t_4^2 - 1)}}$
	$t_2 = sn(K(k_1)(2\eta - 1), k_1')$ $t_4 = \frac{1}{k_1}$ $k_1 = \left(\frac{\vartheta_2(0,q)}{\vartheta_1(0,q)}\right)^2$ $k_1' = \sqrt{1 - k_1^2}, q = e^{-2\pi r}$	$t_4 = \cosh\left(\frac{\pi(1+\eta)}{4r}\right)$ $t_3 = \cosh\left(\frac{\pi(1-\eta)}{4r}\right)$ $k_{E,CPS/PPC'} = \sqrt{1 - k_E^2}$
$h = \infty$	$k_{cell}^c = \frac{K(k')}{K(k)}$ $k = \sin\left(\frac{\pi}{2}\eta\right)$ $k' = \sqrt{1 - k^2}$	$k_{cell}^c = \frac{K(k)}{K(k)}$ $k = \frac{2\sqrt{\pi}}{1+\pi}$ $k' = \sqrt{1 - k^2}$

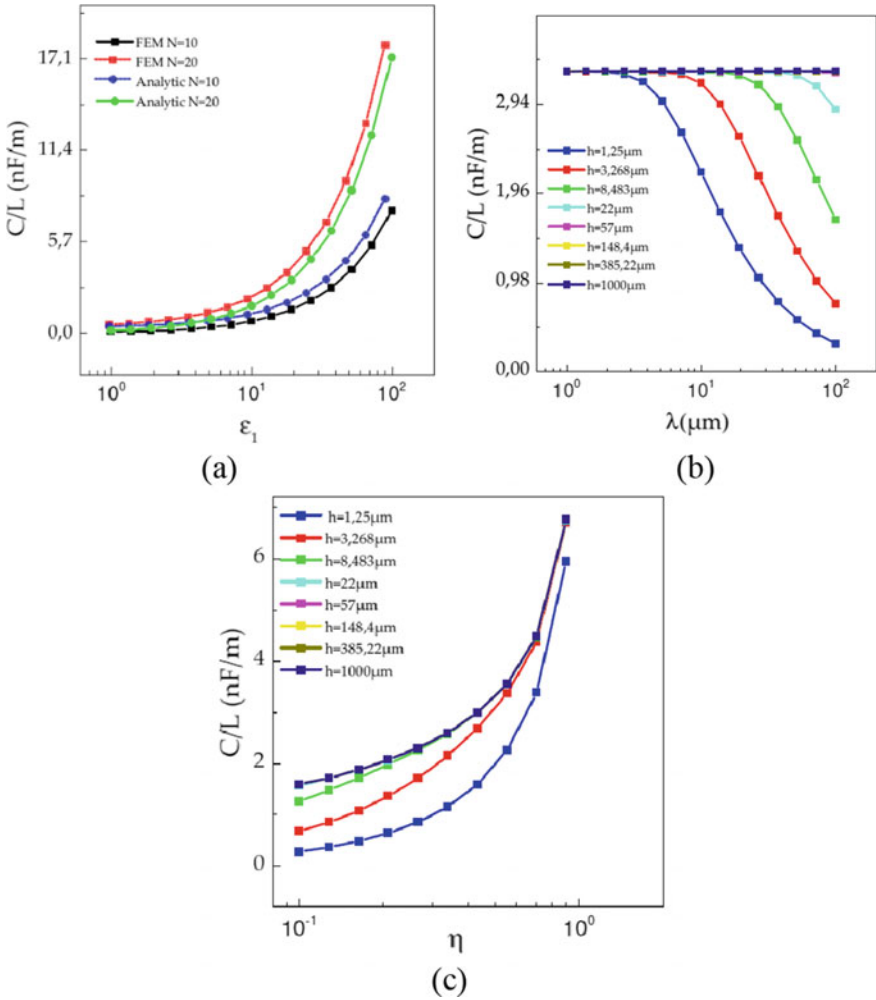


Fig. 4 FEM and analytical evaluation of linear capacitance (C/L) as a function of **a** the relative permittivity of the sample $\epsilon_{r,med}$, **b** electrode periodicity λ , and **c** the metalization ratio η

The third set of simulations was performed by varying the metalization ratio η from 0.1 to 0.9 for 8 layer heights by keeping $\epsilon_{r,med}$ to 80. Capacitance increases with η , which can be explained by the increase of electrode surfaces and the decrease in the gap between the electrodes. For a higher value of η , the impact of the sample thickness becomes less significant due to the decreasing of \mathbf{W}_{eff} , reducing the penetration depth \mathbf{T} at the same time.

2.2.2 Two-Layer Capacitance Calculations

In real interdigitated sensors, the capacitive effect appears not only in the sample direction but also in the substrate. The total capacitance is composed of the addition of sample capacitance (or air in case of open measurement without samples) and the substrate capacitance. The impact of this capacitance must be considered and evaluated. Its calculation is similar to the sample calculation using $\mathbf{K}_{\text{cell}}^c$ factors. \mathbf{K}_{cell} is the geometrical sensor factor, which depends on the unitary $\mathbf{K}_{\text{cell}}^c$ factors and the number of electrodes. The substrate thickness is generally high compared to λ , and the equation for a semi-infinite medium is used. To analyze the impact of the substrate, analytical simulations were performed using Eqs. (8) to (10) with the following parameters: $\epsilon_{r,\text{substrate}} = 4.07$ (relative permittivity of the glass), $\epsilon_{r,\text{air}} = 1$, $\epsilon_{r,\text{sample}} = 80$ (relative permittivity of pure water), $\eta = 0.5$, $w = 3 \mu\text{m}$, $h_{\text{substrate}} = 1 \text{ mm}$, $L = 1 \text{ mm}$ and $h_{\text{med}} = 1 \text{ mm}$. Results are presented in Fig. 5 for air and the sample.

In the case of an open configuration (without a sample), the impact of the substrate capacitance is higher than the effect of the sensing side. If the ratio of relative permittivity between the sample and the substrate is high, the contribution of the substrate stays small, as shown in Fig. 5b. That is why a low-permittivity substrate is more suitable for impedance-based sensors. For example, a silicon substrate has a relative permittivity approximately two to three times higher than glass substrates.

$$C_{\text{substrate}} = (\epsilon_0 \epsilon_{r,\text{substrate}}) \times \left[\left((N-3) \frac{C_I}{2} \right) \times \left(\frac{2C_I C_E}{C_I + C_E} \right) \right] \quad (8)$$

$$C_{\text{sample}} = (\epsilon_0 \epsilon_{r,\text{sample}}) \times \left[\left((N-3) \frac{C_I}{2} \right) \times \left(\frac{2C_I C_E}{C_I + C_E} \right) \right] \quad (9)$$

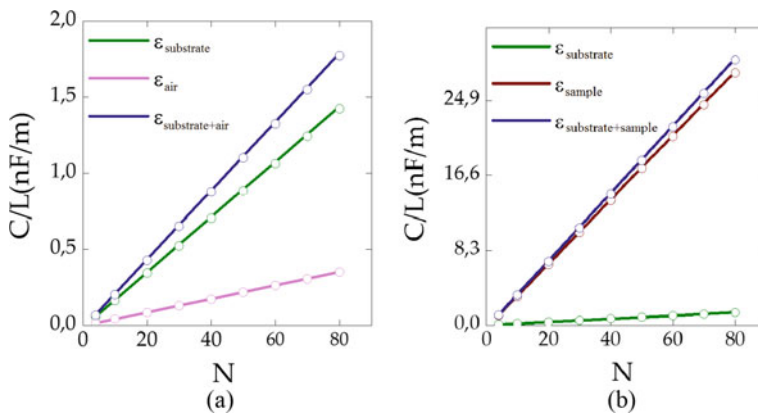


Fig. 5 Impact of the relative substrate permittivity on the global capacitance for a glass substrate **a** without a sample, and **b** with a water-based sample

$$C_{substrate+sample} = (\varepsilon_0(\varepsilon_{r,substrate} + \varepsilon_{r,sample})) \times \left[\left((N-3) \frac{C_I}{2} \right) \times \left(\frac{2C_I C_E}{C_I + C_E} \right) \right] \quad (10)$$

2.2.3 R//C Equivalent Model for Liquid Samples

As biological samples are mainly composed of water, impedance data is commonly analyzed using an **R//C** parallel-based equivalent circuit as a reference. \mathbf{R}_{med} and \mathbf{C}_{med} parameters represent the effects of electrical conductivity and electrical permittivity of the sample medium, respectively. The capacitances of the previous analytical model (upper layer) are now replaced by impedance (or admittance) of the sample medium using Eqs. (11) to (13). The factor \mathbf{K}_{cell} remains the same as before.

$$\underline{Y}_{med} = G_{med} + jB_{med} = \frac{1}{R_{med}} + j\omega C_{med} \quad (11)$$

with

$$C/L = \varepsilon_0 \varepsilon_{r,med} K_{cell} \quad (12)$$

$$R_{med} \times L = \frac{1}{\sigma_{med} K_{cell}} \quad (13)$$

This model presents a cutoff frequency $\mathbf{f}_{c,HF}$, due to the couple $\mathbf{R}_{med} // \mathbf{C}_{med}$. According to Eqs. (12) and (13), $\mathbf{f}_{c,HF}$ does not depend on the electrode geometry but only on the electric and dielectric properties of the sample, as calculated in Eq. (14).

$$f_c = \frac{1}{2\pi RC} = \frac{\sigma_{med}}{2\pi \varepsilon_{med}} \quad (14)$$

To prove this assumption, both analytical and FEM simulations were made with the same sample for two different interdigitated electrode sensors (\mathbf{C}_{S1} and \mathbf{C}_{S2}) with the geometrical parameters resumed in Table 2.

These two sensors were simulated in the presence of a solution (modeled by a parallel piped rectangle) of a semi-infinite thickness, with an electrical conductivity

Table 2 Geometrical parameters for sensors \mathbf{C}_{S1} and \mathbf{C}_{S2}

	N	η	w (μm)	g (μm)	\mathbf{K}_{cell} (m^{-1})
\mathbf{C}_{S1}	40	0.5	3	3	0.97
\mathbf{C}_{S2}	40	0.6	30	20	1.1561

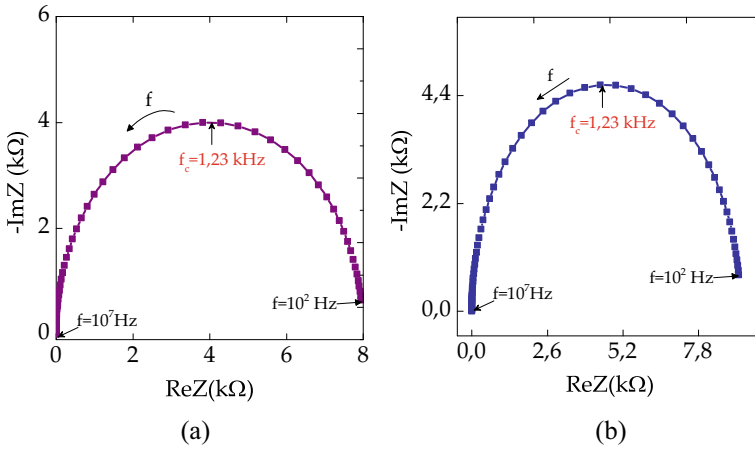


Fig. 6 Nyquist and Bode diagram for simulated sensors C_{S1} and C_{S2} with analytical models (lines) and FEM (rectangles)

of $1 \mu\text{S}/\text{cm}$ and a relative permittivity of 80. Figure 6a and b represent the Nyquist diagram for C_{S1} and C_{S2} sensors, respectively. The Figures demonstrate that the cutoff frequency does not vary for the two geometries: $f_{c,\text{HF}} = 1.23 \text{ kHz}$. One can see that the analytical model provides results that are in perfect cohesion with the FEM simulation results.

2.2.4 Electrical Double Layer

When a metal electrode is immersed in an electrolyte, a double layer is formed at the interface between the electrode and the electrolyte. As is well known, the double layer acts as a barrier for measurements at low frequencies ($<1 \text{ MHz}$). Thus, the determination of its thickness is a paramount parameter. Double layer effects allow us to evaluate the measurement band, optimize the geometrical parameters, and correctly determine the global equivalent circuit model.

The double-layer capacitance is composed of several contributions and is generally represented by the compact layer of “Helmholtz” or “Stern” [16, 17]. Its structure is completed by a “diffusion” layer, composed of electrostatically attracted elements at a distance from the surface of the electrode. The total thickness of the double layer can be defined as the outer limit of the “diffusion” layer that separates it from the solution [18, 19].

The thickness of the double layer induces an electrochemical potential difference between the solution and the electrode. The total capacitance of the double layer C_{DL} is composed of a combination of the compact layer capacitance of Helmholtz (C_{H}) and the diffusion layer capacitance (C_{D}), which can be calculated using Eqs. (15) to (18).

$$\frac{1}{C_{DL}} = \frac{1}{C_H} + \frac{1}{C_D} \tag{15}$$

with

$$C_H = \frac{\epsilon_0 \epsilon_r}{L_H} \tag{16}$$

$$C_D = \frac{\epsilon_0 \epsilon_r}{\lambda_{DEBYE}} \cosh\left(\frac{zeV}{4K_B T}\right) C_D \approx \frac{\epsilon_0 \epsilon_r}{1.5\kappa^{-1}} \tag{17}$$

$$\kappa^{-1} = \sqrt{\frac{\epsilon_0 \epsilon_r K_B T}{2 \times 10^3 n_j z_j^2 e^2}} \tag{18}$$

where λ_D represents the Debye length, K_B the Boltzmann constant, T the absolute temperature, z_j the charge amplitude of each “j” ion, e the elementary charge, and n_j the molar concentration of each “j” ion. This phenomenon (the formation of an electric double layer) occurs on each electrode. One can see this in the model shown in Fig. 7, which gives an equivalent circuit for an interdigitated structure and an example of an equivalent circuit for $N = 4$. R_E and R_I represent the conductive effects of the medium on each interior and exterior electrode.

The total impedance of the equivalent circuit shown in Fig. 7 can be calculated as follows, using Eqs. (19) to (23):

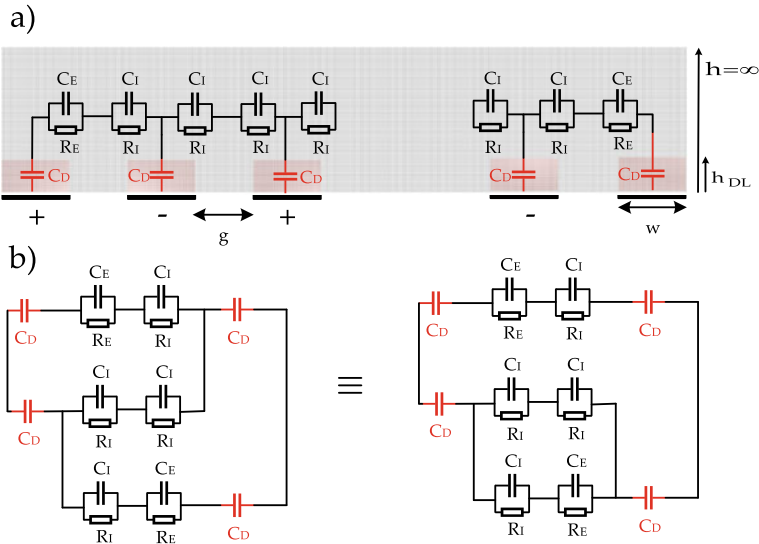


Fig. 7 **a** Electrical equivalent circuit for the interdigitated structure of N electrodes, and **b** an example of four electrodes

$$Y_T = \frac{1}{Z_{i1}} + \frac{(N/2) - 1}{Z_{i,\text{sup}}} + \frac{N - 1}{Z_L} \quad (19)$$

With

$$Z_{i1} = Z_i + 2Z_{DL,i} \quad (20)$$

$$Z_{i,\text{sup}} = \frac{Z_i}{2} + 2Z_{DL,i} \quad (21)$$

$$Z_L = Z_{Sol,L} + 2Z_{DL,L} \quad (22)$$

$$Z_{DL,i} = \frac{1}{j\omega C_{DL,i}}; Z_i = \frac{2R_i}{1 + j\omega R_i C_i}; Z_{DL,L} = \frac{1}{j\omega C_{DL,L}}; Z_{Sol,L} = \frac{R_{sol,L}}{1 + j\omega R_{sol,L} C_{sol,L}} \quad (23)$$

When $\omega \rightarrow 0$ (at very low frequencies):

$$\lim_{\omega \rightarrow 0} \text{Im}(Y_T)/\omega = \lim_{\omega \rightarrow 0} C_T = \frac{1}{4}(2C_{DL,L}(N - 1) + C_{DL,i}) \quad (24)$$

$$\lim_{\omega \rightarrow 0} \text{Re}(Z_T) = \frac{2C_{DL,i}^2 R_i (2 + N) + 4C_{DL,L}^2 R_{sol} (N - 1)}{(2C_{DL,L}(N - 1) + NC_{DL,i})^2} \quad (25)$$

When $\omega \rightarrow \infty$ (at higher frequencies):

$$\lim_{\omega \rightarrow \infty} C_T = \frac{1}{2} \left(\frac{2C_{DL,L} C_{sol} (N - 1)}{C_{DL,L} + 2C_{sol}} + \frac{2C_{DL,i} C_i (C_{DL,i} (N - 1) + C_i N)}{(C_{DL,i} + C_i)(C_{DL,i} + 2C_i)} \right) \quad (26)$$

$$\lim_{\omega \rightarrow \infty} \text{Re}(Z_T) = 0 \quad (27)$$

The double-layer capacity induces a second cutoff frequency at a low frequency, $f_{c,LF}$. This effect can completely predominate the measurements and must be studied before fabrication of the electrodes and their optimization, if necessary. The cutoff frequency can be calculated using Eq. (28), as follows:

$$f_{c,BF} = \frac{1}{2\pi \lim_{\omega \rightarrow 0} Z_T \lim_{\omega \rightarrow 0} C_T} \quad (28)$$

$$f_{c,BF} = \frac{2C_{DL,L}(N - 1) + NC_{DL,F}}{\pi R_i C_{DL,F}^2 (N + 2) + 2\pi R_{S,L} C_{DL,L}^2 (N - 1)}$$

The impact of C_{DL} at a high cutoff frequency can be calculated using Eq. (29):

$$f_{c,HF} = \frac{1}{2\pi R_T \lim_{\omega \rightarrow \infty} C_T} \quad (29)$$

$$f_{c,HF} = \frac{(2C_{DL,L}(N-1) + NC_{DL,F})^2}{\pi X(2C_i^2 R_i(N+2) + 4C_{DL,L}^2 R_{S,L}(N-1))}$$

$$X = \left(\frac{2C_{DL,L}C_{S,L}(N-1)}{C_{DL,L} + 2C_{S,L}} + \frac{C_{DL,F}C_i(C_{DL,F}(N-1) + NC_i)}{(C_{DL,F} + C_i)(C_{DL,F} + 2C_i)} \right)$$

In most cases, C_{DL} is very high compared to capacitance induced by water permittivity and has no significant impact. In this case, the cutoff frequency only depends on C_I/R_I and C_E/R_E , and can be assimilated to Eq. 14.

3 Interdigitated Sensor Optimization

In this section, the effect of each parameter in the global impedance spectrum is analyzed to optimize interdigitated sensors according to the targeted application. The electrodes' wavelength λ is not reviewed in this section. This parameter (depending on \mathbf{w} and \mathbf{g}) is used to evaluate the penetration depth and was already considered in the previous section. To evaluate the impact of the electrode width and gap, it is more suitable to use another indicator as the metalization ratio η .

3.1 Effect of the Number of Electrodes

As before, simulations were performed to study the impact of geometrical parameters on the global impedance spectrum (module and phase) to optimize interdigitated sensors.

First, simulations were performed using both analytical and FEM models by varying the number of electrodes from 10 to 80 by a step of 10. The other parameters were set at $\eta = 0.5$ and $\mathbf{w} = \mathbf{g} = 10 \mu\text{m}$. The thickness of the double layer was calculated using Eq. (15), with $\lambda_D = 80 \text{ nm}$. The liquid sample was considered with an infinite thickness ($\mathbf{h}_{\text{med}} \gg \lambda$), with $\epsilon_{r,\text{med}} = 80$ and $\sigma_{\text{med}} = 1 \mu\text{S/cm}$.

Results are displayed in Fig. 8, with a Bode diagram for module and phase, from which the real part and capacitance are deduced. Both FEM and analytical results are in concordance, demonstrating the validity of the analytical model. One can see that N does not have a significant impact on the phase and cutoff frequencies, as shown in Fig. 9. The low impact observed for the low number of electrodes is due to the peripheral electrodes and became negligible when the number of electrodes was higher than 20. One can conclude that the number of electrodes may influence only by reducing the value of the impedance. This parameter can be used in experimental measurement to adapt the impedance to the desired range to be compatible, for example, with an impedance analyzer.

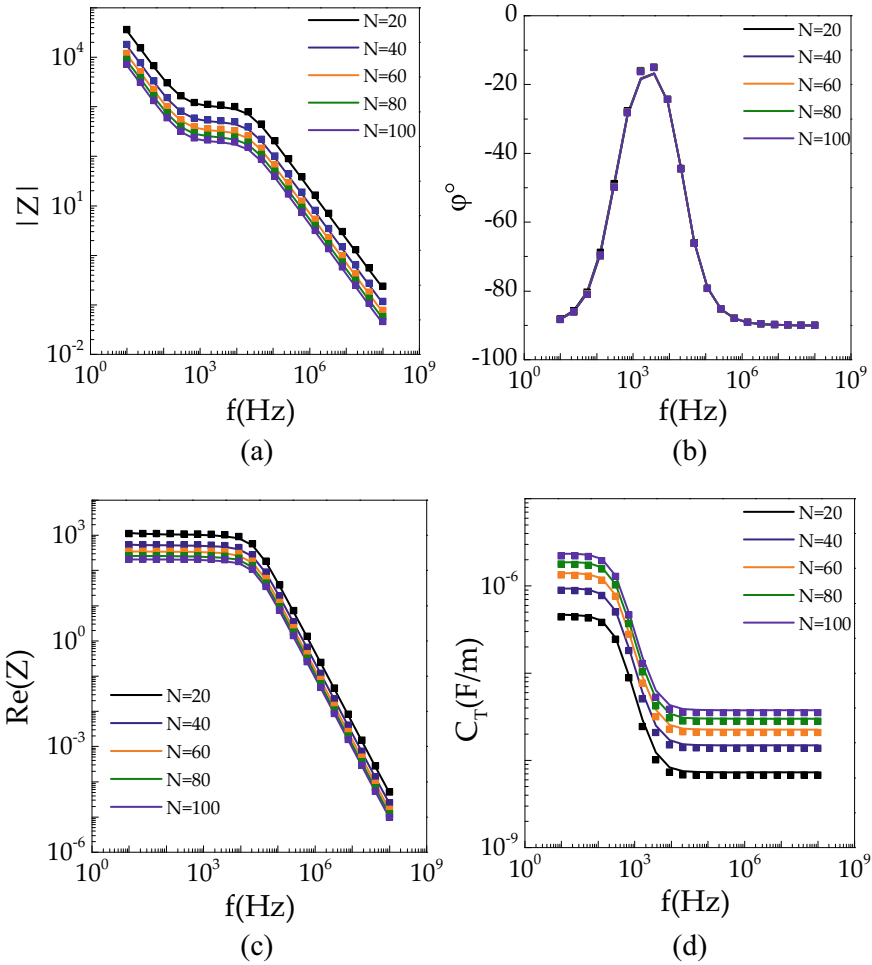


Fig. 8 Bode diagram for analytical (line) and FEM (points) simulations as a function of the number of electrodes N . Diagrams show **a** module, **b** phase, **c** real part, and **d** capacitance extraction

3.2 Effect of the Metalization Ratio

Other simulations were performed to study the impact of the metalization ratio η . The number of electrodes N was set to 20 and h to 4 mm (to consider a semi-infinite layer). η is a function of two other parameters, namely the electrode width w and the electrode gap g (Eq. 4). Thus, simulations were performed by fixing one of the w | g parameters and varying the other, and by fixing η and analyzing the impact of one of the w | g parameters.

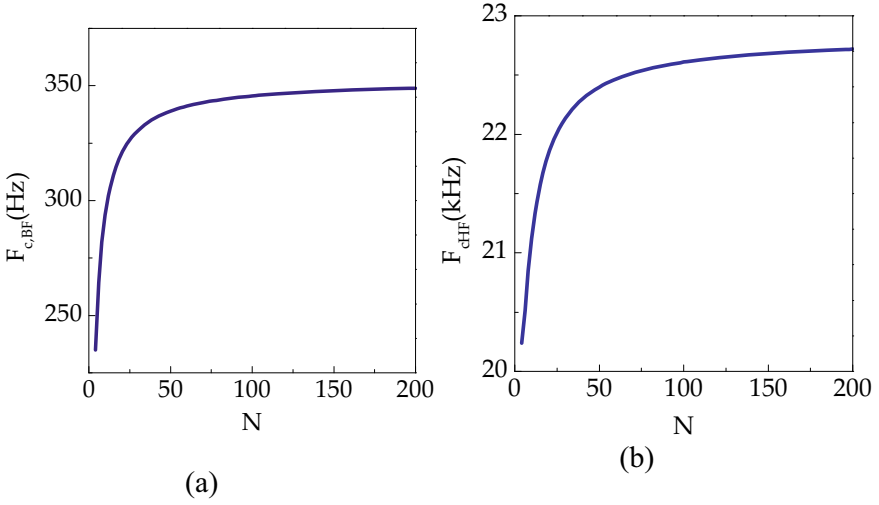


Fig. 9 High and low cutoff frequencies as a function of the number of electrodes N

In a first step, the electrode width w was set to $10 \mu\text{m}$, and the electrode gap g was varied to obtain a metalization ratio η varying from 0.1 to 0.9, using Eq. (30).

$$g = \frac{w(1 - \eta)}{\eta} \quad (30)$$

The results are presented in Fig. 10. A decrease in g causes an increase in the ratio η , resulting in a logarithmic increase of $f_{c,LF}$, which implies a diminution of the useful bandwidth (between $f_{c,LF}$ and $f_{c,HF}$). C_{DL} is not impacted because it only depends on the electrode surface (w , L), and the sample impedance increases as a function of the logarithmic relation of the g/w ratio.

In Fig. 11, the influence of g for an η -maintained constant was studied. For a fixed value of η , increasing g implies increasing w . Since C_{DL} is proportional to w , and impedance depends on the logarithmic relation of g/w , we obtain a logarithmic decrease of $f_{c,LF}$ with increasing g . There is no significant impact on $f_{c,HF}$, because it mainly depends on the sample's intrinsic properties, as explained previously in the ‘‘Electrical double layer’’ section. When $\eta > 0.7$, the electrodes are very close to each other, and the simplified model is no longer valid (see Eq. 3). The electric field is concentrated in a volume that is too confined.

In a second step, the electrode gap g was set to $10 \mu\text{m}$, and the electrode width w was varied to obtain a metalization ratio η from 0.1 to 0.9, using Eq. (31):

$$w = \frac{\eta g}{(1 - \eta)} \quad (31)$$

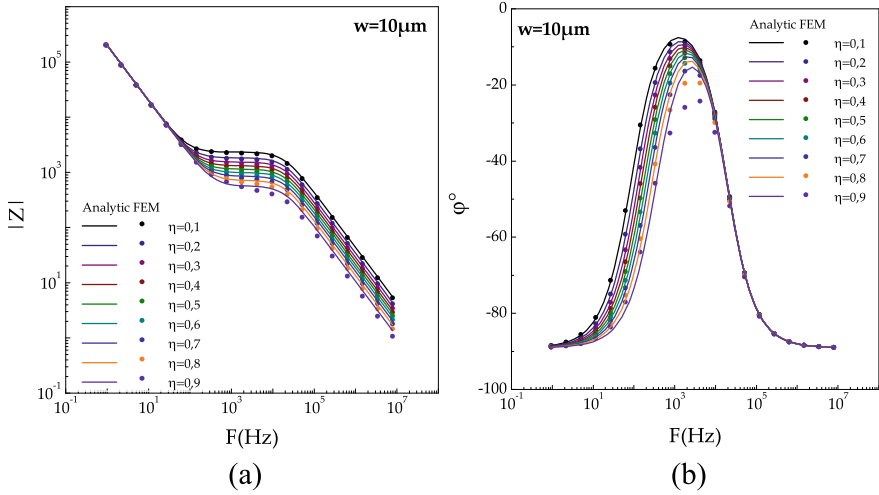


Fig. 10 Simulated impedance as a function of η by setting w to $10 \mu\text{m}$ using the analytical model (lines) and FEM (points). **a** Impedance module, and **b** impedance phase

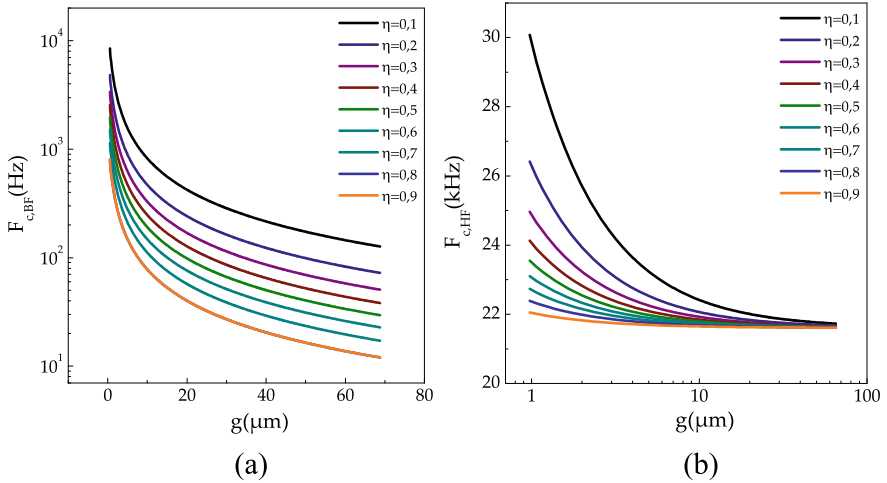


Fig. 11 Simulated cutoff frequencies as a function of g for different η values using the analytical model (lines) and FEM (points). **a** Low cutoff frequency, and **b** high cutoff frequency

Results are shown in Fig. 12. The increasing of ratio η , due to the increase of w , causes a logarithmic increase of $f_{c,LF}$, implying a diminution of the useful bandwidth (between $f_{c,LF}$ and $f_{c,HF}$). C_{DL} is proportional to w because it depends on the electrode surface (w, L). The sample impedance increases as a function of the logarithmic relation of the g/w ratio.

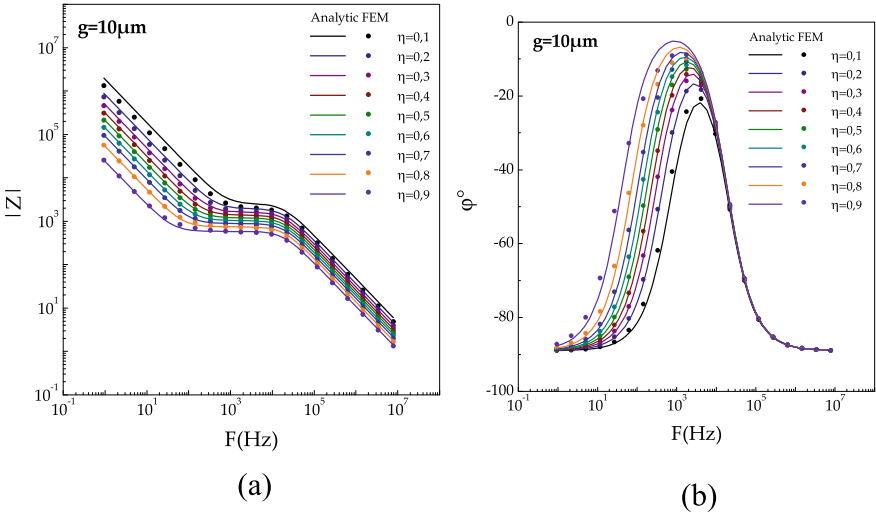


Fig. 12 Simulated impedance as a function of η by setting g to $10 \mu\text{m}$ using the analytical model (lines) and FEM (points). **a** Impedance module, and **b** impedance phase

In Fig. 13, the impact of w with constant η was studied. With a constant η , increasing w implies an increase of g . As C_{DL} is proportional to w , and impedance depends on the logarithmic relation of g/w , we obtain a logarithmic decrease in $f_{c,LF}$ with increasing g . There is no significant effect on $f_{c,HF}$, as it chiefly depends on the sample’s intrinsic properties, as explained above in the “Electrical double layer”

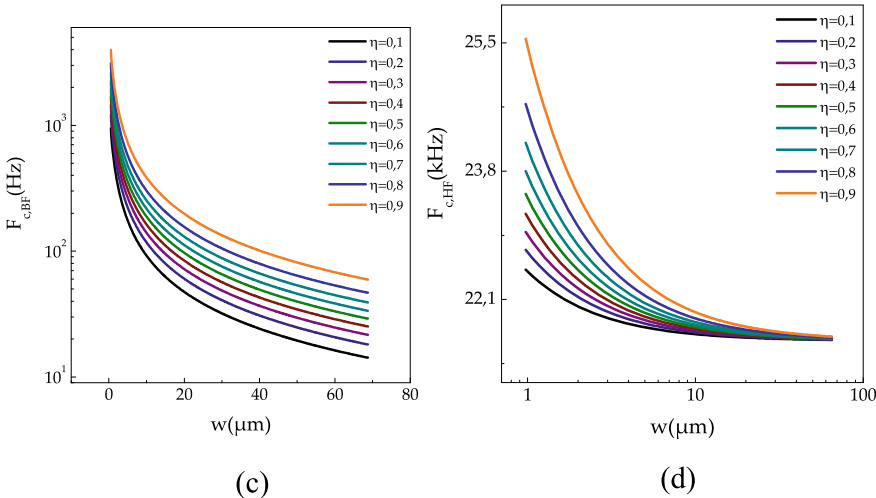


Fig. 13 Simulated cutoff frequencies as a function of w for different η values using the analytical model (lines) and FEM (points). **a** Low cutoff frequency, and **b** high cutoff frequency

section. When $\eta > 0.7$, the electrodes are quite close to each other, the simplified model is no longer valid (see Eq. 3), and the electric field is concentrated in too confined a volume.

From the results of Figs. 10, 11, 12 and 13, one can conclude that the metalization ratio can efficiently contribute to a reduction of the double-layer effect and increase the useful frequency band when g or w are increased. Under these conditions, it is more suitable not to choose too high or too low a ratio of η to keep a good electric field distribution. $\eta = 0.5$ ($g = w$) provide the most uniform electric field distribution between the interdigitated electrodes.

3.3 Effect of Substrate Capacitance

The electrical effect of the substrate (Z_S) is mainly due to its permittivity, ranging from 2 to 14 (relative), depending on the material used, as seen in Table 3. Substrate electrical conductivity is generally very low and neglected. Substrate permittivity adds a capacitive semi-layer in parallel with the characteristic impedance of the biosensors. Global impedance Z_T can be calculated using Eqs. (32) and (33). Substrate impedance is calculated using the same K_{cell} factor as for sample impedance. Due to the low relative permittivity of substrate materials compared to water, its capacitance effect occurs at higher frequencies and has only an impact on $f_{c,HF}$, as shown in Eq. (34). If the relative permittivity of the substrate is low compared to the sample permittivity, the decrease in $f_{c,HF}$ remains minimal. For example, a relative glass permittivity of 4.7 induces a decrease in $f_{c,HF}$ of only 6%, as compared to $f_{c,HF}$ calculated without taking into account glass permittivity. Glass substrate is transparent, resistant to numerous solvents, stable, easy to handle for processing, biocompatible, cheaper than other substrates, and presents a low relative permittivity. For that, it is the more suitable material to use for the substrate.

$$Y_T = \frac{1}{Z_{i1}} + \frac{(N/2) - 1}{Z_{i,sup}} + \frac{N - 1}{Z_L} + \frac{N - 1}{Z_S} \quad (32)$$

Table 3 Electrical relative permittivity and conductivity of different substrate materials

Material	Relative electrical permittivity	Electrical conductivity (σ/m)
PTFE	2.1	$<10^{-9}$
PMMA	2.6 to 3.12 (room temperature)	$<10^{-9}$
Polyimide	3.4	$<10^{-9}$
Glass	3.7 to 10	$<10^{-9}$
Amorphous silicon	11.8	3.10^{-5}

$$Z_S = \frac{2R_{Sub}}{1 + j\omega R_{Sub}C_{Sub}} \quad (33)$$

$$F_{C,H} = \frac{1}{2\pi R_T C_T} F_{C,H} = \frac{1}{2\pi R_T C_T} \quad (34)$$

with

$$R_T = \frac{R_{sol} R_{sub}}{R_{sol} + R_{sub}} \approx R_{sol} \text{ and } C_T = C_{sol} + C_{sub} \quad (35)$$

To verify the previous equations, FEM simulations were executed for an interdigitated sensor with a semi-infinite substrate and a relative permittivity of four on the bottom face. A semi-infinite sample employed a relative permittivity of 80 and a conductivity of $100 \mu\text{S/cm}$ for the upper face. Results are shown in Fig. 14 for both the analytical model calculation and the FEM simulation. One can conclude that the analytical results for the equivalent circuit model are in concordance with the FEM simulations.

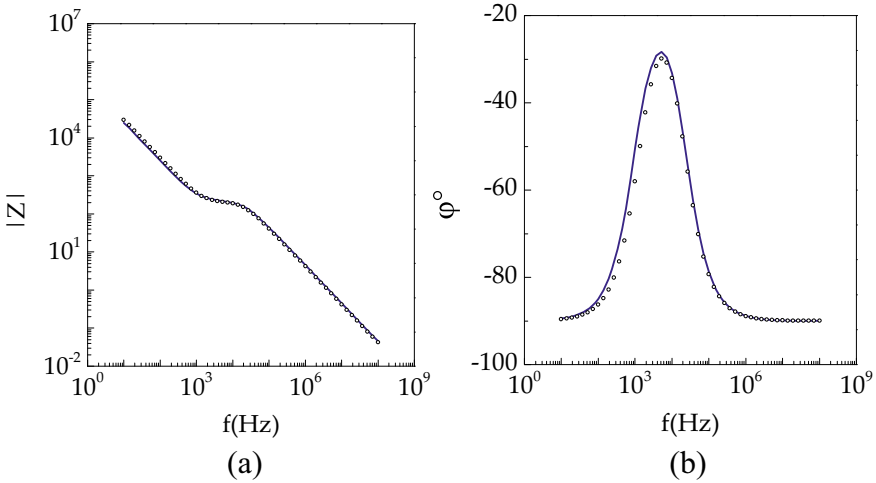


Fig. 14 Results of the analytical evaluation and FEM simulations of an interdigitated sensor with a liquid sample and a glass substrate. Bode diagram for **a** module, and **b** phase

3.4 Optimization Methodology

BIA sensor optimizations are mainly focused on bandwidth improvement, which needs to be wide enough to observe all the useful frequency bands of the sample. For biological samples, useful frequencies are centered around the β dispersion zone. One decade before and after this zone is generally sufficient to characterize a bio sample. These frequencies depend on sample complex conductivity ($\sigma_{\text{samp}}(\omega)$) and can be estimated using the impedance database [20] or models such as Maxwell mixture theory (MMT) [21] or Cole–Cole [22], for example.

Another typical parameter for optimization of interdigitated sensors is the depth of penetration. By varying the parameter λ , it is possible to set the sample thickness desired for analysis. This optimization is particularly interesting when one wants to characterize a thin sample, as for surface cell cultures or cell settling, for example.

The last optimization concerns the impedance range. Low-cost or embedded impedance measurement devices are generally limited in their impedance range and require a sensor with an adapted response.

A better optimization consists of determining the optimum compromise between frequency band, impedance range, and penetration depth. To achieve this, we propose the following methodology:

1. Use a database or models to evaluate the complex conductivity $\sigma_{\text{samp}}(\omega)$ of the samples to characterize.
2. Set the parameter λ as a function of the desired penetration depth, with a metalization ratio η of 0.5 ($\mathbf{w} = \mathbf{g}$).
3. Use equations of previous sections with the complex permittivity of samples to check if the bandwidth is correct. Since the number of electrodes \mathbf{N} and electrodes length \mathbf{L} have no impact on the bandwidth, their value can be set arbitrarily for this step.
4. If the bandwidth is insufficient, the metalization ratio η can be increased by keeping λ constant. It is recommended not to use too high a value of η in order to maintain a correct electric field distribution.
5. If the previous optimization is insufficient, increase the parameter λ to obtain the appropriate bandwidth. This operation reduces the sensitivity by using a penetration depth higher than needed but permits observation of all the useful sample spectrum. This step consists of selecting the best compromise between sensitivity and bandwidth.
6. Set numbers of electrodes \mathbf{N} and length \mathbf{L} to obtain the desired impedance range. It is recommended to use at least 20 electrodes to reduce the effect of outside electrodes on global impedance.

4 Experimentation

To verify our assumption, different sensor designs were fabricated and characterized using biological samples. Various \mathbf{N} , \mathbf{w} , and \mathbf{g} values were tested to validate

their impact on the global impedance spectrum. All measurements of this section were performed at room temperature ($23\text{ }^{\circ}\text{C} \pm 1\text{ }^{\circ}\text{C}$) using an impedance analyzer (E4990A, Keysight Technologies).

4.1 Samples Choices and Modeling

Thus far this work has focused on interdigitated sensor modeling and optimization without discussing the influence of the biological species. To accomplish this, we chose yeast cells (*Saccharomyces cerevisiae*) as a biological model because it is one of the most commonly studied cells. Yeast cells are simple to manipulate, resistant to many ionic concentrations, not pathogenic, and easy to dilute to obtain the appropriate concentration. Deionized water and two calibrated ionic solutions ($1314\text{ }\mu\text{S}/\text{cm}$ and $5000\text{ }\mu\text{S}/\text{cm}$ at $25\text{ }^{\circ}\text{C}$) were used as references for our measurements. Deionized water, with its very low conductivity, is well suited to serve as a reference for electrical permittivity measurements (78 for pure water).

A yeast cell sample can be modeled by its complex conductivity using MMT, as in Eqs. (36) and (37). Calibrated solutions can be readily modeled using the given conductivity and the relative permittivity of water ($\epsilon_{\mathbf{r},\text{water}} \approx 78$), as shown in Eq. (40).

$$\frac{\frac{\sigma_{\text{samp}}(\omega)}{\sigma_{\text{elec}}(\omega)} - 1}{\frac{\sigma_{\text{samp}}(\omega)}{\sigma_{\text{elec}}(\omega)} + 2} = \rho_V \frac{\frac{\sigma_{\text{cell}}(\omega)}{\sigma_{\text{elec}}(\omega)} - 1}{\frac{\sigma_{\text{cell}}(\omega)}{\sigma_{\text{elec}}(\omega)} + 2} \quad (36)$$

$$\sigma_{\text{cell}}(\omega) = \sigma_{\text{mem}}(\omega) \frac{(2\sigma_{\text{mem}}(\omega) + \sigma_{\text{cyt}}(\omega))r_{\text{ext}}^3 - 2(\sigma_{\text{mem}}(\omega) - \sigma_{\text{cyt}}(\omega))r_{\text{int}}^3}{(2\sigma_{\text{mem}}(\omega) + \sigma_{\text{cyt}}(\omega))r_{\text{ext}}^3 + (\sigma_{\text{mem}}(\omega) - \sigma_{\text{cyt}}(\omega))r_{\text{int}}^3} \quad (37)$$

with

$$\sigma_{\text{mem}}(\omega) = \sigma_{\text{mem}} + j\omega\epsilon_{\mathbf{r},\text{mem}}\epsilon_0 \quad (38)$$

$$\sigma_{\text{cyt}}(\omega) = \sigma_{\text{cyt}} + j\omega\epsilon_{\mathbf{r},\text{cyt}}\epsilon_0 \quad (39)$$

$$\sigma_{\text{elec}}(\omega) = \sigma_{\text{elec}} + j\omega\epsilon_{\mathbf{r},\text{elec}}\epsilon_0 \quad (40)$$

σ_{elec} , σ_{cyt} , and σ_{mem} are the electrical conductivity of the electrolyte, the cytoplasm, and the membrane, respectively. $\epsilon_{\mathbf{r},\text{elec}}$, $\epsilon_{\mathbf{r},\text{cyt}}$, and $\epsilon_{\mathbf{r},\text{mem}}$ are their relative electrical permittivities, respectively. \mathbf{r}_{int} and \mathbf{r}_{ext} represent the inner and outer radius of the cell, respectively. ρ_V is the volume ratio of cells in the sample.

4.2 Sample Preparation and Characterization

Yeast cell samples were obtained by dissolving dry cells in water with ratio of 1:6 to obtain a volume ratio of approximately $\rho_V = 0.5$ (hydrated yeast cells have a water percentage around 66%). Deionized water and calibrated solutions are commercial products, which do not need specific preparation.

The intrinsic properties of all samples and their complex conductivity were computed using models presented in the previous section “Samples choice and modeling.” The yeast cells sample was modeled using $\rho_V = 0.5$, $\sigma_{\text{cyt}} = \sigma_{\text{elec}} = 0.3 \text{ S/m}$ [23], $\epsilon_{r,\text{cyt}} = \epsilon_{r,\text{elec}} = 78$, $\sigma_{\text{mem}} = 0 \text{ S/m}$ and $\epsilon_{r,\text{mem}} = 5$ (lipid relative permittivity). Calibrated solutions were modeled using Eq. (40) with conductivity (σ_{elec}) given by the manufacturer and the relative permittivity of water ($\epsilon_{r,\text{water}} = 78$ at 25 °C). As the conductivity of deionized water is unknown, only its relative permittivity was modeled by setting the permittivity of pure water.

To verify the validity of our models, samples were characterized using high precision Liquid Test Fixture **16452A** (Keysight Technologies). Samples complex conductivity was extracted from impedance measurements using the manufacturer’s formula. Both results for modeled and measured conductivities are shown in Figs. 15 and 16, which represent the apparent conductivity and apparent relative permittivity extracted for real and imaginary parts of complex conductivity using Eqs. (41) and (42), respectively.

$$\sigma_{app}(\omega) = \Re(\sigma_{samp}(\omega)) \tag{41}$$

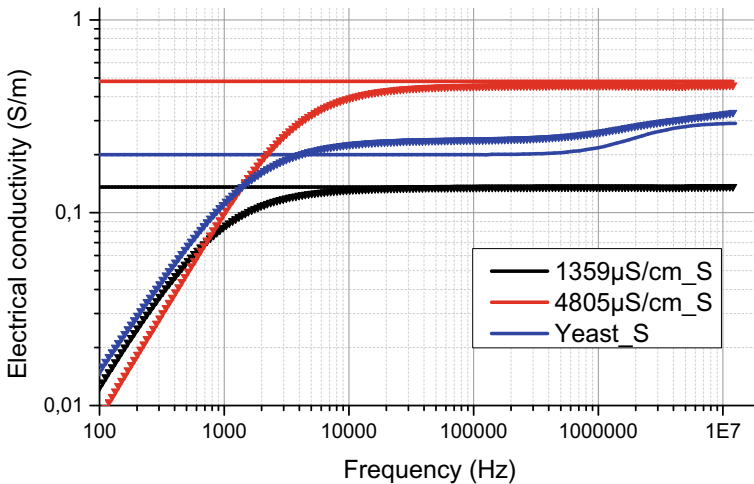


Fig. 15 Apparent conductivity of the calibrated solution and yeast cells sample. Analytical simulation results (lines) and measurements (triangles)

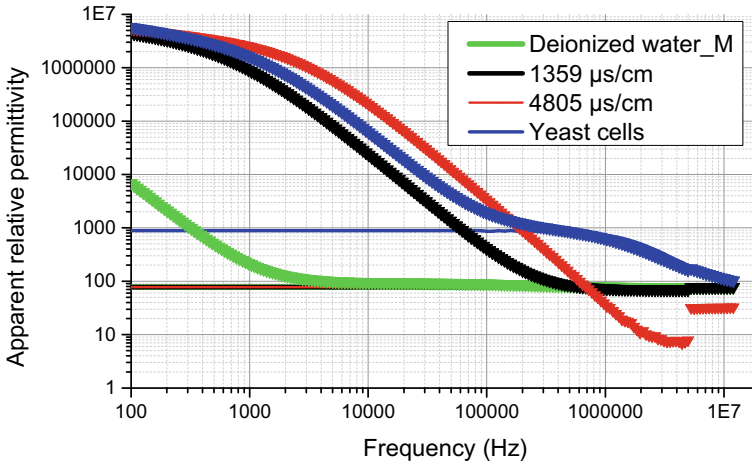


Fig. 16 Apparent relative permittivity of calibrated solutions and yeast cells sample. Analytical results (lines) and measurements (triangles)

$$\varepsilon_{r,app}(\omega) = \Im\left(\frac{\sigma_{samp}(\omega)}{\omega\varepsilon_0}\right) \quad (42)$$

One can see that the analytical model results are in concordance with measurements for upper frequencies, particularly for the cutoff frequencies of β dispersion. As mentioned before, this value is vital for the sensor design. It is necessary for the sensor to have a sufficient bandwidth around the β dispersion to correctly characterize a biological sample. The effect of the double layer, present only in measurement results, occurs at low frequencies and is not included in our analytical models. This choice is motivated because it is not an intrinsic property of the sample and depends mainly on electrode material and surfaces. One can see that this effect is quite the same for the yeast cells and calibrated solutions for both the conductivity and the relative permittivity. For deionized water, this effect occurs at very low frequencies and cannot be compared with other samples. At higher frequencies, the relative permittivity of all samples, except for the calibration solution with highest conductivity ($500 \mu\text{S/m}$), tends to 78 (permittivity of pure water). For the calibration solution with the highest conductivity, the high conductivity makes it difficult to extract the dielectric effect. Finally, for yeast cells, the second plateau is due to the cells membranes capacitances and is for this reason not present in the other measurements.

Results for measured conductivity and relative permittivity for all samples are synthesized in Table 4. The permittivity induced by double-layer effects is not presented, as explained above. The lower values for calibrated solutions can be explained by the lower temperature (conductivity is given for 25°C). This table will serve as a reference for comparison with measurements made with the sensors (see next sections). The high value of apparent permittivity for the first plateau of yeast cells is induced by the high surface capacitance of cell membranes.

Table 4 Geometrical parameters for sensors C1 and C2

Sample	Conductivity (S/m)		Relative permittivity	
	1st plateau	2nd plateau	1st plateau	2nd plateau
Deionized water	0.001	NP*	78	NP ^a
1413 $\mu\text{S}/\text{cm}$ solution	0,136	NP*	78	NP ^a
5000 $\mu\text{S}/\text{cm}$ solution	0.455	NP*	32	NP ^a
Yeast cells	0.238	0.323	860	78

^aNP not present

4.3 Sensor Fabrication

In this section, the impact of geometrical parameters was studied, such as the validity of our proposed methodology. For this, five sensor designs, named C_1 to C_5 , were fabricated. To be comparable, all sensors have the same sensing surface (1 mm \times 1 mm). In this case, L is set to 1 mm for all sensors. For sensors C_3 to C_5 , the smallest electrode dimension (w or g parameters) was set to 5 μm . This represents the classical size of a yeast cell and corresponds to the most usual choice for sensor design. Setting the electrode dimension to the same order of size as the studied cells theoretically permits optimization of detection sensitivity: only one cell layer is enough to significantly modify the electric field between electrodes (setting of penetration depth). It is not useful to use smaller sizes because the investigated depth could be smaller than the cell sizes. Other parameters are set to obtain three different metalization ratios (0.2, 0.62, and 0.8) to study their impact. The C_1 sensor was designed using our proposed methodology. To obtain a sufficient bandwidth for the yeast cell model (approximately one decade before β dispersion), it was necessary to increase the initial cell gap of 5 μm to 20 μm with a metalization ratio of 0.6. The C_2 sensor was proposed to have an intermediate design between C_1 and C_3 .

The sensors' parameters are shown in Table 5.

Sensors were fabricated using biocompatible materials, such as platinum, for electrodes and glass for the substrate. These choices and more details about fabrication were already discussed and presented in previous papers [10, 11]. Images of the five fabricated sensors are shown in Fig. 17.

Table 5 Geometrical parameters for sensors C_1 to C_5

Sensor number	N (μm)	w (μm)	g (μm)	L (μm)	λ (μm)	η	Calculated K_{cell} (m^{-1})
C_1	20	30	20	1000	100	0.6	90
C_2	40	15	10	1000	50	0.6	43
C_3	80	8	5	1000	26	0.62	21
C_4	40	5	20	1000	50	0.2	87
C_5	40	20	5	1000	50	0.8	30

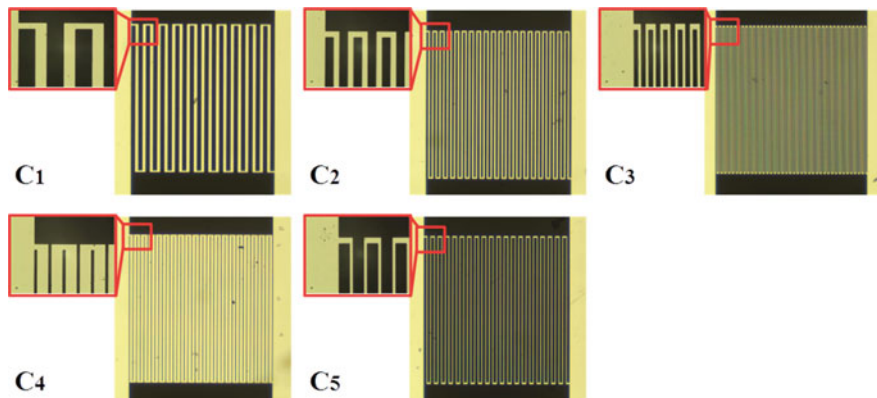


Fig. 17 Optical microscope images of sensors C_1 to C_5 (magnifications $40\times$ and $400\times$)

4.4 Sensor Characterization

All measurements with sensors were performed for a $2\ \mu\text{L}$ volume of the sample deposited on the sensor surface using a micropipette.

The first characterization steps consist of the determination of the sensor cell factor \mathbf{K}_{cell} , which allows for deducing the sample conductivity from its impedance.

The characterization of an impedance-based sensor is typically divided according to the four following steps:

1. Measurement without a sample (unloaded measurement) to determine all capacitive effects of the measurement setup. In our case, capacitance is mainly due to the substrate and air electrical permittivity.
2. Short-circuit measurement to determine the impedances in series with sensors (if possible). This step is unnecessary if the impedance is not too low in comparison to cable and track impedances. This is the case for our sensors.
3. Measurement with calibrated solutions or well-known samples to determine the \mathbf{K}_{cell} factor.
4. Determine the effect of the substrate. Knowing \mathbf{K}_{cell} and the permittivity of air, it is possible to calculate the substrate permittivity.

Results for measurement without samples allows for extracting the apparent capacitance C_{app} from admittance, using Eq. (43). Capacitance was extracted at $f_0 = 1\ \text{MHz}$ because measurements are unstable at very low frequencies due to the high impedance induced. This corresponds to the central frequency in the bandwidth of interest. We obtain 1.02 nF, 1.69 nF, 3.28 nF, 1.11 nF, and 2.1 nF for the sensors C_1 to C_5 , respectively.

$$C_{\text{app}}(\omega_0) = \frac{\Im(\sigma(f_0))}{2\pi f_0} \quad (43)$$

Results for measurements with calibrated solutions are displayed in Fig. 18. One can see first that all sensors except C_4 show a similar spectrum at low frequencies. This part of the spectrum is due to the double-layer effect and depends theoretically on the contact surface of the electrodes with the sample. Since sensors C_1 , C_2 , C_3 and C_5 present a close metalization ratio η (0.6–0.8), their surfaces in contact with sample are quite similar. C_4 shows a very small (0.2) ratio η compared to other sensors, and the effect on the impedance of the double layer is clearly higher than for the other sensors. This is particularly obvious when comparing it to C_1 , which has close to the same cell factor as C_4 . This result confirms our assumptions about the contribution of the parameter η . The increase of this parameter permits reduction of the effect of double-layer capacitance and increases the useful bandwidth.

Another important parameter is the electrode periodicity λ . We discussed the role of decreasing λ in the theoretical section that allows it to decrease penetration depth. Also, we assumed in the methodology section that increasing the electrode periodicity λ can increase the bandwidth of interest. The sensors C_1 , C_2 , and C_3 present similar factor η but three different lambda parameters: 100, 50, and 26, respectively. The

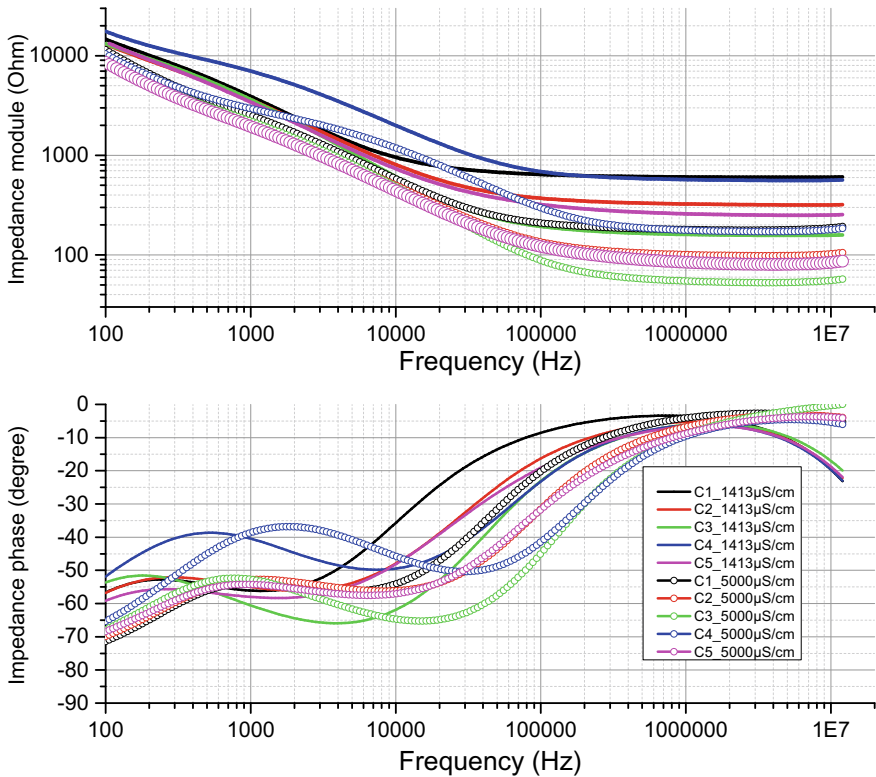


Fig. 18 Impedance in module and phase for sensors C_1 to C_5 for 1413 $\mu\text{S}/\text{cm}$ and 5000 $\mu\text{S}/\text{cm}$ calibrated solutions

Table 6 Measured and calculated K_{cell} for sensors C_1 to C_5

Sensor number	K_{cell} 1413 μ S/cm	K_{cell} 5000 μ S/cm	K_{cell} average	K_{cell} analytical	Error %
C_1	82.35	81.15	81.75	90	9.167
C_2	44.2	44.76	44.48	43	3.44
C_3	21.87	24.00	22.935	21	9.21
C_4	77.83	78.28	78.055	87	10.28
C_5	35.2	36.73	35.965	30	19.88

effects of these parameters are clearly visible in Fig. 18 results, mainly through the phase diagram. C_4 shows a low cutoff frequency approximately twice lower than C_5 , which also presents the same shift with C_6 for the same calibrated solutions. As we fixed the same surfaces for all sensors, it is unnecessary to discuss the effect of the electrodes' number for the same couple (λ , η). Nevertheless, we postulated in the theoretical section that the cell content of one pair of electrodes only depends on η . Following this, one can consider that sensors C_1 , C_2 , and C_3 have the same cell constant and the number of electrodes can be compared. C_3 has twice as many electrodes as C_2 , as does C_2 compared to C_1 . We clearly observe that the impedance module of the plateau decreases by a factor 2 from C_1 and C_2 , and by a factor 2 from C_2 to C_3 , as predicted.

These measurements also allow for determining K_{cell} for each sensor using Eq. (44). σ_{elec} and $\sigma(\omega)$ are the intrinsic conductivity and the complex conductivity of the electrolyte, respectively. f_0 is set to 1 MHz for the electrolyte at 1413 μ S/cm and 3.3 MHz for the electrolyte at 5000 μ S/cm. The results are synthesized in Table 6.

$$k_{cell} = \frac{\sigma_{elec}}{\sigma(f_0)} \quad (44)$$

These results are in concordance with the theoretical approach. The differences between the analytical model and the measures can mainly be explained by fabrication tolerances and some assumed simplifications in the analytical model (considering the semi-infinite layer) as well as the role of temperature (a variation of 1 °C implies approximately a 2% shift in electrolyte conductivity). The determination of K_{cell} permits calculation of the conductivity and permittivity of the samples. The permittivity of the substrate needs to be subtracted from the global measured results and can be calculated using Eq. (45) from the air measurement (Table 7).

$$C_{unload} = \frac{\epsilon_O(\epsilon_{r,sub} + \epsilon_{r,air})}{K_{cell}} \Leftrightarrow \epsilon_{r,sub} = \frac{C_{unload}K_{cell}}{\epsilon_O} - \epsilon_{r,air} \quad (45)$$

Final measurements were performed with biological samples (yeast cells) using the same protocol as the previous measurement. Results are given in Fig. 19 as a Bode diagram of the impedance. Only C_1 displays two distinct ‘‘plateaus,’’ and it allows for measuring electrical properties of the biological sample before and after

Table 7 Measured relative permittivity of substrate for sensors C_1 to C_5

Sensor	C_{unload}	Calculated ϵ_{sub}
C_1	1.02E-12	8.42
C_2	1.69E-12	7.49
C_3	3.2E-12	7.29
C_4	1.11E-12	8.79
C_5	2.1E-12	7.53

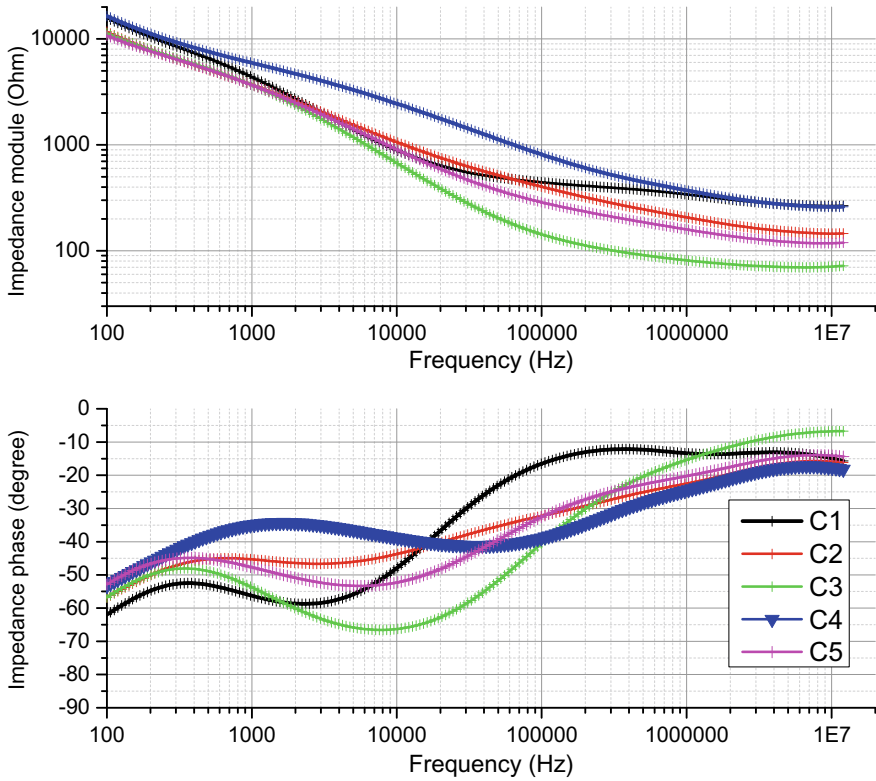


Fig. 19 Impedance in module and phase for yeast cells sample measurement using sensors C_1 to C_5

β dispersion. This is clearly visible in the phase diagram by the presence of two lobes (local maxima) on each side of the β dispersion zone. Other sensors are not correctly optimized, and the double-layer effect occults the first part of the impedance response. This is especially visible by comparing C_1 and C_4 , which have similar K_{cell} but not to the same degree of optimization. Their impedance diagrams are similar at higher frequencies, after β dispersion, but the first plateau is not visible for sensor C_4 . Finally, intrinsic conductivity and permittivity of yeast cells sample were

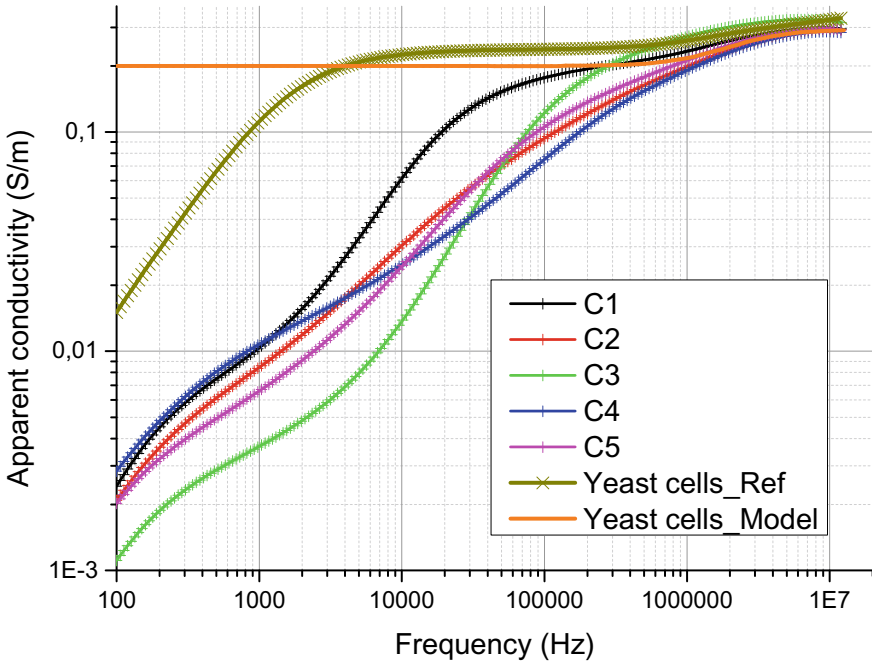


Fig. 20 Conductivity (real part of complex conductivity) of yeast cell samples calculated with the analytical model and extracted from measurement with liquid probe and sensors C_1 to C_5

extracted for impedance measurement using K_{cell} and presented in Fig. 20. These results are in concordance with theory and reference measurement and prove again that sensors others than C_1 are unable to characterize yeast cells samples. The higher gap between C_1 and the liquid text future results can be explained by the fast settling of yeast cells. The time necessary between sample deposition and measurement (1–2 min) is sufficient to obtain a greater cell concentration on the electrodes' surfaces. In terms of optimization, C_1 represents the best compromise between penetration depth and the frequency band of interest for the targeted application, as proposed in the “optimization methodology” section.

5 Conclusion

A complete model for an interdigitated sensor was proposed and validated using FEM simulations. Using this model, the effect of all geometrical parameters on global impedance was studied to propose an optimization methodology. Electrodes with number N and length L permit adjusting impedance values to be compatible, for example, in the range of a measurement device without influencing the bandwidth.

The width and gap of the electrodes mainly influence penetration depth and bandwidth. Electrodes periodicity λ and metalization ratio η , depending only on w and g are more suitable to study the impact of g and w . An increase of η permits a reduction of the double-layer effect and simultaneously increases the useful bandwidth but must be limited to keep a correct uniformity on electric field distribution. A value of 0.6 appears to be the best compromise. The decrease of λ permits a reduction in the penetration depth for surface analysis but simultaneously decreases useful bandwidth. It may be adjusted to obtain the best compromise between the desired penetration depth and sufficient bandwidth. Measurements performed with five different sensors with the same active surface $1\text{ mm} \times 1\text{ mm}$, but different electrodes geometries were performed to validate our model and optimization methodology. The results obtained proved the necessity of optimizing interdigitated sensors using models and is a function of targeted applications. Sensors without sufficient optimization were unable to correctly characterize the biosample and extract its complex conductivity because the double-layer effect was too predominant. Sensor C_1 , with the best optimization, was able to extract all useful parts of the complex conductivity.

Funding

This work was performed with the support of the “Région Grand Est—France” and the European Regional Development Fund (FEDER).

Acknowledgements The authors gratefully thank the MiNaLor skill center of the Institut Jean Lamour (IJL) at the University of Lorraine for technical support.

References

1. L.C. Clark Jr., Monitor and control of blood and tissue oxygen tensions. *Trans. Am. Soc. Artif. Intern. Organs.* **2**(1), 41–48 (1956)
2. J.D. Newman (1997) Chemical sensor analysis, in *IEE Colloquium on Materials Characterization—How Can We Do It? What Can It Tell Us?* (Ref No 1997/150), pp. 6/1–6/3
3. E. Katz, I. Willner, Probing biomolecular interactions at conductive and semiconductive surfaces by impedance spectroscopy: routes to impedimetric immunosensors, DNA-sensors, and enzyme biosensors. *Electroanalysis* **15**(11), 913–947 (2003)
4. C. Gabriel, S. Gabriel, E. Corthout, The dielectric properties of biological tissues: I. Literature Survey. *Phys. Med. Biol.* **41**, 2231–2249 (1996)
5. P. Ertl, R. Heer Interdigitated impedance sensors for analysis of biological cells in microfluidic biochips. *e & i Elektrotechnik und Informationstechnik* **126**(1–2), 47–50 (2009)
6. J. Posseckardt, C. Schirmer, A. Kick, K. Rebatschek, T. Lamz, M. Mertig, Monitoring of *Saccharomyces cerevisiae* viability by non-Faradaic impedance spectroscopy using interdigitated screen-printed platinum electrodes. *Sens. Actuat. B Chem.* **255**, 3417–3424 (2018)
7. J. Wang, Electrochemical nucleic acid biosensors. *Anal. Chim. Acta* **469**(1), 63–71 (2002)
8. M. Ibrahim, J. Claudel, D. Kourtiche, M. Nadi, Geometric parameters optimization of planar interdigitated electrodes for bioimpedance spectroscopy. *J. Electri. Bioimped.* **4**(1), 13–22 (2013)
9. T.-T. Ngo, A. Bourjilat, J. Claudel, D. Kourtiche, M. Nadi, Design and realization of a planar interdigital microsensor for biological medium characterization, in: *Next Generation Sensors and Systems* (Springer, Cham, 2016), pp. 23–54

10. J. Claudel, A.L. Alves De Araujo, M. Nadi, D. Kourtiche, Lab-on-a-chip device for yeast cell characterization in low-conductivity media combining cytometry and bio-impedance. *Sensors* **19**(15), 3366 (2019)
11. A.L. Alves de Araujo, J. Claudel, D. Kourtiche, M. Nadi, Use of an insulation layer on the connection tracks of a biosensor with coplanar electrodes to increase the normalized impedance variation. *Biosensors* **9**(3), 108 (2019)
12. A.V. Mamishev, K. Sundara-Rajan, F. Yang, Y. Du, M. Zahn, Interdigital sensors and transducers. *Proc. IEEE* **92**(5), 808–845 (2004)
13. X. Hu, W. Yang, Planar capacitive sensors—designs and applications. *Sensor Rev.* (2010)
14. R. Igreja, C.J. Dias, Analytical evaluation of the interdigital electrodes capacitance for a multi-layered structure. *Sens. Actuat. A Phys.* **112**(2–3), 291–301 (2004)
15. R. Igreja, C.J. Dias, Extension to the analytical model of the interdigital electrodes capacitance for a multi-layered structure. *Sens. Actuat. A Phys.* **172**(2), 392–399 (2011)
16. D.C. Grahame, The electrical double layer and the theory of electrocapillarity. *Chem. Rev.* **41**(3), 441–501 (1947)
17. D.C. Grahame, Diffuse double layer theory for electrolytes of unsymmetrical valence types. *J. Chem. Phys.* **21**(6), 1054–1060 (1953)
18. K.B. Oldham, A Gouy–Chapman–Stern model of the double layer at a (metal)/(ionic liquid) interface. *J. Electroanal. Chem.* **613**(2), 131–138 (2008)
19. K. Bohinc, V. Kralj-Iglič, A. Iglič, Thickness of electrical double layer. Effect of ion size. *Electrochim. Acta* **46**(19), 3033–3040 (2001)
20. C. Gabriel, *Compilation of the Dielectric Properties of Body Tissues at RF and Microwave Frequencies*. King's Coll London (United Kingdom) Dept of Physics (1996)
21. O. Levy, D. Stroud, Maxwell Garnett theory for mixtures of anisotropic inclusions: application to conducting polymers. *Phys. Rev. B* **56**(13), 8035 (1997)
22. K.S. Cole, Electric impedance of suspensions of spheres. *J. General Physiol.* **12**(1), 29 (1928)
23. K. Asami, T. Hanai, N. Koizumi, Dielectric properties of yeast cells. *J. Membrane Biol.* **28**(1), 169–180 (1976)

Epsilon-Near-Zero Microwave Sensors



Abhishek Kumar Jha

Abstract This chapter introduces epsilon-near-zero (ENZ) waveguide-based sensors as used for dielectric testing of materials. The ENZ waveguide is inherently robust to losses and provides electromagnetic wave (EM) tunneling through the narrow ENZ channel. The theory of the two-port ENZ waveguide is explained using both circuit and numerical analysis. The theoretical and numerical analysis of the electric field under various rectangular waveguide modes inside the ENZ channel suggest that the required features of the ENZ effect are manifested in the TE_{10} mode. The characteristics of the ENZ waveguides viz. the uniform and intensified electric field as well as the high-quality factor, make them a potential candidate for microwave sensor applications. The analytical solution and the conditions related to the dielectric sensing effect are explained using a transmission line model for the ENZ waveguide sensor. Since the ENZ waveguide works around the cutoff frequency of the ENZ channel, tailoring the broader dimension of the waveguide or the dielectric constant of the substrate can help in designing a multifrequency dielectric sensor. Such a multifrequency ENZ sensor could be achieved using multilayer planar technology, which enables single-mode multi-frequency measurement, and is a unique characteristic of the ENZ effect and advantageous for the testing of dispersive materials.

1 Introduction of ENZ Waveguide

Let parallel metallic plates of area A , connected through DC voltage source V , separated by distance d , be filled with a non-magnetic material of relative permittivity ϵ_r , as shown in Fig. 1. The capacitance of such a parallel plate capacitor can be given by:

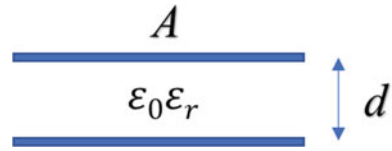
A. K. Jha (✉)

Faculty of Electronics, Telecommunications, and Informatics, Department of Microwave and Antenna Engineering, Gdańsk University of Technology, Gdańsk, Poland
e-mail: abhishek.jha@pg.edu.pl

© The Editor(s) (if applicable) and The Author(s), under exclusive license to Springer Nature Switzerland AG 2021

S. C. Mukhopadhyay et al. (eds.), *Interdigital Sensors*, Smart Sensors, Measurement and Instrumentation 36, https://doi.org/10.1007/978-3-030-62684-6_6

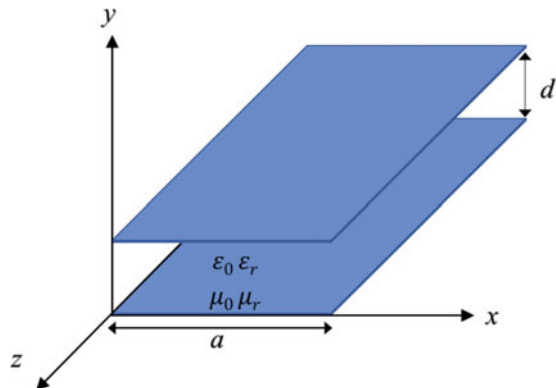
Fig. 1 Parallel plate capacitor



$$C = \frac{\epsilon_0 \epsilon_r A}{d} \quad (1)$$

where ϵ_0 ($=8.854 \times 10^{-12}$ F/m) is the permittivity of free space. In the static case, the value of capacitance given by (1) is constant. Aside from the physical dimensions, the dielectric property of the material plays a decisive part in engineering the capacitance value of a parallel plate capacitor. In general, passive materials possess a dielectric constant greater than one, while metamaterials may have a dielectric constant of less than one. Metamaterials are engineered materials that can be used to manipulate electromagnetic (EM) waves and be created using periodic structures. One example of such a structure is the interdigital sensor, designed using periodic interdigital electrodes [1]. Though the operating principle of a planar interdigital sensor follows the rule of a parallel plate capacitor [2], a parallel plate capacitor under DC conditions does not possess metamaterial characteristics. Recently, the parallel-plate metallic waveguide structures are investigated to show their metamaterial properties with the permittivity and permeability close to zero [3, 4]. Since zero-index metamaterials may decouple the electricity and magnetism, they can be utilized to design interesting devices [5]. The metamaterial behavior can be obtained using a simple modification to the parallel plate structure when excited using a high-frequency signal source. To understand such a phenomenon, let us assume the parallel plate waveguide, as shown in Fig. 2, is connected through a microwave source of angular frequency, $\omega = 2\pi f$. To minimize the fringe field effect, the width of the parallel plate waveguide, a , is kept sufficiently larger than the distance between the parallel plates, d . The gap between

Fig. 2 Parallel plate metallic waveguide



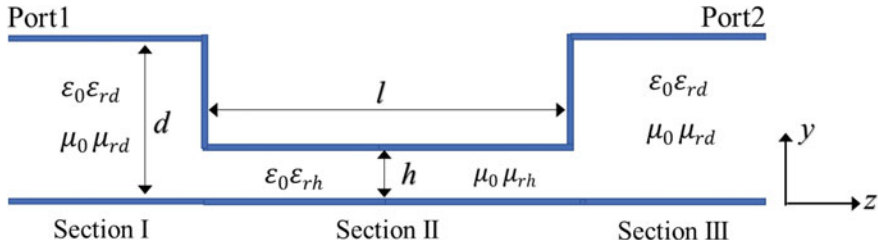


Fig. 3 Parallel plate waveguide with discontinuity

the two-parallel plates is filled with a non-magnetic material (relative permeability $\mu_r = 1$, and the permeability of free space $\mu_0 = 1.257 \times 10^{-6}$ H/m).

Such a parallel plate waveguide supports EM wave propagation in the transverse electric mode (“TE mode”—the z -component of the electric field is zero) and transverse magnetic mode (“TM mode”—the z -component of the magnetic field is zero). Except for the TE and TM modes, the parallel plate waveguide also supports the transverse electromagnetic mode (TEM mode, i.e. the z -components of the electric as well as the magnetic fields are zero), which is the fundamental mode of EM wave propagation. The propagation constant of the TEM mode in the z -direction, k , and the intrinsic impedance of the medium between the two plates, η , are given as $k = \omega(\mu\varepsilon)^{0.5}$ and $\eta = (\mu/\varepsilon)^{0.5}$, respectively, where $\mu = \mu_0\mu_r$ and $\varepsilon = \varepsilon_0\varepsilon_r$ are the permeability and permittivity of the medium between the two metallic plates. The characteristic impedance of the TEM mode, Z_0 , which is the ratio of the forward voltage wave to the forward current wave propagating along the z -axis, i.e. $Z_0 = V_0^+/I_0^+$ (or, the ratio of the backward voltage wave to the backward current wave propagating along the z -axis with a negative sign, i.e. $Z_0 = -V_0^-/I_0^-$) is given by $Z_0 = \eta(d/a)$.

Let us consider the parallel plate waveguide shown in Fig. 2, with a discontinuity of length l comprising a height mismatch at the center, as shown in Fig. 3. For analytical purposes, the parallel plate waveguide with a discontinuity can be divided into three sections, where sections I and III are identical and serve as the input and output ports for the propagation of the EM wave. The characteristic impedance and propagation constant of these sections are given as $Z_{0I} = Z_{0III} = \eta_d(d/a)$, and $k_d = \omega(\varepsilon_d\mu_d)^{0.5}$, respectively, where $\eta_d = (\mu_d/\varepsilon_d)^{0.5}$ is the intrinsic impedance of the medium between the plates, $\varepsilon_d = \varepsilon_0\varepsilon_{rd}$ and for the non-magnetic material $\mu_d = \mu_0\mu_{rd} = \mu_0$. Section II has height h , characteristic impedance $Z_{0II} = \eta_h(h/a)$, and propagation constant $k_h = \omega(\varepsilon_h\mu_h)^{0.5}$, where $\eta_h = (\mu_h/\varepsilon_h)^{0.5}$, $\varepsilon_h = \varepsilon_0\varepsilon_{rh}$ and for the non-magnetic material $\mu_h = \mu_0\mu_{rh} = \mu_0$. If we neglect the shunt admittance at the interface between the mismatched parallel-plate waveguides, the reflection coefficient R and transmission coefficient T can be expressed using transmission line theory [3]:

$$R = \frac{-j(Z_{0I}^2 - Z_{0II}^2) \sin(k_h l)}{2Z_{0I}Z_{0II} \cos(k_h l) + j(Z_{0I}^2 + Z_{0II}^2) \sin(k_h l)}$$

$$T = \frac{2Z_{0I}Z_{02}}{2Z_{0I}Z_{02} \cos(k_h l) + j(Z_{0I}^2 + Z_{0II}^2) \sin(k_h l)} \quad (2)$$

Assuming a total transmission, the EM wave propagation through the parallel plate waveguide with a discontinuity is possible when either $k_h l = p\pi$, where $p = 1, 2, 3, \dots$ or, $Z_{0I} = Z_{0II}$. The first condition of propagation (i.e., $k_h l = p\pi$) signifies Fabry-Pérot resonance, which is quite sensitive to the length of section II and the order of resonating mode p [3]. In contrast, the second condition is independent of the dimension of section II along the direction of wave propagation and provides a unique solution for the zero-order transmission. Considering a significant height mismatch at the two interfaces of section II of the same width a , the zero-order transmission is possible when there is an impedance match, i.e. $\eta_d d = \eta_h h$. For the height mismatched parallel-plate waveguide filled with a non-magnetic material, the condition of wave transmission can be given [3]:

$$\frac{\varepsilon_{rh}}{\varepsilon_{rd}} = \left(\frac{h}{d}\right)^2 \quad (3)$$

From (3), it can be observed that the ratio of relative permittivity depends on the square of the ratio of the height mismatch. For the most practical case, when each section of the parallel plate waveguide with a discontinuity is made of the same passive non-magnetic material, i.e. $\varepsilon_{rh} = \varepsilon_{rd}$, the concept of effective permittivity (ε_{eff}) can be introduced in (3). According to the second condition of total transmission, the concept of effective permittivity is the only approach to reach the impedance match through manipulating the medium property inside section II. The effective intrinsic impedance of section II in terms of ε_{eff} is given as $\eta_h = [\mu_h/(\varepsilon_0 \varepsilon_{eff})]^{0.5}$. To discuss a pragmatic parallel plate waveguide made of a substrate having relative permittivity $\varepsilon_{rd} = 2$ and height mismatch $d = 10h$, the effective relative permittivity of section II is obtained as $\varepsilon_{eff} = 0.02$, which is close to zero. Such a waveguide section is referred to as an epsilon-near-zero (ENZ) medium; the ENZ medium possesses a very high impedance, and extremely large wavelength compared to that in the free space.

From the above discussion, it can be understood that a simple arrangement of height mismatch in a parallel-plate waveguide can modulate the effective permittivity of the medium between two metallic plates. According to Maxwell's equations, the ENZ medium does affect EM wave propagation. When the effective permittivity of a medium approaches zero, the curl of the Maxwell equation vanishes, e.g., $\nabla \times \mathbf{H} = j\omega \varepsilon_{eff} \mathbf{E} \approx 0$. In such cases, Maxwell's equations suggest a quasi-static model of EM wave propagation through the ENZ medium, which means that quasi-static total transmission is possible even at a very high frequency. ENZ media are interesting for radio frequency (RF) and microwave engineering since the EM field can travel along the direction of wave propagation without significant change in phase. This type of EM wave propagation through the ENZ medium is termed 'tunneling'. The tunneling of EM waves through an arbitrarily shaped ENZ medium is also possible that offers a solution of wave transmission through the junctions with high impedance mismatch

[6]. The uniform, quasi-static electric field inside section II (Fig. 3) can be utilized for sensing the dielectric properties of test materials.

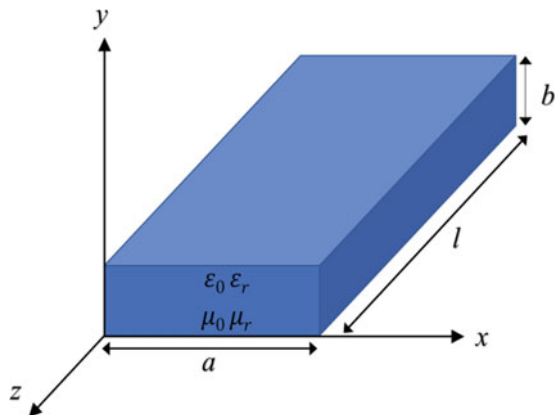
2 Challenges of the ENZ Parallel-Plate Waveguide

Though the parallel-plate waveguide is the most fundamental waveguide to support three propagating modes, i.e., TE, TM, and TEM, the design is not very practical for several reasons. To avoid fringe EM fields, the width of the parallel-plate waveguide must be much greater than the height, i.e. $a \gg d$, which is a prime constraint to practical design. The EM wave excitation in the parallel-plate waveguide is not very pragmatic. Due to the open boundary condition of the parallel-plate waveguide, it suffers from radiation loss. Apart from these fundamental challenges, the above theory of ENZ medium is valid for EM wave propagation in the TEM mode. To provide a concept for developing the ENZ effect at other modes of the waveguide, e.g. the TE mode, a metallic waveguide is considered. Since the metallic waveguide is inherently dispersive, it is an ideal candidate for developing and controlling the ENZ effect, allowing it to be used for sensing applications.

3 Metallic Waveguide: A Dispersive Medium

Let us assume a rectangular metallic waveguide, as shown in Fig. 4, with internal dimensions a , b , and l along the x -axis, y -axis, and z -axis, respectively, and supports the EM wave propagation in the dominant TE_{10} mode. From EM field theory, the propagation constant of a rectangular waveguide that is filled with non-magnetic material can be given as $\beta = [(k)^2 - (k_c)^2]^{0.5}$, where $k_c = [(m\pi/a)^2 + (n\pi/b)^2]^{0.5}$ is the cutoff wavenumber of the TE_{mn} mode, $k = \omega(\mu\varepsilon)^{0.5}$, assuming an air-filled

Fig. 4 Metallic rectangular waveguide as a dispersive medium



waveguide $\mu = \mu_0\mu_r = \mu_0$ and $\varepsilon_e = \varepsilon_0\varepsilon_r$, while m and n are the modal indexes of the TE_{mn} mode. The propagation constant of the rectangular waveguide can also be expressed using the transmission line approach and can be given as $\beta = \omega(\mu\varepsilon_e)^{0.5}$, where $\varepsilon_e = \varepsilon_0\varepsilon_{eff}$ is the effective permittivity of the medium inside the waveguide. In this case, both of the propagation constants can be equated to obtain an expression of the effective permittivity of the non-magnetic medium inside the metallic waveguide [4]:

$$\varepsilon_e = \varepsilon - \frac{1}{\omega^2\mu} \left[\left(\frac{m\pi}{a} \right)^2 + \left(\frac{n\pi}{b} \right)^2 \right] \quad (4)$$

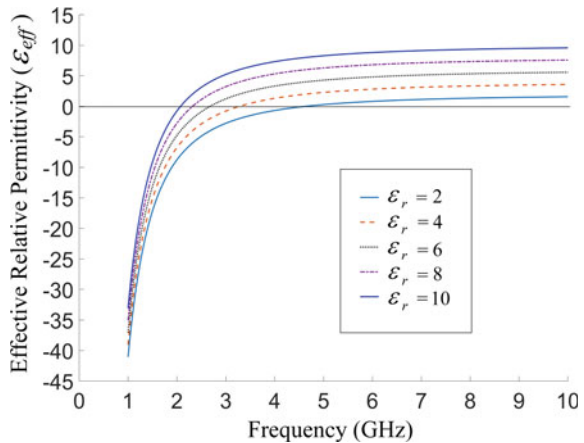
For the dominant TE_{10} mode (i.e., $m = 1, n = 0$), Eq. (4) can be expressed in a simplified form as:

$$\varepsilon_{eff} = \varepsilon_r - \left(\frac{c}{2af} \right)^2 \quad (5)$$

where $c = (\mu_0\varepsilon_0)^{0.5}$ is the speed of light in free space, and $f = \omega/2\pi$ is the linear frequency of operation.

It is interesting to observe that (5) is independent of the height and length of the waveguide but depends inversely on the width of the waveguide. It is to be noted here that the effective permittivity of the medium inside the waveguide also depends on the frequency of operation, which makes the waveguide a highly dispersive medium. For example, let us consider an X-band waveguide with dimension $a = 22.86$ mm that can be filled with dielectric material with various dielectric constants ranging from 2 to 10. Using (5), the effective relative permittivity of the waveguide is calculated for the microwave frequency ranging from 1 to 10 GHz, as shown in Fig. 5. It is interesting to observe from Fig. 5 that the effective medium of such a metallic waveguide is

Fig. 5 Dispersive effective relative permittivity of an X-band rectangular waveguide filled with a non-magnetic material of relative permittivity ε_r



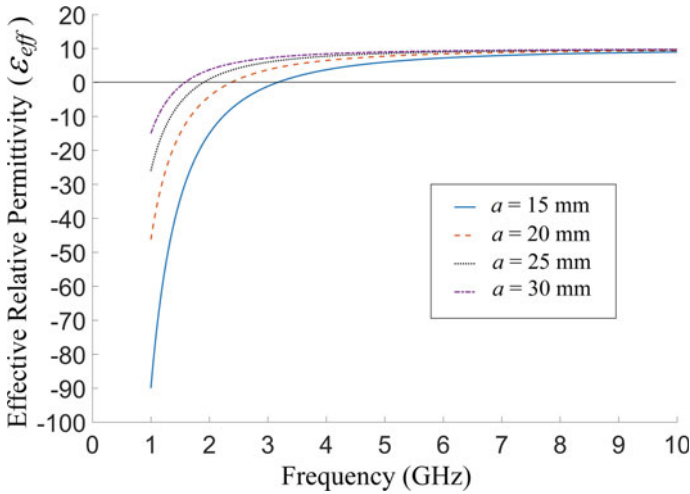


Fig. 6 Dispersive effective relative permittivity of a rectangular waveguide having width a and filled with a material of relative permittivity $\epsilon_r = 10$

quite dispersive, and possesses all possible real values of permittivity, i.e. negative, zero, and positive values. Further note that ϵ_{eff} becomes negative below the cutoff frequency, $f_c = [2a(\mu\epsilon)^{0.5}]^{-1}$, which restricts the wave propagation in the forward direction, and it is mainly due to this reason that the waveguide is also known as a high-pass filter. The epsilon-zero line, i.e. the horizontal line which represents $\epsilon_{eff} = 0$ in Fig. 5, illustrates the region where the metallic waveguide with passive non-magnetic material performs as an ENZ medium.

A similar plot is given in Fig. 6, which shows the dispersive nature of the effective relative permittivity of the metallic waveguide for various values of waveguide width a . It is quite interesting to see that even for a fixed dielectric constant, i.e. $\epsilon_r = 10$, the effective permittivity of the waveguide can be manipulated by changing the value of a . In Fig. 6, the $\epsilon_{eff} = 0$ line separates the negative and positive regions of the effective permittivity of the metallic waveguide. The non-magnetic medium inside the rectangular waveguide near the meeting points of the $\epsilon_{eff} = 0$ line and the dispersive curves drawn for various values of a can be considered an ENZ medium.

4 Metallic ENZ Waveguide

Since the negative permittivity profile of the waveguide is below the cutoff frequency, the effective permittivity near the ENZ frequency region becomes essential to utilize the metallic waveguide as a metamaterial medium. From the expression of guided wavelength, λ_g in the TE_{10} mode [7], i.e.

$$\lambda_g = \frac{\lambda}{\sqrt{1 - (\lambda/\lambda_c)^2}} = \frac{\lambda}{\sqrt{1 - (f_c/f)^2}} \quad (6)$$

it is apparent that at $f = f_c$, the wavelength inside the rectangular waveguide tends to infinity. It may also be noted here that the impedance of the TE₁₀ mode at $f = f_c$ becomes infinite too, and due to this reason, the waveguide operation near the cutoff frequency is avoided in general. However, the property of guided wavelength near $\lambda = \lambda_c$ can be appreciated since tunneling of the EM wave without phase variation is possible over a finite distance. Since the phase variation over a limited distance is constant, the amplitude of the electric field, as well as the magnetic field, remains constant throughout the medium. Though the waveguide is a highly dispersive media for $f > f_c$, as also observed from Figs. 5 and 6, a dispersionless propagation accompanied by low attenuation can be experienced at the tunneling frequency, which is the main advantage of the ENZ medium. From the electromagnetic field theory of rectangular waveguides, the electric field of the TE_{*mn*} mode can be given as in [8]:

$$\begin{aligned} E_x &= -A_{mn} \frac{n\pi}{b} \cos\left(\frac{m\pi}{a}x\right) \sin\left(\frac{n\pi}{b}y\right) e^{-j\beta z} \\ E_y &= A_{mn} \frac{m\pi}{a} \sin\left(\frac{m\pi}{a}x\right) \cos\left(\frac{n\pi}{b}y\right) e^{-j\beta z} \end{aligned} \quad (7)$$

where $A_{mn} = \sqrt{\frac{\epsilon_m \epsilon_n}{ab} \left[\left(\frac{m\pi}{a}\right)^2 + \left(\frac{n\pi}{b}\right)^2 \right]^{-0.5}}$, and $\epsilon_i = \begin{cases} 1, & i = 0 \\ 2, & i \neq 0 \end{cases}$.

From (7), it is recognized that the dominant mode (i.e., $m = 1, n = 0$) possesses a non-zero electric field component along the y -axis, which can be given as:

$$E_y = \sqrt{\frac{2}{ab}} \sin\left(\frac{\pi}{a}x\right) e^{-j\beta z} \quad (8)$$

It is imperative to note from (5) that the effective permittivity profile is independent of the height of the waveguide along the y -direction. Moreover, it is evident from (8) that for a rectangular waveguide of uniform cross-section, the electric field is independent of variation in amplitude and phase along the y -direction, whereas the intensity of the electric field depends on the cross-sectional dimensions a and b . It is interesting to note from (5) and (8) that width a of the waveguide controls the cut-off frequency as well as the effective permittivity of the medium, while height b of the waveguide can modify the strength of the electric field. Since the electric field, as given in (8) appears normal to the top and bottom plates of the waveguide, height b mainly produces a capacitive effect that can be analyzed using the transmission line theory of waveguides. The capacitive effect can be controlled by adjusting the height of the waveguide, where a lower value of b produces a higher capacitive effect that can be explained using the theory of the equivalent voltage and current for a rectangular waveguide. To analyze the transmission line equivalence of the TE₁₀ mode, let us assume an electric field and magnetic field traveling in the waveguide given as

$E_y = (A^+ e^{-j\beta z} + A^- e^{j\beta z}) \sin(\pi x/a)$ and $H_x = -(1/Z_0)(A^+ e^{-j\beta z} - A^- e^{j\beta z}) \sin(\pi x/a)$, where A^+ and A^- represent the amplitudes of the transverse field components along the positive and negative z -axes, respectively, and Z_0 is the characteristic impedance of the TE_{10} mode. From the transmission line model, the equivalent voltage and current waves for the TE_{10} mode can be given as $V = V^+ e^{-j\beta z} + V^- e^{j\beta z}$ and $I = (1/Z_0)(V^+ e^{-j\beta z} - V^- e^{j\beta z})$, where V^+ and V^- represent the amplitude of the voltage wave traveling along the positive and negative z -axes, respectively, and can be estimated from the boundary conditions. The coefficients of the transmission line model and waveguide fields can be compared using the transverse field components, the characteristic impedance, and the power flow of the TE_{10} mode. It is found that the ratio of equivalent coefficients of forward and backward traveling waves are equal and can be given as $V^+/A^+ = V^-/A^- = (ab/2)^{0.5}$ [9]. A change in the height of the waveguide changes the amplitude of the voltage wave, which further supports the theory of capacitive tuning. The findings from the equivalent voltage and current for the rectangular waveguide is also found to be in line with the field expression obtained from the EM field theory given in (8) for the TE_{10} mode.

From the above discussion, it can be concluded that a change in the waveguide height along the y -direction inevitably brings a difference in amplitude of the electric field. The lower height of the rectangular waveguide increases the capacitive effect and the reduced volume available for power flow enhances the electric field concentration of the TE_{10} mode, and termed “energy squeezing”. Total transmission is still possible inside the reduced height of the rectangular waveguide, and is termed “super coupling”, which is explained later in this chapter. The experimental verification of energy squeezing and tunneling through the super coupling effect inside the metallic waveguide is given in [10].

In the recent past, dielectric sensing using waveguide sensors was limited to the sinusoidal variation of the electric field [11]. Nevertheless, the ENZ medium provides a higher intensity of electric field along with EM wave propagation having a “static-like” phase, i.e., with essentially no phase delay. The EM wave tunneling through the ENZ medium with an enhanced electric field and a constant phase in TE_{10} mode may open a new window for dielectric sensing with improved resolution [5].

5 Circuit Analysis of Two-Port Waveguide

Let us consider a two-port lossless waveguide section of length l , propagation constant β , and characteristic impedance Z_0 , as shown in Fig. 4. The two-port scattering coefficients can be given in matrix form from [9]:

$$\begin{bmatrix} S_{11} & S_{12} \\ S_{21} & S_{22} \end{bmatrix} = \begin{bmatrix} 0 & e^{-j\beta l} \\ e^{-j\beta l} & 0 \end{bmatrix} \quad (9)$$

The above scattering matrix gives the typical values of the reflection and transmission coefficients, which considers that either both ends of a waveguide of finite length l terminate with a matched impedance, or that the length of the waveguide is infinitely long. A rectangular waveguide connected to the source and load sections is shown in Fig. 7. In most practical cases, either when the load impedance Z_L or source impedance Z_G is not the same as Z_0 or a discontinuity is present in the waveguide, the reflection coefficients are not zero. A generalized two-port circuit model can illustrate the idea of a practical waveguide and its scattering coefficients. A circuit representation of Fig. 7 is given in Fig. 8, where a waveguide of length l is represented in terms of a T-network having series impedance Z_1 and Z_2 , and shunt impedance Z_3 . The input impedance of the circuit shown in Fig. 8 can be given as $Z_{in} = Z_1 + Z_3 \parallel (Z_2 + Z_L)$. When Z_{in} is known, the reflection coefficient at the source can be given from [9]:

$$S_{11} = \frac{Z_{in} - Z_G}{Z_{in} + Z_G} \quad (10)$$

and the transmission coefficient obtained at the load can be written as [12]:

$$S_{21} = 2\sqrt{\frac{Z_G}{Z_L}} \left(\frac{Z_{in}}{Z_{in} + Z_G} \right) \left(\frac{Z_L}{Z_L + Z_2} \right) \left(\frac{Z}{Z + Z_1} \right) \quad (11)$$

where $Z = Z_3 \parallel (Z_2 + Z_L)$. For a reciprocal system, $Z_1 = Z_2$, while the source and load impedances are real for a practical system, i.e., $Z_G = R_G$ and $Z_L = R_L$. For a

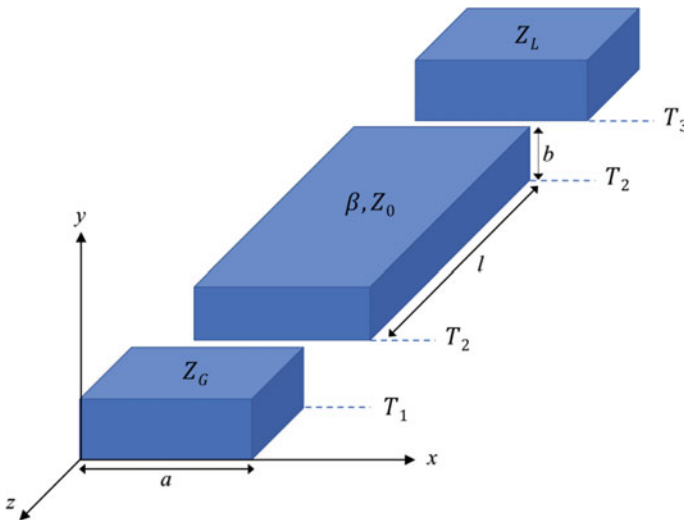


Fig. 7 Two-port rectangular waveguide with source and load sections

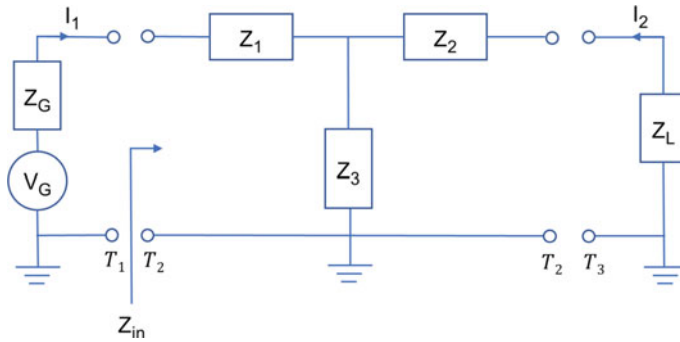


Fig. 8 Circuit representation of a general two-port waveguide

matched and reciprocal two-port system, $Z_G = R_G = Z_L = R_L = Z_0$, which gives $Z_{in} = Z_1 + Z_3 \parallel (Z_1 + Z_0)$ and $Z = Z_3 \parallel (Z_1 + Z_0)$. The simplified expression of the reflection and transmission parameters can be written from [12]:

$$S_{11} = \frac{Z_{in} - Z_0}{Z_{in} + Z_0} \quad S_{21} = 2 \left(\frac{Z_{in}}{Z_{in} + Z_0} \right) \left(\frac{Z_0}{Z_0 + Z_1} \right) \left(\frac{Z}{Z + Z_1} \right) \quad (12)$$

6 Circuit Analysis of Two-Port ENZ Waveguides

As discussed earlier, a discontinuity in terms of the smaller height of the rectangular waveguide augments the ENZ effect near the cutoff frequency. In the previous section, we examined the theory and the circuit model of a general two-port waveguide. Let us suppose that a waveguide of length l , as shown in Fig. 9a, has the same dimensions and material parameters as of the input and output waveguide sections, except height $h \ll b$. The input and output waveguide sections are matched with the characteristic impedance, i.e., $Z_G = Z_L = Z_0$.

The waveguide structure shown in Fig. 9a assumes a capacitive discontinuity connected to matched terminals of characteristic impedance Z_0 . Considering the dominant TE_{10} mode, the waveguide section (T_2T_2) of Fig. 9a can be modeled as an E -plane waveguide discontinuity as shown in Fig. 9b. The E -plane waveguide discontinuity of Fig. 9b can be considered as the capacitive obstacle of finite length l . A detailed analysis of such a waveguide discontinuity is given in [13], where the equivalent circuit model matched with the characteristic admittance of the waveguide, $Y_0 = 1/Z_0$, forms a π -network and shown in Fig. 10a. The shunt susceptance B_a of the π -network accommodates the capacitive effect and the localized evanescent modes at both ends of the narrow waveguide section of height h , whereas the inductive susceptance appearing in series represents the lossless narrow waveguide section of length l . For calculating the scattering matrix in terms of impedance using (12),

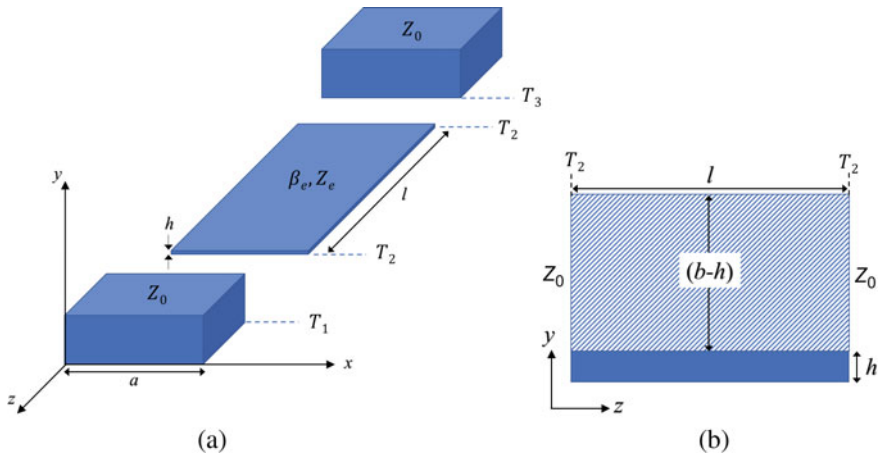


Fig. 9 **a** Two-port rectangular waveguide with a capacitive discontinuity, and **b** side view of the waveguide discontinuity (the dashed area is filled with metal)

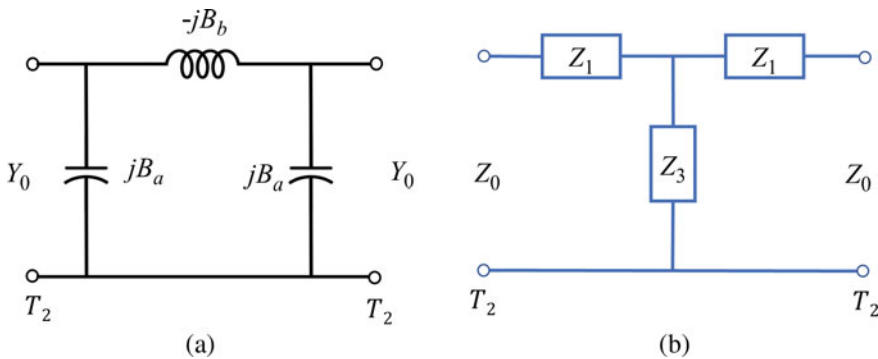


Fig. 10 **a** Equivalent circuit model of the capacitive waveguide discontinuity of finite length l , and **b** the equivalent T-network of (a)

the π -network is transformed into an equivalent T-network, which is matched with the characteristic impedance of the waveguide Z_0 . The T-network of the waveguide discontinuity of length l is shown in Fig. 10b and their respective parameters can be given from [13]:

$$\begin{aligned}
 Z_1 &= j \frac{1}{(2B_b - B_a)} \\
 Z_3 &= -j \frac{B_b}{B_a(2B_b - B_a)}
 \end{aligned}
 \tag{13}$$

where

$$\begin{aligned}
B_a &= B + \frac{1}{\alpha Z_0} \tan\left(\frac{\pi l}{\lambda_g}\right) \\
B_b &= \frac{1}{\alpha Z_0} \csc\left(\frac{2\pi l}{\lambda_g}\right) \\
B &= \frac{1}{Z_0 \lambda_g} \left[\ln \frac{1 - \alpha^2}{4\alpha} \left(\frac{1 + \alpha}{1 - \alpha}\right)^{0.5(\alpha + \frac{1}{\alpha})} + 2 \frac{A + A' + 2C}{AA' - C^2} \right] \\
A &= \left(\frac{1 + \alpha}{1 - \alpha}\right)^{2\alpha} \frac{1 + \sqrt{1 - (b/\lambda_g)^2}}{1 - \sqrt{1 - (b/\lambda_g)^2}} - \frac{1 + 3\alpha^2}{1 - \alpha^2} \\
A' &= \left(\frac{1 + \alpha}{1 - \alpha}\right)^{2/\alpha} \frac{1 + \sqrt{1 - (h/\lambda_g)^2} \coth\left(\sqrt{1 - (h/\lambda_g)^2} \frac{\pi l}{2h}\right)}{1 - \sqrt{1 - (h/\lambda_g)^2} \coth\left(\sqrt{1 - (h/\lambda_g)^2} \frac{\pi l}{2h}\right)} + \frac{3 + \alpha^2}{1 - \alpha^2} \\
C &= \left(\frac{4\alpha}{1 - \alpha^2}\right)^2, \quad \alpha = \frac{h}{b}
\end{aligned} \tag{14}$$

where λ_g is defined in (6). The above equations are obtained by the equivalent static method and valid for $b/\lambda_g < 1$. The value of B gives less than a 5% error for $\alpha < 0.5$, while the error is less than 1% for all values of α when $l/h \geq 1$ [13]. It may be noted from (14) that the susceptances B_a and B_b are expressed in terms of λ_g , therefore, the parameters of the T-network as given in (13) become frequency-dependent. The frequency-dependent reflection and transmission parameters of a metallic waveguide with the capacitive discontinuity of height h and length l can be calculated using (12)–(14). As we have seen from (5) and Figs. 5 and 6 that the waveguide medium close to f_c becomes the ENZ medium, the transmission coefficients calculated near the cutoff frequency of rectangular waveguide would be the response to the ENZ effect.

7 Numerical Verification of Two-Port ENZ Waveguide

To verify the above circuit model, a numerical analysis can be performed using a full-wave EM solver based on the finite element method (FEM). The scattering matrix is calculated for an X-band air-filled waveguide ($a = 22.86$ mm and $b = 10.16$ mm) having a discontinuity of height h over section length l , as shown in Fig. 9. The dimensions of the waveguide discontinuity are chosen such that (13) and (14) remain valid and provide scattering parameters of reasonable accuracy. The height is assumed as $h = 1$ mm, for $h/b \ll 1$, and l is assumed as 40 mm and 50 mm such that $l/h \gg 1$. The transmission coefficients computed using the circuit analysis are plotted along with the results obtained using the numerical analysis.

Fig. 11 Transmission coefficient of X-band ENZ waveguide of length $l = 40$ mm

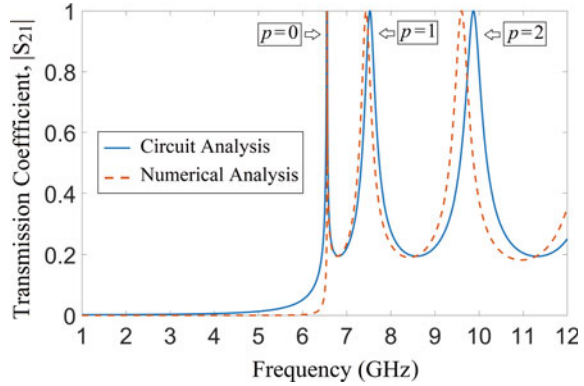
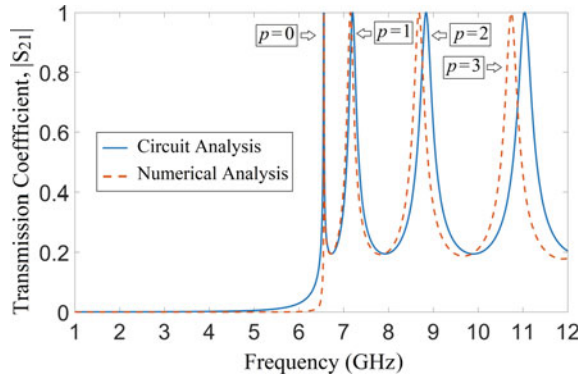


Fig. 12 Transmission coefficient of X-band ENZ waveguide of length $l = 50$ mm



The transmission coefficients for both the X-band waveguides, i.e. for $l = 40$ mm and $l = 50$ mm are shown in Figs. 11 and 12, respectively.

The transmission coefficient is calculated over a broad frequency range, i.e. 1–12 GHz, covering the cutoff frequency of the waveguide and the X-band. From Figs. 11 and 12, it can be observed that the results calculated from the circuit model achieve a good match with the numerical results computed using FEM analysis. It is interesting to note from Figs. 11 and 12 that, although a change in the length of the ENZ waveguide gives new transmission peaks at a frequency higher than f_c , the first transmission peak near f_c remains unchanged. From Figs. 11 and 12 it can be observed that the transmission peaks are associated with the TE_{10p} mode along the ENZ waveguide section. The frequency of the TE_{10p} mode can be given as [7]:

$$f_p = \frac{1}{2\sqrt{\mu\epsilon}} \sqrt{\left(\frac{\pi}{a}\right)^2 + \left(\frac{p\pi}{l}\right)^2} \quad (15)$$

It can be noted from (15) that the frequency of the zero-order transmission related to $p = 0$ is independent of the length of the waveguide, which suggests the frequency

where the ENZ effect is observed. It is evident from Figs. 11 and 12, unlike the EM wave transmission of the TE_{10p} modes ($p \neq 0$), that zero-order EM wave transmission is independent of waveguide length. The modal index of the TE_{100} mode, i.e. $p = 0$, also suggests a similar phenomenon, i.e. the variation in the number of half-wavelengths along the z -direction is zero. It may also be noted from Figs. 11 and 12 that the transmission at f_c observes the smallest 3-dB bandwidth, which provides a higher quality factor compared to the quality factors of TE_{10p} modes ($p \neq 0$). The higher quality factor is quite a desirable parameter when designing EM devices such as sensors and filters.

A tabular representation of various transmission frequencies related to the TE_{10p} modes is provided in Table 1. In this table, the transmission frequency calculated using the circuit analysis, f_{pc} , is compared with the transmission frequency obtained from the numerical analysis, f_{pn} , whereas frequency f_p from (15) is taken as the reference. It may be noted here that unlike f_{pc} and f_{pn} , f_p represents the resonating modes of the rectangular cavity where $p = 0$ signifies the cutoff frequency. For the TE_{100} mode, $f_p \cong f_{pc} \cong f_{pn}$. For the TE_{10p} ($p \neq 0$) mode, though it is observed from Table 1 that $f_p > f_{pc} > f_{pn}$, it is found that f_{pc} closely follows f_{pn} . A lower value of f_{pc} that provides a fair comparison with f_{pn} as compared to f_p is mainly due to the consideration of the shunt susceptance B_a in the circuit analysis. Since it is evident from Table 1 that the EM wave transmission, except the TE_{100} mode, depends on the length of the ENZ waveguide as well as modal index p , it becomes essential to observe the electromagnetic field configuration of the TE_{10p} modes. Therefore, 3D electric field configurations of the air-filled ENZ waveguide ($a = 22.86$ mm, $h = 1$ mm, and $l = 40$ mm) are computed using the FEM based full-wave EM solver. For a correct excitation and reception of the TE_{10} mode, the air-filled X-band waveguide of length 25 mm is connected at the two sides of the ENZ waveguide. The electric fields of three consecutive TE_{10p} modes corresponding to $p = 0, 1$, and 2 are shown in Figs. 13, 14 and 15, respectively.

To better illustrate the electric field, Figs. 13, 14 and 15 are plotted when both the sources at the input and output ports remain simultaneously active. It may be noted here that the representation of the electric fields for Figs. 14 and 15 may differ if analyzed with single port excitation; however, the modal indexes would be the same for both cases. It is observed from Fig. 13 that for the TE_{100} mode, both the

Table 1 Frequency of TE_{10p} modes of X-band ENZ waveguide obtained from circuit theory and numerical analysis

Frequency	l	$p = 0$	$p = 1$	$p = 2$	$p = 3$
f_p (GHz)	40 mm	6.56	7.56	9.96	13.02
f_{pc} (GHz)		6.56	7.53	9.87	12.86
f_{pn} (GHz)		6.56	7.40	9.49	12.13
f_p (GHz)	50 mm	6.56	7.22	8.89	11.14
f_{pc} (GHz)		6.56	7.20	8.84	11.04
f_{pn} (GHz)		6.56	7.15	8.68	10.74

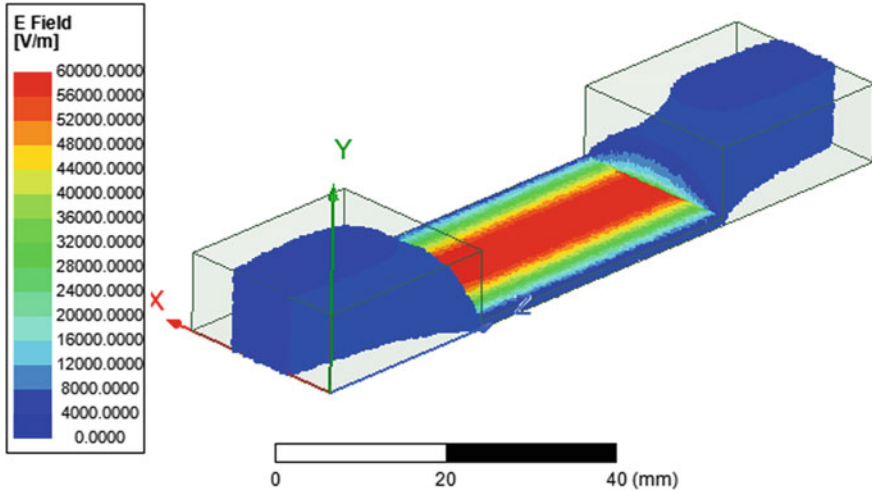


Fig. 13 y -component of the electric field of TE_{100} mode

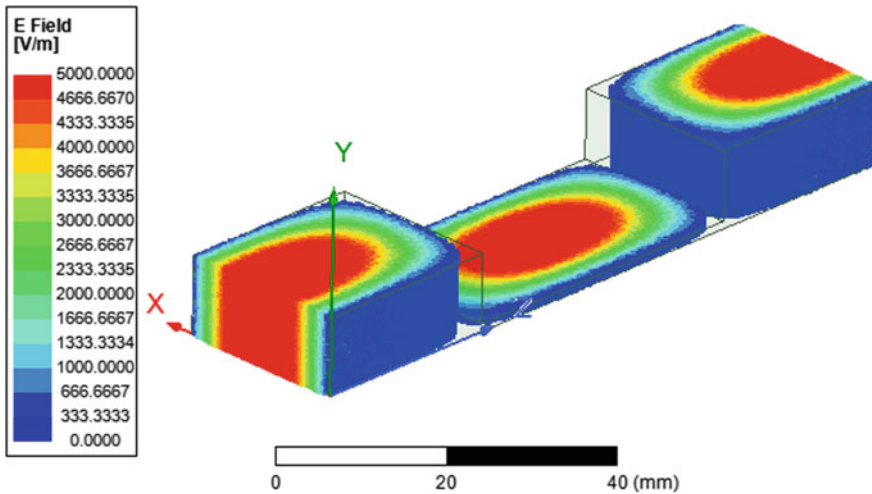


Fig. 14 y -component of the electric field in TE_{101} mode

amplitude and the phase of the electric field remain constant throughout the length of the ENZ medium, and as expected the electric field along the x -axis features a sinusoidal variation. On the contrary, it can be observed from Figs. 14 and 15 that the amplitude and phase of the electric field for the TE_{101} mode and TE_{102} mode feature sinusoidal variation along the length and the width of the waveguide discontinuity.

From Figs. 13, 14 and 15, it is interesting to note that for the TE_{10p} ($p \neq 0$) mode, the electric field representation along the x - and z -directions is sinusoidal, while this

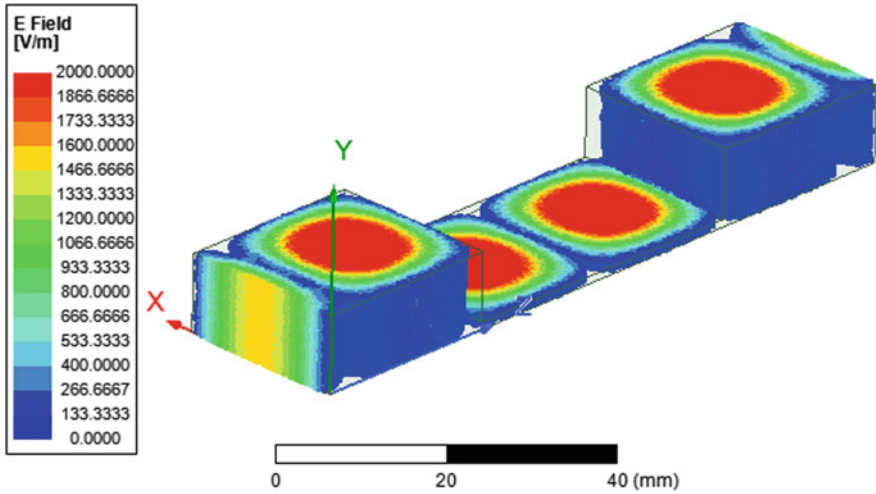


Fig. 15 y -component of the electric field in TE_{102} mode

is not the same for the zero-order transmission. From Fig. 13, it can be observed that the intensity of the electric field along the z -direction, which is uniform throughout the discontinuity of height h and length l , is significantly higher than the intensity of the electric field in the waveguide section of height b . If we assume an ideal power transmission of the TE_{100} mode at a tunneling frequency near f_c , the power flow in each section of the ENZ waveguide should be equal. In this condition, by observing the color map in Fig. 13, it appears that the energy available to a waveguide of height b is squeezed inside the waveguide section of height h and length l . The energy squeezing phenomenon inside a narrowed waveguide, which is mainly due to the ENZ effect, is found to be independent of the shape and size [4]. The total power transmission due to the ENZ effect is possible through sharp bends and twisted channels [6]. To achieve a quantitative understanding of the EM wave tunneling in the ENZ medium, the amplitude of the only non-zero component of the electric field of the TE_{100} mode, i.e. E_y , is computed along the z -axis as well as along the x -axis of the waveguide and given in Figs. 16 and 17, respectively. To highlight the change in the amplitude of the electric field, $|E_y|$ for the ENZ waveguide compared to a conventional waveguide of the same length, the electric field strength of both the waveguides are plotted on the same graph. The electric fields along the z -direction for the regular and ENZ waveguide, as shown in Fig. 16, are numerically calculated in the XY -plane at $(x, y) = (a/2, b/2)$ and $(x, y) = (a/2, h/2)$, respectively. Similarly, the electric fields along the x -direction for the regular and ENZ waveguides, as given in Fig. 17, are calculated in the YZ -plane at $(y, z) = (b/2, l/2)$ and $(y, z) = (h/2, l/2)$, respectively.

As discussed before, the expression of the voltage wave corresponding to the TE_{10} mode and traveling along the z -direction is given by $V(z) = V^+ e^{-j\beta z}$ [9]. Assuming a PEC boundary for a lossless waveguide, the maximum amplitude of the voltage wave

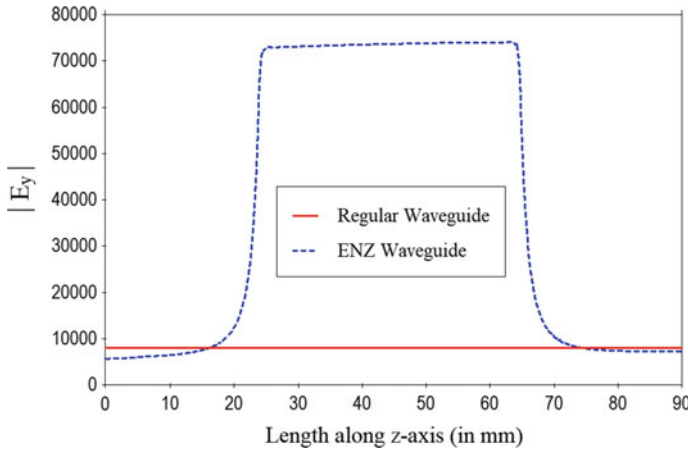


Fig. 16 A comparison between the y-component of the electric fields of the ENZ waveguide and regular waveguide along the z-axis in TE₁₀₀ mode

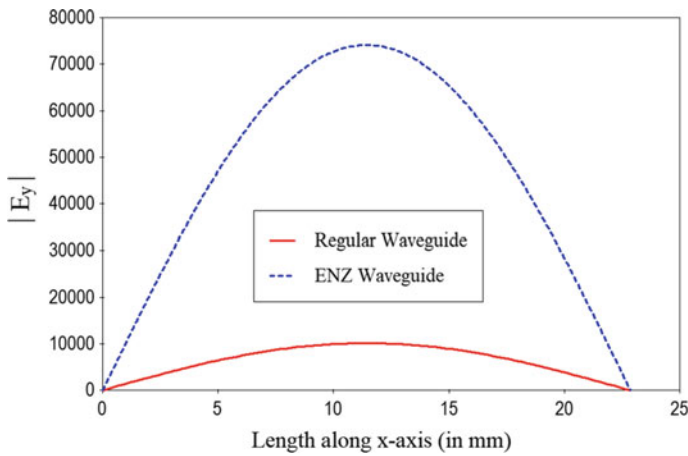


Fig. 17 A comparison between the y-component of the electric fields of the ENZ waveguide and regular waveguide along the x-axis in TE₁₀₀ mode

can be considered to be a constant throughout the waveguide. From the assumption of the quasi electrostatic model, the electric field normal to the top and bottom plates can be given as $E(z) = -\partial V(z)/\partial y$. Let the electric fields in the waveguide of height b and h are E_{by} and E_{hy} , respectively, then ratio of electric fields (E_{hy}/E_{by}) can be expressed as the ratio of the waveguide heights (b/h), which explains the inverse relationship between the strength of the electric field and the height of the waveguide. For the X-band waveguide operating in the TE₁₀ mode, as shown in Figs. 9a and 13 (where $h = 1$ mm and $b = 10.16$ mm), the electric field strength inside a waveguide of height

h is expected to be nearly ten times higher than the electric field strength inside a waveguide of height b . From Fig. 16, a similar effect can be observed for $|E_y|$, where the value of $|E_y|$ between 25 and 65 mm along the z -axis of the ENZ waveguide is recorded to be more than ten times higher compared to the value of $|E_y|$ between 0–25 mm and 65–90 mm. However, the value of $|E_y|$ for a regular waveguide is almost constant and significantly lower, as expected. From Fig. 17, the maximum amplitudes of the half-wave variation along the x -axis, i.e. ($\max|E_y|$) of the ENZ waveguide and the regular waveguide are also found to be in line with the earlier observation.

It may be noted here that the electric fields plotted in Figs. 13, 16, and 17 are at the cutoff frequency of the waveguide, f_c , which provides the guided wavelength of $\lambda_g \rightarrow \infty$. For this reason, the electric field for the regular waveguide along the z -direction, as shown in Fig. 16, has a constant amplitude along the entire length of the waveguide, and so the electric field for the ENZ waveguide outside the discontinuity. At this point, it should be mentioned that the quasi-static electric field of the ENZ waveguide augmented near f_p at the E -plane discontinuity (of height h and length l) is independent of the cutoff frequency of the input and output waveguides. This can be easily demonstrated by tuning the cutoff frequency of the input and output waveguides (say f_{cw}) at a different wavelength such that each part of the waveguide still works in the dominant mode, i.e., $f_{cw}(\text{TE}_{10}) < f_p < f_{cw}(\text{TE}_{20})$. This property of the ENZ effect is very useful in designing waveguides with sharp bends and corners without losing the propagation characteristics at the ENZ frequency. Several 90° and 180° bent ENZ channels are experimentally tested for energy rerouting and super coupling through the rectangular waveguide ($a = 101.4$ mm, $b = 50.8$ mm) operating in TE₁₀ mode [6]. It is practically possible by choosing either a different width a or, the different dielectric material for the input and output waveguide sections as compared to the ENZ waveguide. One example of such an ENZ waveguide is discussed in the next section.

8 ENZ Waveguide as Dielectric Sensor

From the above sections, it is observed that the ENZ waveguide possesses a few interesting features, e.g., a uniform and intensified electric field compared to a conventional waveguide, a higher quality factor as compared to the TE_{10 p} modes ($p \neq 0$), and the tunneling frequency which is almost independent of the length of the ENZ section. The favorable features augmented due to the ENZ effect are appropriate for employing the ENZ waveguide as a sensing device.

The first demonstration of dielectric sensing using the rectangular ENZ waveguide is illustrated in [14] and shown in Fig. 18. The ENZ waveguide in Fig. 18 is almost like that in Figs. 9, 13, 14 and 15 except for a cavity region of length L_{cav} , which is created to locate the dielectric material under test, having relative permittivity ϵ_{cav} . For demonstration purposes, the cavity is created in the middle of an ENZ channel of length L , height a_{ch} , and relative permittivity ϵ_{ch} (shown in blue). The input and

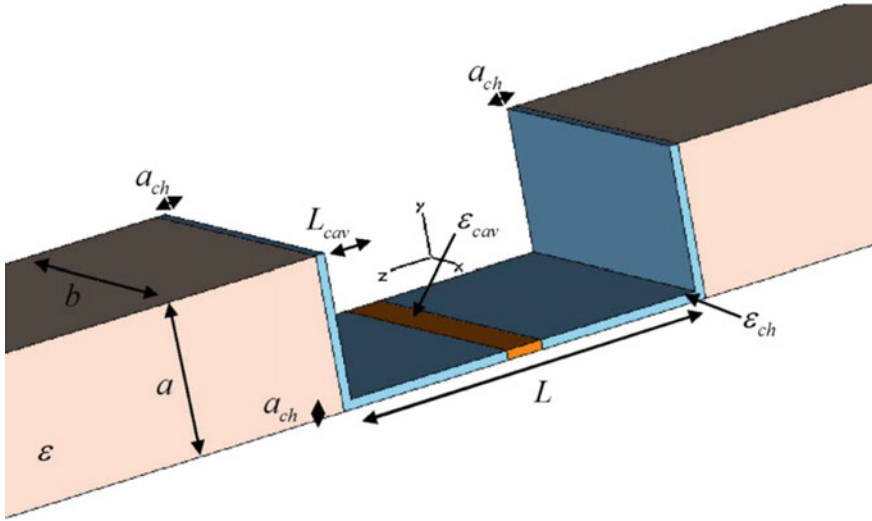


Fig. 18 The geometry of the ENZ waveguide structure proposed as a permittivity sensor. The structure is surrounded by conducting walls (Reprinted with permission from [14]. Copyright ©2008 The American Physical Society.)

output sections of the waveguide joining the E -plane discontinuity have width b , height a and are made of a dielectric material of relative permittivity ϵ . Since the height and relative permittivity of the ENZ channel differ from the input and output waveguide sections, an additional waveguide section of length a_{ch} and height a is attached at each end of the ENZ channel. The additional waveguide sections provide better mode matching and give the characteristic U shape to the ENZ channel, as shown in Fig. 18. As discussed earlier, the ENZ effect is experienced around the cutoff frequency of the narrow section of the waveguide. For ideal transmission through the ENZ section, the cutoff frequency of the input and output waveguide sections must be lower than f_{100} of the E -plane discontinuity, i.e., $\epsilon > \epsilon_{ch}$. It is understood that for a given waveguide, the value of ϵ and ϵ_{ch} is constant while ϵ_{cav} depends on the material under test, which can be evaluated by observing the frequency of ENZ transmission.

The ENZ waveguide, loaded with the test sample, as shown in Fig. 18, can be analyzed using a transmission-line model. Each section of the waveguide can be represented by the effective characteristic impedance $\eta_{eff} = \sqrt{(\mu_0/\epsilon_{eff})}$ and the effective wavenumber $\beta_{eff} = \omega\sqrt{(\mu_0\epsilon_{eff})}$, whereas the matching steps in the U channel can be modeled as voltage transformers with transformation ratio $s = a_{ch}/a$ and parallel reactive loads. As noted in Table 1, the presence of shunt loads slightly downshift transmission frequency; however, they do not notably affect the main features of the ENZ effect. The shunt loads also account for the localized higher-order evanescent mode excitation at the junction of the regular waveguide and the ENZ waveguide, and hence can be neglected. Another good reason for neglecting the reactive loads

of the U channel that appears in the shunt configuration is their high impedance due to $\varepsilon_{eff} \rightarrow 0$, which makes them open-circuit near the tunneling frequency, f_{100} . For a special case, i.e., $\varepsilon_{cav} = \varepsilon_{ch}$ and for identical input and output waveguide sections, the input impedance Z_{in} of the waveguide, as shown in Fig. 18, can be calculated from the transmission line model and given as [4, 14]:

$$Z_{in} = \frac{2s^2\eta_{ch}^2\eta_{wg} + js\eta_{ch}(s^2\eta_{ch}^2 - \eta_{wg}^2)\sin(2\beta_{ch}L)}{s^2\eta_{ch}^2 + \eta_{wg}^2 + (s^2\eta_{ch}^2 - \eta_{wg}^2)\cos(2\beta_{ch}L)} \quad (16)$$

where subscripts ‘*ch*’ and ‘*wg*’ represent the ENZ channel and the input and output waveguide sections, respectively. Total transmission is possible when the input impedance of the overall ENZ waveguide becomes equal to the effective characteristic impedance of the input waveguide section, i.e., $Z_{in} = \eta_{wg}$. For total transmission, the transmission coefficient can be written in terms of the input impedance of the overall waveguide and the characteristic impedance of the input waveguide, and given as:

$$T = \frac{2\eta_{wg}}{Z_{in} + \eta_{wg}} \quad (17)$$

It is interesting to note from (16) that the condition for total transmission is found to be either $L = p\pi/\beta_{ch}$ for $p = 1, 2, 3, \dots$ or $\eta_{wg} = \pm s\eta_{ch}$, where the first condition is related to the Fabry-Pérot resonance of the channel as described earlier for the parallel plate waveguide in Fig. 3. The Fabry-Pérot resonance for the rectangular ENZ waveguide can be verified from Figs. 11 and 12. The second condition refers to the zero-order transmission, where an ENZ waveguide with sharp *E*-plane discontinuity $s \rightarrow 0$ indicates a high channel impedance $\eta_{ch} = \sqrt{(\mu_0/\varepsilon_{ch})}$, which assures $\varepsilon_{ch} \rightarrow 0$. The near-zero relative permittivity of the ENZ channel offers $\beta_{eff} = \omega\sqrt{(\mu_0\varepsilon_{eff})} \rightarrow 0$, which ensures a small phase delay and uniform electric field inside the channel. As explained earlier, the continuity of voltage across the steps at the *E*-plane discontinuity enhances the electric field inside the ENZ channel by a factor of $1/s$ as compared to the electric field in the input and output waveguide sections, which can also be observed in Fig. 16. Due to the interesting properties of the ENZ channel, i.e. the intensified and uniform electric field and the static-like phase, the waveguide arrangement shown in Fig. 18 is utilized for the microwave sensing.

Let us consider the most general case for dielectric sensing based on the arrangement shown in Fig. 18, i.e., the sensing region is filled with a dielectric sample of relative permittivity $\varepsilon_{cav} \neq \varepsilon_{ch}$. Applying the transmission line model to the modified structure, the condition of total transmission for the ENZ frequency can be found after some mathematical manipulation, and given as [14]:

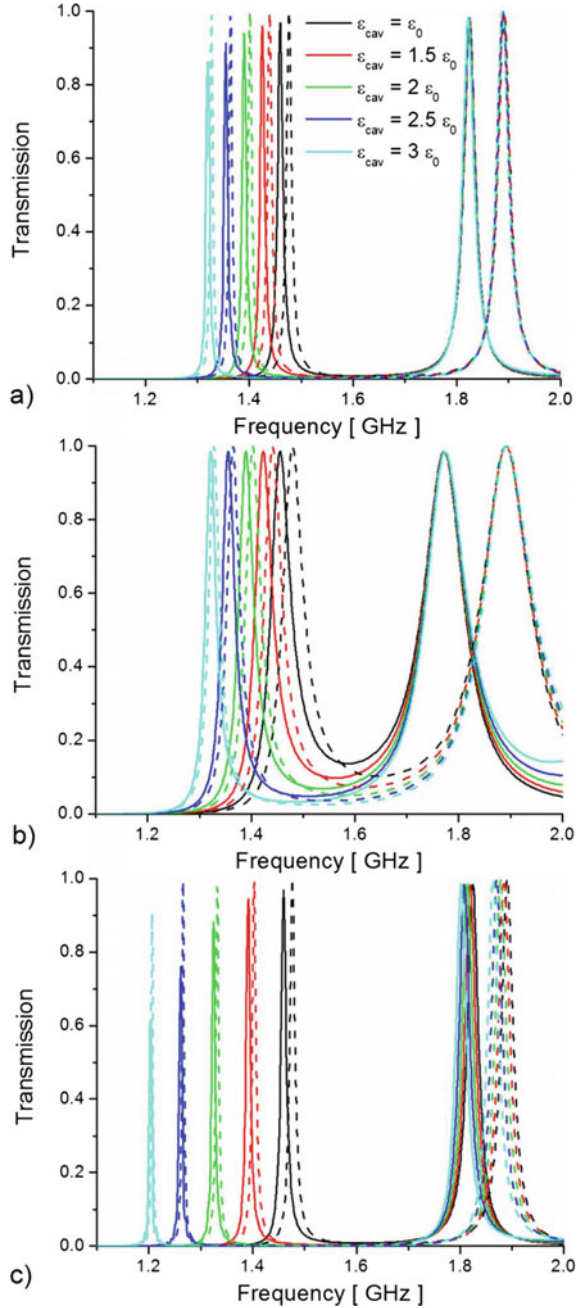
$$\eta_{wg} = \pm s \eta_{ch} \left(1 - \frac{2 \sin(\beta_{cav} L_{cav}) (\eta_{ch}^2 - \eta_{cav}^2)}{\left[(\eta_{ch}^2 - \eta_{cav}^2 + (\eta_{ch}^2 + \eta_{cav}^2) \cos(\beta_{ch} \Delta L)) \sin(\beta_{cav} L_{cav}) \right] + 2 \eta_{ch} \eta_{cav} \cos(\beta_{cav} L_{cav}) \sin(\beta_{ch} \Delta L)} \right) \quad (18)$$

where $\Delta L = L - L_{cav}$ and the subscript ‘cav’ represents the sample parameters. The test sample fits into the cavity made in the middle of the ENZ section for dielectric sensing. From (18), the amount of perturbation caused due to the inclusion of the test sample can be given in terms of the tunneling frequency. To observe the tunneling of EM waves through the loaded ENZ channel, the transmission curves are calculated using the transmission line model, shown as the dashed lines in Fig. 19. The theoretically calculated transmission curves of the loaded ENZ waveguide are compared with the numerical results obtained using the full-wave computational solver, given as the solid lines in Fig. 19. From this figure, it can be seen that the analytical data derived using the transmission line model are in good agreement with the results obtained using full-wave numerical simulations. The agreement between the sets of results justifies the negligence of the reactive shunt loads from the transmission line model, which also suggests that the E -plane discontinuities significantly reduces the excitation of higher-order evanescent modes in the ENZ channel.

The ENZ waveguide dimensions are given in the caption of Fig. 19. The transmission coefficients are calculated using both the transmission line model and the numerical simulation for five typical dielectric test samples, i.e. $\epsilon_{cav}/\epsilon_0 = 1, 1.5, 2, 2.5,$ and 3 . It is observed from Fig. 19 that the shift in tunneling frequency is always toward a lower frequency for $\epsilon_{cav} > \epsilon_{ch}$. The sensitivity of the tunneling frequency was evaluated by changing the dimensions of the ENZ waveguide. Three cases were studied: (a) smaller ENZ height and smaller cavity length, i.e. $a_{ch} = a/64, L_{cav} = L/10$; (b) higher ENZ height and smaller cavity length, i.e. $a_{ch} = a/16, L_{cav} = L/10$; and (c) smaller ENZ height and larger cavity length, i.e. $a_{ch} = a/64, L_{cav} = L/5$.

From Fig. 19a, b, it can be observed that the sensitivity in both cases is of the same order. The sensitivity is defined here as the ratio of the change in tunneling frequency to the change in the relative permittivity of the test dielectric material. For the same length of cavity ($L_{cav} = L/10$), the quality factor calculated for the smaller ENZ waveguide height ($a_{ch} = a/64$) is found to be better than the higher ENZ waveguide height ($a_{ch} = a/16$). From Fig. 19c, it can be observed that increasing the cavity length ($L_{cav} = L/5$) of the ENZ waveguide increases the sensitivity due to an improved perturbation effect, while a better quality factor is obtained due to the smaller ENZ waveguide height ($a_{ch} = a/64$). However, the fundamental Fabry-Pérot resonances in the TE_{101} mode are found to be almost independent of the change in relative permittivity of the test material. The immunity in f_{101} towards the change in the dielectric constant of test material suggests a minimum of the electric field. For the single port excitation of the ENZ waveguides shown in Figs. 9a and 18, a minimum of the electric field in the TE_{101} mode is expected at the center of the ENZ

Fig. 19 Transmission coefficient for the U channel of Fig. 18 with $L = 127$ mm, $b = 2a = 101.6$ mm, $\epsilon = 2\epsilon_0$, and $\epsilon_{ch} = \epsilon_0$: **a** $a_{ch} = a/64$, $L_{cav} = L/10$; **b** $a_{ch} = a/16$, $L_{cav} = L/10$; and **c** $a_{ch} = a/64$, $L_{cav} = L/5$. Solid lines: full-wave simulations; dashed lines: TL model (Reprinted with permission from [14]. Copyright ©2008 The American Physical Society.)



channel. It may be noted from Fig. 19 that the transmission line model and numerical analysis do not match well around Fabry-Pérot resonances. This may be due to the reactive shunt loads that were safely neglected in the transmission line model are now effective due to the larger value of the effective permittivity (i.e., $\epsilon_{eff} > 0$) for the TE_{10p} modes ($p \neq 0$).

From the above discussions, it is confirmed that the ENZ microwave sensor can be designed and fabricated using standard waveguide technology. Since the metallic waveguides are bulky, costly, and not easy to integrate with monolithic microwave integrated circuit (MMIC) and planar devices, the planar technology is very common in practice. In the next section, an ENZ waveguide is designed and fabricated using planar technology. Planar technology allows the easy and cost-effective production of microwave devices, leading to flexibility and novelty in design. Planar technology can be used to design an ENZ microwave sensor operating at multiple frequencies, as explained in the next section.

9 Planar Waveguide as ENZ Microwave Sensor

Dielectric sensing in a metallic waveguide utilizes the tunneling frequency, which occurs near the cutoff frequency of the waveguide. The cutoff frequency of the dominant TE_{10} mode of the waveguide depends on the width of the waveguide and the dielectric constant of the non-magnetic material used in the waveguide. The previous section shows the impact of the dielectric material on the cutoff frequency and the associated ENZ effect. In this section, a fixed dielectric material is used to create the ENZ waveguide cavity, and the width of the ENZ section of the waveguide is varied to observe the ENZ effect. A planar design of the ENZ waveguide cavity is shown in Fig. 20, where the input and output ports are chosen to be the SubMiniature version A (SMA) type 50Ω coaxial lines, which provide easy connection with the vector network analyzer (VNA) for the measurement of transmission coefficients.

The dimensions of the ENZ waveguide cavity are: $a = 41$ mm, $b = 3$ mm, $L = 53$ mm, $L_t = 4$ mm, and $T_t = 1$ mm. The dielectric constant of the substrate is 4.3 and is considered to be lossless in the theoretical analysis. The width of the ENZ section, W_t , is parametrically tuned to a lower value from the initial value (i.e. $W_t = a$). The transmission coefficients are calculated using the full-wave EM solver and given in Fig. 21. From Fig. 21, it can be observed that reducing the value of W_t provides significant control over the ENZ tunneling frequency, f_{100} . It may be noted here that the length of the ENZ waveguide is smaller than the width, which takes the fundamental Fabry-Pérot resonance at a higher frequency than the cutoff of the second-order waveguide mode, i.e. the TE_{20} mode. From (15), the cutoff frequency of the dominant mode, where the ENZ transmission is expected for $W_t = a$, is found to be 1.76 GHz, while the first Fabry-Pérot resonant frequency corresponding to the TE_{101} mode is 18.17 GHz and the cutoff frequency of the TE_{20} mode is 3.53 GHz. Reducing the value of $W_t < a$ tailors the cutoff frequency of the dominant mode of the ENZ waveguide. However, the cutoff of the TE_{10} mode of the external waveguides

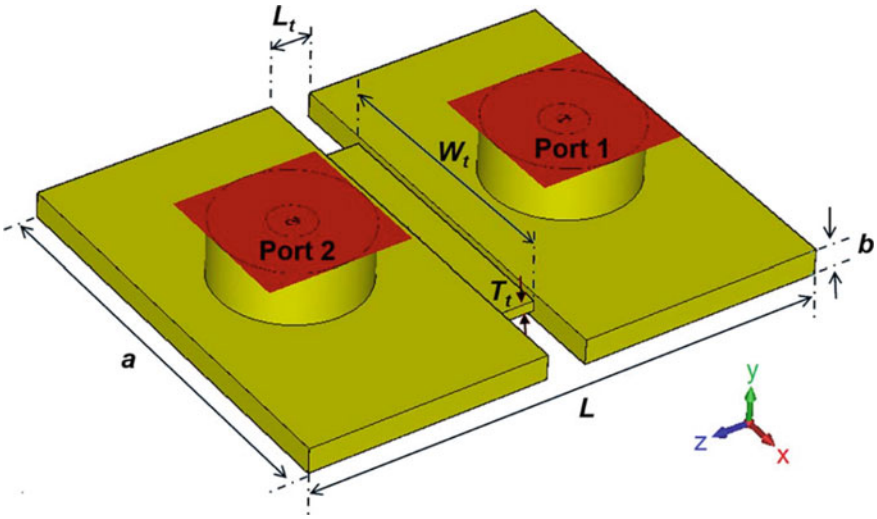


Fig. 20 Single-layer ENZ waveguide based on fully laminated planar technology [15]

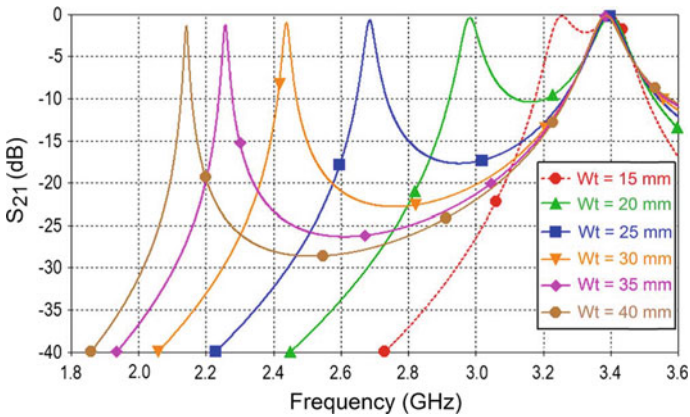


Fig. 21 Variation of the tunneling frequency for various values of W_t [15]

is fixed, and so the cutoff of the TE_{20} mode, which becomes comparable to the cutoff of the dominant mode of the ENZ waveguide at $W_t \sim 0.5a$. In other words, the value of W_t required for tuning of the tunneling frequency must be greater than $0.5a$, which keeps the planar device operating in the dominant mode and below the cutoff frequency of the TE_{20} mode.

10 Multilayer Planar ENZ Sensor: Single-Mode Multiple Frequencies

Since the change in W_t helps in tailoring the tunneling frequency, this useful property can be used to design the ENZ waveguide or ENZ waveguide cavity working at multiple frequencies. The design of the ENZ waveguide cavity, which operates at two frequencies, is given in Fig. 22. In this figure, two ENZ channels of unequal width are stacked vertically and sandwiched between the two external waveguide sections. The width of the second ENZ channel is chosen within the limit of the dominant mode of operation, i.e. $W_t > 0.5a$. The dielectric constant of the lossless substrate is assumed as 4.3 and the dimensions of the two-layer design, as shown in Fig. 22, are: $a = 34$ mm, $b = 4.8$ mm, $L = 41$ mm, $L_t = 4$ mm, $T_{t1} = T_{t2} = T_g = 1.6$ mm, and $W_t = 26$ mm. Similar to the earlier single layer design (Fig. 20) the two-layer design of Fig. 22 is equipped with two SMA type 50Ω coaxial ports for measuring the transmission parameters using VNA.

The two-layer structure described above is modeled in the full-wave EM simulator and the transmission coefficients are calculated. It is found that the unloaded ENZ cavity, as shown in Fig. 22, resonates at two frequencies corresponding to the two transmission peaks. The first ENZ transmission peak is observed at frequency $f_{t1} = 2.49$ GHz, while the second ENZ transmission peak is observed at frequency $f_{t2} = 2.99$ GHz. The electric field is numerically calculated at these two frequencies and shown in Fig. 23. From this figure, it is found that the ENZ channel with a larger width, $W_t = 34$ mm (i.e., channel T1), operates at f_{t1} , while the ENZ channel with a smaller width, $W_t = 26$ mm (i.e., channel T2), operates at f_{t2} . It can be observed from Fig. 23 that the electric field distribution has a half-wave variation along the x -direction while there is no variation along the y -direction, which demonstrates the presence of the dominant mode inside the ENZ tunnels. It is interesting to note that the variation of the electric field inside the tunnel is sinusoidal in the x -direction,

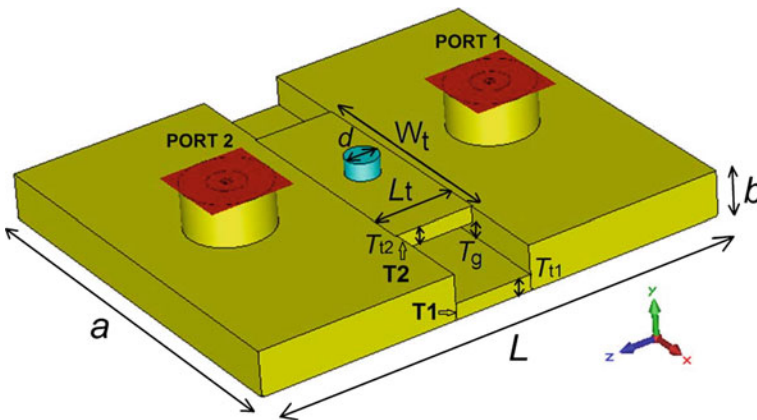


Fig. 22 Two-layer ENZ sensor using fully laminated planar technology [15]

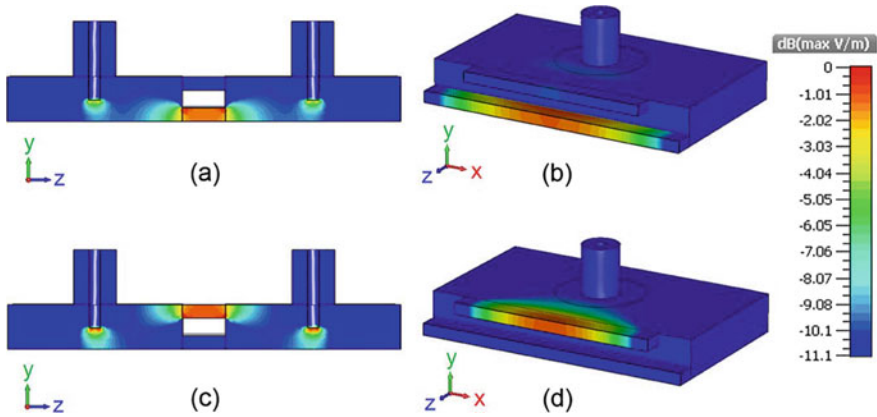


Fig. 23 Electric field distribution: **a** for channel T1 in YZ-plane, **b** for channel T1 in XY-plane with a perspective view, **c** for channel T2 in YZ-plane, and **d** for channel T2 in XY-plane with a perspective view

while it is uniform in the y - and z -directions. From the study of the electric field configuration, it is now easy to recognize the modal indexes, i.e. $m = 1$, $n = 0$, and $p = 0$, which indicates that both the modes are the TE_{100} mode.

It may be noted from Fig. 23 that the electric field at the geometric center of each of the channels is maximum and intensified in comparison to the electric field in the external waveguide sections. Therefore, the geometric center of the ENZ channels is chosen for the sample inclusion and dielectric testing of materials [15, 16]. A cylindrical sample of diameter d , which passes through both the ENZ channels, is considered for the numerical analysis with the arrangement shown in Fig. 22.

For the numerical analysis, the relative permittivity of the test material is varied across a broad range, from 2 to 90, and the tunneling frequencies for the loaded channels, T1 and T2, i.e. f_{s1} and f_{s2} , are calculated. The numerical analysis of the loaded, two-layer ENZ waveguide cavity is also carried out at different values of channel length while the sample diameter is kept constant. The results of the numerical analysis are shown in Fig. 24, where the loaded tunneling frequencies related to channels T1 and T2 are normalized with the unloaded ENZ frequency of channels T1 and T2, respectively. From Fig. 24, it can be suggested that the smaller length of the ENZ channel results in higher sensitivity. The sensitivity, as defined earlier, can be given from the slope of each curve. From Fig. 24, it may be observed that one-unit change in the relative permittivity of the material under test results in a 12 MHz shift in f_{s1} and 18 MHz in f_{s2} . To quantify the result, let us consider a sample with relative permittivity 80 (similar to the dielectric constant of water). For a sample having a relative permittivity close to water, there is almost a 900 MHz and 1100 MHz change recorded in f_{s1} and f_{s2} , respectively, which highlights one of the applications of the multilayer ENZ planar sensor utilizing the single-mode multiple-frequency technique.

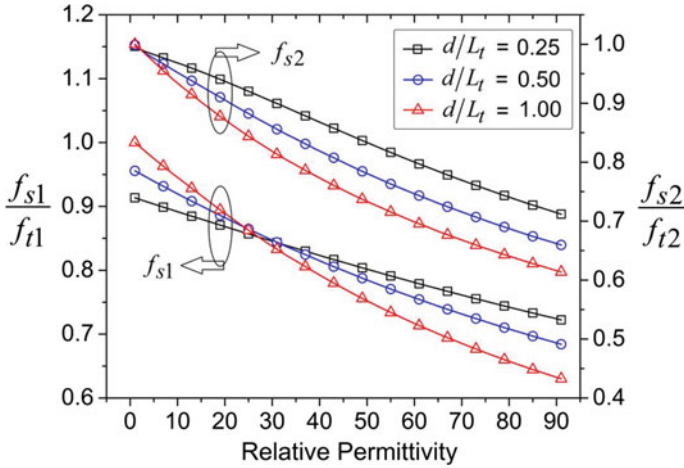


Fig. 24 Normalized tunneling frequency of channels T1 and T2 versus relative permittivity for various ratios of sample diameter to tunnel length [15]

From the above discussions, it can be concluded that the ENZ waveguide and cavity can be utilized as a potential candidate in microwave sensing of a broad range of dielectric materials. The single-layer and multilayered ENZ structure that was created using fully laminated planar technology can also be fabricated using substrate integrated waveguide technology. The multilayered ENZ waveguide sensors provide single-mode multifrequency measurements, which can be very useful in the characterization of dispersive dielectric materials [15].

11 Conclusions

This chapter briefly describes the epsilon-near-zero (ENZ) effect in waveguides as well as the practical realization of metallic and planar ENZ waveguides and cavities. ENZ technology is quite impressive in the creation of a futuristic, bendable, dispersion-less, flexible sensing devices for microwaves to photonics. Though much research is being undertaken towards the technical implementation of epsilon-near-zero (ENZ) and mu-near-zero (MNZ) [] devices, the limitations on utilizing them in sensing technology need to be addressed carefully. One of the fundamental limitations of the ENZ device, i.e. single-frequency operation, has recently been overcome, and the concept of the multi-frequency ENZ microwave sensor has been explained. Moreover, the theory and examples presented here provide the foundations for achieving ENZ transmission or resonance through arbitrary waveguides in microwave systems as well as in the domain of optics. The ENZ transmission (or resonance) can be implemented in a waveguide (or cavity) having bends, twists, and sharp corners in

both the E and H planes, which provides an ample amount of flexibility in designing novel microwave devices and sensors.

References

1. A.V. Mamishev, K. Sundara-Rajan, F. Yang, Y. Du, M. Zahn, Sensors and transducers. Proc. IEEE **92**(5), 808–845 (2004)
2. A.R.M. Syaifudin, S.C. Mukhopadhyay, P.L. Yu, Modelling and fabrication of optimum structure of novel interdigital sensors for food inspection. Int. J. Numer. Model. **25**(1), 64–81 (2012)
3. S. Marcos, G. Silveirinha, N. Engheta, μ -near-zero supercoupling. **195112**, 1–7 (2015)
4. A. Alù, M.G. Silveirinha, N. Engheta, Transmission-line analysis of ϵ -near-zero-filled narrow channels. Phys. Rev. E **78**(1), 016604 (2008)
5. A.M. Mahmoud, N. Engheta, Wave-matter interactions in epsilon-and-mu-near-zero structures. Nat. Commun. **5**(1), 1–7 (2014)
6. B. Edwards, A. Al, M.G. Silveirinha, N. Engheta, Reflectionless sharp bends and corners in waveguides using epsilon-near-zero effects. J. Appl. Phys. **105**(4) (2009)
7. C.A. Balanis, *Advanced Engineering Electromagnetics* (Wiley, USA, 1989).
8. G. Conciauro, M. Guglielmi, R. Sorrentino, *Advanced Modal Analysis: CAD Techniques for Waveguide Components and Filter* (Wiley, England, 2000).
9. D.M. Pozar, *Microwave Engineering*, 4th edn. (Wiley, USA, 2012).
10. B. Edwards, A. Alù, M.E. Young, M. Silveirinha, N. Engheta, Experimental verification of epsilon-near-zero metamaterial coupling and energy squeezing using a microwave waveguide. Phys. Rev. Lett. **100**(3), 1–4 (2008)
11. A.K. Jha, M.J. Akhtar, A generalized rectangular cavity approach for determination of complex permittivity of materials. IEEE Trans. Instrum. Meas. **63**(11), 2632–2641 (2014)
12. J.-S. Hong, *Microstrip Filters for RF/Microwave Applications* (Wiley, USA, 2011).
13. N. Marcuvitz, *Waveguide Handbook* (Peter Peregrinus Ltd., on behalf of the Institution of Electrical Engineers, United Kingdom, 1993).
14. A. Alù, N. Engheta, Dielectric sensing in ϵ -near-zero narrow waveguide channels. Phys. Rev. B Condens. Matter Mater. Phys. **78**(4), 045102 (2008)
15. A.K. Jha, M.J. Akhtar, Design of multilayered epsilon-near-zero microwave planar sensor for testing of dispersive materials. IEEE Trans. Microw. Theory Tech. **63**(8), 2418–2426 (2015)
16. A.K. Jha, M.J. Akhtar, Design of microwave ENZ sensor for contamination detection in liquids using SIW technology. IEEE MTT-S Int. Microw. RF Conf. **2014**, 338–341 (2014)
17. A.K. Jha, N. Delmonte, A. Lamecki, M. Mrozowski, M. Bozzi, Novel MNZ-type microwave sensor for testing magnetodielectric materials. Sci. Rep. **10**, 16985 (2020). <https://doi.org/10.1038/s41598-020-73696-8>

An Overview of Interdigitated Microwave Resonance Sensors for Liquid Samples Permittivity Detection



S. Kiani, P. Rezaei, and M. Fakhr

Abstract Microwave sensors based on electrically small planar resonant elements are investigated in this season. Due to the high sensitivity of these resonators to the properties of their environment, especially the dielectric constant and the loss coefficient, these sensors are of particular importance for the dielectric characterization of solids and liquids and for measuring the composition of materials. This chapter also deals the main advantages and limitations of planar microwave resonant sensors, and several prototypes are reported, mainly including sensors for measuring the dielectric properties of solids, and sensors based on microfluidics (useful for liquid characterization and liquid composition). The proposed sensors have great potential for use in real scenarios (including industrial processes and characterization of bio-samples).

1 Introduction

The measurement of electromagnetic properties is widely used to determine of chemical and biological material, and microwave sensors are one of the devices used in this field. The planar sensors employed in identification of electromagnetic properties in various frequency bands can be used in industry, healthcare and imaging. The material under test can be in liquid, solid or gas state. The planar sensors can be non-resonant (broadband) and resonant (narrow band). Among these, resonant methods have become more popular, especially for applications that require high speed, accuracy and sensitivity in detection. Because resonant elements are sensitive to the properties of their surroundings, microwave sensors based on such elements have been used in many different scenarios, including material characterization, bio-sensing, ambient monitoring, defect detection, motion control, chemical analysis, microfluidics, etc. Furthermore, sensor implementation in planar technology is attractive for various reasons, such as the possibility of development low-profile and low-cost sensors, conformal sensors, recyclable sensors, wearable sensors, integrated

S. Kiani (✉) · P. Rezaei · M. Fakhr
Faculty of Electrical and Computer Engineering, Semnan University, Semnan, Iran
e-mail: sina.kiani@semnan.ac.ir

© The Editor(s) (if applicable) and The Author(s), under exclusive license to Springer Nature Switzerland AG 2021

S. C. Mukhopadhyay et al. (eds.), *Interdigital Sensors*, Smart Sensors, Measurement and Instrumentation 36, https://doi.org/10.1007/978-3-030-62684-6_7

sensors, submersible sensors, or sensors compatible with other technologies (e.g., microfluidics, substrate-integrated waveguide-based sensors, lab-on a-chip sensors, etc.). According to their principle of operation, microwave resonant sensors can be partitioned into: frequency-variation sensors, phase-variation sensors, frequency-splitting sensors, coupling-modulation sensors and differential-mode sensors. In frequency-variation sensors, the desired variable changes the resonance frequency and magnitude for the sensing element based on a resonator. Such sensors are simple and easy to design, and they are very common. Frequency-variation sensors are especially important for characterization of materials, because the resonant frequency of the sensing resonators is perturbed by the presence of a material in contact with it or in close proximity to it [1]. This section is focused on planar sensors based on resonant elements to describe materials such as solids or liquids and four designs: Planar sensor for liquid [2], Microwave sensor for multilayer solid material [3], Sensor for the non-invasive measuring of blood glucose [4], and Dual-frequency microwave sensor for liquid [5] are examined.

2 Modified Planar Sensor for Measuring Dielectric Constant of Liquid Materials

2.1 Abstract

A planar U-shaped resonator is developed for measuring relative permittivity of the liquid materials. Gap sections, coupled lines and central ring resonators (RRs) are used to achieve more sensitivity. Further to increase the resonance sharpness, a tapered double-sided spiral split ring resonator (TDSS-SRR) is presented. In addition same as [6], the ground plane under the proposed cell is removed that results the electric field is focused on the top surface of the resonator. As the permittivity of the liquid under test (LUT) is increased from 26 to 79, the measured resonance frequency of the proposed sensor is varied in the 166.4–287.5 MHz range. Compared to the reported structure [6], the investigated configuration shows better sensitivity in electrical performance. The developed sensor exhibits an improvement in sensitivity of about 45%.

2.2 Proposed Sensor Configuration

As shown in Fig. 1, a modified sensor to constant dielectric detection of liquid is presented by utilizing a TDSS-SRR and U-shaped resonator. Same as the previous work [6], a microstrip line loop is used as all sides of magnetic coupler to excite the proposed TDSS-SRR. This feeding method obtains an inductance with large value, which provides a low Q-factor resonance. The presented TDSS-SRR is

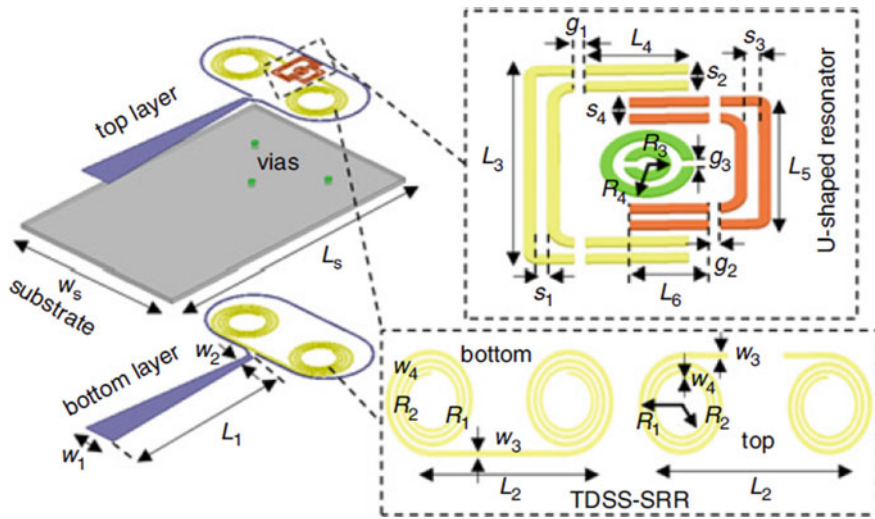


Fig. 1 Schematic diagram of presented sensor configuration

tapered exponentially (from W_3 to W_4 at the bottom and vice versa at the top) to introduce high-impedance circuit that improves resonance values of the sensor. Furthermore, the U-shaped resonator is extended to enhance resonance sharpness and frequency adjustability. The described U-shaped resonator comprised of several coupling sequences. These couplings generate different capacitance values which provide an adjustable and deep resonance. The structure and the equivalent circuit models of the investigated sensor and the conventional sensor [6] are illustrated in Fig. 2.

In [6], L_r and C_r represent equivalent inductance and capacitance of DSS-SRR, respectively. C_1 is the capacitance associated with the interdigital resonator. In the proposed sensor, tapering function provides high-impedance line which results in increasing of L_r and decreasing in C_r values of the conventional DSS-SRR simultaneously. Thus, resonance values of the sensor are improved. Furthermore, the interdigital section (C_1) of [6] is replaced with the U-shaped resonators [coupling and parallel capacitances ($C_1 \dots C_7$ and $C_1' \dots C_4'$)] which in turn intensify the electric fields in the resonance area that increases dielectric loading interaction. So, the sensitivity of the sensor layout will be enhanced.

2.3 Sensor Performance and Comparison

The configuration of the presented microwave sensor is distinct from that reported in [6]: First, an exponential tapering function is presented to enhance the impedance

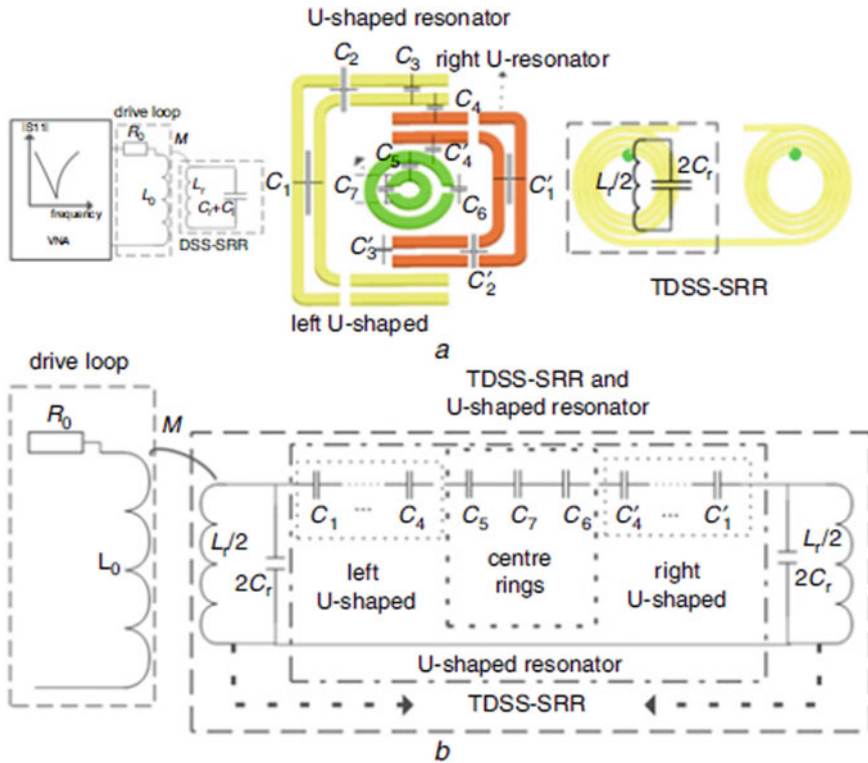


Fig. 2 Circuit model for **a** conventional [6], **b** proposed sensor

[increasing DSS-SRR equivalent inductance (L_r) and decreasing equivalent capacitance (C_r)] of the proposed DSS-SRR, and to improve the resonance values of the sensor. Second, the interdigital resonance section of [6] is replaced by a new resonator with sequential coupling topologies to intensify the interaction between electric field and the loaded liquid material, and to modify sharpness of the resonance. The developed sensor is designed and fabricated on a substrate RO4003 with 20 mil thickness, the length (L_s) and width (W_s) equal to 1.8 and 1.2 cm, respectively. According to Fig. 1, the design parameters of the designed construction are tabulated in Table 1.

Table 1 Detail parameters of proposed sensor (in millimeters)

Substrate		TDSS-SRR				Proposed U-shaped resonator					
W_s	12	w_1	2.1	L_1	12	L_3	2.3	S_2	0.15	g_3	0.2
L_s	18	w_2	0.75	L_2	9.5	L_4	1.05	S_3	0.15	R_3	0.3
h_s	0.508	w_3	0.35	R_2	1.15	L_5	1.8	S_4	0.15	R_4	0.65
		w_4	0.2	R_4	1.55	L_6	0.75	g_1	0.2		
						S_1	0.2	g_2	0.15		

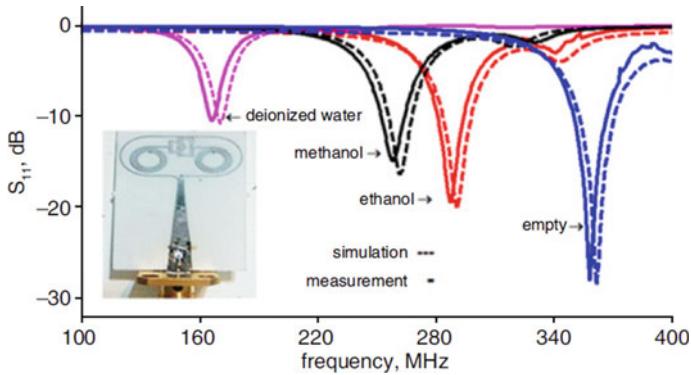


Fig. 3 Simulated and measured S_{11} of proposed sensor

The S-parameters of the investigated configuration are evaluated by employing finite element method with ANSYS high-frequency structure simulator full wave solver. The simulated and measured results of the proposed sensor for permittivity detection of various liquids such as ethanol, methanol and deionized water are plotted in Fig. 3.

Moreover, Fig. 3 illustrates the results for empty (unloaded) case. The good compromise between the results shows the design validity of the proposed sensor. In the measurement process, the relative permittivity of the loaded ethanol–water mixture is varied from 26 to 79 for ethanol concentration between 100 and 0% as reported in [6]. Figure 4 demonstrates that the resonance frequency of the proposed sensor decreases from 287.5 to 166.4 MHz by loading ethanol with concentration from 100 to 0%, respectively.

Although in same condition, this value is shifted from 166 to 117.9 MHz in [6]. As depicted in Fig. 4, for variation of the relative permittivity, the resonance values

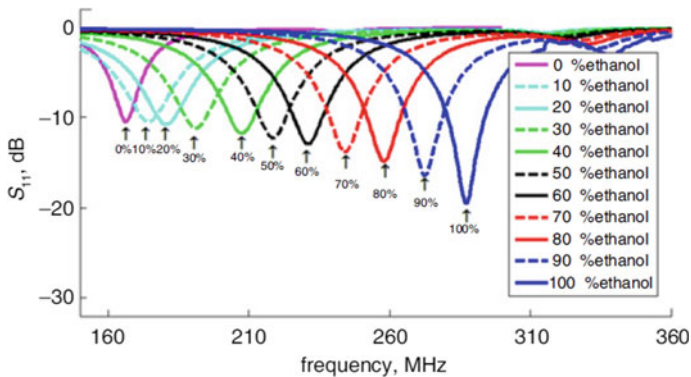


Fig. 4 Measured return loss of proposed sensor in water–ethanol mixture relative dielectric constant detection process

are between -29 and -10 dB in the presented configuration due to high-resonance values. Meanwhile, in the conventional microwave sensor [6], minimum values of the return loss vary from -10 to -4 dB in the operational frequencies. Additionally, the diverse coupling capacitances in the investigated U-shaped resonator make the significant shift in resonance frequencies proportional to dielectric constant variations. The sensitivity of a microwave sensor can be derived as [6]:

$$S = \frac{(f_{01} - f_{02})}{f_{01}} \frac{1}{\Delta\epsilon_r} [\%] \quad (1)$$

where f_{01} and f_{02} are resonance frequencies related to low and high permittivities, respectively. According to (1), the proposed sensor exhibits 0.795% sensitivity for relative dielectric constant change of 53 in water–ethanol mixture, whereas traditional sensor [6] was shown 0.547% sensitivity, similarly. So, compared to [6], the investigated sensor illustrates about 45% detection sensitivity improvement. Furthermore, in the empty case, the resonance value for [6] was about -8 dB, whereas it is about -29 dB in the proposed sensor. Also, the frequency detection resolution (FDR) of sensor for relative permittivity change of (1) can be yielded by (2):

$$\text{FDR} = \frac{(f_{01} - f_{02})}{\Delta\epsilon_r} (\text{GHz}) \quad (2)$$

where $\Delta\epsilon_r$ represents the relative permittivity variation, f_{01} and f_{02} denote upper and lower frequencies in detection process, respectively. Consequently, the FDR for water–ethanol permittivity sensing is about 0.9 and 2.2 MHz for [6] and the proposed sensor, respectively. Therefore, utilizing the designed sensor will be able to improve measurement accuracy of relative permittivity of the liquids. The presented sensor is compared with conventional structure [6] and relevant figure-of-merit parameters are listed in Table 2.

Table 2 Performance comparison among proposed sensor and conventional design [6]

Name	FDR (MHz)	Sensitivity (%)	Frequency (MHz)	Resonance value (empty) (dB)	Electrical size
Conventional [6]	0.9	0.547	300.4	-8	$\lambda_0/50$
Proposed sensor	2.2	0.795	357.8	-29	$\lambda_0/46$

3 Microwave Sensor for Detection of Solid Material Permittivity in Single/Multilayer Samples with High Quality Factor

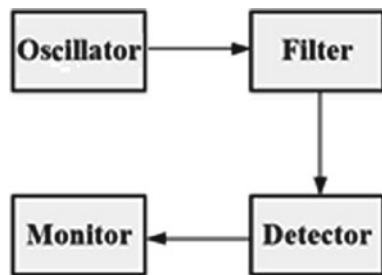
3.1 Abstract

In this study, a planar microstrip sensor based on band-stop filter is presented for determining relative permittivity of single layer and multilayer solid materials. The proposed sensor has been composed from the structure of meandered microstrip line (MML) with T-shaped resonator and an interdigital structure that is connected to ground by via. Interaction between T-shaped resonator and interdigital structure is caused to increase electric field intensity and the high field increase the sensor sensitivity and resolution. The microwave sensor is fabricated on the substrate RO4003 by using single layer technology. The samples of FR4 and RO4350 in single and double layer forms as multilayer is placed on the sensor and the sensor demonstrates different resonance frequencies. When the samples placed on a region of the strong field, interaction among them increase sensitivity and due to high Q-factor, there is a high resolution. The relationship between changing the resonance frequency and variation of the relative permittivity is linear and it determines unknown materials dielectric characterizations. The permittivity of samples changes from 3 to 11 therefore the resonance frequency varies linearly from 3.7 to 5.65 GHz. The proposed sensor shows improvement relative to other similar works in the fields of sensitivity and quality factor.

3.2 Sensor Design

The diagram of the considered sensor is displayed in Fig. 5. This diagram is included an oscillator, a detector, a filter and monitor system which they are needed for the complete measurement system [7]. This structure is introduced as a sensor. There

Fig. 5 Block diagram of unknown solid materials detection



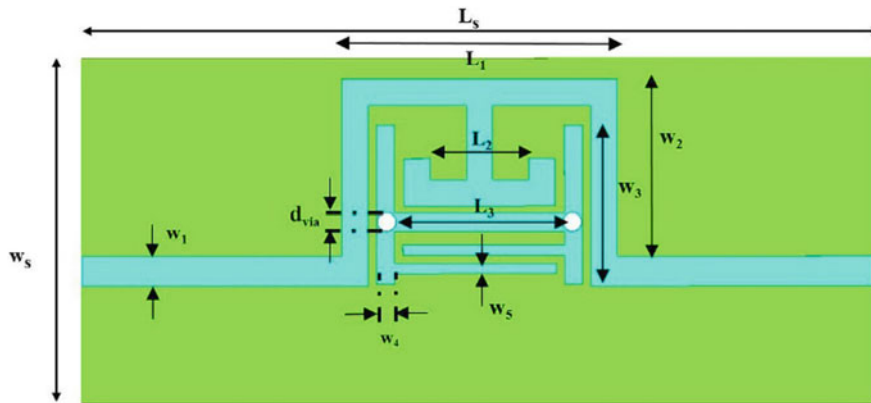


Fig. 6 Geometric layout of the proposed structure

are many ready circuits that can be used as an oscillator, a detector and a monitor in the sensor, while their designing are not different for types of structures, therefore, the most main and important part of a sensor in the presented block diagram is filter. The goal of this research is an investigation of filter as a main part of the sensor. A band-stop microstrip filter is proposed for designing sensor. The parameters of filter such as insertion loss and bandwidth depend on substrate permittivity. When a sample place on the sensor, it can change the frequency response. Variation of frequency response depends on location of sample on the sensor, because when sample place in the region that the electric field intensity is high, it is caused to increase field interaction as a result variation of the resonance frequency. Therefore, changing the resonance frequency can depict added sample characterizations. The proposed band-stop microstrip filter layout is shown in Fig. 6.

The designed filter consists of a T-shaped, MML and interdigital structures. The T-shaped and the MML structures are joined to each other and the interdigital structure is connected to ground by via and this is caused to increase the potential difference between interdigital and MML connected to T-shaped. The electric field is distributed on the MML and interdigital, and the electric field intensity enhances at resonance frequency. Figure 7 displays the electric field distribution.

The location where the field is strong, determines the location of the sample, because when samples are placed in the MML and interdigital structures region where the field is strong it is caused to enhance field interaction between the sample and sensor, and it increases the sensor sensitivity and resolution. The filter parameters are given in Table 3.

The proposed filter is fabricated on a RO4003 substrate with 3.38 dielectric constant, $\tan \delta = 0.0026$ and a thickness of 0.508 mm. Figure 8 shows the filter frequency response without the placement of any sample on the sensor, so that, the resonance frequency is about 5.65 GHz.

Fig. 7 Electric field distribution of the proposed sensor at the resonance frequency

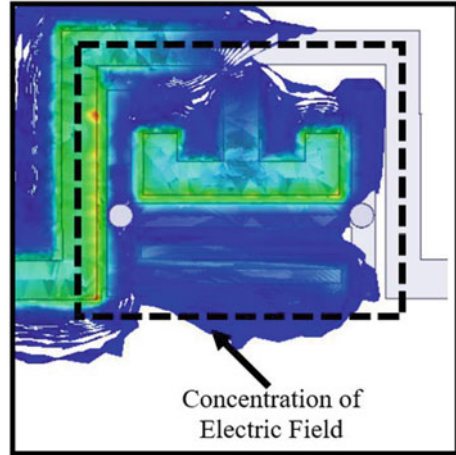


Table 3 The parameters values of the presented filter

Par	L ₁	L ₂	L ₃	W ₁	W ₂	W ₃	W ₄	W ₅	L _S	W _S	d _{via}
Val	10.4	3.7	6.3	1.2	6.5	6	0.7	0.4	30	13	0.7

Par parameters; Val Value (mm)

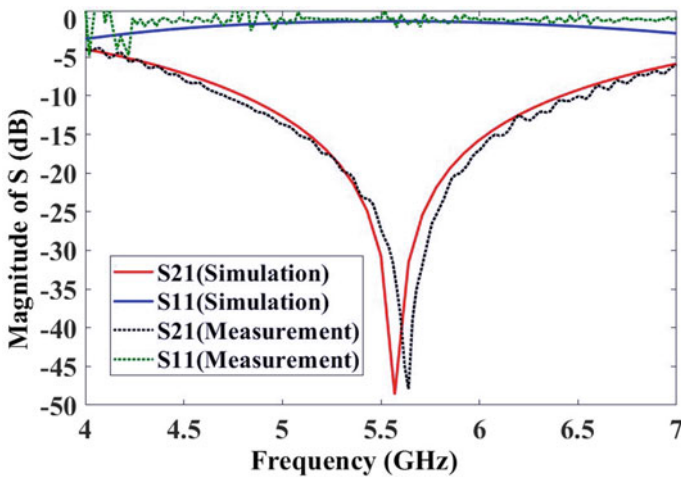


Fig. 8 The frequency response of unloaded filter

According to Fig. 8, in the range shown, the transmission response (S_{21}) doesn't have the pole but it has a transmission zero that it is created in the resonance frequency. When the sample is placed on the sensor, it is expected that the transmission zero is moved. For investigation of sensor, a solid material with different permittivity

are examined. On most sensors, the samples must cover whole of filter while in presented sensor, sensing dimensions is small, so that the sample dimensions is $6.8 \text{ mm} \times 8.4 \text{ mm}$ because this size covers the region of strong electric field while the sample size in [8], is $20 \text{ mm} \times 20 \text{ mm}$, therefore, the sample dimensions are decreased. The proposed sensor will be able to increase accuracy of solids permittivity measurement. The important property of presented filter is a high Q-factor. The Q-factor characterizes a resonance bandwidth relative to its center frequency, therefore increment of Q-factor depicts the high resolution for a sensor. The Q-factor can be derived from [9]:

$$Q = s \frac{f_0}{\Delta f_{\pm 3dB}} \quad (3)$$

where Δf is the +3 dB bandwidth and f_0 is the center frequency. Q-factor is 217 for the unloaded sensor and is 38 for the presented sensor in [8], however the resolution of the presented sensor is increased compared to traditional design of [8]. In presented sensor, different sections are coupled with each other and for achievement of equivalent circuit, circuit model of each section must be obtained. The equivalent circuit model of each part are shown in Fig. 9a. The MML and T-shaped structures are equivalent inductance, the interdigital structure and the open circuit stub are modeled with the capacitance, the via can be modeled with the parallel capacitance and inductance. The equivalent circuit model for the proposed sensor is depicted in Fig. 9b.

In equivalent circuit, CS is the capacitance due to the open circuit stub, LM and LT are the inductances due to the MML and T-shaped structures respectively, and CID is the capacitance due to the interdigital structure. Parallel L_{via} and C_{via} are the inductance and capacitance due to the vias. GMS, GTS, GTID and GIDM are the coupling capacitances due to gap between MML and open circuit stub, T-shaped and open circuit stub, T-shaped and interdigital and, also interdigital and MML, respectively.

3.3 Measurement Results

For validation of measurement, the samples relative permittivity changes from 3 to 11, then resonance frequency is obtained. Also the FR4 and the RO4350 materials place on the sensor and the frequency response behavior is investigated. The relationship between the frequency response behavior and variations of the samples permittivity is caused to detect unknown solid materials dielectric characterizations. The measurements to change the permittivity of the samples are shown in Fig. 10. Figure 11 shows the samples permittivity effective variation.

When the sample relative permittivity increases, the resonance frequency decreases from 4.9 to 3.7 GHz, whereas in the same condition, this value is shifted

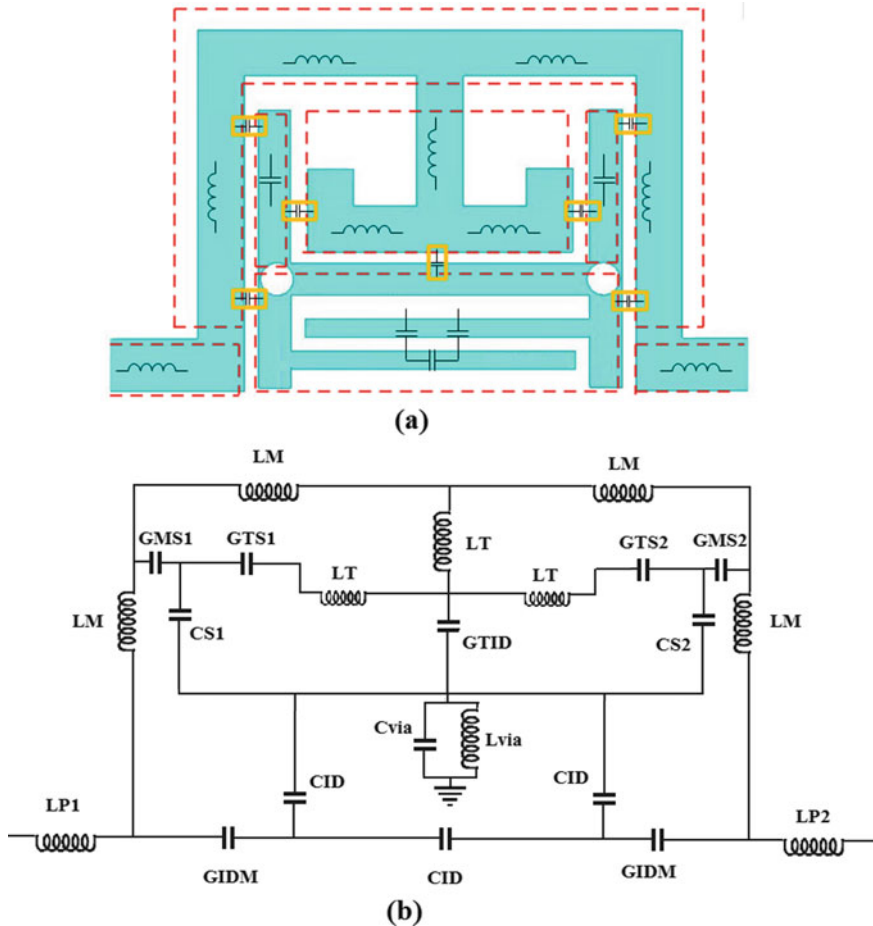


Fig. 9 **a** Equivalent circuit model of each part of the sensor, **b** equivalent circuit model of all the sensor

from 5.2 to 4.1 GHz in [8]. As illustrated in Fig. 11, for changing the relative permittivity, the resonance values are between -50 and -49 dB in the proposed configuration, therefore, it can be said that the resonance value is almost fixed with changing the relative permittivity, while in the proposed sensor of [8], values of resonance change from -41 to -21 dB in the operational frequency. A sample with the grater dielectric constant has a larger downshift of the resonance frequency. However, the sensor sensitivity increases corresponding to the increment of the samples relative dielectric. Corresponding to (1), the considered sensor demonstrates sensitivity of 3.25% for permittivity variation equal to 8 of the samples, whereas sensor of [8] was observed sensitivity of 2.6% , similarly. However, the proposed sensor depicts about significantly improvement in sensitivity compared to [8]. Also, the value of resonance in [8], was about -22 dB in the without sample mode, whereas in the

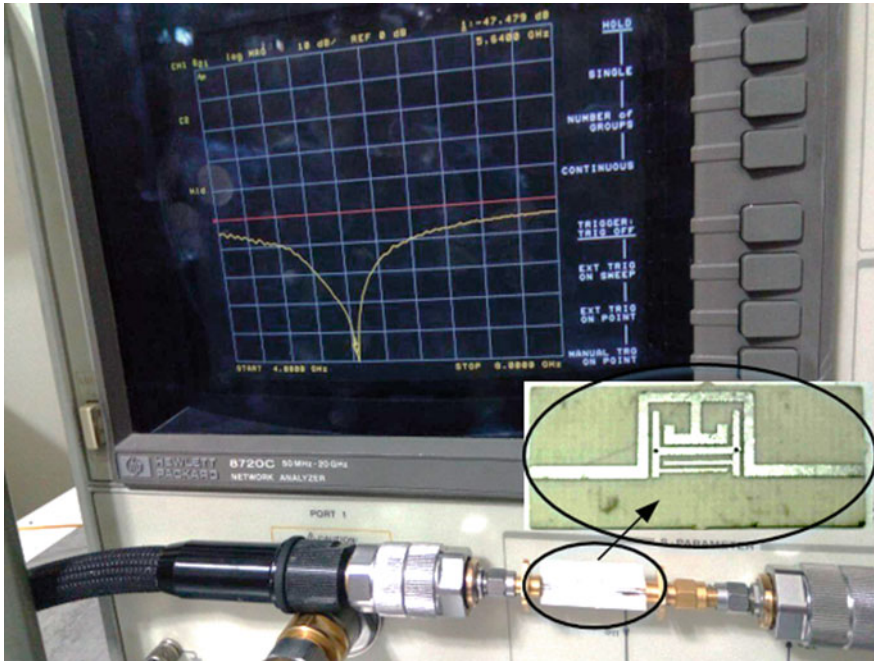


Fig. 10 Measurement of scattering parameters for fabricated prototype

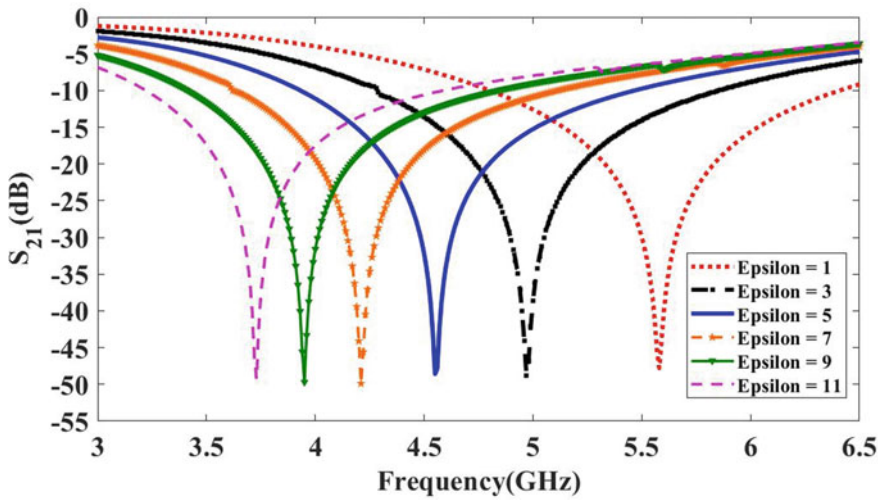


Fig. 11 Variation of the resonance frequency with changing the relative permittivity

Table 4 Comparison between proposed design and different references

Refs.	FDR (GHz)	Sensitivity (%)	Freq. (GHz)	Resonance value (dB) (empty)	Q-factor	Sample size (mm × mm)	MLM
[8]	0.12	2.6	7.6	−22	38	20 × 20	✓
[9]	0.1	2.2	4.53	−15.26	150	2.1 × 1	−
[10]	0.05	2.7	2.1	−11	110	14 × 14	−
This work	0.17	3.25	5.65	−48	217	6.8 × 8.4	✓

MLM Multilayer Measurement

investigated sensor, it is about −48 dB. According to Eq. (2), the FDR for sensing of sample dielectric constant is about 0.17 and 0.12 GHz for the presented sensor and in [8], respectively, however, there is an improvement in FDR compared to traditional structures of [8]. There are many techniques for designing sensor that suffer from low Q-factor with low sensitivity that decrease their abilities of determining small variations in dielectric characterization of unknown materials. The proposed sensor has a high Q-factor compared to work similar to [8], therefor the sensitivity of sensor increase. This depicts that the presented sensor has high sensitivity with the abilities of characterizing and determining a small variation in materials dielectric characterization. The sensor’s sensitivity is introduced as the shift in frequency response versus the changes of the samples relative permittivity and initial frequency. The variation in resonance frequency is relative to the interaction between the sensor and sample electric fields and it is caused to decrease resonance frequency and Q-factor. However, a frequency response with narrower bandwidth and sharper dip indicates a high Q-factor that leads the sensor to characterize and determine changes of materials at narrow-band frequencies. The designed sensor is compared with the traditional structure of [8], and comparative parameters are depicted in Table 4.

For the results validation, the measurement has been implemented and the measured and simulated are compared to each other. In the practical, the FR4 material having 4.6 relative dielectric and loss tangent of 0.02 and RO4350 material having a 3.66 relative dielectric and loss tangent of 0.004 are used as the samples. The sample’s thickness is 1.60 and 1.53 mm, respectively, as in [8]. For measuring, the samples place on the sensor in a region of sensing that have been depicted in Fig. 12, then the sensor with the samples is measured to obtain the frequency response. The proposed sensor structure with the samples of FR4 and RO4350 and position of samples on the sensor are indicated in Fig. 12, and the results of measurement for the presented sensor with the samples of single layer are displayed in Fig. 13.

Figure 13 depicts that with increasing the samples relative dielectric the resonance frequency shifts downward. When the FR4 sample has a relative dielectric more than the RO4350 sample, the resonance frequency relative to FR4 shifts more downward than the RO4350 sample corresponding to reference without samples that was illustrated in Fig. 8. Without any sample, the resonance frequency is at 5.6 GHz, but when the FR4 and RO4350 materials are used as sample, the resonance frequency shifts to

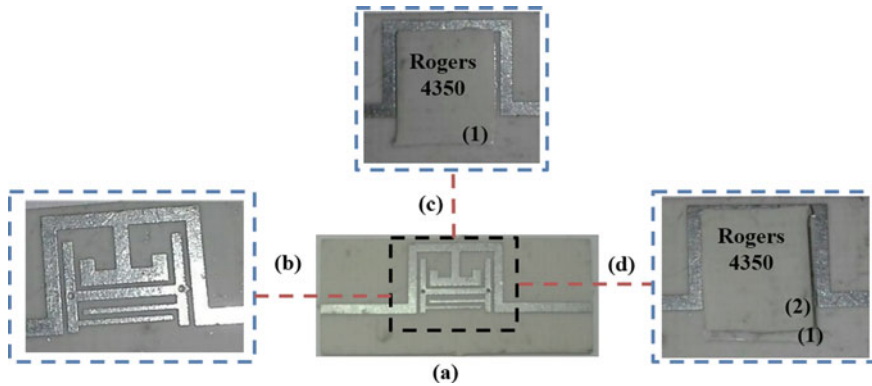


Fig. 12 **a** Picture of the presented sensing, **b** position of sensing, **c** RO4350 sample on the sensor, **d** double RO4350 samples on the sensor

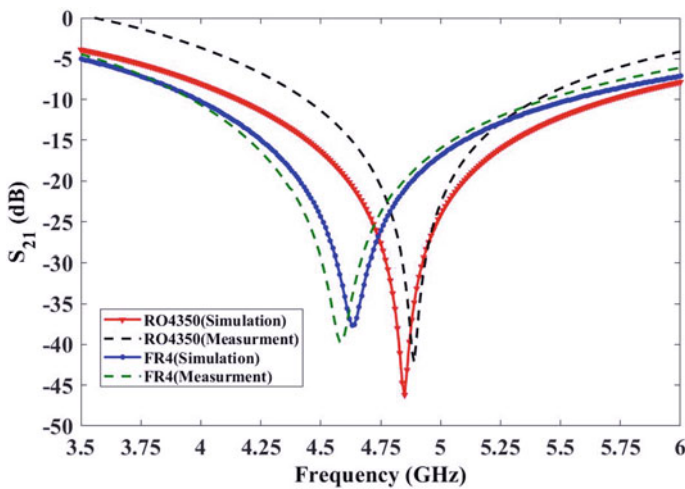


Fig. 13 Simulated and measured frequency response with RO4350 and FR4 samples

4.6 and 4.9 GHz, respectively. To develop the results, for difficult and complicated conditions, samples structure with double sample structures are used as multilayer. In this situation, double samples of RO4350 + RO4350 and FR4 + FR4 are experimented. The measured and simulated transmission coefficient for the double samples are depicted in Fig. 14.

From the Fig. 14 is shown when the sample layer is double, the frequency response as a result resonance frequency shifts downward. When FR4 + FR4 and RO4350 + RO4350 double materials are used as samples, the resonance frequency shifts to 4.5 and 4.7 GHz, respectively. When the sample is placed on the sensor, the electric field distribution of the presented sensor are shown in Fig. 15. Therefore, the proposed

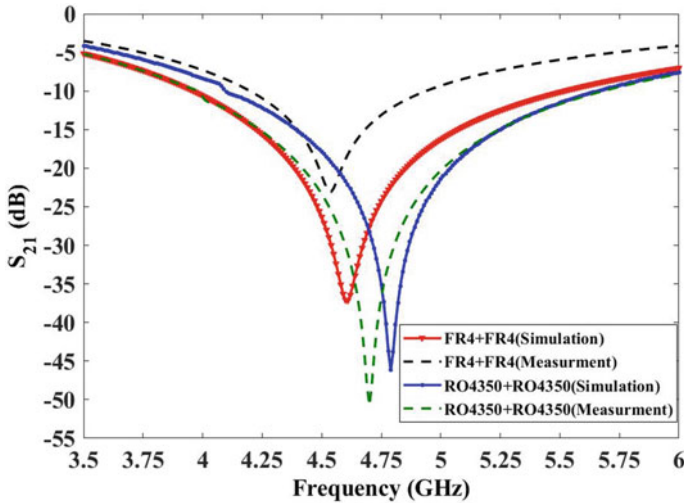


Fig. 14 Simulated and measured frequency response with RO4350 + RO4350 and FR4 + FR4 samples

sensor can detect the permittivity of single layer and multilayer samples. Sensor parameters values for single layer and multilayer samples are indicated in Table 5.

Resonance frequency for single layer and multilayer FR4 sample are 4.58 and 4.5 GHz, respectively. Also resonance frequency for other single-layer and multilayer samples are 4.9 and 4.7 GHz, respectively. Results of Table 5 illustrate that as the sample layer increase, resonance frequency shifted downward. When the simulation and measurement results are close to each other, this demonstrates the validity of the results, thus the low results difference indicates low error. The error is illustrated with the difference between the sample measurement resonance frequency (f_{SM}) and the sample simulation resonance frequency (f_{SS}) relative to the free load resonance frequency (f_{FL}) which is shown in Eq. (4). The values of error are illustrated in Table 5.

$$\text{Error} = \frac{|f_{SM} - f_{SS}|}{f_{FL}} [\%] \tag{4}$$

According to the simulations and measurements implemented, the presented sensor can detect solid materials having relative permittivity of different and unknown. The proposed band-stop filters can be used as a sensor in various applications such as detection of changing blood glucose concentration. Also, Q-factor and FDR of the proposed sensor is more than the traditional paper as [8], therefore the sensitivity and resolution have improved.

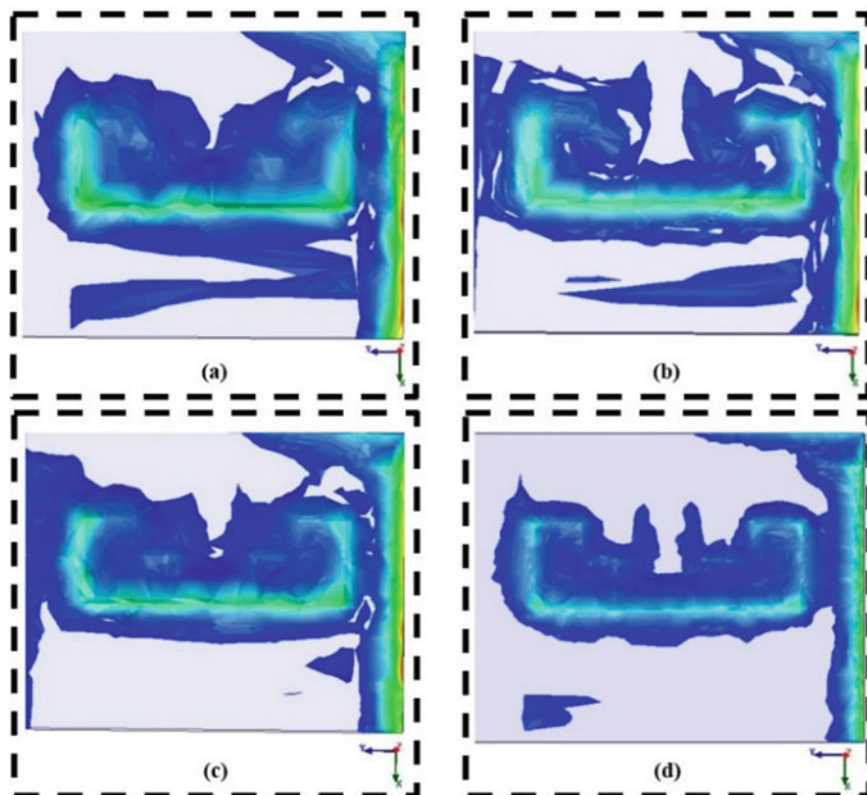


Fig. 15 Electric field distribution of the proposed sensor with the sample at the resonance frequency **a** RO4350 sample on the sensor, **b** double RO4350 samples on the sensor, **c** FR4 sample on the sensor, **d** double FR4 samples on the sensor

Table 5 Value of parameters for single and double samples stations

Samples	Freq. (GHz)	S_{21} (dB)	Q-factor	Error
With single FR4 sample	4.58	-40	82	0.82
With double FR4 samples	4.5	-23	46	1.95
With single RO4350 sample	4.9	-42	188	0.5
With double RO4350 samples	4.7	-51	276	1.8

4 Band-Stop Filter Sensor Based on SIW Cavity for the Non-invasive Measuring of Blood Glucose

4.1 Abstract

In present conditions of world and the prevalence of coronavirus disease (COVID-19), and the dangers that threaten diabetics more than normal people, consideration and monitoring of glucose levels non-destructively in diabetics is felt more than ever. Hence, design and realization of a substrate integrated waveguide (SIW) planar sensor is described for the non-invasive monitoring of blood glucose concentration (BGC). The structure of the presented sensor is similar to a conventional band-stop filter and it is realized by using a modified split ring resonator (SRR) in the central section of the SIW cavity. The slots and interdigital arms on the upper conductor of the SIW cavity are utilized to produce a substantial and localized field enhancement in the sensing region by the SIW technology. Further, the fingertip is used as materials under test and its displacement and fingerprints effects are studied. The fingertips with various glucose values are modelled according to the reported information by Turgul and Kale [11, 12]. Subsequently, these models are placed on the sensing area of the introduced resonator in order to evaluate the performance of the proposed sensor for non-invasive BGC monitoring application. The introduced sensor is then fabricated and measured. The evaluated results indicate that the developed sensor features such as sensitivity, effect of finger placement, and influence of fingerprints have been improved in both the fingertip positioning and fingerprints effects compared to the other works. Also, the resonance frequency shift of the proposed sensor observe that the valuable enhancement of non-invasive BGC detection sensitivity is much more than the previous study.

4.2 Introduction

For a healthy person, blood glucose should be in the normal range. High blood glucose (hyperglycemia) or low blood glucose (hypoglycemia) is dangerous (Fig. 16).

Hypoglycemia can make you weak or even lead to loss of sobriety. On the other hand, hyperglycemia in your blood can also be an emergency or may lead to complications of diabetes. Diabetes is a chronic disease that occurs when the body is unable to produce enough insulin or is unable to use the insulin produced effectively. The disease affects many vital organs such as the eyes, kidneys and heart. Therefore, frequent monitoring of blood glucose is fundamental part of diabetes management. Lifestyle changes and a healthy diabetic diet are the only treatment, as it is not permanently curable. In the current state of the world, COVID-19 is a threat for the health of the general public. Older people and people with chronic medical conditions, such as diabetes, appear to be more vulnerable to COVID-19 virus. We all know that when the coronavirus virus spreads (COVID-19), we should stay at home as much

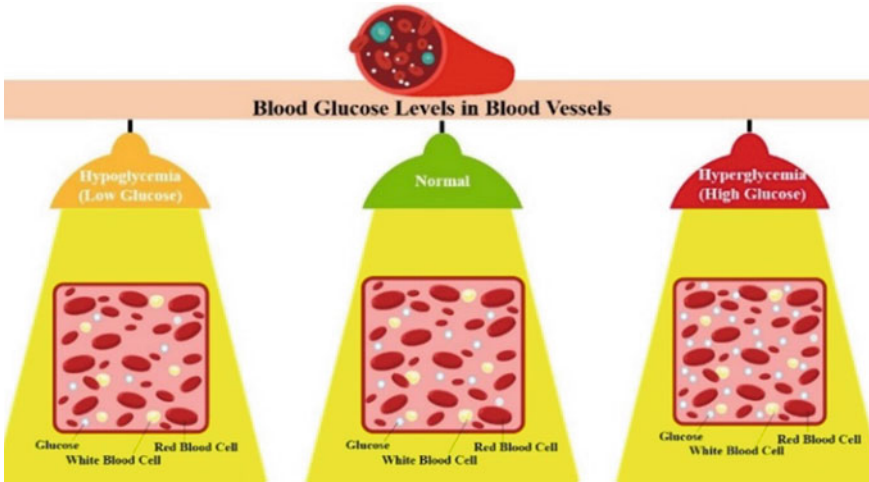


Fig. 16 Different states of blood glucose levels in blood vessels

as possible and not leave the house. This law also applies to patients with diabetes. These patients must abide much more this rule. In fact, people with diabetes need to stay at home and use a kind of smart home health care system for their treatment (Fig. 17).

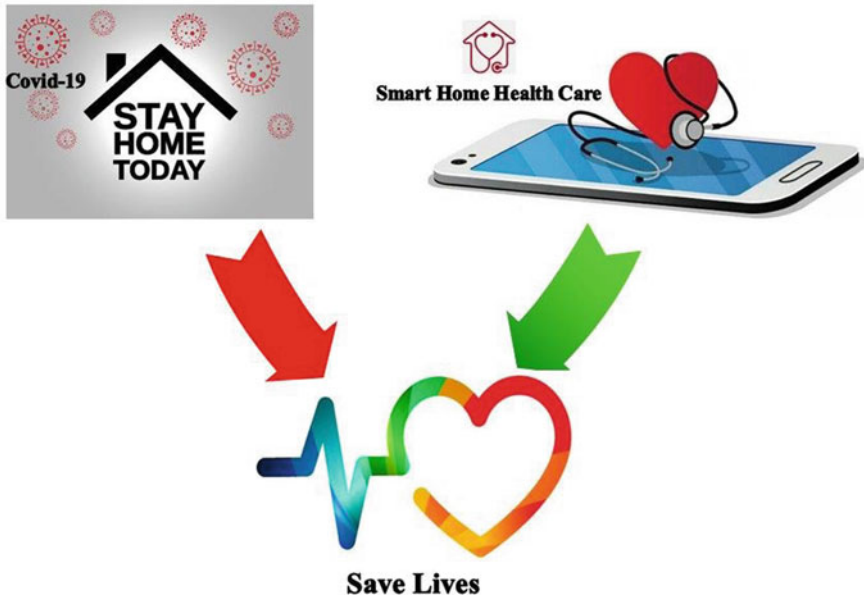


Fig. 17 Necessary actions to save live in present conditions of world

These smart systems allow the patient to use a mobile medical device to perform routine tests and send test information to a real-time health care center. The most common way of diagnose blood glucose for diabetics is through a glucometer, in which a blood sample is taken by stimulating the fingertip and then it is analyzed. At present, these devices remain as the most popular for consumers due to their portability, and their clinical validity has been proven. However, frequent monitoring of blood glucose based on this painful invasive process can be frustrating for the patient. Because it uses lancet devices to stimulate the fingertips to extract blood. And these invasive approaches, such as laboratory and one touch glucometer, increase the risk of blood related infections. In addition, diabetics must bear the cost of tapes and the boredom to perform repeated measurements.

To overcome this distress, a non-invasive patient friendly device is required. In the last few decades, many efforts have been made to develop non-invasive blood glucose concentration monitoring devices. But on the other hand, many presented technologies based on non-invasive have not been accurate enough, have not been able to work for a long time, and they have not reached the stage of wide commercialization. Non-invasive blood glucose concentration monitoring devices are recommended by research groups and companies with the aim of providing a simple, cost-effective, painless and convenient device for measuring glucose levels continuously and for smart home healthcare devices. Some technologies include optical, transdermal techniques, thermal spectrum measurement, breath acetone analysis, impedance spectroscopy, saliva analysis, graphene-based nano-sensors, electrochemical methods that measure glucose level in urine, sweat and interstitial fluid (ISF), contact lenses, acoustic spectroscopy, Raman spectroscopy or a combination of these techniques have been proposed for non-invasive glucose monitoring, and also some have even reached the commercialization stage. Another realized technology is the continuous measurement and control of non-invasive blood glucose using electromagnetic waves due to its ability to penetrate body tissues. These types of systems rely mainly on changes in the permeability (μ) and permittivity (ϵ) of tissues or target cells. And they allow the user to test their glucose levels without daily prick of their finger. Because changes in the concentration of glucose lead to changes in the electromagnetic parameters of ISF under the skin, saliva, tears, sweat, urine and blood in the vessels, and so on. Many studies have consistently suggested promising results and various methods for measuring the electromagnetic properties of blood glucose in tissues. For example, split ring resonators (SRR) and complementary split ring resonators (CSRR), antennas and filters, transmission lines and coaxial, implantable devices, and more can be mentioned.

4.3 Sensor Design

The effective technique for the design of microwave band-stop sensor (BSS) is utilizing the adjacent resonators, which are excited by the electric coupling or direct feeding as illustrated in Fig. 18a and b, respectively. For these planar sensors, a low

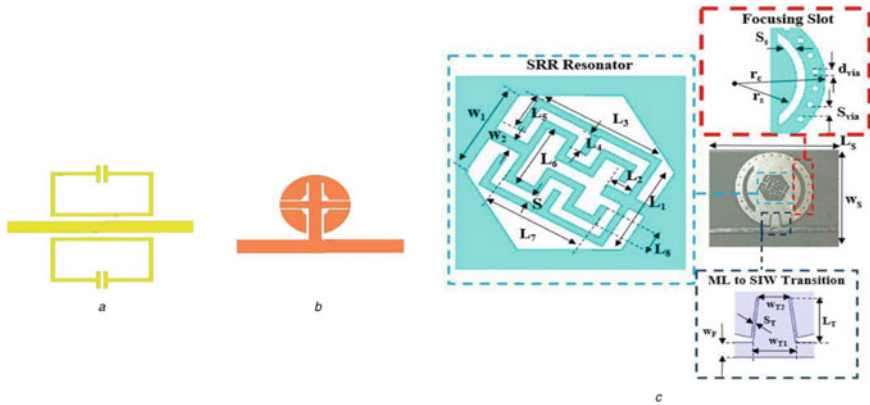


Fig. 18 Microwave BSSs **a** conventional with electric coupling, **b** conventional with direct feeding and **c** proposed sensor structure

Q-factor ($Q < 30$) was attained. The main advantage of direct feed BSS (DF-BSS) in comparison with the coupled excited ones is that their resonance is mainly related to capacitances and inductances in the sensing region. Therefore, the DF-BSS shows more sensitivity when the sample under test (SUT) is displaced or located on the sensing area. Also, employing the SIW cavity in a resonator section of BSS leads to a higher Q-factor. The most significant property of a microwave resonator sensor for BGC monitoring is sensitivity and compact size. Hence, the SIW-based DF-BSS can provide high promise for BGC sensing.

In this research, the proposed BGC sensor is a band-stop configuration based on the SIW cavity which directly fed by a tapered microstrip line (ML), as depicted in Fig. 18c. To create a planar sensing region, a hexagon slot is etched on the top surface of the SIW cavity and a modified SRR is directly connected to the edge of the slot. Traditionally, in SIW cavity, the resonance characteristics strongly depend on the electric field and magnetic field distributions [13]. Furthermore, to concentrate the electric field on the presented sensing spot, the curved slots are inserted into the top plane of SIW cavity, which exhibits strong field confinement that the results in the deeper resonance can be achievable. By the proposed SRR, the electric field coupling is realized for designing the BGC sensor. The investigated SRR includes the meandered rings and open stubs can produce the extended length and more split gaps in small size compared with the conventional SRR. So, the proposed SRR can considerably increase the electric field intensity at specific areas in the close proximity of the sensing region, which allows more interaction between the SUT and the developed sensor and enhances the sensitivity. The equivalent circuit model of the proposed SRR is indicated in Fig. 19. It is derived based on the circuit models presented in [14].

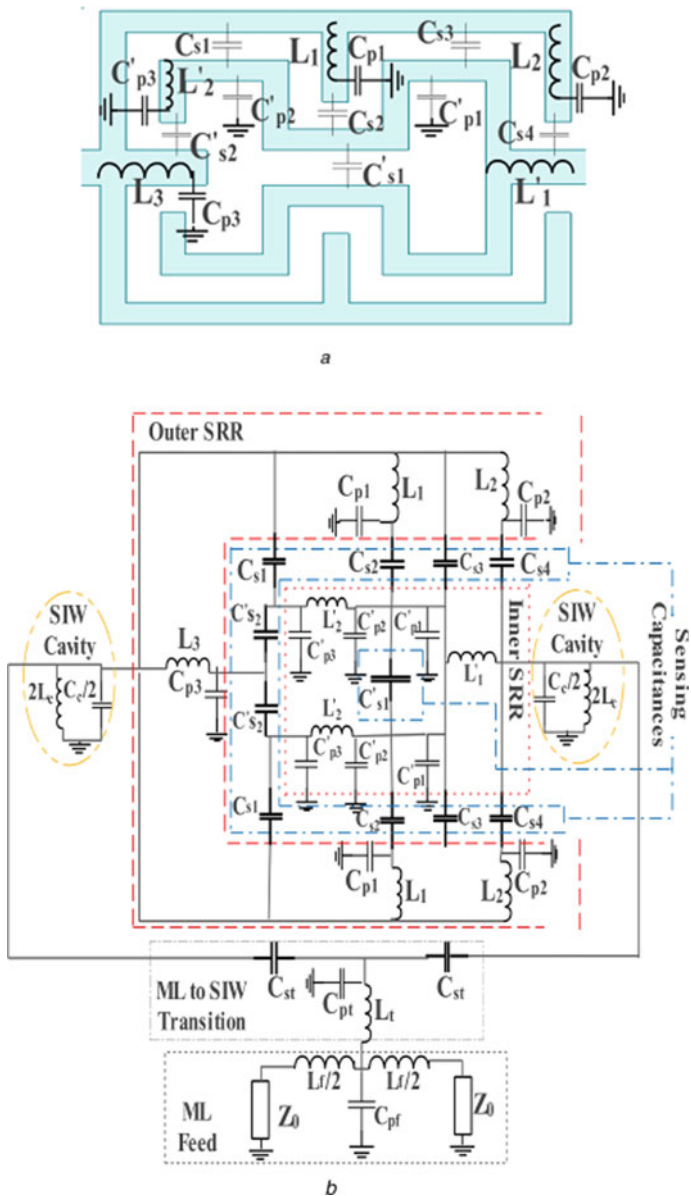


Fig. 19 Equivalent circuit model **a** introduced SRR and **b** circuit model for proposed sensor

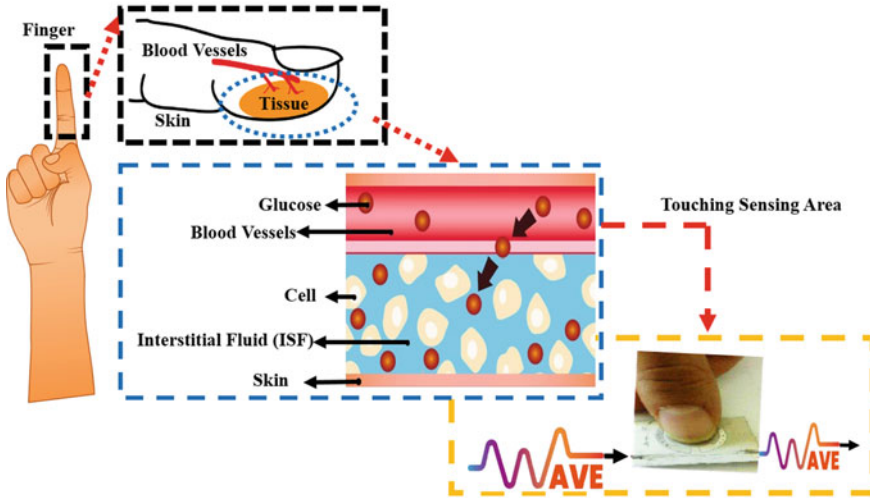


Fig. 20 Finger tissue model and its effect on sensor performance

4.4 Description of Sensor Performance During Loading

The performance of the proposed sensor is based on the measured transmission coefficient of the designed structure. When the user's fingertip is placed at the sensing point, according to the principle of the perturbation, the electromagnetic field distribution disturbs in the surface and inside of the substrate, and the resonance frequency and amplitude of the sensor vary depending on the changes amount in the electromagnetic parameters of the fingertip which is due to the change in glucose levels. From this change in resonance, it can be deduced that the user's glucose level has changed. The finger tissue model is depicted in the Fig. 20.

As one can see from the figure, glucose is present in both the blood vessels and the ISF; and the change of glucose levels in these two parts and their interaction with electromagnetic waves that penetrated into the skin and the resonance frequency change of the sensor leads us to control of blood glucose levels of the user.

4.5 Investigating Environmental and Human Conditions Effective on Results at the Time of Testing

In some previous researches has been demonstrated that fingertip is a good choice for determining blood glucose levels, but non-invasive blood glucose monitoring by resonant sensors is unreliable at microwave frequencies and millimeter waves in this way. They believe that the accuracy of the device and the results are highly dependent on the parameters of physical and chemical properties such as (1) Blood pressure, (2)

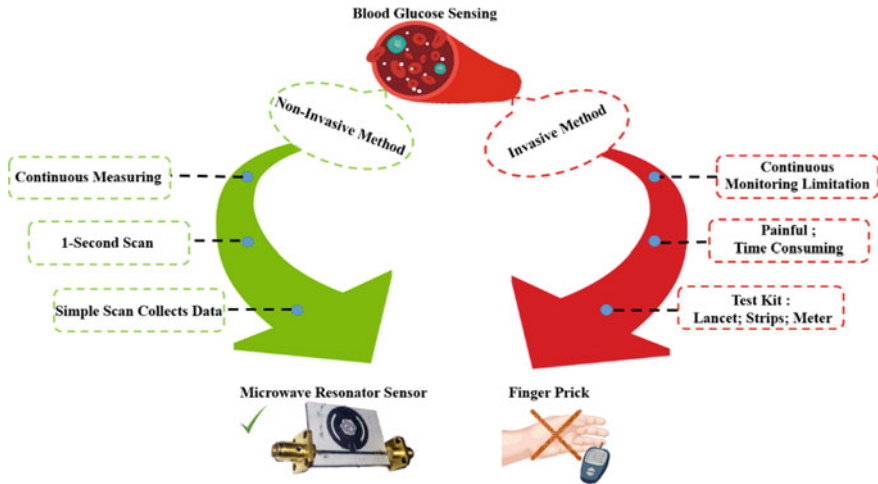


Fig. 21 Comparison between invasive (using a glucometer) and non-invasive (using the proposed glucose sensor)

Body temperature of individuals and the environment, (3) Unwanted electromagnetic radiations from the environment that influence sensor performance, (4) Thickness of the skin, (5) The pressure applied by the fingertip and the position of the fingertip on the sensor, (6) The fingertip arrangement, (7) The sweat and pollutions of the fingertip, and (8) The time of the last meal that the user has eaten. In references [15, 16], it was concluded that if a high field and energy can be concentrated in the whole sensing site, the errors that occur will be largely prevented, which in turn will increase the sensitivity of the sensor. Other cases are also mentioned that should be taken into account when tests performed, it must be first requested from volunteers before the test and six hours must have been passed from their last meal. Before beginning the test process, each volunteer was given about 15 min to rest until their bodies be reached steady state, then their body temperature and blood pressure were taken by a medical staff. Furthermore, each of them was asked to wash their hands to remove any pollution, and finally they were tested at room temperature of 25 °C. Figure 21 shows a comparison between invasive (using a glucometer) and non-invasive (using the proposed glucose sensor) methods.

4.6 Results and Comparison

As shown in Fig. 22, the BGC sensor described in Sect. 4.3 is prototyped and measured to verify the designed configuration. The substrate is Rogers RO4003 with relative permittivity = 3.55 and thickness = 0.508 mm. Dimensions of the fabricated sensor are reported in Table 6.

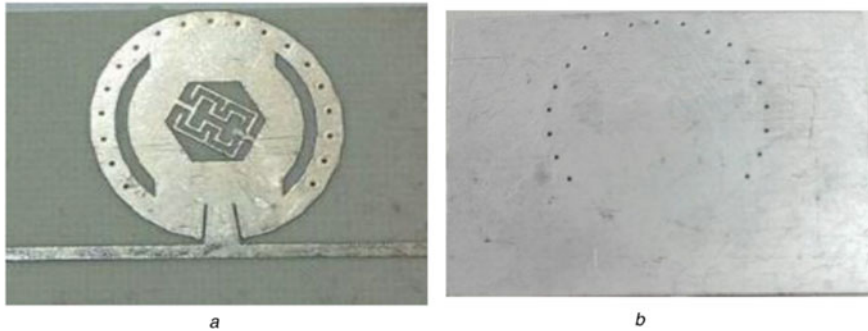


Fig. 22 Fabricated sensor **a** top view and **b** bottom view

Table 6 Detail parameters of the proposed sensor (in millimeter)

Substrate		Focusing slot		ML to SIW transition		Proposed SRR			
W_S	40	d_{via}	0.65	W_F	1.1	L_1	4	L_7	4.1
L_S	30	S_{via}	1.3	W_{T1}	2.8	L_2	1.2	L_8	0.6
h_S	0.5	S_S	1	W_{T2}	2	L_3	5	W_1	4
		r_C	9.5	S_T	0.1	L_4	1	W_2	0.5
		r_S	6	L_T	3	L_5	1.6	S	0.4
						L_6	3.1		

The effects of the SIW cavity, the hexagon slot with the modified SRR and the focusing slots in the proposed sensor performance are studied using the ANSYS high frequency structure simulator (HFSS) and demonstrated in Fig. 23. As indicated in Fig. 23, resonance value is improved when the curved slots are utilized in the proposed structure due to the enhancement of field confinement at sensing place. Also, the measured result for the bare test is plotted in Fig. 23, and a good agreement is detected between the measured and simulated results.

Further, the electric field distribution of the proposed sensor is depicted in Fig. 24. To calculate this distribution in the sensing region of the proposed sensor, a three-dimensional finite element method is accomplished by ANSYS HFSS. As can be seen from Fig. 24, employing the curved slots has a significant influence since the electric field is more concentrated in the SIW cavity center. So, upon loading, the interaction between the electric field and SUT will be enhanced.

When the resonance transmission coefficient is used for permittivity sensing, the Q-factor of the sensor can be obtained from (3) and it can be reached by the formula (3). As can be seen in Fig. 23, f_0 is equal to 5.8 GHz and Δf is about 45 MHz. So, a proper unloaded quality factor ($Q \approx 130$) is attained for the proposed sensor. To peruse the validity of this structure as a sensor, it is needed to have some information about the relation between the dielectric coefficient of blood and its glucose concentration.

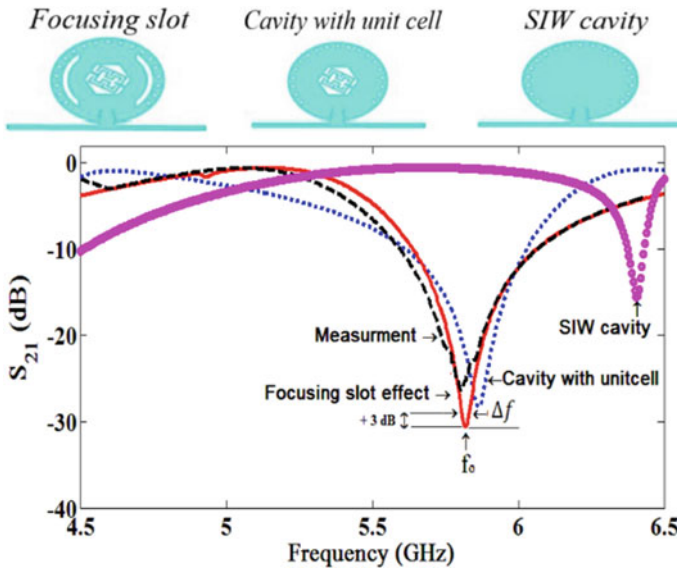


Fig. 23 Simulation and measurement results of the designed sensor in the empty case

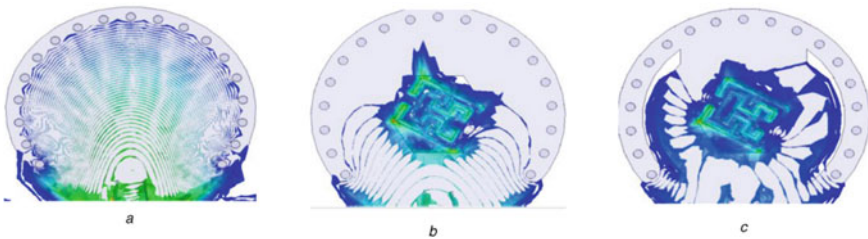


Fig. 24 Effect of sensor components on electric field distribution **a** SIW cavity, **b** hexagon slot and **c** curved focusing slots

This affiliation is derived from [17]. In [17], it was shown that the permittivity of blood decreases as the glucose concentration in the blood increases. Alteration of glucose concentration in the blood causes a shift in the resonance frequency of the band-stop filter. In this research, a fingertip is modelled based on the configuration reported by Turgul and Kale [11, 12], as illustrated in Fig. 25.

The model is then simulated using the ANSYS HFSS software. The overall model size is 4 mm × 5 mm × 10.5 mm. Considering four values of BGC, 105, 255, 400 and 500 mg/dl, this model is placed on the introduced SRR as the SUT and the resonance frequency is shifted to 5.36, 5.395, 5.432 and 5.455 GHz, respectively, as illustrated in Fig. 26a. The resonance shift between the BGC values is about 95 MHz and it is significantly larger than the reported value in [11]. This is due to the proposed SRR that the electric field penetrates in a small area which results in more

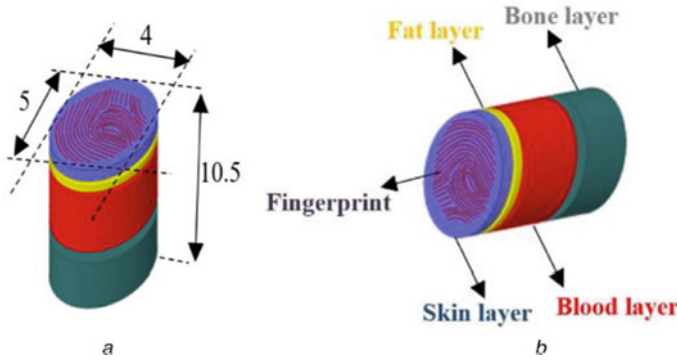


Fig. 25 Fingertip model **a** bottom view and **b** side view (All dimensions are in millimeter)

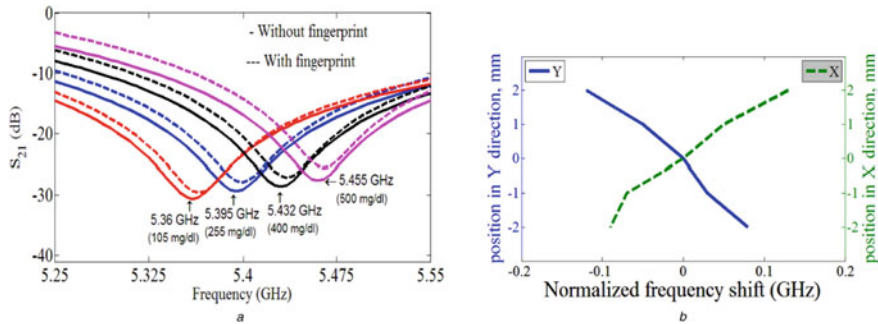


Fig. 26 Performance of the proposed sensor **a** for BGC changes and fingerprint influence and **b** SUT placement effect on the resonance frequency shift

local interaction with SUT. Further, to indicate the sensing accuracy of the proposed sensor, a simplified model of the fingerprint is etched on the skin layer of four utilized fingertip models, as depicted in Fig. 25. In all models, the relevant resonance shifts are <5 MHz, which indicate that the proposed sensor has less influence to fingerprint effect compared to [11], as shown in Fig. 26a. For a microwave BGC sensor, the FDR for BGC value change of 1 mg/dl can be extracted from [2] and can be obtained by (5).

$$FDR = \frac{\Delta F}{\Delta C} (\text{MHz}/(\text{mg}/\text{dL})) \tag{5}$$

where ΔC denotes the BGC variation and ΔF is the relative shift of the resonant frequency. As the value of BGC increases from 105 to 500 mg/dl ($\Delta C = 395$ mg/dl), the resonance frequency of the proposed sensor is shifted from 5.36 to 5.455 GHz ($\Delta F = 95$ MHz), respectively. In [11], the shift of the resonance frequency (ΔF) is 8 MHz, for the same deviation of the BGC value. So, the FDR of the proposed sensor

and conventional configuration [11] are 0.24 and 0.02 MHz/(mg/dl), respectively. Moreover, the effect of the fingertips position placement on the proposed sensor is studied and demonstrated in Fig. 26b. Same as [11], the position of the SUT is changed from -2 to $+2$ mm in both x and y directions individually, and miniaturized proposed sensing area (SRR) shows <130 MHz resonance shifts whereas in [11], the relevant resonance shift was about 250 MHz.

Table 7 summarized the comparison results of the proposed sensor and the previous structure [11]. Also, a measurement procedure is provided for computing the uncertainty of the proposed sensor performance. It includes: (1) Using a GLUCOCARD™ 01-mini blood glucose monitoring system, the BGC values of four patients are measured and (2) By placing their fingertips on the sensing area of the proposed sensor, the measurement of BGC values is repeated again at the same time.

The measured results of the proposed sensor are indicated in Fig. 27. As listed in Table 8, a comparison between the measured results of the proposed sensor and the commercial product is presented. In comparison to the GLUCOCARD™ 01-mini, the proposed sensor shows a maximum measurement error of about 32% for the BGC detection. It is because of the effect of a fingerprint, the difference in fat layer and skin layer thickness and the fingertips placement on the sensing region of the sensor.

Table 7 Comparison between the proposed design and reported sensor [11]

Name	Fingerprint error (MHz)	Placing error (MHz)	BGC variation (mg/dL)	FDR (MHz/(mg/dL))	Resonance value (dB)	Sensing area (mm × mm)
[11]	14	250	100–500	0.02	-14.5	4 × 11
Proposed sensor	<5	<130	105–500	0.24	<-29	4 × 5

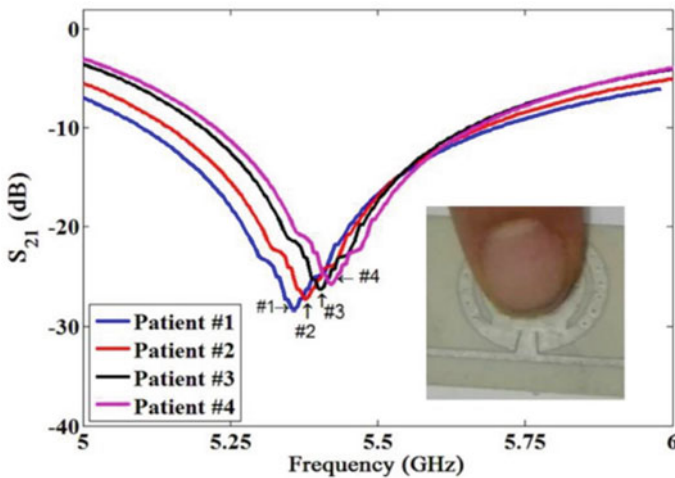


Fig. 27 Measured results of the proposed sensor

Table 8 Comparison with the GLUCOCARD™ 01-mini commercial product

Name	GLUCOCARD™ 01-mini	Proposed sensor		
	Measured BGC (mg/dL)	Measured resonance frequency (GHz)	Calculated BGC (mg/dL)	Measurement error (%)
Patient #1	137	5.36	106	22.5
Patient #2	213	5.374	162	24
Patient #3	271	5.382	196	28
Patient #4	339	5.391	231	32

4.7 Smart Health Care Systems

With the rapid development of wireless communication technology and need to develop smart health care, combining wireless technologies with sensors as wearable, implantable and ingestible devices that monitor the vital signs of the body is very important. Smart systems increase physician–patient communication, speed up disease diagnosis, and reduce health care costs. The function of these systems is like that the patient’s vital signs such as heart rate, blood pressure, oxygen levels and blood glucose levels are sent to a smart phone or a computer through sensors connected to the body. The platform of these transmissions can be wireless communication channels such as Wi-Fi and Bluetooth. Next, the program installed on the interface sends the information to the central server (located in the hospital) via the internet. Then, the information is sent to the relevant physician and the caregivers specified for the patient, which according to the information received, the physician gives the necessary instructions for the process of disease recovery. The process of blood glucose control in the smart health care system for the proposed sensor is shown in Fig. 28. First, the network analyzer obtains the data from the sensor. The data is then processed by a computer, and the data is normalized in a specific range and useful features are selected to assess whether a warning should be generated or not. In the event of an alert, the system will either performs the relevant task directly, or notifies and guides the user or physician accordingly. As stated in article [18], a portable version of the proposed microwave biosensor can be obtained for continuous blood glucose control of diabetics by replacing the vector network analyzer (VNA) with a small radar screen in the testing process; similar to smart watches that monitor the body’s vital signs.

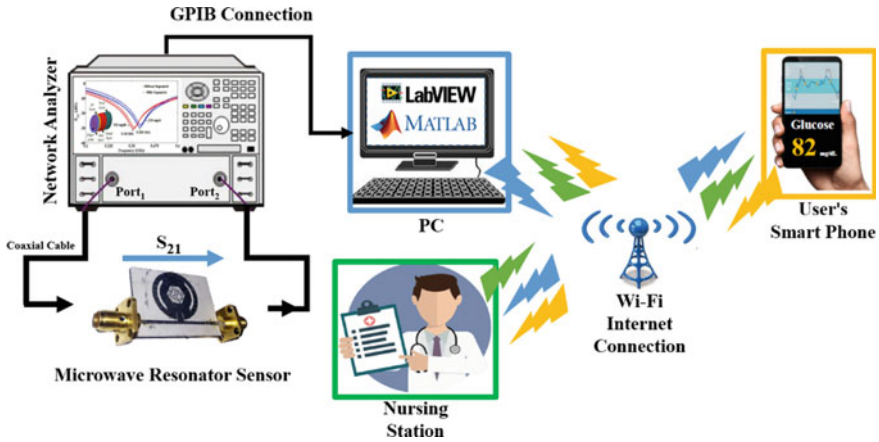


Fig. 28 Smart health care system for the proposed sensor

5 Dual-Sensing and Dual-Frequency Microwave SRR Sensor for Liquid Samples Permittivity Detection

5.1 Abstract

In this research, a microwave sensor based on the SRR has been proposed to detect the real part of the dielectric constant of the liquid sample. The proposed structure composed of non-identical double-split ring resonators (NID-SRRs) which are placed in the inner part of the power divider branches. The proposed sensor has two purposes: (1) Measurement of the permittivity of one sample under test (SUT) in two frequency bands (multi-band), (2) Dual samples under test for simultaneous dielectric detection (multi-sensing). There are several advantages in measuring the permittivity of the SUT with the proposed sensor such as high Q-factor, high sensitivity, compact size, multi-sensing and multi-band. This work investigates resonance frequency variation relative to the samples with different permittivity, such as ethanol, methanol, glucose solution and deionized water (DI water) compared to previous similar works in simulation and experimental results. The permittivity of samples under test varies from 24 to 78 at 25 °C, and the resonance frequency of the simulated sensor would change about from 5.76 to 4.8 GHz at first resonance frequency and 7.85 to 6.35 GHz at second resonance frequency. The proposed structure is fabricated on RO4003 substrate, with 0.508 mm thickness.

5.2 *Design and Fabrication of Microwave Sensor*

To design a high sensitivity microwave sensor, the intensity of the field should be increased by various design methods at the sample placement. As the intensity of the field increases, the field perturbations increase in the presence of a minimum sample value, and in this case the sensitivity of the sensor increases to detect the permeability. Researchers use the different methods such as the meandered line and interdigital structure to increase the field intensity. The designing a microwave sensor based on SRR is a conventional method in recent years and only the used techniques are different. The techniques should provide a high sensitivity and resolution.

The use of multi-channel and multi-band sensors causes several samples to be tested simultaneously, and it reduces error and dimension. The problem of the multi-channel sensors is the mutual influence of channels which the undesirable mutual influence can be reduced by using the power divider.

The requirements for designing the proposed microwave sensor include increasing the sensitivity of the sensor by placing samples at the location of maximum electric field, investigating the capacitance and inductance circuit with an aperture and length of the microstrip line for determining the resonance frequency and design application of the SUT. The sensor design procedure performs step by step.

5.2.1 **NID-SRRs Sensor Design Procedure**

Two sections are considered for designing the proposed microwave sensor, these sections are including power divider, and NID-SRRs sensing mechanism. The power divider structure is a suitable component for microwave and RF devices such as network feed, splitter/combiner and power amplifier. The design idea of the proposed sensor with power divider was taken from [19–21]. The proposed sensor is implemented by using planar SRR technique. The SRR structure is a desirable design due to high Q-factor, high sensitivity, easy fabrication, real time detection, simple field analyzes and simple equivalent circuit model [22]. However, the NID-SRRs is added to power divider design.

5.2.2 **Principle of Sensor**

The resonance frequency must be obtained for determining SUT permittivity. Therefore, the SRR structure could be considered a simple LC equivalent circuit. The relationship between the resonance frequency and equivalent capacitance and inductance is obtained with the formula (6) [22]:

$$f_0 = \frac{1}{2\pi\sqrt{LC}} \quad (6)$$

where the parameters L and C are related to the ring inductance and the split capacitance, respectively. As compared to the circuit model in [23], the presented sensor microstrip transmission line is designed by power divider and SRR which is shown in Fig. 29. The equivalent circuit for the coupled SRR with power divider is presented in Fig. 29a. These parameter of L_s as the inductor is result of a coupling between microstrip line and ring resonator which is described as mutual inductance and is illustrated with M parameter. The resonance frequency changes by C_R capacitance due to ring gap or by L_R inductance due to interaction of microstrip transmission line and SRR. There is a slight resistance in SRR loop that is specified by R_R parameter, and the coupling between microstrip transmission line and SRR is depicted in Fig. 29b. In fact, the involved parameters with transmission line are including L_m (the involved length with microstrip transmission line), W_m (the ring width) and G_m (distance between the ring and microstrip transmission line). These parameters has affected on the feeding, ring resonator and magnetic coupling. To enhance the sensitivity of the NID-SRR sensor, three main parameters including L_m , W_m and G_m are optimized and two operating frequency is obtained. Finally, one of fabricated ring resonators of the proposed sensor is illustrated in Fig. 29c.

Using two ring resonator for the proposed sensor is caused to increase accuracy. Two resonance frequencies are created by two ring resonators and their structure along with the isolation diagrams of two output port are shown in Fig. 30. In the unloaded sensor, the resonance frequencies are appeared at 5.76 and 7.85 GHz. The performance of the presented sensor is based on the resonance frequency variation due to the effect of SUT on the field interaction, because the SUT changes the equivalent inductor and capacitor, thereby vary the field intensity. Moreover, each SRR produces a high Q-factor. A close look at the isolation diagram between the two output ports in Fig. 30c, we find that the isolation of the two output ports is better than 20 dB at operating frequencies and two ports have the least impact on each other.

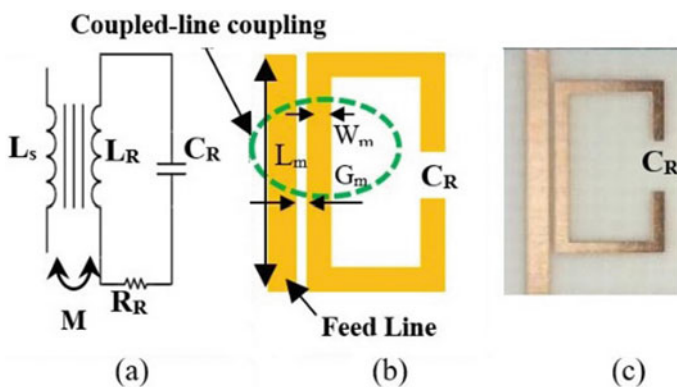


Fig. 29 Equivalent circuit for NID-SRRs sensor **a** LC equivalent circuit that L_s parameter is the inductance of microstrip transmission line with L_R , R_R and C_R parameters of ring resonator, **b** the coupling between microstrip transmission line and SRR, **c** one of rectangular copper ring of proposed sensor. C_R is common capacitor between three features

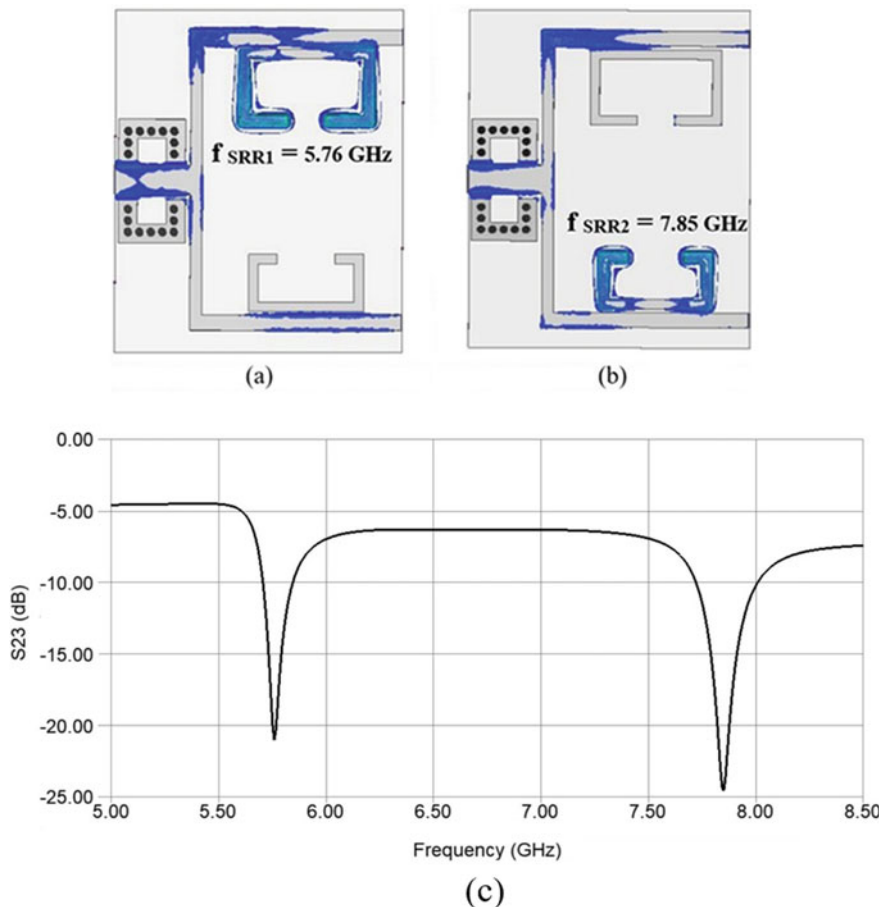


Fig. 30 Concentration of electric field on NID-SRRs in free space that produce two resonance frequency **a** $f_{SRR1} = 5.76$ GHz, **b** $f_{SRR2} = 7.85$ GHz, **c** isolation diagram between two output ports

5.2.3 Sensor Fabrication and the Equivalent Circuit Model

The proposed compact sensor is fabricated on Rogers 4003 substrate with 3.38 dielectric constant, $\tan\delta = 0.0026$ and thickness of 0.508 mm. The fabricated sensor is illustrated in Fig. 31a and the sensor dimension details is observed in Fig. 31b. Parameters values are demonstrated in Table 9. The sensor is fabricated with printed circuit board technology.

In the NID-SRRs sensor, small ring has bigger gap, however produces the higher resonance frequency and the other resonance frequency is generated by the bigger ring resonator. The different parts of the sensor structure must be determined for the presentation of the equivalent circuit model. The presented sensor consists of one power divider and two SRRs. Each SRR is equivalent of a tank circuit that is including

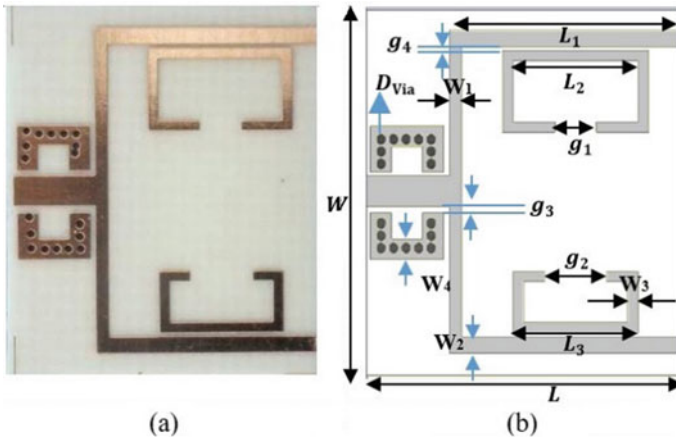


Fig. 31 Structure of NID-SRRs sensor **a** the feature of proposed sensor, **b** dimension of design

Table 9 Parameters values of the presented sensor

Parameters	L_1	L_2	L_3	g_1	g_2	g_3	g_4
Values (mm)	11	7	6	2	3	0.3	0.6
Parameter	W_1	W_2	W_3	W_4	D_{via}	L	W
Value (mm)	0.65	0.8	0.5	1	0.4	15	18

an inductance and a capacitance, power divider is equivalent of a set of inductance, capacitance and resistor. When a sample placed on the sensor, it means that a capacitor is parallel with the tank circuit. The circuit schematic and the resonance frequencies are shown in Fig. 32 and Fig. 33, respectively.

5.3 Simulation and Experimental Measurement Results

In designing the proposed sensor, two main objectives have been considered: (1) The ϵ' detection of two different liquid samples in two frequencies are measured simultaneously under simultaneous dielectric detection (SDD). When a sample (for example, DI water) is placed on the one sensor ring and other sample (for example, ethanol) is located on the other ring, the sensor can measure permittivity of two samples simultaneously. (2) Permittivity detection of one sample in two frequency bands for reduction of measurement error and increasing accuracy. Therefore, to achieve these two purpose, two dissimilar SRRs are added to the power divider structure to create two different resonance frequencies. When a sample is placed on the slots of each SRR, it shifts the resonant frequencies due to the different samples permittivity. In this design, pure ethanol, pure methanol, glucose solution

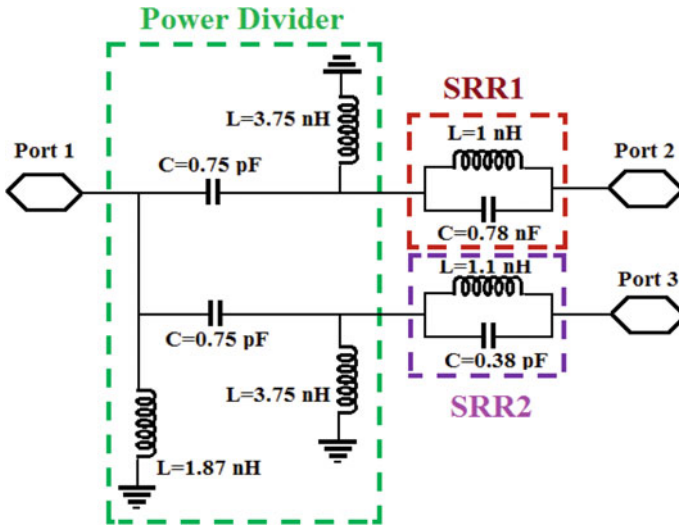
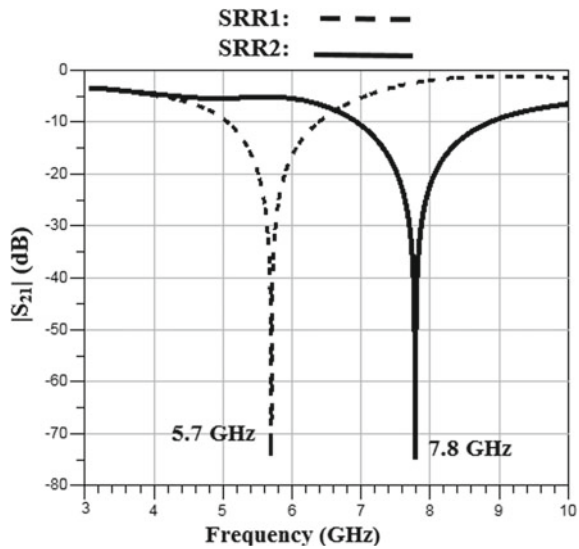


Fig. 32 Equivalent circuit model of the proposed sensor

Fig. 33 Resonance frequencies of free load mode related with SRR1 and SRR2



(0.2 g/ml) and DI water are used as liquid SUTs to assure sensor performance in the measurements. Figure 34a–e shows the both of measured and plotted resonant frequencies with presence of SUT on sensor at two frequencies. The resonance frequency of different SUTs are presented in Table 10.

The measurement setup test is shown in Fig. 35 and the compact fabricated sensor prototype is shown in Fig. 35a. For measuring permittivity, a SUT is injected on a

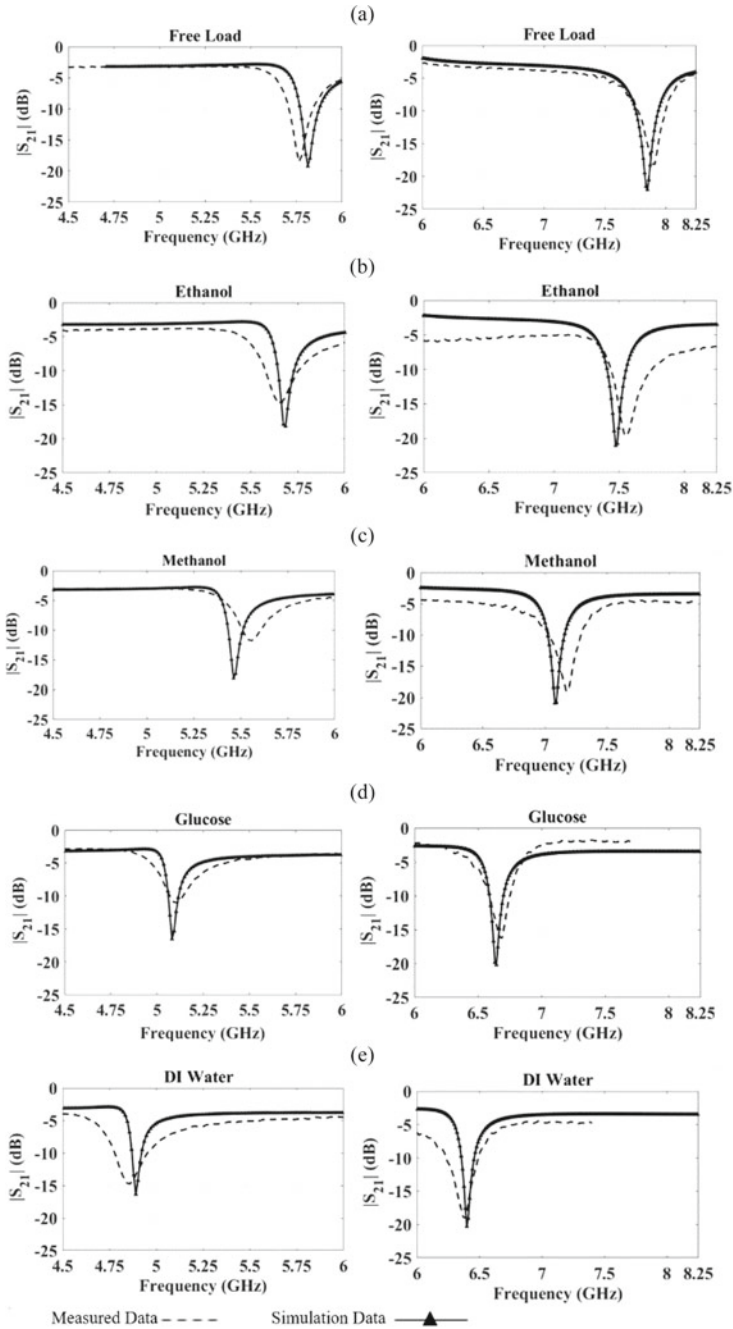


Fig. 34 Simulated and measured S_{21} parameters of different dielectric properties at two resonance frequencies **a** free load, **b** ethanol, **c** methanol, **d** glucose, **e** DI water

Table 10 Resonance frequency value of SUTs

Resonance frequency	Free load	Ethanol	Methanol	Glucose	DI water
	$\epsilon_r = 1$	$\epsilon_r = 24$	$\epsilon_r = 32$	$\epsilon_r = 68$	$\epsilon_r = 78$
f_{SRR1} (GHz)	5.76	5.65	5.52	5.10	4.80
f_{SRR2} (GHz)	7.85	7.56	7.15	6.65	6.35

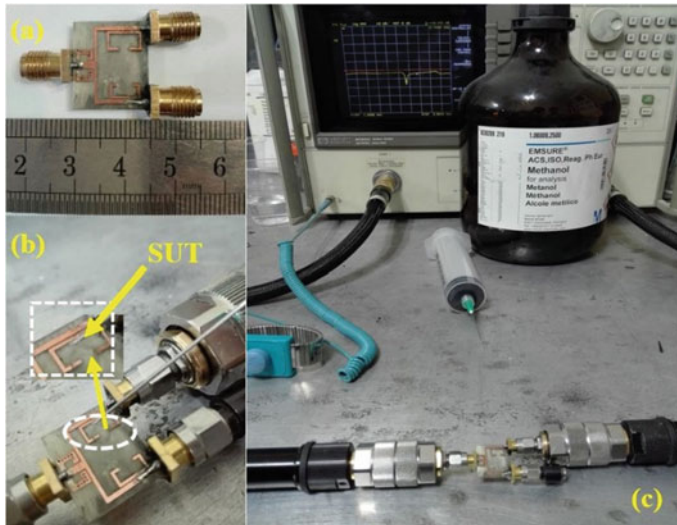


Fig. 35 Experimental measurement of sensor testing environment, **a** proposed sensor under NID-SRRs sensor, **b** situating of SUT on the sensor, **c** measurement of samples with different dielectric using the VNA network analyzer

sensing area that is demonstrated in Fig. 35b. Then, the measurement is performed by VNA, as seen in Fig. 35c.

Figure 36 can be plotted by using the results obtained from experimental tests. In this diagram, the vertical axis represents the resonant frequency of the sensor loaded with the special materials and the horizontal axis represents the permittivity of the materials under test.

In the following the process of measuring the relative permittivity of liquids and for better demonstrating the performance of the sensor, a mixture of water and ethanol with different concentrations are used as samples under test in both channels simultaneously. Then, the permittivity for the different concentrations of water–ethanol solution are interpolated from the diagram of Fig. 36, and their values are compared in Table 11 with the values reported in the reference [24], which are in good agreement.

Stability sensing of sensor is expressed by sensitivity. On other words, this parameter is used for determining accuracy of sensors that is expressed with formula (1). The sensitivity of the proposed sensor is obtained 0.28 and 0.3 corresponding to

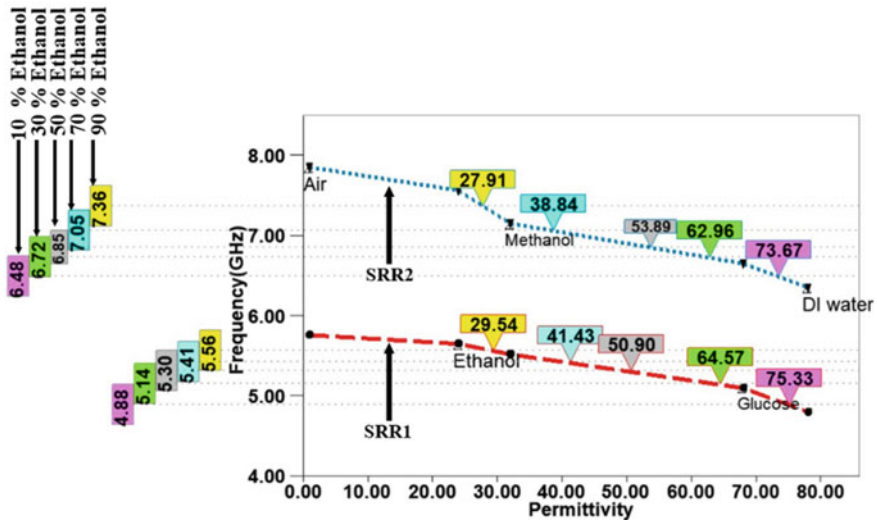


Fig. 36 Resonance frequency diagram of the samples in terms of dielectric constants of the materials under test

Table 11 Permittivity for different concentrations of water–ethanol solution

Water %	Ethanol %	Dielectric constant in [24]	This work			
			Dielectric constant		Frequency (GHz)	
			CH1	CH2	CH1	CH2
0	100	24	24	24	5.65	7.56
10	90	30	29.5	27.9	5.56	7.36
30	70	41	41.4	38.8	5.41	7.05
50	50	51	50.9	53.8	5.3	6.85
70	30	62	64.5	62.9	5.14	6.72
90	10	73	75.3	73.6	4.88	6.48
100	0	78	78	78	4.8	6.35

SRR1 and SRR2 respectively, and the relative permittivity is changed from 24 to 78. For determining the sensor resolution is used from FDR that can be given by Eq. (2). The FDR of the proposed sensor is obtained 0.016 and 0.022 corresponding to SRR1 and SRR2 respectively. Comparison of Q-factor between sensors can be reached by the formula (3). In the presented sensor, Q-factor values are 280 and 110 at frequencies of 5.76 GHz and 7.78 GHz respectively, which is appropriate compared to similar works. Table 12 shows comparison among different parameters for the presented NID-SRR sensor and previous works. For determining validity of the sensor, the measurement and simulation results are compared on each other, when their different is low, this shows the error value is small. The error is illustrated in

Table 12 Performance comparison between proposed sensor and previous works

References	Frequency (GHz)		Sensitivity (%)		FDR (MHz)		Q-factor		DLSDD	Size (mm × mm)	Published in
	CH1	CH2	CH1	CH2	CH1	CH2	CH1	CH2			
[21]	2	5	0.014	0.004	3	0.2	40	60	No	>270	Microw. Opt. Tech. Lett., 2012
[23]	2.1	-	0.14	-	3	-	130	-	No	625	Sensors Actuators A: Physical, 2013
[25]	2	-	0.4	-	7	-	35	-	No	>270	IEEE Sensors J., 2014
[26]	3.1	-	0.003	-	0.1	-	250	-	No	>270	IEEE Trans. Microw. Theory Techn., 2014
[6]	0.3	-	0.55	-	1	-	30	-	No	200	IEEE Sensors J., 2015
[27]	17.1	-	0.1	-	20	-	120	-	No	>270	Sensors, 2016
[28]	9.5	-	0.09	-	8	-	38	-	No	>270	IEEE Sensors J., 2016
[29]	4.68	-	0.16	-	7	-	70	-	No	>270	IEEE Trans. antennas propagation, 2016
[30]	5.84	-	0.03	-	2	-	75	-	No	>270	IEEE J. Electromag., RF Microw. Med. Biology, 2017
[31]	2.1	-	0.04	-	0.8	-	525	-	No	>270	Microw. Opt. Tech. Lett., 2017
[2]	0.358	-	0.8	-	2	-	120	-	No	216	Electron. Lett., 2017
[32]	3.23	-	0.04	-	1	-	60	-	No	<270	J. Applied Physics, 2017

(continued)

Table 12 (continued)

References	Frequency (GHz)		Sensitivity (%)		FDR (MHz)		Q-factor		DLSDD	Size (mm × mm)	Published in
	CH1	CH2	CH1	CH2	CH1	CH2	CH1	CH2			
[33]	2.47	-	0.95	-	23	-	50	-	No	>270	J. Applied Physics, 2017
[34]	2.27	-	0.012	-	0.27	-	487	-	No	>270	IEEE Microw. Wirel. Compon. Lett, 2017
[35]	2	3.32	0.15	0.1	2	3	30	30	No	>270	Sensors, 2017
[36]	6	-	0.008	-	0.45	-	50	-	No	>270	Sensors, 2017
[37]	0.975	-	0.17	-	2	-	30	-	No	>270	IEEE Sensors J., 2017
[38]	4.62	-	0.01	-	0.8	-	230	-	No	875	J. Electrochemical Soc., 2017
[39]	4.1	-	0.08	-	3	-	40	-	No	625	J. Electrochemical Soc., 2017
[40]	0.58	-	0.4	-	1	-	70	-	No	>270	J Sensors and Sensor Systems, 2018
[41]	3.45	-	0.16	-	5	-	35	-	No	>270	Modern Physics Lett. B, 2018
[42]	4	-	0.6	-	22	-	25	-	No	324	J. Electromag. Waves Applications, 2019
[43]	1.51	-	0.6	-	10	-	100	-	No	900	Applied Physics A, 2018

(continued)

Table 12 (continued)

References	Frequency (GHz)		Sensitivity (%)		FDR (MHz)		Q-factor		DLSDD	Size (mm × mm)	Published in
	CH1	CH2	CH1	CH2	CH1	CH2	CH1	CH2			
[44]	2.52	-	0.1	-	1	-	35	-	No	>270	IEEE Microw. Wirel. Compon. Lett., 2018
[45]	5.76	-	0.08	-	5	-	80	-	No	>270	IEEE Microw. Wirel. Compon. Lett., 2018
[46]	0.96	-	0.13	-	1	-	60	-	No	>270	Sensors Actuators A, 2018
[47]	2.188	-	0.5	-	8	-	87	-	No	>270	Sensors, 2018
[48]	5.81	-	0.14	-	8	-	190	-	No	>270	Sensors, 2018
[49]	8.26	-	0.04	-	4	-	70	-	No	>270	Sensors, 2018
[50]	5.26	-	0.1	-	5	-	1080	-	No	>270	Sensors, 2018
[51]	2.564	-	0.15	-	3.8	-	76	-	No	>270	Sensors, 2018
[52]	2.3625	-	0.02	-	1	-	50	-	No	560	IEEE Sensors J., 2018
[53]	2.03	-	0.026	-	1	-	105	-	No	>270	IEEE Trans. Instrum. Meas., 2019
[54]	2.5	-	0.27	-	9	-	55	-	No	>270	IEEE Trans. Microw. Theory Techn., 2018
[55]	9.25	-	0.07	-	6	-	95	-	No	232	J. Electrochemical Soc., 2018

(continued)

Table 12 (continued)

References	Frequency (GHz)		Sensitivity (%)		FDR (MHz)		Q-factor		DLSDD	Size (mm × mm)	Published in
	CH1	CH2	CH1	CH2	CH1	CH2	CH1	CH2			
[56]	4.3392	-	0.04	-	1.86	-	400	-	No	>270	Int. J. RF Microw. Computer-Aided Eng., 2019
[57]	2.4	-	0.5	-	11	-	40	-	No	750	Sensors, 2019
[58]	0.1342	-	0.57	-	0.76	-	47	-	No	1000	Sensors, 2019
[59]	2.52	-	0.46	-	12	-	44	-	No	>270	IEEE Trans. Antennas Propag., 2019
[60]	4.34	-	0.04	-	1.7	-	46	-	No	>270	IEEE Sensors J., 2019
[61]	4.4	-	0.04	-	1.93	-	400	-	No	>270	Scientific Reports, 2019
[62]	6.83	8.27	0.05	0.04	3	4	42	40	Yes	360	Scientific Reports, 2018
[63]	0.33	-	0.5	-	1.6	-	100	-	No	1500	IEEE Sensors J., 2019
[64]	2.45	5.8	0.17	0.07	4	3	120	100	No	240	J. Electron. Mater., 2020
[65]	1.95	-	0.2	-	6	-	50	-	No	800	Sensors, 2020
Proposed sensor	5.76	7.85	0.28	0.3	16	22	280	110	Yes	270	Measurement, 2020

DLSDD Dual of Liquid SDD

Table 13 Value of parameters for samples

Samples	Frequency (GHz)		Resonance value (dB)		Q-factor		Error	
	CH1	CH2	CH1	CH2	CH1	CH2	CH1	CH2
Ethanol	5.65	7.56	-15	-20	75	61	0.52	1.14
Methanol	5.52	7.15	-12	-20	40	55	1.04	0.88
Glucose	5.10	6.65	-12	-17	43	45	0.34	0.25
DI water	4.80	6.35	-15	-20	40	43	1.04	0.63

Eq. (4). The error of the proposed sensor for two channels are depicted in Table 13. Application of the presented sensor is high in variety of industries. Measuring blood glucose concentrations based on interactions of electromagnetic fields with biological tissues is one of its applications in the medical industry. Perhaps the proposed sensor can be used in sensing pH or glucose in biological material such tear, saliva and sputum, therefore such topics can be considered for future work.

6 Conclusion

Finally, a review of several techniques is reported for implementing planar microwave resonant sensors in this chapter. According to studies conducted, in designing a resonant sensor, according to the principle of their operation, namely the resonant frequency variation at the time of presence of the sample under test, there are several main purposes which must be achieved. These aims are: (1) It must be easily integrated with other parts of microwave and electric circuits (2) It ought to be highly sensitive to small volume of sample. In other words, the quality factor of the sensor should be as large as possible and there should be high concentrated field in the sensing area. (3) Be compact, and (4) It should be possessed easy and low cost fabrication.

Acknowledgements In this section, authors must first mention two eminent professors of telecommunications (Prof. Mojgan Daneshmand and Prof. Pedram Mousavi) who are no longer with us; and we are very grateful for their achievements and scientific services [66, 67]. Also, we appreciate the Semnan University, which supported us in conducting research.

References

1. F. Martín et al., Microwave sensors based on resonant elements. *Sensors* **20**(12), 3375–3382 (2020)
2. M. Karami et al., Modified planar sensor for measuring dielectric constant of liquid materials. *Electron. Lett.* **53**(19), 1300–1302 (2017)

3. S. Kiani, P. Rezaei, M. Navaei, M.S. Abrishamian, Microwave sensor for detection of solid material permittivity in single/multilayer samples with high quality factor. *IEEE Sens. J.* **18**(24), 9971–9977 (2018)
4. S. Kiani, P. Rezaei, M. Karami, R.A. Sadeghzadeh, Band-stop filter sensor based on SIW cavity for the non-invasive measuring of blood glucose. *IET Wirel. Sens. Syst.* **9**(1), 1–5 (2019)
5. S. Kiani, P. Rezaei, M. Navaei, Dual-sensing and dual-frequency microwave SRR sensor for liquid samples permittivity detection. *Measurement* **160**, 107805 (2020)
6. L. Benkhaoua et al., Miniaturized quasi-lumped resonator for dielectric characterization of liquid mixtures. *Sens. J.* **16**(6), 1603–1610 (2016)
7. R. Baghbani, M.A. Rad, A. Pourziad, Microwave sensor for noninvasive glucose measurements design and implementation of a novel linear. *IET Wirel. Sens. Syst.* **5**(2), 51–57 (2015)
8. M.N. Rahman, M.T. Islam, M. Samsuzzaman, Design and analysis of a resonator based metamaterial for sensor applications. *Microw. Opt. Technol. Lett.* **60**(3), 694–698 (2018)
9. I.M. Rusni, A. Ismail, A.R.H. Alhawari, M.N. Hamidon, N.A. Yusof, An aligned-gap and centered-gap rectangular multiple split ring resonator for dielectric sensing applications. *Sensors* **14**(7), 13134–13148 (2014)
10. A. Ebrahimi, J. Scott, K. Ghorbani, Differential sensors using microstrip lines loaded with two split ring resonators. *IEEE Sens. J.* **18**(14), 5786–5793 (2018)
11. V. Turgul, I. Kale, Influence of fingerprints and finger positioning on accuracy of RF blood glucose measurement from fingertips. *Electron. Lett.* **53**(4), 218–220 (2017)
12. V. Turgul, I. Kale, Simulating the effects of skin thickness and fingerprints to highlight problems with non-invasive RF blood glucose sensing from fingertips. *IEEE Sens. J.* **17**(22), 7553–7560 (2017)
13. S. Kiani, P. Rezaei, M. Karami, R.A. Sadeghzadeh, Substrate integrated waveguide quasi-elliptic bandpass filter with parallel coupled microstrip resonator. *Electron. Lett.* **54**(10), 667–668 (2018)
14. A. Ebrahimi et al., Compact dual-mode wideband filter based on complementary split-ring resonator. *IEEE Microw. Wirel. Compon. Lett.* **24**(3), 152–154 (2014)
15. M. Saadat-Safa, V. Nayyeri, A. Ghadimi, M. Soleimani, O.M. Ramahi, A pixelated microwave near-field sensor for precise characterization of dielectric materials. *Sci. Rep.* **9**(1), 13310 (2019)
16. C.H. Tseng, C.Z. Wu, A novel microwave phased-and perturbation-injection-locked sensor with self-oscillating complementary split-ring resonator for finger and wrist pulse detection. *IEEE Trans. Microw. Theory Tech.* **68**(5), 1933–1942 (2020)
17. Y. Nikawa, T. Michiyama, Non-invasive measurement of blood-sugar level by reflection of millimeter waves, in *Asia-Pacific Microwave Conference*, Yokohama, Japan, Dec 2006, pp. 47–50
18. S. Kiani, P. Rezaei, M. Fakhr, A CPW-fed wearable antenna at ISM band for biomedical and WBAN applications. *Wirel. Netw.* <https://doi.org/10.1007/s11276-020-02490-1> 1–11 (2020)
19. R. Mirzavand et al., High-resolution balanced microwave material sensor with extended dielectric range. *IEEE Trans. Ind. Electron.* **64**(2), 1552–1560 (2017)
20. K. Staszek et al., Low-cost microwave vector system for liquid properties monitoring. *IEEE Trans. Ind. Electron.* **65**(2), 1665–1674 (2018)
21. J. Shao et al., Dual-band radio-frequency device for sensing dielectric property changes in microfluidic channel. *Microw. Opt. Tech. Lett.* **54**(12), 2691–2694 (2012)
22. G. Galindo-Romera et al., Submersible printed split-ring resonator-based sensor for thin-film detection and permittivity characterization. *IEEE Sens. J.* **16**(10), 3587–3596 (2016)
23. W. Withayachumnankul et al., Metamaterial-based microfluidic sensor for dielectric characterization. *Sens. Actuators A Phys.* **189**, 233–237 (2013)
24. P.R. Sathesh Babu et al., Solubility enhancement of cox-II inhibitors by cosolvency approach. *Dhaka Univ. J. Pharm. Sci.* **7**(2), 119–126 (2008)
25. A. Ebrahimi et al., High-sensitivity metamaterial-inspired sensor for microfluidic dielectric characterization. *IEEE Sens. J.* **14**(5), 1345–1351 (2014)

26. A.A. Abduljabar et al., Novel microwave microfluidic sensor using a microstrip split-ring resonator. *IEEE Trans. Microw. Theory Technol.* **62**(3), 679–688 (2014)
27. M.U. Memon et al., Microwave chemical sensor using substrate-integrated-waveguide cavity. *Sensors* **16**(12), 1829–1840 (2016)
28. E. Silavwe et al., A microfluidic-integrated SIW lab-on-substrate sensor for microliter liquid characterization. *IEEE Sens. J.* **16**(21), 7628–7635 (2016)
29. Y. Seo et al., Microfluidic eighth-mode substrate-integrated-waveguide antenna for compact ethanol chemical sensor application. *IEEE Trans. Antennas Propag.* **64**(7), 3218–3222 (2016)
30. N. Meyne et al., Resonant microwave sensors for picoliter liquid characterization and non-destructive detection of single biological cells. *IEEE J. Electromag. RF Microw. Med. Biol.* **1**(2), 98–104 (2017)
31. A.A.M. Bahar et al., Dielectric analysis of liquid solvents using microwave resonator sensor for high efficiency measurement. *Microw. Opt. Technol. Lett.* **54**(12), 2781–2784 (2017)
32. R.A. Awang et al., Meta-atom microfluidic sensor for measurement of dielectric properties of liquids. *J. Appl. Phys.* **121**(9), 094506–094512 (2017)
33. V. Rawat et al., ISM (Industrial Scientific and Medical standard) band flex fuel sensor using electrical metamaterial device. *Appl. Phys. A Mater. Sci. Process.* **123**(1), 75–79 (2017)
34. A.A.M. Bahar et al., High-efficiency microwave planar resonator sensor based on bridge split ring topology. *IEEE Microw. Wirel. Compon. Lett.* **27**(6), 545–547 (2017)
35. N. Jankovic et al., A microwave microfluidic sensor based on a dual-mode resonator for dual-sensing applications. *Sensors* **17**(12), 2713–2729 (2017)
36. V. Radonić et al., Microfluidic EBG sensor based on phase-shift method realized using 3D printing technology. *Sensors* **17**(4), 892–906 (2017)
37. P. Véléz et al., Microwave microfluidic sensor based on a microstrip splitter/combiner configuration and split ring resonators (SRRs) for dielectric characterization of liquids. *IEEE Sens. J.* **17**(20), 6589–6598 (2017)
38. M. Bakir, Electromagnetic-based microfluidic sensor applications. *J. Electrochem. Soc.* **164**(9), B488–B494 (2017)
39. O. Altintas et al., Fluid, strain and rotation sensing applications by using metamaterial based sensor. *J. Electrochem. Soc.* **164**(12), B567–B573 (2017)
40. T. Reinecke et al., Design and evaluation of split-ring resonators for aptamer-based biosensors. *J. Sens. Sens. Syst.* **7**(1), 101–111 (2018)
41. O. Akgol et al., Metamaterial-based multifunctional sensor design for moisture, concrete aging and ethanol density sensing applications. *Modern Phys. Lett. B* **32**(23), 1850271–1850282 (2018)
42. J. Cai et al., A metamaterials-loaded quarter mode SIW microfluidic sensor for microliter liquid characterization. *J. Electromagn. Waves Appl.* **33**(3), 261–271 (2019)
43. X. Wang et al., High-Q sensor for permittivity detection based on spiral resonator. *Appl. Phys. A* **124**(11), 740–748 (2018)
44. E. Massoni et al., Enhanced cavity sensor in SIW technology for material characterization. *IEEE Microw. Wirel. Compon. Lett.* **28**(10), 948–950 (2018)
45. B.D. Wiltshire et al., 3D printing microfluidic channels with embedded planar microwave resonators for RFID and liquid detection. *IEEE Microw. Wirel. Compon. Lett.* **29**(1), 65–67 (2018)
46. J. Wu et al., Design and validation of liquid permittivity sensor based on RCRR microstrip metamaterial. *Sens. Actuators A Phys.* **280**, 222–227 (2018)
47. Z. Wei et al., A high-sensitivity microfluidic sensor based on a substrate integrated waveguide re-entrant cavity for complex permittivity measurement of liquids. *Sensors* **18**(11), 4005–4022 (2018)
48. A. Salim et al., TM₀₂ quarter-mode substrate-integrated waveguide resonator for dual detection of chemicals. *Sensors* **18**, 1964–1982 (2018)
49. A. Salim et al., Simultaneous detection of two chemicals using a TE₂₀-mode substrate-integrated waveguide resonator. *Sensors* **18**(3), 811–829 (2018)

50. M.U. Memon et al., Microfluidic high-Q circular substrate-integrated waveguide (SIW) cavity for radio frequency (RF) chemical liquid sensing. *Sensors* **18**(1), 143–156 (2018)
51. A. Salim et al., Low-cost and lightweight 3D-printed split-ring resonator for chemical sensing applications. *Sensors* **18**(9), 3049 (2018)
52. E.L. Chuma et al., Microwave sensor for liquid dielectric characterization based on metamaterial complementary split ring resonator. *IEEE Sens. J.* **18**(24), 9978–9983 (2018)
53. C.G. Juan et al., Concentration measurement of microliter-volume water-glucose solutions using q factor of microwave sensors. *IEEE Trans. Instrum. Meas.* **68**(7), 2621–2634 (2019)
54. M. Abdolrazzagli et al., Strongly enhanced sensitivity in planar microwave sensors based on metamaterial coupling. *IEEE Trans. Microw. Theory Tech.* **66**(4), 1843–1855 (2018)
55. M. Bakır et al., Microfluidic and fuel adulteration sensing by using chiral metamaterial sensor. *J. Electrochem. Soc.* **165**(11), B475–B483 (2018)
56. A.A.M. Bahar et al., Microfluidic biochemical sensor based on circular SIW–DMS approach for dielectric characterization application. *Int. J. RF Microw. Comput. Aided Eng.* **29**(9), e21801 (2019)
57. X. Zhang et al., High-sensitivity microwave sensor for liquid characterization using a complementary circular spiral resonator. *Sensors* **19**(4), 787–801 (2019)
58. Y. Liang et al., An LC wireless microfluidic sensor based on low temperature co-fired ceramic (LTCC) technology. *Sensors* **19**(5), 1189–1200 (2019)
59. S.Y. Jun et al., Liquid sensor/detector using an EBG structure. *IEEE Trans. Antennas Propag.* **67**(5), 3366–3373 (2019)
60. A.M. Gargari et al., Passive matched mushroom structure for a high sensitivity low profile antenna-based material detection system. *IEEE Sensors J.* **19**(15), 6154–6162 (2019)
61. A.A.M. Bahar et al., Real time microwave biochemical sensor based on circular SIW approach for aqueous dielectric detection. *Sci. Rep.* **9**(1), 5467–5479 (2019)
62. H. Zhou et al., Multi-band sensing for dielectric property of chemicals using metamaterial integrated microfluidic sensor. *Sci. Rep.* **8**(1), 14801–14812 (2018)
63. C. Lee et al., Open complementary split-ring resonator sensor for dropping-based liquid dielectric characterization. *IEEE Sens. J.* **19**(24), 11880–11890 (2019)
64. Y. Khanna et al., Dual-band microwave sensor for investigation of liquid impurity concentration using a metamaterial complementary split-ring resonator. *J. Electron. Mater.* **49**(1), 385–394 (2020)
65. Y. Abdulkarim et al., Novel metamaterials-based hypersensitized liquid sensor integrating omega-shaped resonator with microstrip transmission line. *Sensors* **20**(3), 943–961 (2020)
66. M. Daneshmand, Being an electromagnetic engineer: it is not a job, it is a lifestyle [women in engineering]. *IEEE Antennas Propag. Mag.* **61**(4), 116–119 (2019)
67. M. Moghaddam, A.K. Iyer, N. Behdad, A. Kishk, F. Vipiana, L. Shafai, S. Noghianian, R. Dahle, remembering prof. Mojgan Daneshmand and prof. Pedram Mousavi [in memoriam]. *IEEE Antennas Propag. Mag.* **62**(2), 124–125 (2020)

IDC Planar RF Sensors for Dielectric Testing and Applications



M Jaleel Akhtar, Nilesh K Tiwari, and Greeshmaja Govind

Abstract In recent years, the design and implementation of various types of sensors in the radio frequency (RF) and microwave frequency region for material characterization and testing has gained a lot of attention from various researchers around the globe. The characterization and testing of dielectric materials in the RF and microwave frequency band primarily involves estimating the dielectric properties of materials in the specified frequency band for design and development of various types of modern RF devices and circuits. However, the RF dielectric testing procedure has also become quite attractive for several real-world applications apart from estimating the dielectric properties of materials due to the fact that it is basically a non-invasive and non-destructive process. The RF sensor is a generic term quite often used to represent the electronic device or the hardware, which is required to be designed and developed to facilitate the accurate testing of dielectrics in the RF and microwave frequency regime. In the earlier days, the conventional RF sensors were primarily based on the metallic waveguide or the coaxial line structures. The metallic waveguides or the coaxial lines are basically non-planar bulky structures, employed in the past to design various RF circuit components and devices. However, in modern times, these non-planar structures are mostly replaced with the planar configurations in order to realize the compact RF devices and components. It is mainly due to this reason that the planar RF sensor has emerged as the viable alternative to the conventional waveguide and coaxial sensors for the characterization and testing of dielectric materials in the specified frequency range. The planar RF sensors offer small size, lightweight, compact design, and ease of integration with other RF circuits based on the planar technology. Now, as mentioned earlier, apart from the direct applications of material testing, the planar RF sensors are now also being employed for certain indirect applications in the food, agricultural and biomedical industries. For these industries, the major application emerging in recent years has been to detect the quality of various types of edible and medical products. It appears that in order to achieve accurate dielectric testing and to successfully realize various types of indirect industrial applications mentioned above, the sensitivity of

M. J. Akhtar (✉) · N. K. Tiwari · G. Govind
Department of Electrical Engineering, Indian Institute of Technology, Kanpur, India
e-mail: mjakhtar@iitk.ac.in

© The Editor(s) (if applicable) and The Author(s), under exclusive license to Springer Nature Switzerland AG 2021

S. C. Mukhopadhyay et al. (eds.), *Interdigital Sensors*, Smart Sensors, Measurement and Instrumentation 36, https://doi.org/10.1007/978-3-030-62684-6_8

the designed planar sensor should be reasonably high. As a matter of fact, the sensor with higher sensitivity is most suited to detect any type of adulteration in the edible or the medical grade product. In the last few decades, it has emerged that the planar RF sensors employing the concept of electrically small structures have reasonably higher sensitivity, thus being well suited to accurately estimate the complex permittivity of materials. These electrically small configurations are usually realized using the engineered planar structures in order to achieve excellent sensitivity due to the concentrated electric field, which are becoming quite popular in recent years for direct application in the RF industry to perform the dielectric testing of materials and media. The split ring resonator (SRR), the complementary split ring resonator (CSRR), and the interdigital capacitor (IDC) structures may be considered as a few of the basic engineered structures for these types of applications. However, the IDC structure is found to be more appropriate for certain dielectric testing applications than that of the CSRR and SRR due to its relatively high sensitivity and the overall compact size, as it can directly be etched on the main signal line, thus providing quite high sensitivity. This chapter is mainly focused on the IDC based planar RF sensor and its implementation for various dielectric testing applications. A detailed analysis, including the theoretical description involving the quasi static model and the electromagnetic model of a typical IDC based sensor structure, along with the associated dielectric sensing mechanism, is provided. Both the resonant and the non-resonant variants of the IDC structure including their working principle relevant to the dielectric sensing mechanism are discussed in detail. Finally, the use of the planar IDC RF sensors for various industrial, environmental, and biomedical applications based on their design configurations are discussed.

1 Introduction

The dielectric testing in the RF microwave frequency region mainly involves the estimation of the complex permittivity of the test specimen in terms of the measured parameters. In the recent past, several methods have been proposed for the dielectric testing of materials depending on the requirement of various factors such as the frequency range, the desired accuracy, availability of sample volume, the sensitivity etc. In the most general sense, the dielectric testing in the RF and microwave frequency region may be divided into two categories, i.e., the resonant technique and the non-resonant technique. The non-resonant technique is usually employed for the wideband dielectric testing of materials using the measured scattering parameters with moderate accuracy. On the other hand, the resonant technique mainly employs the narrowband measurement but with improved accuracy. Recently, the use of the resonant technique has also been explored for the multi-band dielectric testing of materials in the RF and microwave frequency band. Both the resonant and non-resonant methods usually employ some hardware widely known as the sensor structure for the sample placement, in order to facilitate the measurement of required set of scattering parameters in the specified frequency band. The involved

sensor structures may be broadly classified into two categories viz. the non-planar and the planar sensor structures. The use of planar sensor structures has substantially increased over the non-planar counterparts in recent years, due to their compact size and ease of integration with the modern RF circuits. The dielectric testing using the non-resonant planar sensors primarily employs the microstrip line, the coplanar waveguide (CPW), the substrate integrated waveguide (SIW) based structures. On the contrary, the resonant dielectric testing using the planar sensors can be carried out using the simple planar cavity and associated resonators. It is worth mentioning that the sensitivity of the planar resonant sensor structures is usually better as compared to the non-resonant structures. However, it is required to be further improved for a few specific dielectric testing applications where the sensitivity becomes quite crucial. More specifically, the RF sensors for various industrial, humanitarian, and biomedical applications require substantially higher value of sensitivity in order to identify the purity or concentration of the virgin sample in the presence of even small contamination. It is to be noted that the mischievous practice of contaminating the virgin fluid with some cheap adulterant is quite common, especially in the developing world today, which costs many human lives. As a matter of fact, the quality monitoring agencies are continuously exploring novel mechanisms and methods in order to detect and identify possible contamination in various types of edible and biomedical fluids. Nevertheless, in a real scenario, adulteration detection is not an easy task due to quite close similarity between the adulterant and virgin fluids. Moreover, the concentration of the adulterant is usually kept at such a small level that it cannot easily be identified. The situation becomes more complicated concerning the packaged food industries, where only some sort of non-invasive sensing mechanism can be employed.

Additionally, for specific biomedical applications where the available sample volume remains quite small, it becomes extremely difficult to ascertain the quality of the medical grade product using conventional methods. For these types of applications, the RF sensors have recently been explored as different samples, including the reference liquid and the adulterant, possess different dielectric properties in the specified frequency range. Additionally, in the RF and microwave frequency range, the overall dielectric testing procedure is totally non-invasive, and appropriate compact planar RF sensors may be designed to facilitate the measurement wirelessly. Therefore, it can be said that the design of planar non-invasive RF sensor structures with improved sensitivity may help to ascertain the quality of various medical grade liquids.

It has recently been demonstrated that the integration of some engineered structure to a planar transmission line helps to attain the relatively improved sensitivity with an overall compact sensor topology. The improved sensitivity of these engineered structures based sensing elements may primarily be attributed to the enhanced electric field localization in the sensing region. For these types of applications, three basic types of sensing elements viz., the SRR (split ring resonator), the CSRR (complementary split ring resonator), and the IDC (interdigital capacitor) structures have mainly been utilized in the literature, depending on the specific usage. For example, the CSRR elements show relatively higher sensitivity for dielectrics than that of the

SRR elements. On the contrary, the SRR elements help to design the dielectric sensors with relatively improved resolution than that of the CSRR elements. Nonetheless, both the CSRR and the SRR sensing elements are usually excited using coupling from the main signal line, i.e., the sensing structures are designed in proximity coupling with the main transmission line. This type of indirect coupling of the sensing elements somewhat reduces their sensitivity depending on the actual coupling coefficient and their positions relative to the transmission line. On the other hand, the IDC structures can directly be etched on the main transmission line, which certainly helps to attain improved sensitivity due to the enhanced electric field of the main line. It is mainly due to this reason that various industrial applications have been realized using the IDC sensor structures in the recent past. In this chapter, both the non-resonant and resonant topologies of the IDC structures are described, and their usage for various industrial and the microfluidic biomedical applications are discussed.

2 Basic Theory and Working Principle

The planar interdigital capacitor may be viewed as the modified configuration evolved from the conventional parallel plate capacitor as depicted in Fig. 1 [1, 2]. From this figure, it can be visualized that the simple IDC structure may be realized by arranging both the metallic electrodes of the conventional capacitor on a single side. It can also be observed from this figure that the electric field originated from the signal/positive electrode and terminated on the ground/negative electrode results in the formation of the simple IDC structure with the field hump along the path. This type of uniplanar IDC structure with bulging of the field on its top can effectively be utilized to realize the enhanced interaction of the electric field with the material under test (MUT), loaded on the top of the structure [1, 2]. The strength of the electric field in the given area can be further enhanced by introducing more number of metallic electrode patterns, as shown in Fig. 2, which basically represents a typical IDC structure.

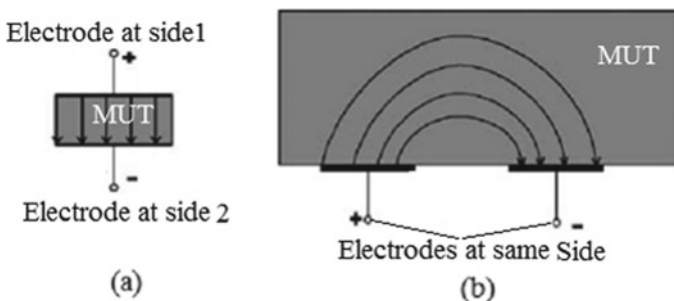
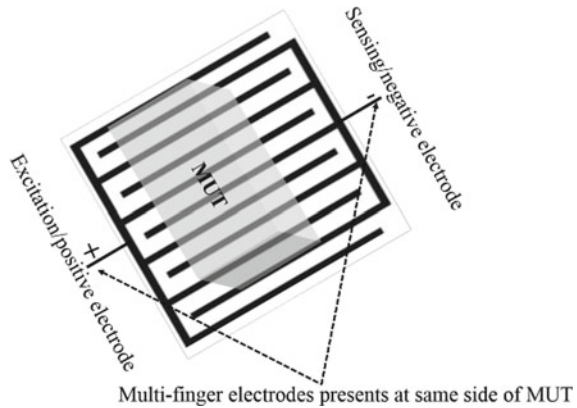


Fig. 1 A fringing field dielectric sensor as: **a** a parallel-plate capacitor, double sided access to MUT, **b** the corresponding IDC topology, one-sided access to the MUT

Fig. 2 A typical geometrical structure of the MUT loaded conventional planar IDC



From Figs. 1 and 2, it can be ascertained that the pair of electrodes are mainly used here to realize the capacitance, thereby producing the electric field in the region in order to facilitate the enhanced interaction of the IDC structure with the MUT [1, 2]. The interaction of the electric field with the material loaded on the IDC structure certainly modifies the distribution of the electric field as compared to its unperturbed state, i.e., when the IDC is not loaded with the material. This disturbance in the unperturbed electric field basically modifies various parameters under investigation such as the capacitance, the impedance, etc. The change in values of parameters under observation can then be related to the dielectric properties of the loaded sample at the specified frequency. It basically means that the planar IDC structure can conveniently be employed for the realization of a compact dielectric sensor over the desired frequency range. It is mainly due to this reason that in the recent past, various RF sensor topologies have been realized using the conventional/modified IDC structures with their implementation on the planar transmission lines.

The RF sensing mechanism usually involves the recording of change in the measured scattering parameters corresponding to a change in the dielectric properties expressed by the dielectric constant and the loss tangent of the specimen at the specified frequency range. The test material possessing certain dielectric properties at the specific frequency point basically governs the RF/microwave response of materials. Thus, the dielectric properties of test specimen helps to understand its actual behaviour in response to the electromagnetic waves. It basically means that each dielectric test specimen appropriately modifies the incident EM wave properties represented in terms of the scattering parameters. Hence, one can retrieve the dielectric properties of specimens in terms of the corresponding measured scattering data by performing its careful inverse processing. The dielectric testing mechanism using the RF sensors, including the IDC inspired structure, can be understood using either with the lumped circuit model or with the electromagnetic wave approach. For a better understanding of the actual RF sensing mechanism using the IDC structure, a quick overview of the quasi-static/lumped equivalent model and the electromagnetic analysis approach is provided here.

2.1 Quasi-Static Analysis

From the simple quasi-static point of view, the IDC structure may be considered as the equivalent capacitance between the two patterned electrodes separated with a finite distance. Here, it is to be noted that depending on the actual configuration, the IDC structure may also be modelled as the combination of the resistance-capacitance-inductance. The inductance of the IDC structure may be attributed to the associated metallic part, while the finite resistance depicts the loss associated with the structures. In this section, several typical examples of the IDC structures represented as lumped capacitors to facilitate sensing of dielectric materials are described.

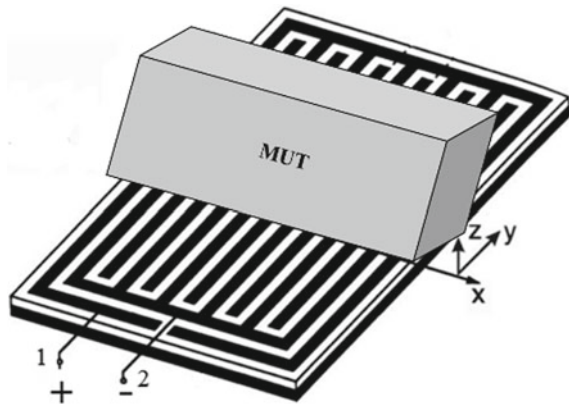
Figure 3 shows a typical IDC structure with the sample loaded on top of it, and its corresponding lumped equivalent model [1, 2]. From this Figure, it may be visualized that the effective capacitance of the structure will be modified once it is loaded with the material under test due to the change in the effective dielectric constant of the medium between two electrodes, 1, 2, leading to the capacitance (C_{12}). Further, if we approximate the C_{12} as a parallel plate capacitor with finite fringing field then it may be written as function of material dielectric constant [1, 2]

$$C_{12}(C_{IDC}) \equiv f(\epsilon_{rMUT}) \approx \epsilon_0 \epsilon_{rMUT} \frac{A}{d} \quad (1)$$

where, d corresponds to the inter-electrode distance, and A represents an effective cross-sectional electrode area and ϵ_0 , ϵ_r have their usual meaning.

Now, it becomes quite evident that any change in the dielectric constant of MUT accordingly reflects the changes in the measured capacitance parameter. Here, it is worth mentioning that a change in the IDC capacitance can identically be related with the equivalent change in the measured parameters, i.e., the impedance/admittance (z_m/y_m) and the propagation constant (γ_m) as [3]

Fig. 3 A typical arrangement of the MUT loaded IDC sensor



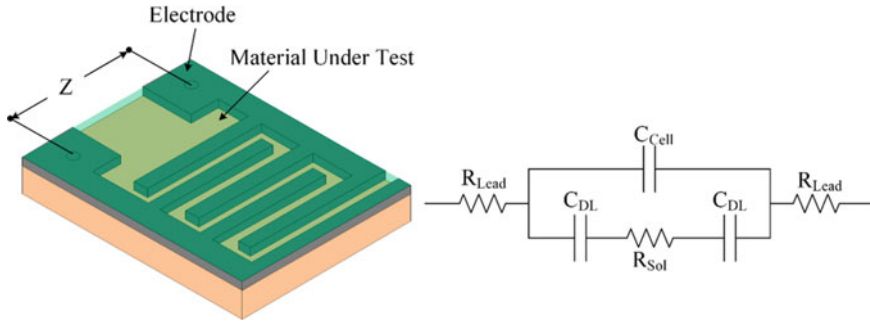


Fig. 4 A typical interdigitated electrode: **a** configuration of the cell, **b** simplified equivalent circuit. *Source* [4] M. R. R. Khan, and SW Kang, Sensors: MDPI, vol. 15, 2015, pp. 13201–13221 © 2015 CC

$$\begin{aligned}
 \gamma_m &= \sqrt{(R + j\omega L)(G + j\omega C)} \Big|_{\text{IDC}} \\
 z_m &\equiv 1/\gamma_m = \sqrt{(R + j\omega L)/(G + j\omega C)} \Big|_{\text{IDC}}
 \end{aligned}
 \tag{2}$$

From (1), (2), it can be followed that a change in any of the measured parameters such as the impedance/admittance, the propagation constant, etc., can be used to estimate the dielectric property of the material under investigation.

Similarly, the RF sensing mechanism can be realized using other variants of the IDC structure by observing a change in the measured capacitance corresponding to a change in dielectric properties of the MUT. For example, Fig. 4 shows a typical configuration of the IDC structure along with its approximated equivalent lumped equivalent circuit model [4], which can be employed for the RF dielectric sensing.

Here, the direct capacitive coupling between the two electrodes is modelled by the cell capacitance C_{Cell} , whereas the layered capacitor represented by two double-layered capacitances C_{DL} is connected in series with the resistance of the MUT solution (R_{Sol}). The total series resistance of the connecting wires is represented here using the lead resistance R_{Lead} . The cell capacitance (C_{Cell}), in the present situation, can approximately be related with the dielectric constant of the medium (material under test) as $C_{\text{cell}} = \epsilon_0 \epsilon_r \text{Sol} / K_{\text{cell}}$, with K_{cell} being the constant representing the geometry of the cell. From the given equivalent circuit, it may again be postulated that any change in the dielectric constant of the medium between the excitation and sensing electrodes changes the associated capacitance of the IDC structure [4].

Similarly, the working principle of other planar IDC based sensors, coupled to CPW, can also be analyzed using a quasi-static approach conforming to their equivalent lumped circuit model. For example, the measured value of capacitance corresponding to the MUT loaded configurations has been employed to effectively observe the dielectric properties of various biological grade liquids [5], [6]. The CPW fed IDC sensor topology can be realized with either the two port configuration [5], or one port configuration [6]. A typical single port IDC based sensor structure, as shown in Fig. 5, can equivalently be modelled as a combination of the conductance and the

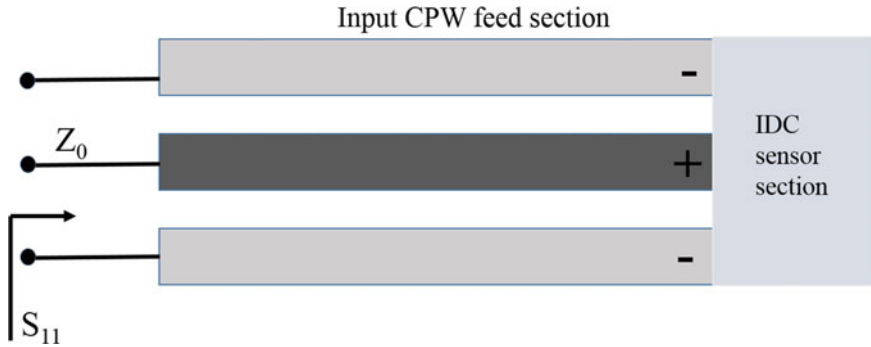


Fig. 5 Typical schematic of CPW fed one port IDC sensor configuration

capacitance [6]. Thus, the approximate equivalent impedance of the sensing region in the present situation may be expressed as [6]

$$Z_{IDC} = 1/(G_S + j\omega C_S) \equiv Z_0 \frac{1 + S_{11}}{1 - S_{11}} \quad (3)$$

Here, S_{11} represents the measured reflection coefficient of the sensing region loaded with the MUT. The measured reflection coefficient in the present situation provides the conductance (G_S) and capacitance (C_S) of the sensing region, which will be the function of the dielectric permittivity of the loaded sample [6].

From the above-described examples, it can easily be ascertained that the IDC based planar structures, usually modelled as lumped capacitors, may be employed for RF dielectric sensing either with one port or two port topologies over the desired frequency range. It is also to be noted that most of these IDC sensor structures employed for the dielectric property estimation of the material under test over the broad frequency range have quite compact topologies. However, inclusion of an appropriate inductance along with the IDC structure helps to realize the resonant sensor structure, which may be used for quite accurate dielectric sensing over a narrow frequency band. Under these situations, the overall structure may be viewed as the resonant IDC sensor topology having dedicated resonant frequency, governed by the actual value of various geometrical parameters. The resonance phenomenon associated with these structures basically helps to attain quite strong localized electric field in the sensing region at the corresponding resonant frequency, which eventually leads to improved dielectric sensing due to substantially higher material-field interaction. A typical IDC sensor topology making use of a spiral inductive arrangement is shown in Fig. 6 [3], where it can be observed that the IDC structure, in this case, is embedded inside the spiral inductive element.

The overall resonant frequency f_{rsens} of the sensor shown in Fig. 6 can be estimated using the equivalent inductance and capacitance shown in the figure, which can be given as [3]

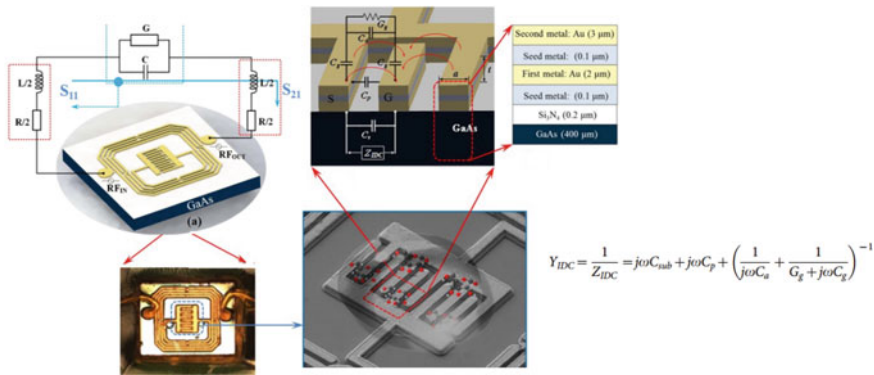


Fig. 6 Resonant IDC inspired label-free biosensor **a** 3D layout of the resonator using an interdigital capacitor and intertwined spiral inductor, and the equivalent circuit in terms of R, L, C and G, **b** image of the resonator surface bearing the glucose sample, **c** SEM image of the IDC and schematic image of the glucose sample using water and glucose molecules, **d** enlarged schematic view of a portion of the IDC including the equivalent circuit along with the different layers of the IPD fabrication process of the resonator and the equivalent admittance of capacitor (Y_{IDC}). *Source* [3] N. Kim, K. Adhikari, R. Dhakal, et al., Scientific Reports, vol. 5, No. 7807, 2015, © 2015 CC

$$f_{rsens} = \frac{1}{2\pi\sqrt{LC}} \Big|_{IDC} \tag{4}$$

An equivalent circuit shown in this figure comprises various circuit elements where R represents the total resistive loss associated with the spiral inductor having inductance (L), C represents the effective capacitance of the IDC, and G shows the equivalent leakage conductance (G). In these types of IDC resonant sensor structures, the resonant frequency changes with a change in the equivalent IDC capacitance which depends on the dielectric constant of the MUT [3]. It implies that the dielectric constant of the MUT can be estimated using the resonant IDC structure by recording a relative change in the resonant frequency. Here it is to be noted that the capacitance of the IDC structure can be related to the dielectric constant of the MUT using the relationship provided in (1). Apart from the resonant frequency parameter, the change in admittance of the IDC cell can also be used as the additional parameter to estimate the permittivity of the test specimen, as shown in Fig. 6 [3].

There are some other variants of the resonant IDC RF sensor structures presented in the literature to estimate the dielectric constant of the test specimen by measuring the resonant frequency under different loading conditions. The CPW fed IDC-like resonator and its corresponding equivalent circuit are provided systematically in the work reported by Zhu et al. [7]. Recently, the modified CPW fed resonant IDC-like structure has been reported for dielectric testing [8]. The actual resonator structure and its approximate equivalent resonant circuit model are shown in Fig. 7 [7, 9, 10]. This resonator can also be viewed as the combination of the open and short stubs, etched on the CPW line [11].

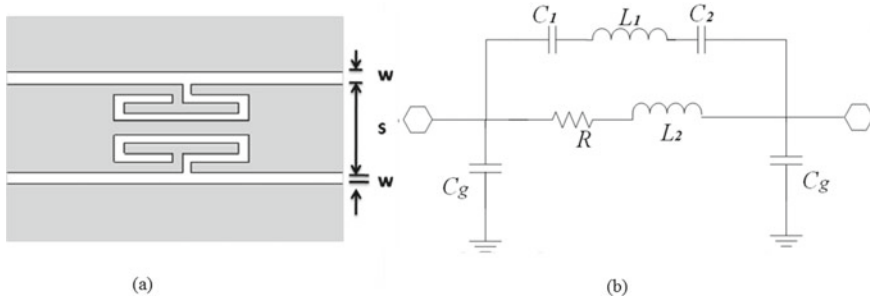


Fig. 7 IDC-like resonant sensor, **a** CPW fed resonator with modified series stubs, **b** an approximate equivalent circuit model. *Source* [11] © 2015 IEEE

In Fig. 7a, the width of the signal line is represented by s , and the spacing between the signal and ground line is shown with the symbol w . The approximated equivalent circuit contains various circuit elements corresponding to the combination of open and short stub etched on the CPW line [11]. Here, the capacitances C_1 , C_2 represent the equivalent IDC-like resonator capacitances, mainly responsible for the dielectric sensing, and L_1 , L_2 , R represent the associated inductance and resistance with C_g as the static device capacitance. The IDC inspired resonator capacitance ($C_{\text{IDC}} \equiv f(C_1, C_2)$) and the resonator inductances ($L_{\text{IDC}} \equiv f(L_1, L_2)$) are mainly responsible for generating the resonant frequency as per the relationship provided in (4), with C_{IDC} depending on the MUT dielectric property as per relationship (1).

2.2 Equivalent Electromagnetic Field Analysis

In the previous subsection, the equivalent lumped circuit approach was mainly utilized to qualitatively explain the RF dielectric sensing mechanism of the IDC structure. This subsection will mainly focus on the electromagnetic field analysis approach to qualitatively explain the RF dielectric sensing mechanism of IDC structures, which is quite important for the high frequency measurement. For this type of analysis, let us consider the electric field lines between the positive/signal and ground/receiving electrode of the IDC structure, as shown in Fig. 8 [4].

Now, if the MUT is loaded on top of the IDC structure, then the induced field of the IDC structure starts to interact with the MUT, as shown in Fig. 8. This interaction basically modifies the strength of the received electric field on the receiving end of the IDC structure as compared to that of the unloaded condition. In the RF and microwave frequency range, it is more convenient to measure the electromagnetic field strength in terms of the scattering parameters rather than expressing it in terms of the traditional voltage-current, inductance/capacitance parameters. These kinds of RF measurements are usually performed using the vector network analyzer (VNA) which can record the complex scattering parameter (S-parameters) corresponding to

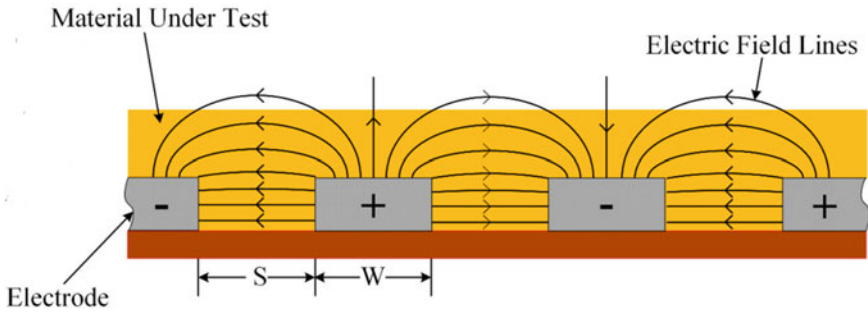


Fig. 8 Electric field of the coplanar IDC structure. *Source* [4] M. R. R. Khan, and SW Kang, *Sensors: MDPI*, vol. 15, 2015, pp. 13201–13221 © 2015 CC

the device under test with its exposure to RF source. Here, one should always keep in mind that even though the S-parameters are better suited for the RF measurement, the overall mathematical formulation of the multi-layered structures is not quite straight forward due to the involved reflection/transmission wave parameters. Therefore, for a detailed analysis and formulation, the measured S-parameters should be converted to the corresponding transmission parameters using the well-established matrix conversion [12]. Thereafter, the derived transmission/ABCD matrix of the multi-layered structure may be transformed into the S-parameters for immediate comparison with the measured data and to estimate the dielectric properties of the test specimen. Let us consider a typical CPW coupled IDC inspired capacitive sensing section as shown in Fig. 9, where the overall structure is accordingly represented in terms of the effective propagation constant (γ_{IDCeff}) and the effective impedance (Z_{IDCeff}) of the sensor section [12].

The transmission matrix, derived in terms of the measured S-parameters, corresponding to the sensor section can be related with the relevant parameters as follows [12]

$$\begin{bmatrix} S_{11m} & S_{12m} \\ S_{21m} & S_{22m} \end{bmatrix} \triangleq \begin{bmatrix} A_S & B_S \\ C_S & D_S \end{bmatrix} = \begin{bmatrix} \cosh(\gamma_{IDCeff} l_{IDC}) & Z_{eff} \sinh(\gamma_{IDCeff} l_{IDC}) \\ \sinh(\gamma_{IDCeff} l_{IDC})/Z_{IDCeff} & \cosh(\gamma_{IDCeff} l_{IDC}) \end{bmatrix}$$

Measured S parameters \Rightarrow Sensor ABCD = $f(\gamma_{IDCeff}, Z_{IDCeff})$ (5)

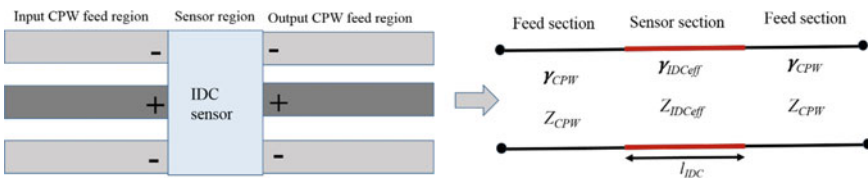


Fig. 9 A typical schematic of CPW fed IDC based sensor topology and its equivalent transmission line model

where, γ_{IDCeff} , and Z_{IDCeff} can usually be related with the effective dielectric properties of the sensing region (6).

$$Z_{IDCeff} = \sqrt{\frac{\mu_0}{\epsilon_{IDCeff}}}, \gamma_{IDCeff} = \sqrt{\mu_0 \epsilon_{IDCeff}} \tag{6}$$

From relationships (5) and (6), one can easily interpret that the change in effective dielectric constant over the sensing region changes the measured S-parameters accordingly. It basically means that one can effectively estimate the dielectric properties of the test specimen over the desired frequency range based on the measured S-parameters of the sensor section loaded with the specimen.

Now, in a similar way, the electromagnetic analysis approach can also be used to understand the operation of the resonant IDC inspired structures where the IDC capacitance is integrated with an inductive element. These types of resonant IDC-like structures mainly store the electric energy over the sensing region at the corresponding resonant frequency, as shown in Fig. 10 [11]. Therefore, when the material is loaded on the top of the sensing region, a substantial interaction between the MUT and the electric field of the sensor region takes place resulting in a slight change in the original unloaded electric energy of the resonant IDC inspired sensor. The basic working principle of these sensors can qualitatively be understood with the help of small material perturbation theory [13]. As per the small material perturbation approach, the placement of test sample over the sensing region of planar resonant

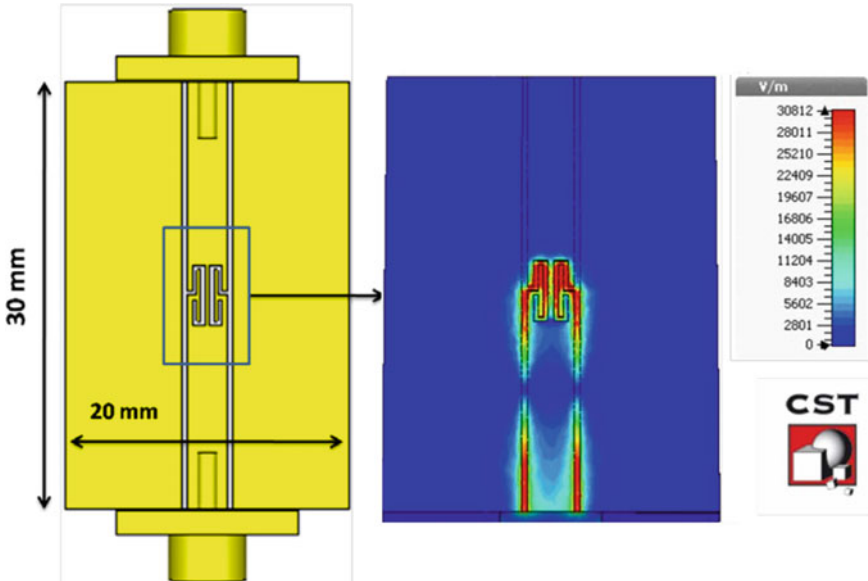


Fig. 10 CPW fed IDC-like resonant sensor comprising of modified stubs with plot of associated electric field at resonant frequency. *Source* [11] © 2015 IEEE

sensors perturbs the parent electric field of the unperturbed resonator. It results in a shift in the resonant frequency and Q -factor of the designed sensor as compared to its unperturbed value. This change in the resonant frequency and Q -factor of the cavity can be related to the material property of the sample under test using the relationship (7). It is important to note that the relation in (7) mainly represents the perturbation of the electrical energy when a purely dielectric test specimen is placed in the sensing region [13].

$$\frac{\omega - \omega_0}{\omega} = - \frac{\int_{V_s} \Delta \varepsilon E \cdot E_0^* dV}{2 \int_{V_c} \varepsilon_1 E \cdot E_0^* dV} \quad (7)$$

where, the parameters V_s , V_c in the above equation represent the sample and the cavity volume, respectively with ω_0 , E_0 and ω , E representing the value of the angular resonant frequency and electric field of the resonant IDC structure before and after loading the test specimen, respectively. The parameters $\Delta \varepsilon$ and ε_1 in the expression represent the relative change in the complex permittivity and the complex permittivity of the MUT, respectively.

For many practical situations, the resonant IDC structures are used for the concentration detection of individual constituent in the given liquid solution. Under these types of scenarios, the relative change in the complex permittivity ($\Delta \varepsilon$) may be viewed as the difference between values of the dielectric constant corresponding to the mixture solution and that of the pure sample. The relationship (7) can then be rewritten for the negligibly small field perturbation (8) in conjunction with the standard dielectric mixing formulae (9).

$$\frac{f_s - f_0}{f_s} = \left(\frac{1 - \varepsilon_{rS}}{2} \right) \frac{\iiint_{V_s} E_0^* \cdot E_s dV}{\iiint_{V_c} |E_0|^2 dV} \quad (8)$$

In (8) f_0 and f_s represent the unloaded (without sample) and the loaded (with liquid sample) resonant frequency corresponding to the dielectric constant of test liquid ε_{rS} . The test liquid in the present situation expressed by ε_{rS} can be represented in terms of the dielectric constant of the constituent liquid 1 (ε_{rP}) and that of the constituent liquid 2 (ε_{rA}) with the corresponding volume fraction v_P , and v_A , respectively, as shown in Eq. (9), using the LLL dielectric binary mixing relationship [14].

$$\varepsilon_{rS} = (v_P \cdot \varepsilon_{rP}^{1/3} + v_A \cdot \varepsilon_{rA}^{1/3})^3, v_P + v_A = 1 \quad (9)$$

From the relationships (7)–(9), it may be concluded that the extent of perturbation of the electric field in the vicinity of the sensing region under loaded condition would depend upon volume proportions and dielectric constants of the constituent liquid 1 and the constituent liquid 2. Hence, in principle, the resonant IDC sensor can suitably be used to test the purity level of the reference liquid (constituent liquid 2) by detecting the level of contamination of the adulterant liquid (constituent liquid

1) in it, which is basically facilitated by observing the relative shift in the measured resonant frequency of the sensor under loaded condition.

From the above discussion, it may be inferred that the dielectric sensing mechanism can suitably be realized using the IDC sensors in order to estimate dielectric properties of materials in the RF and microwave frequency range. Moreover, the overall dielectric sensing mechanism of these IDC based RF planar sensors can be explained using the quasi-static equivalent circuit approach as well as that of the electromagnetic field approach. It is mainly due to this reason that in the recent past, the planar RF sensors based on the IDC inspired structures have been implemented for various applications, including accurate estimation of dielectric properties of materials. A few practical applications of the IDC inspired RF planar sensors are provided below to demonstrate the industrial usage of these types of IDC sensors.

3 Industrial Applications of IDC Inspired RF Sensors

3.1 IDC-Based Glucose Biosensor

A highly stable IDC glucose biosensor with solvatochromic-dye-containing sensing membrane with wide dynamic range and high sensitivity has recently been proposed [15]. The working principle of the dielectric sensing membrane loaded IDC glucose biosensor is primarily based on the recording of a relative change in the IDC capacitance corresponding to the change in the glucose concentration placed over the IDC sensing membrane. In other words, the dielectric property of the IDC sensing membrane gets changed in this case after its immersion in the test glucose solution which eventually changes the IDC capacitance and the phase between two electrodes. A typical experimental setup containing the IDC based glucose bio-sensing system is presented in Fig. 11 [15].

As the basic operation of the proposed IDC glucose biosensor is based on the observation of a relative change in the capacitance of the IDC sensor, hence an AC voltage is applied to produce an electric field between the two electrodes of the sensing membrane loaded IDC structure [15]. The impedance of the IDC structure changes after application of the electric field to the dielectric/sensing material of the IDC, and subsequently the dielectric constant of the sensing system also changes with a variation in the test glucose concentration. In this work, the desired liquid test solution is prepared by dissolving the glucose substances with the deionized (DI) water whereas Nile-red is employed as the IDC sensing membrane for all the demonstrated results. The proposed sensing membrane loaded IDC glucose bio-sensing system works on the capacitor principle, and hence, the phase difference between the reference signal and the target glucose solution gets increased with an increase in the glucose concentration, as shown in Fig. 12a. Moreover, the variation in IDC capacitance corresponding to the change in the test glucose concentration is depicted in Fig. 12b. From this Figure, it can also be noticed that the measured

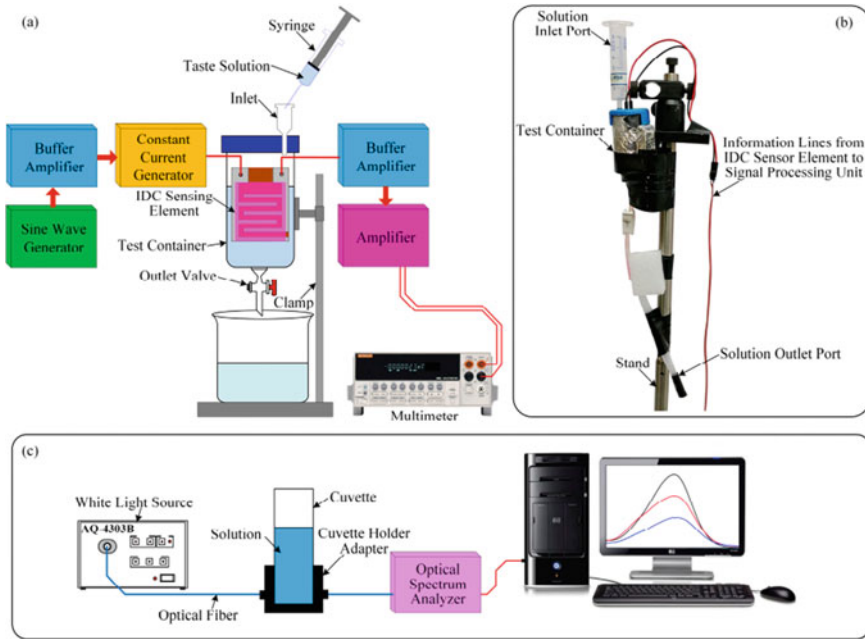


Fig. 11 A typical experimental setup: **a** schematic diagram of the IDC inspired glucose biosensing system; **b** photograph of the various parts of the proposed IDC bio-sensing system; and **c** schematic diagram for measuring the optical properties of different sensing solutions under different concentrations. *Source* [15] M. R. R. Khan, A. Khalilian and SW Kang, Sensors: MDPI, vol. 18, s16020265, 2016 © 2016 CC

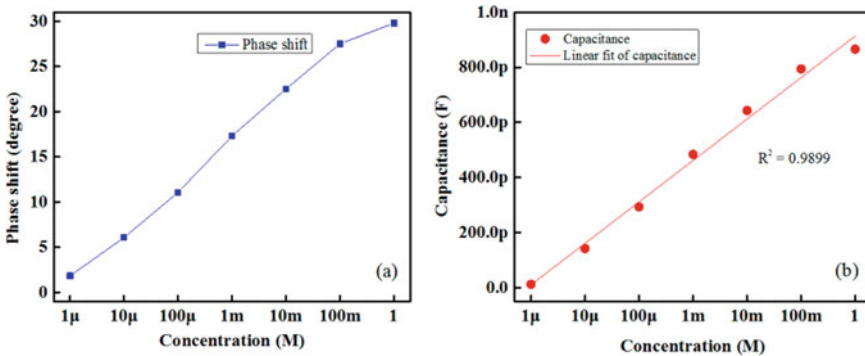


Fig. 12 Response of the IDC inspired sensor for different glucose concentration (M), **a** variation in phase shift, **b** variation in capacitance. *Source* [15] M. R. R. Khan, A. Khalilian and SW Kang, Sensors: MDPI, vol. 18, s16020265, 2016 © 2016 CC

change in the capacitance value increases proportionally with an increase in the glucose concentrations from $1 \mu\text{M}$ to 1 M [15].

In summary, the above glucose biosensing system is based on the interdigitated capacitor (IDC) integrated with the dielectric sensing membrane which can effectively record the variation in the glucose concentration from $1 \mu\text{M}$ to 1 M with quite linear sensing response. Moreover, a typical CPW fed IDC sensor topology has also been employed for various biomedical sensing applications including the detection of living cell concentration and yeast suspension in host medium [15].

3.2 Integrated Passive Device Biosensor Using Resonant IDC Topology

For detection of glucose in water-glucose solution, a passive IDC biosensor has been implemented [3]. The design of this sensor is based on the usage of an intertwined spiral inductor coupled with an interdigital capacitor, which basically helps to concentrate the electromagnetic field over the sensing region (IDC) eventually resulting in providing quite high sensitivity ($199 \text{ MHz/mg mL}^{-1}$). Therefore, this sensor configuration possesses an ultralow detection limit of 0.033 mM . The measured S-parameters, and the derived parameters, i.e., the propagation constant (γ), impedance (Z), capacitance (C), inductance (L), resistance (R), and conductance (G), are utilized here to estimate the glucose concentration. The experimental setup along with the employed sensor in this scenario is shown in Fig. 13 [3].

The resonant IDC sensor, shown in Fig. 13, is used to detect the glucose concentration in human serum and water-based solution, where the glucose sample ($5 \mu\text{L}$)

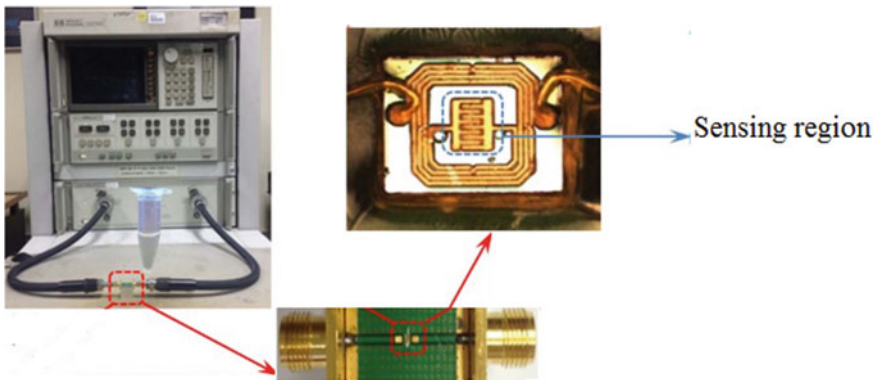


Fig. 13 Scheme for the S-parameters measurement of a typical IDC inspired resonator, **a** bio-sensing resonator connected with the VNA for the measurement of S-parameters, **b** enlarged view of the resonator, **c** FIB image of the resonator surface bearing the glucose sample. *Source* [3] N. Kim, K. Adhikari, R. Dhakal, et al., Scientific Reports, vol. 5, No. 7807, 2015, © 2015 CC

with various concentration is dropped on the resonant sensor and the corresponding S-parameters are being measured [3]. The measured S-parameters of the empty resonator and the resonator loaded with different samples under test are presented in Fig. 14, where for all the cases, the resonant frequency shifts downward from the unloaded frequency (2.246 GHz). In this situation, the obtained changes in the measured S-parameters may be interpreted as the effective interaction between the MUT and capacitor/inductor of the resonator corresponding to different concentration of glucose solution. It may be observed from Fig. 14, that the measured S-parameters of the resonator change in accordance with the MUT. For example, the obtained resonant frequency of the resonator is 0.642 GHz and 1.189 GHz for glucose samples with minimum (0.25 mg/mL) and maximum concentrations (5 mg/mL), respectively. Here, the measured resonant frequency is at the minimum value for the considered maximum glucose concentration due to the involved negative correlation between the glucose dielectric constant and its concentration. It is also to be noted

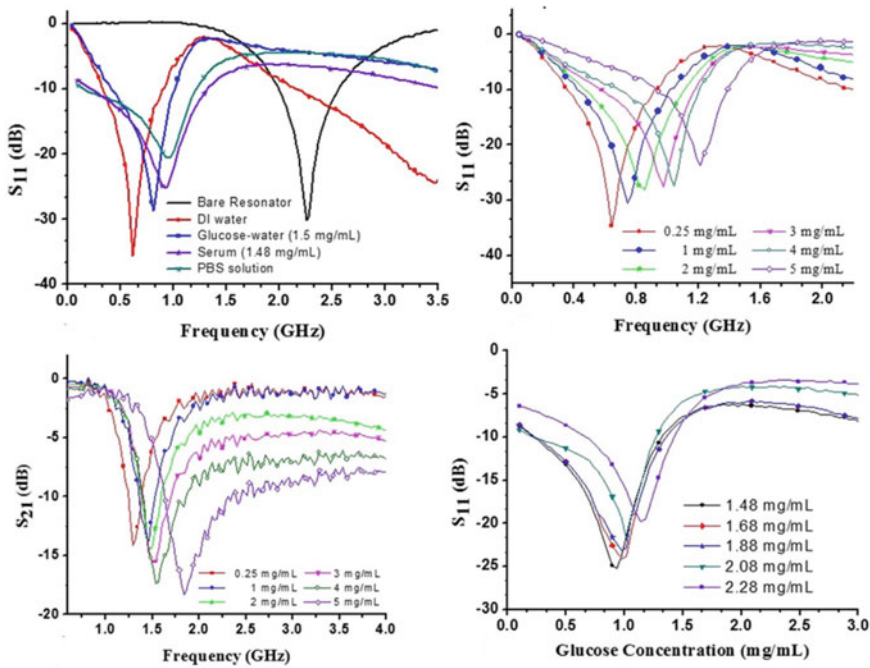


Fig. 14 Dielectric characterization. **a** Shift in the resonant frequency under various conditions, **b** shift in the resonant frequency and variations in the reflection coefficient (S_{11}) magnitude for water-glucose samples of varying concentrations (0.25 to 5 mg/mL), **c** shift in the frequency and magnitude of the transmission coefficient (S_{21}) at transmission zero, **d** shift in the resonant frequency and variations in the magnitude of the reflection coefficient (S_{11}) for serum samples with glucose concentrations varying from 1.48 to 2.28 mg/mL. Source [3] N. Kim, K. Adhikari, R. Dhakal, et al., Scientific Reports, vol. 5, No. 7807, 2015, © 2015 CC

that the increased glucose concentration broadens the resonator bandwidth due to the increase in the overall loss [3].

Next, the propagation constant (γ) and impedance (Z) is derived from the measured S-parameters corresponding to different glucose concentrations by employing various standard relationships, (3), (5) and (6). The derived propagation constant (γ) and impedance (Z) can further be utilized to extract the corresponding equivalent circuit parameters of resonators (2), [3]. A typical parameter variation is shown in Fig. 15, where, the variation in parameter values corresponding to a change in glucose concentration can be noticed.

Therefore, the highly sensitive IDC biosensor described above can be used for the possible diabetic detection using the measurement carried out in the specified RF range.

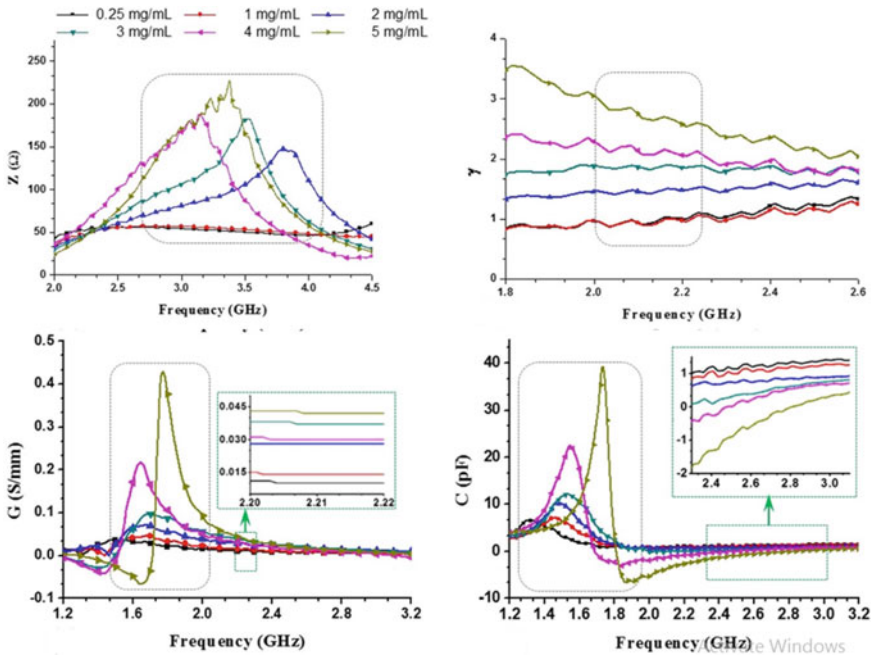


Fig. 15 Variation of various secondary parameters related to IDC inspired resonant biosensor with varying glucose concentrations, **a** impedance, **b** propagation constant, **c** conductance, **d** capacitance. Source [3] N. Kim, K. Adhikari, R. Dhakal, et al., Scientific Reports, vol. 5, No. 7807, 2015, © 2015 CC

3.3 Resonant IDC-Inspired Sensor for Edible Oil Adulteration Detection

The microstrip fed IDC inspired resonant sensor is also utilized to detect the presence of adulteration in common edible oils at the ISM (industrial, scientific and medical) frequency band (5.85 GHz) [16]. It basically measures the relative change in the resonant frequency corresponding to the different concentrations of contaminants in edible oil. The considered sensor structure with optimized values of different geometrical dimensions and enlarged view along with the associated electric field distribution over the sensing region is presented in Fig. 16.

From the electric field plot shown in Fig. 16b, it can be noticed that the maximum field is concentrated around the resonant sensing structure of the sensor which basically facilitates the high sensitivity of the sensor. The plot of shift in the resonant frequency and variation in the insertion loss for change in the dielectric properties of the test specimen is shown in Fig. 17, to show its dielectric sensitivity.

A typical experimental setup and the S-parameters corresponding to different oil samples are presented in Fig. 18, where it can be noticed that measurement of different edible oils results in different resonant frequencies although the difference in the dielectric properties of these oil samples is relatively small, as observed from Table 1 [16].

Therefore, the adulteration of targeted edible oil with other cheaper substitute can easily be identified with this type of IDC inspired sensor due to the associated difference in their dielectric properties [16]. A typical plot corresponding to the change in resonant frequency for various adulteration levels is shown in Fig. 19, where a noticeable shift in the resonant frequency can easily be observed.

Thus, the IDC inspired planar RF sensor can suitably be employed to detect the purity of various standard edible oils for possible adulteration with other types of cheap oils.

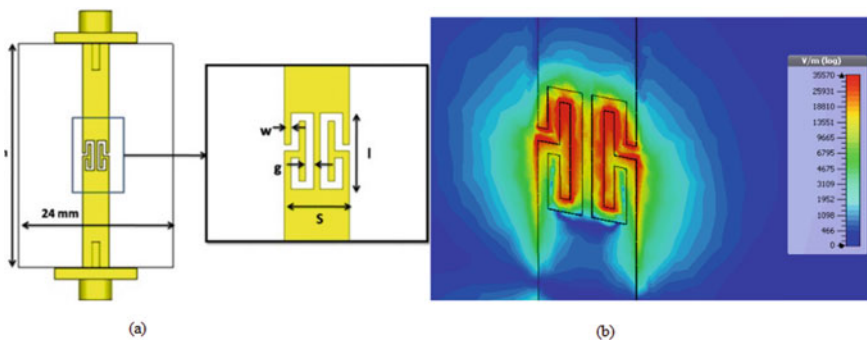


Fig. 16 Numerical design, **a** structure of the sensor with dimensions, $W = 0.4$ mm, $g = 0.5$ mm, $S = 4$ mm. $I = 4.7$ mm with enlarged view of resonant structure, **b** electric field variation in the proposed sensor at the resonant frequency. Source [16] © 2016 IEEE

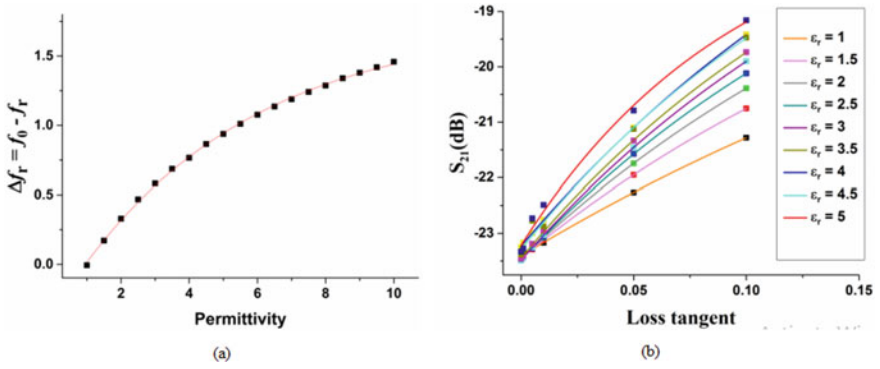


Fig. 17 A typical numerical data, **a** change in resonant frequency (GHz) corresponding to different relative permittivity values, **b** the insertion loss under loaded condition corresponding to different loss tangent values. *Source* [16] © 2016 IEEE

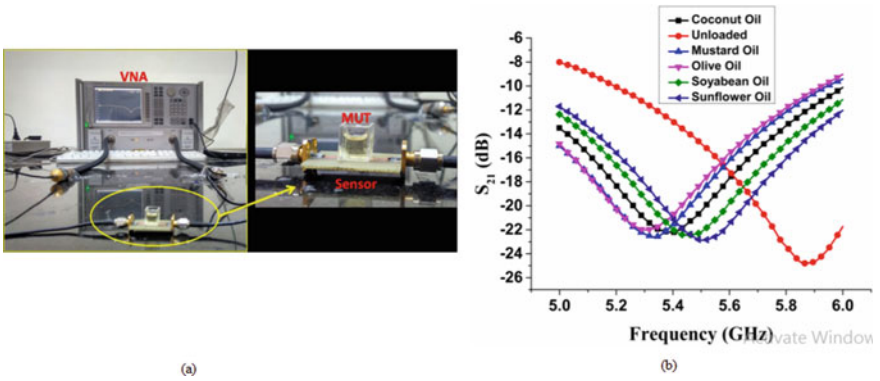
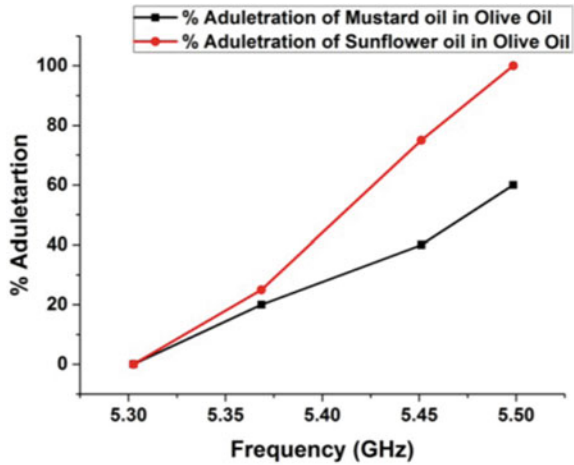


Fig. 18 Experiment, **a** measurement setup for edible oil adulteration detection, **b** measured S_{21} plot for different edible oil samples, employed in [16]. *Source* [16] © 2016 IEEE

Table 1 Measured permittivity and loss tangent of edible oil samples

MUT measured loss	Measured permittivity	Measured loss tangent
Olive oil	2.9839	0.0353
Coconut oil	2.5815	0.0313
Soyabean oil	2.4238	0.0276
Sunflower oil	2.1686	0.0152
Mustard oil	2.0412	0.0041

Fig. 19 The percentage adulteration as a function of measured resonant frequency of the test specimen. *Source* [16] © 2016 IEEE



The applicability of the above IDC RF sensor is also tested for other industrial applications such as the petrochemical industry where the oil spill is a common undesired incidence [17]. To emulate the real scenario, the petroleum chemical is carefully spilled over the water medium and accordingly, the change in measured resonant frequency for different concentrations of the spill is recorded as shown in Fig. 20. In this Figure, at first, the S-parameters corresponding to petroleum sample and water medium are recorded separately to get the preliminary idea about the corresponding resonant frequencies. Thereafter, the S-parameters corresponding to different spill concentrations are measured to record the individual resonant frequency which is then plotted against the corresponding spill concentration to get the quantitative interpretation about the sensor performance. From the plot, it is obvious that even the presence of a small spill can easily be detected with the IDC inspired RF resonant sensor.

It can thus be inferred that the application of the IDC inspired resonant sensor is quite adaptable for various industrial grade applications.

3.4 IDC-Inspired Planar Resonant RF Sensor for Retrieval of Permittivity

The modified IDC structure, integrated with the SRR topology, has recently been utilized to attain an improved sensitivity, as compared to that of the simple SRR based RF sensor, as shown in Fig. 21.

From the plot shown in Fig. 21, one can easily notice the strong concentration of the electric field over the IDC sensing region which eventually leads to improved sensitivity. The prototype of the sensor and corresponding S-parameters of various MUT are presented in Fig. 22, where it is observed that the obtained S-parameter changes

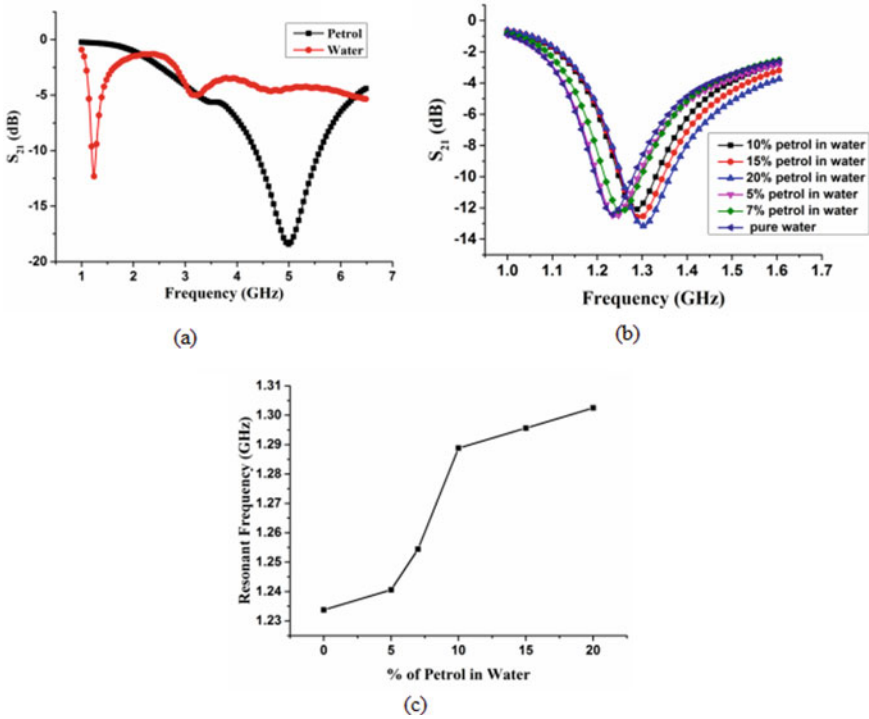


Fig. 20 Measured results, **a** S_{21} plot for pure water and petrol, **b** S_{21} plot for different amount of petrol spill, **c** Variation in resonant frequency with change in % of petrol spill over water. *Source* [17] © 2016 IEEE

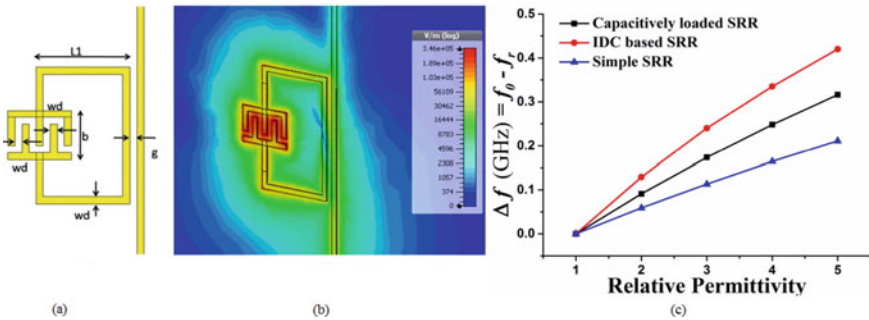


Fig. 21 Numerical analysis, **a** structure of IDC—SRR based dielectric sensor with dimensions , $L_1 = 4 \text{ mm}$, $L_2 = 7 \text{ mm}$, $g = 0.3 \text{ mm}$, $w_d = 0.3 \text{ mm}$. $b = 1.5 \text{ mm}$. **b** Electric field configuration near IDC based SRR at 2.45 GHz, **c** sensitivity improvement of IDC-SRR topology. *Source* [18] © 2017 IEEE

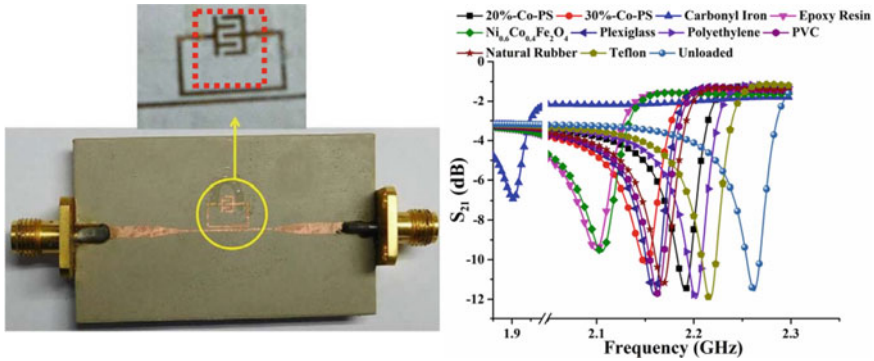


Fig. 22 Resonant sensor, **a** fabricated prototype of IDC-SRR dielectric sensor with an enlarged view of the resonant structure, dotted lines inscribed area represents the position of the sample, **b** measured S_{21} plot for different dielectric and magneto-dielectric materials. *Source* [18] © 2017 IEEE

Table 2 Measured permittivity of different dielectric and magneto-dielectric materials

MUT	Measured	ϵ_r	% Error
Carbonyl Iron	5.84	5.5 [31]	6.18
$Ni_{0.6}Co_{0.4}Fe_2O_4$	3.23	–	–
30% Cobalt-polystyrene	2.74	–	–
20% Cobalt-polystyrene	2.34	–	–
Teflon	2.09	2.1 [8]	0.48
PVC	2.62	2.65 [8]	1.13
Polyethylene	2.23	2.26 [8]	1.33
Plexiglas	2.65	2.6 [8]	1.92
Natural rubber	2.57	–	–
Epoxy resin	3.29	3.5 [33]	6.00

in accordance with the dielectric properties of test specimen, which is quite obvious from the earlier discussed theory. The measured S-parameters are then employed in conjunction with the developed empirical model [18], to estimate the dielectric constant of test specimens.

From Table 2 [18], it can be ascertained that the sensor prototype can suitably be employed for quite accurate estimation of the dielectric constant of test samples.

3.5 IDC-Based Microfluidic Sensor for Glucose Monitoring

The IDC integrated SRR structure based high-sensitive resonant microwave microfluidic RF sensor has recently been implemented for detecting glucose concentration in

aqueous medium. To facilitate the measurement of lossy liquids/fluids, a microfluidic channel is accordingly positioned over the IDC region of the SRR. In present application, aqueous solutions with various glucose concentrations (0 to 5000 mg/dl) are characterized based on the shift in the resonant frequency and the normalized peak attenuation of the measured S-parameters. The measured sensitivity of the IDC inspired resonant sensor is found to be $2.60\text{E-}02 \text{ MHz/mgdl}^{-1}$ [19]. The schematic of the resonant IDC sensor along with its electric field over the IDC sensing region and PDMS integrated complete sensor topology is presented in Fig. 23 [19].

The electric field plot shown in Fig. 23b clearly demonstrates the strong field confinement leading to an improved interaction between the field and aqueous solutions, which are basically loaded on the sensor through the designed PDMS channel. The in-lab experimental setup along with the fabricated prototype of the resonant sensor are shown in Fig. 24.

Figure 24 also includes the plot of the insertion loss which depicts a substantial notch at the measured resonant frequency of the IDC based resonator. Afterwards, the S-parameters corresponding to the loading of different glucose concentrations are measured to record the individual resonant frequency and notch level and accordingly to develop the graph between them, as shown in Fig. 25. The generated graph helps to develop the empirical relationship between the resonant frequencies/notch-levels and

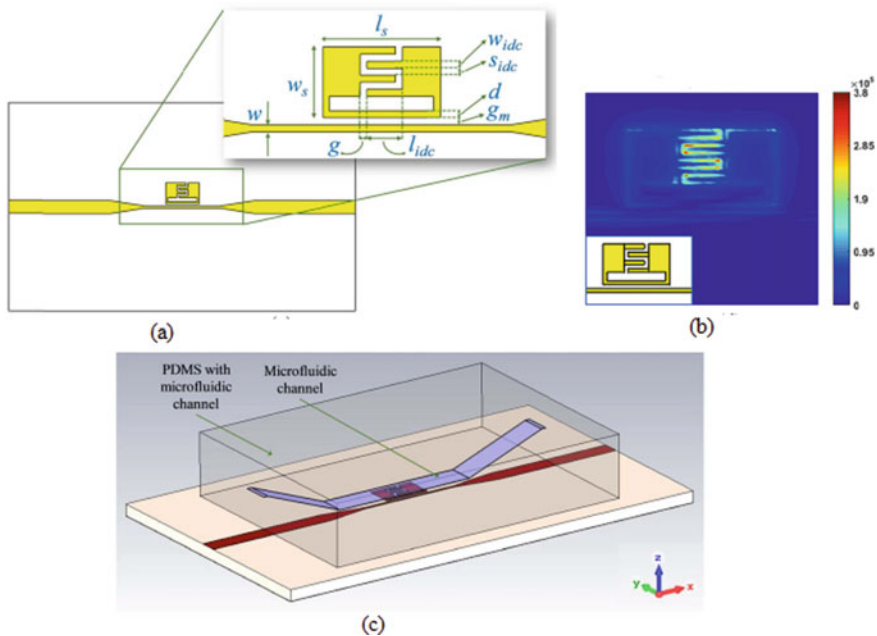


Fig. 23 A typical numerical data related to IDC inspired resonant element, **a** schematic design with parameters of the sensor, **b** electric field distribution (V/m) of the sensor design ($f_0 = 4.18 \text{ GHz}$), **c** perspective view of the sensor. Source [19] © 2019 IEEE

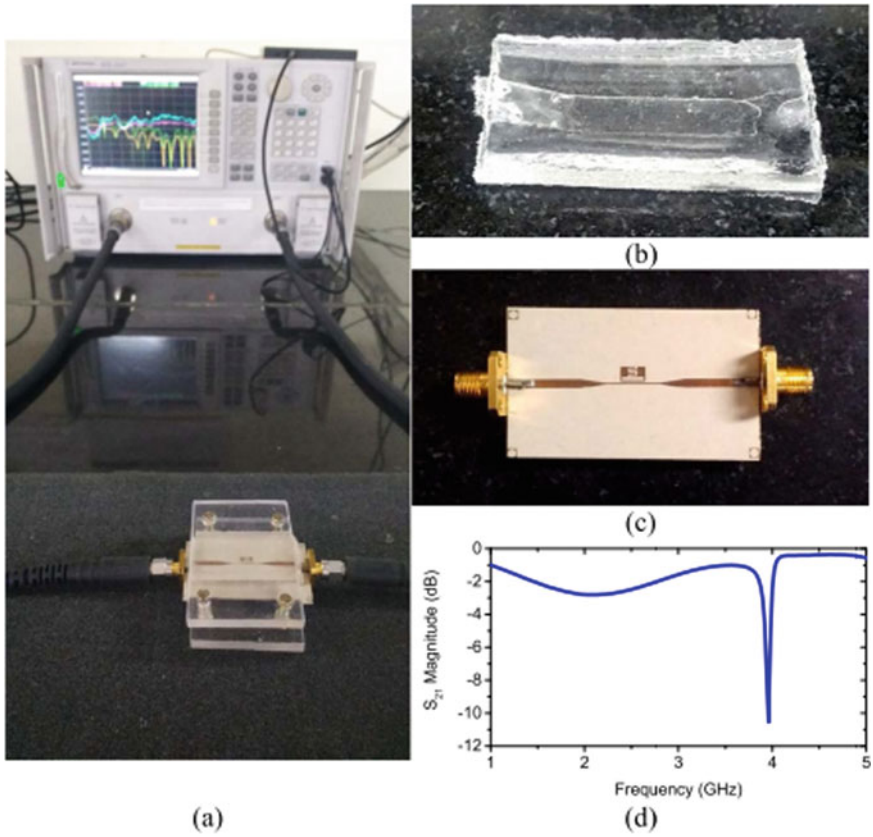


Fig. 24 Typical setup employed in [18], **a** experimental arrangement, **b** top view of the fabricated sensor, **c** non-planar PDMS microfluidic channel, **d** measured magnitude of transmission parameter. *Source* [19] © 2019 IEEE

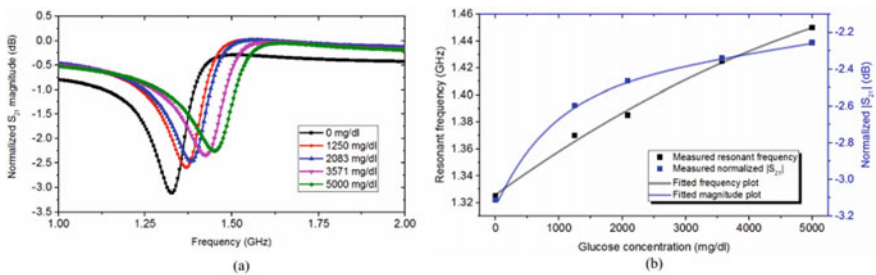


Fig. 25 Typical measured parameters, **a** transmission parameters corresponding to different glucose concentrations, **b** resonant frequency and transmission minimum magnitude variations plot as a function of glucose concentration. *Source* [19] © 2019 IEEE

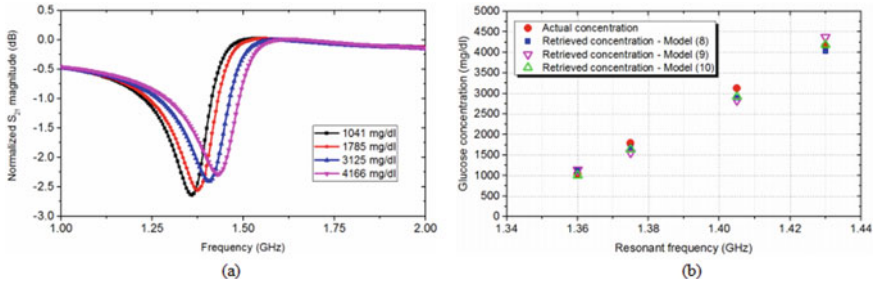


Fig. 26 Sensor prototype performance, **a** measured transmission parameters of unknown glucose samples for various concentrations, **b** Retrieved glucose concentrations from measured resonant frequency and peak attenuation in **a** using developed empirical relationships. *Source* [19] © 2019 IEEE

the measured glucose concentrations, to estimate the unknown glucose concentration [19].

Finally, to ascertain the applicability of designed sensor, the resonant frequency and notch level corresponding to the unknown glucose concentrations are measured (Fig. 26a), where, the developed empirical modelling is employed to ascertain the considered concentration level, as shown in Fig. 26b. This Figure shows that the IDC based resonant sensor can quite suitably be employed for an accurate estimation of glucose concentration in the targeted aqueous solutions.

3.6 Dual Band IDC-Based Resonant Sensor

Apart from the single band IDC resonator-based RF sensor described above, the multiband RF sensors based on the concept of IDC resonator may also be designed and developed in order to test the targeted liquid samples over different frequency points. A typical example of the CPW fed dual band IDC sensor along with its electric field distribution at the respective resonant frequencies, 2.45 GHz and 5.85 GHz, is shown in Fig. 27. The actual values of various parameters along with the detailed design procedures are available in the earlier reported work [20]. From the electric field plot, it can be seen that both the resonant IDC elements facilitate the relatively strong electric energy confinement over the IDC inspired sensing region at the corresponding resonant frequencies that leads to quite substantial interaction between the MUT and the electric field at the designated frequencies [20].

Thus, it can be postulated that an integration of IDC-like resonant elements with the RF transmission line leads to design of multi-band RF sensor with different resonant frequencies corresponding to various resonating elements. A typical measurement setup along with the measured S-parameters corresponding to the dual band IDC CPW based RF sensor loaded with different chemicals under test, is shown in

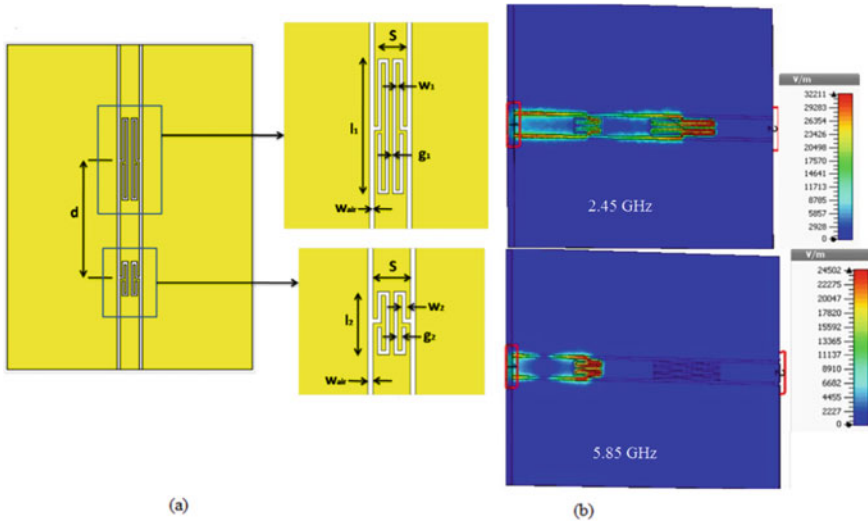


Fig. 27 IDC inspired resonator: **a** geometry of CPW etched dual band sensor with magnified view of the sensing area at with resonant frequency of 2.487 GHz and 5.825 GHz, **b** electric field distribution at 2.49 GHz and 5.825 GHz. *Source* [20] © 2015 IEEE

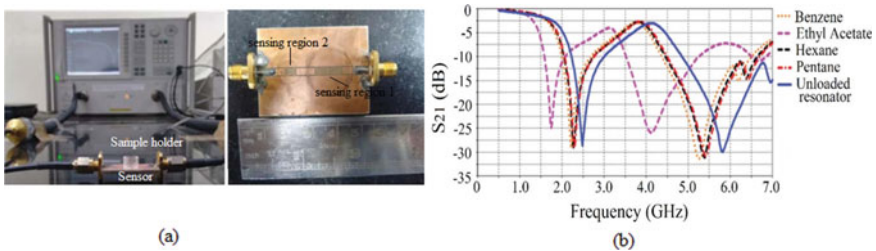


Fig. 28 Experimental image, **a** measurement setup and fabricated dual band resonator, **b** measured S_{21} magnitude corresponding to the resonant frequency for different samples. *Source* [20] © 2015 IEEE

Fig. 28. From this Figure, it can clearly be noticed that the IDC resonant sensor can conveniently be used for the dual band application.

3.7 IDC-Inspired Wireless Sensing System for Testing of Biological Samples

In this configuration, the wireless RF sensing system comprising of ultra-wideband transmitter-receiver antenna and highly sensitive IDC inspired structure is employed

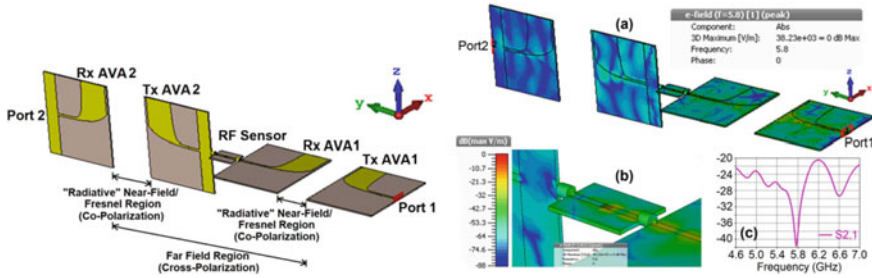


Fig. 29 A typical wireless sensing system, **A** detailed setup used for numerical analysis, **B** Anti-clockwise: **a** 3D electric field intensity in entire wireless sensor, **b** enlarged view of the electric field intensity at 2D plane of resonant sensor, **c** transmitted signal observed at Port 2. *Source* [21] © 2018 IEEE

for assessment of glucose and saline concentration, which are quite crucial for various biomedical applications as shown in Fig. 29 [21].

The RF sensor system, shown in Fig. 29, basically provides the cost-effective wireless sensing technique, where the ultra-wideband printed antennas, operational in 1–18 GHz with highest gain of 7 dBi, are incorporated. The wireless sensor of the proposed RF system helps to attain the relatively higher sensitivity (60 MHz per/unit change in dielectric constant of liquid sample) due to the presence of IDC inspired resonant structure in sensor topology [21]. From this, figure, it is also evident that the electric field concentration over the sensor area is quite substantial to facilitate the effective MUT-field interaction which can be noted from the received transmission coefficient plot where strong notch level can be observed at the resonant frequency. A typical experimental setup, employed for wireless sensing system in [21], to accomplish the in-lab testing of biological samples, i.e., glucose and saline solutions, is presented in Fig. 30.

The prepared glucose and saline solution (water based) can then be placed in the designated sample holder to record the corresponding S-parameters in order to visualize a change in their profile. From the measured S-parameters data shown in Fig. 31, a quantitative relationship between the glucose/saline concentration and measured resonant frequency can be generated, as shown in Fig. 32. From this Figure, it can be ascertained that the measured resonant frequency varies in proportion to the concentration of glucose/saline in liquid medium, here water. Therefore, for the particular biomedical application, where it is required to assess the actual saline/glucose concentration remotely, the IDC inspired wireless RF sensing system can effectively be employed [21].

It may be noted that in addition to above specified applications, the IDC based RF sensors have also effectively been utilized for the non-destructive wideband dielectric testing of biological liquids and cell suspensions, especially for the smaller sample volume [12]. For such type of applications, an IDC-like element has been modelled as an electrically small discontinuity, within the sensing region of the miniaturized planar transmission-line sensor [12]. The IDC inspired sensors have also

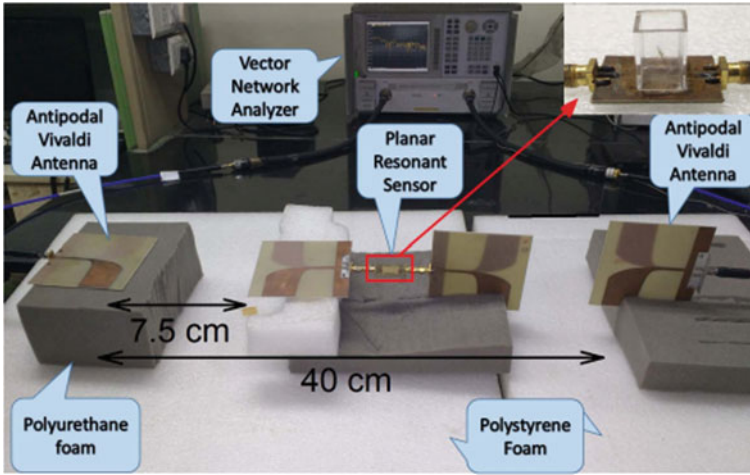


Fig. 30 A typical wireless sensing measurement setup with inset shows the sensor with the cuvette for liquid sample measurement. *Source* [21] © 2018 IEEE

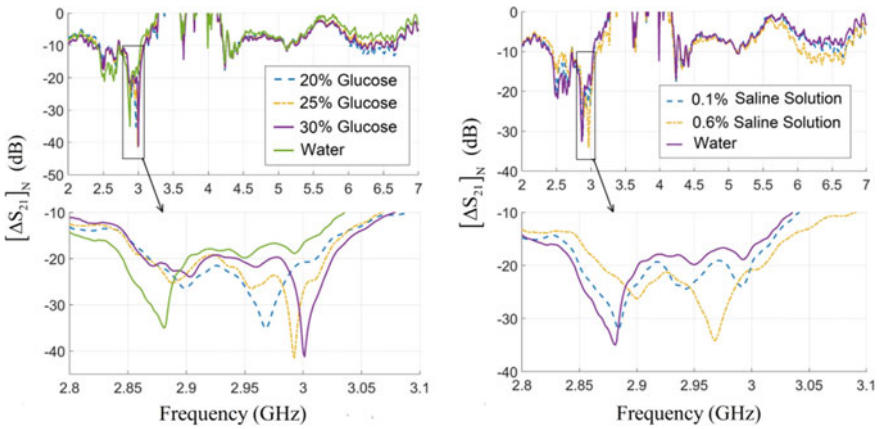


Fig. 31 Normalized transmission data of **a** glucose solution, **b** water based saline solution with enlarged view of the marked regions. *Source* [21] © 2018 IEEE

been explored for the wideband dielectric property estimation of various biological samples including the protein solution [12].

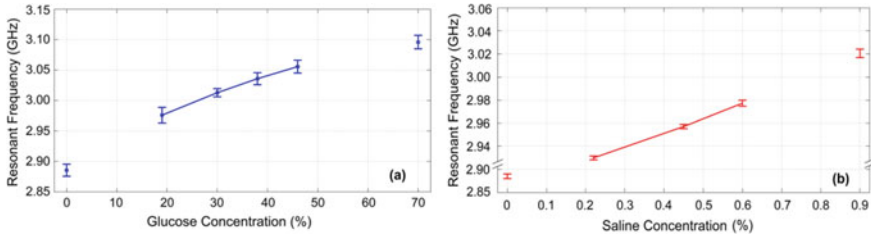


Fig. 32 Performance curve of **a** glucose (w/v) and **b** saline (v/v) samples with various concentration in water solution. Error bars represent a standard deviation calculated from $N = 8$ measurements. Source [21] © 2018 IEEE

4 Conclusion

The main focus of this chapter has been to provide an overview of the basic operating principle of various IDC based planar RF sensors, and their implementation for dielectric testing applications. To this end, the detailed analysis procedure of the IDC element using the quasi-static model and the electromagnetic model has been described. The dielectric sensing mechanism of some typical IDC based sensor structures has also been provided in the chapter. A number of resonant and non-resonant types of IDC structures relevant to the dielectric sensing applications have been discussed. Finally, various planar IDC RF sensor configurations proposed in the literature for industrial, environmental, and biomedical applications have also been described.

References

1. A.V. Mamishev, K. Sundara-Rajan, F. Yang, Y. Du, M. Zahn, Interdigital sensors and transducers. *Proc. IEEE* **92**(5), 808–845 (2004)
2. S.C. Mukhopadhyay, Smart nitrate sensor: internet of things enabled real-time water quality monitoring, smart sensors. *Meas Instrum.* **35** (2019), ISBN: 978-3-030-20094-7 (Print) 978-3-030-20095-4 (Online)
3. N. Kim, K. Adhikari, R. Dhakal et al., Rapid, sensitive and reusable detection of glucose by a robust radiofrequency integrated passive device biosensor chip. *Sci. Rep.* **5**(7807), 1–9 (2015)
4. M.R.R. Khan, S.W. Kang, Highly sensitive multi-channel IDC sensor array for low concentration taste detection. *Sensors: MDPI* **15**, 13201–13221 (2015)
5. T. Chen, D. Dubuc, M. Poupot, J. Fournie, K. Grenier, Accurate nanoliter liquid characterization up to 40 GHz for biomedical applications: toward noninvasive living cells monitoring. *IEEE Trans. Microw. Theory Tech.* **60**(12), 4171–4177 (2012)
6. X. Bao et al., A planar one-port microwave microfluidic sensor for microliter liquids characterization. *IEEE J. Electromagn. RF Microw. Med. Biol.* **2**(1), 10–17 (2018)
7. L. Zhu, K. Wu, Accurate circuit model of interdigital capacitor and its application to design of new quasi-lumped miniaturized filters with suppression of harmonic resonance. *IEEE Trans. Microw. Theory Tech.* **48**(3), 347–356 (2000)

8. T. Chretiennot, D. Dubuc, K. Grenier, A microwave and microfluidic planar resonator for efficient and accurate complex permittivity characterization of aqueous solutions. *IEEE Trans. Microw. Theory Tech.* **61**(2), 972–978 (2013)
9. G.D. Alley, Interdigital capacitors and their application to lumped-element microwave integrated circuits. *IEEE Trans. Microw. Theory Tech.* **18**(12), 1028–1033 (1970)
10. K. Hettak, N. Dib, A. Sheta, S. Toutain, A class of novel uniplanar series resonators and their implementation in original applications. *IEEE Trans. Microw. Theory Tech.* **46**(9), 1270–1276 (1998)
11. H. Samant, A.K. Jha, M.A.H. Ansari, M.J. Akhtar, Design of CPW fed IDC resonator for non-invasive testing of chemical solvents, in *IEEE 16th Annual Wireless and Microwave Technology Conference (WAMICON) 2015* (Cocoa Beach, FL, 2015), pp. 1–4
12. N. Meyne née Haase, G. Fuge, H. K. Trieu, A. Zeng and A.F. Jacob, Miniaturized transmission-line sensor for broadband dielectric characterization of biological liquids and cell suspensions. *IEEE Trans. Microw. Theory Tech.* **63**(10), 3026–3033 (2015)
13. L.F. Chen et al., *Microwave Electronics: Measurement and Materials Characterization* (Wiley, West Sussex, England, 2004) ISBN: 9780470844922 (Print), 9780470020463 (online). <https://doi.org/10.1002/0470020466>
14. S.O. Nelson, Permittivity and density relationships for granular and powdered materials, in *IEEE Antennas and Propagation Society Symposium, 2004*, vol. 1 (Monterey, CA, USA, 2004), pp. 229–232
15. M.R.R. Khan, A. Khalilian, S.W. Kang, Fast, highly-sensitive, and wide-dynamic-range interdigitated capacitor glucose biosensor using solvatochromic dye-containing sensing membrane,” *Sensors: MDPI* **18**(1)–(13), s16020265 (2016)
16. M.S. KT, A.K. Jha, M.J. Akhtar, Nondestructive technique for detection of adulteration in edible oils using planar RF sensor, in *IEEE MTT-S International Microwave and RF Conference 2016, IMaRC 2016* (New Delhi, 2016), pp. 1–4
17. M.S. KT, N.K. Tiwari, A.K. Jha, M.J. Akhtar, Microwave planar resonant sensor for detection of oil spills, in *Mediterranean Microwave Symposium 2016, MMS 2016* (Abu Dhabi, 2016), pp. 1–4
18. K.T.M. Shafi, A.K. Jha, M.J. Akhtar, Improved planar resonant RF sensor for retrieval of permittivity and permeability of materials. *IEEE Sens. J.* **17**, 5479–5486 (2017)
19. G. Govind, M.J. Akhtar, Metamaterial-inspired microwave microfluidic sensor for glucose monitoring in aqueous solutions. *IEEE Sens. J.* **19**, 11900–11907 (2019)
20. H. Samant, A.K. Jha, M.J. Akhtar, Design of coplanar dual band resonator sensor for microwave characterization of dispersive liquids, in *IEEE MTT-S International Microwave and RF Conference 2015, IMaRC 2015* (Hyderabad, 2015), pp. 249–252
21. A.K. Jha, Z. Akhter, N. Tiwari, K.T.M. Shafi, H. Samant, M.J. Akhtar, M. Cifra, Broadband wireless sensing system for noninvasive testing of biological samples. *IEEE J. Emerg. Sel. Top. Circuit. Syst.* **8**, 251–259 (2018)

Biomedical Application of Interdigital Sensors



Nasrin Afsarimanesh, Ghobad Shafiei Sabet, and S. C. Mukhopadhyay

Abstract Interdigital or interdigitated electrodes have been extensively employed as a fundament to create various types of sensors for quite some time. The significant benefits of this type of sensors such as high sensitivity, ease of fabrication, reusability etc., have led to their applications in a variety of sectors in the field of science and technology. Biomedical application of interdigital sensors is one of the most prominent applications of them, which has recently attracted so much attention among researchers. In biomedical sector, sensors have been connected to different types of signal-conditioning circuits to process and transfer data to the monitoring part of the system. Based on the application for which interdigital sensors have been used, design, processing material, configuration and size of the sensors have been largely varied. These parameters vary the performance of the sensors in terms of efficiency and sensitivity. This chapter studies different types of interdigital sensors developed for biomedical applications and some of their challenges.

1 Introduction

During the last few decades, interdigital sensors have been extensively employed in many different applications [1–4], due to their promising features such as miniaturization size, rapid response, no radiation, and the low cost of fabrication [5, 6]. Some important benefits of interdigital sensors are their simple and low-cost fabrication method and the possibility to utilize them in many various applications with no need to make main changes in the design [7–9]. Apart from these features, another advantage could be the ability to link sensors with instrumentation to develop lab-on-chip devices. In addition, the sensitivity of interdigital sensors could be enhanced by adjusting the dimension of the sensors [10]. However, not much work has been done

N. Afsarimanesh (✉) · G. Shafiei Sabet
DGUT-CNAM Institute, Dongguan University of Technology, Dongguan, China
e-mail: afsarimanesh.n@gmail.com

S. C. Mukhopadhyay
Macquarie University, Sydney, Australia

© The Editor(s) (if applicable) and The Author(s), under exclusive license
to Springer Nature Switzerland AG 2021

S. C. Mukhopadhyay et al. (eds.), *Interdigital Sensors*, Smart Sensors, Measurement
and Instrumentation 36, https://doi.org/10.1007/978-3-030-62684-6_9

to evaluate the effect of geometry of interdigital sensors on their operation [10–13]. Another significant advantage of planar interdigital sensors is the single-side access to the material under test (MUT) when there is a restriction to use both sides of the MUT [14]. The non-destructive testing (NDT) feature [15, 16] is another advantages which makes interdigital sensors more useful in in vitro analysis and process-control applications [17]. Igreja et al. studied the problems related to the design of interdigital electrodes for a multi-layer structure. In this study, an analytical tool was employed to analyze the NDT and material characterization of this type structure [18]. Li et al. provided a thorough investigation on the effects of the design parameters and geometry of interdigital sensors on their performance. They used finite element simulations to evaluate the effects of width and thickness of substrate on sensor performance [19].

Interdigital sensors follow the same working principle as parallel-plate capacitors. The planar structure of the electrodes offers a non-invasive, low signal-to-noise ratio, and single-sided measurement of the tested samples. When the electrodes slowly open, the electric field is stretched to a wider space, which then produces a fringing electric field. By changing the position of the electrodes to a co-planar configuration, the fringing electric field becomes foremost between the working and sensing electrodes [20]. The conversion from a parallel-plate capacitor to a planar interdigitated sensor is shown in Fig. 1 [17]. The repeated nature of the electrodes causes a stronger signal compared to those gained by only one pair of electrodes. When a low amplitude AC signal is applied to the electrodes, an electric field is produced between the planar electrodes. Since the electrodes are placed in a planar structure, the caused electric or magnetic fields bulges out from one electrode to another electrode of opposite polarization. The form of the produced field would differ depending on the space between the electrodes. In conventional sensors, the two electrodes are considered as excitation and reference electrodes. During the biomedical tests, samples would be in contact or proximity with the sensing surface of these devices. As the electric field is formed and moves from one electrode to another, these fields enter through the MUT. The rate of penetration varies by changing the gap between the electrodes [21]. When the bulging electric field moving between the electrodes enters through the MUT, it creates an electrical displacement to cope with the applied field which happens because of the ionic and faradic currents flowing between the electrode-electrolyte interfaces. The change in the electric field subsequently changes the capacitance.

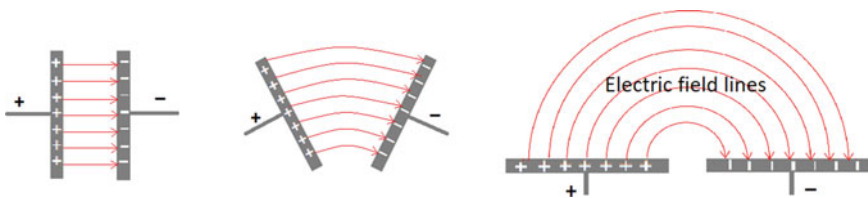


Fig. 1 Schematic of the transition from a parallel-plate capacitor to a planar sensor that provides one-sided access to MUT

This variation in capacitance could be used to determine the characteristics of the MUT.

Generally, the planar interdigital sensors are useful in determining capacitance, dielectric constant, and bulk conductivity in various mediums [22]. In some biomedical applications, the interdigital sensors measure the rate of applied strain. These sensors are made of flexible materials. The working principle of flexible sensors [23] is somewhat different from the sensors with rigid substrates. Due to the flexible structure of these sensors, any changes in the overall dimension of the sensor causes a change in the response of the sensor which would be a result of the strain-induced on the sensor. Figure 2 illustrates the working principle of interdigital flexible sensors used in biomedical applications. When the flexible interdigital sensor is bent, some parameters of the sensor such as the space between the electrodes (d), the length (L) and the width (W) of the sensor change. These variations would offer a significant change in the overall structure, producing a change in the capacitance of the sensor [24].

This book chapter reviews applications of interdigital sensors in biomedical sectors. Sensors have been designed and fabricated with different dimensions and materials based on the specific applications for which they can be employed. Table 1

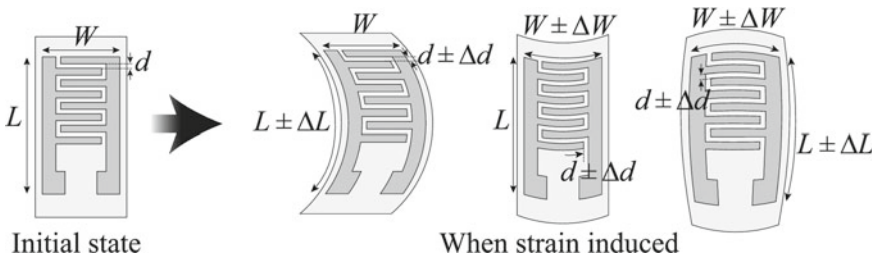


Fig. 2 Working principle of flexible planar interdigital sensors [24]

Table 1 Substrate and electrodes materials, and the dimension of some Interdigital Sensors developed for biomedical applications

Substrate material	Electrodes material	Dimensions (width, gap, and thickness)	Reference
Polyimide-PDMS	Brass Sheet	127 μm thickness and 5 μm gap	[25]
Silicon	Gold	800 nm width, 120 nm thickness and 400 nm gap	[26]
PDMS	Conductive fabric	10 mm length, 57 μm thickness, 1.5 mm width and 1 mm gap	[24]
Silicon	Gold	2.5 mm length, 25 μm width, 500 nm thickness and 25 μm gap	[27]
PDMS	Graphite	18 mm length, 2 mm width and 1.5 mm gap	[28]

Table 2 Comparative study of different kinds of interdigital sensors based on electrochemical sensing for different kinds of applications

Sensor materials	Sensitivity	Linear response	Detection range	Reference
Copper, chromium, polyimide	45.78 mV/decade	1 μ M – 1 M	1 μ M – 1 M	[29]
Gold, 2-mercaptoethylamine	0.22 nF.pg ml ⁻¹	5 pg ml ⁻¹ – 1 ng ml ⁻¹	1.34 pg ml ⁻¹	[30]
Reduced graphene, oxide	180 k Ω /% RH	0–75%	0–100%	[31]
Polyaniline, reduced graphene oxide	457.4 μ A mM ⁻¹ cm ⁻²	0.4–183.7 mM	0.1 μ M	[32]
Carbon Nanotubes	2.72 kPa ⁻¹	0–20 kPa	0–140 kPa	[33]
Hollow MXene spheres, Reduced graphene, Aerogel	609 kPa ⁻¹	0–10 kPa	6.4–10 kPa	[34]

Table 3 Comparative study of different kinds of interdigital sensors based on strain sensing for different kinds of applications

Sensor materials	Gauge factor	Detection limit (%)	Reference
Palladium, PET	55	0.3	[35]
Silicone elastomer, Conductive-knit fabric (Shieldex [®])	0.3	0.6	[36]
Liquid crystal polymer, Polyimide	1.38	0.145	[37]
PDMS, Conductive fabric (VeilShield)	0.87	0.1	[24]
Carbon black, Barium titanate, Ecoflex	1.7	1	[38]

summarizes some significant interdigital sensors developed for biomedical applications. The dimensions of each of these prototypes depend on their application, as well as the material that was being processed. Tables 2 and 3 elaborate the differences in the sensing parameters of each of the prototypes for different applications based on electrochemical sensing and strain sensing, respectively.

2 Biomedical Applications of Interdigital Sensors

Sensors used in biomedical applications should meet certain requirements to provide similar or even better results than the conventional available systems. These systems need to be easy to use, small-size, low-cost, and reliable [39]. The need for a low amount of sample and a rapid analysis are the requirements for the imminent applications of biomedical sensing devices. Thus, the opportunity of miniaturization and automation are the incentive for novel advances. An important approach is the possibility of using such sensing devices for the detection of a biomarker in different

body fluids and tissue extracts [40]. Therefore, study on sensing devices is determined by the attention to design special sensors, which could be later utilized for quick and reliable measurements in various biomedical applications. The market for such devices has been projected to grow by around 15% every year [39]. To develop such sensing systems, some research has been done to develop lab-on-a-chip devices [41–43] in which all the steps such as sampling, preparation, examination and reporting are joint and automated [44]. For point-of-care testing [45–47], all these jobs must be combined to develop a complete sensing system which can take over different biomedical applications for detection and treatment of diseases, and ultimately, employ them as portable and handheld biomedical devices [48–50].

There are several benefits in using interdigital sensors, which make them fit for biomedical applications. One of the most considerable benefits is single-side access to the MUT. This feature makes it possible to infuse the sample with magnetic, electric, or acoustic fields from only one side. Besides, the output signal can be adjusted by changing the number of interdigitated electrodes, the space between them, as well as the dimension of the sensing area. The capability of being used in non-destructive testing is another advantage of interdigital sensors, which makes them more appropriate for online analysis and process-control uses [17].

A novel interdigital capacitive (IDC) strain sensor for wireless structural health monitoring applications was reported by Hung et al. [25]. In this work, the sensors were fabricated by laser-micromachining technique [51]. The wireless monitoring system was created using a commercial wireless module which could offer simultaneous multi-modality monitoring [52]. A graphical user interface was developed for data storage and presentation, and online data evaluation. The sensitivity of the sensor was evaluated in both stretching and bending modes, proving 0.025% of the limit of detection for strain. The gauge factor was estimated in the range of 6 to 9 which is much more than those of the commercial strain gauges. The bending detection of the developed sensors is consistent up to 20°. Hysteresis and temperature behavior were also studied, exhibiting expectable results. Finally, the proposed sensing device was formed with both single and multiple sensors for a real-time structural health monitoring application. The block diagram of the developed wireless structural health monitoring is shown in Fig. 3.

Another interesting work in this sector was presented by Chen et al. [53], in which the sensors were formed by printing the interdigital electrodes on plastic films for monitoring and analyzing the density of tumor cells. The sensor responses were verified with cell culture solutions formed with deionized water and PBS solutions. Finally, the responses were investigated using the electrochemical impedance spectroscopy technique. The thickness of substrate was around 500 microns and gold-based ink was directly printed to create the conductive electrodes. The shape of the electrodes was created using stainless steel masks. The dimension of the electrodes included width and gap of 100 microns and 20 microns, respectively. The samples were tested inside a PDMS chamber, used to load samples by attaching the films on the chamber following to the plasma treatment. The frequency range used for the experimental purpose was from 1 kHz to 1 MHz. Lee et al. reported a graphene-based electrochemical sensing microneedles for diabetes monitoring and

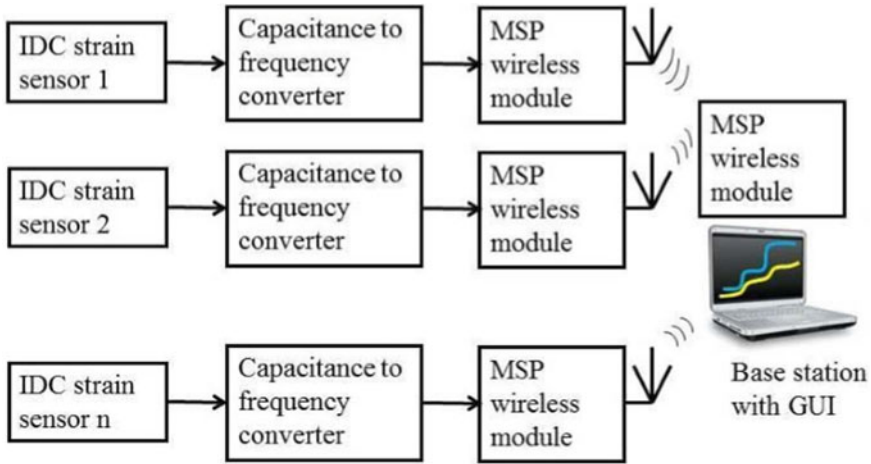


Fig. 3 The block diagram of the structural health monitoring system using the developed IDC strain sensors [25]

therapy [54]. Monitoring of the biomarkers and physiological signals was done with sweat control and transcutaneous drug delivery system to accomplish a suitable point-of-care therapy for diabetes. The sensing system involved bare graphene doped with gold and gold mesh to increase the electrochemical activity. The developed system contained different elements such as a heater, and some sensors like temperature, humidity, glucose and pH sensors, along with some polymeric needles. These components were joined to form a sensing device for the thermal activation of drugs. The performance of the proposed system was evaluated by testing it on a diabetic mouse by delivering Metformin. The sensor was formed using a bilayer formed with a serpentine gold mesh and gold-doped CVD-formed graphene. These layers qualified to high conductivity, mechanical reliability and optical transparency for the system. The measurements were taken from the doped-graphene layer and compared with that of the gold mesh layer, due to the higher electrochemical activity in the former layer. Changes in current and impedance values were determined using cyclic voltammetry, which was the result of charge transfer and redox reactions. The highest charge transfer resistance was in the gold layer, which was compensated by the doped-graphene layer because of the conducting sites appear in the electrochemically active regions. The stability of the doped graphene layer was further confirmed by the temperature-dependent impedance measurements. The excellent electrochemical interactive capability was proved by functionalizing the doped layer with different kinds of monomers. The model was then shifted to a thin silicone patch to create a patterned electrochemically-functionalized hybrid sensing system. Resistance modulation of the graphene and gold mesh layers is done to create the heater, tremor sensor and temperature sensor. Any variation in relative humidity is determined with respect to the corresponding variation in the impedance of the interdigitated PEDOT electrodes to show the presence of sweat on the skin. The

electrochemical reactions of the doped graphene layer due to the reduction of the hydrogen peroxide from the glucose oxide was estimated to determine the change in the glucose level. The pH was also measured, where fluctuations in electrochemical signals were determined due to Polyaniline (PANI)/GP hybrid in combination with the Ag/AgCl counter electrode. The shared operation was done by real-time *in vitro* testing of artificial sweat. The diabetic patch was exposed to a minimum of 20 μl of the sample to define the starting point for glucose and pH sensing. The response of pH and glucose respect to the change in temperature was examined, where the sensitivity of glucose and pH were realized to be somewhat reduced and then constant, respectively. The recordings related to high glucose level triggered the heaters to dissolve phase-change material (PCM) [55] and hence, bio-resorbable microneedles released Metformin as feedback transdermal drug delivery to the glucose detection. It was reported that fundamentally soft materials improve the conformal adaptivity of devices with the human skin and thus enhances the efficiency of biochemical sensors and drug delivery.

Elsholz et al. reports an automated electrical method for to detect and measure pathogens, which are mainly involved in urinary tract infections [26]. Interdigital sensors with gold electrodes were fabricated for sensitive investigation. These sensors were developed on standard 6-inch silicon wafers. The area of the sensor were $9 \times 10 \text{ (mm)}^2$, including 16 electrodes with the diameter of 500 μm . The gold electrodes functionalized by thiol-modified oligonucleotides were employed as the capturing probes. The electrical signals were produced by amperometric redox cycling and captured by a unique multi-potentiostat. The device output signals were position specific current and changed over time with respect to the levels of analyte. The authors expressed that if two additional biotins are added into the affinity binding complex, the sensitivity of the system enhances more than 60%. The LOD for the developed system had been calculated to be 0.5 $\text{ng}/\mu\text{L}$. The control of fluidics, as well as the multichannel electrical information and data management, have all been fully automated.

Nebling et al. [56] presented development of a completely electrical sensor for the detection of viral DNA. The electronic detection was based on interdigital ultra-microelectrode arrays developed using the silicon technology. Oligonucleotide capture probes were coated on the gold electrodes using the thiol—gold self-assembling technique. The nanoscale electrodes were developed to carry out a sensitive detection of enzyme activity by signal enhancing redox recycling of hydroxylaniline (HA). Multiplexing and serial details were identified using a CMOS ASIC module [57] and a computer-controlled multi-channel potentiostat. A 16-channel multi-potentiostat fitted out with two multiplexers was employed for electrochemical measurements. In this work fundamental of the silicon-based electrical biosensor was introduced for different experimental setups and for the detection of virus DNA in real unpurified multiplex samples. It was claimed that quick and quantitative assessment for all types of affinity assays was strong and particle tolerant. The developed electrical biochip and structure of the measurement system are depicted in Fig. 4.

Chen et al. presented the design and fabrication of an interdigital surface acoustic wave (SAW) [58, 59] gas sensor as a virtual sensor array, linked with an imaging

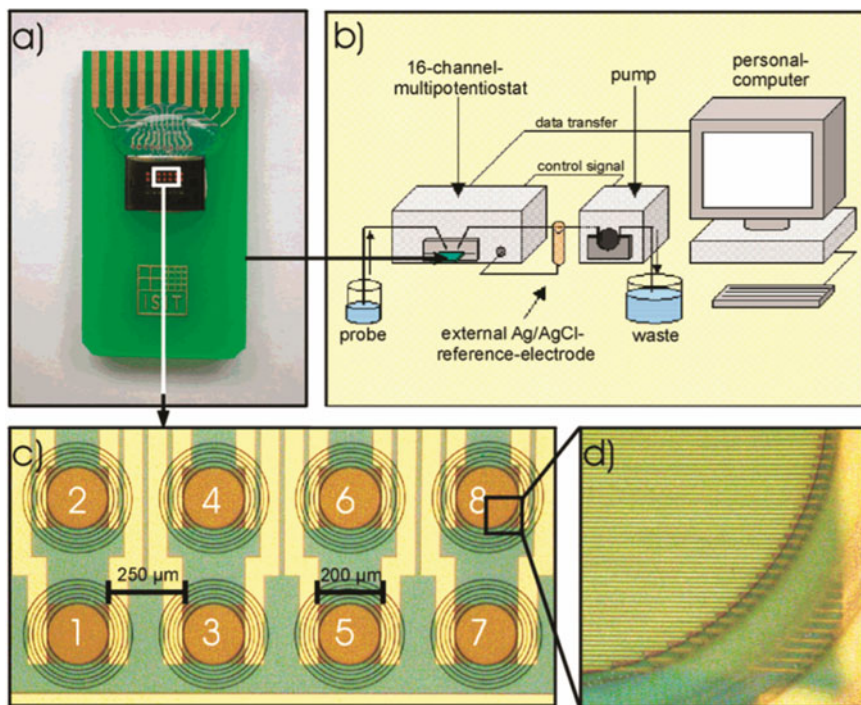


Fig. 4 **a** chip on PCB; **b** 16-channel multi-potentiostat with chip and flow-through cell connected to the reference electrode, pump, and computer; **c** chip positions; **d** submicrometer interdigitated electrode fingers and the three-dimensional polymeric ring structures [56]

detection method for non-invasive diagnosis of lung cancer [60]. It consisted of a gas path made of a two-bag system, solid-phase microextraction (SPME) [61] and a capillary column. A pair of SAW sensors were utilized to recognize chemical compounds. One of the sensors were coated with a thin polyisobutylene (PIB) film. This electronic noise could be employed to determine the quality and quantity of eleven volatile organic compounds (VOCs) [62] which are recognized as the biomarkers of lung cancer according to the pathological research. Following, an improved artificial neural network (ANN) [63] algorithm merged with an imaging method was developed for the recognition of an anomaly among patients. Finally, the electrical noise was calibrated by eleven VOCs separated into three levels and was later used to identify patients with lung cancer in a hospital. The experimental outcomes showed that this type of electronic noise could be beneficial to identify patients with lung cancer. Another research group [13] developed interdigitated electrode arrays for impedance-based measurement of Hs578T breast cancer cells [64]. Gold interdigitated electrodes were patterned on 4-inch glass substrates using photolithography and metal deposition technologies. The 3000 PY photoresist [65] was used to pattern the electrodes and contact pads. The substrate was layered with a 15 nm of chromium

and then 20 nm of gold. Then, the photoresist film was removed using acetone. Finally, SU-8 photoresist [66] was employed to create a passivation layer. In this phase, only the electrodes and contact pads were exposed. Eventually, a passivation layer was created using the SU photoresist. This layer was then baked to produce an inert polymer resin. The proposed device was then diced and 6 mm cultivation chamber was attached and sealed using gradually heated photoresist near the outer edges of the chamber. Former to the impedance measurements, the Hs578T breast tumor cells were cultured. The device was first rinsed and then the sample was kept on the electrodes for 20 min and removed before the cellular inoculation. The device was then immunized with a small amount of cell suspension with a concentration of 14.67×10^4 cells/ml. 200 μ l of medium was then added to the culture slots. An incubation period of 24 h was given to ensure proper devotion of the cells to the electrodes. Lastly, impedance variation was measured using an Agilent 4294A impedance analyzer in a frequency range of 100 Hz to 10 MHz. System calibration was done using the manufacturer protocol. Baseline measurements were conducted using medium, followed by the measurements of cellular impedance.

Afsarimanesh et al. developed a smart sensing system for the prognostic monitoring of bone health [27]. They designed and fabricated a selective interdigital gold electrode sensor on a silicon substrate for the recognition and quantification of the C-terminal telopeptide of Type-I collagen (CTx-I), which is one of the most significant biomarkers of osteoporosis [67, 68]. The electrochemical impedance spectroscopy (EIS) technique was employed to measure the changes in impedance for different levels of CTx-I samples. A MEMS sensor with an area of 10×10 mm², including a sensing area of 2.5×2.5 mm² was developed, and impedance measurements were conducted using a HIOKI-3536 LCR meter. Molecularly imprinted polymer (MIP) technology was used to develop the selective coating material [69] and some optimization experiments were performed to determine the optimum coating thickness. Samples with different levels of CTx-I were measured using the proposed system and the results were confirmed using a standard ELISA kit. The proposed sensing system exhibited the LOD of 0.09 ppb. This group had also proposed a microcontroller-based system that could quantify the concentration of CTx-I and transfer data to an IoT-based cloud server. The information could be given to the health practitioner and a detailed investigation could therefore be started for prognostic detection and treatment [27]. Figure 5 shows the graphical illustration of the proposed sensing system.

Nag et al. reported the design, development and implementation of a novel strain-induced graphite/PDMS sensor for biomedical applications [70]. The sensors was developed using 3D printing technique [71, 72], in which acrylonitrile thermoplastic polymer was used as the filament. The electrodes of the sensor patch were made of Graphite and PDMS was used to create the substrate. The electrodes were formed in an interdigitated configuration with the casting of graphite powder on the 3D printed molds. Figure 6a depicts the proposed strain-induced graphite/PDMS sensor. They used the COMSOL simulation results to intricate the working principle of the sensor patches. EIS technique was used to measure impedance variations of sensor patches at different operating conditions. The maximum bending radius confirmed by the

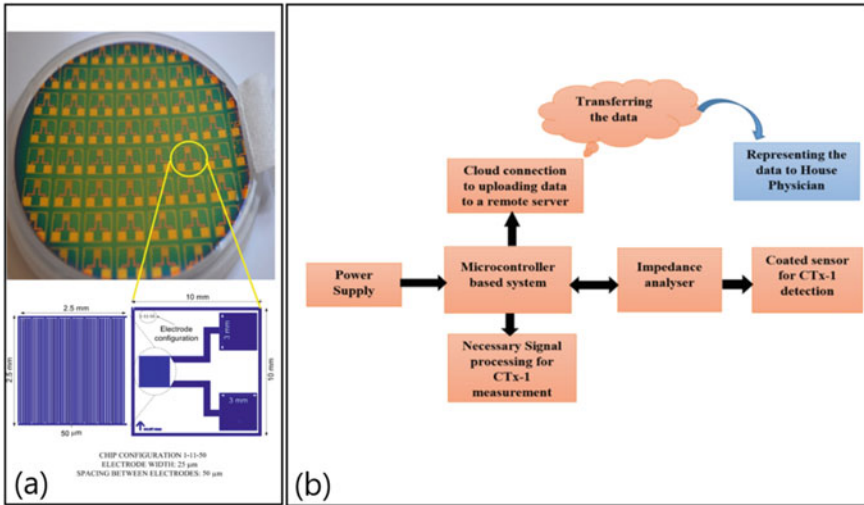


Fig. 5 a Configuration of the interdigitated gold electrode sensor. b Block diagram of the smart sensing system for prognostic monitoring of bone loss [27]

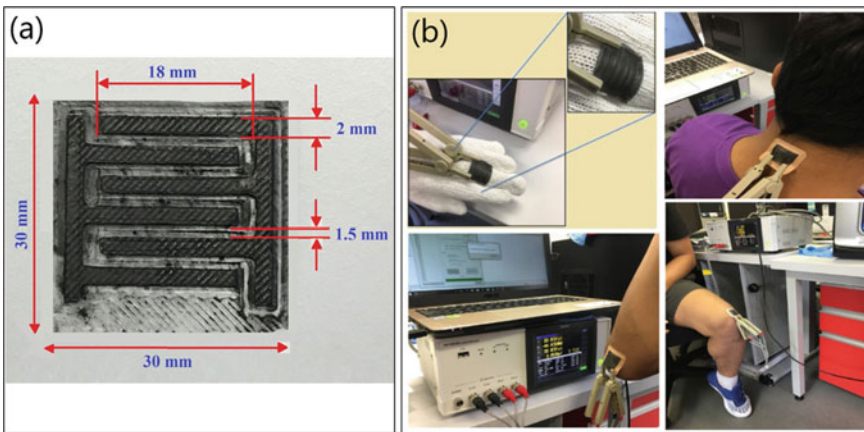


Fig. 6 a Dimension and configuration of the developed strain-induced graphite/PDMS induced sensor. b Attachment of the sensor patch on the finger, elbow, neck, and knee to monitor their movements based on the strain-induced of the sensor patches [70]

proposed sensor patches was 6 mm. Strain-sensing tests were successfully done based on the bending of the different parts of the body, such as a finger, elbow and knee (Fig. 6b) where the sensor patches were attached. Promising outcomes have been shown by the developed sensor patches to demonstrate their capability to be used in the biomedical applications [70].

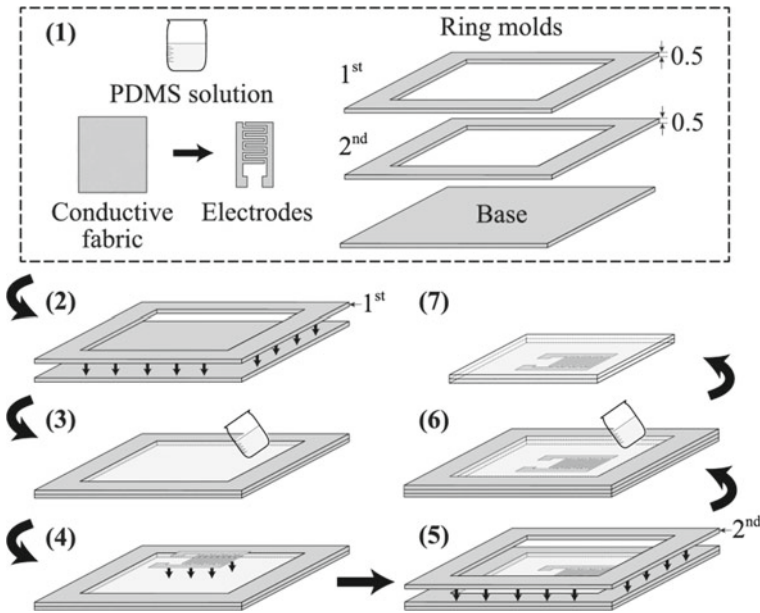


Fig. 7 Schematic illustration of the fabrication steps of the transparent sensor [24]

Another paper presented by the same group, reported the development of a novel transparent strain sensor for wearable sensing biomedical applications [24]. They fabricated flexible interdigitated-electrode sensors using a PDMS-embedded conductive fabric and fruitfully confirmed applications of the sensor in sensing different strains. The fabrication process is illustrated in Fig. 7. The proposed sensor was characterized based on its transparency and electromechanical performance. Later, the sensors were tested in different physiological sensing situations, such as the sensing of the movement of different parts of the body and tactile sensing. Aside from great optical transparency (70%), the sensor showed prominent sensing results that approve the applicability of the proposed sensor for detection of flexible and transparent strain sensors for wearable sensing applications [73–75].

3 Challenges of the Existing Sensors

Though interdigitated sensors have many different applications, there are yet some ambiguities that need to be addressed. While the sensors are characterized and used for strain sensing, they are mainly used for electrochemical sensing, because of their specific construction. This decreases the chances of using them as flexible prototypes [76]. The multi-functional nature of these sensors can be further emphasized by using flexible polymers as substrates. This can be advantageous as sensors can be used for both electrical and mechanical attributes. Another feature that should be changed

for these sensors is the addition of selectivity for taking particular analyte. Although existence of selectivity helps to enhance the sensitivity for a particular molecule, the reusability of the sensor always remains as a limitation. The sensors need to be designed with the selective material intact to the sensor [77]. This should be well-thought-out with an extra step of removal of the captured analyte to make the sensors ready for the next measurement. This way, the electrodes can preserve a constant sensitivity, together with using the same sensor for a longer period. Moreover, to add multi-functionality, an array of electrodes should be involved in every sensor for electrochemical sensing, so that more than one analyte can be detected. Another matter that should be discussed is the minimization of the capacitance formed by the fringe effect. This should be altered by reducing the interference and noise affecting the device. Optimizing the signal-conditioning circuit related to the sensor is one of the ways to do this. Another problem that should be noted is the electronic waste produced by the used sensors. When sensors are used, they are discarded, either because they are damaged, or they have lost their sensitivity. This creates a huge amount of electronic waste, considering the use of sensing devices in every part of science and technology. One of the solutions to overcome this problem could be using organic materials to develop the substrates and electrodes of sensors, which after its use, will slowly decompose with time. The use of glassy carbon electrodes or allotropes of carbon like graphene [78, 79], carbon nanotubes [80, 81] to create the electrodes could be a wise choice. Polymers like polydimethylsiloxane (PDMS) [24, 82], polyethylene [83, 84], poly-vinyl chloride (PVC) [85, 86] and others could be considered as an alternative for substrates. This will significantly reduce the microelectronic waste produced by the sensors.

4 Conclusions and Outlook

The chapter presents the importance of the usage of interdigital sensors in biomedical sector. Interdigitated electrodes have been developed using different kinds of materials, depending on the applications. Some of the advantages of interdigital sensors were their simple structure and working principle, easy alteration, low input voltage and possibility to be used in different applications. The customization of the interdigital sensors with their dimension, interdigital gap and electrical permittivity related to various applications is one of the most important advantages of interdigital sensors. There are many other numerous sectors where interdigitated sensors have been implemented due to their mentioned advantages. The applications of interdigital sensors could be further extended to new sectors by joining them with the available techniques. The development of array of sensors can prepare these sensors for different sorts of applications, with each one for a certain use. On the other hand, interdigital sensor fabrication techniques can be controlled to prepare each of these sensors specific for a particular analyte. This would not only make the array of sensors multi-functional but would also cut the cost of the sensors. The bacterial and pathological detection is another area that could be further studied to recognize very low scale

microorganisms. With the current progress in medical science, a lot of new viruses are coming up, which need to be recognized. Interdigital sensors, having a simple fabrication procedure, could be selected as a popular possibility for their large-scale detection.

References

1. T. Faes, H. Van der Meij, J. De Munck, R. Heethaar, The electric resistivity of human tissues (100 Hz-10 MHz): a meta-analysis of review studies. *Physiol. Meas.* **20**(4), R1 (1999)
2. N. Afsarimanesh et al., Smart sensing system for the prognostic monitoring of bone health. *Sensors* **16**(7), 976 (2016)
3. A.I. Zia, S.C. Mukhopadhyay, P.-L. Yu, I.H. Al-Bahadly, C.P. Gooneratne, J. Kosel, Rapid and molecular selective electrochemical sensing of phthalates in aqueous solution. *Biosens. Bioelectron.* **67**, 342–349 (2015)
4. L. Guan, X. Feng, G. Xiong, J. Xie, Application of dielectric spectroscopy for engine lubricating oil degradation monitoring. *Sens. Actuator. A* **168**(1), 22–29 (2011)
5. N.F. Sheppard, R.C. Tucker, C. Wu, Electrical conductivity measurements using microfabricated interdigitated electrodes. *Anal. Chem.* **65**(9), 1199–1202 (1993)
6. S.C. Mukhopadhyay, Sensing and instrumentation for a low cost intelligent sensing system, in 2006 SICE-ICASE International Joint Conference, pp. 1075–1080, (2006) IEEE
7. P. Van Gerwen et al., Nanoscaled interdigitated electrode arrays for biochemical sensors. *Sens. Actuator. B: Chem.* **49**(1–2), 73–80 (1998)
8. S. Mukhopadhyay, C. Gooneratne, S. Demidenko, G.S. Gupta, Low cost sensing system for dairy products quality monitoring, in 2005 IEEE Instrumentation and Measurement Technology Conference Proceedings, vol. 1, pp. 244–249 (2005), IEEE
9. A. Rivadeneyra, J. Fernández-Salmerón, J. Banqueri, J.A. Lopez-Villanueva, L.F. Capitan-Vallvey, A.J. Palma, A novel electrode structure compared with interdigitated electrodes as capacitive sensor. *Sens. Actuator. B: Chem.* **204**, 552–560 (2014)
10. M. Ibrahim, J. Claudel, D. Kourtiche, M. Nadi, Geometric parameters optimization of planar interdigitated electrodes for bioimpedance spectroscopy. *J. Electr. Bio.* **4**(1), 13–22 (2019)
11. T. Shi, C. Xie, S. Huang, R.A. Williams, M. Beck, Capacitance-based instrumentation for multi-interface level measurement. *Meas. Sci. Technol.* **2**(10), 923 (1991)
12. H. Wang, W. Yin, W. Yang, M. Beck, Optimum design of segmented capacitance sensing array for multi-phase interface measurement. *Meas. Sci. Technol.* **7**(1), 79 (1996)
13. F. Alexander Jr, D.T. Price, S. Bhansali, Optimization of interdigitated electrode (IDE) arrays for impedance based evaluation of Hs 578T cancer cells. *J. Phys.: Conf. Ser.* **224**(1), 012134 (2010), IOP Publishing
14. A.S. Abu-Abed, R.G. Lindquist, Capacitive interdigital sensor with inhomogeneous nematic liquid crystal film. *Prog. Electromagn. Res.* **7**, 75–87 (2008)
15. J. Blitz, *Electrical and Magnetic Methods of Non-Destructive Testing*. Springer Science & Business Media (2012)
16. K. Kosmas, C. Sargentis, D. Tsamakias, E. Hristoforou, Non-destructive evaluation of magnetic metallic materials using Hall sensors. *J. Mater. Process. Technol.* **161**(1–2), 359–362 (2005)
17. A.V. Mamishev, K. Sundara-Rajan, F. Yang, Y. Du, M. Zahn, Interdigital sensors and transducers. *Proc. IEEE* **92**(5), 808–845 (2004)
18. R. Igreja, C. Dias, Analytical evaluation of the interdigital electrodes capacitance for a multi-layered structure. *Sens. Actuator. A* **112**(2), 291–301 (2004)
19. X.B. Li, S.D. Larson, A.S. Zyuzin, A.V. Mamishev, Design principles for multichannel fringing electric field sensors. *IEEE Sens. J.* **6**(2), 434–440 (2006)
20. X. Hu, W. Yang, Planar capacitive sensors—designs and applications. *Sensor Rev.* **30**(1), 24–39 (2010)

21. M.S.B.A. Rahman, S.C. Mukhopadhyay, P.L. Yu, Novel sensors for food inspections. *Sens. Transducer.* **114**(3), 1 (2010)
22. P. Geng et al., Self-assembled monolayers-based immunosensor for detection of *Escherichia coli* using electrochemical impedance spectroscopy. *Electrochim. Acta* **53**(14), 4663–4668 (2008)
23. A.J. Bandonkar, J. Wang, Non-invasive wearable electrochemical sensors: a review. *Trends Biotechnol.* **32**(7), 363–371 (2014)
24. A. Nag et al., A transparent strain sensor based on PDMS-embedded conductive fabric for wearable sensing applications. *IEEE Access* **6**, 71020–71027 (2018)
25. H. Cao et al., Development and characterization of a novel interdigitated capacitive strain sensor for structural health monitoring, **15**(11), 6542–6548 (2015)
26. B. Elsholz et al., Automated detection and quantitation of bacterial RNA by using electrical microarrays. *Anal. Chem.* **78**(14), 4794–4802 (2006)
27. N. Afsarimanesh, M.E.E. Alahi, S.C. Mukhopadhyay, M. Kruger, Development of IoT-based impedometric biosensor for point-of-care monitoring of bone loss. *IEEE J. Emerg. Sel. Top Circuit. Syst.* **8**(2), 211–220 (2018)
28. A. Nag, S. Feng, S. Mukhopadhyay, J. Kosel, D.J.S. Inglis, A.A. Physical, 3D printed mould-based graphite/PDMS sensor for low-force applications, **280**, 525–534 (2018)
29. M.R.R. Khan, S.-W. Kang, Highly sensitive multi-channel IDC sensor array for low concentration taste detection. *Sensors* **15**(6), 13201–13221 (2015)
30. H.A. Zeinabad, H. Ghourchian, M. Falahati, M. Fathipour, M. Azizi, S.M. Boutorabi, Ultra-sensitive interdigitated capacitance immunosensor using gold nanoparticles. *Nanotechnology* **29**(26), 265102 (2018)
31. G. Hassan, M. Sajid, C. Choi, Highly sensitive and full range detectable humidity sensor using PEDOT: PSS, methyl red and Graphene oxide materials. *Sci. Rep.* **9**(1), 1–10 (2019)
32. L. Li, H. Liu, B. Li, Y. Guo, L. Qing, B. Wang, Design and construction of polyaniline/reduced graphene oxide three-dimensional dendritic architecture on interdigital electrode for sensitive detection nitrite, *Macromol. Res.* pp. 1–10 (2019)
33. C. Wang et al., An ultra-sensitive and wide measuring range pressure sensor with paper-based CNT film/interdigitated structure. *Sci. China Mater.* 1–10 (2019)
34. M. Zhu et al., Hollow MXene Sphere/Reduced Graphene Aerogel composites for Piezoresistive sensor with ultra-high sensitivity. *Adv. Electro. Mater.* (2019)
35. F. Liu, W. Shao, G. Xu, L. Yuan, Response characteristics of strain sensors based on closely spaced nanocluster films with controlled coverage. *Chin. J. Chem. Phys.* **32**(2), 213 (2019)
36. O. Atalay, Textile-based, interdigital, capacitive, soft-strain sensor for wearable applications. *Materials* **11**(5), 768 (2018)
37. R. Zeiser, T. Fellner, J. Wilde, Capacitive strain gauges on flexible polymer substrates for wireless, intelligent systems. *J. Sens. Sens. Syst.* **3**(1), 77–86 (2014)
38. E. Cholleti, J. Stringer, M. Assadian, V. Battmann, C. Bowen, K. Aw, Highly stretchable capacitive sensor with printed carbon Black electrodes on barium titanate elastomer composite. *Sensors* **19**(1), 42 (2019)
39. E.J.M.S. Simon, Technology, Biological and chemical sensors for cancer diagnosis. **21**(11), 112002 (2010)
40. S. Jimenez-Fernandez, P. De Toledo, F. Del Pozo, Usability and interoperability in wireless sensor networks for patient telemonitoring in chronic disease management. **60**(12), 3331–3339 (2013)
41. J.P. Laffleur, A. Jönsson, S. Senkbeil, J.P.J.B. Kutter, Bioelectronics, “Recent advances in lab-on-a-chip for biosensing applications.” **76**, 213–233 (2016)
42. C.D. Chin, V. Linder, S.K. Sia, Lab-on-a-chip devices for global health: Past studies and future opportunities. **7**(1), 41–57 (2007)
43. H.A. Stone, A.D. Stroock, A.J.A.R.F.M. Ajdari, Engineering flows in small devices: microfluidics toward a lab-on-a-chip. **36**, 381–411 (2004)
44. A. Romani et al., Capacitive sensor array for localization of bioparticles in CMOS lab-on-a-chip, in 2004 IEEE International Solid-State Circuits Conference (IEEE Cat. No. 04CH37519), pp. 224–225 (2004), IEEE

45. A.K. Yetisen, M.S. Akram, C.R. Lowe, Based microfluidic point-of-care diagnostic devices. **13**(12), 2210–2251 (2013)
46. A. Kaushik, A. Vasudev, S.K. Arya, S.K. Pasha, S.J.B. Bhansali, Bioelectronics, Recent advances in cortisol sensing technologies for point-of-care application. **53**, 499–512 (2014)
47. W. Suntornsuk, L.J.E. Suntornsuk, Recent applications of paper-based point-of-care devices for biomarker detection. **41**(5–6), 287–305, 2020
48. M. Prgomet, A. Georgiou, J.I. Westbrook, The impact of mobile handheld technology on hospital physicians' work practices and patient care: a systematic review. **16**(6), 792–801 (2009)
49. F.M. Mncube-Barnes, B.L. MSIS, O. Esuruoso, P.N. Gona, S.D. Msc, Mobile access to Clinical information at the point of care. **8**(3) (2016)
50. S.J.B.A. Choi, Powering point-of-care diagnostic devices. **34**(3), pp. 321–330 (2016)
51. K. Ahmed, C. Grambow, A.-M.J.M. Kietzig, Fabrication of micro/nano structures on metals by femtosecond laser micromachining. **5**(4), pp. 1219–1253 (2014)
52. K.E. Wartenberg, J.M. Schmidt, S.A.J.C.C.C. Mayer, Multimodality monitoring in neurocritical care. **23**(3), pp. 507–538 (2007)
53. L. Chen, J. Guo, Printed interdigital electrodes on plastic film for tumor cells density monitoring. *Electrophoresis* **36**(16), 1859–1861 (2015)
54. H. Lee et al., A graphene-based electrochemical device with thermoresponsive microneedles for diabetes monitoring and therapy. **11**(6), p. 566 (2016)
55. A. Waqas, Z.U. Din, Phase change material (PCM) storage for free cooling of buildings—a review. *Renew. Sustain. Energy Rev.* **18**, 607–625 (2013)
56. E. Nebling, T. Grunwald, J. Albers, P. Schäfer, R. Hintsche, Electrical detection of viral DNA using ultramicroelectrode arrays. *Anal. Chem.* **76**(3), 689–696 (2004)
57. A. Andreev et al., Architectural floorplan for a structured ASIC manufactured on a 28 NM CMOS process lithographic node or smaller, ed: Google Patents (2015)
58. R. Takpara et al., Development of flexible SAW sensors for non-destructive testing of structure, in *AIP Conference Proceedings*, vol. 1706(1) (AIP Publishing, 2016), p. 070003
59. J.-J. Cai, H. Chen, Y. Guan, S. Chou, and E. Jeng, “Study on the polymer-coated Surface Acoustic Wave sensors for organic vapor detection,” in *2016 5th International Symposium on Next-Generation Electronics (ISNE)*, 2016, pp. 1–2: IEEE
60. X. Chen et al., A study of an electronic nose for detection of lung cancer based on a virtual SAW gas sensors array and imaging recognition method. *Meas. Sci. Technol.* **16**(8), 1535 (2005)
61. D.D. Manning, K.C. Schreiber, K.J. Fredeen, G.E. Riehm, G. Weaver, J.R. Laverack, *Solid Phase Micro-Extraction (SPME) Devices*, ed: Google Patents (2018)
62. A. Mirzaei, S. Leonardi, G. Neri, Detection of hazardous volatile organic compounds (VOCs) by metal oxide nanostructures-based gas sensors: a review. *Ceram. Int.* **42**(14), 15119–15141 (2016)
63. D. Livingstone, *Artificial Neural Networks: Methods and Applications*. Springer (2008)
64. É. Caron-Beaudoin, R. Viau, J.T. Sanderson, Effects of neonicotinoid pesticides on promoter-specific aromatase (CYP19) expression in Hs578t breast cancer cells and the role of the VEGF pathway. *Environ. Health Perspect.* **126**(4), 047014 (2018)
65. M. Mahmoodian, B. Pourabbas, M. Hosseini, S. Mohajerzadeh, Patterning ability of conducting polypyrrole thin films by positive photoresist. *J. Mater. Sci.: Mater. Electron.* **26**(2), 898–908 (2015)
66. C.D. Joye, J.P. Calame, M. Garven, B. Levush, UV-LIGA microfabrication of 220 GHz sheet beam amplifier gratings with SU-8 photoresists. *J. Micromech. Microeng.* **20**(12), 125016 (2010)
67. N. Afsarimanesh, S.C. Mukhopadhyay, M. Kruger, Sensing technologies for monitoring of bone-health: a review. *Sens. Actuators, A* **274**, 165–178 (2018)
68. N. Afsarimanesh, S. Mukhopadhyay, M. Kruger, K. Marlena, Biosensors for the measurement of C-terminal telopeptide of type I Collagen (CTX-I). *J. Osteoporos. Phys. Act.* **5** (2017)
69. N. Afsarimanesh, S.C. Mukhopadhyay, M. Kruger, Molecularly imprinted polymer-based electrochemical biosensor for bone loss detection. *IEEE Trans. Biomed. Eng.* **65**(6), 1264–1271 (2017)

70. A. Nag, N. Afsarimanesh, S. Feng, S.C. Mukhopadhyay, Strain induced graphite/PDMS sensors for biomedical applications. *Sens. Actuators, A* **271**, 257–269 (2018)
71. T. Han, A. Nag, N. Afsarimanesh, S.C. Mukhopadhyay, S. Kundu, Y. Xu, Laser-assisted printed flexible sensors: a review. *Sensors* **19**(6), 1462 (2019)
72. T. Han, S. Kundu, A. Nag, Y. Xu, 3D printed sensors for biomedical applications: a review. *Sensors* **19**(7), 1706 (2019)
73. W. Gao et al., Fully integrated wearable sensor arrays for multiplexed in situ perspiration analysis. *Nature* **529**(7587), 509 (2016)
74. R. Varatharajan, G. Manogaran, M.K. Priyan, R. Sundarasekar, Wearable sensor devices for early detection of Alzheimer disease using dynamic time warping algorithm. *Clust. Comput.* **21**(1), 681–690 (2018)
75. W. Wang, T. Yang, H. Zhu, Q.J.A.P.L. Zheng, Bio-inspired mechanics of highly sensitive stretchable graphene strain sensors. **106**(17), 171903 (2015)
76. A. Nag, S.C. Mukhopadhyay, J. Kosel, Wearable flexible sensors: a review. *IEEE Sens. J.* (2017)
77. N. Stasyuk, O. Smutok, G. Gayda, B. Vus, Y. Koval'chuk, M. Gonchar, Bi-enzyme L-arginine-selective amperometric biosensor based on ammonium-sensing polyaniline-modified electrode. *Biosens. Bioelectron.* **37**(1), 46–52 (2012)
78. A. Nag, A. Mitra, S.C. Mukhopadhyay, *Graphene and Its Sensor-based Applications: A Review* (Physical, Sensors and Actuators A, 2017)
79. Y. Zhao, X.-G. Li, X. Zhou, Y.-N. Zhang, Review on the graphene based optical fiber chemical and biological sensors. *Sens. Actuator. B: Chem.* **231**, 324–340 (2016)
80. T. Han, A. Nag, S.C. Mukhopadhyay, Y. Xu, *Carbon Nanotubes and Its Gas-Sensing Applications: A Review* (Physical, Sensors and Actuators A, 2019)
81. I.V. Zaporotskova, N.P. Boroznina, Y.N. Parkhomenko, L.V. Kozhitov, Carbon nanotubes: sensor properties. A review. *Modern Electron. Mate.* **2**(4), 95–105 (2016)
82. T.H. da Costa, J.-W. Choi, A flexible two dimensional force sensor using PDMS nanocomposite. *Microelectron. Eng.* **174**, 64–69 (2017)
83. Y. Wang, X. Wang, W. Lu, Q. Yuan, Y. Zheng, B. Yao, A thin film polyethylene terephthalate (PET) electrochemical sensor for detection of glucose in sweat. *Talanta* (2019)
84. M. Akiyama et al., Flexible piezoelectric pressure sensors using oriented aluminum nitride thin films prepared on polyethylene terephthalate films. *J. Appl. Phys.* **100**(11), 114318 (2006)
85. G. Zhou et al., Highly sensitive wearable textile-based humidity sensor made of high-strength, single-walled carbon nanotube/Poly (vinyl alcohol) Filaments. *ACS Appl. Mater. Interfaces.* **9**(5), 4788–4797 (2017)
86. Z.C. Kennedy et al., 3D-printed poly (vinylidene fluoride)/carbon nanotube composites as a tunable, low-cost chemical vapour sensing platform. *Nanoscale* **9**(17), 5458–5466 (2017)

Fabrication of Interdigital Electrodes for Monolithic Biosensing



Nireekshan Kumar Sodavaram and S. C. Mukhopadhyay

Abstract Interdigital electrodes/contacts (IDCs) based sensors are widely used in a variety of chemical and biological sensors, which presents promising advantages such as high sensitivity, low electron mobility, enhanced gate conductivity and increased signal to noise ratio. In particular, interdigitating (or interlocking) the electrodes can be valuable for organic field-effect transistors (OFET) designed using conducting polymers and peptides as semiconducting material. The current chapter discusses the finite-element numerical modelling along with the design and fabrication of IDC-based OFETs.

1 Introduction

An organic field-effect transistor (OFET) hold great potential in various applications such as the detection of cell growth, bacteria [1, 2], toxins [3], disease progression, etc. The methods available for the fabrication include electrochemical, electrolyte gated [4] and bioinspired peptide-based thin-film nanostructures [5]. The structure of an OFET is almost similar to a normal metal-oxide thin-film transistor but fabricated via solution processing of organic semiconducting materials.

Over the last few years, polythiophenes are the most studied organic semiconductors in the field of OFET. Particularly, pentacene, (13,6-*N*-Sulfinylacetamidopentacene or SAP) and poly(3-hexylthiophene), P3HT, a p-type donor and regioregular semiconducting organic material due to its regular end-end arrangement of the side chain, solubility and efficient π - π stacking of the conjugated backbones [5–7]. Recently, peptide-based nanostructures derived from natural amino acids have also shown excellent semiconducting properties that can be used in the fabrication of OFET [8]. Peptides can self-assemble into ordered nanostructures via non-covalent interactions such as electrostatic interaction, hydrogen bonding, van der Waals interactions and hydrophobic interactions to form fibrous networks [9].

N. K. Sodavaram · S. C. Mukhopadhyay (✉)
School of Engineering, Macquarie University, North Ryde, NSW 2109, Australia
e-mail: Subhas.Mukhopadhyay@mq.edu.au

© The Editor(s) (if applicable) and The Author(s), under exclusive license to Springer Nature Switzerland AG 2021

247

S. C. Mukhopadhyay et al. (eds.), *Interdigital Sensors*, Smart Sensors, Measurement and Instrumentation 36, https://doi.org/10.1007/978-3-030-62684-6_10

At appropriate concentrations, these self-assemble peptides form hydrogels that are biocompatible and has the potential in the fabrication of OFETs for the detection of various toxins and cancerous cell growth inside the human body [10, 11].

In general, an OFET comprises of three major components that include the (1) organic material, insulating layer, and source and drain metal IDC. The insulating layer can be made of a variety of dielectric materials such as silicon dioxide (SiO_2) and aluminium dioxide (Al_2O_3). In contrast to the fabrication of a general metal-oxide-field-effect transistor (MOSFET), the OFET devices are built using a bottom-up approach that begins with the patterning and deposition of IDC on the substrates, solution processing of the organic material and deposition of the solution-processed organic material on the substrate. Figure 1 shows the conceptual diagram of the OFET configuration topologies. Since, OFET fabrication involves the solution processing of the organic semiconductor, which is deposited via spin coating, drop-casting and Langmuir Blodgett method, Backgate (BG) and bottom contact (BC) configuration are more preferred to avoid the contact with the gate or other encapsulation materials thereby circumventing contamination of the organic material [12].

IDC comprises of two interlocking comb-patterned arrays of metallic electrodes connected from a set of interdigitating electrode fingers and offers various benefits to OFETs including high sensitivity, low electron mobility, enhanced gate conductivity and increased signal to noise ratio [13]. In OFET design settings, these electrode fingers are deposited on silicon (Si) substrate with a thin oxide layer, where the bulk Si acts as a back gate.

When the peptide is spin-coated, drop casted or deposited via Langmuir Blodgett method onto the silicon substrate allow it to form a hydrogel, the back gate controls the

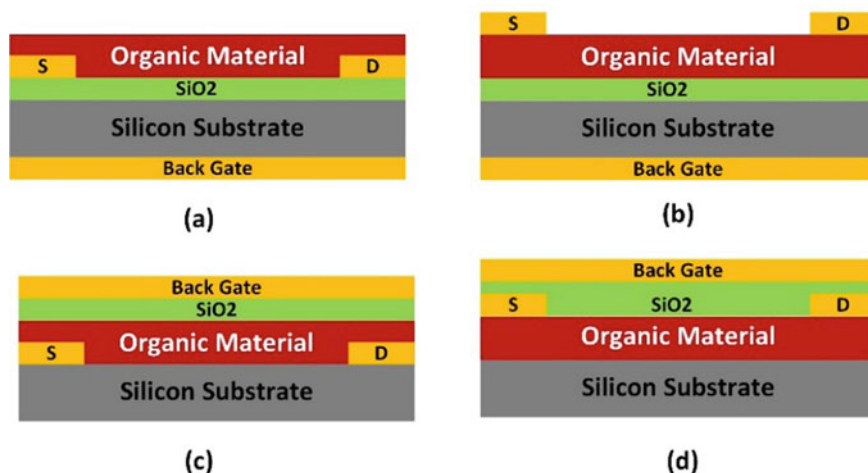


Fig. 1 Conceptual diagram of OFET configuration topologies. **a** The Backgate (BG) and bottom contact (BC), **b** Backgate (BG) and top contact (TC), **c** top gate (TG) and bottom contact (BC), **d** top gate (TG) and top contact (TC)

channel between the IDC forming the basis of metal-oxide-silicon (MOS) capacitor. The principle of operation depends on the electrodynamics of the two parallel plate capacitors (bulk Si at the bottom and the conducting polymer at the top). IDCs were the source and drain patterns initially used in MOS field-effect transistors (FET) to achieve a better width-to-length ratio with the limited layout space [14]. The device structure of the first organic light-emitting field-effect transistor (OLET) also comprised of interdigital source and drain electrodes [15]. There is a wealth of literature supporting the design and fabrication of IDC-based OFETs [16–23]. M.M Maters et al. investigated two solution-processed IDC-based OFETs (pentacene and PTV) for gate-voltage and temperature dependence of the mobility of (amorphous) organic transistors [24]. Supachai Ritjareonwattu et al. fabricated an ion-sensitive IDC-based OFET using P3HT as the semiconductive layer and PMMA as the gate insulator [25]. Akram R. Nasser designed, fabricated and reported on a porous silicon p-type IDC-based extended gate OFET for pH sensing [26]. Francesca Leonardi et al. fabricated an IDC based electrolyte gated OFETs (DB-TTF:PS blend and deposited by BAMS) using a low-cost technique compatible with roll-to-roll processes [27]. Stefano Casalini described an IDC potentiometric sensor based on electrolyte gate OFETs for dopamine detection [28].

2 Modelling of OFET with IDC in the Channel

Field-effect is a phenomenon which propels the operation of a conventional OFET and is composed of three terminals, the gate, the drain and the source. The voltage applied to the drain assists in the charge injection in the channel. When a voltage is applied to the back gate, a thin charge layer occurs between the source and drain and the current starts to flow. The variation in the magnitude of the current flowing between the source and drain can be controlled by varying the voltage applied to the source and drain contacts [29] (Fig. 2).

Numerical system modelling can aid in the optimization of initial design models. Over the last few years, computer-aided design (TCAD) based Silva ATLAS 2D finite-element numeric simulator has been widely used to predict OFET electrical behaviour along with internal physical mechanics associated with system operation [29, 30]. As an example, a back gate (BG) and bottom contact (BC) OFET with pentacene as the organic conducting layer is chosen for the finite-element numerical modelling. Figure 3 shows the structure of a pentacene IDC OFET. It was generated using Silvaco's ATLAS to study its electrical characteristics by varying the drain-source voltage (V_{ds}) with a constant gate-source voltage (V_{gs}).

Various standard models such as the drift–diffusion are employed by the Silvaco's ATLAS for modelling the transportation behaviour of charge carriers. The static and dynamic behaviour of IDC-based OFET studied by Poole–Frenkel mobility model of mobility $\mu_{PF} \propto \mu_0(T) \exp(\gamma \sqrt{E})$, where μ_0 is the zero-field mobility and E is the electric field.

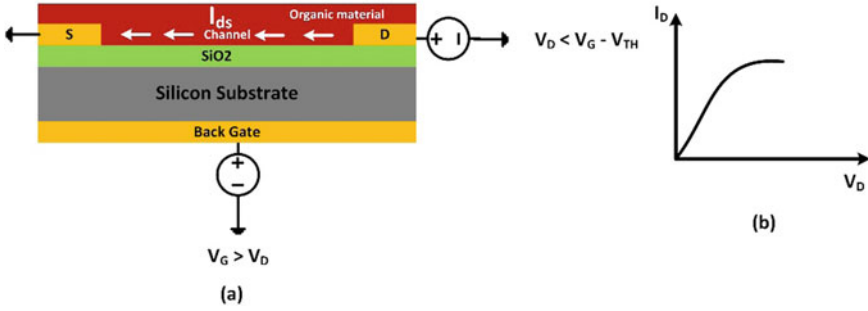


Fig. 2 Conceptual diagram of the OFET device linear mode OPERATION ($V_G < V_D$) and ($V_D < V_G - V_{TH}$)

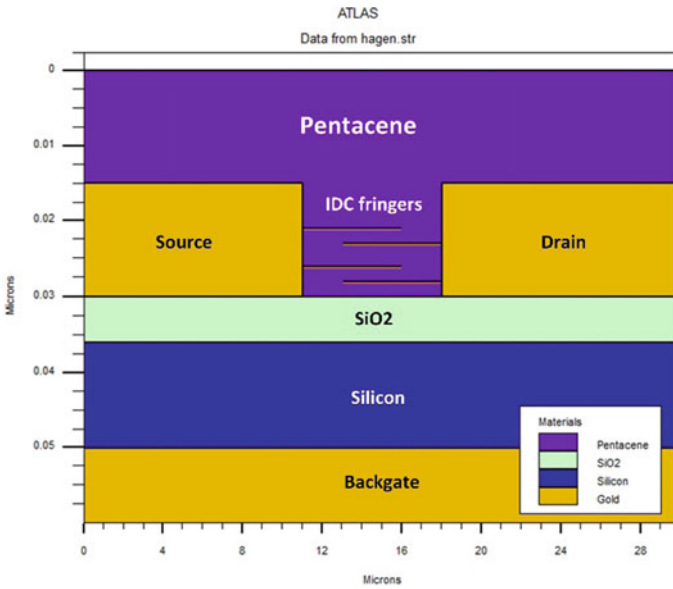


Fig. 3 The Backgate (BG) Bottom Contact (BC) OFET with IDCs between the source and drain electrodes and the pentacene organic semiconducting layer created using Silvaco’s ATLAS

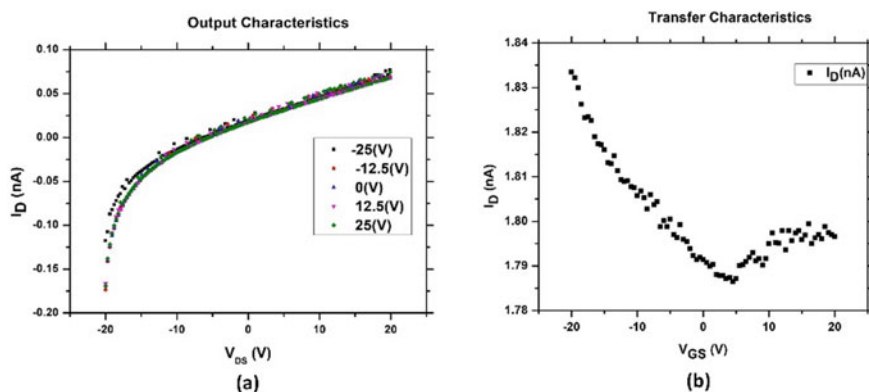
Material Parameters

The IDC-based OFET with pentacene semiconductor layer is designed using the back gate (BG) and bottom contacts (BC) configuration. The designed structure has a channel length of 10 μm and a channel width of 100 μm (Figure). The record of simulation parameters is listed in Table 1.

Figure 4a shows the output characteristics obtained by varying the drain-source voltage (V_{DS}) from -20 V to 20 V keeping the Gate voltage (V_G) at $-25, -12.5,$

Table 1 Finite-element simulation parameters of IDC OFET with pentacene semiconductive layer

2D simulation parameters	Value
Thickness of pentacene	30 nm
The thickness of dielectric (t_{ox})	5.7 nm
The thickness of the gate electrode (t_g)	10 nm
Thickness of S/D electrodes (t_g/t_d)	15 nm
Channel width (W)	100 μm
Channel Length (L)	10 μm
Energy Band Gap	2.8
Electron affinity	2.49 eV
Intrinsic p-type doping	$2 \times 10^{17} \text{ cm}^{-3}$
Work function of Gold (Au) electrode	5 eV
Pool Frenkel factor (betap.pfmob)	$7.758 \times 10^{-8} \text{ eV}(\text{V}/\text{cm})^{1/2}$
Deltap.pfmob	1.7992×10^{-2}
N_{TA}	$2.5 \times 10^{18} \text{ cm}^{-3} \text{ eV}^{-1}$
N_{TD}	$1 \times 10^{18} \text{ cm}^{-3} \text{ eV}^{-1}$
WTA	0.129
WTD	0.5
EGA	0.62
EGD	0.78
WGA	0.15
WGD	0.15

**Fig. 4** **a** The Output characteristics of pentacene OFET. **b** The Transfer characteristics of pentacene OFET

0, 12.5 and 25 V, (b) shows the transfer characteristics obtained by varying the gate-source voltage (V_{GS}) keeping the drain-source voltage constant (V_{DS}).

In addition to studying the device physics of IDC OFET, electrostatics study is also required to analyse the electrical field potential of IDCs [31]. The electrostatic AC/DC module available in COMSOL multiphysics can assist in finite-element-analysis (FEA). The physics interface solves Gauss law for the electric field potential using the scalar electric potential variable along with charge conservation according to Gauss' law for the electric displacement field. Also, it provides an interface for defining the constitutive relation and its associated properties such as the relative permittivity [31, 32]. The ordinary differential equations (ODE) used for solving the electrostatic model of IDCs are given below.

$$E = -\nabla V \tag{1}$$

$$\nabla \cdot (\epsilon_0 \epsilon_r E) = \rho_v \tag{2}$$

Figure 5 shows the three-dimensional (3D) structure of a Gold (Au) IDCs created in COMSOL.

The voltage across the IDC can be mathematically expressed as

$$V_C = I_C Z_P \tag{3}$$

where I_C is the steady current flowing through the MIDE based sensor. The change in voltage across the MIDE can be expressed as

$$\Delta V_C = I_C \Delta Z_P \tag{4}$$

Figure 6 shows the 3D Multislice electric potential plot of the IDC.

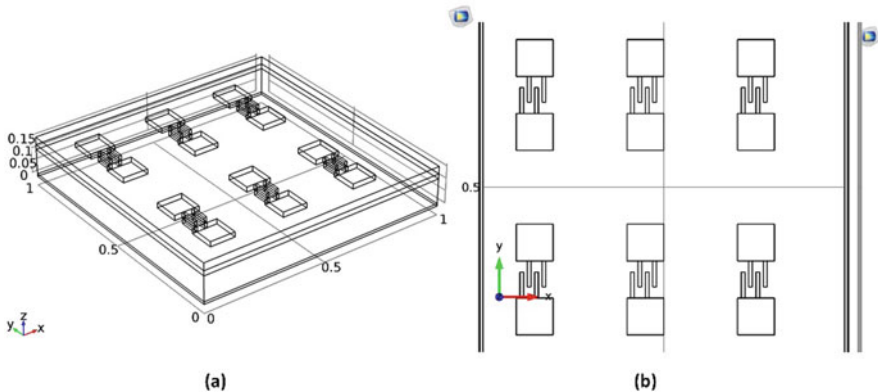


Fig. 5 The structure of IDC based OFET. **a** 3D view showing the substrate, oxide layer, source-drain contacts and IDCs. **b** Top view showing the source-drain contacts with IDC between them

3 Fabrication of OFET with IDC in the Channel

The fabrication process of an OFET involves a host of activities including (1) Wafer cleaning, (2) Dicing of the wafer into small substrate devices, (3) Geometrical patterning of the substrates, (2) Photolithography, (3) Deposition of source-drain IDCs, (4) Preparation of organic material (active layer), (5) Solution processing, (6) Surface treatment of the substrate and IDCs, (6) Deposition of the organic material (spin coating), (7) electrical characterisation of the OFET [33–35].

To avoid the complex substrate patterning and photolithography stages, pre-patterned and evaporated IDC-based OFET chips can be purchased from Ossila (organic electronic scientists) who provide a wide variety of components, equipment and materials for enabling high-level of scientific research [36].

Prefabricated OFET Chips

Ossila has developed high-density, prefabricated OFET chips with thermally evaporated gold (Au) IDCs [37]. Figure 2 shows the geometrical structure of IDC and Table 2 enumerates the individual details and dimensions, of the prefabricated OFET substrate (Fig. 7).

Platinum OFET Chips

Ossila developed a new range of robust and reusable platinum OFET chips patterned using photolithography and sputtering of titanium adhesion layer to provide extremely robust contact [38]. Table 3 enumerates the individual details and dimensions, of the prefabricated OFET substrate.

It allows harsh cleaning procedures using solvent sonification, plasma etching and swabbing. Figures 5 and 8.

Interdigitated ITO Substrates for OFET and Biosensing

Ossila pre-patterned Indium Tin Oxide (ITO) OFET and sensing substrates consisting of interdigitated fingers to act as the source and drain electrodes. The substrate is made of high-quality soda-lime float glass with a 20 nm coating of SiO₂. The transparent

Table 2 The geometrical details of the interdigitated electrodes 18 mm × 50 μm constant channel length substrate (S233)

Geometry	Interdigitated
Arrangement	20 identical OFETs
Channel width	18 mm
Channel length	50 μm

Table 3 The geometrical details of the interdigitated electrodes 22.6 × 5 μm constant channel length substrate (S411)

Geometry	Interdigitated
Arrangement	20 identical OFETs
Channel width	22.6 mm
Channel length	5 μm

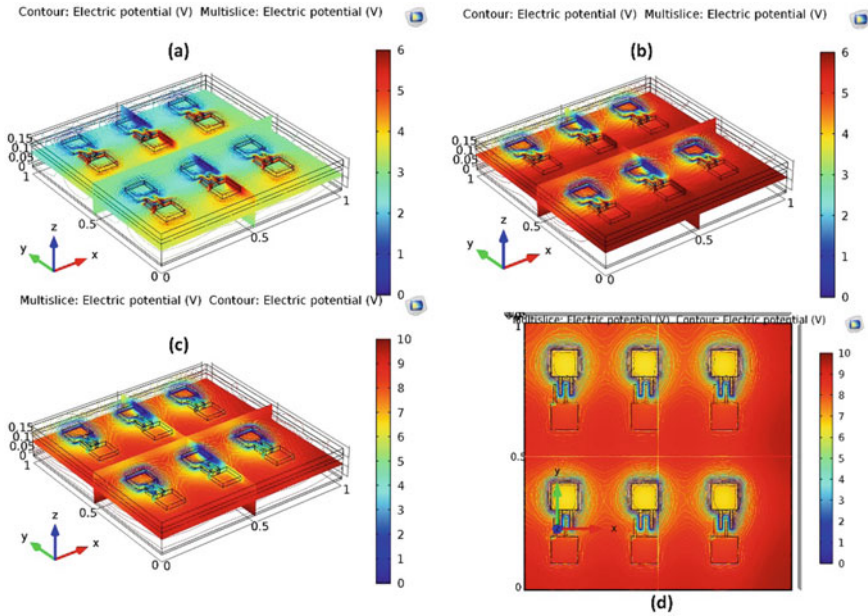


Fig. 6 3D Multislice plot of IDC based OFET

nature of the ITO supports optoelectronic experiments including photoconductivity, photo-induced doping-based sensing. OFET can be fabricated by simply depositing the organic material (semiconductor) on the purchased ITO substrate [39].

3.1 Wafer Cleaning and Back Gate Deposition

The fabrication of OFET always emanates with the choice of the wafer. A wide range of substrate wafers are used in the fabrication including silicon, polyimide (Kapton), flexible polymeric substrates like the indium tin oxide coated polyethylene terephthalate (ITO coated PET), etc. The OFETs are commonly fabricated at the device level with a back gate (BG) and bottom contact (BC) configuration. Therefore, the wafer needs a back gate deposition followed by dicing before the actual fabrication commences. The process involves (a) immersing the wafer into acetone followed by rinsing in IPA, (2) protection of smooth surface side using a thin layer of photoresist and PDMS, (3) Gold evaporation on the rough surface, (4) Dicing of the wafer into small substrates. Figure 9a shows the silicon wafer protected with a thin layer of photoresist and PDMS. The protection is achieved by spin coating the AZ1518 photoresist and polydimethylsiloxane (PDMS) solution 10:1 with the curing agent (b) shows the wafer with Chrome(Cr)/Gold(Au) back gate. The back gate is achieved by thermal evaporation of Cr/Au electrode using Angstrom thermal evaporator.

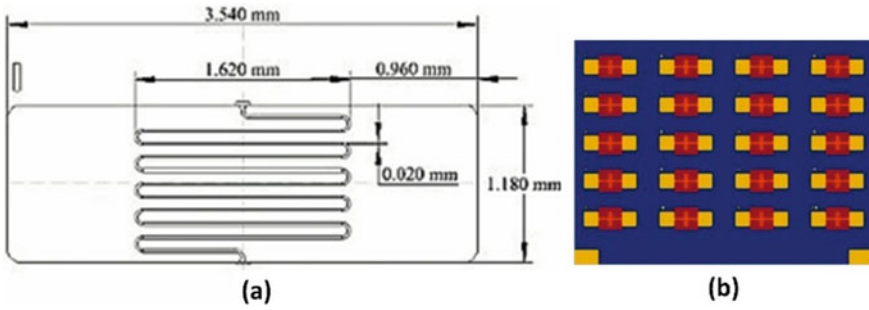


Fig. 7 The photograph of prefabricated OFET chips. **a** the geometry of the interdigitated electrodes, **b** top view of the chip. Taken from the Ossila website [37]

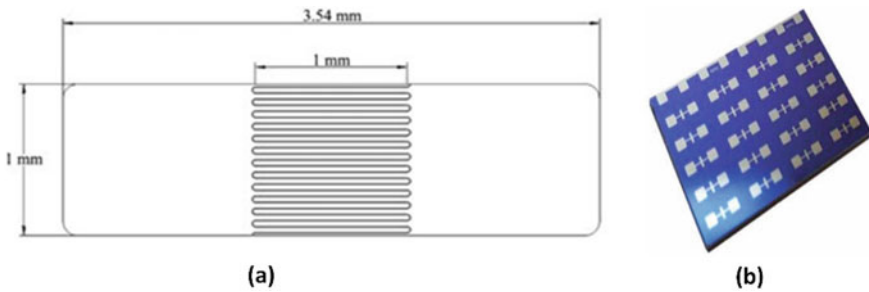


Fig. 8 The photograph of the platinum OFET chips, **a** the geometry of the interdigitated electrodes, **b** the top view of the chip. Taken from ossila website [38]

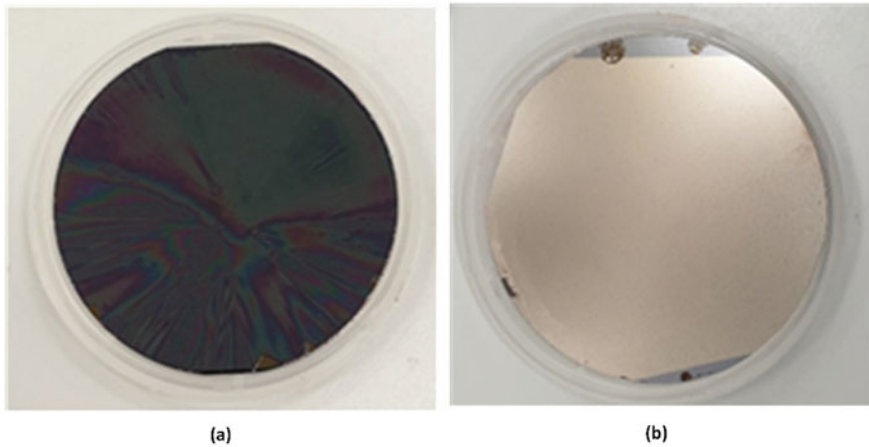
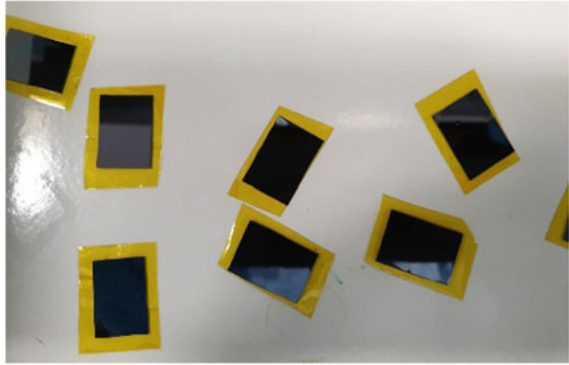


Fig. 9 **a** The photograph of a silicon wafer coated with a thin layer of AZ1518 photoresist and PDMS; **b** back gated silicon wafer via thermal evaporation of chrome (Cr)/Gold (Au)

Fig. 10 The photograph of silicon substrates after dicing



3.2 *Wafer Dicing*

Wafer dicing is a process of cutting thin silicon wafers into small substrates that involve mechanical sawing using a laser or a diamond scriber. Figure 10 shows the diced substrates [40].

3.3 *Photomask Design and Patterning*

Geometrical patterning of a substrate is an essential part of fabricating OFET that helps in the lithography and deposition stages of metal IDCs. The patterning of substrates can be realised by designing a custom-made photomask, photolithography and thermal evaporation.

Patterning via Custom Photomask

Photomasking is a process, where a computer-aided geometry is transferred to a thin layer of fused silica substrate (photomask). The standard photomasks use chrome as the absorption material. The transparent image developed on the photomask is the master template and is transferred onto a substrate via contact mask aligner (MJB3). The custom photomask would be valuable for applications that require specific geometrical and spacing (length and width) between the IDC source and drains.

A custom photomask can be designed using the layout editor software [41]. The photomask geometrical design considerations depend on the various parameters, which include wafer size, die size, device minimum feature size, layout grid, manufacturing grid, floor planning, etc. Figure 11 shows the mask of the designed source-drain and IDCs using the layout editor software.

Almost all the layout editors enable to export the mask pattern to GDSII file format which will be needed for developing a chrome or glass-based photomask.



Fig. 11 The source-drain and IDC mask designed using the layout editor

3.4 OFET Device Fabrication using Photolithography

Photolithography (aka optical lithography) is a process that involves the transferring of geometric patterns onto the substrates using a custom-designed photomask to a light-sensitive chemical photoresist on a diced device substrate. The general process includes substrate cleaning, Soft baking, photoresist deposition, thermal annealing, mask aligning, exposure and developing.

Substrate Cleaning

To obtain a good yield in the fabrication of OFET devices, initial substrate cleaning is a mandatory step, which helps in getting rid of organic residues on the surface of the substrate. Table 4 lists the cleaning procedure of silicon substrates.

Applying Photoresist

The photoresist is a light-sensitive material that varies its chemical and physical properties when exposed to the light. Photoresist also assists in transferring the geometrical pattern onto the diced device substrates. To obtain good evaporation of a metal IDC, it is important to optimise the application of photoresist. AZ 1518 and AZ P4330 are more frequently employed in the photolithography process.

Table 4 The cleaning process protocol

Procedure	Time	Process
Cleaning 1	1 min	Sonication in acetone
Cleaning 2	1 min	Sonication in IPA
Cleaning 3	5 min	Immersion in IPA
Blow-drying	Few minutes	Compressed gas

Table 5 The process parameters of the spin coating of AZ1518 photoresist

Process		AZ 1518
Spin coating	Speed (RPM)	4000
	Acceleration (RPM/s)	5800
	Time (s)	60

Spin Coating

Spin coating is the most common technique for most of the photoresists. The parameters that are vital in achieving good photolithography include spin speed and photoresist film thickness. The spin coating process should be able to dispense right amount on to the surface of the substrate and consists of four steps: (1) Applying the resist to the substrate, (2) Acceleration to the desired RPM, (3) Spinning at a constant RPM and, (4) Deceleration. Table 5 lists the recommended process parameters for the spin coating of AZ 1518 photoresist.

Soft Baking

The thin layer of photoresist obtained after spin coating contains some residual solvents that may introduce some built-in stresses caused by the shear forces during the spin coating process. Stress in the photoresist layer significantly impairs the quality of the pattern transfer during mask aligning and developing stages. To remove the residual solvents, a soft baking step is involved before the mask aligning and exposure. Prebaking ensures that the resist film has uniform properties both across the wafer and from wafer to wafer in a lot. Table 6 lists the parameters for the soft baking process.

Mask Alignment and Exposure

In the mask alignment stage (SUSS MJB3 mask aligner), the actual pattern transfer is transferred from the photomask to the photoresist coated substrate by the polymerisation of the selected areas of photo-resist. This is achieved by repeatedly aligning the mask to a pattern and exposing the selected area of photo resist-substrate to ultraviolet light through the mask. As per the procedure, the custom photomask should first be loaded into the machine. Then the substrate must be placed and glued on to the chuck. At this point, the substrate must be moved up to get in contact with the mask by manoeuvring the contact lever counterclockwise until the contact light on the front panel illuminates. When a satisfactory contact alignment has been achieved, the exposure time must be set to initiate the exposure.

The important parameters that help to achieve better IDCs on the substrate are the contact mode and exposure time. The exposure time can be calculated by the

Table 6 The parameters for the soft baking process after spin coating of AZ1518 photoresist

Process		AZ 1518
Soft baking	Temperature	100 °C
	Time (s)	180

Table 7 Process parameters for mask alignment and pattern transfer

Process		AZ1 1518
Mask alignment	Contact	Tight contact between the photomask and the substrate (as close as possible for thin structures)
	Exposure time (s)	90

following expression

$$Exposure\ time(s) = \frac{Photoresist\ specific\ dose\ (\frac{mJ}{cm^2})}{UV\ light\ intensity\ (\frac{mW}{cm^2})} \tag{5}$$

where the photoresist specific dose is normally provided by the photoresist developers and UV light intensity is calibrated on SUSS MJB3 mask aligner. The table lists the optimised mask alignment and exposure parameters. Table 7 shows the process parameters for mask alignment.

Development

After the geometrical patterns are transferred to the photoresist that is applied to the substrate, it needs to be developed to produce the final three-dimensional pattern structures. The developing process is the most important step and ascertains the final the quality of IDC metal evaporation or deposition. AZ 351 B is the general; purpose developer used in the development stage. The developed needs to be diluted with De ionised (DI) water in 1:4 ratio. The process involved in the developing includes submerging each substrate in the diluted developer solution and agitating for 45 s followed by submerging and agitation in DI water for 60 s. After the structures are visible clearly, blow-dry the substrates using compressed air. Table 8 lists the process parameters for developing three-dimensional pattern structures.

Inspection

To determine the quality of the transfer, from the photomask image to the three-dimensional structures, an optical microscope is employed and inspected at 40 to 100x. The pattern structures are inspected for (1) underexposure, where the pattern is incompletely transferred, (2) overexposure, where the features formed are wider and larger, (3) overdevelopment, where too much photoresist has been removed from the edges. If the quality of the three-dimensional structures is of good quality,

Table 8 Process parameters for the development after pattern transfer

Process		AZ1 1518
Development	AZ 351 developer in DI water (1:4) agitation time (s)	45
	DI water agitation time	60
	Blow-drying	Nitrogen compressed air

the substrates must be prepared for loading into thermal evaporator for metal IDC deposition. Figures 12 and 13 shows one of the source-drain electrodes and 3 μm channel.

Thermal Evaporation (Deposition) of IDC

In general, the thermal evaporation is realized using Angstrom Engineering thermal and electron beam evaporator. The thermal evaporation is conducted in a vacuum chamber and the chamber is usually pumped down to a base pressure of 2×10^{-6} mbar. After the chamber reaches the base pressure, the substrates are loaded onto the substrate holder. A chromium adhesion layer and gold (Au) crystals are loaded on to the two boats inside the chamber. The thickness achievable via thermal evaporation include 5 nm chromium and 50 nm gold.

Lift-Off

In the thermal evaporation, the Cr/Au metal is deposited all over the substrate and only desired patterns of IDC with channels are needed. There Lift-off process is employed to release the final IDC structure via a wet etching process. In general, acetone is used as the solvent for lift-off. The procedure involves soaking the substrates in acetone for thirty minutes followed by slight agitation or sonification for 30 s.

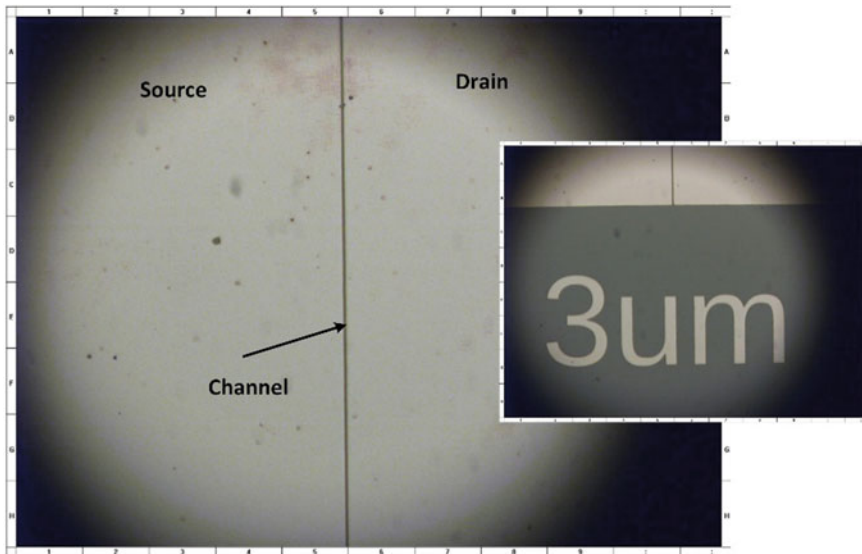
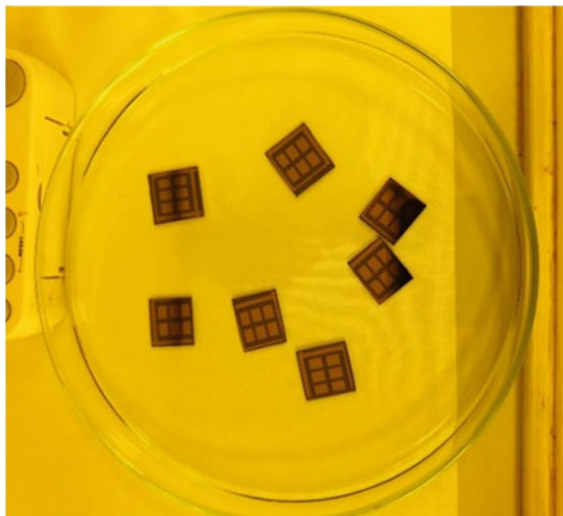


Fig. 12 The image of a 3 μm channel on OFET showing the source-drain electrodes

Fig. 13 The image of silicon substrates after the lift-off process



3.5 Solution Processing and Deposition of the Organic Material (P3HT)

Before, the deposition (spin coating) of the organic material, surface treatment is essential for improving the charge transport in the organic material that occurs in the dew monolayers near the interface between the organic material and oxide layer. Also, molecular parameters of the organic material must be modified by controlling the regioregularity, molecular weight, side-chain length and doping level along with circumventing the contact resistance that impairs the OFET performance. Self-assembled monolayers (SAMs) are good candidates for effective surface treatment due to their high-packing density, being only a few nm thick and allowing interface control with end-functional groups. Among various SAMs with different binding groups, such as carboxyl groups, thiols and silanes, phosphonic acid self-assembled monolayers (PA-SAMs) have attracted attention due to readily assembling on activated metal oxides because their reaction is not limited by the contents of surface hydroxyl groups and supplies their hydroxyl moieties [42].

Surface Treatment

The first surface modification is the 2,3,4,5,6-pentafluorothiophenol (PFBT) treatment of Cr/Au IDCs, where the substrates are plasma-treated using oxygen for 30 s at 100 W followed by immersing Substrates immersed in 2.5 mMol/l solution of PFBT in IPA at room temperature [43].

The second surface modification is the Octadecyltrichlorosilane (OTS) treatment of oxide (dielectric) layer [44]. The OTS surface treatment is steered inside a nitrogen glove box and the process involves the following.

- (1) A solution of OTS (25 μL) is mixed in cyclohexane (anhydrous grade 1 mil).
- (2) 50 ml of cyclohexane is poured into an annealing beaker along with adding OTS solution prepared earlier to obtain a final solution of 60 ml with OTS at a concentration of 1 mMol/l.
- (3) The substrates are immersed in the above solution for 20 min followed by rinsing in cyclohexane and blow-dry.

Solution Preparation

As an example, pentacene has been used as the organic semiconducting material and the process is compatible with most of the polymeric materials. The following is the process for preparing the pentacene solution [45, 46].

- (1) A 5 mg/ml 13,6-*N*-sulfinylacetamidopentacene precursor is dissolved in a vial consisting of anhydrous chloroform: Trichlorobenzene (99:1).
- (2) The vial is placed on a hot plate (70 °C) with a stirrer bar for 30 min.
- (3) The solution is allowed to cooled down to room temperature and then filtered with a 0.45 μm PTFE (hydrophobic) filter.
- (4) The solution is stored overnight on a hot plate at 30 °C to prevent excessive aggregation of the pentacene molecules.

Spin Coating

The pentacene solution is then deposited onto the substrate via spin coating and drop-casting inside a nitrogen glovebox.

- (1) 30 μl pentacene solution is dropped in the middle of the substrate loaded onto the spin coater.
- (2) The substrates are spun at a speed of 1000 RPM for 10 s followed by 2000 RPM for 60 s.
- (3) Substrates annealed at 90 °C for 30 min.

3.6 Electrical Characterisation of OFET

Steady-state drain-source voltage (V_{ds}) and drain current (I_{D}) measurements were performed at room temperature using an Agilent 4156 C parametric analyzer with two source-measure units. All measurements were performed at a scan rate of 1 V/s under a nitrogen glovebox atmosphere with <1 ppm water and oxygen content.

Figures 14 and 15 shows the output characteristics of the pentacene OFET with IDCs in the channel. The output characteristics of the physical device almost correlate to the I-V characteristics of the OFET device model from the TCAD Silvaco's ATLAS simulator. Besides, the IDCs in the channel has assisted in improving the current characteristics of the physical device, which in turn may be valuable in ameliorating the OFET device performance, particularly when the organic material is a poor semiconductor.

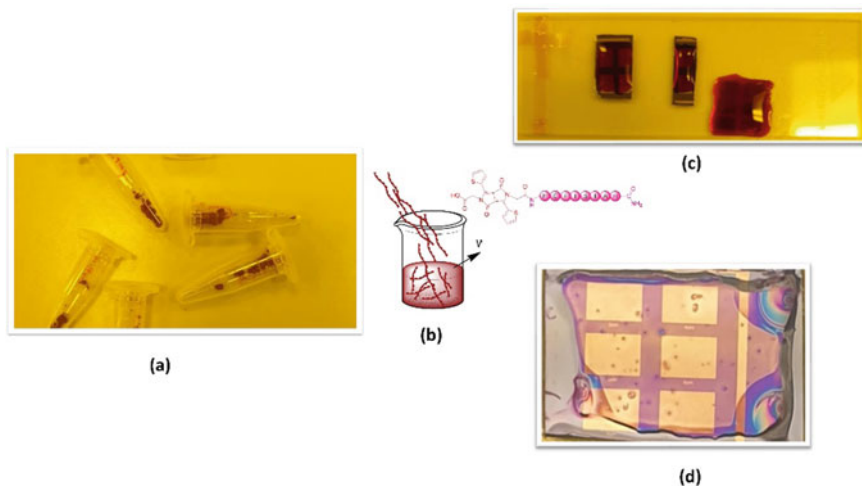


Fig. 14 The collage of images showing the process of making solution-processed OFET, **a** the organic material in powdered form, **b** solution processing, **c** drop-casted films, **d** spin-coated films

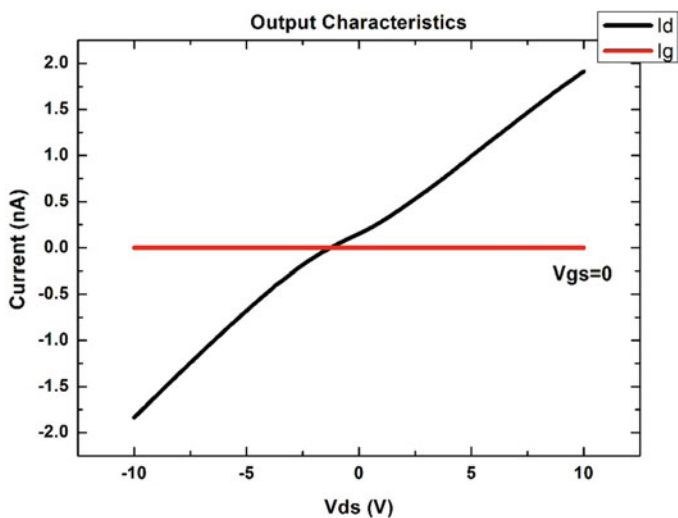


Fig. 15 The output characteristic of the pentacene OFET from Agilent 4156 C semiconductor parametric analyser

4 Conclusion and Future Possibilities

The chapter has described the finite element modelling and the fabrication of organic field-effect transistor (OFET) with interdigital electrodes/contacts in the channel for monolithic biosensing. As an example, pentacene (13,6-*N*-sulfinylacetamidopentacene precursor) has been chosen as an organic semiconductor for fabrication purposes. The output characteristics of the physical device almost correlate to the I-V characteristics of the OFET device model from the TCAD Silvanco's ATLAS simulator. Besides, the IDCs in the channel has shown to improve the drain current characteristics (I_D) of the device, which would potentially be valuable in the fabrication of peptide-based OFETs. In future, this design procedure can be extended to self-assembled peptide-diketopyrrolopyrrole (TDPP) based OFETs, in particular, peptides inspired by the protein-protein β -interface as they have shown potential to form nano-fibres.

References

1. X. Liu, M. Marrakchi, D. Xu, H. Dong, S. Andreescu, Biosensors based on modularly designed synthetic peptides for recognition, detection and live/dead differentiation of pathogenic bacteria. *Biosens. Bioelectron.* **80**, 9–16 (2016)
2. M.E.E. Alahi, S.C. Mukhopadhyay, Detection methodologies for pathogen and toxins: a review. *Sensors* **17**(8), 1885 (2017)
3. B.D. Malhotra, S. Srivastava, M.A. Ali, C. Singh, Nanomaterial-based biosensors for food toxin detection. *Appl. Biochem. Biotechnol.* **174**(3), 880–896 (2014)
4. L. Kergoat, B. Piro, M. Berggren, G. Horowitz, M.C. Pham, Advances in organic transistor-based biosensors: from organic electrochemical transistors to electrolyte-gated organic field-effect transistors. *Anal. Bioanal. Chem.* **402**(5), 1813–1826 (2012)
5. B. P. Silva Santos, J. J. Rubio Arias, M. de Fátima Vieira Marques, J. G. de Melo Furtado, L. A. Silva, R. A. Simão, Synthesis and characterization of poly (3-Hexylthiophene) for organic solar cells, in *Macromolecular Symposia*, Vol. 383, No. 1 (2019), p. 1700078
6. S. Pretl, M. Kroupa, A. Hamáček, T. Džugan, J. Řeboun, J. Čengery, haracterization of the organic field-effect transistor based on solution-processed P3HT, in *33rd International Spring Seminar on Electronics Technology, ISSE 2010*. (IEEE, 2010), pp. 24–29
7. S.P. Tiwari, W.J. Potscavage Jr., T. Sajoto, S. Barlow, S.R. Marder, B. Kippelen, Pentacene organic field-effect transistors with doped electrode-semiconductor contacts. *Org. Electron.* **11**(5), 860–863 (2010)
8. T. Cipriano, G. Knotts, A. Laudari, R.C. Bianchi, W.A. Alves, S. Guha, Bioinspired peptide nanostructures for organic field-effect transistors. *ACS Appl. Mater. Interfaces.* **6**(23), 21408–21415 (2014)
9. J. Wang, K. Liu, R. Xing, X. Yan, Peptide self-assembly: thermodynamics and kinetics. *Chem. Soc. Rev.* **45**(20), 5589–5604 (2016)
10. J. Chen, X. Zou, Self-assemble peptide biomaterials and their biomedical applications. *Bioactive Mater.* **4**, 120–131 (2019)
11. J. Li, R. Xing, S. Bai, X. Yan, Recent advances of self-assembling peptide-based hydrogels for biomedical applications. *Soft Matter* **15**(8), 1704–1715 (2019)
12. X. Tao, V. Koncar, Textile electronic circuits based on organic fibrous transistors, in *Smart Textiles and their Applications* (Woodhead Publishing, 2016), pp. 569–598

13. Y. Taniike, S. Ikeda, T. Yoshioka, Panasonic Corp. *Biosensor with interdigitated electrodes*. U.S. Patent 7,022,218 (2006)
14. S.Ding, Highly sensitive biosensors with interdigitated electrode arrays (2018)
15. C.F. Liu, X. Liu, W.Y. Lai, W. Huang, Organic light-emitting field-effect transistors: device geometries and fabrication techniques. *Adv. Mater.* **30**(52), 1802466 (2018)
16. A. Hepp, H. Heil, W. Weise, M. Ahles, R. Schmechel, H. von Seggern, Light-emitting field-effect transistor based on a tetracene thin film. *Phys. Rev. Lett.* **91**(15), 157406 (2003)
17. K. Besar, S. Yang, X. Guo, W. Huang, A.M. Rule, P.N. Breyse, I.J. Kymissis, H.E. Katz, Printable ammonia sensor based on organic field effect transistor. *Org. Electron.* **15**(11), 3221–3230 (2014)
18. H.T. Yi, M.M. Payne, J.E. Anthony, V. Podzorov, Ultra-flexible solution-processed organic field-effect transistors. *Nat. Commun.* **3**(1), 1–7 (2012)
19. J. Song, J. Dailey, H. Li, H.J. Jang, L. Russell, P. Zhang, P.C. Searson, J.T.H. Wang, A.D. Everett, H.E. Katz, Influence of bioreceptor layer structure on myelin basic protein detection using organic field effect transistor-based biosensors. *Adv. Func. Mater.* **28**(37), 1802605 (2018)
20. T.T.K. Nguyen, H.V. Tran, T.T. Vu, S. Reisberg, V. Noël, G. Mattana, M.C. Pham, B. Piro, Peptide-modified electrolyte-gated organic field effect transistor. Application to Cu²⁺ detection. *Biosens. Bioelectron.* **127**, 118–125 (2019)
21. B. Anımurbey, Ç. Çakırlar, S.P. Mucur, M. Yasin, S. Berber, Influence of Al₂O₃ nanoparticles incorporation on the dielectric properties of solution processed PVA films for organic field effect transistor applications. *J. Mater. Sci.: Mater. Electron.* **30**(20), 18384–18390 (2019)
22. A. Kösemen, High-performance organic field-effect transistors fabricated with high-k composite polymer gel dielectrics. *J. Electron. Mater.* **48**(12), 7819–7826 (2019)
23. P. P. Cielecki, T. Leissner, M. Ahmadpour, M. Madsen, H. G. Rubahn, J. Fiutowski, J. Kjelstrup-Hansen, Photo-induced and electrical degradation of organic field-effect transistors. *Org. Electron.* 105717 (2020)
24. M. Matters, D.M. De Leeuw, M.J.C.M. Vissenberg, C.M. Hart, P.T. Herwig, T. Geuns, C.M.J. Mutsaers, C.J. Drury, Organic field-effect transistors and all-polymer integrated circuits. *Opt. Mater.* **12**(2–3), 189–197 (1999)
25. S. Ritjareonwattu, Y. Yun, C. Pearson, M.C. Petty, An ion-sensitive organic field-effect transistor incorporating the ionophore valinomycin. *IEEE Sens. J.* **12**(5), 1181–1186 (2011)
26. A.R. Nasser, G.M. Ali, A porous silicon P-type interdigitated extended-gate field effect transistor pH sensor. *Silicon* **11**(4), 2095–2102 (2019)
27. F. Leonardi, S. Casalini, Q. Zhang, S. Galindo, D. Gutiérrez, M. Mas-Torrent, Electrolyte-gated organic field-effect transistor based on a solution sheared organic semiconductor blend. *Adv. Mater.* **28**(46), 10311–10316 (2016)
28. S. Casalini, F. Leonardi, T. Cramer, F. Biscarini, Organic field-effect transistor for label-free dopamine sensing. *Org. Electron.* **14**(1), 156–163 (2013)
29. C.M. Hussain (Ed.), *Handbook of Nanomaterials for Industrial Applications* (Elsevier, 2018)
30. A.D.D. Dwivedi, S.K. Jain, R.D. Dwivedi, S. Dadhich, Numerical simulation and compact modelling of low voltage pentacene based OTFTs. *J. Sci. Adv. Mater. Dev.* **4**(4), 561–567 (2019)
31. B.G. Sonmez, O. Ertop, S. Mutlu, Modelling and realization of a water-gated field effect transistor (WG-FET) using 16-nm-thick Mono-Si film. *Sci. Rep.* **7**(1), 1–8 (2017)
32. L.Q. Jun, G.W. Bin Djaswadi, H.F. Bin Hawari, M.A.B. Zakariya, August. Simulation of interdigitated electrodes (IDEs) geometry using COMSOL multiphysics, in *2018 International Conference on Intelligent and Advanced System (ICIAS)* (IEEE, 2018), pp. 1–6
33. S. MacKay, P. Hermansen, D. Wishart, J. Chen, Simulations of interdigitated electrode interactions with gold nanoparticles for impedance-based biosensing applications. *Sensors* **15**(9), 22192–22208 (2015)
34. T. Minari, C. Liu, M. Kano, K. Tsukagoshi, Controlled self-assembly of organic semiconductors for solution-based fabrication of organic field-effect transistors. *Adv. Mater.* **24**(2), 299–306 (2012)

35. R. Dheepika, P. Mohamed Imran, N.S. Bhuvanesh, S. Nagarajan, Solution-processable unsymmetrical triarylamine: towards high mobility and ON/OFF ratio in bottom-gated OFETs. *Chem. A Eur. J.* **25**(66), 15155–15163 (2019)
36. E.V. Agina, A.S. Sizov, D.S. Anisimov, A.A. Trul, O.V. Borshchev, D.Y. Paraschuk, M.A. Shcherbina, S.N. Chvalun, S.A. Ponomarenko, Thiophene-based monolayer OFETs prepared by Langmuir techniques, in *Organic Field-Effect Transistors XIV; and Organic Sensors and Bioelectronics VIII*, vol. 9568, (International Society for Optics and Photonics, 2015), p. 95680Z
37. V. Kostianovskii, B. Sanyoto, Y.Y. Noh, A facile way to pattern PEDOT: PSS film as an electrode for organic devices. *Org. Electron.* **44**, 99–105 (2017)
38. Prefabricated OFET test chips (High density) Ossila 2020. <https://www.ossila.com/collections/ofet-test-chips>
39. Platinum OFET test chips (high density) Ossila 2020. <https://www.ossila.com/collections/ofet-test-chips>
40. Interdigitated ITO substrates for OFET sensing Ossila 2020 <https://www.ossila.com/collections/ito-ofet-substrates-masks>
41. S.Y. Luo, Z.W. Wang, Studies of chipping mechanisms for dicing silicon wafers. *Int. J. Adv. Manuf. Technol.* **35**(11–12), 1206–1218 (2008)
42. Layout editor <https://layouteditor.com/download?release=20110914>.
43. S. Jang, D. Son, S. Hwang, M. Kang, S.K. Lee, D.Y. Jeon, S. Bae, S.H. Lee, D.S. Lee, T.W. Kim, Hybrid dielectrics composed of Al₂O₃ and phosphonic acid self-assembled monolayers for performance improvement in low voltage organic field-effect transistors. *Nano Convergence* **5**(1), 20 (2018)
44. S. Choi, F.A. Larrain, C.Y. Wang, C. Fuentes-Hernandez, W.F. Chou, B. Kippelen, Self-forming electrode modification in organic field-effect transistors. *J. Mater. Chem. C* **4**(35), 8297–8303 (2016)
45. S. Li, D. Guérin, K. Lmimouni, Improving the performance of OFET by tuning the occurrence of charge transport based on pentacene interaction with SAM functionalized contacts. *Microelectron. Eng.* **195**, 62–67 (2018)
46. M.J. Dong, C.L. Tao, X.H. Zhang, G.P. Ou, F.J. Zhang, Fabrication of pentacene organic field-effect transistors with polyimide gate dielectric layer. *Optoelectron. Lett.* **3**(6), 432–434 (2007)

Interdigital Sensing System for Kidney Health Monitoring



S. N. Prabhu, C. P. Gooneratne, K. A. Hoang, S. C. Mukhopadhyay, A. S. Davidson, and G. Liu

Abstract The kidney diseases are recognized by high levels of serum creatinine and blood urea nitrogen (BUN) caused by deteriorating glomerular ultrafiltration rate. These diseases are a serious problem and can be seen in individuals of any age and sex but significantly in old age populations. There is generally minor or no symptoms of kidney diseases are seen until significant loss of kidney function and/or disease states related to a kidney (renal) malfunction are worsen in individuals. The creatinine and BUN are considered as biomarkers for kidney healthcare. Ultrasound, CT scan, blood test, sedimentation of urine, the output of urine as well as a urinalysis test are standard techniques for measuring the serum electrolytes, serum creatinine, BUN and kidney function levels. Any of these tests are useful in the diagnosis of

S. N. Prabhu (✉)

School of Engineering, Macquarie University, Level 2, 221 (Data Acquisition Room), 9 Wally's Walk (E6A), Sydney, NSW 2109, Australia
e-mail: sumedha.prabhu@hdr.mq.edu.au

C. P. Gooneratne

Drilling Technology, Saudi Aramco, Dhahran, Saudi Arabia
e-mail: chinthaka.gooneratne@gmail.com

K. A. Hoang

School of Engineering, Macquarie University, 9 Wally's Walk (E6A), Sydney, NSW 2109, Australia
e-mail: ky-anh.hoang@students.mq.edu.au

S. C. Mukhopadhyay

School of Engineering, Macquarie University, Level 3, 313, 9 Wally's Walk (E6A), Sydney, NSW 2109, Australia
e-mail: subhas.mukhopadhyay@mq.edu.au

A. S. Davidson

Macquarie University Clinic, Macquarie University, 2 Technology Place, Sydney, NSW 2109, Australia
e-mail: andrew.davidson@mq.edu.au

G. Liu

Faculty of Engineering, Graduate School of Biomedical Engineering, University of New South Wales, Kensington, NSW 2052, Australia
e-mail: guozhen.liu@unsw.edu.au

© The Editor(s) (if applicable) and The Author(s), under exclusive license to Springer Nature Switzerland AG 2021

267

S. C. Mukhopadhyay et al. (eds.), *Interdigital Sensors*, Smart Sensors, Measurement and Instrumentation 36, https://doi.org/10.1007/978-3-030-62684-6_11

kidney diseases and their progression in each stage. They help in treatment methods and decisions associated with drug regimens. These techniques are also helpful in understanding the degree of improvement/declining status in diseased kidney healthcare after medical treatment. Since the noticeable changes in kidney disease stages (maintenance/progression/improvement) are very slow, therefore most of the drugs which are prescribed are useful in long term care of kidney health than that of faster healing of diseased stage. Due to the slower rate of kidney healthcare progression, the ultrasound and/or CT scan studies are needed after longer time intervals; where a medical practitioner can be able to distinguish the difference between previous and current kidney health status. Although the daily formation of the creatinine and BUN are constant, the noticeable changes in creatinine and BUN are visible in two weeks. That is why the detection and quantifying of biomarkers such as creatinine and BUN are of high significance. The level of BUN is also linked with other organ disease conditions but the rise in serum creatinine levels is specifically linked with kidney disease. Therefore, serum creatinine levels are highly useful with the ultrasound and/or CT scan to identify loss of kidney function and kidneys' subsequent response to the drug regimens. Frequent visits to pathology labs are necessary but also inconvenient for kidney patients. Currently, there is the unavailability of techniques to detect levels of creatinine at home. Although blood testing is standardised for measurement of serum creatinine, it is invasive as it involves venepuncture. This method is time consuming, costly, requires pathology experts in venepuncture as well as for performing sample analysis, and the results are complicated for a patient to understand from home. Therefore, it is necessary to develop a home-based electrochemical biosensing detection system which is rapid, cost-effective, easily operable, interpretation and internet friendly Point-of-Care (PoC) diagnostic device sensing system. The PoC device can establish a trustable domestic measuring profile for kidney disease patients. The device can be utilised as a prognostic as well as a prophylactic care modem at a patient understanding level, that indicates the frequent minor changes in levels of serum creatinine thus helpful in kidney healthcare. This will help as an indicator to the patient and a medical practitioner in detecting changes in serum creatinine at early-stage thus helpful in better revival. In current work, we would like to describe our research on the development of highly specific polymer for the detection of creatinine from heat-inactivated serum samples and the making of electrochemical impedance spectroscopy (EIS)-based sensing system. The Molecularly Imprinted Polymer (MIP)-EIS combined system is further developed to make a home operable and internet connectable PoC diagnostic device and it has been cross-verified by using commercially developed Creatinine Colorimetric Assay Kit.

1 Introduction

The structure and functioning of kidneys, renal health along with the significance of creatinine levels are explained below in Sect. 2. Currently available methods for management of creatinine levels in humans and their margins are discussed in Sect. 3.

Why there is a specific need for home-based kidney healthcare monitoring of patients by doctors over the internet is also discussed in Sect. 3.

2 Structure and Functioning of Kidneys, Renal Health with Creatinine Levels

The human kidneys are two organs having a bean-like structural shape and located on the right and left side of the body inside retroperitoneal space. Figure 1 shows an anterior, posterior and superior transverse view of the human kidneys. The kidneys filter blood plasma, thus removing the waste products of metabolism as well as toxic substances from the body followed by excreting them from the urine. This process also involves the maintenance of constant composition and volume of the blood, called homeostasis.

During this process, blood enters the kidney via the renal artery which further divides into smaller arteries. The arteries further divide into arterioles. The arterioles come in contact with the structural and functional units of the kidneys called nephrons. Figure 2 depicts the ultrastructure of the nephron. The nephrons help in the process of filtration of blood and formation of urine. The filtered blood then passes through venules, followed by several large veins and finally leaves the kidney via the renal vein. The collection of formed urine is done within collecting ducts and further it goes out of the kidney with the help of ureters. The single kidney consists of about a million number of nephrons. A nephron has two parts, i.e. a Bowman's capsule as well as a renal tubule. The renal tubules of numerous nephrons join to a shared collecting duct. In total three steps are involved in the urine formation. The glomerular ultrafiltration takes place within the Bowman's capsule. The tubular reabsorption and the secretion take place within the renal tubule. The collecting duct helps in the maintenance of the level of water inside the body. Blood arrives the Bowman's capsule through the afferent arteriole. Then it passes through a bundle of a network of capillaries called the glomerulus. Later it leaves the Bowman's capsule through the efferent arteriole. The lumen size of afferent arteriole is noticeably higher than that of the efferent arteriole. This creates a flow of blood with big size inlet and a smaller size outlet resulting in the hydrostatic blood pressure within a bunch of capillaries. It is significantly higher than normal blood pressure. The osmotic, as well as hydrostatic pressures within the Bowman's capsule, allows passing of water and solutes from blood plasma via an ultrafiltration membrane inside the Bowman's capsule space of nephrons. The filtration membrane performances are similar to a sieve permitting specifically passing of small molecules. Which includes water, glucose, amino acids, inorganic ions, and various metabolic waste products including BUN as well as creatinine. Along with ultrafiltration, the kidney has other important functions. Kidney converts a precursor of vitamin D in its active form, the calcitriol. It also synthesizes the hormones erythropoietin and renin. The fluid passed from nephrons is called as a glomerular ultrafiltrate.

Urinary System

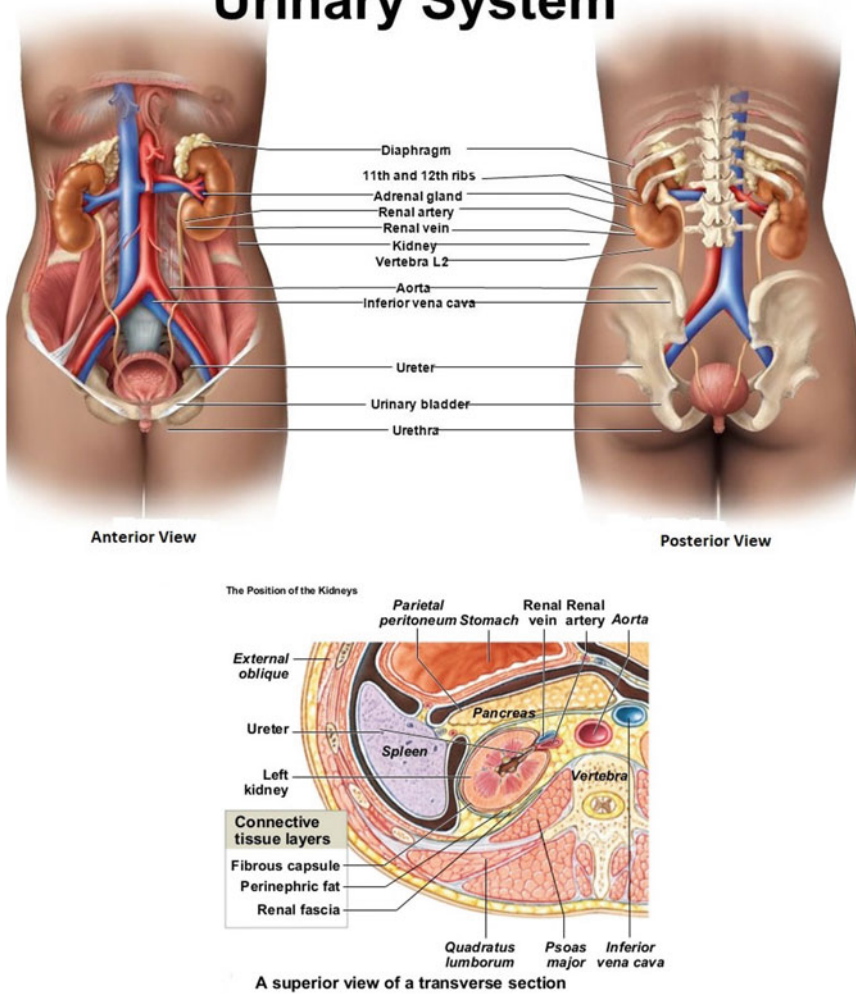


Fig. 1 An anterior, posterior and superior view of a transverse section of human kidneys [1, 2]

The net quantity of produced filtrate every minute is called a glomerular filtration rate. The glomerular filtration rate is constant via multiple feedback mechanisms within the kidneys called renal autoregulation. The glomerular filtration rate is also under freedom and control of hormones and it is usually accomplished with the help of rhythmic constriction and dilation of the afferent arteriole. It also causes the fall and rise of glomerular blood pressure. A healthy person generates about 150–180 L of total glomerular filtrate. Just 1% of this produced filtrate is considered excreted urine whereas the remaining 99% is reabsorbed in the blood as the filtrate passes from the lengthy renal tubule. It is due to the efferent arteriole. Just after leaving

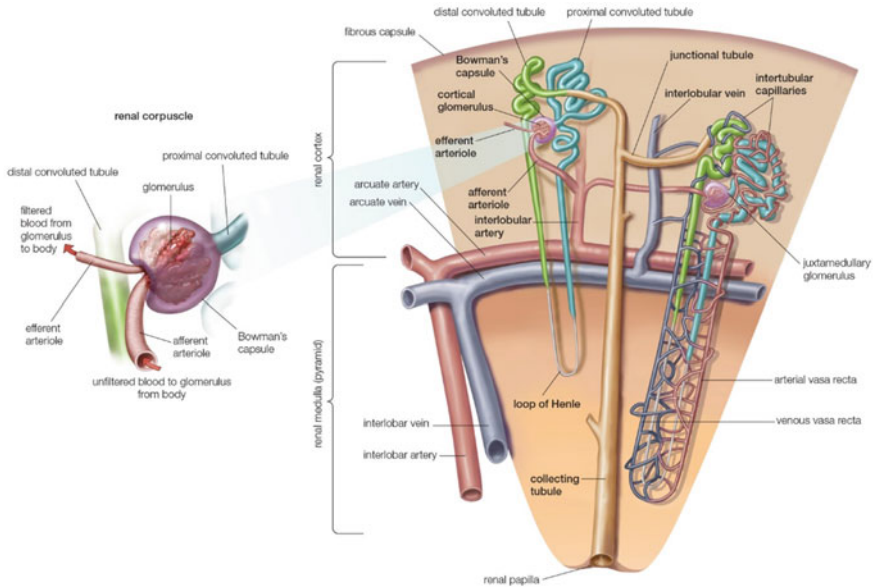


Fig. 2 An ultrastructure of the nephron [3]

the Bowman’s capsule, the filtrate passes through the branches which protrude out from the network of capillaries, called peritubular capillaries, bordering the renal tubule. The initial part of renal tubule called the proximal convoluted tubule reabsorbs around the two-third amount of the filtrate. During this, water and solutes are transferred via the epithelial cells which make the lining of the tubule inside the extra tubular space. Further, it is taken care of by the peritubular capillaries. The absorption of sodium is utmost significant because it generates an osmotic pressure which allows water as well as an electrical gradient that passes negatively charged ions. The levels of sodium within the epithelial cells are maintained at lower levels because of the sodium–potassium pumps which continually pump sodium ions outside within the extracellular space. This phenomenon generates a concentration gradient which provides the diffusion of sodium from the tubular fluid inside the cells. The absorption of sodium ions is performed by symport proteins. They also bind glucose molecules and few other solutes. Almost all glucose, as well as amino acid molecules, are reabsorbed inside the blood. Around half of nitrogenous waste products are reabsorbed into the bloodstream.

The kidneys reduce levels of metabolic wastes inside the blood to a homeostatic level but do not completely remove their presence from the body. Few reabsorptions are also taken care of by the paracellular route via the tight junctions within the epithelial cells. Simultaneously, the tubular secretion wherein the further waste products such as drugs and other solutes leave the bloodstream to join the tubular fluid also takes place. The reabsorption and secretion processes take place within the Loop of Henle, a nephron loop, as well as also inside the distal convoluted tubule. These parts

of the renal tubule have few more vital functions. The key function of the Loop of Henle is to generate and preserve an osmolarity gradient within the medulla region of the kidney that permits the collecting ducts in the concentration of the urine at the further phase. The ascending limb of the Loop of Henle dynamically pumps sodium ions out thus creating the medulla region of the kidney into the salty region. The descending limb of the Loop of Henle is permeable for water but significantly not so permeable for sodium ions. Water leaves the tubule by the process of osmosis. Later the remaining filtrate becomes increasingly concentrated as it further moves towards the base level. The ascending limb of the Loop of Henle is permeable to ions but not with the molecules of water. Due to this, the concentrated filtrate loses sodium ions as it moves upward and converts into increasingly and gradually diluted at the topmost region of the Loop of Henle. The medulla region is in balance with the Loop of Henle and it also has the identical gradient of salinity, i.e. salted at the lowest region. Reabsorption, as well as the process of secretion within distal convoluted tubule, are underneath the regulation of several hormones. This one is kidneys' response towards the needs of the body and regulations in the urine composition as per necessity. The collecting duct collects tubular fluid from numerous nephrons. The key functioning of the collecting duct is concentrating the urine as well as conservation of water inside the body. This is made probable because of the gradient of osmolarity formed through the Loop of Henle. As filtrate gets salty within deeper regions of the medulla, the filtrate lacks the amount of water content as it passes further downwards towards the collecting duct. The hormones also control the collecting duct. Under hormonal control, it can regulate the quantity of reabsorbed water according to the hydration status of the body. During the time of dehydration, additional water is reabsorbed into the blood and the minor amount of water is excreted via the formation of concentrated urine and vice versa [4].

Acute kidney injury (AKI), is also acknowledged as acute renal failure. It is an unexpected, speedy loss of functioning of the kidney, characteristically within few days/weeks. The kidneys function is to filter blood plasma, removal of metabolic wastes products through urine. Meanwhile, it also adjusts the composition of urine for keeping the accurate balance of numerous blood components. In AKI, metabolic wastes saturate and fluid, electrolyte as well as acid–base disorders may progress rapidly. Out of the various likely complications, utmost serious are overloading of potassium—a condition called hyperkalemia. It also leads to an excess of fluid volume—a condition called hypervolemia. Typically, both kidneys must fail for AKI condition to get diagnosed. Although AKI can be caused by fast-developing intrinsic kidney disease. This is quite common due to an underlying condition outside the kidney. The causes are differentiated as prerenal, renal or postrenal. The most common cause is prerenal. The nephrons form urine. Blood enters into the nephrons via the afferent arteriole. Then it passes through a bunch of capillaries called the glomerulus, where the process of filtration takes place. Then the blood leaves via the efferent arteriole. Blood pressure inside the glomerulus is high enough to enable filtration. It is accomplished by having the significantly larger diameter of afferent arteriole than that of the efferent arteriole. It creates a blood flow with a big size inlet and small size outlet. The prerenal AKI is generally because of inadequate blood

flow to the kidneys. Main causes comprise depletion in extracellular fluid volume and reduced blood pressure, together with reducing the glomerular filtration rate. Generally, mechanisms of autoregulation inside the kidney dilate the afferent arteriole in response to a loss of blood volume. Resulting in compensation of a certain degree of low blood flow. AKI progresses when severe hypoperfusion is there, or when related mechanisms are conceded in patients along with pre-existing chronic kidney disease (CKD). Medicines which result in dilation of the efferent arteriole or constriction of the afferent arteriole, reduce the glomerulus pressure and may result in the progression of AKI. In patients with prerenal AKI with healthy kidneys, a renal function naturally returns to normal post resolving of the underlying condition, or the suspension of causing drug is performed. Kidney disease causes related to intrinsic problems inside the kidney, naming necrosis or inflammation of any of its' components such as the renal tubules, glomeruli, and interstitium. Postrenal causes include several types of obstruction in the storing or vacating parts of the urinary system. They are counted from a microscopic obstruction within renal tubules, blocking of ureters by kidney stones, the urethral obstacle in men because of an enlarged prostate. Few AKI might include problems at higher than one level including renal hypoperfusion. A prerenal cause might occasionally severe to induce renal tubule cells ischemia, resulting in intrinsic kidney disease. The cells death results in cellular debris which can clog the tubules, and become a postrenal cause. Originally, AKI symptoms are usually disguised by the pre-existing condition. Whereas in later stages, noticeable symptoms are because of the build-up of nitrogenous wastes, turbulences of fluid as well as electrolyte imbalance. The output of urine might not be reduced in this case. The diagnosis of AKI is dependent on renal function tests, including serum electrolytes, serum creatinine, BUN, sedimentation of urine, the output of urine as well as a urinalysis test. The underlined reason needs to be determined. Prerenal causes are typically superficial. Usually, ultrasound is done for detecting the postrenal blockage. The process of treatment goals in addressing the original cause. Nearly all patients might also need electrolyte and fluid management, or they may be recommended to go for the dialysis depending upon the degree of AKI [4].

CKD is a steady loss of renal function, characteristically developed over months or years. Several conditions, including internal and external to the kidneys, can be a reason for increasing injury to the kidneys over the period, resulting in CKD. Among these, the utmost known reasons are diabetes as well as hypertension. Both directly injure blood vessels inside the kidney and also destroy the renal tissue. An AKI, if not fully cured, might also develop in CKD. The renal disease severity is assessed depending upon the glomerular filtration rate. The glomerular filtration rate is an indicator of the wellbeing of the blood filtration process taken care by the kidneys. The glomerular filtration rate is measured as a function of serum creatinine. As creatinine is a waste product, it accumulates and saturates within blood plasma when kidney function deteriorates. The measurement counts the patients' gender, age as well as the race. Symptoms of CKD develop gradually over a while, developing from renal insufficiency towards the end-stage renal failure. Every so often, the primary loss of renal tissue will not result in any noticeable symptoms. It is due to the remaining healthy tissue. They become further active and by increasing their functionality they

compensate for the loss of tissue, which is also called renal adaptation. Generally, the noticeable symptoms are observed when a major part of kidney function is lost by that time. The capability to concentrate urine is typically the initial thing to get hampered, subsequently lead to recurrent visits to the lavatory, particularly during night time. Additional primary signs can be counted as a loss of appetite, fatigue, along with reduced mental capacity. As the kidneys eliminate metabolic waste products, maintain pH of blood, water/electrolyte balance, and produce numerous hormones, the damaged kidney functioning, results in numerous health-associated complications. The build-up of poisonous nitrogenous wastes causes a series of indications like vomiting, nausea, confusion as well as seizures. Reduced elimination of hydrogen ions results in raised acidity of blood also called metabolic acidosis. Reduced elimination of potassium leads to overloading of potassium within the blood, called hyperkalaemia. The hyperkalaemia might result in a group of conditions called cardiac arrhythmia. Hyperkalemia typically occurs within the advanced stages only, but extreme potassium intake or drug usage preventing in the excretion of potassium might rapidly decline the patient renal health and they may experience the condition in previous stages. Declining excretion of phosphate leads to a condition called hyperphosphatemia. Declining renal production of the active form of vitamin D the calcitriol, result in lowered levels of blood calcium, called hypocalcemia. The lower level of blood calcium stimulates the parathyroid hormone (PTH) production by the parathyroid gland. The PTH endorses release of calcium from bones for raising the levels of blood calcium. This system ultimately results in overactivation of the parathyroid gland, also called secondary hyperparathyroidism. It can develop even beforehand of the occurrence of hypocalcemia. Due to continuous loss of bone calcium and adding it to the rise levels of blood calcium, the bones turn out to be thinner and weaker. This condition called renal osteodystrophy. The symptoms comprise of painful bones and joints and significantly increased fracture risks. Declining renal secretion of a hormone called erythropoietin, which is a promoting factor for the formation of red blood cell, can result in anaemia. The renal function tests help in diagnosis, including analysis blood as well as urine. The ultrasound is prescribed which helps in detecting kidney status along with confirmation of the presence/absence of renal obstruction. Ultrasound aids in differentiating AKI and CKD depending upon the size of each kidney. The treatment and drug regiments target to govern the root causing conditions, followed by addressing the complications. It also involves the prescription of specific nutritional supplements as well as multiple diet restrictions. End-stage kidney disease necessitates a process of dialysis or the transplantation of kidney [4]. Figure 3 displays a healthy versus diseased kidney.

The AKI, CKD, kidney obstruction, severe dehydration as well as side effects of certain medications which result in rising levels of serum creatinine. Kidney diseases can get diagnosed in a person at any age but mostly in old age populations. BUN and creatinine are biological waste products excreted by kidneys. The creatinine is an instinctively formed non-enzymatic degradation by-product of a substance called creatine [6]. It is formed during daily muscular building and usage process. The levels of creatinine play a vital part in the calculation of functioning of the kidneys. The normal creatinine range in human serum is 0.5–1.1 mg/dL (5–11 ppm) for females

Fig. 3 A healthy versus diseased kidney [5]



whereas it is 0.6–1.2 mg/dL (6–12 ppm) for male. It is due to the gender-based body composition of males having more mass of lean muscles [7]. Levels over 15 ppm in adults need medical attention and levels over 60 ppm indicate severe damage to one or both the kidneys. Kidneys eliminate creatinine by cleaning blood plasma through glomerular ultrafiltration, for maintaining homeostasis within the body. The amount of creatinine in the serum helps in the measurement of the glomerular ultrafiltration rate and thus acts as an indicator of kidneys functioning [6]. The damage caused to kidneys results in the decrease in qualitative as well as quantitative functioning of one or both kidneys. The damage leads to significantly noticeable changes resulting in rising levels of BUN as well as creatinine, and a reduction in levels of both in the urine. The raised levels of serum creatinine show symptoms such as dropping of the frequency or amount of urine, dark urine, urethritis, the urgency with urination, haematuria, fatigue, muscular swelling in ankles or feet, vomiting, nausea, confusion and seizure [8–19]. It is very difficult to identify kidney diseases at early stages therefore prognostic and prophylactic kidney healthcare is very important.

3 Methods Available for Creatinine Levels Management and Their Margins

Traditionally when an individual gets diagnosed with kidney disease they are prescribed with routine blood check-up, ultrasound and/or CT scan. These are commercially available standard techniques. The blood check-up helps in understanding serum creatinine and BUN levels precisely thus helpful in knowing the waste

content of the blood. The technique of CT scan uses x-rays and computers for creating three-dimensional pictures of patients' renal system. An ultrasound uses sound waves to create a picture of patients' renal system. These three techniques are well developed, pre-standardized and practised everywhere. They are time-consuming, costly, only performed by a clinical technician, and a patient needs to visit pathology lab. The results are uninterpretable to them so they need to visit a medical practitioner for understanding their kidney health conditions.

There is a need for a precise, home-based, portable, easily interpretable, rechargeable, internet friendly, cost and time-effective sensing system for long-distance monitoring of kidney patients by doctors over the internet. The development of this kind of device will be supportive for kidney patients as it will significantly reduce their visits to pathology labs along with kidney healthcare clinics and will help them in understanding their creatinine status right at home. This system will be also helpful to medical practitioners as they can easily monitor their patient located over the long-distance with the help of PoC diagnostic devices' internet connectivity and secure data transfer process.

4 Motivation

It is described in the above section that there are some difficulties and restrictions related to the existing methodologies used for prognostic as well as prophylactic care of kidney health. The reason which encouraged us towards the fabrication of creatinine specific selective sensor and development of a LoRaWAN-based complete sensing system is to make a patient-friendly kidney health system. Currently, creatinine values cannot be monitored from home. The patient needs to visit the pathology lab for the blood test and/ or need to go for an ultrasound and/or CT scan quite frequently depending on their creatinine levels and underlined disease conditions. The results are not patient-friendly in understanding and they need to visit a medical practitioner to understand their kidney health status. There is a lack of patient-friendly device which can be utilised by the patient for their regular check-up. There is lacking a simple device which will help existing patients to save the cost of medical check-up cost related to creatinine level rise and kidney healthcare maintenance. This system currently based on sensing of creatinine levels from heat-inactivated serum samples due to human ethical issues. In future, this system can be further developed for using human blood for detection of levels of creatinine at home. The currently developed sensing system is home-based, precise, portable, rechargeable, reusable, cheaper, time-effective, and user friendly in understanding levels of creatinine anywhere with the help of internet connectivity. This system can be operated at one end and the results can be monitored from anywhere in the world with the help of internet connectivity. This is an additional advantage of this device making it useful in future for medical practitioners for easy kidney healthcare monitoring of their patients from long distance.

5 Functioning Pattern of Interdigital Sensors

The working of interdigital (ID) sensors as well as details about their heavy permeation depth is explained in-depth in the following sections.

6 The Working of ID Sensors

The planar ID sensors are composed of finger alike or comb alike repetitive pattern of parallel electrodes on a substrate. The electrodes are used for building up the capacitance associated with the electric fields which pass through the sample under test (SUT) and transmits vital information related to the properties of the used sample [20]. One of the significant positive-side of the planar ID sensors is the one-sided access to the SUT. This property aids to pass the sample solution along with acoustic or electromagnetic fields from only single-side. The power of the output signal could be monitored by altering the total number of comb-like electrodes, the total sensing area of the ID sensor, and the ID electrode spacing in-between them. The non-destructive single-sided sample access is an additional benefit of these sensors; thus, this property makes them useful in testing of real biological samples as well as in other applications [21].

The planar ID sensors follow the working principle of parallel plate capacitors. The gradual transition from parallel-plate to a planar plate capacitor is displayed in Fig. 4, wherein the electrodes allow access to SUT by opening up in only a single side of the sensor. The electrode pattern of the sensor can be kept uniform or repeated multiple times, to get a signal as well as to keep the signal to noise ratio in a good range [22]. The structural pattern of an ID sensor is shown in Fig. 5. Wherein an alternating current is supplied as an excitation voltage to the positive terminals, an electric field is generated from positive and moves towards the negative terminal. The electric field protrudes out from SUT from the excitation electrode and is collected by

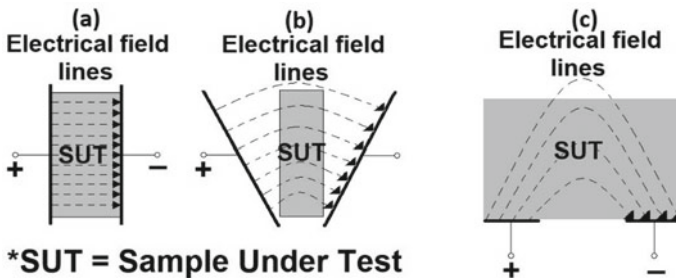
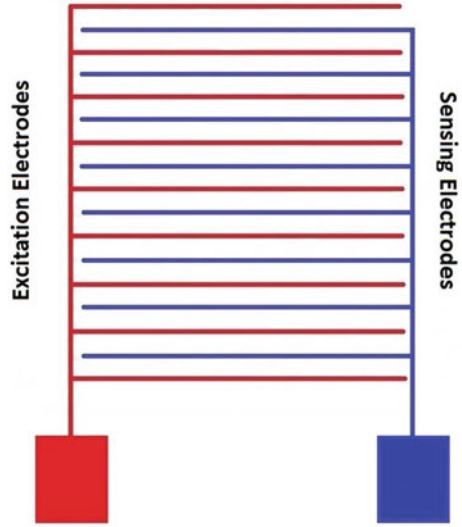


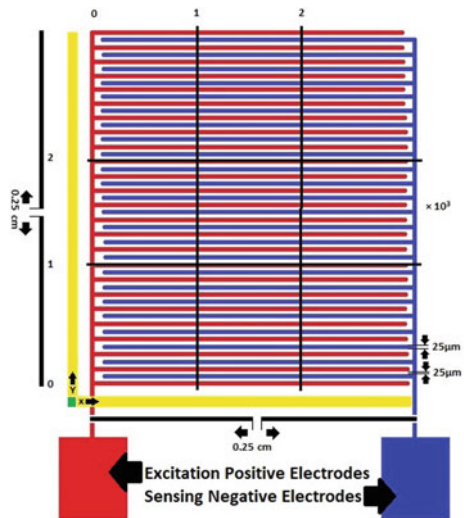
Fig. 4 Electrical field lines of the parallel-plate capacitor as well as the planar ID sensor. The evolution of electric field lines and gradual transition from parallel-plate to a planar plate capacitor **a** parallel plate capacitor, **b** intermediate stage and **c** ID sensor

Fig. 5 Structural pattern of a typical ID sensor



a negative sensing electrode. It transmits important information related to the characteristic properties of SUT namely density, concentration, impedance and many more. Figure 6 displays the structural pattern of currently developed microelectromechanical systems (MEMS) planar ID sensor. Figure 7 displays the electric field generated in-between excitation positive electrodes and sensing negative electrodes for varying pitch lengths-where the distance in-between two adjacent electrodes having identical polarization. The varying pitch lengths show varying penetration, as described in

Fig. 6 The structural pattern of currently developed MEMS planar ID sensor



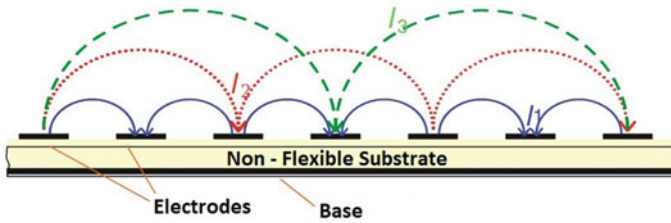


Fig. 7 Electric field having various pitch-lengths [23]

Fig. 7. The depth of penetration increases by increasing the net pitch length, but it results in weakening of the electric field.

7 Heavy Permeation Depth Planar ID Sensors

The presented ID sensors are designed with more repetitions of sensing and excitation electrodes, to raise the penetration depth of the electric field. Various structural designs have been studied from available literature [24–26]. Figure 7 denotes the excitation pattern for an excitation-sensing electrode pattern in an ID sensing design. These ID sensors have been manufactured depending on a very simplified geometrical pattern. Figure 6 displays the structural configuration of an ID sensor having the configuration of 1-1-25, presenting the presence of one sensing electrode between two consecutive excitation electrodes. A time-dependent sine wave electrical charge is provided to the positive excitation electrodes of the ID sensors. The alternating charge passes through the SUT; from positive excitation electrode towards the direction of the negative sensing electrode. This phenomenon transmits important information about the properties of SUT when it is in superficial contact with the detecting sensor [20, 21].

These sensors were fabricated at King Abdullah University of Science and Technology, Saudi Arabia as a research tie-up between School of Engineering, Macquarie University and King Abdullah University of Science and Technology. The sensor fabrication is done by etching and photolithography technologies on a single silicon/silicon dioxide wafer having 4 in. diameter and 525 μm thickness. In total 36 number of working sensors were designed on a single wafer chip. The single sensor has dimensions of 10 mm \times 10 mm and sensing area 6.25 mm². The MEMS technology is used for the manufacturing process of these ID sensors. It involved multiple steps such as coating of photoresist, ID sensor pattern transfer using UV exposure, plasma etching metal deposition done by DC magnetron sputtering process followed by lifting off. The thin-film electrodes were made by sputtering with 500 nm of gold on the surface of chromium to provide a firm attachment of ID electrodes over the base substrate. In a further stage, the printed wafer surface is coated with Parylene C layer of 1 μm layer thickness. The Parylene C acts as a protective covering on the

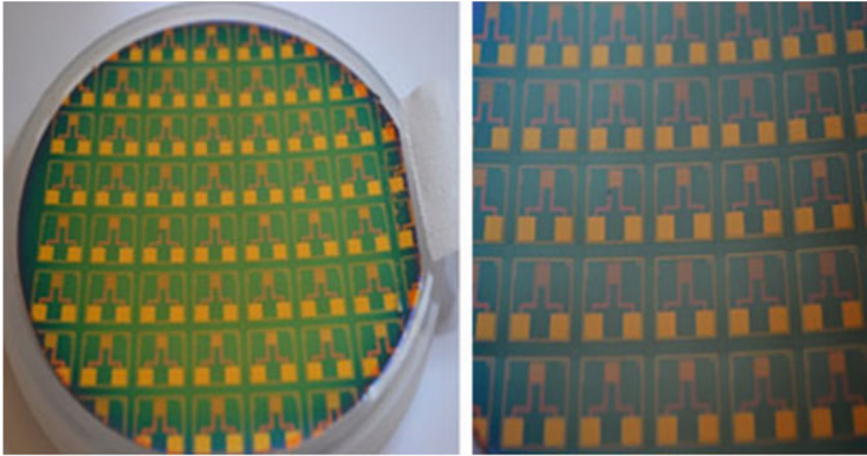


Fig. 8 The MEMS planar ID sensors on silicon wafer chip [28]

sensing area of ID sensors from corrosion associated with close contact of SUT with the sensing area. The coating also prevents the accumulation of moisture inside the silicon/silicon dioxide base substrate. The moisture interference might hamper the dielectric properties of SUT and result in a change in performance of the sensor. In the final stage, the bonding pads were allowed to open with the help of the plasma etching process [27]. Figure 8 shows MEMS planar ID sensors on silicon wafer chip.

The ID sensors have numerous applications in manufacturing lines [29], monitoring of environmental parameters [26, 30–33], moisture as well as humidity detection system [34, 35], gas sensing [36], detection of photosensitive materials [37]. It is developed based on the ID pattern for identification of hazardous pollutants in seafood [24, 33]. One of the ID sensors were made for determining phthalates from the water-based samples [30–32].

8 EIS Technique

The EIS technique is a well-known standard technique for measuring the capacitive as well as resistive properties of sample materials by providing a minor alternative current (AC) signal. The main advantages of using the EIS technique are testing of the sample in a non-destructive manner, one-sided sample access, label-free identification of components for various chemical and biological investigation purposes. Various applications of EIS has been testified including the identification of fat percentage inside meat [38], levels of toxins from shellfish [24], levels of bacterial endotoxins in food [39], the content of phthalates in juices and water [31], a study of corrosive behaviour of materials [40, 41] as well as detection of electrical properties for the process of soybean coagulation [42]. The technique has various applications

in several research areas including, mechanism of corrosion [43], detection of coating [44, 45], battery optimization [46] as well as biological sensing [47].

From the list of methods currently available for the process of measurement of impedance, frequency response analyser (FRA) has turned into a practising standard for quantification of EIS. The FRA is a FastTrack method for practical evaluation of the change in impedance. The technique analyses the system impedance for a broad range of frequencies and does a comparison of outcomes with the standard data. The main benefit of the comparative analysis process is noise reduction but may result in the weakening of the generated signal. The FRA is a solo sine wave contribution methodology involving a minor amplitude AC signal of a pre-decided frequency. It is put over the direct current (DC) bias potential, which is provided to the electrode and it is followed by the measurement of subsequent AC is performed. With lower amplitude AC, the system relies pseudo-linear. The protocol is reanalyzed at pre-decided optimum frequency range. The impedance measurements are taken five times and their average data are taken for analysis. For finalizing the systems' strength, repeatability as well as linearity, the current method is considered practical for a reversible as well as a stable system within the equilibrium. Due to the above purpose, immediate impedance calculations are needed for non-stationery systems [48–50].

The study of the impedance of a linear system is quite simple when compared with non-linear systems. During the EIS analysis, a small AC voltage is provided to the electrochemical cell. Because of the small current, the receiving system is a non-linear. Inside a non-linear system, the outcome related to current will carry harmonics of the excitation voltage frequency and might get hampered by the harmonics.

The EIS can be measured with the help of a minor AC signal followed by measurement of the phase angle in the current signal concerning the provided signal. In EIS the impedance is calculated with a low excitation signal for measuring the electrochemical cell response as a pseudo-linear. Within a linear system, the charge outcome to the sine wave excitation signal at the same frequency, a shift in phase angle is seen in Fig. 9.

The impedance is described as the calculation of the power of the electrical circuit to resist the flowing of electrical charge when the voltage is provided. Within an AC circuit, the impedance is shown as a composite value which includes real resistive as well as imaginary reactance.

The Nyquist plot displays an imaginary impedance part against the real impedance for every single excitation frequency. It offers various advantages. The resistance of the solution can be studied very effortlessly with the Nyquist plot. The Nyquist plot can be used for calculating the EIS parameters, such as solution resistance (R_s), double-layer capacitance (C_{dl}), electrode polarization resistance (R_p). The solution resistance (R_s) can be obtained by an inducing arc on to the X-axis. The main disadvantage of the Nyquist plot is related to its' inability to indicate anything about frequency thus, making it troublesome in the calculation of the double-layer capacitance [49]. The phase shift and the impedance against frequency can be represented by the Bode plot. The main difference between Nyquist and Bode plot is that the Bode plot represents information about the frequency at one of its axes. Therefore,

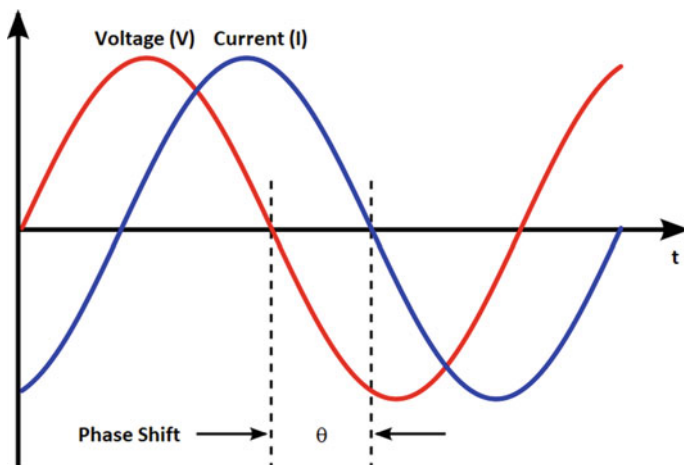


Fig. 9 The shifting of the phase in the current signal concerning the applied voltage

the Bode plot helps in better understanding of the relationship between frequency and impedance.

The Randle's equivalent circuit is commonly used [51] for the interpretation as well as analysing the EIS outcomes in electrical presentation as described in Fig. 10. The model is useful in describing diffusion, as well as kinetics procedures, take place at the borders between electrodes. It involves the resistance of the solution (R_s) in a sequence connection to the analogous fusion of double-layer capacitance (C_{dl}) to the charge transfer resistance (R_{ct}) when the Warburg impedance (W_1) is used in series [47]. The Randle's equivalent circuit model is named after Randle [52]. The circuit diagram consists of two resistors (R_1 and R_2), two capacitors (C_1 and C_2) and Warburg impedance (W_1). It incorporates solution resistance (R_s) (R_1) and

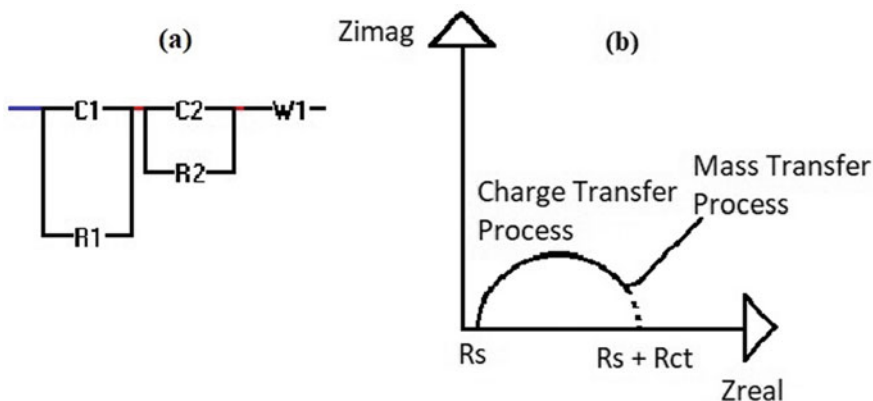


Fig. 10 The Randle's equivalent circuit along with the Nyquist plot for that equivalent circuit

solution charge transfer resistance (R_{ct}) (R_2) are in parallel in combination connected to capacitances C_1 and C_2 in a series connection with Warburg impedance W_1 [47].

The EIS experimental results in electrical research as displayed in Fig. 10a. The Nyquist plot has a semi-circular area and a 45° angular line, shown in Fig. 10b. Within this, the impedance of faradic reaction involves an active charge transfer resistance (R_{ct}) (R_2) as well as an electrochemical diffusion component, also called a Warburg element (W_1). At the high-frequency range, the semicircular region displays a slower charge transfer whilst the straight line indicates a significantly faster mass-transfer at a low range of frequency. The charge transfer resistance is measured with the help of inducing the semicircle to Z_{real} axis shown in Fig. 10b. Whereas the solution resistance (R_s) (R_1) can be calculated by inducing measurements to the real axis (X real ordinate) value at the higher-frequency intercept, the one which intercepts close to the origin of the Nyquist plot (Fig. 10b). The charge transfer resistance (R_{ct}) (R_2) can be calculated by extrapolating the semi-circle with Z_{real} axis as shown in Fig. 10b. Both $C_1 + C_2$ capacitance can be calculated from the frequency at the highest of the semi-circular region in the Nyquist plot using the following Eq. (1).

$$\omega = 1/R_{ct} \times (C_1 + C_2) \quad (1)$$

To get the Randle's equivalent parameters, the adjustment of the model circuit to the experimentally obtained data need to be done with the help of the complex non-linear least-square (CNLS) curve fitting technology.

9 Experiments with the Developed Sensing System

For developing the smart sensing system, the MEMS sensor is supposed to be selective to creatinine and it should be able to attract and adsorb the creatinine for its detection as well as quantification purpose. MIP-based detection technology is used to make the sensor specifically selective for the analyte, the creatinine. The MIP polymer is synthesised chemically and it is coated on the MEMS sensor for making the sensors' sensing area functionalised for creatinine from the serum samples. The specifically selective nature of functionalised MEMS sensor helped in precise detection of creatinine levels from serum samples.

10 Experimental Set-Up

The experimental set-up includes humidity meter and a digital thermometer, the MEMS ID sensor, SUT, MIP polymer coating suspension, and a high precision Hioki 3536 LCR meter. The LCR meter is connected to the computer through the RS232 connection port, for data collection and analysis. The MEMS sensor is connected to excitation as well as sensing electrode with the help of specifically made jig

having gold pin connectors shown in Fig. 11. The measurement system set-up is diagrammatically represented in Fig. 12.

The EIS experiments were done using the Hioki 3536 LCR meter. The experiments are done by use of the slow mode of equipment testing. A 1 V alternative current is

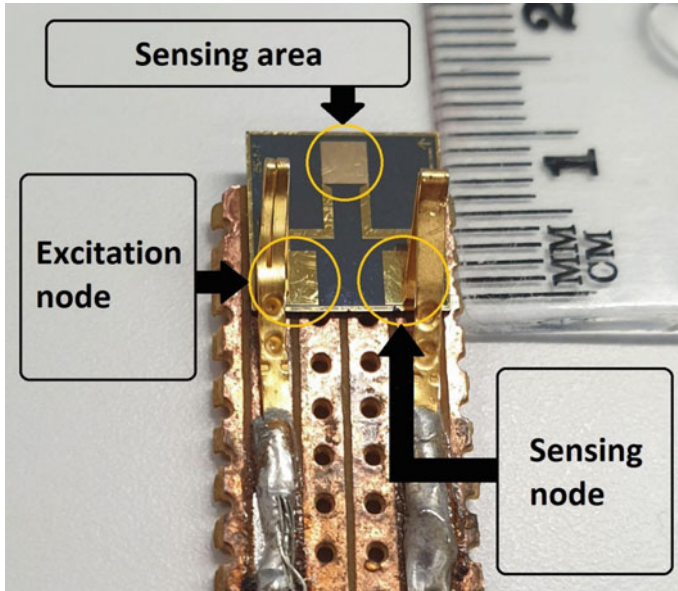


Fig. 11 Different parts of the MEMS planar ID sensor having 1-1-25 configuration

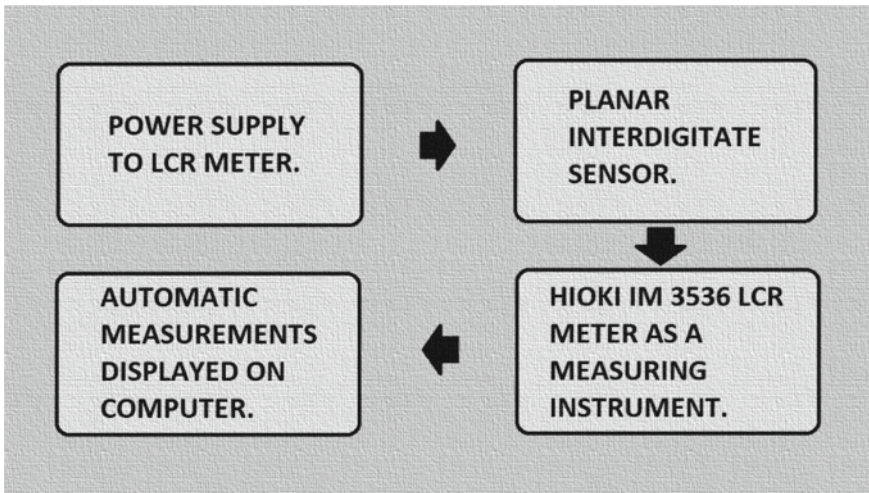


Fig. 12 The block diagrammatic representation of the measurement system set-up

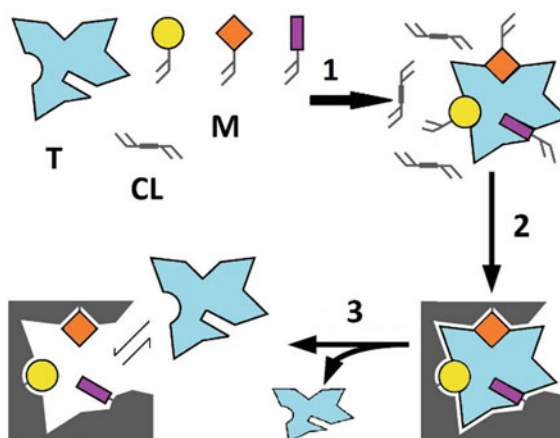
applied to the sensor with the help of the gold pin connector and the frequency is swept between 10 Hz and 100 kHz. All the experiments were repeated thrice and the average of the results is used to confirm the reproducibility and trustworthiness of the obtained results.

11 Synthesis of MIP Particles for Creatinine

For introducing creatinine associated specificity as well as selectivity to the designed MEMS-based planar ID sensors, the sensing area is coated with the MIP particles. The technique of molecular imprinting is non-expensive which permits the synthesis of artificial binding sites inside chemically synthesised synthetic polymer particles. Figure 13 shows the functioning principle of MIP technology. In MIP technology, a template (T) molecule is uniformly mixed along with a monomer (M) molecule. In the next step cross-linker (CL) molecule assembles a self-generated structural geometry (1). The process of polymerization of all the additions results into systematic production of a structure which is heavily cross-linked and has imprinted sites (2) for the targeted template (creatinine). In the last step, template molecules were extracted (which were locked within the polymer powder matrix) with the help of the soxhlet extraction process (Fig. 14). The process helps in leaving empty cavities that in future allows specifically selective recognition as well as binding of the targeted creatinine molecule (3) [53].

The MIPs have significant applications in the various branches of clinical analysis, medical diagnosis as well as the targeted drug delivery process. MIP permits the formation of artificial receptors having binding sites similar to natural binding sites. The advantage of using MIP is that the polymer powder can withstand much harsher conditions including higher levels of temperature, pressure and pH. The MIP

Fig. 13 The functioning principle of MIP technology



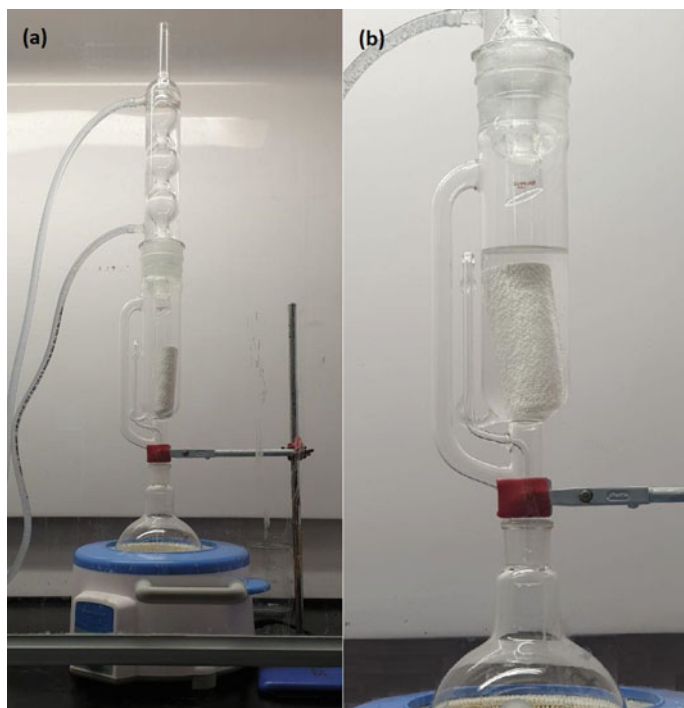


Fig. 14 Soxhlet extraction process for MIP. **a** Assembly of soxhlet extraction apparatus, **b** Creatinine molecule extraction from MIP powder kept inside cellulose thimble filter suspended inside AcOH solution

synthesis can be synthesised in large quantities along with having significant reproducibility [54]. These chemically synthesised synthetic MIP polymer powder is a decent alternative to naturally available sensitive biological receptors.

The popular alternative methodologies to synthesise MIP are processes of bulk polymerization and precipitation polymerization. In the current work, the process of precipitation polymerization is used for synthesising the specifically selective polymer powder for creatinine molecule [55].

For the conventional MIP bulk polymerization process, the polymers are formed in bulk quantity and then the polymer needs crushing, grinding as well as sieving processes to achieve desire sizing of polymer powder. During all these processes significant quantity of template recognition sites is damaged and overall it is also a time inefficient process. When compared the process of bulk polymerisation, the sphere-shaped polymer powder is quite simply synthesised using precipitation polymerization. Therefore, in current creatinine specific MIP synthesis, the precipitation polymerization process is preferred.

The process of precipitation polymerization for synthesizing MIP powder for creatinine template is explained in our previous work [55]. The creatinine is used as a template. Methacrylic acid (MAA) as a monomer, 2,2-azoisobutronitrile (AIBN) as

a reaction initiator whereas divinylbenzene (DVB) is used as a cross-linker molecule. All the reagents are purchased from Sigma-Aldrich, Australia. A uniform reaction mixture is prepared by mixing the creatinine template, MAA monomer and DVB a cross-linker in the ratio proportion of 2:0.510:7.5. The AIBN reaction initiator and acetonitrile: toluene in the ration proportion of 3:1 were added and the flask is purged with nitrogen gas for 15 minutes. Later the solvent mixture is shifted inside a hot water bath at 60 °C for 24 h. to complete the process of MIP polymerization. The polymer is separated from the other reaction solvent mixture after 24 h. In the subsequent stage, the creatinine template molecule is extracted from the polymer powder matrix using soxhlet extraction process by using the acetic acid (AcOH) as a solvent for 24 h long acid reflux process. It helped in proper extraction of creatinine template molecules from the polymer matrix and generation of empty spaces inside the formed polymer. These spaces are highly specific and selective for recognition and binding to their target i.e. creatinine molecules from the samples. The complete extraction of the template molecule is successfully validated with the help of the standard process of liquid chromatography-mass spectrometry (LC-MS) instrument analysis. The LC-MS is used to analyse the remaining eluent from the completed soxhlet extraction for detecting the presence of extracted creatinine molecules inside the leftover AcOH solvent. After that, the static adsorption of creatinine molecules with the MIP polymer powder is tested by using ultra-high-performance liquid chromatography (UHPLC) technique for detecting the functionality and saturation levels of MIP powder. The analysis technique of UHPLC helped in confirming the specific selective adsorption attraction of MIP polymer for creatinine from the serum sample solutions [55].

12 Functionalization of Sensors Sensing Area and EIS Test

In the first step, the MEMS-based ID sensors' air profiling is done at 1 V AC and the frequency is swept between 10 Hz and 100 kHz. It helped in the characterization of the sensor as well as finalizing the optimal operating frequency. In the second step, the MEMS-based sensors' sensing area is functionalised by using MIP polymer coating. The self-assembled single (SAS) layering technology along with acrylic resin is used for the MIP polymer coating process. 200 μ L of acrylic resin, 1 g of MIP polymer and 1.5 mL of acetone were mixed inside a glass beaker. The functionalization is done by use of PTL-MM01 dip coater instrument to make the uniform coating layer on the sensing area. The dipping and withdrawal of the sensing area of a sensor is done at a uniform speed of 200 mm/min. Due to the quick evaporation of acetone, the coating suspension becomes a solidified coat on the sensing area. Figure 15 displays the functionalisation process of the MEMS ID sensor.

After functionalization of the sensing area, the sensor is again characterized by using the EIS technique. This helped in understanding the changes concerning the non-functionalized sensing area. In the third step, the serum samples having the serum creatinine concentrations of 6, 10 and 14 ppm were analysed by adding 5 μ L of a sample on the sensing area. Finally, the air profiling of the MEMS sensor is done once

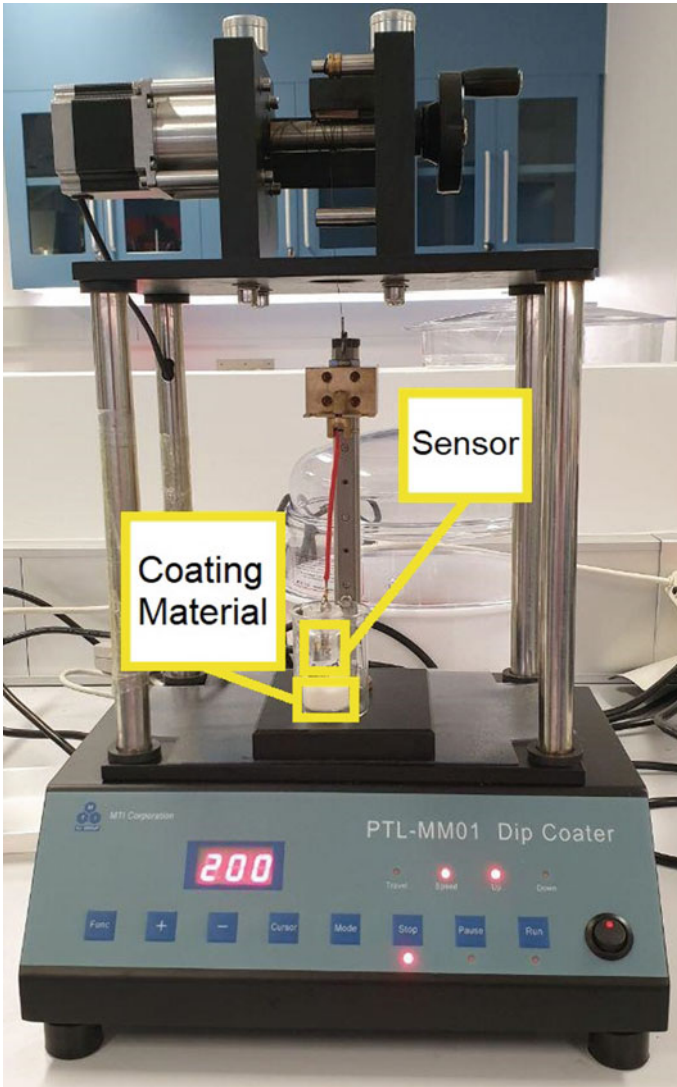


Fig. 15 The process of functionalization of MEMS ID sensor

again using the EIS technique and the Hioki 3536 LCR meter instrument. Figure 16 displays the representation of steps necessary in making the creatinine specific MIP-coated functionalised biological sensing surface for specific adsorption of creatinine on the surface of MEMS ID sensors.

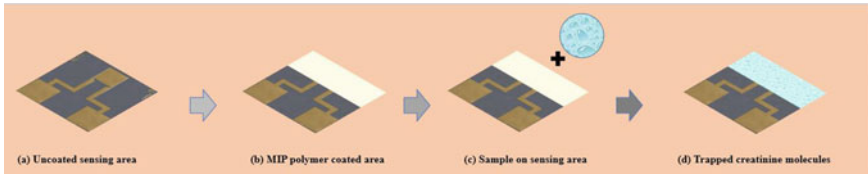


Fig. 16 Schematic representation of the steps required in preparing the MEMS ID sensing area for creatinine sensing

13 Preparation of Creatinine Spiked Serum Samples

For EIS analysis, a concentrated serum stock of 100 ppm creatinine level is prepared by mixing 1 mg of creatinine powder inside 10 mL of heat-inactivated human serum purchased from Sigma-Aldrich, Australia. The creatinine spiked serum samples stock is stored inside the refrigerator for preserving its active functionality. A serial dilution technique is utilised for making the serum samples having lower creatinine concentrations of 6, 10 and 14 ppm from the original stock. The pure serum with zero levels of creatinine content is used as a control solution for all other different samples having different creatinine concentrations.

14 Development of Microcontroller-Based PoC Diagnostic Device as a System for Impedance Measurement

After a successful EIS analysis, the sensing system is further developed for making a PoC diagnostic device system. For making a portable PoC diagnostic device for kidney health monitoring, a microcontroller-based sensing system is developed for measuring the creatinine levels from heat-inactivated serum creatinine samples. The data is transferred to the Internet of Things (IoT)-based cloud server. The received data can be provided to the medical practitioner with the help of IoT technology. The creatinine levels and their relation with kidney health status can be checked with this PoC diagnostic device. This device will be also helpful prognostic as well as prophylactic care of kidney health. The device can also turn helpful in long-distance treatment management.

The 1020 Hz frequency is used as an optimum operating frequency. AD5933 impedance analyzer [56] is utilised for the collection of impedance data which is generated because of varying serum creatinine concentration levels. The Inter-Integrated Circuit protocol [57] is used for obtaining the MIP-coated biosensors' impedance data. A rechargeable battery of 3.7 V is used for power supply to the microcontroller. Finally, the calculated serum creatinine concentration level is sent to an IoT-based cloud server for providing the collected data to a medical practitioner for patients' kidney healthcare analysis. The microcontroller accepts the collected

impedance data from the impedance analyzer and utilizes the standard calibration graph to measure the correct serum creatinine concentration level.

The microcontroller board of PoC diagnostic device has an inbuilt LoRaWAN chip and that assisted in joining of PoC diagnostic device with the aid of gateway for transmitting of the calculated data to the remotely located server. Adafruit is free IoT-based cloud server, and it is utilised for storage of measured data. The Adafruit cloud server can be utilised from any remote location by using internet access and thus helps the medical practitioner for observing their patients' serum creatinine data for the kidney health monitoring. The Cayenne Low Power Payload (LPP) library is used for calculated data transfer to the preferred personalised channel within the Adafruit website. CayenneLPP is a library, and it practices LoRaWAN protocol for transferring the measured serum creatinine sample data to Adafruit cloud server. Figure 17 denotes the flow process of the developed PoC device system. The electrical circuit diagram of the PoC diagnostic device is displayed in Fig. 18. Figure 19 shows the flow of the PoC diagnostic device software process for creatinine concentration calculation and data transfer to the IoT cloud server. Figure 20 display the actual PoC diagnostic device prototype system whereas Fig. 21 demonstrates online data streaming from the developed PoC diagnostic device for 10 ppm serum sample.

The experiments for obtaining the standard calibration graph are done by testing three known serum creatinine samples. A 20 μ l of serum creatinine sample is added on the MIP-coated sensing area of MEMS ID sensor using autopipette. A 10 min' delay time is given for adsorption of creatinine molecules to the MIP coating and then the surface is rinsed using Milli-Q water. The measurement is performed using the PoC diagnostic device. The 1020 Hz frequency is used as an optimum operating frequency as per previous results.

15 Experiments Using Creatinine Colorimetric Assay Kit

The developed LoRaWAN-based PoC diagnostic device is connected to the MIP-functionalised sensor. The MIP-functionalised sensor helps in measuring the creatinine concentration from the serum samples. The measured data is sent to the PoC diagnostic device via a gold pin connecting jig and further, it is processed by the in-build system within the LoRaWAN-based PoC diagnostic device. The standard plot of Creatinine Colorimetric Assay Kit helps in validating the results obtained using LoRaWAN-based PoC diagnostic device.

The human serum male AB plasma, USA origin, sterile-filtered is locally purchased from Sigma-Aldrich, Australia. The Creatinine Assay Kit (Colorimetric/Fluorometric) is used in this protocol, as it is suitable for faster, precise and sensitive measurement of levels of creatinine from biological samples including urine, serum/plasma, cell culture supernatant, as well as cerebrospinal fluid (CSF). It is locally purchased from Abcam. The Creatinine Colorimetric Assay Kit is an enzyme-probe coloured product based standardised testing for measuring the creatinine concentration from real samples. The kit contained creatininase (lyophilised),



Fig. 17 Flow process of the PoC device system

creatinine standard (10 μmol) (lyophilised); creatinase (lyophilised), creatinine enzyme mix (lyophilised), creatinine assay buffer and creatinine probe in DMSO (200 μl). The experiments are done using the Creatinine Colorimetric Assay Kit to obtain the standard plot by using standard serum samples having pre-calibrated creatinine concentrations. The standard plot results of Creatinine Colorimetric Assay Kit are further used to validate the detected values of LoRaWAN-based PoC diagnostic device. The developed LoRaWAN-based PoC diagnostic device is connected to the

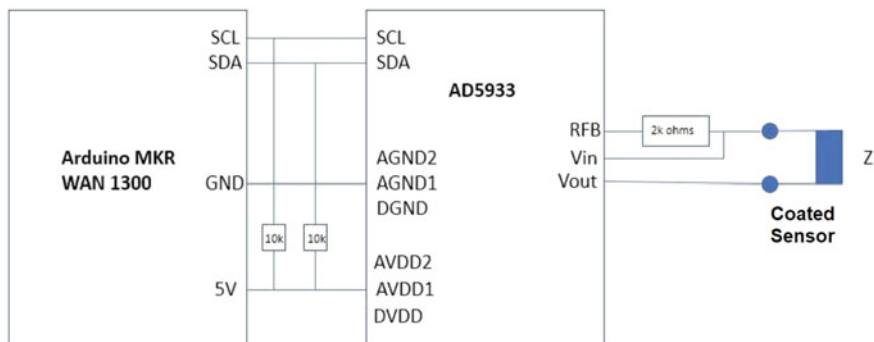


Fig. 18 Electrical circuit diagram of PoC device system

MIP-functionalised sensor. The MIP-functionalised sensor helps in measuring the creatinine concentration from the serum samples. The measured data is sent to the PoC diagnostic device via a gold pin connecting jig and further, it is processed by the in-built system within the LoRaWAN-based PoC diagnostic device. The standard plot of Creatinine Colorimetric Assay Kit helps in validating the results obtained using LoRaWAN-based PoC diagnostic device.

16 Creatinine Colorimetric Assay Reagent Preparation

The Creatinine Colorimetric Assay Kit contained multiple small vials. All the vials are carefully centrifuged at low speed before opening them in a lab environment. All the reagents were taken out from the -20°C and thawed at 4°C ice-cold water bath for 12 min before making their aliquots. Once opened all the opened aliquot vial are not restored at -20°C temperature to avoid the possibility of cross-contamination associated interferences or false-positive results. All the unused aliquot vials are stored at -20°C temperature to preserve their functional stability and to protect from light.

16.1 Creatinine Standard

The small vial containing creatinine standard in a powdered form is reconstituted by using $100\ \mu\text{l}$ of Milli-Q water for generating 100 mM creatinine standard. The 100 mM standard is aliquot in 10 vials so that the sufficient volume of solution will be available for use during every single assay and multiple freeze/thaw cycles can be avoided to a single cycle. Only one vial is used and rest all 9 aliquot vials were stored at -20°C .

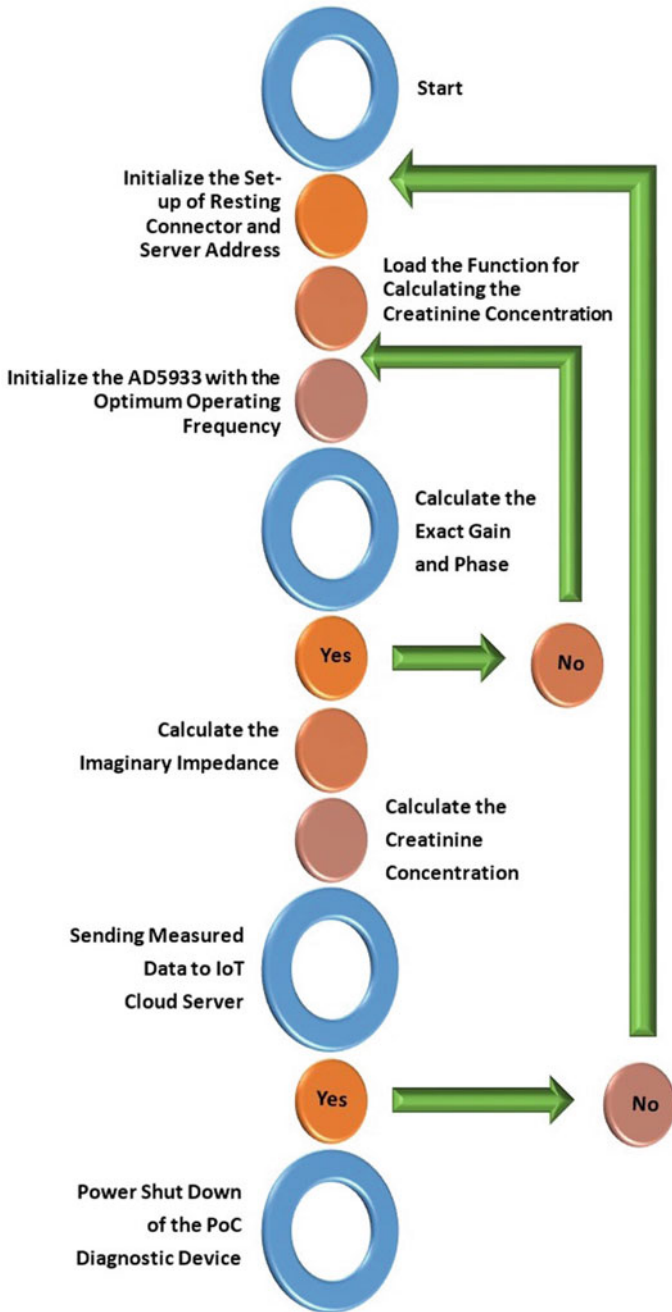


Fig. 19 The flow of the PoC diagnostic device software process for creatinine concentration calculation and data transferring to the IoT cloud server

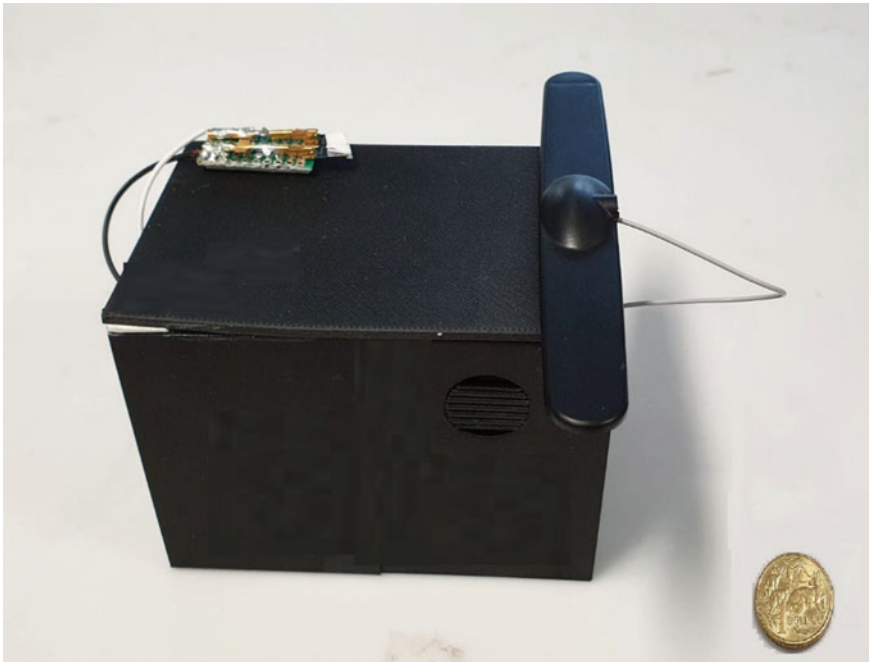
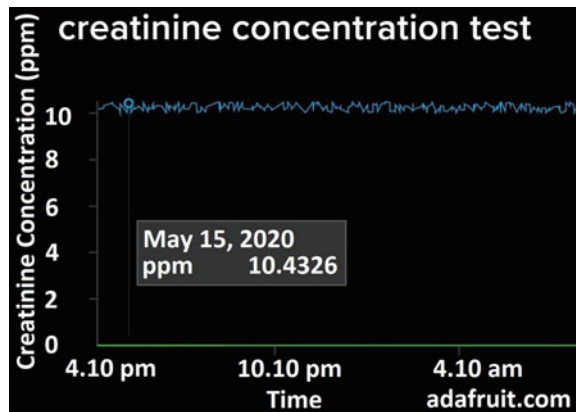


Fig. 20 PoC diagnostic device prototype system

Fig. 21 Online data from the developed PoC diagnostic device for 10 ppm



16.2 Creatinine Assay Buffer

The creatinine assay buffer is used as supplied without any further reconstitution. The assay buffer is equilibrated at room temperature before its use. It is stored inside the freezer at $-20\text{ }^{\circ}\text{C}$ post usage.

16.3 Creatine Probe

The creatine probe is also used as supplied in the kit. It is warmed by placing it inside 37 °C water bath for 1–5 min for thawing one of its integral content, the DMSO solution before its use. The DMSO acquired solidity whilst stored at –20 °C as well as at lab standard room temperature. It requires melting for a few minutes at 37 °C before use. The melted probe is also aliquot in vials for having sufficient volume for performing the desired number of assays. All extra vials are stored at –20 °C. The thawed probe is used immediately.

16.4 Creatininase

The creatininase is an enzyme which works on creatinine and converts it into creatine. The creatininase is reconstituted with 220 µl of creatinine assay buffer for generating the 3 aliquots. The aliquot in use is kept in an ice-cold water bath to keep enzyme functionality intact. Rest 2 aliquots were stored at –20 °C for further use.

16.5 Creatinase

The creatinase is an enzyme which works on creatine and converts it into sarcosine. The creatinase is reconstituted with 220 µl of creatinine assay buffer for generating the 3 aliquots. The aliquot in use is kept in an ice-cold water bath to keep enzyme functionality intact. Rest 2 aliquots were stored at –20 °C for further use.

16.6 Creatinine Enzyme Mix

The sarcosine is specifically oxidised to produce a reaction product which further reacts with creatinine probe to generate the reddish-pink coloured end product. The creatinase enzyme mix is reconstituted with 220 µl of creatinine assay buffer for generating the 3 aliquots. The aliquot in use should be kept in an ice-cold water bath to keep enzyme functionality intact. Rest 2 aliquots were stored at –20 °C for further use.

Table 1 Samples dilutions used for making the standard Creatinine Colorimetric Assay plot [58]

Creatinine working standard	Volume of creatinine working standard (μl)	Creatinine assay buffer (μl)	Final volume of creatinine working standard in well (μl)	End concentration of creatinine in well (nmol/well)
1	0	150	50	0
2	6	144	50	2
3	12	138	50	4
4	18	132	50	6
5	24	126	50	8
6	30	120	50	10

17 Experiments with Creatinine Colorimetric Assay Kit

The experiments were done with creatinine colorimetric assay kit to perform cross-validation of developed PoC diagnostic device is explained below.

17.1 Preparation of Working Standards

The set of working standards were always prepared freshly just before their every use. The set of working standard dilutions were discarded immediately after finishing experiments due to their inability to store well over an hour.

17.1.1 Procedure:

1. Creatinine working standard of 1 nmol/ μl concentration (1000 μl quantity) is made by diluting 10 μl of 100 mM creatinine working standard in 990 μl of creatinine assay buffer.
2. The 1 nmol/ μl creatinine working standard is used for preparing standard samples. These samples dilutions were used for making the standard plot as shown in Table 1 in a 96 well clear microtiter plate.
3. Each dilution reading is repeated twice and the average colorimetric reading value is taken for plotting a creatinine working standard graphical plot.

17.2 Preparation of Samples

The set of test samples were in ppm range and as the Creatinine Colorimetric Assay Kit working range is in ppb, therefore all the test serum samples were diluted 1000

times by using a pure serum before they were analysed with the help of this kit. The dilution of test samples helped in ensuring that the readings will be in the standard value range. Freshly prepared test samples were used every time for analysis.

18 Creatinine Colorimetric Assay Procedure

The procedure for creatinine colorimetric assay is explained below.

18.1 Setting the Reaction Wells

1. Standard wells = Standard working dilutions of 50 μl .
2. Test sample wells = samples of 50 μl .
3. Sample background control wells = 50 μl pure serum samples with zero creatinine content as a blank (control).

18.2 Creatinine Reaction Mix

1. In each 96 well microtiter well, 50 μl of reaction mix is added for the reaction. Total 1500 μl of reaction mix is prepared and used for all creatinine working standard and creatinine test sample wells.
2. A 100 μl of background reaction mix is also prepared and used for both pure serum samples with zero creatinine content. Table 2 shows the preparation procedure for creatinine reaction mix as well as background reaction mix.
3. All the contents from each 96 well microtiter well were mixed by using a 1 G-force at 37 $^{\circ}\text{C}$ for 1 h.

Table 2 Preparation procedure for creatinine reaction mix and background reaction mix [58]

Component	Reaction mix (μl)		Background reaction mix (μl)	
	Each well (50 μl)	All 30 wells (1500 μl)	Each well (50 μl)	All 2 wells (100 μl)
Assay buffer	42	1260	44	88
Creatinase	2	60	2	4
Creatininase	2	60	0	0
Enzyme mix	2	60	2	4
Creatinine probe	2	60	2	4

4. The coloured reaction output is read by using SPECTROstar Nano microplate reader at an optical density (OD) 570 nm. The Creatinine Colorimetric Assay Kit procedure has been illustrated in the flow chart pattern in Fig. 22.

Total of 30 reaction wells is used for every single analysis. 6 working standards were made and analysed in duplicates ranging from well no. A1–A12. 8 samples were analysed in duplicates at room temperature ranging from well no. B1–C4. 1 pure serum samples with zero creatinine concentration is used as blank (control) samples in duplicates from well no. C5–C6. The Colorimetric Assay Kit results are shown in Fig. 23 and working standard plot is shown in Fig. 24.

19 Creatinine Colorimetric Assay Kit Data Analysis

1. As all the values were taken in duplicates, the average is taken for all 6 creatinine working standards, 8 test samples and a set of pure serum sample used as a blank (control).
2. As the value of background control, pure serum (blank) is significant, it is subtracted from all the test sample readings. The blank value (creatinine working standard #1) was subtracted from all the other creatinine working standard and test sample readings. It helped in getting the corrected absorbance.
3. To get the final concentration of creatinine the values of corrected absorbance of each standard were plotted.
4. The creatinine working standard plot is drawn for concentration 0–10 ppb range.
5. The values for creatinine concentrations for 6, 10 and 14 ppm serum test samples were obtained by multiplying the results with 1000 times (ppb to ppm conversion factor). As Creatinine Colorimetric Assay is used as a standard diagnostic method in pathology labs, it helped in standardising and validating the values obtained from MIP-coated MEMS sensor of LoRaWAN-based PoC diagnostic device.

20 Results and Discussions

Three known concentration serum samples (6, 10, 14 ppm) were tested by using the developed ID PoC diagnostic device. The serum sample with zero creatinine content is considered as the standard control. All the experiments were done at laboratory temperature and 31% humidity level. The testing of samples is done immediately after preparing the serum samples. The imaginary part of the impedance with the range of frequencies for all three creatinine serum concentrations for developed MEMS planar ID sensing using the EIS technique is shown in Fig. 25. As shown in Fig. 25, the capacitive reactance ($Z_{\text{imaginary}}$) presents significant changes—specifically at a lower range of frequencies concerning the change in serum creatinine concentrations. Therefore, capacitive reactance ($Z_{\text{imaginary}}$) is decided as the measuring parameter

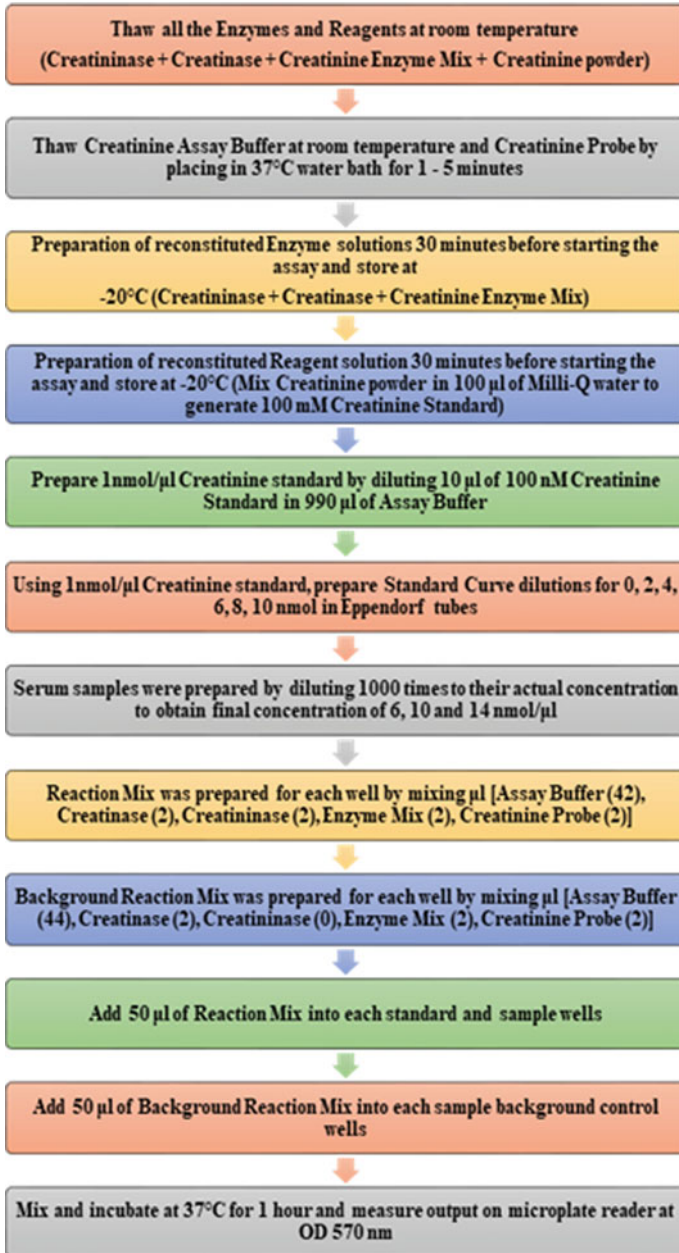


Fig. 22 The flowchart of commercial Creatinine Colorimetric Assay

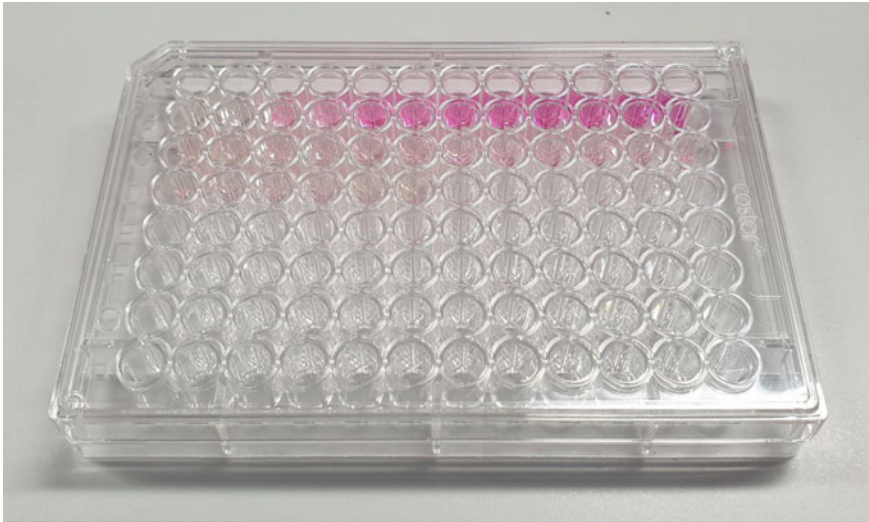


Fig. 23 The coloured product of Creatinine Colorimetric Assay Kit after incubation for an hour at 37 °C

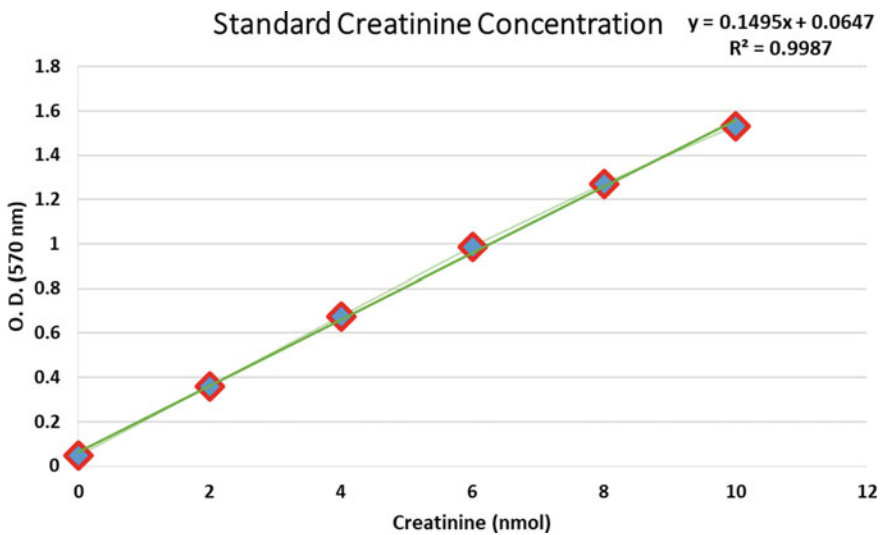


Fig. 24 The standard plot of Creatinine Colorimetric Assay

for further making and developmental process of the PoC diagnostic device. The 1020 Hz frequency is chosen as an optimum operating frequency for working of PoC diagnostic device. This is related to the dielectric properties of SUT.

The real part of impedance (Z_{real}) versus frequency range for the same serum creatinine concentrations (6, 10, 14 ppm) is plotted in Fig. 26. Not many changes

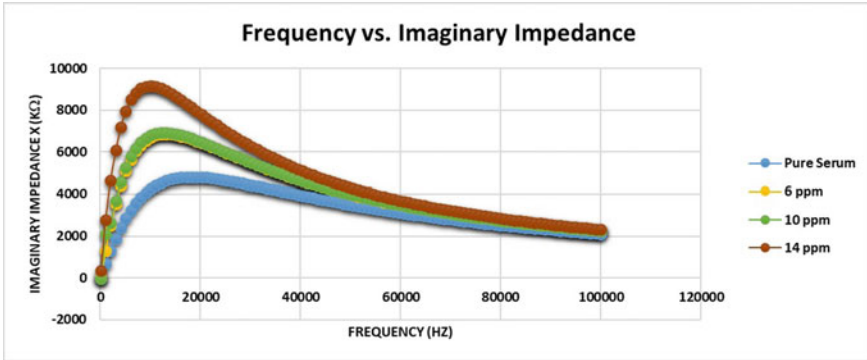


Fig. 25 Imaginary impedance versus a range of frequencies

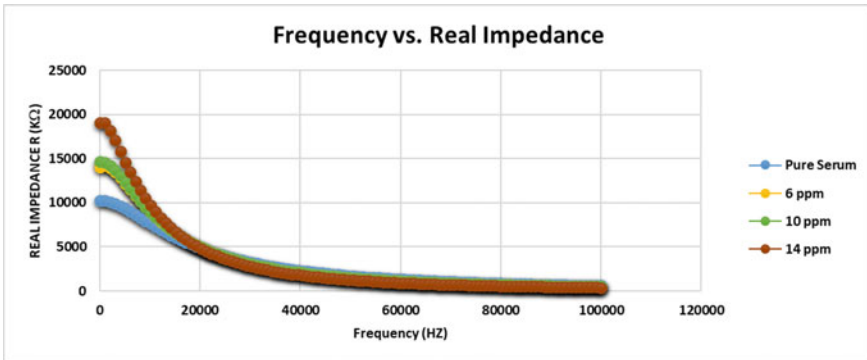


Fig. 26 Real impedance versus a range of frequencies

are observed in the real part of the impedance (Z_{real}) which is associated with the ionic properties of the serum samples as well as the Faradic current. The Nyquist plot is depicted in Fig. 27 for the impedance spectra obtained for all three serum creatinine concentrations for the frequency range of 10–100 kHz. It can be said that the semicircle diameter of Nyquist plots is raised by rising the serum creatinine concentrations.

The 1020 Hz is considered as the optimal operating frequency because at that frequency the MEMS ID sensor clearly distinguishes every serum creatinine concentration. The sensitivity of the MEMS ID sensor concerning creatinine serum samples is calculated by using the reactance (X) values at 1020 Hz frequency range using the following Eq. (2):

$$Sensitivity(\%) = \frac{(Z_{imaginary}(\text{control}) - Z_{imaginary}(\text{sample}))}{Z_{imaginary}(\text{control})} \tag{2}$$

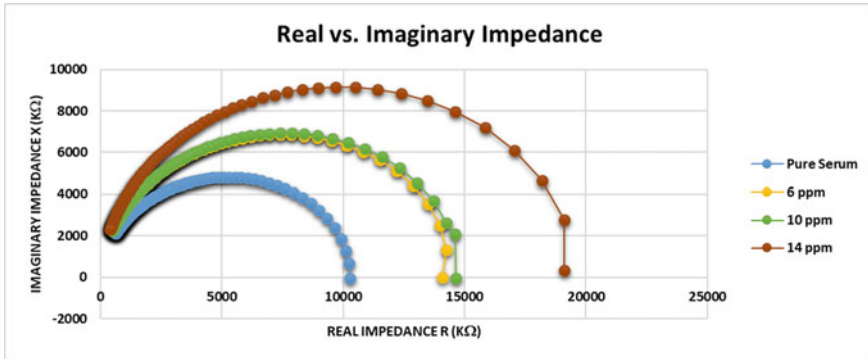


Fig. 27 Nyquist plot of various creatinine concentrations

The serum creatinine concentrations vs. the sensitivity of reactance curve for MEMS ID sensor is plotted at an optimal operating frequency of 1020 Hz (Fig. 28). The plotted curve can be used for finding the serum creatinine concentrations of any unknown serum samples.

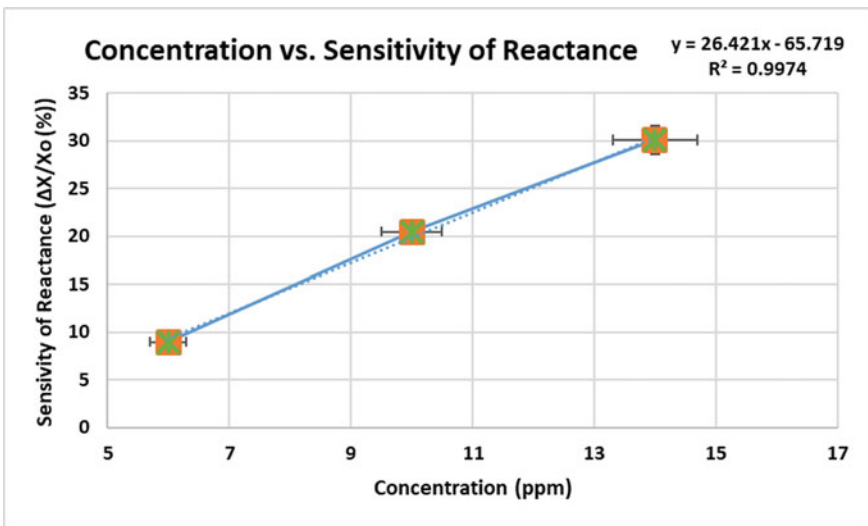


Fig. 28 The reference curve for concentration versus sensitivity of reactance for MEMS ID sensor

21 Calibration Graph and Measurement of Unknown Sample

Figure 29 displays the calibration graph of the developed PoC diagnostic device. All the measurements were repeated five number of times to obtain the mean values, and further, they are used for plotting the PoC associated calibration graph (Table 3). The adsorption associated functioning capacity of MIP-coating layer is refreshed post completion of every measurement with the help of immersion of coated sensing area in 1% AcOH solution by using Milli-Q water for 20 min.

The MEMS ID sensor offers its values of reactance and resistance at all conditions. The value of impedance significantly differs when the serum creatinine sample constitutes of any contamination. The value of reactance concerning to the pure serum having zero levels of creatinine concentration is considered as the normal value of the sensor output.

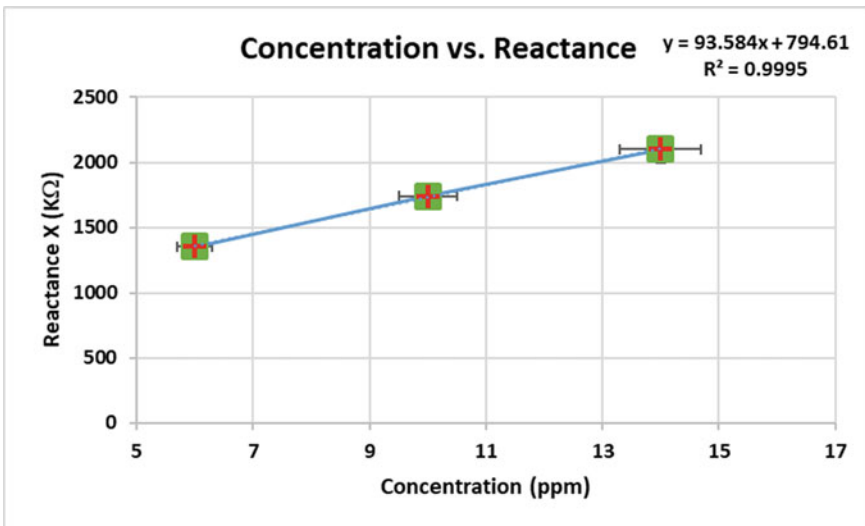


Fig. 29 Calibration graph of PoC diagnostic device showing concentration versus reactance

Table 3 The mean values of reactance and standard deviation for various serum creatinine concentrations

Serum Creatinine Concentration (ppm)	Reactance (kΩ) ^a	Standard Deviation (Ω)
6	1311.89	438.59
10	2107.71	1001.32
14	2773.72	1472.26

^aThe mean values are obtained after an average of five times measurements

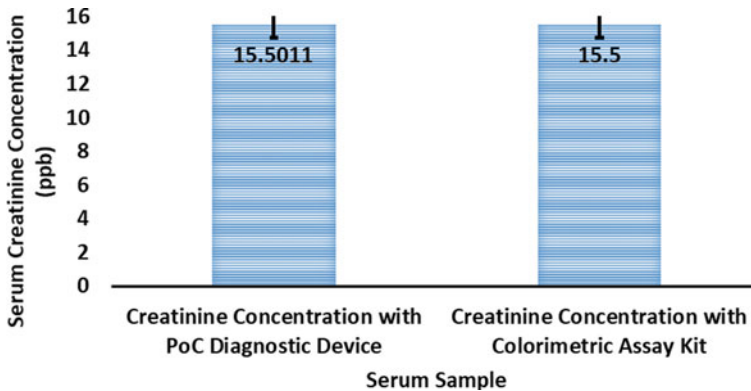


Fig. 30 Comparative study between the PoC diagnostic device results and the Creatinine Colorimetric Assay Kit results

An unknown serum creatinine concentration is measured with the help of developed MEMS ID sensing system. The creatinine concentration of that unknown sample is found out to be 15.5011 ppm. The results were cross-verified with the Creatinine Colorimetric Assay Kit results and the error rate value is negligible for the unknown serum sample. Figure 30 shows a comparative study between the PoC diagnostic device results and the Creatinine Colorimetric Assay Kit results.

22 CNLS Impedimetric Curve Fitting

The CNLS is used for calculating the equivalent circuit. It is also used for checking the component parameters with the help of experimental data fitting with its theory-based predicted response depending on Randle's model. The model infers the protocols performed within the biochemical cell in its' equivalent circuit. The CNLS analysis for Nyquist plot is shown in Fig. 31. The red square-shaped points on the graph show the experimentally noted data and the green line displays the theoretically formfitting response for the equivalent circuit. The predicted equivalent circuit for the EIS CNLS analysis process is displayed inside Fig. 32.

The mathematical algorithm practices statistical analysis for calculating the mean square r_c^2 value for experimentally noticed values inside the obtained spectrum using CNLS with the help of the Eq. (3) given below [59, 60]:

$$r_c^2 = \sum_{i=1}^N \left[\frac{(Z'_i \text{ observed} - Z'_i \text{ calculated})^2}{(Z'_i \text{ observed})^2} + \frac{(Z''_i \text{ observed} - Z''_i \text{ calculated})^2}{(Z''_i \text{ observed})^2} \right] \quad (3)$$

where,

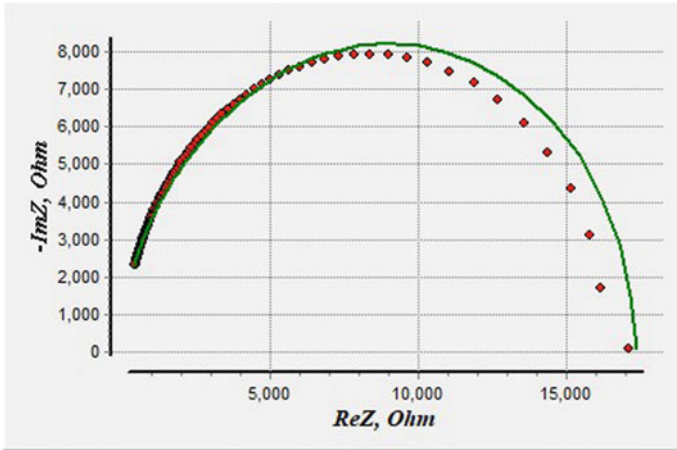
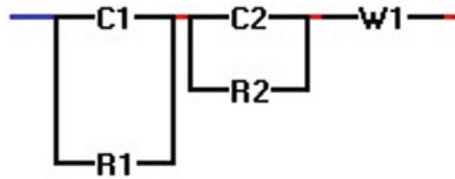


Fig. 31 CNLS analysis curve for Nyquist plot

Fig. 32 The equivalent circuit for CNLS analysis



- Z'_i observed The observed value of real impedance.
- Z'_i calculated The calculated value of real impedance.
- Z''_i observed The observed value of imaginary impedance.
- Z''_i calculated The calculated value of imaginary impedance.
- r^2_c Displays the deflection between the data values obtained with experimental results and the optimal solution in this above equation.

Table 4 displays the calculated component parameters of the equivalent circuit. The C_1 and C_2 represent capacitor 1 and capacitor 2. The R_1 and R_2 represent resistor 1 and resistor 2 whereas, the $W1$ represents the Warburg element. The error rate for serum samples is found out to be $< 11\%$ for the equivalent parameters from the presented circuit. It helps in understanding which component parameter is most sensitive and changes its' values as per change in serum creatinine concentrations. In the currently used circuit, the component R_2 (resistor 2) is found to be the most sensitive parameter and its' value increases uniformly with an increase in serum creatinine concentration.

Table 4 Equivalent circuit parameter values

Component parameters	Values of the parameters 0 ppm pure serum	Values of the parameters 6 ppm	Values of the parameters 10 ppm	Values of the parameters 14 ppm
C_1	$1.2626 \times E^{-09}$	$2.0220 \times E^{-09}$	$2.1458 \times E^{-09}$	$2.4702 \times E^{-09}$
C_2	$2.4363 \times E^{-09}$	$1.0017 \times E^{-09}$	$9.6198 \times E^{-10}$	$8.9768 \times E^{-10}$
R_1	4324.9	2122.9	2028.9	1713.9
R_2	10,593	13,266	15,307	17,569
Aw_1	35,289	1122	484.28	1732.1
$r^2_{\text{amplitude}}$	0.0033280	0.00059503	0.00065365	0.0007507

23 Conclusion

Three known standard creatinine serum samples were tested with the help of PoC diagnostic device. The results were checked with the help of a commercially available standard technique called Creatinine Colorimetric Assay Kit. The reference curve of PoC diagnostic device is plotted and it is used for calculating the concentration of unknown serum creatinine serum sample. Later, the concentration of creatinine from an unknown sample is also measured with the help of developed PoC diagnostic device. The results of the PoC diagnostic device are cross-verified with the results obtained using the Creatinine Colorimetric Assay Kit and the error rate is found to be negligible for the developed PoC diagnostic device sensing system.

References

1. An anterior, posterior view of human kidneys, <https://y7177.com/sa/anato/uro/kidney/kidney.htm>. Accessed 24 Jan 2019
2. A superior view of a transverse section of a human kidney, <https://slideplayer.com/slide/12632070/>. Accessed 24 Jan 2019
3. An ultrastructure of the nephron, <https://www.britannica.com/science/nephron>. Accessed 24 Jan 2019
4. Structure and Functioning of Kidneys, Renal Health with Creatinine Levels, <https://www.aliamedicalimages.org/BrowseImages/browse-topics/urology-browse-topics/>. Accessed 23 Jan 2019
5. A.D. Paul, C. Girish, T.N. Shilpa, K. Manogna, A.G. Susmitha, Renal vascularisation causing end-stage failures and outcomes: a pooled analysis of community-based studies. *Int. J. Pharm. Sci. Drug Res.* **9**(5), 256–262 (2017)
6. M. Wyss, R. Kaddurah-Daouk, Creatine and creatinine metabolism. *Physiol. Rev.* **80**, 1107–1213 (2000)
7. Levels of creatinine, https://www.medicinenet.com/creatinine_blood_test/article.htm#what_are_considered_high_creatinine_levels. Accessed 24 Jan 2019
8. Kidney Damage (Acute Renal Failure), https://cancer.unm.edu/cancer/cancer-info/cancer-treatment/side-effects-of-cancer-treatment/less-common-sideeffects/organ-problems/kidney-damage-acute-renal-failure/#_edn1. Accessed 25 Jan 2019

9. J.P. Cata, A.M. Zavala, A.V. Meter, U.U. Williams, J. Soliz, M. Hernandez, P. Owusu-Agyemang, Identification of risk factors associated with postoperative acute kidney injury after cytoreductive surgery with hyperthermic intraperitoneal chemotherapy: a retrospective study. *Int. J. Hypertherm. Therm. Ther.* **34**, 538–544 (2018)
10. T. Dagle, S. Misirlioglu, S. Tanju, B. Afsar, F. Selcukbiricik, S. Erus, D. Vatansever, E. Balik, C. Taskiran, S. Dilege, N.M. Mandel, D. Bugra, T. Yalti, M. Kanbay, Hyperthermic intraperitoneal chemotherapy is an independent risk factor for development of acute kidney injury. *J. Balkan Union Oncol* **23**, 1528–1533 (2018)
11. D. Katagiri, E. Noiri, R. Matsuura, R.C. Harris, Acute kidney injury: transition to chronic kidney disease. *Hum. Pathobiochem.* 269–277 (2019)
12. H. Izzedine, M.A. Perazella, Anticancer drug-induced acute kidney injury. *Kidney Int. Rep.* **2**, 504–514 (2017)
13. M. Aapro, V. Launay-Vacher, Importance of monitoring renal function in patients with cancer. *J. Cancer Treat. Rev.* **38**, 235–240 (2012)
14. V. Sahni, D. Choudhury, Z. Ahmed, Chemotherapy-associated renal dysfunction. *Nat. Rev. Nephrol.* **5**, 450–462 (2009)
15. S.L. Kane-Gill, S.L. Goldstein, Drug-induced acute kidney injury: a focus on risk assessment for prevention. *Crit. Care Clin.* **31**, 675–684 (2015)
16. G.S. Pazhyattil, A.C. Shirali, Drug-induced impairment of renal function. *Int. J. Nephrol. Renovasc. Dis.* **7**, 457–468 (2014)
17. I. Glezerman, M.G. Kris, V. Miller, S. Seshan, C.D. Flombaum, Gemcitabine nephrotoxicity and hemolytic uremic syndrome: report of 29 cases from a single institution. *Clin. Nephrol.* **71**, 130–139 (2009)
18. J. Radhakrishnan, M.A. Perazella, Drug-induced glomerular disease: attention required! *Clin. J. Am. Soc. Nephrol.* **10**, 1287–1290 (2015)
19. V. Launay-Vacher, S. Oudard, N. Janus, J. Gligorov, X. Pourrat, O. Rixe, J. Morere, P. Beuzeboc, G. Deray, Prevalence of renal insufficiency in cancer patients and implications for anticancer drug management. *Cancer* **110**, 1376–1384 (2007)
20. A.S. Abu-Abed, R.G. Lindquist, Capacitive interdigital sensor with inhomogeneous nematic liquid crystal film. *Progress Electromag. Res.* 75–87 (2008)
21. A.V. Mamishev, K. Sundara-Rajan, F. Yang, Y. Du, M. Zahn, Interdigital sensors and transducers. *Proc. IEEE* 808–845 (2004)
22. Y. Chen, C. Zhu, M. Cao, T. Wang, Photoresponse of SnO₂ nanobelts grown in situ on interdigital electrodes. *Nanotechnology* **18**, 285–502 (2007)
23. M.S.A. Rahman, S.C. Mukhopadhyay, P.-L. Yu, Novel planar interdigital sensors, in *Novel Sensors for Food Inspection: Modelling, Fabrication and Experimentation* (Springer, 2014), pp. 11–35
24. A.M. Syaifudin, K. Jayasundera, S. Mukhopadhyay, A low cost novel sensing system for detection of dangerous marine biotoxins in seafood. *Sens. Actuators: B Chem.* **137**, 67–75 (2009)
25. A.M. Syaifudin, S. Mukhopadhyay, P. Yu, Electromagnetic field computation using COMSOL multiphysics to evaluate the performance of novel interdigital sensors. *Appl. Electromag. Conf. AEMC 2009*, 1–4 (2009)
26. A.M. Syaifudin, M. Yunus, S. Mukhopadhyay, K. Jayasundera, A novel planar interdigital sensor for environmental monitoring. *Sens. IEEE*, 105–110 (2009)
27. S.N. Prabhu, S.C. Mukhopadhyay, C. Gooneratne, A.S. Davidson G. Liu, Interdigital sensing system for detection of levels of creatinine from the samples, in *2019 13th International Conference on Sensing Technology (ICST)* (2019), pp. 1–6
28. M.S. Abdul Rahman, S.C. Mukhopadhyay, P.-L. Yu, Novel planar interdigital sensors, in *Novel Sensors for Food Inspection: Modelling, Fabrication and Experimentation. Smart Sensors, Measurement and Instrumentation*, vol. 10 (Springer, 2014)
29. Y. Yang, G. Chiesura, G. Luyckx, T. Vervust, F. Bossuyt, J. Vanfleteren et al., In situ on-line cure monitoring of composites by embedded interdigital sensor, in *16th European Conference on Composite Materials (ECCM-16)* (2014)

30. A.I. Zia, A.M. Syaifudin, S. Mukhopadhyay, P. Yu, I. Al-Bahadly, C.P. Gooneratne et al., Electrochemical impedance spectroscopy based MEMS sensors for phthalates detection in water and juices. *J. Phys Conf. Ser.* 012–026 (2013)
31. A.I. Zia, S.C. Mukhopadhyay, P.-L. Yu, I. Al-Bahadly, C.P. Gooneratne, J. Kosel, Rapid and molecular selective electrochemical sensing of phthalates in aqueous solution. *Biosens. Bioelectron.* **67**, 342–349 (2015)
32. A. Zia, S. Mukhopadhyay, I. Al-Bahadly, P. Yu, C.P. Gooneratne, J. Kosel, Introducing molecular selectivity in rapid impedimetric sensing of phthalates, in *Instrumentation and Measurement Technology Conference (I2MTC) Proceedings, 2014 IEEE International* (2014), pp. 838–843
33. A. Syaifudin, K. Jayasundera, S. Mukhopadhyay, A novel planar interdigital sensor based sensing and instrumentation for detection of dangerous contaminated chemical in seafood, in *Instrumentation and Measurement Technology Conference, I2MTC'09* (IEEE, 2009), pp. 701–706
34. J. Fischer, H. Dejmokva, J. Barek, Electrochemistry of pesticides and its analytical applications. *Curr. Org. Chem.* **15**, 2923–2935 (2011)
35. M. Khafaji, S. Shahrokhian, M. Ghalkhani, Electrochemistry of levo-thyroxin on edge-plane pyrolytic graphite electrode: application to sensitive analytical determinations. *Electroanalysis* **23**, 1875–1880 (2011)
36. L. Li, F. Yang, J. Yu, X. Wang, L. Zhang, Y. Chen et al., In situ growth of ZnO nanowires on Zn comb-shaped interdigitating electrodes and their photosensitive and gas-sensing characteristics. *Mat. Res. Bull.* **47**, 3971–3975 (2012)
37. M. Dhull, A. Arora, Design of MEMS based microheater for enhanced efficiency of gas sensors. *J. Therm. Sci. Eng. Appl.* **2**, 16–21 (2015)
38. S.C. Mukhopadhyay, C.P. Gooneratne, A novel planar-type biosensor for noninvasive meat inspection. *IEEE Sens. J.* **7**, 1340–1346 (2007)
39. M.S.A. Rahman, S.C. Mukhopadhyay, P.-L. Yu, J. Goicoechea, I.R. Matias, C.P. Gooneratne et al., Detection of bacterial endotoxin in food: New planar interdigital sensors based approach. *J. Food Eng.* **114**, 346–360 (2013)
40. C. Xhoffer, K. Van den Bergh, H. Dillen, Electrochemistry: a powerful analytical tool in steel research. *Electrochim. Acta* **49**, 2825–2831 (2004)
41. C.V. Vidal, A.I. Muñoz, Effect of physico-chemical properties of simulated body fluids on the electrochemical behaviour of CoCrMo alloy. *Electrochim. Acta* **56**, 8239–8248 (2011)
42. X. Li, K. Toyoda, I. Ihara, Coagulation process of soymilk characterized by electrical impedance spectroscopy. *J. Food Eng.* **105**, 563–568 (2011)
43. C. Liu, Q. Bi, A. Leyland, A. Matthews, An electrochemical impedance spectroscopy study of the corrosion behaviour of PVD coated steels in 0.5 N NaCl aqueous solution: Part II.: EIS interpretation of corrosion behaviour. *Corros. Sci.* **45**, 1257–1273 (2003)
44. A. Ghasemi, V. Raja, C. Blawert, W. Dietzel, K. Kainer, Study of the structure and corrosion behavior of PEO coatings on AM50 magnesium alloy by electrochemical impedance spectroscopy. *Surf. Coat. Technol.* **202**, 3513–3518 (2008)
45. R.M. Souto, M.A.M. Laz, R.L. Reis, Degradation characteristics of hydroxyapatite coatings on orthopaedic TiAlV in simulated physiological media investigated by electrochemical impedance spectroscopy. *Biomaterials* **24**, 4213–4221 (2003)
46. D. Andre, M. Meiler, K. Steiner, C. Wimmer, T. Soczka-Guth, D. Sauer, “Characterization of high-power lithium-ion batteries by electrochemical impedance spectroscopy, I. Experimental investigation. *J. Power Sour.* **196**, 5334–5341 (2011)
47. F. Lisdat, D. Schäfer, The use of electrochemical impedance spectroscopy for biosensing. *Anal. Bioanal. Chem.* **391**, 1555–1567 (2008)
48. B.-Y. Chang, S.-M. Park, Electrochemical impedance spectroscopy. *Annu. Rev. Anal. Chem.* **3**, 207–229 (2010)
49. G. Instruments, Basics of electrochemical impedance spectroscopy. *Gamry Inst. Complex Impedance Corros.* **130** (2007)

50. I.I. Suni, Impedance methods for electrochemical sensors using nanomaterials. *Trends Anal. Chem.* **27**, 604–611 (2008)
51. J.R. Macdonald, E. Barsoukov, Impedance spectroscopy: theory, experiment, and applications. *History* **1** **8** (2005)
52. J.E.B. Randles, Kinetics of rapid electrode reactions. *Discuss. Faraday Soc.* **1**, 11–19 (1947)
53. K. Haupt, A.V. Linares, M. Bompard, B.T.S. Bui, Molecularly imprinted polymers, in *Molecular Imprinting* (Springer: Berlin/Heidelberg, Germany, 2012), pp. 1–28
54. M.J. Whitcombe, N. Kirsch, I. Nicholls, A. Molecular imprinting science and technology: A survey of the literature for the years 2004–2011. *J. Mol. Recognit.* **27**, 297–401 (2014)
55. S.N. Prabhu, S.C. Mukhopadhyay, A.S. Davidson, G. Liu, Highly selective molecularly imprinted polymer for creatinine detection, in *2019 13th International Conference on Sensing Technology (ICST)* (Sydney, Australia, 2019), pp. 1–5
56. Analog Devices AD5933: Impedance Analyzer, https://www.analog.com/media/en/technical_documentation/datasheets/AD5933.pdf. Accessed 9 Feb 2020
57. S. Prabhu, C. Gooneratne, K.A. Hoang, S. Mukhopadhyay, IoT-associated impedimetric biosensing for point-of-care monitoring of kidney health. *IEEE Sens. J.* (2020)
58. Creatinine Colorimetric Assay Kit, [https://www.abcam.com/ps/products/65/ab65333/documents/ab65333%20Glucose%20Assay%20kit%20Protocol%20v11a%20\(website\).pdf](https://www.abcam.com/ps/products/65/ab65333/documents/ab65333%20Glucose%20Assay%20kit%20Protocol%20v11a%20(website).pdf). Accessed 10 Feb 2020
59. A. Zia, A. Syaifudin, S. Mukhopadhyay, I.H. Al-Bahadly, P. Yu, C.P. Gooneratne et al., MEMS based impedimetric sensing of phthalates, in *2013 IEEE International Instrumentation and Measurement Technology Conference (I2MTC), IEEE International* (2013), 855–860
60. M.S. Abdul Rahman, S.C. Mukhopadhyay, P.-L. Yu, J. Goicoechea, I.R. Matias, C.P. Gooneratne et al., Detection of bacterial endotoxin in food: new planar interdigital sensors based approach. *J. Food Eng.* **114**, 346–360 (2013)

Recent Advancement of Interdigital Sensor for Nitrate Monitoring in Water



Md. Eshrat E. Alahi, Yun Hui, Fahmida Wazed Tina, Fowzia Akhter, Anindya Nag, Tianzhun Wu, and S. C. Mukhopadhyay

Abstract Water contamination is a significant problem in all over the world, and it is crucial to monitor the contaminating nutrients regularly for keeping the groundwater or drinking water safe. The nitrate ion has a remarkable impact on human health and the environment, and excessive use of this ion might damage the ecological system and the natural environments. Nitrate ions can be detected through various laboratory-based methods or in-situ sensor-based methods to develop a monitoring system. But for the last few years, the Interdigital sensor is used to detect the nitrate ions due to their reasonable fabrication costs and secure sensing mechanism. Some such sensors have high sensitivity with a reasonable limit of detection (LOD). Others might have a reasonable sensitivity with the reduced cost, where the proposed detection method uses a sensor-based portable sensing system. This chapter discusses the different working principles and fabrication methods of the Interdigital sensor for nitrate ions detection in water.

1 Introduction

Nitrogen is the most common natural element in the environment, and 80% of the air we breathe contains nitrogen [1]. It can be found in many forms in the air, such as Nitrogen (N_2), Nitrous oxide (N_2O), Nitrogen dioxide (NO_2), Nitric oxide (NO), and

Md. E. E. Alahi (✉) · Y. Hui · T. Wu

Shenzhen Institutes of Advanced Technology, Chinese Academy of Sciences, Beijing, China
e-mail: aalahi@yahoo.com

F. W. Tina

Faculty of Science and Technology, Nakhon Si Thammarat Rajabhat University, Tha Ngio, Thailand

A. Nag

Department of Electrical Engineering, CEMSE Division, the King Abdullah University of Science and Technology, Thuwal 23955, Saudi Arabia

F. Akhter · S. C. Mukhopadhyay

Faculty of Science and Engineering, Macquarie University, Sydney, Australia

© The Editor(s) (if applicable) and The Author(s), under exclusive license to Springer Nature Switzerland AG 2021

S. C. Mukhopadhyay et al. (eds.), *Interdigital Sensors*, Smart Sensors, Measurement and Instrumentation 36, https://doi.org/10.1007/978-3-030-62684-6_12

Ammonia (NH_3) [2]. Some of these gases combine with rainwater and go the water as nitrate and ammonium ions. They mix with the soil and groundwater. Consumption of the nitrate ion has several health benefits for the human body, such as improving blood flow, cardio-vaso-protective effects, and reducing blood pressure. However, adverse effects can occur due to an excessive intake of nitrate ions for the human body, primarily through drinking water, such as gastric, cancer, and Parkinson's diseases. Infants can suffer the diseases, called "blue baby syndrome" or methemoglobinemia [3], which reduces the oxygen level of the blood [4]. It affects infants of six months old. The unnecessary use of fertilizers in the agriculture field and general mishandling of the use of natural resources are also liable for the agitation of the global and local nitrogen cycle. Waste materials can be another anthropogenic source of nitrates in water. Nitrate in an aquatic medium stimulates the excessive production of algae and phytoplankton, which leads to eutrophication. They consume oxygen from water during the decomposition process, which affects the fish or other aquatic life. These problems have been identified widely all over the world, and as a result, different international and government organizations have created frameworks to control the level within the environment and in food products, with appropriate regulations in most industrialized countries. Therefore, monitoring the environmental fate of nitrates has gained increasing importance in global water monitoring research.

The need and desire to monitor nitrates is undeniable, yet monitoring their presence can present a significant challenge to the research community. There are similar ions available in water, such as nitrate, ammonium, phosphate, and sulfate, where they have a similar molecular structure. Therefore, improved detection methods are essential for avoiding any kind of interference that can be encountered in various water sources, such as the environment, industries, food, and industrial activities. Over the years, many analytical methods and sensing methods have been developed to overcome the difficulties to identify the nitrate ion in various media. Many different methods are used to determine nitrate ion in water, with the spectrometric method being the most common [5–11]. Other laboratory-based methods, such as spectrophotometric, conductimetric, or electrochemical detection, are frequently used with the combination of ion-exchange chromatography or ion-selective electrode [12] for nitrate detection. They are appropriate for the detection of a wide variety of environmental samples, such as water for drinking, ground and surface water, waters from acid rain, and wastewater [8, 13–19]. All these methods have good high accuracy, sensitivity, and good reproducibility. However, these methods require trained technicians, massive and costly instruments, produce a lot of chemical waste and comprehensive treatment of the samples beforehand.

Interdigital electrodes [20] are the most used periodic electrode structure for various applications. It has many applications [21–23] for the last few decades due to the favorable aspects. One of the significant benefits of the interdigital sensor is its simple fabrication methods and low-cost sensing method in many real-time applications. Some of the favourable aspects of interdigital sensors are sensor's geometry, fabrication technique, choice of materials, and numerical modeling. Among the many

advantages of using an interdigital sensor, it can integrate with various instrumentations to design labs on a chip device. Therefore, it has been used for the last few decades in various applications, and nitrate detection is one of them.

In this chapter, the working principle of the interdigital sensor will be discussed to understand the functionality and usefulness of the method. Some fabrication methods will also be discussed, including the application of an interdigital nitrate sensor for water monitoring. And finally, conclusions and future research directions will be discussed.

2 Working Principle

2.1 Electric Field Sensing

The interdigital sensor has the same working principle of operation as the more conventional parallel-plate capacitor or coaxial cylinder dielectric sensor cell. A small alternating current (AC) voltage is applied to the electrodes to measure the impedance of those electrodes. A bulging electric field generates from the positive electrode and goes to the negative electrode, which is similar to the single capacitor. The material under test (MUT) can be provided on one side of the sensing surface to measure the capacitance and conductance, which solely depends on the dielectric properties of the materials. The combination of the electrode can be varied based on the applications. It is a direct measurement method where the sinusoidal AC signal can be varied with various frequencies. The varied frequency signal provides extensive information on the material. Since the induced impedance is directly related to the changes of various physical, chemical, and structural properties of materials, this method provides the nondestructive evaluation of vital parameters in a variety of industrial and scientific applications [24, 25]. Figure 1 illustrates the transformation of the coplanar interdigital sensor.

Usually, the capacitance between two coplanar strips is comparable to the stray capacitance of the electrodes due to the conduction with the electrical excitation source. The coplanar stripe pattern could be repeated many times to boost an easily computable electrode structure. The permeation depth of the fringing electric fields

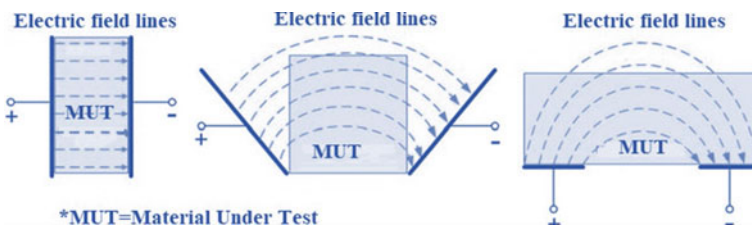


Fig. 1 Electric field intensity of parallel-plate capacitors and coplanar interdigital sensors [26]

Fig. 2 MEMS-based Interdigital sensor [27]

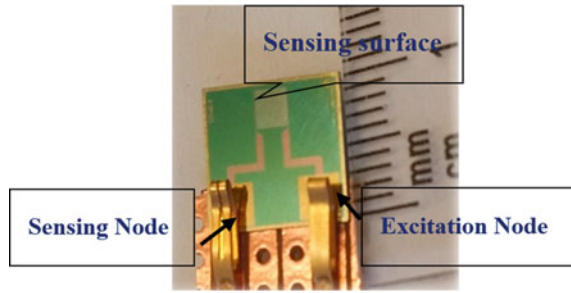
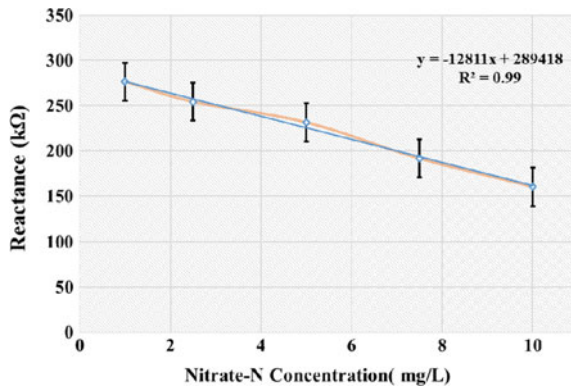


Fig. 3 Calibration standard for nitrate-N measurement [28]



above the interdigital electrodes is related to the pitch gap between the driven fingers and is independent of frequency (Fig. 2).

There are some studies [27–31] have been conducted on interdigital sensors to develop a low-cost sensing system for nitrate measurement. In a low-cost sensing system, Electrochemical Impedance Spectroscopy (EIS) is used for measurement in where a small alternating signal is provided to the anode, and an output signal is produced at the cathode. In this method, the impedance measurement is done through an LCR meter. The sensitivity of the sensor depends on the length, width, and pitch gaps, as well as on the electrodes' materials and the sensing area. A smart sensor used for nitrate detection in water was reported by Alahi et al. [28]. In this sensor, temperature compensation was added to improve the sensitivity, and the detection limit was 0.01–0.5 mg/L. On the silicon substrate, gold electrodes were used for excitation and Sensing. The pitch gap of the electrodes was 25 μm , and the dimension of the sensing surface was 2.5×2.5 mm. This advanced sensor was able to measure nitrate in water and transfer the measured data to the cloud for real-time monitoring. Another study by Alahi et al. [28, 32] explained the principle of selective material for nitrate detection. An imprinting polymer technique was used for material development, and the detection range was from 1–10 mg/L. This developed material was used as a coating material on the interdigital sensor for nitrate detection in the

lake, stream, river, and canal water. The calibration curve (Fig. 3) was developed in terms of reactance, and later, it was used to measure unknown nitrate samples.

A Graphene-based electrode (Fig. 4) was used for nitrate detection in water [29, 30] with a detection limit of 1–70 mg/L. The sensitivity was improved significantly by printing graphene on Kapton tape. It was also proposed to use temperature compensation for further improvement of the sensitivity of the sensor. This sensor was robust, cost-effective, easy to operate, and useful for nitrate measurement. Alahi et al. [27, 33] developed an interdigital sensor based on FR4 and the Internet of Things for nitrate measurement and found it extremely useful for nitrate detection from creek, stream, lake water in real-time. Table 1 summarises the various characteristics of planar interdigital sensors.

Fig. 4 Graphene-based interdigital sensor [30]

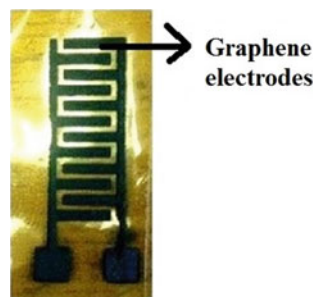


Table 1 Various Planar Interdigital sensor with different characteristics

Type of sensor	Sensor's response	Limit of detection (LOD)	Linear range	Application	Ref.
MEMS sensor	$-115,543 \Omega/0.1 \text{ ppm}$	0.01 mg/L	(0.01–0.5) mg/L	Smart sensing system for agricultural industry	[27]
Graphene Sensor	$-667.97 \Omega/\text{ppm}$	1 mg/L	1–70 mg/L	IoT-enabled smart sensing system	[29]
MEMS-based coated sensor	$-12,811 \Omega/\text{ppm}$	1.06 mg/L	1–10 mg/L	Smart sensing system for water quality measurement	[28]
FR4-based sensor	$-51.76 \Omega/\text{ppm}$	1 mg/L	1–40 mg/L	Water quality monitoring	[2]
FR4-based coated sensor	–	–	5–100 mg/L	Nitrate, phosphate and nickel detection	[34]

2.2 Interdigital Sensing based on Magnetic Field

The sensing method is called the low-frequency interdigital sensor that measures capacitance and conductance function in the region of the electro-quasi-static estimate to Maxwell equations. It is also important to mention that the magneto-quasi-static analog of these sensors is also called as meandering winding magnetometers [24, 35–39]. Figure 5 illustrates a standard structural design of this type of sensor. The interdigital pattern is carried out by the insulating substrate and windings instead of the conducting electrodes. The conducting electrode patterned interdigital section is discussed in the previous section. When the electric current goes across the windings, it stimulates the eddy currents in the conducting MUT. Due to the variation of material properties, the change of mutual inductance between secondary and primary windings occurs. The voltage of secondary winding is given by the time rate of change of magnetic flux crossing through the secondary winding, which comes from the current of the primary winding. The induced voltage can become very small at low frequencies. It can also be possible to replace the secondary winding with a magneto-resistive sensor to operate at very low frequencies, down to dc for overcoming this low-frequency limitation.

After conducting much research on impedance-based sensors, it has been proved that they are excellent at measuring physical properties and suitable for direct measurement. A Planar Electromagnetic Sensor Array (PESA) is one of those sensors which measures physical properties in terms of impedance. PESA is convenient for in-situ measurement. It is highly reliable, cost-effective, and shows a quick response. During measuring nitrate in water samples, different properties of the sample (i.e., conductivity, dielectric properties, and permeability) can be estimated [40–43]. It is essential to enhance the sensor's sensitivity, which can be done by optimizing the sensor design and configuration. A planar electromagnetic sensor used for nitrate

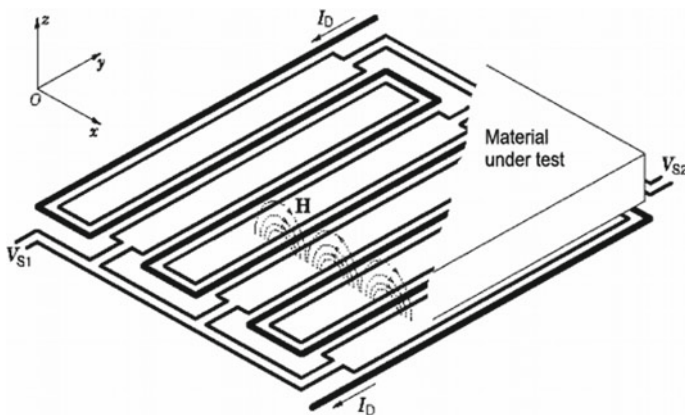


Fig. 5 A meandering winding magnetometer for measuring high conductivity and magnetic materials [38]

detection in an aqueous medium was reported by Yunus et al. [41]. This sensor's performance was measured through two different arrangements: series and parallel connections. It was found that series connection showed better performance during nitrate detection in terms of the sensor's sensitivity. Therefore it is better to use a series connection for electromagnetic sensors. The material of the electrodes is another important thing on which the sensitivity of the sensors also depends. In the previously reported work, gold electrodes were used due to the attraction of nitrate ions towards gold. However, for developing a high-sensitivity sensor, it is required to use a high-dielectric substrate to increase the penetration depth of the electric field. Usually, there are three configurations to design the electrodes: parallel, star, and delta. Nor et al. [42] reported a sensor array with a thin substrate on a Printed Circuit Board (PCB), which was made by using a conventional PCB fabrication technique. This designed sensor had several coils or loops of electrodes that were spiral or square. The sensitivity of the sensor also depends on the distance between the coils. The impedance of a sensor can be increased by increasing the distance between the two electrodes and decreasing their area [15].

3 Fabrication Techniques

Various materials can be used to fabricate the interdigitated structure for various applications. After the raw materials are chosen for a particular sensing device, the fabrication technique processes these materials to produce the sensor prototypes with a definite shape and structure. One particular type of fabrication technique is chosen based on the following attributes:

1. **Raw materials:** The type of raw materials that are being used to develop the sensor decides which technique would have a better capability to process them comparatively with the best efficiency. The costing of the material is also an essential factor in deciding the fabrication method.
2. **The dimension of the Sensor:** The dimensions of the sensors can be significantly varied with the techniques used for fabrication. For example, the dimensions go down to a few micrometers in the screen printing method, while the photolithography method will reduce the dimension to a few nanometres.
3. **Application:** The use of the sensors can also decide the technique chosen for their fabrication. Some of the applications like monitoring of body movements or physiological parameters would require much smaller and sensitive sensors compared to the applications like water quality monitoring.

There are various fabrication techniques available; some of the conventional techniques are discussed below:

1. **Photolithography** [44, 45]: Lithography or photolithography is the most common and standard technique to developed sensors. This is done by using light (ultra-violet) for patterning a design on a solid substrate. The UV light

transfers the design developed on the photo-mask or uploaded on the system. There are two types of photolithography processes based on the template.

- a. **Masked lithography** [46]: This is the process where a mask or a template is present above the photoresist coated substrate. The intensity of the UV lights falls on the solid substrate via the template forming the pattern on the substrate.
- b. **Mask-less lithography** [47]: Here, the targeted design is already uploaded on the system. The photoresist contained substrate is scanned by the UV light over the substrate to form the uploaded design.

There are two different photoresists available to coat the solid surface:

There are two different photoresists available to coat the solid surface:

- a. **Positive photoresist** [48]: In the positive photoresist, the UV light exposed parts on the substrate can be removed through the subsequent treatment processes while the rest of the parts stay. This resist is then treated so that the design on the substrate engraves permanently.
- b. **Negative photoresist** [49]: In negative photoresist, the photoresist part exposed with the UV light, which remains on the substrate. The whole part removes from the surface.

Figure 6 shows the use of positive and negative photoresist on masked photolithography [50].

The next process is the exposing process to develop and the photoresist from the surface. Tetramethylammonium hydroxide (TMAH) [51] or Su-8 [52], is used as developing the surface. The developing chemical is soluble with the resist that has to be removed, which is then done with the etching process. Etching can of two different types:

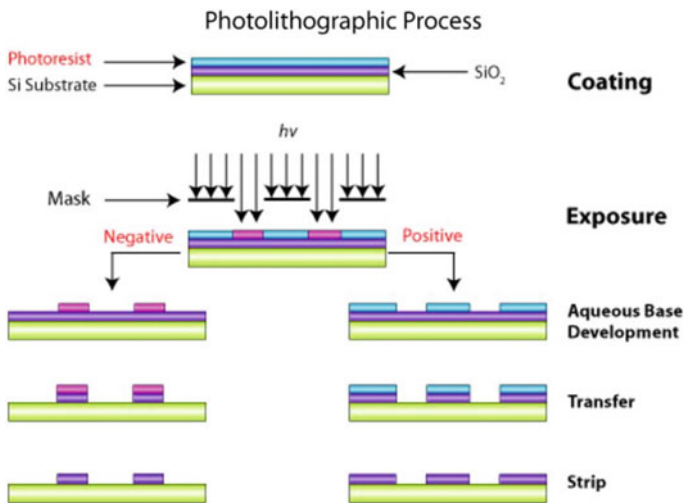
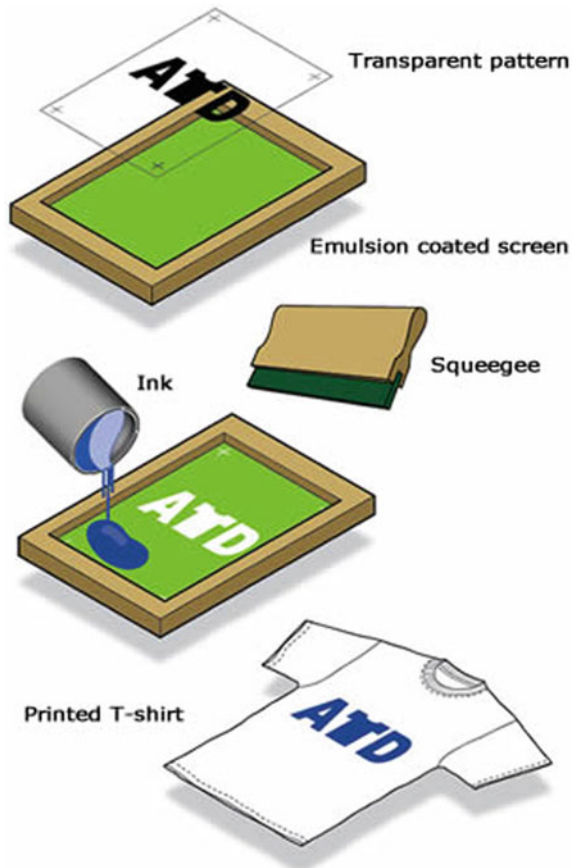


Fig. 6 Schematic diagram for the masked photolithography with positive and negative photoresist [50]

- a. **Wet etching** [53]: In the wet etching process, the exposed substrate is treated with specific chemicals to remove the soluble resist. It is a pervasive process in Microelectromechanical systems (MEMS) to develop the isotropic patterns on the exposed substrate.
 - b. **Dry etching** [54]: Dry or plasma etching is widely used for anisotropic patterns on the exposed substrate. It is done with oxygen inside a vacuum chamber where the plasma hits the top surface of the photoresist to react with the developed resist and remove it from the substrate.
2. **Screen printing** [55, 56]: This technique has been used since the early nineteenth century, where it was mostly used for commercial applications. It was around the last two decades, where the use of this technique had been done mostly in sensor development. In this technique, a mesh is employed to shift inks from one side to the other side except the regions blocked by the mesh. The flow of the ink is crucial as it restricts the thickness of the substrate. This builds a pattern on the substrate that is transferred from the mesh. Figure 7 shows an example of screen printing where the developed design on the coated screen is shifted on the printed shirt with the ink poured over the screen [57].
- There are many commercially available conductive inks like silver [58], graphene [59], which are used to create the electrodes via the explained technique on the substrate. The major advantage of using the technique is flexibility in the type of materials that can be utilized as a substrate while transferring the ink. Some of them are polymers [60], fabrics [61], circuit boards [62], etc. Even though the technique is used for a long time for manufacturing various electronic devices, it is not as efficient as other techniques as the finished products are not very specific with this technique.
3. **Laser printing** [63, 64]: Even though lasers are in use for a long time, the introduction of this technique has been done for the last two decades [65, 66]. This technique is advantageous compared to other ones because of the following reasons:
 - a. Unlike photolithography, no sample mentioned above preparation time is required to complete the process.
 - b. Fragile and flexible materials can be cut using this technique, which cannot be achieved by techniques like screen printing.
 - c. The finished products have relatively smooth edges that are perpendicular to the surface. Therefore, it is not necessary to have extra steps to refine the end product.

In this process, the substrate is carried under the laser to scan or curve out parts of the substrate to form an initial design. The proportion of sample removes from the initial cut, which also depends on the characteristics of the material and the settings parameters of the specific laser system. There are different kinds of laser machines available in the market, which vary according to the maximum output power generated by the nozzle of the laser machine. Other essential attributes that can vary the thickness of the curved sample are:

Fig. 7 Schematic diagram for the different steps followed in screen printing [57]

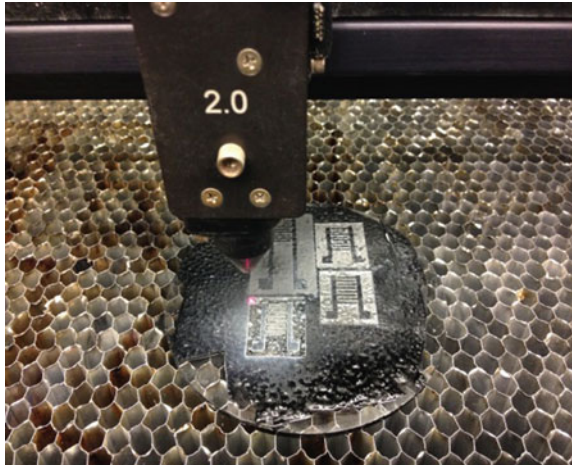


- Z-axis: This Z-axis regulates the height of the platform below the laser nozzle to keep the material in the designated location.
- Speed: It determines the speed of the nozzle to move over the sample. In the case of laser printing, there has to be a trade-off between the input power and speed of the nozzle for obtaining the optimal features.
- Frequency: It determines the frequency of the laser nozzle moving over the sample.

Figure 8 shows an example of laser printing where interdigitated shaped sensors prototypes are generated from Carbon Nanotube (CNT) and PDMS based nanocomposite. A universal laser system was used to develop the sensor where the input power was 12 Watts in the fabrication process.

- Inkjet printing** [67, 68]: Ink-jet printing technique for printed electronics has been established from the laser printers using for printing documents. The concept of using inkjet printers developed with substituting the ink with any conductive

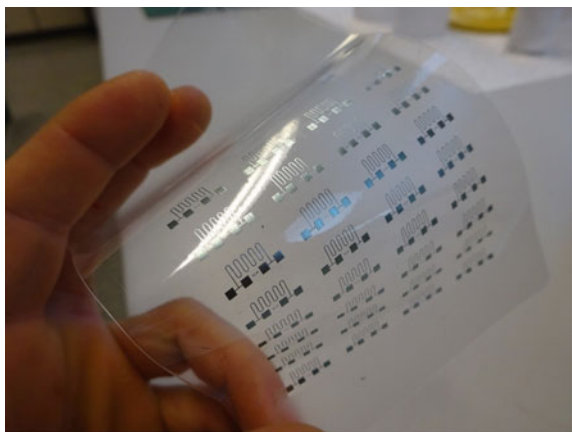
Fig. 8 The laser printing process is done on the sample to generate sensor prototypes [63]



inks to build the sensing part on any sensing substrate [69]. Figure 9 shows an example of a temperature sensor developed by inkjet printing on a PET substrate [70]. There are several advantages of utilizing this technique for fabrication associated with other techniques. Some of them are:

- a. The fabricating devices are not expensive. It is essentially a printer with the use of different conductive inks to print on the substrate for fabrication purposes.
- b. High-quality sensing devices can be accomplished by following this technique.
- c. The required time for completing the process is very less. This is beneficial in particular in the case of the fabrication of enormous scale devices.
- d. They are very more comfortable to use and can be controlled by any non-specialist users.

Fig. 9 Ink-jet printing is done on the PET substrate to develop a temperature sensor [70]



Some common types of conductive inks used in the inkjet printing process are silver [71], carbon [72], copper [73]. There are two types of inkjet printers:

- a. **Continuous printing:** In this process, a continuous stream of ink is pump after a reservoir to break down the liquid droplets by the wave created by a piezoelectric crystal contained by the laser. An electrostatic field charges the broken droplets for creating a charging electrode. The field is different in conformity with the deviation of the charge, which is desired for each droplet. The charged droplets are passed across another electrostatic field for deflecting them on the substrate material where they are printed. The charged droplets start the division on their way by the wave to the point where they come out. They are also divided by uncharged or guard droplets to minimize the repulsion between them.
- b. **Drop-on-demand (DOD) printing:** The technique is divided into two more categories:
 - **Thermal based DOD:** Here, the cartridges consist of a series of mini-heaters through a pulse of passed current for heating it. It then heats up the ink in the reservoir, thus increasing its pressure and form the bubble of ink. The constructing bubble runs out on the directed substrate as a droplet to form the desired structure. The process increases its pressure, the heating, and the condensation of the ink along with its surface tension. It also leads to a drawing effect on the ink from the reservoir, thus causing a series of droplets on the substrate.
 - **Piezoelectric based DOD:** This is similar to the thermal-based DOD, except the point that the mini heaters are replaced by piezoelectric material for changing its shape to provide a necessary voltage to it. The change in shapes increases the pressure to form a bubble and squeezes out of the droplet.
5. **Casting [22, 74]:** This technique is similar to screen printing, which has also been used for many years for commercial applications. This technique was also used for the fabrication of flexible interdigital sensors until the last decade or so. This process is done with a template forming a mold of the desired shape. A liquid or semi-liquid material would then be poured on the mold, which would then be solidified to have the shape of that mold. After the material has solidified, it is cast off the molded and used as a separate device. In the case of flexible sensors, the liquid or semi-liquid material that would be poured would be the conductive material that would solidify and form the electrodes. On top of the solidified mold, a layer of different material like a polymer would be poured solidified and cast to form the substrate for the sensor. The schematic diagram for the explained steps is shown in Fig. 10 [22]. This method was followed to form a flexible sensor with PDMS as the substrate and a nanocomposite of Multi-walled Carbon Nanotubes (MWCNTs) and PDMS as the electrode material.

There are some significant advantages of using this technique which are:

- a. It can be possible to develop complex structures with this process as the design of the desired interdigitated electrodes would be the design of the mold.

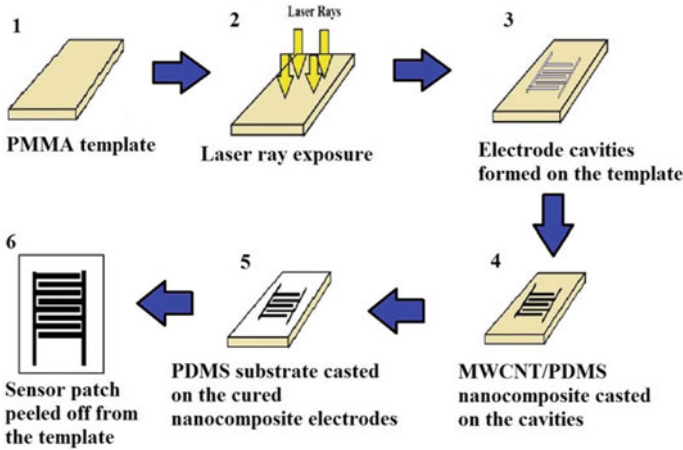


Fig. 10 Schematic diagram for the individual steps followed in the casting technique to develop a strain-sensitive sensor prototype [22]

- b. It is not expensive than other MEMS-based standard fabrication techniques like photolithography or laser printing.
- c. The method is flexible to get any shape of desired prototypes.

Even though the casting technique has been used significantly lately [75, 76], some limitations curb its use to no small extent. Some of the limitations are:

- a. Micro-structures cannot be obtained with this technique.
- b. The electrodes' sensitivity is not as high as the ones developed with other methods, such as laser cutting techniques or printing techniques. This is for the reason that the second material (preferably a polymer) poured over the first solidified material decreases the conductivity of the electrodes.
6. **Weaving** [77, 78]: This one is comparatively a recent one which is used to develop flexible electronics Compared to the previously mentioned techniques. The technique is mainly used to develop fabric embedded sensors [79, 80]. Handlooms or any weaving device follow this process. This reason because this technique is comparatively newer; the weaving machines designed for developing fabric embedded flexible sensors are still high in cost and need to be handled by specialists. Figure 11 shows an example of the weaving technique, where the woven silk stripes were used as glucose sensors [81].

Some of the advantages of using this technique are:

- a. The person using the sensor won't have to wear anything separately as the sensor would be embedded in the textile.
- b. The sensor can be designed with a single step. There are no individual steps in developing the electrodes and substrates separately.

Fig. 11 A handloom used to weave silk strips, which would be used as glucose sensors [81]



- c. The sensors can be developed with any substrate without scrutinizing much into their characteristics. This is because the conductive material would be woven on the garments [82].

4 Conclusion

The working principle of the interdigital sensor is explained in this chapter. Their advantage and drawbacks are also explained, which might be helpful for the readers. Various fabrication methods are also discussed. Some methods are useful for low-cost sensor developments, and some are useful for highly sensitive sensor developments. Most of the interdigital sensors for nitrate detections are used for in-situ measurements, and it is also a significant research point to find out the reasonable methods to reduce the fabrications cost with high sensitivity.

References

1. E. Berner, R. Berner, *The Global Water Cycle Prentice Hall*, New Jersey (1987)
2. M.E.E. Alahi, S.C. Mukhopadhyay, Detection methods of nitrate in water: a review. *Sens. Actuators, A* **280**, 210–221 (2018)
3. H.H. Comly, Cyanosis in infants caused by nitrates in well water. *J. Am. Med. Assoc.* **129**(2), 112–116 (1945)
4. P. Brimblecombe, D. Stedman, Historical evidence for a dramatic increase in the nitrate component of acid rain. *Nature* **298**(5873), 460–462 (1982)
5. M.S. Finch, D.J. Hydes, C.H. Clayson, B. Weigl, J. Dakin, P. Gwilliam, A low power ultra violet spectrophotometer for measurement of nitrate in seawater: introduction, calibration and initial sea trials. *Anal. Chim. Acta* **377**(2–3), 167–177 (1998)
6. M.A. Ferree, R.D. Shannon, Evaluation of a second derivative UV/visible spectroscopy technique for nitrate and total nitrogen analysis of wastewater samples. *Water Res.* **35**(1), 327–332 (2001)

7. M. Abbas, G. Mostafa, Determination of traces of nitrite and nitrate in water by solid phase spectrophotometry. *Anal. Chim. Acta* **410**(1–2), 185–192 (2000)
8. K.M. Miranda, M.G. Espey, D.A. Wink, A rapid, simple spectrophotometric method for simultaneous detection of nitrate and nitrite. *Nitric Oxide* **5**(1), 62–71 (2001)
9. K. Sastry, R. Moudgal, J. Mohan, J. Tyagi, G. Rao, Spectrophotometric determination of serum nitrite and nitrate by copper–cadmium alloy. *Anal. Biochem.* **306**(1), 79–82 (2002)
10. T.A. Doane, W.R. Horwath, Spectrophotometric determination of nitrate with a single reagent. *Anal. Lett.* **36**(12), 2713–2722 (2003)
11. A. Drolc, J. Vrtovšek, Nitrate and nitrite nitrogen determination in waste water using on-line UV spectrometric method. *Biores. Technol.* **101**(11), 4228–4233 (2010)
12. M.J. Moorcroft, J. Davis, R.G. Compton, Detection and determination of nitrate and nitrite: a review. *Talanta* **54**(5), 785–803 (2001)
13. A. Dudwadkar, N. Shenoy, J. Joshi, S.D. Kumar, H. Rao, A. Reddy, Application of ion chromatography for the determination of nitrate in process streams of thermal denitration plant. *Sep. Sci. Technol.* **48**(16), 2425–2430 (2013)
14. X.-H. Pham et al., Electrochemical detection of nitrite using urchin-like palladium nanostructures on carbon nanotube thin film electrodes. *Sens. Actuators B: Chem.* **193**, 815–822 (2014)
15. X. Wang, Y. Wang, H. Leung, S.C. Mukhopadhyay, M. Tian, J. Zhou, Mechanism and experiment of planar electrode sensors in water pollutant measurement. *IEEE Trans. Instrum. Meas.* **64**(2), 516–523 (2014)
16. B. Schazmann, D. Diamond, Improved nitrate sensing using ion selective electrodes based on urea–calixarene ionophores. *New J. Chem.* **31**(4), 587–592 (2007)
17. B.A. Pellerin, B.A. Bergamaschi, B.D. Downing, J.F. Saraceno, J.D. Garrett, L.D. Olsen, Optical techniques for the determination of nitrate in environmental waters: guidelines for instrument selection, operation, deployment, maintenance, quality assurance, and data reporting. *US Geological Survey Techniques and Methods*, pp. 1–D5, (2013)
18. A.A. Ensafi, M. Amini, Highly selective optical nitrite sensor for food analysis based on Lauth’s violet–triacyetyl cellulose membrane film. *Food Chem.* **132**(3), 1600–1606 (2012)
19. G. Pandey, R. Kumar, R.J. Weber, Real time detection of soil moisture and nitrates using on-board in-situ impedance spectroscopy, in *2013 IEEE International Conference on Systems, Man, and Cybernetics* (IEEE, 2013), pp. 1081–1086
20. M.E.E. Alahi, S.C. Mukhopadhyay, Interdigitated Sensor and Electrochemical Impedance Spectroscopy (EIS), in *Smart Nitrate Sensor* (Springer, 2019), pp. 43–52
21. A. Nag, M.E.E. Alahi, S. Feng, S.C. Mukhopadhyay, IoT-based sensing system for phosphate detection using graphite/PDMS sensors. *Sens. Actuators, A* **286**, 43–50 (2019)
22. A. Nag, S. Mukhopadhyay, J. Kosel, Transparent biocompatible sensor patches for touch sensitive prosthetic limbs, in *2016 10th International Conference on Sensing Technology (ICST)* (IEEE, 2016), pp. 1–6
23. N. Afsarimaneh, M.E.E. Alahi, S.C. Mukhopadhyay, M. Kruger, Development of IoT-based impedometric biosensor for point-of-care monitoring of bone loss. *IEEE J. Emerg. Sel. Top. Circuits Syst.* **8**(2), 211–220 (2018)
24. N.J. Goldfine, A.P. Washabaugh, J.V. Dearlove, P.A. von Guggenberg, Imposed ω -k magnetometer and dielectrometer applications, in *Review of Progress in Quantitative Nondestructive Evaluation* (Springer, 1993), pp. 1115–1122
25. Y. Sheiretov, M. Zahn, Dielectrometry measurements of moisture dynamics in oil-impregnated pressboard. *IEEE Trans. Dielectr. Electr. Insul.* **2**(3), 329–351 (1995)
26. M.E. Alahi, L. Xie, A.I. Zia, S. Mukhopadhyay, L. Burkitt, Practical nitrate sensor based on electrochemical impedance measurement, in *2016 IEEE International Instrumentation and Measurement Technology Conference Proceedings* (IEEE, 2016), pp. 1–6
27. M.E.E. Alahi, X. Li, S. Mukhopadhyay, L. Burkitt, A temperature compensated smart nitrate-sensor for agricultural industry. *IEEE Trans. Ind. Electron.* (2017)
28. M.E.E. Alahi, S.C. Mukhopadhyay, L. Burkitt, Imprinted polymer coated impedimetric nitrate sensor for real-time water quality monitoring. *Sens. Actuators B: Chem.* **259**, 753–761 (2018)

29. M.E.E. Alahi, A. Nag, S.C. Mukhopadhyay, L. Burkitt, A temperature-compensated graphene sensor for nitrate monitoring in real-time application. *Sens. Actuators, A* **269**, 79–90 (2018)
30. M.E.E. Alahi, S.C. Mukhopadhyay, Graphite/PDMS capacitive sensor for nitrate measurement, in *Smart Nitrate Sensor* (Springer, 2019), pp. 73–89
31. M.E.E. Alahi, S.C. Mukhopadhyay, Temperature compensation for low concentration nitrate measurement, in *Smart Nitrate Sensor* (Springer, 2019), pp. 53–72
32. M.E.E. Alahi, S.C. Mukhopadhyay, Preparation and characterization of the selectivity material of nitrate sensor, in *Smart Nitrate Sensor* (Springer, 2019), pp. 91–113
33. M.E.E. Alahi, N. Pereira-Ishak, S.C. Mukhopadhyay, L. Burkitt, An internet-of-things enabled smart sensing system for nitrate monitoring. *IEEE Internet Things J.* **5**(6), 4409–4417 (2018)
34. A. Azmi, A.A. Azman, S. Ibrahim, M.A.M. Yunus, Techniques in advancing the capabilities of various nitrate detection methods: a review. *Int. J. Smart Sens. Intell. Syst.* **10**(2) (2017)
35. M. Zaretsky, J. Melcher, Complex permittivity measurements of thin films using microdielectrometry, in *Conference on Electrical Insulation & Dielectric Phenomena—Annual Report 1986* (IEEE, 1986), pp. 462–471
36. N. Goldfine, Y. Sheiretov, A. Washabaugh, V. Zilberstein, S. Kenny, P. Crowther, Materials characterisation and flaw detection for metallic coating repairs. *Insight* **42**(12), 809–814 (2000)
37. M.E. Van Steenberg, A. Washabaugh, N. Goldfine, Inductive and capacitive sensor arrays for in situ composition sensors, in *2001 IEEE Aerospace Conference Proceedings (Cat. No. OITH8542)*, vol. 1 (IEEE, 2001), pp. 1/299–1/309
38. A.V. Mamishev, K. Sundara-Rajan, F. Yang, Y. Du, M. Zahn, Interdigital sensors and transducers. *Proc. IEEE* **92**(5), 808–845 (2004)
39. N. Goldfine, V. Zilberstein, J.S. Cargill, D. Schlicker, I. Shay, Meandering winding magnetometer array eddy current sensors for detection of cracks in regions with fretting damage. *Mater. Eval.* **60**(7), 870–877 (2002)
40. G. Ellis, I. Adatia, M. Yazdanpanah, S.K. Makela, Nitrite and nitrate analyses: a clinical biochemistry perspective. *Clin. Biochem.* **31**(4), 195–220 (1998)
41. M.A.M. Yunus, S.C. Mukhopadhyay, Novel planar electromagnetic sensors for detection of nitrates and contamination in natural water sources. *IEEE Sens. J.* **11**(6), 1440–1447 (2010)
42. A.S.M. Nor, M.A.M. Yunus, S.W. Nawawi, S. Ibrahim, Low-cost sensor array design optimization based on planar electromagnetic sensor design for detecting nitrate and sulphate, in *2013 Seventh International Conference on Sensing Technology (ICST)* (IEEE, 2013), pp. 693–698
43. M.A.M. Yunus, S. Mukhopadhyay, A. PUNCHIHewa, Application of independent component analysis for estimating nitrate contamination in natural water sources using planar electromagnetic sensor, in *2011 Fifth International Conference on Sensing Technology* (IEEE, 2011), pp. 538–543
44. N. Herzer, S. Hoepfner, U.S. Schubert, Fabrication of patterned silane based self-assembled monolayers by photolithography and surface reactions on silicon-oxide substrates. *Chem. Commun.* **46**(31), 5634–5652 (2010)
45. S. Khumpuang, H. Maekawa, S. Hara, Photolithography for minimal fab system. *IEEE Trans. Sens. Micromachines* **133**(9), 272–277 (2013)
46. D.J. Harris, H. Hu, J.C. Conrad, J.A. Lewis, Patterning colloidal films via evaporative lithography. *Phys. Rev. Lett.* **98**(14), 148301 (2007)
47. A. Nag, A.I. Zia, X. Li, S.C. Mukhopadhyay, J. Kosel, Novel sensing approach for LPG leakage detection: Part I—operating mechanism and preliminary results. *IEEE Sens. J.* **16**(4), 996–1003 (2016)
48. H.S. Lee, J.-B. Yoon, A simple and effective lift-off with positive photoresist. *J. Micromech. Microeng.* **15**(11), 2136 (2005)
49. S. Sugiura, K. Sumaru, K. Ohi, K. Hiroki, T. Takagi, T. Kanamori, Photoresponsive polymer gel microvalves controlled by local light irradiation. *Sens. Actuators, A* **140**(2), 176–184 (2007)
50. Photoresists. <https://www.photochembsu.com/applications/photoresists.html>
51. E. Barborini et al., Batch fabrication of metal oxide sensors on micro-hotplates. *J. Micromech. Microeng.* **18**(5), 055015 (2008)
52. P. Data, SU-8 Developer

53. D. Zhuang, J. Edgar, Wet etching of GaN, AlN, and SiC: a review. *Mater. Sci. Eng.: R: Rep.* **48**(1), 1–46 (2005)
54. R.A. Powell, *Dry Etching for Microelectronics* (Elsevier, 2012)
55. S. Ohta, S. Komagata, J. Seki, T. Saeki, S. Morishita, T. Asaoka, All-solid-state lithium ion battery using garnet-type oxide and Li₃BO₃ solid electrolytes fabricated by screen-printing. *J. Power Sources* **238**, 53–56 (2013)
56. S. Khan, L. Lorenzelli, R. Dahiya, Bendable piezoresistive sensors by screen printing MWCNT/PDMS composites on flexible substrates, in *2014 10th Conference on Ph. D. Research in Microelectronics and Electronics (PRIME)* (IEEE, 2014), pp. 1–4
57. *Meshed screen printing*. <https://www.polyestermeshfabric.com/technology/use-screen-printing.html>
58. S. Merilampi, T. Laine-Ma, P. Ruuskanen, The characterization of electrically conductive silver ink patterns on flexible substrates. *Microelectron. Reliab.* **49**(7), 782–790 (2009)
59. J. Ping, J. Wu, Y. Wang, Y. Ying, Simultaneous determination of ascorbic acid, dopamine and uric acid using high-performance screen-printed graphene electrode. *Biosens. Bioelectron.* **34**(1), 70–76 (2012)
60. D.A. Pardo, G.E. Jabbour, N. Peyghambarian, Application of screen printing in the fabrication of organic light-emitting devices. *Adv. Mater.* **12**(17), 1249–1252 (2000)
61. I. Locher, G. Tröster, Screen-printed textile transmission lines. *Text. Res. J.* **77**(11), 837–842 (2007)
62. A.C. Siegel, S.T. Phillips, M.D. Dickey, N. Lu, Z. Suo, G.M. Whitesides, Foldable printed circuit boards on paper substrates. *Adv. Func. Mater.* **20**(1), 28–35 (2010)
63. A. Nag, S.C. Mukhopadhyay, J. Kosel, Flexible carbon nanotube nanocomposite sensor for multiple physiological parameter monitoring. *Sens. Actuators, A* **251**, 148–155 (2016)
64. A. Nag, S.C. Mukhopadhyay, J. Kosel, Tactile sensing from laser-ablated metallized PET films. *IEEE Sens. J.* **17**(1), 7–13 (2016)
65. J.A. Barron, B.R. Ringeisen, H. Kim, B.J. Spargo, D.B. Chrisey, Application of laser printing to mammalian cells. *Thin Solid Films* **453**, 383–387 (2004)
66. A.J. Birnbaum, H. Kim, N.A. Charipar, A. Piqué, Laser printing of multi-layered polymer/metal heterostructures for electronic and MEMS devices. *Appl. Phys. A Mater. Sci. Process.* **99**(4), 711–716 (2010)
67. S.Z. Hossain et al., Development of a bioactive paper sensor for detection of neurotoxins using piezoelectric inkjet printing of sol–gel-derived bioinks. *Anal. Chem.* **81**(13), 5474–5483 (2009)
68. C.M. Homenick et al., Fully printed and encapsulated SWCNT-based thin film transistors via a combination of R2R gravure and inkjet printing. *ACS Appl. Mater. Interfaces* **8**(41), 27900–27910 (2016)
69. M. Singh, H.M. Haverinen, P. Dhagat, G.E. Jabbour, Inkjet printing—process and its applications. *Adv. Mater.* **22**(6), 673–685 (2010)
70. *Inkjet printing*. https://www.ikts.fraunhofer.de/en/departments/energy_bio-medical_technology/materials_and_components/HT_ElectrochemistryCatalysis/material_inks.html
71. W. Shen, X. Zhang, Q. Huang, Q. Xu, W. Song, Preparation of solid silver nanoparticles for inkjet printed flexible electronics with high conductivity. *Nanoscale* **6**(3), 1622–1628 (2014)
72. S. Wang et al., Inkjet printing of conductive patterns and supercapacitors using a multi-walled carbon nanotube/Ag nanoparticle based ink. *J. Mater. Chem. A* **3**(5), 2407–2413 (2015)
73. Y. Farraj, M. Grouchko, S. Magdassi, Self-reduction of a copper complex MOD ink for inkjet printing conductive patterns on plastics. *Chem. Commun.* **51**(9), 1587–1590 (2015)
74. V. Eswaraiah, K. Balasubramaniam, S. Ramaprabhu, Functionalized graphene reinforced thermoplastic nanocomposites as strain sensors in structural health monitoring. *J. Mater. Chem.* **21**(34), 12626–12628 (2011)
75. L. Lin et al., Transparent flexible nanogenerator as self-powered sensor for transportation monitoring. *Nano Energy* **2**(1), 75–81 (2013)
76. G. Latessa, F. Brunetti, A. Reale, G. Saggio, A. Di Carlo, Piezoresistive behaviour of flexible PEDOT: PSS based sensors. *Sens. Actuators B: Chem.* **139**(2), 304–309 (2009)

77. S. Takamatsu, T. Imai, T. Yamashita, T. Kobayashi, K. Miyake, T. Itoh, Flexible fabric keyboard with conductive polymer-coated fibers, in *Sensors, 2011 IEEE* (IEEE, 2011), pp. 659–662
78. N. Chen, J. Engel, S. Pandya, C. Liu, Flexible skin with two-axis bending capability made using weaving-by-lithography fabrication method, in *MEMS 2006 Istanbul. 19th IEEE International Conference on Micro Electro Mechanical Systems, 2006* (IEEE, 2006), pp. 330–333
79. J.B. Lee, V. Subramanian, Weave patterned organic transistors on fiber for E-textiles. *IEEE Trans. Electron Devices* **52**(2), 269–275 (2005)
80. K. Cherenack, C. Zysset, T. Kinkeldei, N. Münzenrieder, G. Tröster, Woven electronic fibers with sensing and display functions for smart textiles. *Adv. Mater.* **22**(45), 5178–5182 (2010)
81. *Weavers Turn Silk Into Diabetes Test Strips*. <https://www.npr.org/sections/goatsandsoda/2015/01/08/375442225/weavers-turn-silk-into-diabetes-test-strips>
82. U. Briedis, A. Valisevskis, M. Grecka, Development of a smart garment prototype with enuresis alarm using an embroidery-machine-based technique for the integration of electronic components. *Procedia Comput. Sci.* **104**, 369–374 (2017)

Temperature and Humidity Compensated Graphene Oxide (GO) Coated Interdigital Sensor for Carbon Dioxide (CO₂) Gas Sensing



Fowzia Akhter, Saima Hasan, Md. Eshrat E. Alahi,
and S. C. Mukhopadhyay

Abstract A low-cost, low-power planar interdigital carbon dioxide (CO₂) sensor is proposed in this research. A well-known dielectric material graphene oxide (GO) is used as a coating material to induce selectivity towards CO₂. The proposed sensor has been characterized and calibrated for detecting various CO₂ concentrations, temperature and humidity. A temperature and humidity compensation mechanism is also included for improving the accuracy in CO₂ concentration measurement in unknown samples. The reproducibility, repeatability, cross-sensitivity, stability, response, and recovery time test results are promising for developing a cost-effective, smart CO₂ gas monitoring system for both indoor and outdoor environments.

1 Introduction

Fabrication and implementation of a cost-effective, energy-efficient, stable, highly-sensitive, and miniature carbon dioxide (CO₂) sensor are one of the promising research areas because of the rising atmospheric CO₂ concentration up to 408 ppm due to the industrial revolution [1]. The emission of CO₂ gas increases the global temperature by trapping the solar energy, which in turn alters the energy balance of the planet such as weather patterns and water supplies. The real-time monitoring of CO₂ gas in the atmosphere promotes detecting environmental hazards at an early stage and provide adequate time for implementing an effective countermove [2–4]. Tracking the indoor CO₂ level in the smart premises is also essential as these data help to understand the indoor air quality and to optimize the necessary ventilation rates for the wellness of the occupants [5–7]. Therefore, development of a feasible, low-cost CO₂ sensor applicable for both the indoor and outdoor air quality monitoring is the demand of the current situation. This research proposes a micro-electromechanical

F. Akhter (✉) · S. Hasan · S. C. Mukhopadhyay
Department of Engineering, Macquarie University, Sydney, Australia
e-mail: fowzia.2k3@gmail.com

Md. E. E. Alahi
Shenzhen Institute of Advanced Technology, Chinese Academy of Sciences, Shenzhen, China

© The Editor(s) (if applicable) and The Author(s), under exclusive license
to Springer Nature Switzerland AG 2021

S. C. Mukhopadhyay et al. (eds.), *Interdigital Sensors*, Smart Sensors, Measurement
and Instrumentation 36, https://doi.org/10.1007/978-3-030-62684-6_13

system (MEMs)-based graphene oxide (GO) coated interdigital sensor for CO₂ detection. The cross-sensitivity towards temperature and humidity has also been studied, and a compensation mechanism has been proposed for improving the accuracy of the sensor. This fast response sensor is able to differentiate various CO₂ concentrations ranging from 400 to 4000 ppm. The reproducibility, reusability, cross-sensitivity are also carried out, and the outcomes are promising to develop a CO₂ sensing system in real-time.

2 Types of CO₂ Sensor

There are various types of CO₂ sensors, such as optical, metal oxide semiconductor-based sensor and graphene-based sensors. These are discussed in this section.

2.1 Optical Sensors

Optical CO₂ sensors are the most commercially available sensors that measure the CO₂ level using a specific wavelength of light. The operating mechanism is based on the infrared signal adsorption characteristics of CO₂. The adsorption wavelength for each gas is different due to their quantized vibrating energy, and for CO₂, these wavelengths are 2.7, 4.3, and 15 μm [8]. Figure 1 refers to the working principle of a typical NDIR, which consists of two identical tubes. The reference tube is filled with non-absorbing gas such as helium, nitrogen, and synthetic air. Another one is referred to the measurement cell, which contains the sample gas. Monochromators and Filters are two essential elements in the optical sensors for obtaining monochromatic beams of infrared light having a broad wavelength range. When the infrared light passes through both the tubes, the sample gas absorbs the infrared signal and attenuates signals that fall on the detector. The difference between the attenuated signal and the un-attenuated signal is studied to determine the amount of CO₂ gas in the measurement cell.

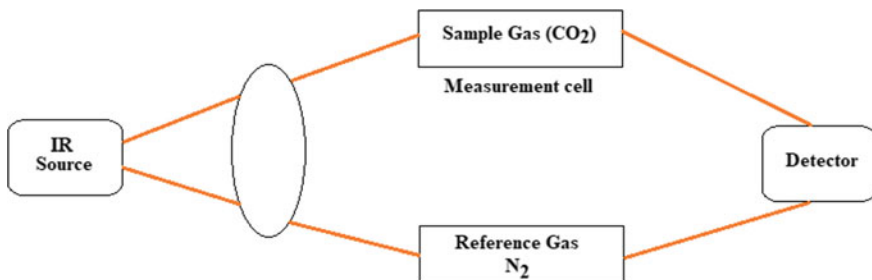


Fig. 1 The working principle of optical carbon dioxide (CO₂) gas sensor [10]

These sensors are highly-accurate, fast, stable and not cross-sensitive to other gas in the same wavelength. However, the drawbacks of these sensors are expensive, bulky and consume high power. It also needs regular calibration using a reference gas for accurate measurements [9].

2.2 Metal Oxide Semiconductor (MOS) Sensor

A Metal Oxide Semiconductor (MOS) sensor consists of a thin film or metal strip, which is exposed to the air under test. A constant electric current runs through this strip. When the monitored gas comes in contact with the stripe, a chemical reaction happens between the strip and target molecules. As a result, the current flowing through the strip changes. This changing characteristic is studied to identify gas [11]. There are various metal oxides used for gas sensing application. Among those, the most commonly used metal oxides are SnO_2 , WO_3 , CuO , ZnO , and In_2O_3 . The sensor's resistance decreases as soon as the sample gas comes in contact with the MOS sensor. The amount of gas concentration is studied from the value of change in resistance [12]. In most cases, the sensor's filament is heated to 300–500 °C by the electric current. A MOS sensor is selective to a particular gas at a specific temperature. Therefore, it is necessary to find the operating temperature for achieving maximum sensitivity [13].

The attractive features of the sensors are high-sensitivity, simple fabrication, low-cost, handy, long-life, higher signal strength, applicable for measuring a wide range of gases and vapors, suitable to use in hard-wired and low budget gas detection systems. However, these sensors require operating temperature higher than 100 °C to achieve an acceptable sensitivity, and also cross-sensitive towards other gases [14] (Fig. 2).

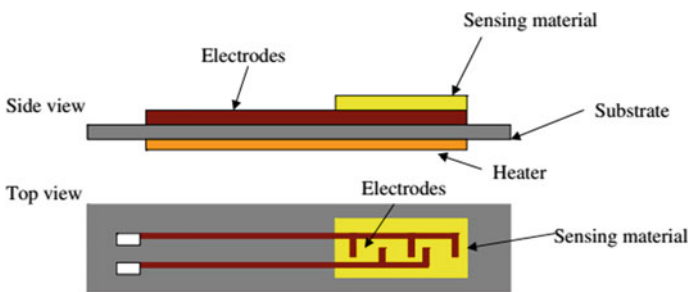


Fig. 2 Schematic diagram of a typical MOS [10]

2.3 Graphene Based CO₂ Sensor

As the Metal oxides based sensors operate at a temperature higher than 100 °C, the researchers are looking for an alternative. Currently, interest to develop carbon-based CO₂ sensors such as Graphene, and Graphene Oxide (GO) and Carbon nanotubes (CNTs) is growing. Compared to other coating materials, Graphene Oxide exhibits high electron mobility at room temperature [15]. The sensitivity of GO is also very high at ambient temperature. GO is more convenient than CNTs for microfabrication because of the planar nanostructure. GO can measure the lowest level of target gas, including all the atoms exposed to the environment [16–18]. Moreover, it has also been demonstrated that Graphene-based compound has an exceptional CO₂ adsorption capacity [19].

A number of studies have been done using GO at room temperature for sensing of CO₂ gas. Among them, Hafiz et al. presented an indoor CO₂ sensing system using a Hydrogen plasma reduced graphene oxide resistive sensor. The sensor's response and recovery time are very fast, about 4 min. The detection range of this sensor is from 300 to 1500 ppm. This type of sensor is suitable for the regions where temperature and humidity are constant for example, in the thermally isolated buildings [20].

Yoon et al. proposed a graphene-based CO₂ sensor functioning at room temperature. The sensor response and recovers very fast, such as 8 s and 10 s, respectively. The temperature of the sensor is varied up to 60 °C, but no significant changes are observed on the sensor's response. Impact of humidity change is not analyzed on the proposed sensor. The detection range of the sensor is 10–100 ppm only [21].

Shaban et al. proposed nanoporous graphene oxide (NGO) based CO₂ gas sensor with a detection range of 1000 ppm. The response time is moderate, 25 s. However, recovery time is higher than 10 min. The sensor's performance is analyzed at 20 °C and varied humidity range from 20.2 to 69.9%. This type of sensor is applicable only for thermally insulated indoor environment only as the temperature and humidity both varies under the field conditions [22].

Fan et al. analyzed the performance double-layer graphene-coated sensor for CO₂ and humidity sensing at room temperature. The sensor is able to detect 250–1000 ppm CO₂ with a response and recovery time of 5.5 s and 8.5 s respectively. The relative humidity is varied from 20 to 100%, and the sensor's performance is recorded. The sensor shows a faster response and recovery time for humid is for humidity 600 ms and 300 ms, respectively. The influence of humidity is also minimized by red reducing the relative humidity to below ~3%. The Graphene shows a notable amount of cross-sensitivity towards temperature. However, the impact of temperature on the proposed sensor's performance is not analysed [23]. A summary of the reviewed works on the graphene-based CO₂ sensors is mentioned in Table 1.

It is understood from the above discussions that the cross-sensitivity of humidity is analysed in some research on CO₂ sensing. However, there is no reported CO₂ sensor applicable to the outdoor environment where the impact of both the temperature and humidity changes are included. Therefore, this research proposes a GO coated planar interdigitated sensor for selective detection of CO₂ gas. A compensation mechanism

Table 1 A comparative study of the existing CO₂ sensor

Material used	Detection range (ppm)	Working condition		Response time (s)/Recovery time (s)	References
		Temperature (°C)	Humidity (%)		
Hydrogen plasma reduced graphene oxide	300–1500	23	68	240/240	[20]
Graphene sheet	10–100	22–60	44	8/10	[21]
Nanoporous graphene oxide (NGO)	1000	20	20.2–69.9	25/674.7	[22]
Double-layer graphene	250–1000	25	20–100	5.5/8.5 for CO ₂ 600 ms/300 ms for humidity	[23]
Vanadium oxide (VO ₂) and Graphene oxide (GO)	200–1000	26	–	150/250	[24]
Pure and Gd-doped cerium oxide (CeO ₂)	800	250	–	–	[25]
LaOCl-coated ZnO nanowires	500–4000	400	–	5/18	[26]
Graphene	400–2000	Room temperature	–	3/long recovery	[27]
RGO-PEI	1000–15,000	Room temperature	Ambient humidity	14/14 for the single layer) 43/120 for the bi-layer	[28]
SnO ₂ nanowires (NWs) with LaOCl	250–4000	400	–	3–20/4–19	[29]
GO	400–4000	10–60	40–90	3/5	This work

has also been proposed to improve the accuracy of CO₂ measurement at a real-life scenario.

3 Preparation of the Proposed CO₂ Sensor

A (micro-electromechanical system) MEMS interdigital sensor is fabricated and coated with GO for the application of CO₂ gas sensing. An Interdigitated sensor has been used in this research due to their high sensitivity, ease of manufacturing, less weight and size compared to other resistive sensors.

3.1 MEMs Sensor Fabrication

Firstly, Coventorware[®] software is utilised for designing the interdigitated electrodes (IDE) patterns. After that, a five-inch transparent mask is prepared by a mask writer. A positive photoresist (EC13027) is spin-coated on a Si wafer with a thickness of 525 μm . For better attachment of photoresist on the Silicon wafer, pre-baking is performed at a temperature of 150 $^{\circ}\text{C}$. Later on, a 200 mJ/cm^3 constant dose of ultra-violet (UV) light is applied for transferring the IDE patterns on the photoresist-coated wafer. Then, the wafer is washed with chemicals and plasma etched for removing the residue of the photoresist present in the trenches. Later, 20 nm of chromium (Cr) and 500 nm of gold (Au) are sputtered on the substrate applying DC magnetron technique. After that, the wafer is dried with nitrogen flow. After that, 1 μm coating of parylene C is coated on the sensing surface for protecting it from Faradic currents and oxidation. Figure 3a presents the fabrication steps, Fig. 3b shows the fabricated wafer and Fig. 3c refers to the configuration of the sensor (1-5-50). The proposed sensor has five sensing electrodes for an excitation electrode having 50 microns gap between two successive electrodes. This configuration is selected due to a higher output of electric field between the sensing electrode and the excitation electrode [30].

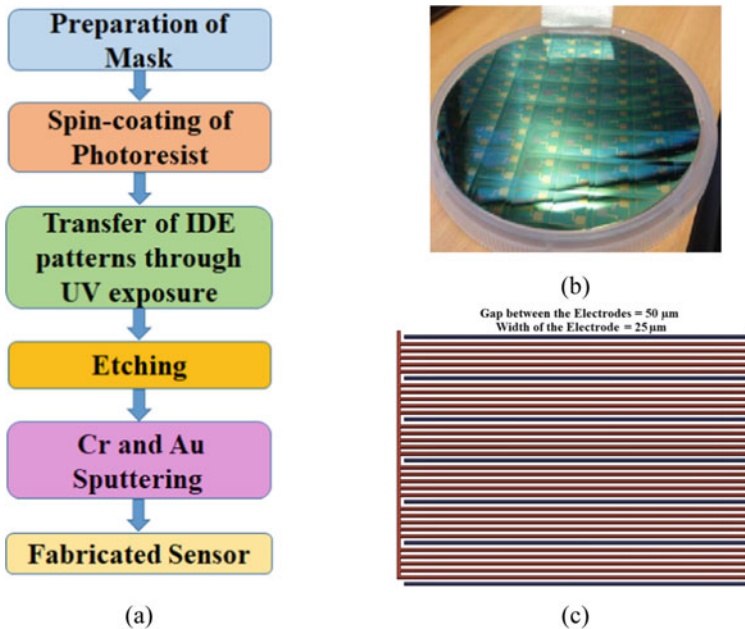


Fig. 3 a Steps of the fabrication process, b fabricated sensors on silicon wafer, and c IDE configuration of the sensor (1-5-50)

3.2 Functionalizing GO Coating for CO₂-Sensing

The highly concentrated Graphene Oxide (GO) dispersed in H₂O (2 mg/mL) is brought from Sigma-Aldrich Australia. To prepare the CO₂ sensitive layer, it is sonicated for 24 h so that it adequately dispersed in water. The sensor is washed thoroughly using ethanol and dried with nitrogen gas flow prior to coating with the GO solution. The GO thin film is formed on the sensor's sensing area using a spin coater at 200 rpm for 60 s. Spin coating technique is used in this research as it provides a more uniformed film of the coated material. The thickness of the coating can also control these mechanisms [31].

3.3 Coating Characterization

The Fourier-transform infrared spectroscopy (FTIR) is done to understand the functional groups exist in GO. Figure 4 shows the FTIR spectrum, where five prominent peaks are observed. The broad peak at 3255 cm⁻¹ refers to the presence of hydroxyl groups and stretching mode of the O–H bond. A sharp peak at 1700 cm⁻¹, 1382 cm⁻¹, 1249 cm⁻¹, and 1056 cm⁻¹ conveys the existence of the carboxyl, C–OH, C–O–C, and C–O groups, respectively. As the bond lengths of these functional groups are higher than the C=O bond of CO₂, CO₂ gas molecules are successfully adsorbed on the GO film [32]. As soon as the proposed sensor exposed to CO₂, the sensor's gas electrical properties change due to the adsorption of the gas molecules on the

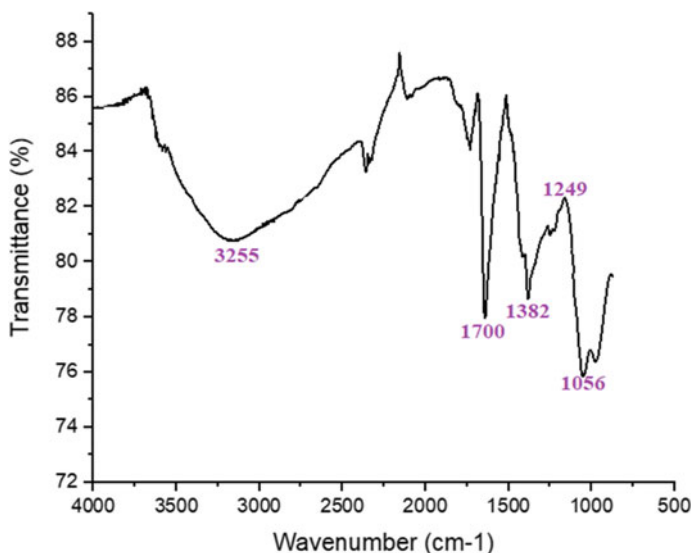


Fig. 4 Fourier-transform infrared spectroscopy (FTIR) of graphene oxide (GO)

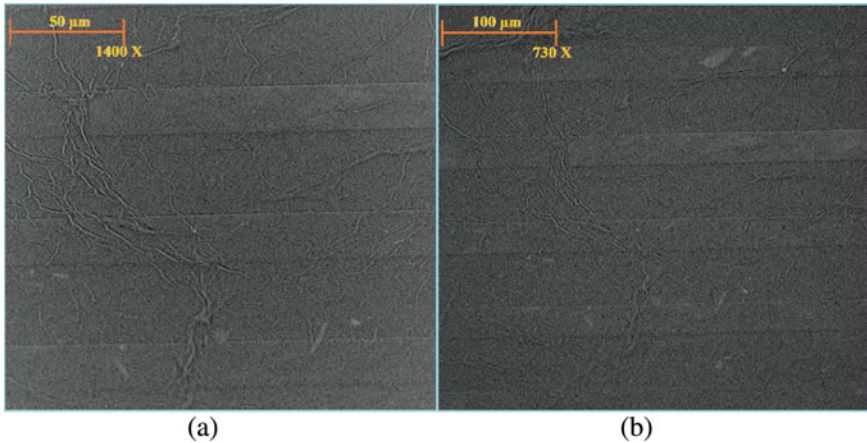


Fig. 5 SEM images of the coated surface at different magnification (a) 50 μm , and (b) 100 μm

sensing area. This change in electrical properties is studied to determine the amount of CO_2 concentration. A thin film is formed on the sensing area once the sensor is dried after performing the spin coating. The Scanning Electron Microscopy (SEM) is applied for understanding the quality of GO film. Figure 5 displays the SEM images of the GO film. The images convey that the coating materials are uniformly spread on the sensing surface, and there are very few wrinkles on the film. The thin film is sufficient to carry out the Electrochemical Impedance Spectroscopy (EIS) analysis.

4 Operating Principle

The temperature, humidity, and CO_2 sensing experiments are conducted using a planar interdigital sensor. These sensors give access to the Material Under Test (MUT) in only one-side. An electric field is formed between the excitation and sensing electrode as soon as a low-amplitude alternating electrical voltage is applied to the excitation electrode (Fig. 6). When a MUT comes in close contact with the sensing surface, the sensor's impedance changes due to the change in an electric field. This changing behaviour of the electric field is analyzed to determine the characteristics of the MUT. The analysis is carried out applying various impedimetric mechanism. These sensors are widely used for environmental [33], biomedical [34], and industrial [35], applications.

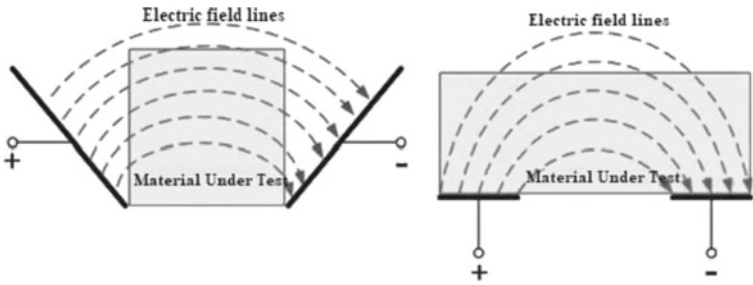


Fig. 6 Schematics of the operating mechanism [35]

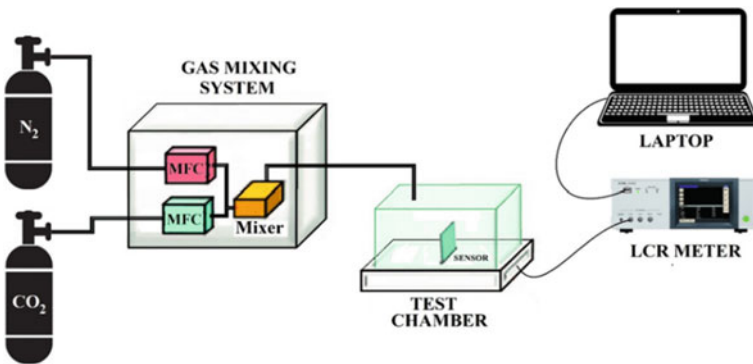


Fig. 7 Experimental setup for the detection of CO₂

5 Experimental Setup

The proposed GO coated sensor is kept inside an incubator (Heraeus BBD6220). The temperature and humidity of the incubator are maintained constant. A two-input mixer is connected with the chamber for mixing the N₂ and CO₂ gas, as shown in Fig. 7. The temperature and humidity of the chamber are precisely controlled. Two mass flow controllers (MFCs) are used to control the CO₂ and N₂ flow rates. The flow rates of N₂ and CO₂ are adjusted to achieve CO₂ concentration ranging from 400 to 4000 ppm for gas sensing experiment. The effect of temperature and humidity is analysed in the nitrogen environment only.

6 Experimental Results and Discussions

This work is focused on developing a CO₂ sensor which will be suitable for both the indoor and outdoor environments. The temperature and humidity change considerably in a real-life scenario. As a result, the efficiency of the sensor may

degrade. Therefore, the performance of the sensor has been investigated for various temperature, humidity and CO₂ concentrations. In addition to that, a compensation mechanism is proposed to improve the accuracy of the proposed sensor.

6.1 Effect of Temperature

The effect of temperature variation on the proposed sensor is determined first. The experiment is conducted in the incubator. The sensor is connected to the Hioki IM 3536 impedance analyser via a clamp. The sensor is profiled for EIS measurement for a wide range of frequency from 10 to 10 kHz. Each experiment is conducted five times, and the average data were accounted for analysis. The temperature of the incubator is varied from 10 to 60 °C keeping the humidity constant at 40%. The real part of impedance (R) correspond to various temperature is plotted in Fig. 8 as the real impedance change significantly as compared to the imaginary impedance for various temperatures.

To determine the relationship between temperature and resistance, a frequency of 1.3 kHz is selected, and resistance at this point is taken into consideration. This frequency is considered as it falls in a sensitive region where temperatures are distinguishable. Figure 9 displays the relationship between the temperature and the real impedance. This curve can be considered as a standard for measuring the unknown samples. The coefficient of determination, R² is 0.9985 conveys well-correlation between real impedance and the temperature. Thus, the following equation can be used to measure the temperature:

$$T_c \text{ (}^\circ\text{C)} = \frac{7 \times 10^6 - R_{Tc}}{59,149} \tag{1}$$

Here, T and R_T denote calculated temperature and real impedance correspond to a specific temperature, respectively. The temperature correlation factor, α_T is 59,149 Ω/°C.

Fig. 8 Variation of the real part of impedance (R) with respect to frequency for various temperatures

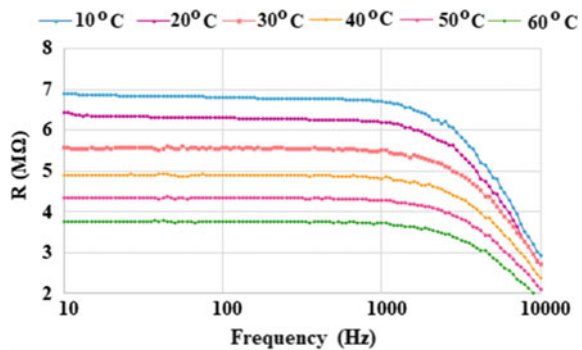
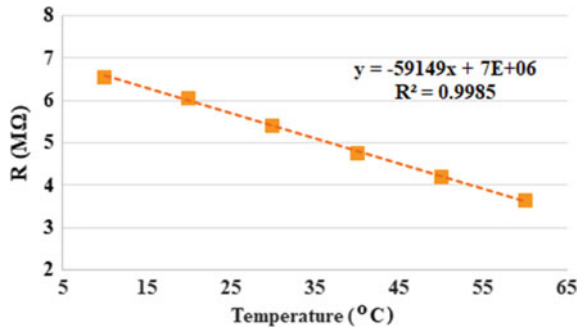


Fig. 9 Relationship between real impedance (R) and temperature at 1.3 kHz frequency



6.2 Effect of Humidity

The effect of humidity on the GO coated sensor is also analyzed. The temperature of the incubator is maintained at 30 °C, and the humidity is varied from 40 to 90%. The responses of the sensor are obtained for a wide range of frequency from 10 to 10 kHz. Figure 10 shows the variation of the sensor’s resistance for different values of humidity. The higher the amount of humidity, the lower the sensor’s resistance value. The significant change in the sensor’s resistance proves that the water molecules are successfully adsorbed on the GO film. With the adsorption of a single molecule of water, the hydrogen bond between inter molecules of water accelerates further adsorption of molecules.

The changes in reactance for different humidity is less significant than changes in resistance. So, change in sensor’s resistance for various humidity values are included in this chapter (Fig. 10) and the calibration standard is developed by plotting the value of measured resistance as a function of humidity at 1.3 kHz (Fig. 11). This relationship can be stated in the form of equation as below:

$$H(\%) = \frac{1 \times 10^6 - R_H}{5679.4} \tag{2}$$

Fig. 10 Variation in the real impedance with respect to frequency for various humidity values

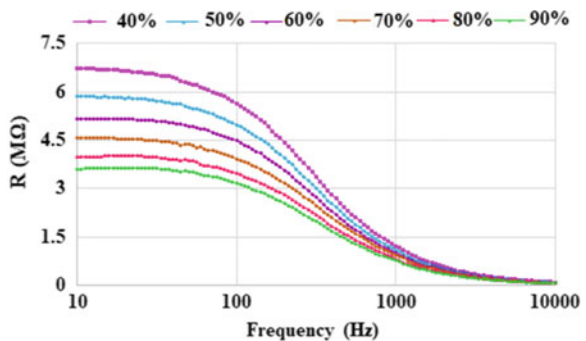
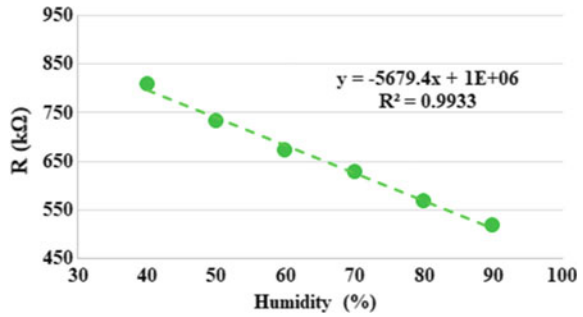


Fig. 11 Relationship between humidity and real impedance at 1.3 kHz frequency



Here, R_H refers to the real impedance corresponds to a particular humidity, and H denotes the calculated humidity. Resistance per unit change of humidity, α_H is $5679.4 \Omega/\%H$.

6.3 Response Towards Differently Concentrated CO₂

The responses of the sensor for various CO₂ concentrations in an N₂ environment are also recorded. The gas concentration is varied from 400 to 4000 ppm. The proposed sensor’s responses of the for various CO₂ concentrations is shown in Fig. 12. The resistance values decrease when the CO₂ concentrations increase. The CO₂ molecules function as a donor for GO thin film. This initiates the charge transfer between the GO thin film and CO₂. As a result, the concentration of electron on the GO film increases, the electrical conductance enhances and the sensor’s resistance reduces. The massive drop in resistance conveys that CO₂ is effectively adsorbed on the GO film.

It is evident from Fig. 12 that, the sensor exhibits a considerable amount of changes at lower frequencies. Thus, a frequency of 1.3 kHz is selected to determine the concentration of CO₂ gas with respect to the sensor’s resistance value, as shown in

Fig. 12 Variation in real impedance for various CO₂ concentrations

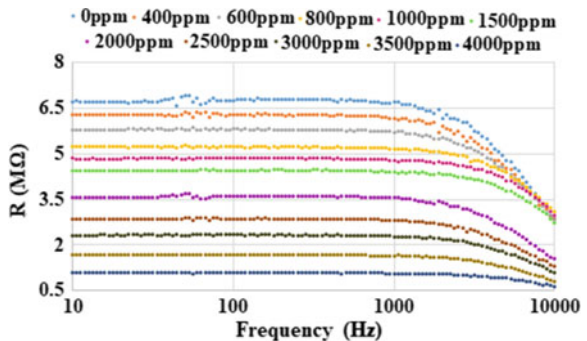


Fig. 13 Relationship between the real impedance (R) and CO₂ concentrations at 1.3 kHz frequency

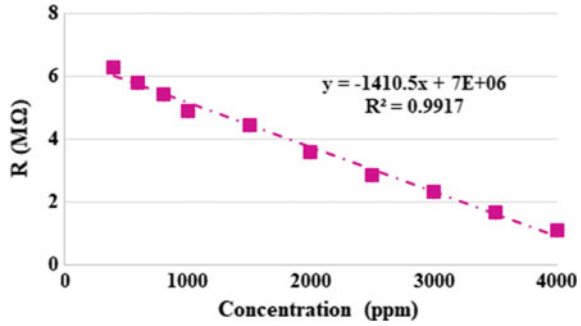


Fig. 13. The value of R² is 0.991, which implies that the accuracy of the results will be quite high using this calibration equation. This relationship between the CO₂ concentration and sensor’s resistance is stated by the following equation:

$$C = \frac{7 \times 10^6 - R_{s\text{ence}}}{1410.5} \tag{3}$$

As the sensor reacts with the variation of temperature and humidity, the actual real impedance is amended by two correlation factors, α_T and α_H. R_{actual} is the real impedance, including temperature and humidity effect, which can be determined by the following formula:

$$R_{\text{actual}} = R_{\text{sence}} + \alpha_T(T - 25) + \alpha_H(H - 40) \tag{4}$$

Finally, the final equation for determining CO₂ concentration as a function of sensor’s resistance is:

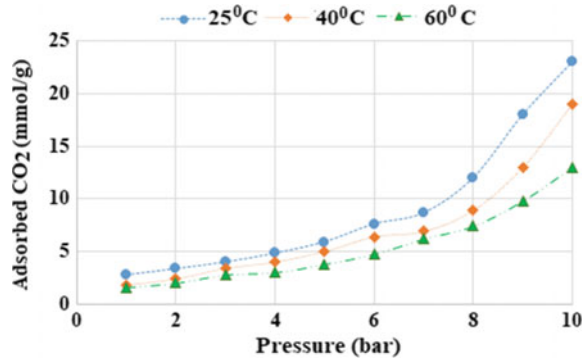
$$C_{\text{actual}} = \frac{7 \times 10^6 - R_{\text{actual}}}{1410.5} \tag{5}$$

6.4 Adsorption Study

The exposure of CO₂ gas to the sensor inside the vacuum chamber causes a reduction in the resistance values, which implies an increase in conductance. As CO₂ functions as a donor, the adsorption of CO₂ gas increases the electron concentration in the GO thin film, thus enhances the electrical conductance. Therefore, it is essential to measure the CO₂ adsorption isotherms on GO coated sensor. The Brunauer–Emmett–Teller (BET) surface area measurement of GO is conducted in this research.

The CO₂ gas adsorbed amount in mole is calculated by obtaining the number of CO₂ gas moles inside the system before and after the adsorption mechanism.

Fig. 14 Adsorption capacity of CO₂ with the variation of temperature



The number of moles of gas in the system can be calculated by the following equation:

$$abn^3 + aVn^2 + (RT + Pb)V^2n - PV^3 = 0 \quad (6)$$

where, a and b are the van der Waals constants, n is the number of moles of CO₂ gas present in the volume, V; T and P are the temperature and pressure of the system, respectively [36].

Figure 14 displays the CO₂ adsorption isotherms on GO film at various temperatures for the pressure ranging from 0 to 10 bar. As the pressure increases, the CO₂ uptake increases drastically. This is because of the multilayer adsorption of CO₂ molecules in pores at high pressures. Having no plateau in the adsorption isotherm for investigated pressure range conveys that GO is able to adsorb more CO₂ at higher pressure. The maximum adsorption capacities of 23, 19 and 13 mmole/g are observed at 10 bar pressure for 25°, 40° and 60 °C temperatures, respectively.

6.5 Measurement of Unknown Sample

To measure the CO₂ concentrations in unknown samples, five gas samples are collected in gas sampling bags from several parts of Sydney, Australia. These samples are inserted into the gas sensing chamber, and the sensor's data are recorded at 1.3 kHz operating frequency. The value of the CO₂ concentration measured by the proposed sensor is calculated using Eq. 5. The CO₂ concentration in those five samples is also measured using the standard gas chromatography (GC) method for validation. As the CO₂ concentrations in most samples are not adequate for measuring the range of concentrations that the sensor can detect, some CO₂ samples are mixed to elevate the concentration of CO₂. Table 2 shows the experimental results, which conveys that the coated sensor can accurately measure CO₂ concentration with an error of less than 2%, which promotes the reliability of the developed sensor.

Table 2 Measurement of unknown sample and validation of measurement

No	Developed sensor (ppm)	Gas chromatography method (ppm)	Error (%)
1	451	445	1.34
2	875	890	1.68
3	1593	1622	1.78
4	2345	2570	0.97
5	3285	3715	0.80

Table 3 Measurement error before and after temperature and humidity compensation

No	Sensor system		GC method (ppm)	Error rate before compensation (%)	Error rate after compensation (%)
	Before compensation (ppm)	After compensation (ppm)			
1	530	451	460	15.21	1.95
2	702	613	625	12.32	1.92
3	940	895	870	8.04	2.87
4	1325	1215	1240	6.85	2.01
5	1985	1868	1832	8.35	1.96

6.6 Significance of Compensation Mechanism

An experiment is designed to demonstrate the impact of temperature and humidity compensation to achieve higher accuracy. Five gas samples are inserted into the gas sensing chamber, where the temperature is set to 30 °C and humidity is maintained at 60%. The amount of CO₂ present in the gas sample is determined using both the sensor and gas chromatographic (GC) method. The CO₂ concentration before and after application of the compensation mechanism is calculated by using Eqs. 3 and 5, respectively. All the results are summarized in Table 3. The percentage of error is more than 15% before application of the compensation mechanism.

6.7 Sensitivity and Impact of Background Gas

Figure 15 shows the sensitivity of the resistance (R) of the proposed sensor for CO₂ gas detection. The variation of sensitivity in percentage is obtained applying the following equation:

$$Sensitivity (\%) = \frac{(R_{N_2} - R_{CO_2})}{R_{N_2}} \times 100 \quad (7)$$

Fig. 15 Percentage change of sensitivity for various CO₂ gas concentrations in N₂ and air environment

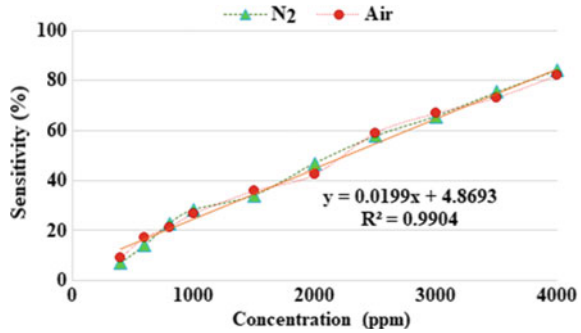


Fig. 16 Response and recovery time response of the GO coated CO₂ sensor when exposed to 4000 ppm CO₂

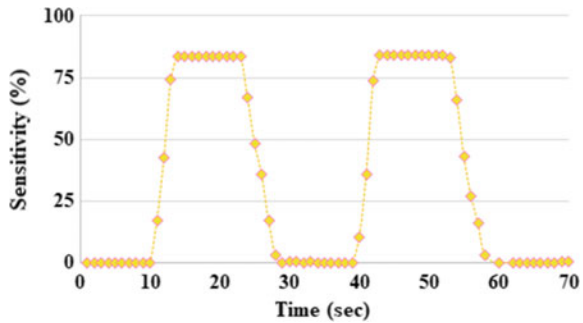


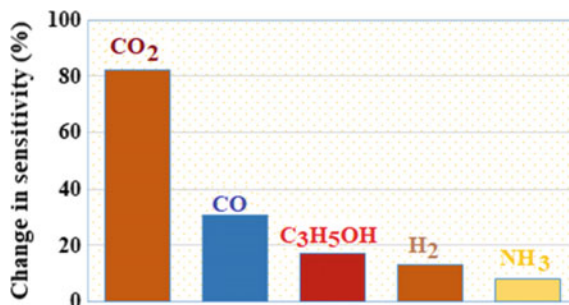
Figure 15 shows that there is a linear relationship between the resistive values of the sensor and CO₂ concentration. It is evident from the results that the resistance (R) has the most significant role to play for the functionality of the proposed CO₂ gas sensor.

All the experiments are conducted in a similar manner using air as the background gas for preparing standard samples for CO₂ gas to understand the impact of the background gas on the sensor’s sensitivity. It is found that the sensitivity of the sensor is similar irrespective of background gas according to Fig. 16. This is because of taking initial resistance, R_{N_2} or R_{air} such that N₂ or air is the base gas while obtaining the sensor’s performances. Moreover, GO is more sensitive to CO₂. Thus, the performance of the sensor is not affected by the background gas.

6.8 Response and Recovery Time

The response and recovery time of the sensor is calculated by operating the sensor at 1.3 kHz and measuring the sensor’s resistance when the Gas is ON and OFF. Relative change of resistance is considered for determining response and recovery time as the resistance values change significantly for the proposed sensor. The response time is referred to the time needed for the change in relative resistance, reaching 90% of

Fig. 17 % sensitivity of the sensor towards different gases such as CO₂ (4000 ppm), CO (50 ppm), C₃H₅OH (50 ppm), H₂ (25 ppm) and NH₃ (25 ppm)



the steady-state value after CO₂ is injected. The recovery time is the time taken for the sensor attaining a resistance 10% higher than the initial value in N₂. The sensor is exposed to 4000 ppm CO₂ until the sensors saturate, and finally desorbed with nitrogen until the resistances returned to their initial values. The average response time and recovery time for CO₂ gas detection are 3 s and 5 s, respectively, as calculated from Fig. 16.

6.9 Cross Sensitivity

The sensor's sensitivity towards various gases in addition to CO₂ is examined at ambient environment. The sensor's response is recorded individually for each gas, and the sensitivity is calculated applying Eq. 7. Figure 17 shows the results of this experiment. The sensor responds 2.6, 4.8, 6.3 and 10.25 times lower for CO, C₃H₅OH, H₂ and NH₃ respectively as compared to the response for CO₂. These results clearly suggest that the sensor highly selective towards CO₂.

6.10 Reproducibility

Five CO₂⁻ sensitive sensors are prepared, and the reproducibility test is conducted at 25 °C and 40% humidity by exposing it towards 400, 1000, 2000, 3000, and 4000 ppm of CO₂. The sensor's outcomes are summarized in Table 4. The performances of all the sensors are almost the same towards a sample. The maximum relative standard deviation (RSD) is found as 0.47%. This proves the outstanding reproducibility of the proposed sensor.

However, it is necessary to clean and dry the sensor before applying the CO₂-sensitive coating. It is also required to sonicate GO solution for the long term for proper dispersion. Adequate attention should also be given while placing the sensor inside the glove box and choosing the operational parameters for spin-coating. In the case of preparing a particular concentration of CO₂ gas sample, the flow rate

Table 4 Reproducibility test of the proposed sensor

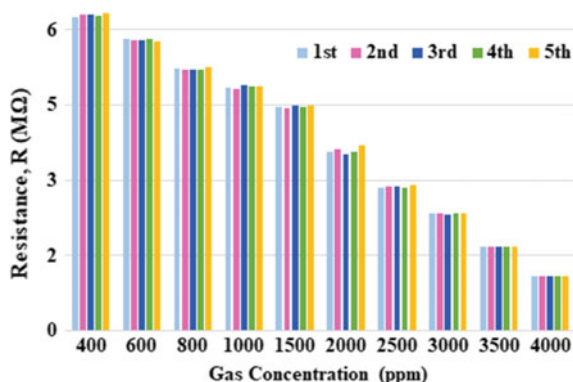
Sensor number	Actual concentration (ppm)	Measured concentration by sensors (ppm)	RSD (%)
1	400	403	0.47
2		400	
3		405	
4		404	
5		402	
1	1000	1005	0.41
2		1000	
3		1015	
4		1012	
5		1007	
1	2000	2010	0.23
2		2000	
3		2006	
4		2009	
5		2012	
1	3000	3005	0.22
2		3000	
3		3009	
4		3017	
5		3013	
1	4000	4010	0.12
2		4000	
3		4006	
4		4013	
5		4009	

and time for CO₂ gas and N₂ flow should be finely controlled to achieve the target concentration.

6.11 Repeatability

The real impedance values are measured for the differently concentrated CO₂ gas samples for observing the repeatability test of the sensor. The experiment is repeated for five times, and the experimental results are shown in Fig. 18. Figures 18 shows

Fig. 18 Repeatability test for differently concentrated CO₂ samples



the experimental results. It is found that the sensor's response for a particular concentration does not deviate from its first performance. The value of RSD is below 2%. Therefore, the sensors show outstanding repeatability towards various CO₂ samples.

7 Chapter Summary

The fabrication and application of a novel interdigital CO₂ sensor operating at the ambient environment are successfully presented in this chapter. A thin layer of GO is formed on the sensor's sensing surface to make it selective to CO₂. The performance of the sensor for various temperature, humidity and CO₂ concentrations are studied. Experimental results prove that the sensor can distinguish a wide range of CO₂ concentrations. The compensation of temperature and humidity effect promotes higher accuracy. Validation of all the results using laboratory-based method confirms the reliability of the sensor. The results obtained from the cross-sensitivity, reproducibility, and repeatability tests are highly encouraging to develop a smart environmental monitoring system for both the outdoor and indoor conditions. This research will have a high impact on the detection of environmental hazards beforehand and taking necessary countermeasure in the early stage.

References

1. Latest Cape Grim Greenhouse gas data. <https://www.csiro.au/en/Research/OandA/Areas/Assessing-our-climate/Latest-greenhouse-gas-data>. Accessed 3 Jan 2019
2. J.A. Rudd, R. Horry, R. Lyle Skains, You and CO₂: a public engagement study to engage secondary school students with the issue of climate change. *J. Sci. Educ. Technol.* **29**, 230–241 (2020)

3. F. Akhter, S. Khadivizand, J. Lodyga, H.R. Siddiquei, Md.E.E. Alahi, S.C. Mukhopadhyay, Design and development of an IoT enabled pedestrian counting and environmental monitoring system for a smart city, in *Proceedings of the 13th International Conference on Sensing Technology (ICST)*, Sydney, Australia, 2–4 November, 2019
4. F. Akhter, S. Khadivizand, H.R. Siddiquei, Md.E.E. Alahi, S. Mukhopadhyay, IoT enabled intelligent sensor node for a smart city: pedestrian counting and ambient monitoring. *Sensors* **3374**, 1–19 (2019)
5. Y. Al horr, M. Arif, M. Katafygiotou, A. Mazroei, A. Kaushik, E. Elsarrag, Impact of indoor environmental quality on occupant well-being and comfort: a review of the literature. *Int. J. Sustain. Built Environ.* **5**, 1–11 (2016)
6. A. Steinemann, P. Wargock, B. Rismanchi, Ten questions concerning green buildings and indoor air quality. *Build. Environ.* **112**, 351–358 (2017)
7. A. Schiewecka, E. Uhdea, T. Salthammera, L.C. Salthammerb, L. Morawskac, M. Mazaheric, P. Kumar, Smart homes and the control of indoor air quality. *Renew. Sustain. Energy Rev.* **94**, 705–718 (2018)
8. S. Moumen, I. Raible, A. Krauß, J. Wöllenstein, Infrared investigation of CO₂ sorption by amine based materials for the development of a NDIR CO₂ sensor. *Sens. Actuators B: Chem.* **236**, 1083–1090 (2016)
9. Y. Wang, M. Huo, M. Zeng, L. Liu, Q.Q. Ye, X. Chen, D. Li, L. Peng, J.Y. Yuan, CO₂-responsive polymeric fluorescent sensor with ultrafast response. *Chin. J. Polym. Sci.* **36**, 1321–1327 (2018)
10. S. Neethirajan, D.S. Jayas, S. Sadistap, Carbon dioxide (CO₂) sensors for the agri-food industry—a review. *Food Bioprocess Technol.* **2**, 115–121 (2009)
11. A. Dey, Semiconductor metal oxide gas sensors: a review. *Mater. Sci. Eng. B* **229**, 206–217 (2018)
12. Bo. Zhang, P.-X. Gao, Metal oxide nanoarrays for chemical sensing: a review of fabrication methods, sensing modes, and their inter-correlations. *Front. Mater.* **6**, 1–20 (2019)
13. N.B. Tanvir, O. Yurchenko, Ch. Wilbertz, G. Urbanab, Investigation of CO₂ reaction with copper oxide nanoparticles for room temperature gas sensing. *J. Mater. Chem. A* **4**, 5294–5302 (2016)
14. H. Ji, W. Zeng, Y. Li, Gas sensing mechanisms of metal oxide semiconductors: a focus review, nanoscale. *R. Soc. Chem.* **11**, 22664–22684 (2019)
15. W. Tian, X. Liu, W. Yu, Research progress of gas sensor based on graphene and its derivatives: a review. *Appl. Sci.* **1118**, 1–21 (2018)
16. M. Yang, Y. Wang, L. Dong, Z. Xu, Y. Liu, N. Hu, E.S.W. Kong, J. Zhao, C. Peng, Gas sensors based on chemically reduced holey graphene oxide thin films. *Nanoscale Res. Lett.* **14**, 1–8 (2019)
17. D. Iruretagoyena, M.S.P. Shaffer, D. Chadwick, Adsorption of carbon dioxide on graphene oxide supported layered double oxides. *Adsorption* **20**, 321–330 (2014)
18. A.T. Smith, A.M. LaChance, S. Zeng, B. Liu, L. Sun, Synthesis, properties, and applications of graphene oxide/reduced grapheneoxide and their nanocomposites. *Nano Mater. Sci.* **1**, 31–47 (2019)
19. M. González-Barriuso, C. Pesquera, F. González, Á. Yedra, C. Blanco, CO₂ capture by amino-functionalized graphene oxide. *Chem. Eng. Trans.* **75**, 637–642 (2019)
20. S.M. Hafiz, R. Ritikos, T.J. Whitcher, N.Md. Razib, D.C.S. Bien, N. Chanlek, H. Nakajima, T. Saisopa, P. Songsiriritthigul, N.M. Huang, S.A. Rahman, A practical carbon dioxide gas sensor using room-temperature hydrogen plasma reduced graphene oxide. *Sens. Actuators B: Chem.* **193**, 692–700 (2014)
21. H.J. Yoon, D.H. Jun, J.H. Yang, Z. Zhou, S.S. Yang, M.M.-C. Cheng, Carbon dioxide gas sensor using a graphene sheet. *Sens. Actuators B: Chem.* **157**, 310–313 (2011)
22. M. Shaban, S. Ali, M. Rabia, Design and application of nanoporous graphene oxide film for CO₂, H₂, and C₂H₂ gases sensing. *J. Mater. Res. Technol.* **8**, 4510–4520 (2019)
23. X. Fan, K. Elgammal, A.D. Smith, M. Ostling, A. Delin, M.C. Lemme, F. Niklaus, Humidity and CO₂ gas sensing properties of double-layer graphene. *Carbon* **127**, 576–587 (2018)

24. S.E. Zaki, M.A. Basyooni, M. Shaban, M. Rabia, Y.R. Eker, G.F. Attia, M. Yilmaz, A.M. Ahmed, Role of oxygen vacancies in vanadium oxide and oxygen functional groups in graphene oxide for room temperature CO₂ gas sensors. *Sens. Actuators A* **294**, 17–24 (2019)
25. A.A. Aboud, H. Al-Keleshb, W.M.A.E. Roubay, A.A. Farghali, A. Hamdedein, M.H. Khedr, CO₂ responses based on pure and doped CeO₂ nano-pellets. *J. Mater. Res. Technol.* **7**, 14–20 (2018)
26. N.V. Hieu, N.D. Khoang, D.D. Trung, L.D. Toan, N.V. Duy, N.D. Hoa, Comparative study on CO₂ and CO sensing performance of LaOCl-coated ZnO nanowires. *J. Hazard. Mater.* **244–245**, 209–216 (2013)
27. A.D. Smith, K. Elgammal, X. Fan, M.C. Lemme, A.D.M. Rasander, L. Bergqvist, S. Schroder, A.C. Fischer, F.Niklaus, M. Ostling, Graphene-based CO₂ sensing and its cross sensitivity with humidity. *RSC Adv.* **7**, 22329–22339 (2017)
28. Y. Zhou, Y. Jiang, G. Xie, M. Wu, H. Tai, Gas sensors for CO₂ detection based on RGO–PEI films at room temperature. *Chin. Sci. Bull.* **59**, 1999–2005 (2014)
29. D.D. Trung, L.D. Toan, H.S. Hong, T.D. Lam, T. Trung, N.V. Hieu, Selective detection of carbon dioxide using LaOCl-functionalized SnO₂ nanowires for air-quality monitoring. *Talanta* **88**, 152–159 (2012)
30. M.E.E. Alahi, L. Xie, S.C. Mukhopadhyay, L. Burkitt, A temperature compensated smart nitrate-sensor for agricultural industry. *IEEE Trans. Ind. Electron.* **6**, 7333–7341 (2017)
31. A. Nag, A.I. Zia, X. Li, S.C. Mukhopadhyay, J. Kosel, Novel sensing approach for LPG leakage detection: Part I—Operating mechanism and preliminary results. *IEEE Sens. J.* **16**, 996–1003 (2016)
32. R.M.D. Castillo, A.G. Calles, R.E. Morales, H.H. Coronado, Adsorption of CO₂ on graphene surface modified with defects. *Comput. Condens. Matter* **16**, 1–11 (2018)
33. F. Akhter, A. Nag, Md.E.E. Alahi, H. Liu, S.C. Mukhopadhyay, Electrochemical detection of calcium and magnesium in water bodies. *Sens. Actuators: A. Phys.* **305**, 1–9 (2020)
34. N. Afsarimanesh, S.C. Mukhopadhyay, M. Kruger, Molecularly imprinted polymer-based electrochemical biosensor for bone loss detection. *IEEE Trans. Biomed. Eng.* **65**, 1264–1271 (2018)
35. Md.E.E. Alahi, N. Pereira-Ishak, S.C. Mukhopadhyay, L. Burkitt, An Internet-of-Things enabled smart sensing system for nitrate monitoring. *IEEE Internet Things J.* **5**, 4409–4417 (2018)
36. G. Li, P. Xiao, P. Webley, Binary adsorption equilibrium of carbon dioxide and water vapor on activated alumina. *Langmuir* **25**, 10666–10675 (2009)

Development of Dual-Friction Drive Based Piezoelectric Surface Acoustic Wave Actuator



Basudeba Behera 

Abstract This chapter deals with the modeling and simulation of a dual friction-drive (DFD) piezoelectric motor driven by a Rayleigh surface acoustic wave. Different techniques of modeling of SAW devices are discussed along with finite element simulation of resonator and delay line. The proposed SAW motor involves a cubical shaped object called slider which is kept tightly between two piezoelectric stators preferably identical in nature. The stator is typically made of lithium niobate facing each other, while each stator having an IDT placed on both ends. A Rayleigh SAWs is generated on the surfaces of both stators when sinusoidal excitations applied to the pair of IDTs on one side and the wave interacts with the slider. A sufficient amount of preload is applied externally; the generated SAWs generate frictional forces on the two surfaces contacting the slider and makes a translational motion to the slider. The reverse direction of motion of the slider can be performed by changing the excitation conditions to the pair of IDTs on the opposite side. The chapter describes the modeling of IDTs including characteristics, principles, and generation of surface waves, and finally, through finite element simulation, it discusses the operation of SAW motor along with displacement of the slider, contact pressure, and forces acting on the slider.

1 Introduction

Piezoelectric materials have provided a great scope to explore the facilitated miniaturization of actuators and motors with enormous mechanisms to construct ultrasonic motors [1–3]. The advent of surface acoustic wave (SAW) motors led to improved resolution and high-power-density operation [4, 5]. Persistent development in SAW motors resulted in light-weight, very high speed, and feasibility of sub-nanometer stepping resolution [6, 7]. A SAW linear motor [8] typically uses a piezoelectric

B. Behera (✉)

Department of Electronics and Communication Engineering, National Institute of Technology
Jamshedpur, Jamshedpur 831014, Jharkhand, India
e-mail: basudeb.ece@nitjsr.ac.in

© The Editor(s) (if applicable) and The Author(s), under exclusive license
to Springer Nature Switzerland AG 2021

S. C. Mukhopadhyay et al. (eds.), *Interdigital Sensors*, Smart Sensors, Measurement
and Instrumentation 36, https://doi.org/10.1007/978-3-030-62684-6_14

substrate like lithium niobate (LiNbO_3) or (LN) [9] as stator along with aluminum electrodes arranged in comb-shape known as IDTs [10] placed at both ends of the stator [11] to generate Rayleigh wave when potential is applied. A slider, basically a movable object is placed tightly with suitable external preload on the surface of the stator [12] through a lubricated guide rail to minimize friction at the top surface of the slider. The working principle of the SAW motor [13] utilizes the interaction of frictional force between the slider and the stator generated by the elliptical motion of the contact points on the surface due to the propagation of Rayleigh wave [8]. This mechanism drives the slider in the direction opposite to the direction of SAW propagation. To create high contact friction force at the interface of the slider and the stator, a high adequate preload along with lubricated guide rail used to provide preload makes the system heavy and bulky. The chapter presents a proposed DFD SAW motor that replaces the lubricated guide rail by the second stator which is identical and facilitates the motion of the slider using friction-drives from both the bottom and top sides of the slider.

2 Generating Surface Acoustic Waves

The stator used in SAW motor aims to generate Rayleigh waves with large amplitude. SAW devices can be made up of fabricating IDTs on the surface of piezo substrates to generate Rayleigh SAW can be modeled, and the functions of IDT can be described using feasible techniques for example delta function method or discrete source, impulse response method, the coupling of mode (COM) method, piezoelectric permittivity method, matrix representation, numerical techniques using equations, and equivalent circuit method [14, 15]. The finite element method (FEM) is a technique that allows simulating the devices with any number of IDT fingers and easy visualization of the device response to the applied boundary conditions [15, 16]. This section describes the simulations of conventional SAW devices such as one-port SAW resonators and SAW delay line devices by FEM using COMSOL Multiphysics.

The generation of traveling or standing waves on an elastic medium occurs when the particles in the medium are displaced from their equilibrium positions by an external force together with the elastic restoring forces [17]. The three possible trajectories of the particles in motion on the elastic medium are linear, elliptical, and circular polarization [17, 18]. The motion of the particles can be resolved into two components, namely longitudinal component, and shear component. A English scientist Lord Rayleigh in 1885 has published a research paper on surface acoustic wave entitled “On wave propagation along the plane surface of an elastic solid” based on his study of seismic waves. The particle displacement in elastic Rayleigh wave has surface normal and surface parallel components concerning the direction of wave propagation.

3 Structure of Resonators and Delay Lines

The electrodes patterned with high conductive metals such as Aluminum, Platinum in a comb structure on the surface of a piezo substrate in a SAW device is known as an interdigital transducer (IDT) [18]. Aluminum (Al) is generally used for fabricating IDT having properties of conducting and physical properties using photolithography [19]. Figure 1a shows an IDT with bond pads for electrical connection fabricated on a piezo substrate. The electrical potential applied to the IDT electrodes produces an electric field which will cut the piezo substrate as illustrated in Fig. 1b and generate stresses at the surface of the piezo substrate. Application of sinusoidal wave excitation results in a series of alternate compression and expansion regions propagating on the surface of the substrate and on both sides of the IDT [19] as SAW.

When a sinusoidal potential with period T is applied, the vibrations add positively if the center-to-center distance between IDT fingers p is equal to the half of the acoustic wavelength λ for the excitation frequency as shown in Fig. 1a [19].

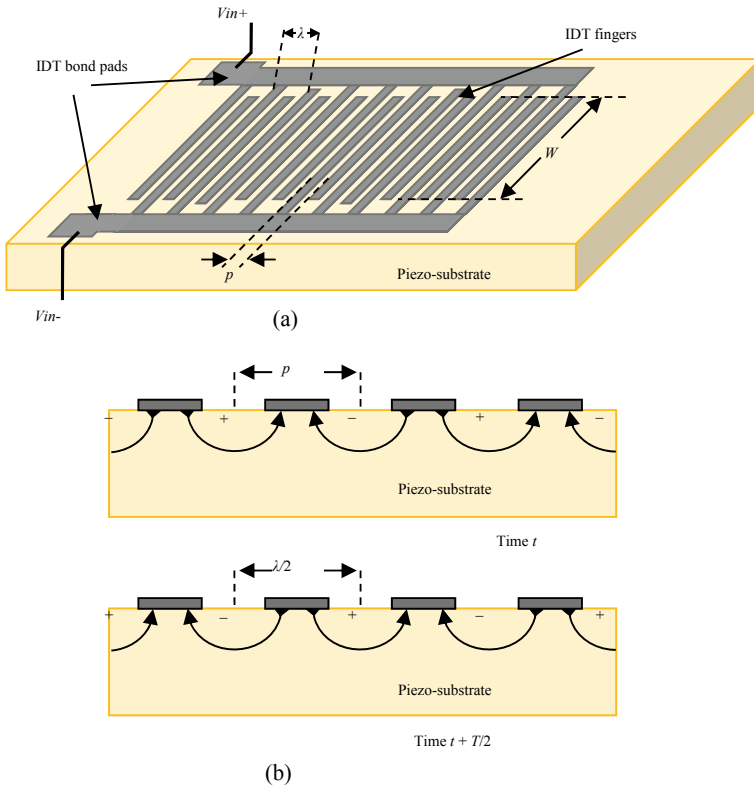


Fig. 1 a Interdigital transducer (IDT) with bond pads on a piezo-substrate. b Polarities of applied potentials on IDT fingers at time t and at time $t + T/2$

Figure 1b illustrates the constructive generation of SAW on a piezo substrate. The stress wave generated at time t by a pair of IDT fingers travels a distance of half acoustic wavelength ($\lambda/2$) in the time interval of half period ($T/2$) with the speed of SAW phase velocity c . As shown in Fig. 1b, at time $t + T/2$, the generated stress wave reaches the neighbor IDT finger pair where it adds constructively to the stress wave produced during the next half cycle of the input sinusoid [19].

The deformed waves generated by each finger pair can be added constructively with the deformed waves generated by other finger pairs in the subsequent cycles of input excitation resulting in resonance. The resonance frequency or the synchronous frequency f_0 is related to the pitch p of the IDT fingers and SAW phase velocity c as given in Eqs. (1) and (2).

$$f_0 = \frac{c}{\lambda} \tag{1}$$

$$\lambda = 2p \tag{2}$$

where wavelength is denoted by λ . The number of finger pairs of the IDTs determines the operating bandwidth of the SAW device. The 3 dB bandwidth f_b of a SAW device with N number of IDT finger pairs can be estimated [20] as given in Eq. (3).

$$f_b = \frac{0.88 f_0}{N} \tag{3}$$

4 Basic Configurations of SAW Devices

The SAW devices are generally operated in two different ways: resonator and delay line. A SAW delay line type device is a two-port device as shown in Fig. 2, where an IDT is fabricated at either end of the substrate separated by a distance of a few wavelengths [15]. One IDT called as a transmitter IDT, on electrical excitation, generates SAW that propagates towards the other IDT called a receiver IDT which

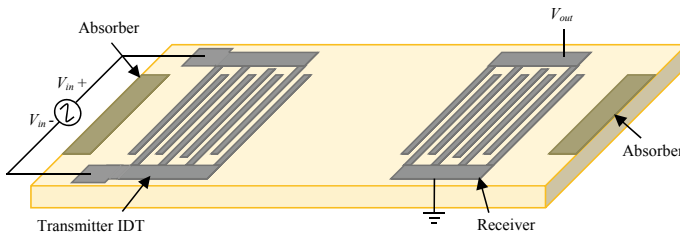


Fig. 2 Schematic diagrams of the SAW delay line device [22]

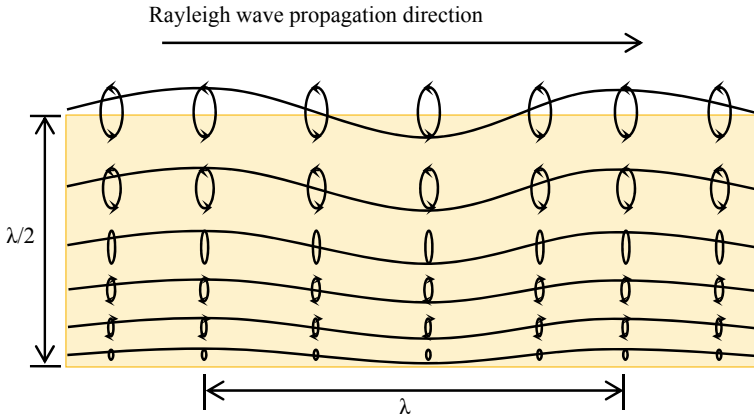


Fig. 3 Schematic of motion trajectories of points in the substrate during the propagation of Rayleigh SAW [23]

converts the SAW in electrical output. Figure 3 shows the schematic of the motion trajectories of the points when SAW propagates on the free surface of a semi-infinite elastic body. A Rayleigh wave traveling from left to right results in anticlockwise elliptical motion of the points on the surface of the stator as shown in Fig. 3 [21].

The amplitude of SAW falls exponentially with the depth inside the substrate. The SAW resonator devices are divided into two types: one port resonator and two-port resonator. In resonators, SAW of the specific frequency generated by the IDT propagates within the substrate block such that the wave is reflected back and forth within the confinement causing resonance. In one-port SAW resonator, a bidirectional IDT is fabricated with a set of reflectors on either side [18]. The reflectors could be made of shorted metal strips or grooves. At the Bragg frequency, the periodicity of the reflector electrodes is equal to half the wavelength, so that the reflections from individual fingers are in phase and add coherently. Strong reflections are obtained when $N|r_{sl}| > 1$, where N is the number of reflector fingers, and r_{sl} is the reflection coefficient of a finger. Typically, $|r_{sl}|$ is about 2% and N is 200 or more [18].

A one-port SAW resonator can also be made by using a large number of IDT fingers without reflectors. In this device, multiple reflections within the IDT lead to standing waves and the device resonates at a particular frequency. In the case of the two-port resonator, a set of reflectors is fabricated on each outer side of the pair of adjacent IDTs. Two-port resonators are used in high stability oscillators [18]. The conventional SAW devices are discussed in detail and simulated based on a finite element simulation method (FEM) using COMSOL Multiphysics [14] as below.

5 Finite Element Method (FEM)

The finite element method (FEM) is a numerical technique that provides approximate solutions to the governing differential or integral equations of a complicated system through a discretization process [24, 25]. FEM is used to solve the problems of engineering disciplines such as the areas of stress/strain analysis of solid structures, heat conduction analysis, and fluid dynamics. The domain of the system (physical/mathematical) can be defined or subject to frequent changes (moving boundary problems such as transient-free surface water flow, large deformation problems, etc.) [25].

6 Results and Discussions for SAW Resonators

The results of the simulation of conventional SAW resonator are shown in Fig. 4. The total displacement profile, x -displacement profile, and y -displacement profile of the resonator at the resonance frequency f_r of 8.37 MHz are shown for substrate depth of about 3.75λ .

The resonance frequency of the resonator is identified as the frequency for which the susceptance crosses zero value. Figure 4a shows plot of total displacement as a function of normalized frequency and peak at the resonance frequency. The normalized frequency is expressed as $\eta = 2pf/v_0$, where, $v_0 = 3990$ m/s is the free surface velocity of the substrate. The curves of harmonic admittance per period as a function of normalized frequency for conventional SAW resonator are shown in Fig. 4b. Figure 4b shows the closer view of the curve of harmonic admittance per period as a function of normalized frequency near the resonance frequency. In the case of the real device, it would be lower due to the finite aperture, attenuation, and damping. This simulation does not consider the attenuation or damping and assumes the infinite width of the aperture of IDT fingers in x_2 direction.

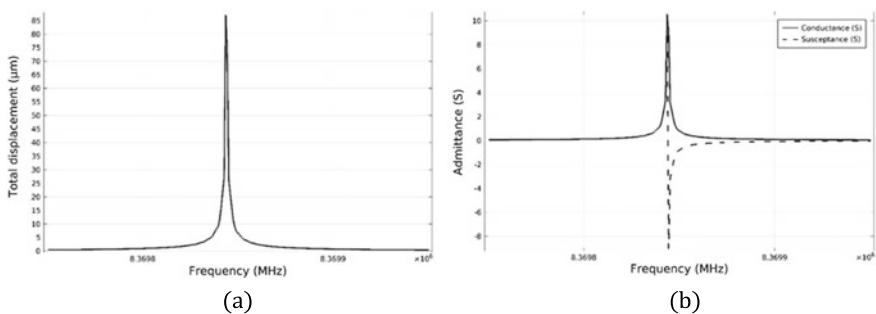


Fig. 4 FEM simulation of a SAW resonator, **a** plot for total displacement as a function of normalized frequency, **b** plot of harmonic admittance as a function of normalized frequency

The free surface resonance frequency f_0 calculated from the Eigenmode analysis of the piezo substrate is 8.37 MHz. The resonance frequency is affected by the mechanical and electrical properties as mass loading, and conductivity of the metallic IDT fabricated on the piezo substrate effects SAW phase velocity and it requires consideration of these factors while designing [19, 26].

The quality factor Q_r at the resonance frequency of the convention SAW resonators is calculated from Fig. 4b. The expression for quality factor is given as [15, 27]

$$Q_r = \frac{f_r}{\Delta f} \quad (4)$$

where, Δf is the bandwidth at half of the peak conductance [15, 27] (see Fig. 4b). The capacitance ratio which is a measure of the resonator performance is calculated from Fig. 4c. The capacitance ratio γ is expressed as [15]

$$\gamma = \frac{f_r^2}{f_a^2 - f_r^2} \quad (5)$$

where f_a is anti-resonance frequency (see Fig. 4c). The capacitance ratio for the conventional SAW resonator computed from the simulation is 28.

7 Simulation of One-Port SAW Resonator Based on FEM in 3D

In this section, a conventional SAW resonator with a finite aperture having an infinite number of IDT fingers with a simplified model is simulated. For 3D simulation, a piezo solid application mode of COMSOL Multiphysics is used. The simulation is carried out taking a half wavelength consisting of a single electrode of antiperiodic IDT fingers is used. The dimensions used for 3D simulation are the same as 2D simulation except for the depth of piezo-substrate h_s and aperture W . The depth of piezo-substrate is truncated to 5λ since SAW energy concentrates near the substrate depth of one wavelength (Fig. 5).

The simplified model is used to reduce the number of nodes and reduce computation cost. The bottom surface of the substrate is fixed and all other boundaries are stress-free. It is possible by modeling a thin strip of a thickness of W in x_2 direction and applying zero displacement constraint in the x_2 direction on both side boundaries normal to the direction of wave propagation. Rayleigh SAW has no variation and no component of displacement vectors in the x_2 direction [28]. The antiperiodic boundary condition is applied to the left (Γ_L) and right (Γ_R) sides of the periodic section. The Eigenmode analysis is performed to compute the resonance frequency of the SAW resonator.

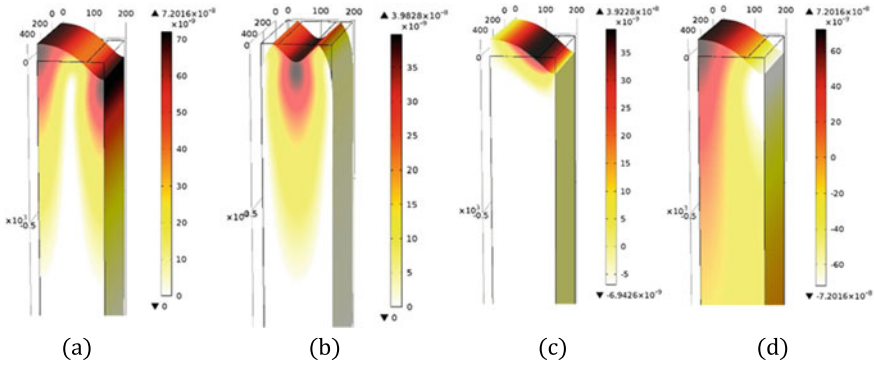


Fig. 5 Displacement profiles at resonance frequency 8.282835 MHz, **a** total displacement profile, **b** *x* displacement profile with a deformed shape, **c** *y* displacement profile with the deformed shape. *Note* For simplicity, the substrate length shown in the Figure is 2λ .

The resonance frequency is identified from the list of Eigenmode frequencies and their displacement amplitude, the mode of vibration, and the charge distribution on the IDT fingers are studied. At the resonance frequency, the displacement is maximum between the fingers of the resonator while at anti-resonance frequency the displacement is maximum in the middle of the finger. The charge distribution is symmetry and antisymmetric at resonance and antiresonance frequencies.

8 Simulation of a Conventional SAW Delay Line

The conventional SAW delay line device has been simulated using FEM by many researchers [29–31]. In this section, a conventional SAW delay line device is simulated to compare the simulation results with the proposed SAW delay line device configuration described.

9 Simulation Methodology

A SAW delay line device with a delay of 3λ ($\lambda = 1200\ \mu\text{m}$) is simulated by FEM using COMSOL Multiphysics. In this simulation, three pairs of IDT fingers for transmitter IDT and receiver IDT fabricated at the two ends of the piezo substrate are considered. The dimensions used for simulations are as follows: electrode width (*d*) $100\ \mu\text{m}$, electrode pitch (*p*) $200\ \mu\text{m}$, depth of the piezo substrate $400\ \mu\text{m}$ (1λ), and thickness of IDT fingers $0.2\ \mu\text{m}$ [32]. YX LiNbO₃ piezoelectric material is used as a piezo substrate and aluminum metal is used as IDT electrodes. 3D geometry of the SAW delay line device used for simulation is shown in Fig. 6. The following boundary conditions are applied to the model.

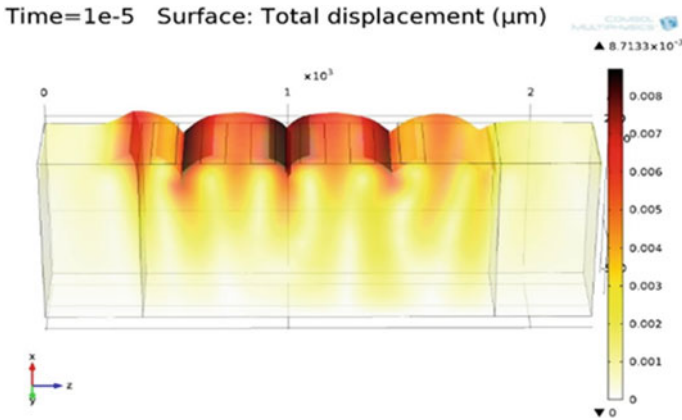


Fig. 6 Results of simulation of a conventional SAW delay line device, **a** total displacement profile at time 10 ns

The top surface of the substrate is assumed stress-free and the bottom surface is fixed in its position. The critical damping is assumed at the edge of the transmitter B_L , receiver B_R , and bottom of the substrate B_B to avoid reflections of the acoustic waves. The alternate fingers are shorted and 1 V sinusoidal driven voltage of its resonance frequency is applied. The resonance frequency is about 8.37 MHz. An optimized mesh density is used for the simulation. To analyze the propagation of SAW over the delay line, transient analysis is performed using direct solver SPOOLS available in COMSOL Multiphysics [33] with the time interval of 10 ns for a duration up to 1 μ s. The displacements and potential at the receiver electrode are recorded at every instant.

The transient analysis of the SAW delay line device is performed for the time duration of 1 μ s. Figure 6 shows the total displacement profile of the SAW delay line device at time 1 μ s. The output electrical potential, x displacement, and y displacement are measured at the receiver IDT electrodes. The plots of output potential, x displacement and y displacement as a function of time are shown in Fig. 7a, b. The output electric potential of 0.3 V is obtained at the receiver IDT electrodes. In the SAW delay line device, the delay time is one of the important parameters. The delay time calculated from the free surface velocity of 3478 m/s is 1 μ s. x displacement and y displacement of about 6 nm and 6 nm are obtained at time 1 μ s.

10 Dual Friction-Drive (DFD) SAW Motor

The proposed SAW motor which uses the dual friction-drive (DFD) concept made up of two identical Lithium Niobate stators placed mirror-image manner and a cubical structured slider placed in between them. The stators are attached to glass substrates for support to protect damage and uniform preload to the system as shown in Fig. 8.

Fig. 7 Results of simulation of a conventional SAW delay line device, **a** displacement of the particle in the tangential direction, **b** displacement of the particle in the normal direction

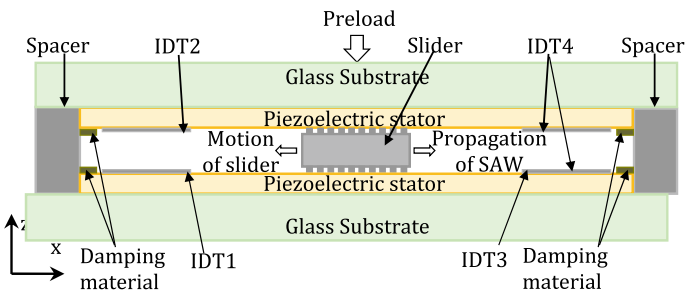
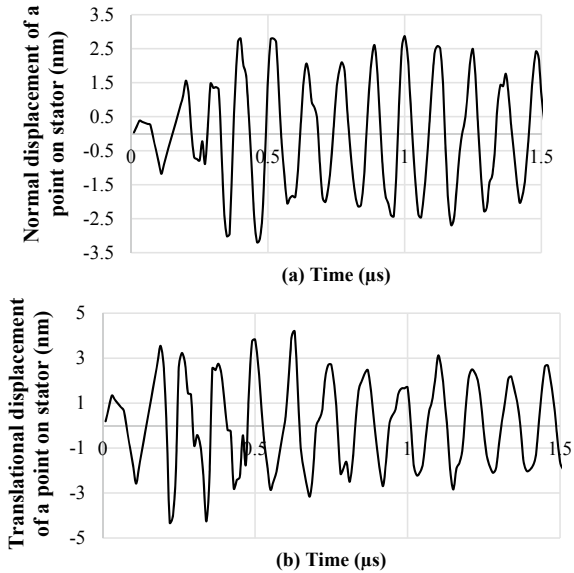
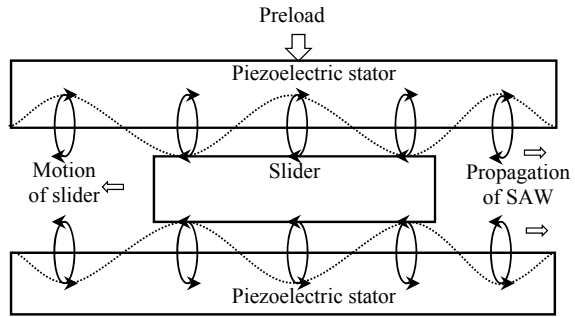


Fig. 8 Schematic of a DFD SAW motor with cuboid slider [34]

The proposed DFD SAW motor able to avoid the disadvantages associated with the conventional SAW motor, the slider is driven with double force, as well as impactfully simplifying the motor arrangement.

The stator is made of a 128° rotated Y cut X propagated Lithium Niobate piezoelectric material generating Rayleigh SAW with high coupling coefficient and IDTs are fabricated at both ends. The IDT is made of aluminum electrodes fabricated in a comb-shaped structure with bond pads to facilitate the electrical connections. Preferably the slider is made of silicon material and cuboid in shape. The spacers help to maintain the gap and alignment between the stators.

Fig. 9 Schematic showing SAW motor implementing the dual friction-drive technique with slider having no projections [37]



11 Principle of Operation of DFD SAW Motor

The principle operation of the proposed DFD SAW motor is based on the Hertz contact theory [35]. As represented in Fig. 8, when a sinusoidal potential is applied to IDT1 and IDT3 of the left side of the top and bottom stators as shown in Fig. 8, it generates SAWs that propagate in horizontal-direction on the surfaces depicted in Fig. 9. The points on the surface of the top stator make clockwise elliptical motion about their mean position while the points on the surface of the bottom stator make anticlockwise elliptical motion. The slider moves in the direction of motion of the points due to the transfer of velocity of the surface component through frictional force [8, 36]. When the potential is applied to IDT2 and IDT4 placed at the right side of the motor, the direction of motion of the slider will be in the opposite direction. Finite element simulation provides an appropriate way to understand the insight operation of the motor.

12 Finite Element (FE) Simulation of DFD SAW Motor

The three-dimensional geometry is taken up to carry out Finite element simulation of the proposed SAW motor in COMSOL Multiphysics. Both piezoelectric and solid mechanics modules are coupled to execute the physics of the motor. The delay line made by taking on an LN substrate of width $400\ \mu\text{m}$ ($1\ \lambda$), length $2000\ \mu\text{m}$ ($5\ \lambda$) and height $800\ \mu\text{m}$ ($2\ \lambda$) and placing IDT of the thickness of $0.2\ \mu\text{m}$, width $100\ \mu\text{m}$ ($\lambda/4$), aperture $400\ \mu\text{m}$ ($1\ \lambda$), and having an array of 6 fingers. A silicon slider is placed in the active region having a length of $400\ \mu\text{m}$ and width $400\ \mu\text{m}$ as shown in Fig. 10.

When it comes to simulation of any model the domain setting of COMSOL Multiphysics, it plays a crucial role. The piezoelectric element is assigned to the stator, and linear elements are assigned to IDTs and sliders. The properties of Lithium Niobate such as coupling coefficients, elastic coefficients, relative permittivity, Poisson’s ratio, Young’s modulus, and density [38] and are listed in Table 1. Due to the high

Fig. 10 Geometry of the DFD SAW motor used in the simulation

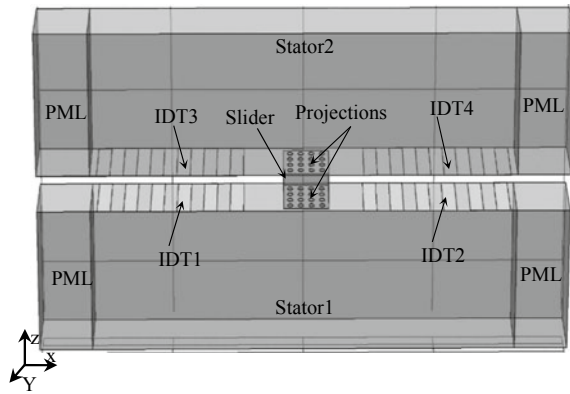


Table 1 Selected parameters applied to the settings of the domains for simulation

Sl. No	Parameter	Symbol	Value
1	Resonance frequency applied	f	8.28 MHz
2	Preload	F_n	2.63 mN
3	Static coefficient of friction	μ_s	0.45
4	Dynamic coefficient of friction	μ_d	0.15
5	Young's modulus slider	E_1	169 GPa
6	Poisson's ratio slider	ν_1	0.3
7	Young's modulus stator	E_2	173 GPa
8	Poisson's ratio stator	ν_2	0.345

conductive, low cost, and lightweight properties of the aluminum (Al), it is used for IDTs formation while Silicon is assigned to the slider. Perfect matching layers (PML) are applied to the boundaries of the SAW devices to absorb unutilized waves and avoid reflection of waves [39]. To keep the slider in contact with the stators, an adequate amount of preload of 2.63 mN is applied to the assembly. The piezoelectric stator and the silicon slider create a contact pair where the stator is playing the role of the master which will drive and the slider plays the role of a slave which will be driven by the master. The contact surface between the stator and slider is assigned with a dynamic coefficient of friction of 0.15 to match up with the atmospheric conditions. To analyze the structure, the whole structure needs to be divided into several small elements which are called meshing. Here for this structure is divided into triangular-shaped meshing with swept meshing for all the domains to cover up the interaction portion perfectly and error-free analysis of the physics of the model [25].

13 Results and Discussion

The simulation is carried out with an application of excitation voltage of 150 V and resonance frequency of 8.28 MHz. The reported literature conveys that a SAW motor has a dead zone typically below $30 V_{peak}$ where the slider unable to make any motion [40]. When a potential of 150 V is applied to the stator surface, it makes displacement both in normal and translational directions and can be detected by points on the surface of 10 nm and 16 nm, respectively. The displacement in normal direction initially deforms a lot but as the time progresses it diminishes and becomes negligible as shown in Fig. 11.

The mechanism of friction-drive at the interface area of the stator and slider experiences two states i.e. stick and slip zones [41] in each cycle of the Rayleigh wave. The slider experiences stick conditions both at the trough and crest of the SAW wave and the contact point exerts a tangential force on the slider [28] which forces to move the slider. As per the Hertz contact theory [35], Fig. 12 shows the tangential force on the slider at the crest moves the slider in the direction opposite to the direction of wave propagation. The motion of the slider is opposed by the tangential force at the trough but as at the crest generates much greater force than that at the trough, the motion of the slider is least affected [40]. Other than this

Fig. 11 Simulated result for the displacement in the normal direction of the slider

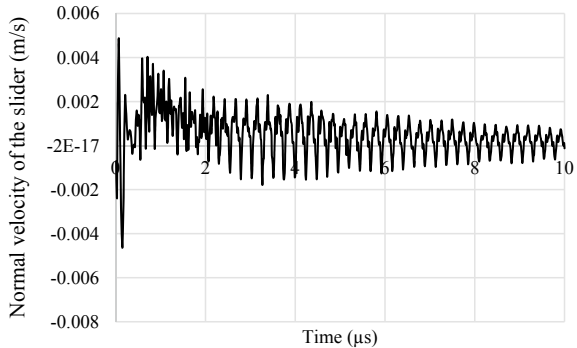
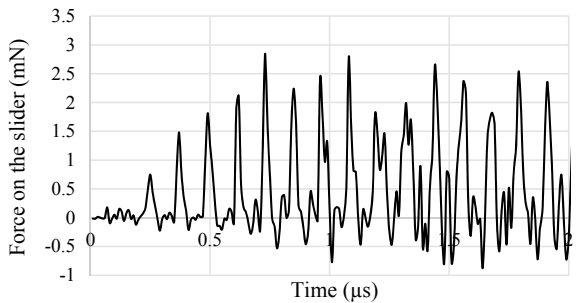


Fig. 12 Graph for the tangential force impacted on the surface of the slider



activity, the rest of the time of the propagation of the wave, the slider experiences slip condition which causes loss in frictional force, and thrust is not produced.

Figure 13 shows the snapshot of the motion of the slider during the simulation. The slider displaces a distance of $0.26 \mu\text{m}$ at end of $10 \mu\text{s}$ in a horizontal direction. The achieved motion occurs with the application of potential 150 V in a continuous-wave excitation manner to both stators without any difference in phase. Figure 14 represented a magnified view of the motion of the slider for excitation of 150 V with step incremental motion.

Three different voltages viz. 100, 150, and 180 V are applied to check the variation in motion of the slider. Figure 15 shows the motion of the slider of displacement of

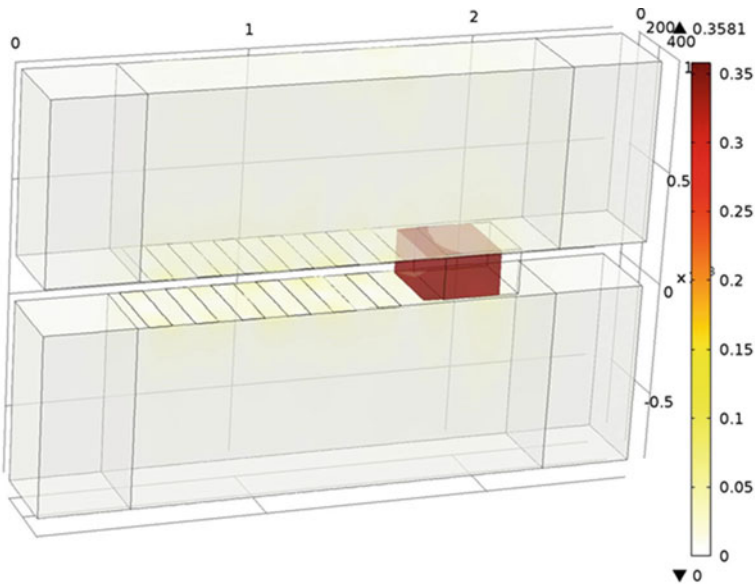


Fig. 13 Translational displacement of $0.25 \mu\text{m}$ of the slider at the end of $10 \mu\text{s}$

Fig. 14 The stepwise motion of the slider for the application of excitation of 150 V

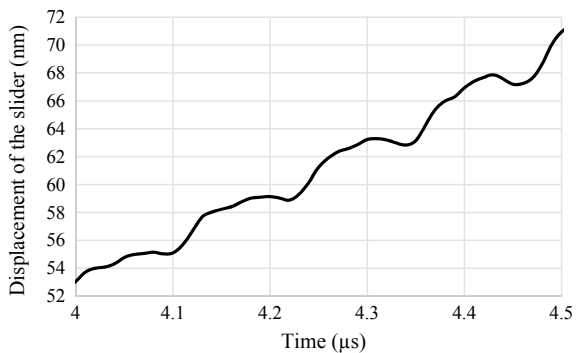
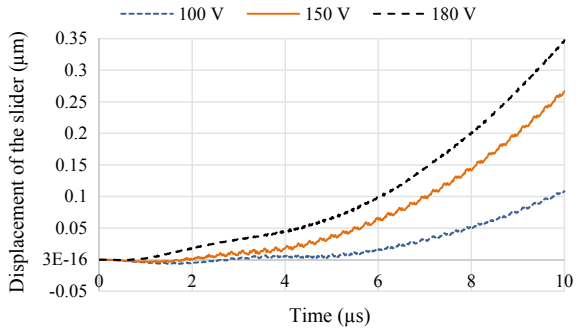


Fig. 15 Translational displacement of the slider for the application of three different voltages



0.35 μm, 0.26 μm, and 0.1 μm for the application of 180 V, 150 V, and 100 V respectively at the end of 10 μs.

Figure 16 shows the results of the simulation for the translational motion of the slider with a continuous excitation wave along the horizontal direction. Thus, the slider can make a translational motion in both forward and reverse directions along the horizontal axis.

When continuous Rayleigh wave propagates under the slider, the motion of the slider picks to movement at a constant speed of motion due to the inertia of motion which converts the stepwise motion to continuous motion. Figure 17 shows a compar-

Fig. 16 Steady-state velocity of the slider at the end of 0.02 s

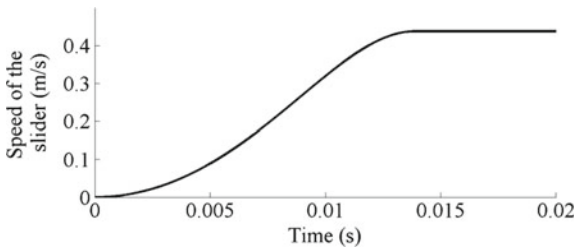
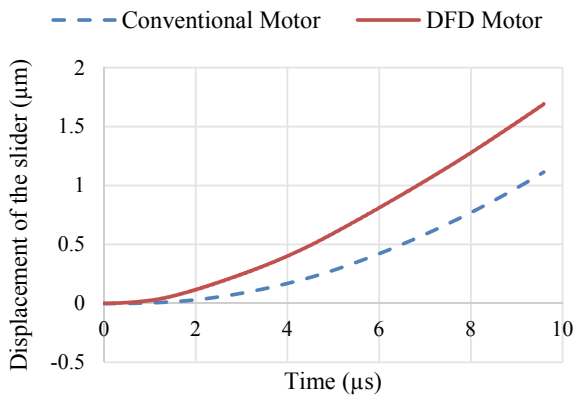


Fig. 17 Comparison between conventional and DFD SAW motor with projections



ative simulation result for the movement of the slider in conventional SAW motor and Proposed DFD motor. The slider in the proposed DFD SAW motor makes a displacement of around $1.75\ \mu\text{m}$ as compare to the conventional SAW motor where it makes around $1\ \mu\text{m}$ movement. The proposed DFD motor can be utilized to drive an external load such as micromirrors, small screws, etc.

14 Conclusions

This chapter presents piezoelectricity, the equation of motion, and the solution to surface waves in piezoelectric media. Simulations based on FEM using COMSOL Multiphysics to determine the free surface SAW phase velocity and adequate mesh density for the simulation are performed. Simulation of one-port SAW resonator is done so that the results will be used to compare the proposed DFD SAW device configuration. To find out the delay time and attenuation in the output electric potential, the Simulation of the SAW delay line is carried out. The device parameters such as velocity dispersion, reflection coefficient, and effective permittivity as a function of the metallization ratio are presented. The basic design of SAW motor has to be optimized with the help of modeling techniques. The proposed DFD motor leads to an extraordinarily compact and less weight structure. The FEM simulation of the SAW motor is performed and presented to explain the operation of DFD SAW motor. The forces acting on the surface of the cubical slider and the subsequent displacement and velocity of the slider are studied. The displacement of 0.1 , 0.26 , and $0.35\ \mu\text{m}$ for the application of 100 , 150 , and $180\ \text{V}$ of the slider is observed at the end of $10\ \mu\text{s}$. Finally the comparative simulation study of a conventional SAW motor and proposed DFD SAW motor is presented.

References

1. T. Morita, Review on miniature piezoelectric motor. Elsevier Sens. Actuators Phys. **103**, 291–300 (2003)
2. B. Behera, H.B. Nemade, Recent developments of piezoelectric motors with diverse operating principles. ISSS J. Micro Smart Syst. 1–13 (2017)
3. B. Behera, Design and investigation of a dual-friction drive based LiNbO_3 piezoelectric actuator employing a cylindrical shaft as slider. IEEE Sens. J. **19**(24), 1–1 (2019)
4. M.K. Kurosawa, Ultrasonic linear motor using traveling surface acoustic wave, in *Proceedings of IEEE Ultrasonics Symposium*, 2009, pp. 1096–1105
5. K. Uchino, Piezoelectric ultrasonic motors: overview. Smart Mater. Struct. **7**(3), 273–285 (1998)
6. T. Shigematsu, M.K. Kurosawa, K. Asai, Sub-nanometer stepping drive of surface acoustic wave motor, in *Third IEEE Conference on Nanotechnology*, 2003, pp. 299–302
7. Y. Nakamura, M.K. Kurosawa, T. Shigematsu, Effects of ceramic thin film coating on friction surfaces for surface acoustic wave linear motor, in *IEEE Ultrasonics Symposium*, 2003, pp. 1766–1769

8. T. Morita, M.K. Kurosawa, T. Higuchi, Simulation of surface acoustic wave motor with spherical slider. *IEEE Trans. Ultrason. Ferroelectr. Freq. Control* **46**(4), 929–934 (1999)
9. Y. Kusminov, *Lithium Niobate Crystals* (Cambridge International Science Publishing, 1997)
10. A.V. Mamishev, K.S. Rajan, F. Yang, Y. Du, M. Zahn, Interdigital Sensors and Transducers. *Proc. IEEE* **92**(5), 808–845 (2004)
11. K. Uchino, *Advanced Piezoelectric Materials Science and Technology*, 1st edn. (Woodhead Publishing Limited, New Delhi, 2010)
12. T. Shigematsu, M.K. Kurosawa, K. Asai, Nanometer stepping drives of surface acoustic wave motor. *IEEE Trans. Ultrason. Ferroelectr. Freq. Control* **50**(4), 376–385 (2003)
13. H. Gu, D. Ma, S. Zhang, L. Cheng, X. Shui, Theoretical analysis of non contact linear motors driven by surface acoustic waves, in *Proceedings of the IEEE*, 2008, pp. 3–6
14. D. Royer, E. Dieulesaint, *Elastic Waves in Solids II*, 1st edn. (Springer, New York, 1999)
15. K. Hashimoto, *Surface Acoustic Wave Devices in Telecommunications Modelling and Simulation*, 1st edn. (Springer, Chiba, Japan, 2000)
16. C.C.W. Ruppel, T.A. Fieldly, *Advances in Surface Acoustic Wave Technology, Systems and Applications*, vol. I (World Scientific Publishing Co. Pte. Ltd., 2001)
17. B.A. Auld, *Acoustic Fields and Waves in Solids*, vol. II, 1st edn. (Wiley, Canada, 1973)
18. D. Morgan, *Surface Acoustic Wave Filters With Applications to Electronic Communications and Signal Processing*, 2nd edn. (Elsevier Academic Press, Oxford, 2007)
19. D. Royer, E. Dieulesaint, *Elastic Waves in Solids: Free and Guided Propagation*, vol. I, 1st edn. (Springer, Northampton, England, 1996)
20. M. Thompson, *Surface-Launched Acoustic Wave Sensors : Chemical Sensing and Thin-Film Characterization* (Wiley, 1997)
21. D. Royer, *Elastic Waves in solids*, 1st edn. (Springer, France, 1996)
22. B. Behera, H.B. Nemade, Investigating translational motion of a dual friction-drive surface acoustic wave motor through modeling and finite element simulation. *Simul. Trans. Soc. Model. Simul. Int.* 1–9 (2018)
23. B. Behera, H.B. Nemade, Modelling and finite element simulation of a surface acoustic wave driven linear motor. *Procedia Eng.* **144**, 1411–1418 (2016)
24. V.K. Varadan, K.J. Vinoy, S. Gopalakrishnan, *Smart Material Systems and MEMS : Design and Development Methodologies*, 1st edn. (Wiley, England, 2006)
25. D.S.H. Lo, *Finite Element Mesh Generation*, 1st edn. (CRC Press, New York, 2015)
26. C.S. Hartmann, D.T. Jr. Bell, R.C. Rosenfeld, Impulse model design of acoustic surface-wave filters. *IEEE Trans. Microw. Theory Tech.* **21**(4), 14 (1973)
27. J. Koskela, V.P. Plessky, M.M. Salomaa, SAW/LSAW COM parameter extraction from computer experiments with harmonic admittance of a periodic array of electrodes. *IEEE Trans. Ultrason. Ferroelectr. Freq. Control* **46**(4), 806–816 (1999)
28. M.K. Kurosawa, T. Shigematsu, Friction drive simulation of a surface acoustic wave motor, in *Proceedings of Ens'07*, 2007, no. December, pp. 8–13
29. M.Z. Atashbar, B.J. Bazuin, M. Simpeh, S. Krishnamurthy, 3D FE simulation of H2 SAW gas sensor. *Sens. Actuators B. Chem.* **112**, 213–218 (2005)
30. N. Ramakrishnan, A.K. Namdeo, H.B. Nemade, R. Paily, Simplified model for FEM simulation of SAW delay line sensor. *Eng. Prpcedia* **41**, 1022–1027 (2012)
31. Y.L. Rao, Nanostructure enhanced surface acoustic love wave devices for biosensing applications (2008)
32. W. Richard, H.M. Gerard, J.H. Collins, M. Reeder, H.J. Shaw, Design of surface wave delay lines with interdigital transducers. *IEEE Trans. Microw. Theory Tech.* **17**(11), 9 (1969)
33. C. Multiphysics, M. Guide, COMSOL multiphysics modeling guide, in *COMSOL Multiphysics*, 2005, pp. 01–348
34. B. Behera, H.B. Nemade, S. Trivedi, Modelling and finite element simulation of a dual friction-drive SAW motor using flat slider, in *IEEE International Ultrasonics Symposium*, 2016, pp. 1–4
35. K.L. Johnson, *Contact Mechanics* (Cambridge University Press, 1, 1985).
36. B. Behera, H.B. Nemade, Dual friction-drive SAW motor utilizing cylindrical shaft as external load driver. *Ferroelectr. Lett. Sect.* **45**(1–3), 8–13 (2018)

37. B. Behera, H.B. Nemade, Finite element simulation of a saw motor based on dual friction-drive. *Mater. Today Proc.* **4**(9), 9594–9599 (2017)
38. T. Shigematsu, M.K. Kurosawa, Friction Drive of an SAW motor. Part V: design criteria. *IEEE Trans. Ultrason. Ferroelectr. Freq. Control* **55**(10), 2288–2297 (2008)
39. S.J. Ippolito, K. Kalantar-Zadeh, D.A. Powell, W. Wlodarski, A 3-dimensional finite element approach for simulating acoustic wave propagation in layered SAW devices, in *IEEE Ultrasonics Symposium*, 2003, pp. 303–306
40. M.K. Kurosawa, T. Shigematsu, Friction drive simulation of a SAW motor with slider surface texture variation. *Adv. Sci. Technol.* **54**, 366–371 (2008)
41. T. Shigematsu, M.K. Kurosawa, Friction drive modeling of SAW motor using classical theory of contact mechanics, in *10th International Conference on New Actuators*, 2006, no. June, pp. 444–447

Basudeba Behera received the Bachelor of Engineering in Electronics and Instrumentation Engineering and the Master of Technology in Electronics and Communication Engineering from GIET University, Odisha, India in 2006 and 2009 respectively. He completed his Ph.D. degree in the Department of Electronics and Electrical Engineering from the Indian Institute of Technology Guwahati (IITG), Assam, India in 2017. Currently, he is working as a full-time faculty member (Assistant Professor) at the National Institute of Technology Jamshedpur (NITJSR). He has been involved in research on Piezoelectric and SAW devices, Ultrasonic Motors, mostly in Modeling, simulation, and fabrication of the Sensors and Actuators.

Interdigital Sensor for IoT Applications



M. Adhikary

Abstract Internet of Things (IoT) is the technological means for making wireless interconnection of multiple “smart” instruments feasible by employing radio frequency signals. Since day by day, the need for automated instruments is increasing with exponential growth, the new technologies supporting that feature are coming up. One main aspect of the interconnection of the instrument is the logic behind their interconnection. For example, a “smart room” is supposed to sense the ambient temperature and humidity of the room and respond to the same by controlling the temperature and humidity of the “smart air conditioning system” or the “smart fan”. Several mobile-based IoT applications like IFTTT (If This Then That) [1], etc. have come up in the market which can set the logic behind the operation of interconnected IoT devices. The fundamental building block of any smart system is the sensor. Since interdigital sensors have multiple benefits including, high sensitivity, wider tuning range, the feasibility of planar interconnection with other system modules, they are widely used in modern IoT devices capable of actuating the device upon sensing certain physical parameters. A generalized sensor is what is capable of sensing the dielectric constant of a substance or a substrate since in many passive sensor modules either the dielectric constant or the loss tangent is the main signifier of any physical change. However, to measure a passive sensor, expensive instruments such as Vector Network Analyzer, Signal Generator, Spectrum Analyzer, etc. are required. That is why there is a major necessity for stand-alone sensing systems that can measure some physical parameters and translate that into some electrical signals without the necessity of the expensive off-the-shelf instruments. The capability of the integrated system can be further extended to make it IoT compatible so that the measured data can be made available at cloud storage for real-time monitoring of the signal at distant locations also. With this technique, the cost of the proposed system can be cut down to a great extent. This chapter will give an overview of a kind of interdigital sensor-based system which can be potentially applied for monitoring of dielectric

M. Adhikary (✉)

Department of Electrical Engineering, Indian Institute of Technology Kanpur, Kanpur, India
e-mail: moitreya@iitk.ac.in

Staff Systems Engineer, Maxlinear Inc., Bangalore, India

© The Editor(s) (if applicable) and The Author(s), under exclusive license to Springer Nature Switzerland AG 2021

369

S. C. Mukhopadhyay et al. (eds.), *Interdigital Sensors*, Smart Sensors, Measurement and Instrumentation 36, https://doi.org/10.1007/978-3-030-62684-6_15

constant of a substrate, which transmits the sensor information at a distance utilizing IoT capability.

1 Introduction and Literature Review

Over the years, the use of microwave material sensors has increased extensively in the field of chemical and medical industries due to their accuracy, compact size, lightweight, low cost, and easy planar design [2]. The basic principle of a microwave sensor is the change in transmission, reflection, and scattering characteristics of the sensor device when the microwave field of the sensor interacts with the material under test. These sensors are utilized to characterize the electrical properties of the materials such as permittivity, permeability, and conductivity. A significant improvement in the sensitivity of resonant type sensors has been observed in recent works over the non-resonant type sensors [3–6]. The measurement of these quantities is not that straightforward as these cannot be determined directly. Instead, special measurement techniques and numerical methods are employed to extract the permittivity out of the variations in transmission and reflection characteristics of the sensor caused by the material placed over the sensor. The modern microwave sensors for the material characterization are mostly based on Split Ring Resonator (SRR), Complementary Split Ring Resonator (CSRR), the Interdigital capacitor, etc.

In recent years, various techniques have been employed for the realization of wireless and portable dielectric sensing systems, many of them are based on RF identification (RFID) scheme [7–9]. RFID is the use of radio waves to read and capture the information stored on the tag attached to the object. Wireless sensing of complex permittivity of liquids based on RFID is presented in [10]. A wireless sensing system is designed by integrating planar antennas at the two ends of the sensor which serves as tag antennas. Similar planar antennas are attached to the Vector Network Analyzer (VNA) port 1 and port 2 as Tx reader antenna and Rx reader antenna which couple the RF energy to the sensor and receives the energy from the sensor at other port respectively. Another approach of non-invasive testing of biological samples using a broadband wireless sensing system is presented in [11]. The system employed ultra-wideband transmitter–receiver antennas and planar sensors for the testing. However, the RF signal to excite the planar sensors in both [10, 11] is provided using Vector Network Analyzer (VNA). The presented systems are distance-dependent as increasing the distance between the reader and tag antennas affects the RF energy coupling. An application of facilitating the distant measurement of material permittivity, a negative resistance oscillator based active tag integrated antenna design is proposed in [12].

The exponential growth in wireless and mobile communication technologies in the last decade has resulted in the integration of one or more communication modules in almost every object around us. It has led the industries and academia to conduct a wide range of research and development to realize applications such as 5G, the Internet of Things (IoT) and smart skins (SS) that interconnect different objects

with sensing and processing capabilities which can communicate with each other at high speed without human interaction [13–15]. IoT enabled interdigital sensor related research is being widely carried out to perform various tasks including kidney health monitoring, Nitrate percentage in soil, biosensor that determines the stage of bone loss in patients, etc. With the growing world of interconnectivity and automation of things, objects, and devices, a wide range of industrial and academic research have been done to make the devices, equipment's remotely accessible and to get the availability of collected data at a distant location for further analysis.

In this work, an approach of integrating standalone Internet of Things (IoT) enabled RF Sensor system has been proposed, which measure the transmission coefficients of microwave material sensor which can be used to characterize the dielectric properties of materials by applying the curve fitting and some sophisticated artificial neural network-based algorithms on resonance frequency shift data for different materials loaded on the sensor. The calculated values of transmission coefficients are made available at internet cloud storage so that it could be accessed at any location. Various sub-components employed in the proposed system are designed, fabricated, and tested as described in the latter sections. The values of the calculated transmission coefficient of the sensor at different frequencies in the present situation have been plotted in real-time at the cloud storage, which can be accessed and analyzed at any location. Unlike conventional systems where it requires expensive measurement equipment for the characterization of a sensor, this standalone system can perform the same measurement with considerable accuracy and send the data to the cloud for remote monitoring and analysis.

2 System Design Principle

The complete functional block diagram of the proposed IoT enabled automated system along with various sub-components chain is shown in Fig. 1. To facilitate the characterization of an RF sensor, the design of the proposed system combines various sub-components, software, and services that have been employed such as Oscillators, Rectifiers, power supply, Arduino Uno microcontroller, NodeMCU chip, Arduino IDE, cloud storage, etc.

A. *Role of Oscillator*

The role of oscillators is to provide a stable frequency RF signal output with a sufficient amount of RF power. Wilkinson power divider is integrated into both oscillators so that an equal amount of RF power signal could be taken as an output from two ports. A tunable negative resistance Voltage Controlled Oscillator (VCO) is designed and fabricated, as shown in Fig. 2, to be integrated into a broadband RF sensor system in which S_{21} of the sensor sample is plotted for a range of frequencies. In further stage to reduce the external load-pull effect on the oscillator performance (reduction of frequency tuning range) by the sensor and other loaded networks are

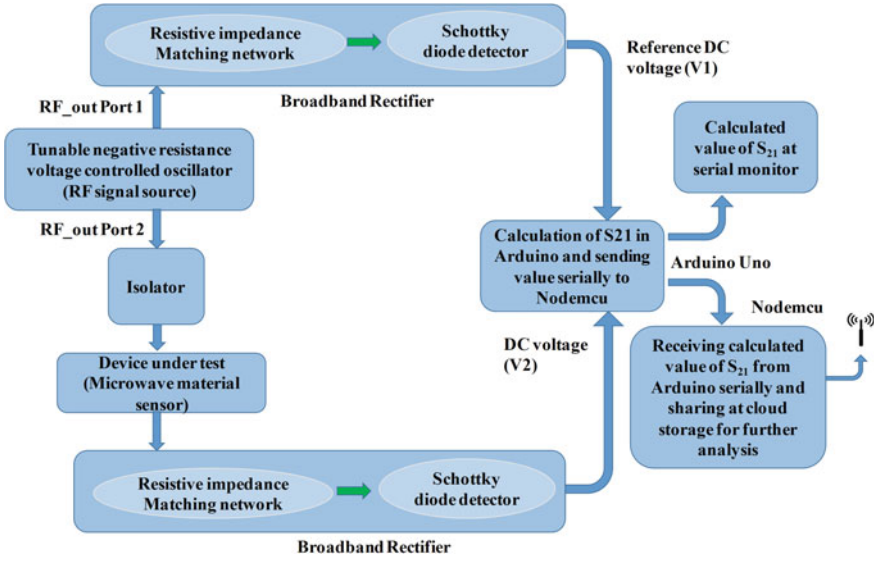
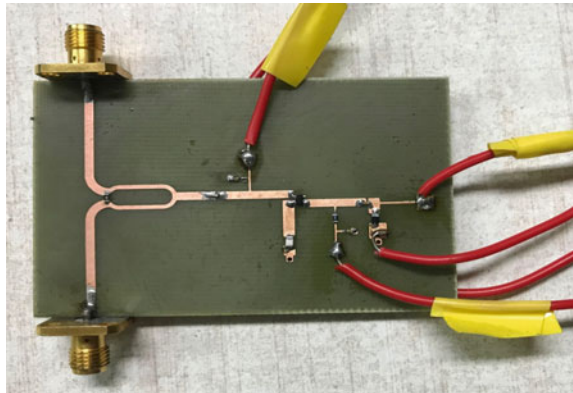


Fig. 1 Simplified functional block diagram of the system

Fig. 2 Fabricated oscillator working as signal source



alleviated by using an isolator. Even though the isolator can somehow mitigate the load-pull effect, it is difficult to be integrated with standard planar circuitry and hence it is replaced in a later stage by close to unity gain buffer amplifier which is planar.

B. Role of Rectifiers

To convert RF power signal coming out of the tunable oscillator to corresponding DC voltage level, two similar broadband rectifiers using Villard Doubler topology [16] are designed as shown in Fig. 3 and fabricated which covers the complete range of VCO output signal frequencies. One converts the reference RF signal coming out of the oscillator to DC voltage and another to convert RF signal coming through the

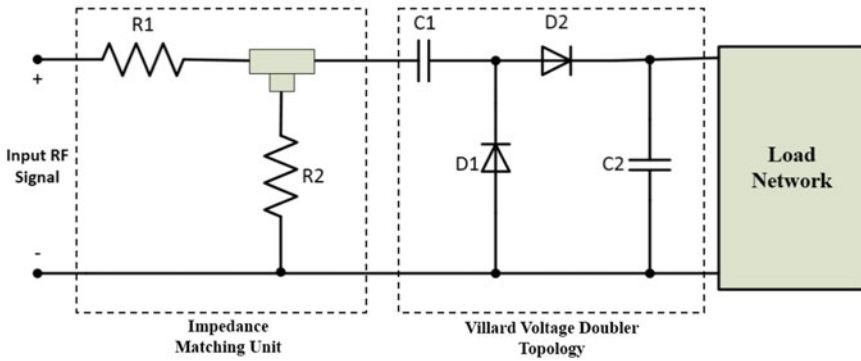


Fig. 3 Block diagram of the proposed broadband rectifier design showing impedance matching unit and Villard voltage doubler stage

Sample sensor to corresponding DC voltage. If transmission loss (S_{21}) of the sample under test is negative at that frequency, then DC voltage termed as DC_out2 (Ref. to Fig. 1) will be less in magnitude due to less RF power being transferred from oscillator to rectifier.

C. Role of Microcontroller

The microcontroller is an integrated circuit that can be programmed for specific applications in an embedded system. There are various microcontrollers available such as Arduino Uno, Raspberry Pi, etc., which mainly differ in terms of the input/output pins, memory, processor, etc. In the present situation, the Arduino Uno has been used to implement the proposed integrated sensor system. The main role of Arduino here is to read the DC voltages provided at the output of rectifiers and accordingly calculate the magnitude of S_{21} of the material sensor in the dB scale. The computed S_{21} data of the material sensor are also sent to the NodeMCU Wi-Fi chip using this Arduino through serial communication to facilitate the sharing of sensor data at the cloud storage. Arduino Uno is programmed using Arduino IDE (Integrated Development Environment) software to read the voltages, to calculate the S_{21} , and to send data serially (Fig. 4).

D. Wi-Fi Connectivity

The proposed integrated RF sensor system is made IoT enabled by connecting the system with nearby Wi-Fi using the NodeMCU chip, which can be configured using the open-source platform. NodeMCU includes an ESP8266 System on Chip (SoC) developed by Espressif System, which can be programmed to connect with nearby Wi-Fi. The role of NodeMCU in the RF sensor system is to serially receive the real-time calculated values of S_{21} sent by the Arduino and share the received data to the internet through Wi-Fi. The NodeMCU here has also been programmed using the Arduino IDE software to receive the data serially, to make the connection with Wi-Fi, and to send the data at cloud storage for further processing (Fig. 5).

Fig. 4 Arduni MCU (© Google)

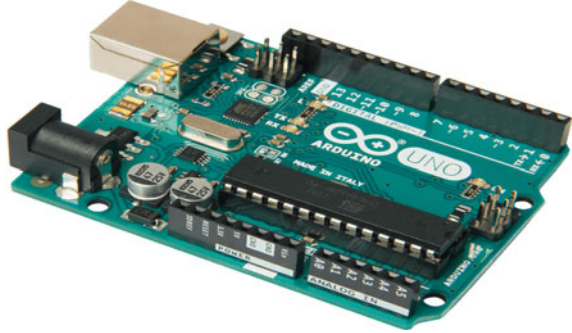
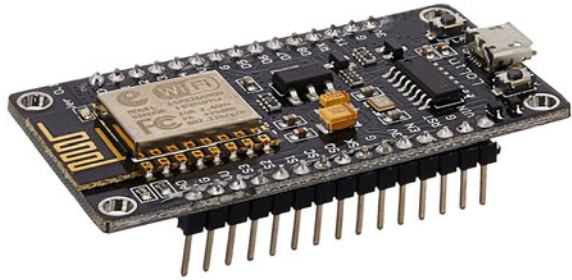


Fig. 5 NodeMCU WiFi unit (© Google)



E. Cloud Storage

Various online IoT platforms provide free channel storage for the Internet of Things (IoT) applications. Some of these are Microsoft Azure IoT Suite, Thingspeak IoT platform, Google cloud's IoT platform, Cisco IoT cloud connect, etc. In this work, the Thingspeak IoT platform (Fig. 2) is utilized to collect and plot the calculated values of S_{21} at a distant location. Thingspeak gives access to a private channel in the cloud having a unique ID and Application Programming Interface (API) write key. Channel ID and API write key have been fed in the scratch Code burned in NodeMCU chip. Data Stored in the channel can be visualized in MATLAB and data can also be downloaded for further post-processing (Fig. 6).

F. Microwave Material Sensor

Microwave material sensors are widely used in material characterization industries. The main objective of the sensor system is to find the dielectric constant and loss tangent of the material under test. However, since many physical parameters are correlated with the dielectric constant of the sensing material under the effect of change in the corresponding physical parameters, it is obvious that they can in general be considered as generalized sensing system. Interdigital sensors are mostly used in dielectric characterization industry owing to their high sensitivity and wide tuning range. In this chapter, some modern design aspects of interdigital sensors will be

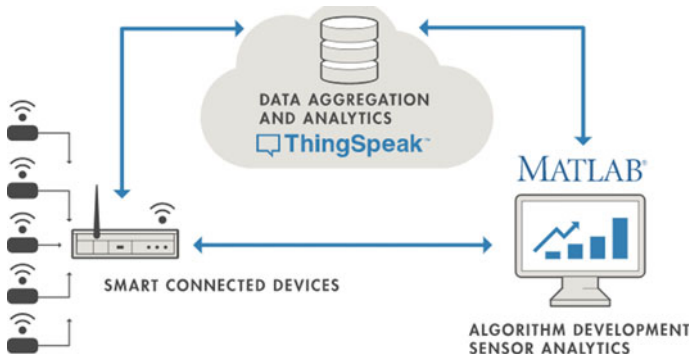


Fig. 6 ThinkSpeak cloud platform (© Google)

Fig.7 IDCSRR sensor



discussed. The present sensor system in discussion uses a kind of interdigital complementary split ring resonator (IDCSRR) to enhance the sensitivity as shown in Fig. 7. Since, the objective of the chapter is to deal with interdigital system, further details are provided in the next section of the chapter.

G. Buffer Amplifier

For the purpose of making the system fully planar, the isolator can be replaced by using two identical unity gain buffer amplifiers on either side of the VCO output ports to reduce the external load-pull effect. The simulated performance of the proposed buffer amplifier and its effect on improving the matching of the reflection type CSRR sensor are shown in Fig. 8.

H. Performance of the system for material sensing

The complete system set up to measure the magnitude of S_{21} is designed using the scheme depicted in Fig. 9. Before calculating the values of S_{21} , the tuning range of Oscillator has been tested again with the help of signal analyzer after integrating the oscillator with sensor and rectifiers. It had been found that due to impedance mismatch provided by the sample sensor to the oscillator, the tuning range of the oscillator was affected adversely. The lowest and highest oscillator frequency after connecting the sensor at one of the ports of the oscillator was found to be 2.37 GHz and 2.44 GHz respectively. Initially, the S_{21} characterization of the sensor has been done

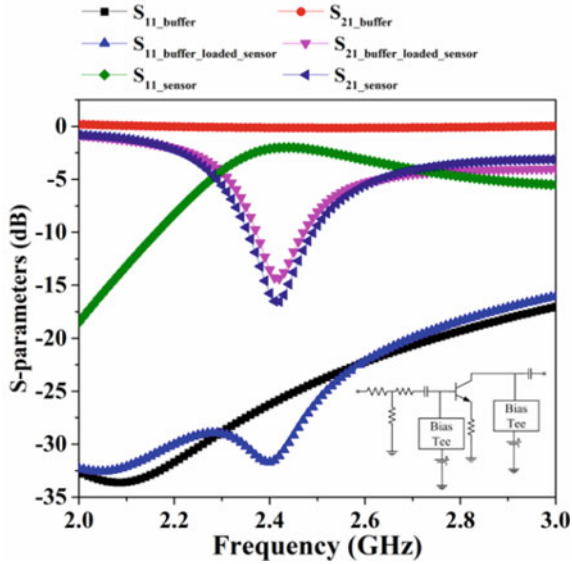


Fig. 8 S-parameter responses of the standalone sensor and the sensor loaded with buffer amplifier, inset: simplified schematic of buffer

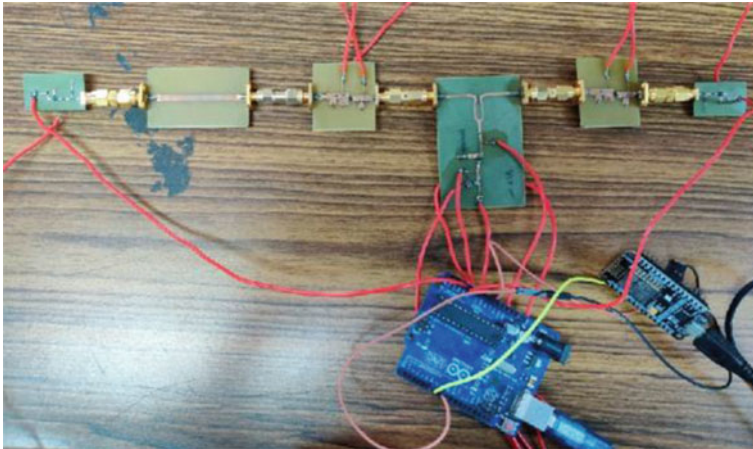


Fig. 9 Overall IoT sensor system with the IDCSRR sensor (shown under dashed box)

for the same frequency range 2.37 to 2.44 GHz, but tuning range of the oscillator has been improved with the use of an isolator. By varying the DC voltage across Varactor diode of the oscillator, the magnitude of S_{21} of the CSRR sensor has been calculated for all tuning range of VCO, and calculated values are being sent to the Thingspeak cloud for real-time plotting of the data. Figure 10 shows the plotted graph of S_{21}

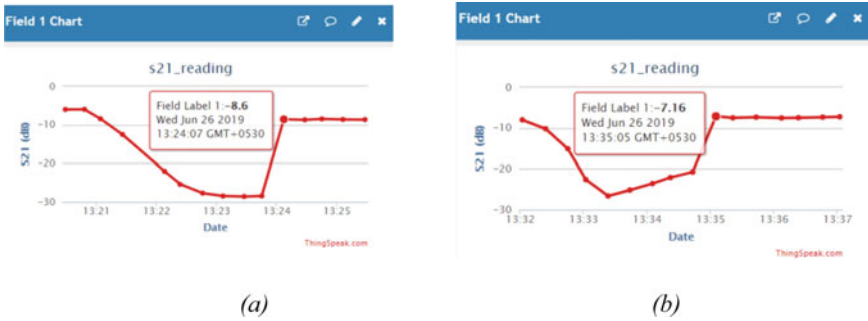


Fig. 10 Real-time plot of the magnitude of S_{21} of **a** unloaded, **b** loaded CSRR sensor at cloud storage

values of the unloaded sensor with respect to time at which data was sent to the cloud. The S_{21} is calculated as the ratio of DC_{out2} to DC_{out1} .

The look up table is generated for variation of oscillator frequencies with respect to reverse biased voltage applied so that it can be corresponded to frequency scale in Arduino real time serial plotter and to generate S_{21} data points versus frequency during post analysis. The Y-axis data has been downloaded in CSV format from the website for further post-processing. Similarly, the same procedure has been followed for the CSRR sensor in the material loaded condition, as shown in Fig. 15. The material RT/Duroid 5880 of permittivity 2.2 and thickness 0.127 mm and loss tangent of 0.0009, has been placed over IDC/SRR of the sensor so that shift in resonance frequency can be noticed using RF sensor system (Fig. 11).

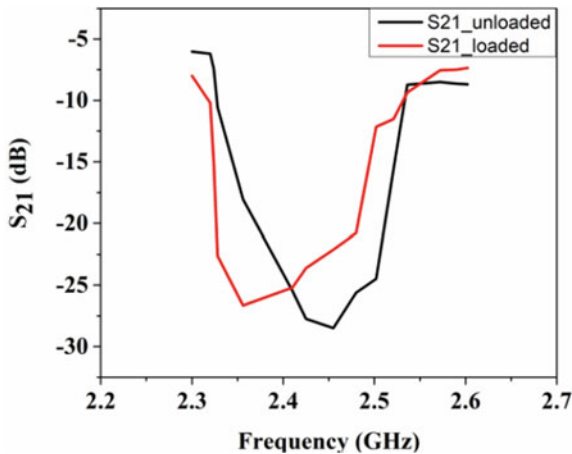


Fig. 11 Curves of S_{21} magnitudes of the IDC/SRR sensor with both loaded and unloaded conditions, calculated using the proposed IoT enabled sensor system as shown in Fig. 9

3 Interdigital Split Ring and Complementary Split Ring Resonators

In rectangular shaped split ring resonator (SRR), the maximum electric field is confined to the dielectric gap of the SRR at resonance, and it is used as a sensing region for material characterization. Figure 12 shows the structure of a conventional rectangular SRR based planar microwave sensor and the electric field distribution. To improve the sensitivity, the SRR based dielectric sensor can accordingly be modified. The confinement of electric field in the gap of the SRR can be improved by increasing the effective capacitance of this gap, which can be achieved by maximizing the local area of the ring on both sides of the gap resulting into a capacitive loaded SRR structure as shown in Fig. 13a. Figure 13b shows the electric field of

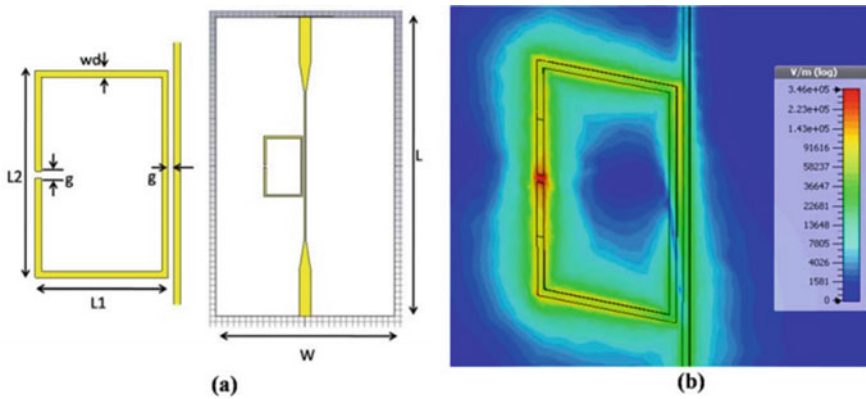


Fig. 12 a Conventional split ring resonator, b electric field magnitude distribution [© 17]

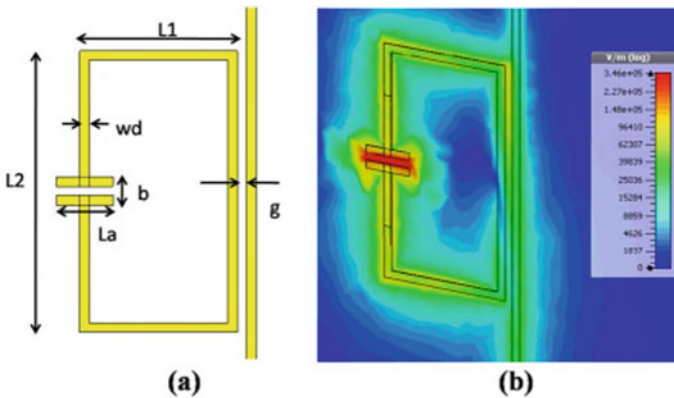


Fig. 13 a Improved split ring resonator, b electric field magnitude distribution [© 17]

the proposed capacitive loaded SRR structure magnetically coupled to the microstrip line. Comparing the electric field of the capacitive loaded SRR with that of the simple SRR shown in Fig. 13b at the resonant frequency, it can be observed that the modified SRR structure improves the electric field in the gap area, increasing the sensitivity. The field in the gap region of the SRR is further improved to obtain higher sensitivity by introducing an IDC in the gap of SRR as shown in Fig. 14a. The IDC based structure shown in Fig. 14a basically provides higher effective capacitance as compared the previous structures.

Since in case of SRR the microstrip line carrying the signal is perturbed by using the magnetic coupling from the line and the resonator, a further enhancement in the design can be achieved if the design is made underneath the microstrip line, as a perturbed structure on the ground plane. This generates the basis of IDCSSRR sensor.

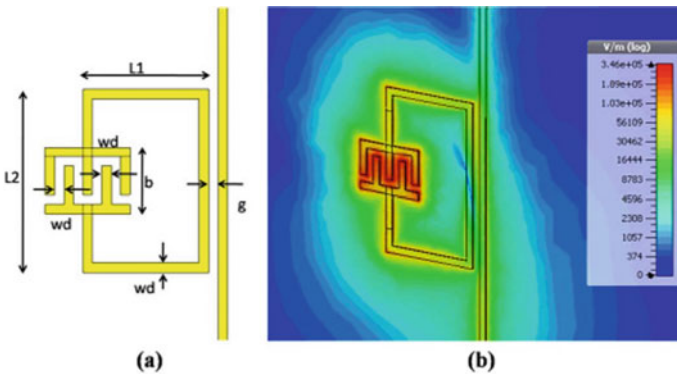


Fig. 14 a Interdigital split ring resonator, b electric field magnitude distribution [© 17]

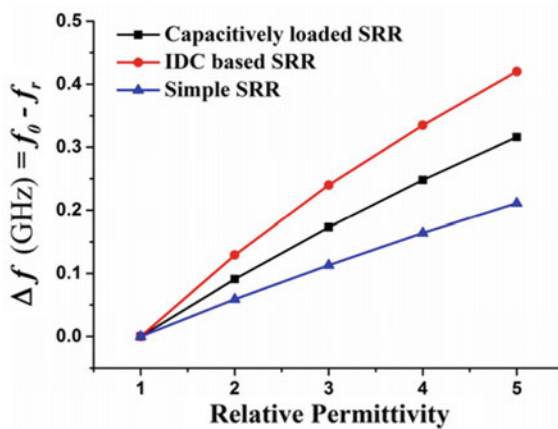


Fig. 15 Sensitivity comparison of different dielectric sensor designs having nearly similar design footprint

IDCSRR sensor achieves more sensitivity than the IDSRR sensors and has better design flexibility since there is no limitation on the coupling gap of the microstrip line and the sensor element. The comparison of the sensitivity of different sensing elements are shown in Fig. 15.

4 Equivalent Circuit Modelling and Analysis of Interdigital SRR

The IDSRR sensor resonator can be equivalently modelled as a coupled resonator circuit consisting of the equivalent mutual inductance and self capacitance of the resonator (Fig. 16a). Owing to the difficulty in modelling or quantifying the mutual inductance value, it can be equivalently decomposed into a series tank circuit [18] as depicted in Fig. 16b. The S_{21} of the equivalent circuit and the actual resonator performance can be compared to be almost identical from ADS simulation (Fig. 17). From the equivalent modelling it can be found that the interdigital line based sensor can provide almost 3 times the effective sensing capacitance than its conventional SRR counterpart. Hence IDSRR is more effective for sensing low permittivity materials. Similar analysis can be carried out for IDCSRR. Owing to the formation of the meander line on the ground IDCSRR has better sensitivity to magneto dielectric materials.

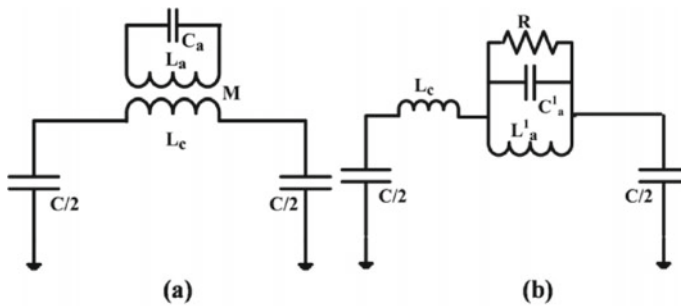
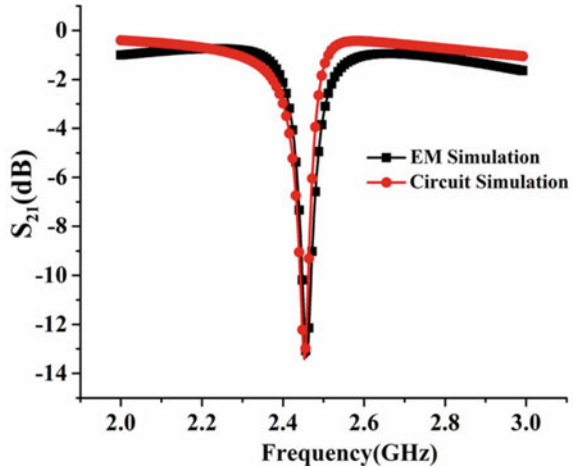


Fig. 16 Proposed equivalent circuit for IDC-SRR based dielectric sensor

Fig. 17 Comparison of S_{21} plot of full-wave and ADS simulation



5 Generalized Integration of Resonators with Interdigital Structures

5.1 Conclusions

This chapter deals with a generalized IoT enabled RF sensor system comprising of the RF oscillator, the rectifier and the Arduino microcontroller, with heart of the system being an interdigital CSRR sensor. The focus has been on integrating various components of the RF integrated circuits in order to realize a generic topology of the RF system containing the source as well as the detector. The major objective was here to make the proposed RF system IoT enabled so that the measured data could be accessed from distant location using simple Wi-Fi network. The IoT enabled automated RF sensor system measures the magnitude of S_{21} of the Dielectric Material Microwave Sensor for a range of frequencies and shares the calculated data at the private cloud storage channel through Wi-Fi in real-time. All the fabricated sub-components such as oscillators and rectifiers have been integrated together along with the Arduino Uno and NodeMCU Wi-Fi module to realize a complete IoT enable RF sensor system. Testing and verification of the proposed system have been done by calculating the magnitude of S_{21} of the microwave sensor under both loaded and unloaded conditions. The measured data have been compared with the corresponding data obtained using the Vector Network Analyzer. The plot of the measured S_{21} data has been generated at the private cloud channel in real time so that data can be downloaded at any location and analyzed for post-processing applications. The system is very much cost effective and can be employed in material characterization industries.

References

1. <https://platform.ifttt.com/docs>
2. L.F. Chen, C.K. Ong, C.P. Neo, V.V. Varadan, V.K. Varadan, *Microwave Electronics, Measurement and Materials Characterization* (Wiley, New York, NY, USA, 2004).
3. A.K. Jha, M.J. Akhtar, An improved rectangular cavity approach for measurement of complex permeability of materials. *IEEE Trans. Instrum. Meas.* **64**(4), 995–1003 (2015)
4. A.K. Jha, M.J. Akhtar, A generalized rectangular cavity approach for determination of complex permittivity of materials. *IEEE Trans. Instrum. Meas.* **63**(11), 2632–2641 (2014)
5. A.K. Jha, M.J. Akhtar, Improved resonator method for microwave testing of magnetic composite sheets. *IEEE Trans. Magn.* **51**(9) (2015). Art. no. 4003709
6. M.A.H. Ansari, A.K. Jha, M.J. Akhtar, Design and application of the CSRR-based planar sensor for noninvasive measurement of complex permittivity. *IEEE Sens. J.* **15**(12), 7181–7189 (2015)
7. A. Vena, E. Perret, D. Kaddour, T. Baron, Toward a reliable chipless RFID humidity sensor tag based on silicon nanowires. *IEEE Trans. Microw. Theory Techn.* **64**(9), 2977–2985 (2016)
8. A. Lazaro, R. Villarino, D. Girbau, A passive harmonic tag for humidity sensing. *Int. J. Antennas Propag.* (2014). Art. no. 670345
9. S.D. Nguyen et al., Approach for quality detection of food by RFID-based wireless sensor tag. *Electron. Lett.* **49**(25), 1588–1589 (2013)
10. H. Lobato-Morales et al., Wireless sensing of complex dielectric permittivity of liquids based on the RFID. *IEEE Trans. Microw. Theory Techn.* **62**(9), 2160–2167 (2014)
11. A.K. Jha et al., Broadband wireless sensing system for non-invasive testing of biological samples. *IEEE J. Emerg. Select. Topics Circuits Syst.* **8**(2), 251–259 (2018)
12. M. Adhikary, A. Biswas, M.J. Akhtar, Active integrated antenna based permittivity sensing tag. *IEEE Sens. Lett.* **1**(6), 1–4 (2017). Art no. 3501104
13. S. Prabhu, C. Gooneratne, K.A. Hoang, S. Mukhopadhyay, IoT-associated impedimetric biosensing for point-of-care monitoring of kidney health. *IEEE Sens. J.* <https://doi.org/10.1109/JSEN.2020.3011848>
14. M.E.E. Alahi, N. Pereira-Ishak, S.C. Mukhopadhyay, L. Burkitt, An internet-of-things enabled smart sensing system for nitrate monitoring. *IEEE Internet Things J.* **5**(6), 4409–4417 (2018). <https://doi.org/10.1109/JIOT.2018.2809669>
15. M.E.E. Alahi, L. Xie, S. Mukhopadhyay, L. Burkitt, A temperature compensated smart nitrate-sensor for agricultural industry. *IEEE Trans. Industr. Electron.* **64**(9), 7333–7341 (2017)
16. Hewlett Packard, Application Note 963, Impedance matching techniques for Mixers and Detectors
17. K.T. Muhammed Shafi, A.K. Jha, M.J. Akhtar, Improved planar resonant RF sensor for retrieval of permittivity and permeability of materials. *IEEE Sens. J.* **17**(17), 5479–5486 (2017). <https://doi.org/10.1109/JSEN.2017.2724942>
18. J. Naqui, M. Duran-Sindreu, F. Martin, Modeling split-ring resonator (SRR) and complementary split-ring resonator (CSRR) loaded transmission lines exhibiting cross-polarization effects. *IEEE Antenn. Wireless Propag. Lett.* **12**, 178–181 (2013)

Some Applications of Interdigital Sensor for Future Technologies



J. K. Roy and S. C. Mukhopadhyay

Abstract This chapter focuses on the application of Interdigital sensors considering future technologies. The interdigital sensor is interdigital electrodes with a dielectric. The geometric and physical structures with different types of dielectric materials formed a variety of sensor and transducer designs. Its physical and chemical principles behind the operation vary so much in different fields of science and technology, generating varieties of applications in reality. The chapter of the book highlights a few important applications of interdigital sensors considering capacitive, dielectric, piezo acoustic, chemical, biological, and micro-electro-mechanical varieties. These applications may play a great role in future technologies.

1 Introduction

The term “Interdigital” does not have direct analogs in English. Thus, this most frequent term is often replaced by periodic, microstrip, comb, and grating, as well as such variations as interdigitated and combed. However, in practice, every microstrip circuit cannot be termed as interdigital. Similarly, every interdigital circuit is not periodic in practice. The term *interdigital*, selected for use throughout this paper, refers to a digit like or comb-like periodic pattern of parallel in-plane conducting electrodes used to build up the capacitance associated with the electric fields that penetrate the into the material sample or sensitive coating [1].

The first interdigital electrode design has been found in the patent of Nicola Tesla, which was issued in 1891 [2]. In this patent drawing, each “finger” is a rectangular plate, immersed in an insulating liquid. The total capacitance of the “electrical

J. K. Roy (✉)

Eureka Sciencetech Research Foundation, Kolkata, West Bengal, India

e-mail: jkroy.cal51@gmail.com

S. C. Mukhopadhyay

School of Engineering, Macquarie University, Sydney, NSW 2109, Australia

e-mail: Subhas.Mukhopadhyay@mq.edu.au

condenser” increases approximately linearly with the number of plates. This principle is used in the design capacitors as well. The interdigital sensor has two components, conducting a comb-like pair of electrodes and a substrate. The electrode pairs are in the same plane for sensing operation; therefore, this type of sensors called a planner interdigital sensor. The planner interdigital sensor is converted to a planer interdigital capacitive sensor if electrodes of the sensor are covered by insulating material. In either case, the measuring parameter is impedance. Therefore, it is also called an impedimetric interdigital sensor. During the last two decades, planar interdigital sensors have been widely used in a wide range of applications [3], due to its simplicity and low cost. Ayoub Bourjilat et al. [4] in 2017 studied the modelling of an interdigital sensor designed for conductivity measurement. It concluded with a new design of equivalent circuit of the sensor and explicit theoretical relation with geometry, no of combs substrate permittivity, and exciting frequency of the voltage applied. This equation was validated with the Finite element method. The authors took the example of electrodes interdigitated sensors with the following geometrical parameters ($N = 40$, $\eta = 0.5$, $w = 3 \mu\text{m}$, $K_{cell} = 0.97$). The sensor is evaluated in the presence of a solution modelled by a semi-infinite thickness rectangle Fig. 1 with an electrical conductivity of $1 \mu\text{S} / \text{cm}$ and a relative permittivity of 80. Figure 2 is the Nyquist diagram of the sensor. The theoretical model is in perfect coherence with the simulation results (the triangles and rectangles represent the theoretical results) [4].

Another equivalent circuit is double layer dielectric, which is more practical in a sense.

A double layer of dielectric is formed between the electrode. The thickness of the double layer is an important parameter in low frequency ($<1 \text{ MHz}$) measurements because it allows us to determine the measurement band, optimize the geometric parameters and correctly determine the equivalent circuit model. In a geometric

Fig. 1 a Geometry of Planner Interdigital sensor [4]. b Equivalent circuit [4]

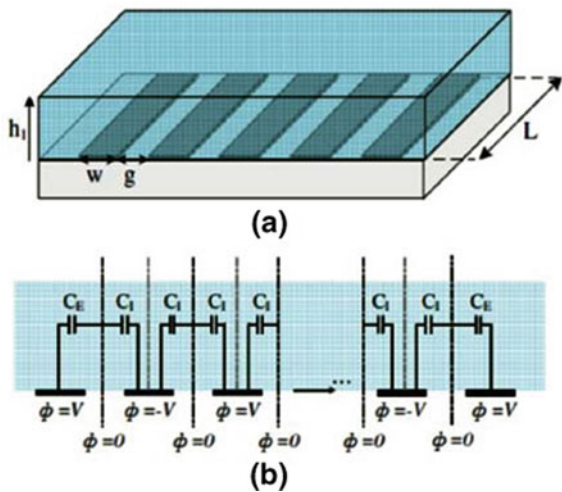
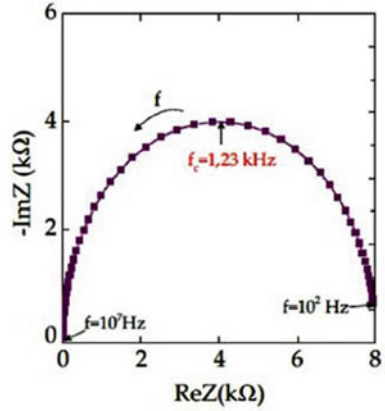


Fig. 2 Nyquist diagram for an interdigitated electrode structure [4]



sense, the double layer is represented by the compact layer of “Helmholtz” or “Stern” [5]. The double-layer phenomena occur on the entire electrode surface and can be modelled for a 4-electrode system, as shown in Figs. 3, 4.

In order to study the impact on the number of electrodes on impedance and phase ϕ .

The authors [4] considered number of electrodes varies from 10 to 80, the metalization ratio is $\eta = 0.5$, $w = g = 10 \mu m$. The thickness of the double layer is dDL

Fig. 3 Double layer interdigital sensor configuration [4]

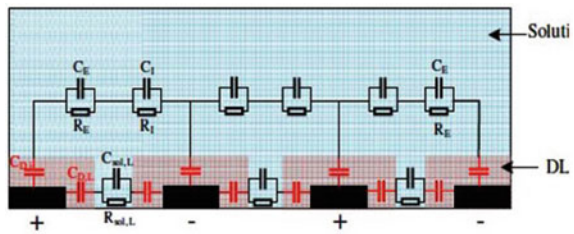
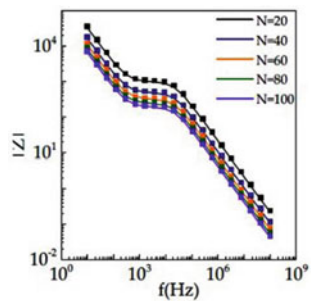


Fig. 4 Effect of Impedance with number of electrodes



= 80 nm. From the simulation study, it has been concluded that the number of electrodes does not have a significant impact on the phase; the number of electrodes only decreases the value of the impedance.

The important findings by the authors [4] are summarised and valuable in designing the Planar interdigital sensors.

- The double-layer model is more practical and suitable for analysis.
- The real part of the sensor impedance decreases with the number of electrode segments
- At the higher frequency of excitation capacitive part plays an effective role
- At a lower frequency of excitation, the resistive part plays an effective role.
- The sensor is maximum sensitive with a change in the value of permittivity of the layer/test liquid.
- The number of electrodes does not have a significant impact on the phase
- The geometry, permittivity of the substrate, and excitation frequency and voltage are important in the selectivity of the sensor.

The properties, as mentioned above of the planar interdigital sensor, make it suitable for large areas of applications in various engineering domains.

The impedance of the interdigital sensor is the measurand; the impedance values at the different physical conditions of the sensor are the data. For analysis Nyquist and Bode plots [6, 7] are drawn from the impedance data during experimentation. Standard impedance analyzers can be used during measurement. The impedance analyzer has an inbuilt low voltage sinusoidal source. The frequency of the source can be control from the front control of the analyzer, or the analyzer can be programmed for sweep frequency at a constant amplitude. There is voltage, and current probes in pairs are available, which can directly be interfaced with the sensor. The impedance spectroscopy needs very low ac voltage for excitation, which also can be programmed in the Instrument. The Instrument has a communication port for computer application (Fig. 5).



Fig. 5 A typical Impedance analyzer (Hioki LCR meter IM3536) [8]

So using software and a laptop interfaced with the analyzer can get Nyquist and Bode plot instantly. The impedance data during experimentation can be stored in the instrument memory, and the data file for each sweep is available for the study.

A group has made a detailed study of the Interdigital Sensor of researchers on various applications of interdigital sensors [9]. They made detail comparative studies on the following issues:

- (a) The comparative studies of chemical sensing by interdigital sensors for the various applications.
- (b) The comparative studies of strain sensing by interdigital sensors at various applications.
- (c) Uniformity and repeatability of the interdigital sensor during measurement.

Usually, the planar interdigital sensors are employed to detect capacitance, dielectric constant, and bulk conductivity in different mediums [9]. For some other type of biomedical applications, where the quantity of induced strain is measured, the interdigital sensors used are formed of flexible material. The operating principle of these sensors [9] is slightly different from that of the ones with rigid substrates.

This type of flexible interdigital sensor is very suitable for biomedical applications.

The manufacturing of the interdigital sensor is great art. It can be done by lithography and chemical etching using a mask. The fabrication can be done by vacuum or chemical deposition of metal on the substrate, or the prototype can be made using a 3-D printer. In the fabrication process, Aninda Nag et al., in the year 2015, developed a maskless lithography process [10], which enhances the performance of the Interdigital Sensor.

Capacitive Interdigital sensors can be formed in a single layer or multilayer to enhance performance. R. Igreja and C. J. Dias have made the analytical method of the interdigital sensor for a multi-layered structure in the year 2011.

To explore future technologies of Interdigital Sensors let us discuss some pertinent applications of the sensors technical domain wise:

The applications are divided into the following domains,

1. Sensors for process Industry
2. Sensors for environmental pollution measurement
3. Sensors for Human and Animal health
4. Sensors for the assessment of food quality
5. Sensors for Non Destructive testing
6. Sensors for other applications.

2 Application of Interdigital Sensors

The literature survey has been made on Interdigital sensor applications for the determination of process parameters. Not much work has been done in this domain for the last ten years; even no Industrial product based on the interdigital sensor is available

in the process industry market. This area has enough scope for the future development of the process sensor.

Let us discuss some application of Interdigital sensor in Industry.

2.1 Liquid Level Measurement Using Interdigital Capacitive Sensor [12]

Capacitive liquid level transmitter is very common in Industry for level measurement. The gage glass type non-contact level transmitter works the same with the working principle of the Interdigital capacitance sensor [11]. However, the capacitive gauge glass and simple immersion type Interdigital capacitive level sensor are suffering from fringe capacitance, which is sensitive to the excitation frequency, however for low accuracy, less than $\pm 2\%$, IDC sensor is good and rugged. The cost of the sensor is very less compared to other level sensors.

A simplified, low-cost liquid level transmitter was developed by Sayyed Faizan Ali et al.; in 2019, using the Interdigital Capacitive sensor [12] for measuring any type of conducting or insulating type of liquid. The sensor is fabricated from a copper-clad FR4 sheet. An interdigital pattern is created through the masking and etching process. The length of the sensor is 150 cm. The pattern is printed with an interdigital electrode gap of 0.5 mm, as shown in the Fig. 6.

The prototype was built in a laboratory and studied with the experimental setup as shown in Fig. 7.

The capacitance value of the sensor varies with the water level and measured through a modified DeSauty bridge. The bridge is made null when there is no water level. The bridge output varies with the water level in the tank. The output AC voltage is converted to DC voltage using a precision rectifier. The DC signal from the rectifier circuit is then processed for offset nulling, full-scale calibration using the Operational amplifier based simple signal conditioner circuit. Because of interdigital character,

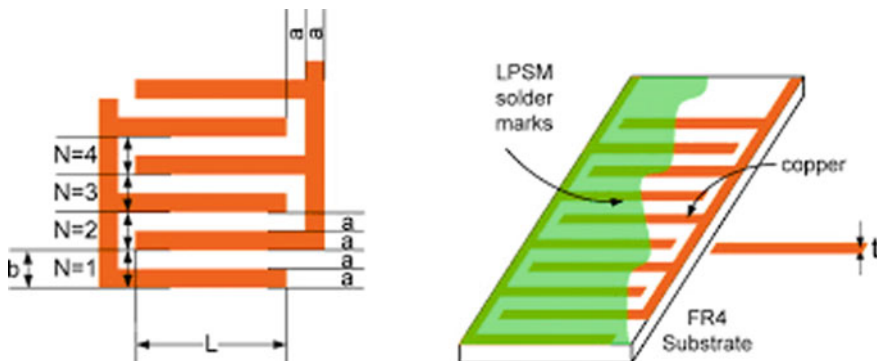


Fig. 6 Design of interdigital capacitive level sensor

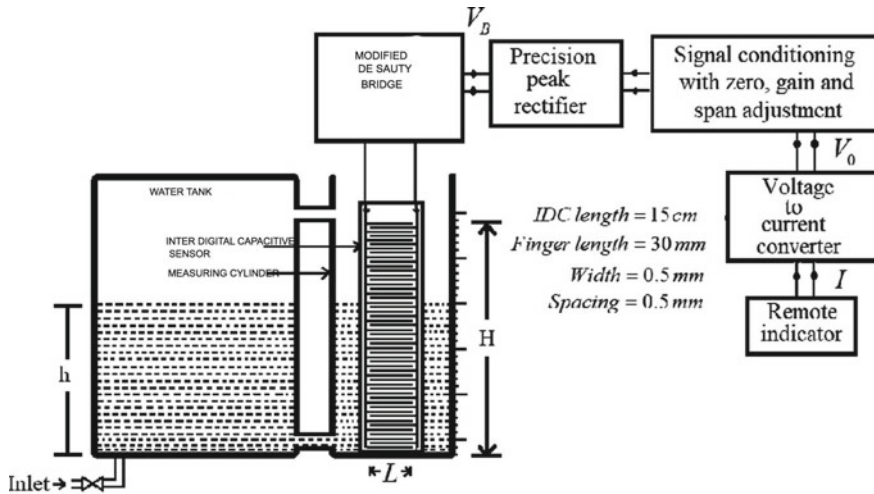


Fig. 7 Experimental setup and signal conditioning [12]

the capacitance increases linearly with the liquid level. Hence the voltage output of the signal conditioner also follows the liquid level. A simple Digital Volt Meter can be used for local monitoring, or the voltage can be fed to voltage to current converter with calibrated current range 4-20 mA.

The IDC level sensor has been tested for mineral water, tap water, river water, and distilled water found. The level measure is consistent with the physical level, as shown in Fig. 8a and b. The Fig. 8c is the uncertainty in the measurement, which was calculated from the large measurement data, as shown in Fig. 8c.

2.2 Chemical Sensing

There is a large number of various applications of the Interdigital Sensor in chemical sensing discussed in the literature. Interdigital sensors are used in the detection of toxic or non-toxic gases, chemicals, moisture, and organic impurities. The comb-like electrodes are coated with a thin layer of material, which is sensitive to the concentration of chemicals present within its atmosphere. The outputs of measurement are changes in resistance and capacitance between electrodes pairs. The sensing mechanism works when the sensor is exposed to ambient having chemicals. The interaction of the ambient chemicals with the sensitive coating material changes the coating material's conductivity, the effective thickness of the coated sensitive layer, and dielectric constant, and. The change in effective thickness and conductivity results in a resistance change, and the change of effective thickness of the sensitive layer and change of dielectric constant due to the ambient chemicals, changes the capacitance of the sensor. Interdigital chemical sensors are inexpensive to manufacture. It

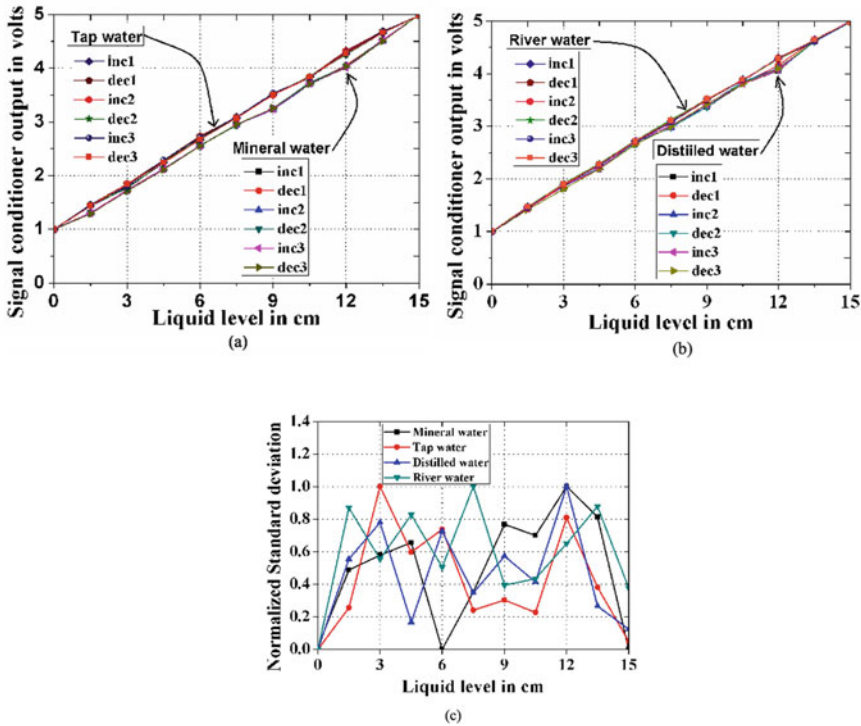


Fig. 8 Experimental data and measurement error [12]

can be integrated on a chip consisting of the sensor element and signal processing electronics.

2.3 The Concentration Measurement of Gases and Vapours Using Interdigital Sensor

A major application of interdigital sensors is to monitor the concentration of certain gases in the ambient atmosphere. The adsorption of gases has to be reversible to reach a stable equilibrium with their concentration in the gas phase. The most important factor in gas monitoring is the sensing material. A wide variety of sensitive materials have been reported for chemical sensing. Two major classes of materials are inorganic semiconductor oxides and organic polymers that are conducting or insulating.

Organic films have low melting points; therefore, they must be run at low temperatures, i.e., well below 100 C for polymers. In contrast, semiconductor oxides are typically run at higher temperatures between 300 and 500 C, depending on the target chemicals. The detection of CO has been given considerable attention due to recent

concerns of CO emissions as a global warming factor. A low-cost CO sensor in thick-film technology has been developed using BaTiO and various semiconducting oxides [13]. It is found that in this case, the best composition of gas sensing material is CuO-BaTiO La O CaCO. Also, the sensitivity increases with decreasing CO concentration. A sodium carbonate-based CO sensor has also been reported [14]. In this sensor, an encapsulated solid-state reference electrode is used to achieve a nearly drift-free response to CO change (drift 0.5 mV/24 h). Heteropolysiloxane exhibits a high sensitivity to SO gas, and so is used as the sensing material for SO [15]. Co-condensation with the hydrophobic propyltrim ethoxylate (PTMS) reduces the response to humidity present in the air. This sensor was fabricated with gold thin-film technology on a silica glass substrate with nickel as an adhesive layer. A SAW transducer is included in the sensor system to reduce the overall cross-sensitivity of the system to humidity. Undoped, Pd-doped, and Pt-doped SnO -based thin-film chemical sensors have been used to determine the concentration of NO, CO, CH, and H [16] quantitatively. The different contributions from contacts, surface, bulk, and grain boundaries to the sensor response were separated using different electrode configurations at different frequencies of electrical excitation.

Another example of an interdigital sensor used as a gas detector is the highly selective NO detection using Bi O -based materials. Doped and undoped Bi O (a p-type semiconductor material) were used to detect NO. It has notable sensitivity and remarkable selectivity as compared to other components in exhaust gases, such as CO, CH, C H, C H, iso-C H, and H [17]. Also, the response time is very short, normally less than 2 to 3 min. The sensitivity for various test gases is monitored using simple two-terminal measurements. Electrically conductive polymers poly(3-hexylthiophene) were investigated as ultrasensitive chemical sensors for hydrazine and monomethylhydrazine vapour [18]. It is demonstrated that concentrations in the 0.1–100 ppb range of these highly toxic species can be monitored with an accuracy of $\pm 20\%$. The sensor can be used for both dosimetry and real-time detection of d-Cellulose derivatives, such as ethylcellulose, cellulose acetate, and cellulose propionate. The method can also be used for the detection of different organic compounds in the gas phase, e.g., ketones, alkanes, alcohols, aromatic, and chlorinated hydrocarbons [19]. A quartz microbalance (QMB) is coupled with an IDC to measure changes of masses upon molecule/polymer interactions in this experiment. For different compounds, capacitance changes are mainly determined by the dipole moments of the analyte molecules.

The most commonly used sensor array is the planar structure, which consists of two planar lumped electrodes manufactured in conventional thin-film technology on an insulating substrate. The mechanism is based on the interaction between the surface of the layer and the gas molecules. Different electrode geometries and their relationship with sensor sensitivity are being investigated [20]. It is found that a very small electrode gap can achieve high sensitivity.

2.4 The pH Measurement of Liquid Using Interdigital Sensor

Chuang et al. developed a flexible interdigital sensor coated with a thin film of polyaniline [21]. As the redox state of PANDB changed after the reaction with different pH values, the impedance change was several times the original impedance before the reaction. It meant not only that the magnitude of impedance change could be easily detected by simple electronic equipment, but also that the resolution of the pH sensor was very high. In addition, the variations of impedance in an ambient environment and at different bending angles were less than 1%. Thus, the pH sensor was able to provide a reliable and stable result and would be suitable even for samples that cannot be measured on-site, as is the case in fieldwork. This study has been concluded that the feasibility of sensing pH values using a low-cost, disposable, flexible IDT-electrode sensor with a PANDB layer.

Krister Hammarling et al., 2018 developed a hydrogel-based pH Sensor [22], which is a flexible Interdigital sensor (Fig. 9). Schematic of the different sensor layers and their thicknesses (left picture). Layers from the bottom and up are Mylar as substrate. The Interdigital pattern made of gold, SU8 as an electric protection layer and AOBAE is the pH-sensitive layer. The middle picture is a photo of a manufactured sensor (with SU8 and AOBAE on top). The right-hand picture shows an enlargement of the middle pictures lower part, with measurements of conductor width, W , and the gap, G , between the conductor.

The sensors were fabricated with 105 μm thick Mylar (PET) film. 30 nm thin gold layer was formed on the Mylar substrate by using a Quorum Q150T ES sputter (Quorum Technologies, UK) system. The 355 nm nanosecond pulsed laser ablation system is used with spatial resolution in the order of 10 μm to pattern an Interdigital capacitance structure. In this design, the width of the conductive lines and distance between the lines was 120 μm and 40 μm respectively; The active, pH-sensitive ABOAE layer was deposited in a layer by a blade coating technique. AOBAE is the pH-sensitive hydrogels, and the full form is acryl terminated oligo beta-amino ester's (AOBAE). The characterization of interdigital pH-sensors was made by submerging each sensor in liquids having defined pH levels. The capacitance values were measured using a digital smart LCR meter (HP 4284A). This smart meter is connected with a computer having a LabVIEW program (National Instruments, Austin, TX, USA).

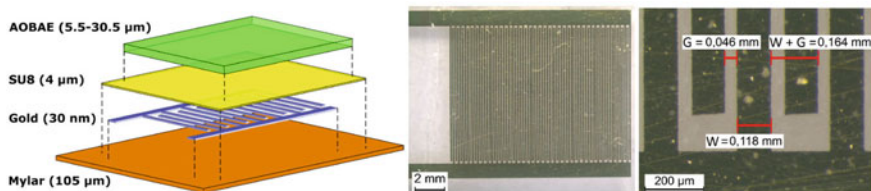


Fig. 9 Interdigital pH sensor [22]

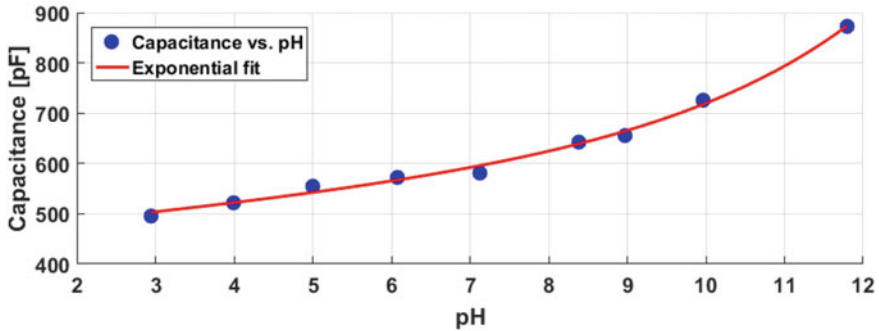


Fig. 10 Experimental data: capacitance –vs–pH [22]

Using LabVIEW, measurement, and control had been done during experimentation. The developed sensor was fitted in a holder with all cables fixed and kept as short as possible. A motorized lab jack was used to lift /down the different pH-buffers. Before the measurement of the sensor capacitance, the pH buffer solutions with pH values ranging between 2.94 and 11.80 were used as reference solutions. The Reference pH measurements were performed on the buffers using a Metrohm 632 pH-meter (Metrohm AG, Herisau, Switzerland). The calibration data is shown in Fig. 10. The specific interest to develop this Interdigital flexible pH sensor by authors was to monitor the pH level of Industrial effluents in landfills, recycling zones, and mine deposits. The heavy metal is highly toxic for humans, and heavy metal disrupts the pH level. Therefore, by measuring the pH level, the level of heavy metal leakage in the environment can be monitored at the site without chemical analysis.

Mary Lewis & Gerd Scheying of Robert Bosch GmbH in 2004 reported [23] the development of potentiometric sensor device for the measurement of pH. The sensor is thick film silver electrodes on a glass–ceramic base and interdigital in structure. The pH measurement range is 2–12 pH. The electrodes of the sensor made using thick-film technology and have an interdigital structure on the substrate. The sensor can be manufactured in mass production with precision. Further, the sensor because of its interdigital structure without a reference electrode can be mounted on the vitreous surface, especially in automobiles and industrial plants, where the sensor device is exposed to high mechanical stress. It can be used without any problems.

The Proton exchange membrane fuel cell (PEMFC) is used as an emergency generating set during a power interruption and crisis. The performance and the life of internal components of PEMFC are affected by the acidic environment [24].

This type of fuel cell developed mainly for transport applications, stationary, and portable fuel-cell applications—for example, an electric car driven by the Fuel cell. Figure 11a depicts the operation of the PEMFC, and Fig. 11b shows an application of the fuel cell. The distinguishing features include a lower operating temperature/pressure ranges (50–100 °C) and have special proton-conducting polymer electrolyte membrane. The PEMFCs generate electricity and operate on the opposite principle to PEM electrolysis, which consumes electricity.

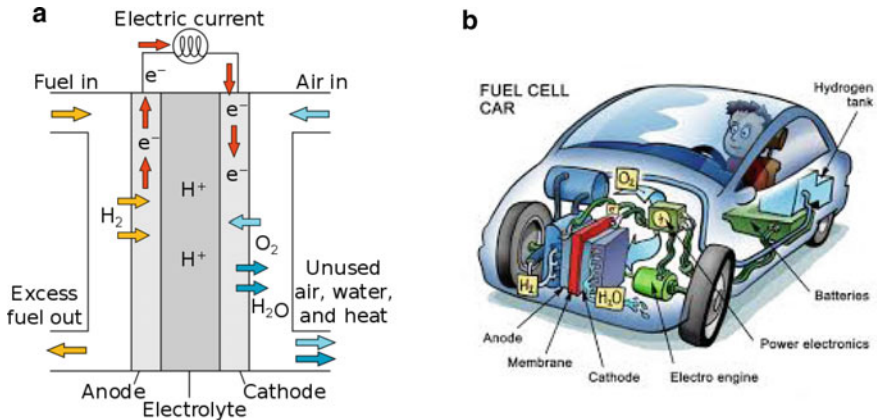


Fig. 11 Courtesy: Wikipedia

When the operating temperature of the fuel cell and the relative humidity is too high, the working efficiency of the fuel cell will decrease, and shorten the life of the internal component. pH sensors are brittle, bulky, and expensive, so the sensor cannot be embedded inside the fuel cell. The micro-electro-mechanical systems (MEMS) technology is used to develop flexible micro pH sensors. The advantages of flexible micro pH sensors include their flexibility against the acidic environment, and it can be placed anywhere in a fuel cell. Chi-Yuan Lee et al., in 2016 had been reported this development [24]. The developed pH sensor is flexible and interdigital. The MEMS technology is used to develop the flexible micro pH sensor on the polyimide (PI) flexible substrate. The thickness of the PI is 50 μm . The PI. Polymer has properties of high temperature resistance, compression resistance, high flexibility, and good durability. It is fabricated using MEM technology. The size is very small. The coating layer is Hydrogel based and acid-sensitive.

2.5 The Role of Interdigital Sensor in Soil and Water Pollution

Nitrogen is one of the essential elements for the growth of all plants and animals in the water, as it is a major component of the supply of protein [25, 26]. Therefore, Nitrate-nitrogen ($\text{NO}_3\text{-N}$) is used in agriculture to increase plant and animal production in the form of fertilizer. Some fertilizers also used ($\text{NO}_2\text{-N}$) as the source of Nitrogen. However, nitrite or nitrate contamination is a common problem in the surface and groundwater in agricultural areas [26]. In some countries with high domestic cattle concentration, the $\text{NO}_3\text{-N}$ or $\text{NO}_2\text{-N}$ concentration in groundwater is higher than the threshold concentration (Table 1), and the urine of agricultural livestock is the main source of nitrate contamination [26]. Cows are inefficient users of Nitrogen

Table 1 Drinking water standard and health advisory [27]

Chemicals	Standards			Health advisory		
	Status	MCLG (mg/L)	MCL (mg/L)	10-kg child		RfD
				One day mg/L	10 day mg/L	
Nitrate (as N)	F	10	10	10 ¹	10 ¹	1.6
Nitrite (as N)	F	1	1	1 ¹	1 ¹	0.16

F = Final, MCLG = Maximum Contaminant Level Goal

MCL = Maximum Contaminant Level

¹These value is calculated for a 4 kg infant are protective for all age group

but excrete a large proportion (around 80%) of Nitrogen that they consume in their urine. Elevated NO₃-N concentrations in surface waters can stimulate the growth of unwanted algae and aquatic plants. Due to the rapid urbanization and development of agriculture worldwide, there is an increased risk of water pollution. The purity of water in these bodies can be degraded to the point of it being unsuitable for drinking or any domestic use, even after following a standardized purification procedure. Nitrate contamination is also a common problem in the surface water and groundwater in the agricultural area. When the nitrate level exceeds 1 mg/L, the consumption of water may cause the death of infants. NO₃-N concentrations are measured using the spectrophotometric method in the laboratory. This method requires expensive equipment and trained staff to conduct measurements. Another in situ measurement for the Detection of Nitrate or Nitrite is Raman Spectrophotometer, which is very costly and not comfortable for the measurement of large samples.

In 2015, a group of researchers from Massey University, New Zealand, reported the development of Interdigital based Sensor to Nitrate and Nitrite in soil and water.

Figure 12 is the design of the Interdigital Sensor. The sensor configuration is 1:5, which means that it has five sensing electrodes are present for one excitation electrode. The sensor is uncoated with dielectric. There are six groups of parallel sensing electrodes.

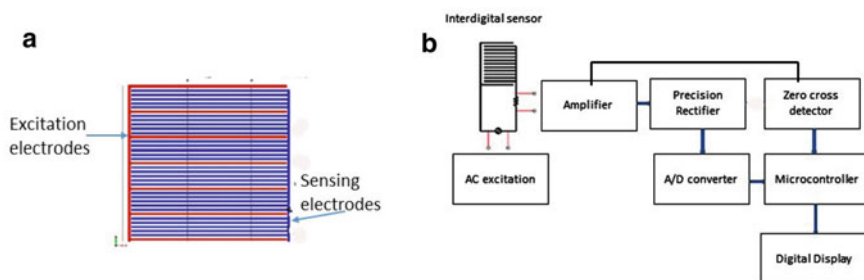


Fig. 12 Design of the interdigital sensor and its signal processing for nitrate and nitrite measurement in soil and water

The sensor is excited with sinusoidal ac voltage from a function generator. The sensor is connected to the AC source with a series load resistance. When the sensor is dipped to the water, then current flows through the circuit. The voltage drop across the load resistance is the measuring AC signal. The AC voltage output depends on the impedance value of the sensor, which depends on the Nitrate concentration in the water. The AC signal from the sensor is converted to DC voltage using OPAMP based precision rectifier. The DC signal after rectification fed to the A/D converter of the microcontroller. The same AC signal output is fed to the zero-cross detector. The microcontroller with digital display gives the digital value of nitrate or nitrite concentration in terms of impedance. After the calibration, the sensor was immersed into water samples collected from water bodies near the agricultural field, and the reading was taken. From the calibration data, the real concentration of the test sample was calculated. This type of sensor is disadvantageous because it is responsive to both the version of N.

In continuation of this research, the same group of researchers developed a highly selective Ion Imprinted Polymer-based Interdigital Capacitive Sensor for Nitrite Detection [28]. In this case, the sensor has a thin layer of Ion imprinted polymer (IIP), which is sensitive to nitrite ion, and the sensor becomes selective to the $\text{NO}_2\text{-N}$ only.

Ion Imprinted Polymers (IIP) are synthesized on the principles of enzyme phenomenon whereby a polymer is altered by a polymerization [28], which takes place in the presence of a template that could be later removed to create cavities to recognize only the analyte of interest. This specific and selective affinity for the target species decreases the chances of competition with other different types of ions. There are three types of imprinting: non-covalent, sacrificial spacer, and covalent. Non-covalent imprinting is the most widely used form, and it is based on the ability of the template molecule to produce strong intermolecular, non-covalent interactions (e.g., van der Waals/electrostatic interactions and hydrogen bonding) with the functional monomers. The exclusion of the template affords a cavity that, regarding size, shape, and functionality, corresponds to the template molecule and acts as the site for the recognition of specific ions. The experimental study was done with a standard solution of Nitrite at different concentrations and the water sample for nitrite concentration testing. The results show [28] that the development has extraordinary potential to develop a low-cost, in-situ measurement system to detect nitrite contamination with real-time monitoring.

A similar method was implemented [29] for nitrate detection with a different template, such as the Interdigital capacitive sensor is selective to Nitrate concentration, and the result was promising and quite satisfactorily.

Haoyue Luo et al. [30] developed an effective, fast, and highly selective nanogold film interdigital electrode sensors for Nitrite detection. The Chrome-black T was modified to the surface of the nanogold film interdigital electrodes by electrochemical polymerization. The chrome-black T has an affinity of nitrite ions. The sensor was calibrated with standard Nitrite solutions of strength 1 mol/L, 10 – 1 mol/L, 10 – 2 mol/L, 10 – 3 mol/L, 10 – 4 mol/L, and 10 – 5 mol/L laboratory. The developed interdigital electrode sensors can detect the very low concentration of nitrite solution

conveniently and quickly within 30 s. The novel nanogold film interdigital electrode sensors can be used in the Detection of Nitrite in blood, body fluid, food, and drinking water.

2.6 Interdigital Sensor in Toxicity Measurement

The biosensor is an analytical device, conjugated with a bioreceptor and a transducer unit. It has been used in many research areas [31, 32]. For example, the detection of different types of analytes, bacteria, viruses, and especially pathogen bacteria. These are important targets of a biosensor to sense and identify. The important fields of application of biosensor are clinical diagnosis at the point of care, food technology for assessment of food quality and water safety to prevent the human from dangerous diseases. Useful research has been made to detect pathogen bacteria using developed IDEA and 3D-IDEA impedimetric transducer [30] having interdigitated electrodes arrays with high selectivity. 3D-IDEA sensors were fabricated using conventional microelectronics fabrication techniques. The interdigitated electrode arrays were formed on a silicon wafer with a 2.5 μm thick thermal silicon oxide layer. The electrode material is a highly conducting tantalum silicide deposited using magnetron sputtering.

The interdigital pattern formed using the lithographic method. Biosensing platform has been made with p(NIPMAM) microgels on the sensor barrier by micro-contact imprinting. The scheme of the biofunctionalization process of 3D-IDEA impedimetric transducer with E.Coli bacteria is shown in Fig. 13.

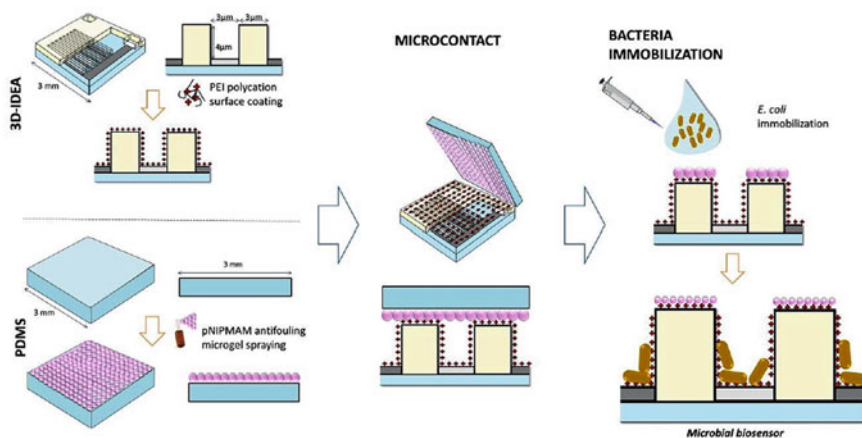


Fig. 13 Scheme of the biofunctionalization process of 3D-IDEA impedimetric transducer with E.coli bacteria [30] Courtesy: [32]

The IDEA & 3D- IDEA are a useful tool for different microbial biosensing applications, including the detection of bacteria and the determination of bacterial endotoxins. He used Electrochemical Impedance Spectroscopy (EIS) technique for the measurement impedance and found 3D-IDEA impedimetric is a highly selective and reproducible method for characterization of the sensor and the biosystem as a whole.

In the pathological practice, the bone loss can be monitored and detected by regular examination of serum or urine C-terminal telopeptide of type 1 collagen (CTX-1). The rapid, portable, and low-cost point-of-care devices are highly essential. Nasrin Afsarimanesh et al. reported an Internet of Things (IoT)-based selective, sensitive, and quick for the quantification of CTx-1 levels in serum [33]. A capacitive interdigital sensor was coated with artificial antibodies, prepared by molecular imprinting technology. Electrochemical impedance spectroscopy was used to evaluate the resistive and capacitive properties of the sample solutions. The processing system is IoT enabled microcontroller-based system for the measurement of the level of CTx-1 in serum and data transmission to the cloud server. The data is accessible to the medical practitioner, and a detailed investigation can start for early detection and treatment. The working zone of the developed sensing system is 0.1–2.5 ppb and linear, which covers the normal reference range of CTx-1 in serum, with a limit of detection of 0.09 ppb.

Anindya Nag et al. reported the development of Transparent biocompatible sensor patches for touch-sensitive prosthetic limbs in the year 2016 [34]. The transparent, flexible sensor patches were developed using a casting technique with polydimethylsiloxane (PDMS) as a substrate and a nanocomposite of carbon nanotubes (CNTs) and PDMS as interdigital electrodes. The electrodes act as strain sensitive capacitor. The prototypes were used as touch-sensitive sensors attached to the limbs. Experiment results show the sensitivity of the patches towards tactile sensing. The results are very promising and can play a key role in the development of a cost-efficient sensing system attached to prosthetic limbs.

A study was conducted on the detection and concentration measurement of estrone glucuronide (EIG), an important metabolite of the ovarian hormone estradiol, by using the Electrochemical Impedance Spectroscopy (EIS) technique [35]. A miniature planar Inter-digital capacitive sensor fabricated on a single-crystal silicon substrate with sputtered gold electrodes coupled with EIS was used to measure conductivity, permeability, and dielectric properties of the said hormone metabolite. The result and analysis confirmed that the fabricated sensor together with EIS could provide a rapid and successful low-cost sensing system, which can help a lay user to determine peak time for feminine reproductive fertility at home without submitting samples for an expensive and time-consuming costly laboratory test.

In the late 19th and early twentieth century, many peoples became ill due to the consumption of seafood like raw oysters, clams & mussels. Domoic acid is one of the key chemicals of seafood contamination. A.R.Mohd. Saifuddin et al..in 2008 successfully fabricated an interdigital sensor [36], which can detect domoic acid inside mussels. In that research, the electromagnetic interaction of an interdigital planer Sensor with chemical contamination in seafood was investigated. Food poisoning

caused by endotoxins or Lipopolysaccharide (LPS) is associated with Gram-negative bacteria. Two major foodborne pathogens, *Escherichia coli*, and *Salmonella* are examples of Gram-negative bacteria that cause a large number of outbreaks of food poisoning.

New types of planar interdigital sensors have been reported with different coating materials to assess their response to endotoxins [37]. A carboxyl-functional polymer, APTES (3-Aminopropyltriethoxysilane), and Thionine were chosen to be coated onto the FR4 interdigital sensors. These sensors were observed to have better sensitivity and selectivity to the target biomolecules of LPS. There are many other food and tannery related applications of the interdigital sensor. For example, the detection of trace amount of Pathlate contamination in bottled water and fruit juices [38–40], quality assessment of dairy products [41], noninvasive meat inspection [42], assessment of sheepskin property [43], looseness estimation of leather during the manufacturing process in a tannery [44] and many others. The safety of food and the environment has been a major concern of food technologists and health scientists in recent years. There exists a strong need for rapid and sensitive detection of different components of foods and beverages along with the foodborne and waterborne pathogens, toxins, and pesticide residues with high specificity. Biosensors present attractive, efficient alternative techniques by providing quick and reliable performances. There is very good potential for the application of biosensors for monitoring food quality and safety in food and bioprocessing industries [45].

2.7 Interdigital Sensor in Wound Health Monitoring

The most effective and economical treatment of chronic wounds is to cover the wound with suitable medication and dressing to heal quickly. For certain chronic wounds like leg ulcers for people with diabetes, compression therapy is provided using bandages and stocking. The compression bandage provides a pressure of 60 mm Hg over the sub bandage. Mehmood et al. [46] developed a prototype telemetry system for chronic wound health monitoring, having an IC chip-based telemetry circuit in a flexible PCB, two miniature Interdigitated flexible pressure sensors, and two numbers flexible interdigitated moisture sensor. The pressure sensor consists of two interdigitated electrically conductive traces placed under a thin conductive polymer sheet coated with carbon-based ink (Fig. 14). The pressure causes the conductive poly sheet to bent, touches a portion of the conductive fingers of the interdigitated electrodes, and decreases the resistance between the sensor terminal.

Voltage signals are digitized by 10-bit analog to digital converter. The digital data then transmitted to smart mobile through RF trans-receiver (Bluetooth). The schematic diagram developed PCB is shown in Fig. 16, and the flexible PCB and the Sensor mounting) is given in Fig. 17a and b. The performance of the Pressure Sensor and Moisture Sensor is given in Figs. 14b and 15b. The information on the pressure as well as dryness is available in smart mobile in real-time, which will be helpful for the better management of the chronic wound.

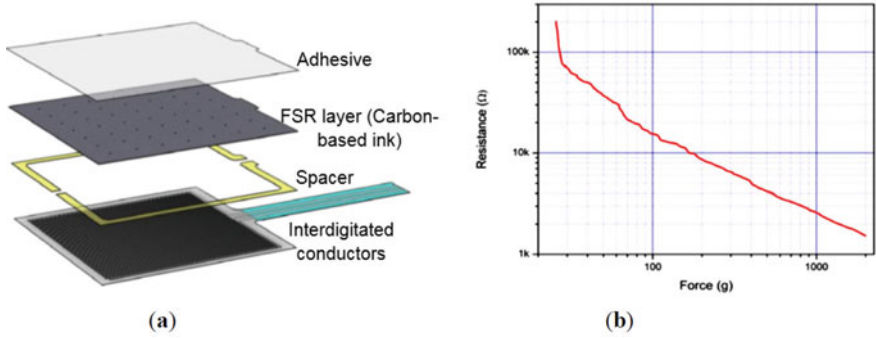


Fig. 14 a Interdigital pressure sensor b The pressure sensor characteristics

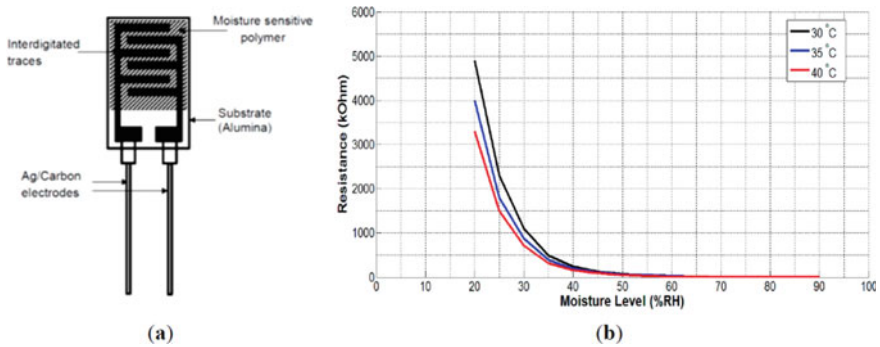


Fig. 15 a Interdigital moisture sensor b The moisture sensor characteristics

2.8 Interdigital Sensor in Kidney Health Monitoring

The Kidney [47] filter the waste of the body from the blood. It regulates pH, salt, and potassium level. It also produces hormones that regulate blood pressure. The kidneys are also responsible for activating a form of vitamin D that helps the body to absorb calcium for building bones and regulating the muscle function. Maintaining kidney health is important to overall health and general well-being [47]. Early-stage diagnosis of kidney disease is important for better revival. Kidney function can be qualitatively as well as quantitatively checked by monitoring levels of creatinine in urine or serum samples. Prabhu et al.; reported the development of fast, portable, cost, and time-effective Point of Care (PoC) devices for monitoring kidney health. In this research, an Internet of Thing (IoT)—associated creatinine specific, precise, fast, and cost and time-effective PoC diagnostic device for the monitoring of creatinine levels from serum has been carried out. The circuit diagram of the IoT enabled Kidney health monitoring system is shown in Fig. 18.

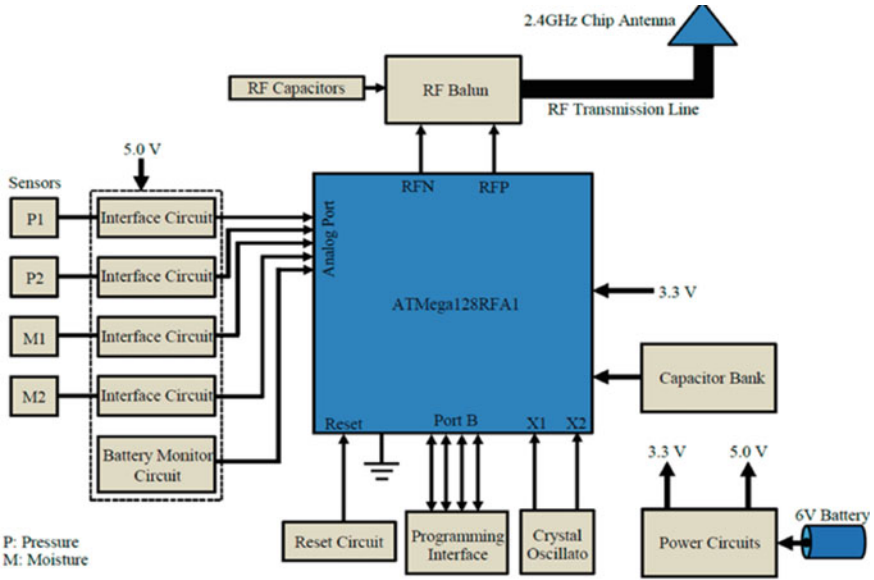
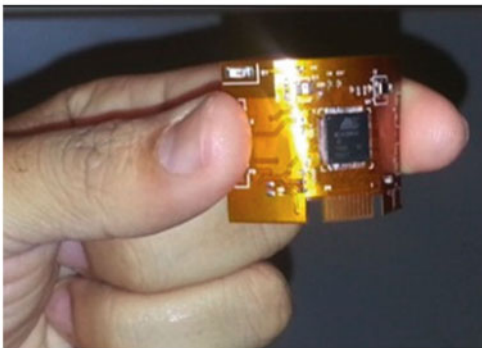


Fig. 16 a Schematic diagram of the Telemetry system



(a)



(b)

Fig. 17 a Flexible circuit b Implementation of the sensors and telemetry system

An interdigital sensor coated with creatinine selective Molecularly Imprinted Polymer (MIP) by using Electrochemical Impedance Spectroscopy (EIS) for determining impedance properties of the sample under test. The picture of the developed prototype is shown in Fig. 19. A low power microcontroller-associated diagnostic device was fabricated for the quantitative measuring of creatinine levels from serum,

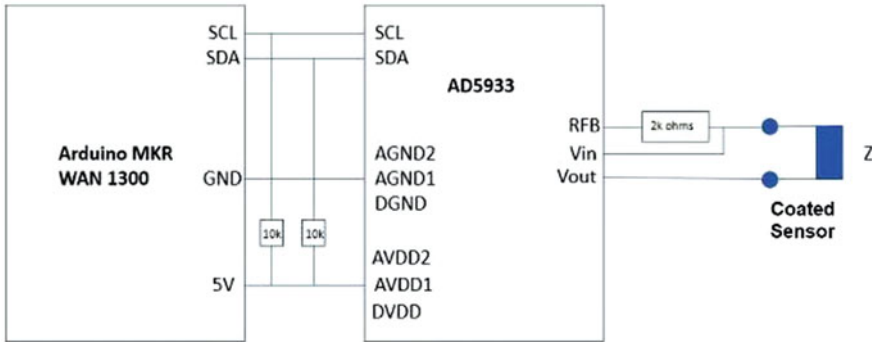


Fig. 18 Circuit diagram of the IoT enabled Kidney health monitoring system

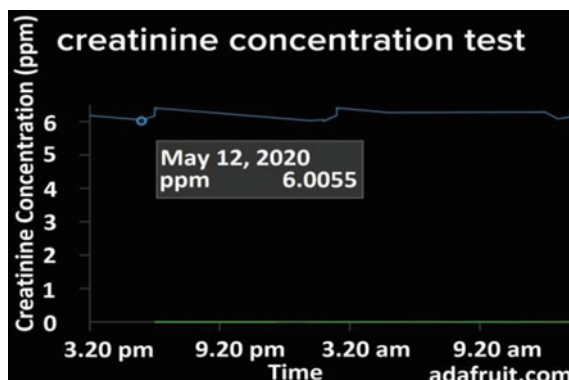
Fig. 19 The picture of the developed prototype



which transfers data to an IoT-associated cloud server. The collected data can be stockpiled, and it is accessible to concern (Fig. 20).

Oncologists/nephrologists located over distance for a long-distance patient health-care facility can visualise the data for diagnosis. The developed sensing system covers a wide range of 5–12 ppm (normal) up to 50 ppm (highest upper limit of detection), which is over thrice the acceptable creatinine range in serum levels, which is suitable for prognostic and prophylactic PoC care facility for kidney patients. The presented biosensor system is fast, easy, handy, but sensitive detection testing by using the presented PoC diagnostic device, and the verification of the device is performed using standard Creatinine Colorimetric Assay Kit [48].

Fig. 20 Online data from the developed PoC diagnostic device for 6 ppm [48]



3 Acceptability of Interdigital Sensor in Industry and Consumer Domain

When we talk about sensor development, then the following prerequisites are coming in to question—the quality ranking of the sensor and its usability on a mass scale as a consumer product or industrial product. The pre-requisites are:

- Selectivity:** The sensing device should be highly selective for the target analyte and show minimum or no cross-reactivity with moieties having a similar chemical structure.
- Sensitivity:** The sensing device should be able to measure in the range of interest for a given target analyte with minimum additional steps such as pre-cleaning and preconcentration of the samples.
- The linearity of response:** The linear response range of the system should cover the concentration range over which the target analyte is to be measured.
- Reproducibility of signal response:** When samples having the same concentrations are analyzed several times, they should give the same response.
- Quick response time and recovery time:** The biosensor device response should be quick enough so that real-time monitoring of the target analyte can be done efficiently. The recovery time should be small for the reusability of the biosensor system.
- Stability and operating life:** As such most of the biological compounds are unstable in different biochemical

Let us discuss the scenario of interdigital impedimetric or capacitive sensor-

- Selectivity:** In the case of an Interdigital sensor, the selectivity is achieved using Molecularly Imprinting technology, which leaves cavities in the Polymer Matrix with an affinity for a chosen “template” molecule. The selectivity depends on the accuracy of the template formation in the polymer. It is expected that the sensor will be used in the environment, where several types of molecules coexist in the form of mixtures. Suppose particular molecules have a lesser diameter than the

diameter of the template molecule. There will be cross-sensitivity, which may be prominent in nature and will act as noise. In that case, the interdigital sensor will not be 100% selective.

- b. Sensitivity: The sensitivity of the interdigital sensor depends on the electrode material, dielectric, geometry, and design. The optimized sensitivity can be obtained through the proper design of the interdigital sensor.
- c. The linearity of response: The method of measurement is impedimetric, Digital programmable LCR meter is used for measurement of impedance. The impedance curve is not linear. This phenomenon is the limitation of Impedance spectroscopy, so direct digital readout of the parameter sensed with proper scaling is hard to achieve. There is enough scope of research of signal processing of the interdigital sensor signal for direct evaluation of parameters using artificial intelligence.
- d. Reproducibility of the signal: The interdigital sensor needs proper cleaning each time before measurement to get reproducible data. So it is difficult to use in a process online. For laboratory or in-situ sample measurement, the interdigital sensor works well.
- e. Quick response and recovery time: For the interdigital sensor, the measurement needs some time to stabilize for the next measurement recovery time is also slow compare to other physical sensors. Therefore, the interdigital sensor could not be used in the real-time measurement.
- f. Stability and operating life: The stability and operating life of a sensor depend on how it is fabricated. In the case of the interdigital sensor for biological and chemical detection, the stability and operating life depend on ambient conditions such as temperature, pressure, and humidity as well as it depends on the coating layer of the interdigital sensor. The stability and operating life of the interdigital sensor are poor compared to the other physical sensor like thermocouple, RTD, etc. However interdigital capacitive sensor has better operating life compare to the Interdigital impedimetric sensor.

4 Future Trends of Interdigital Sensors

The concepts of the interdigital sensor are simplest other than sensors available around us. Flexibility in design makes interdigital sensors versatile. The interdigital sensor can be manufactured in bulk scale easily. Volume-wise the cost of raw material in the fabrication of the sensor is considerably low. With the cutting edge technology of IC fabrication, the array of interdigital sensors with a variety of chemical selectivity can be fabricated in a very small area of a substrate, which will bring the reality of Lab on a Chip in the future. Similarly, the sensor array with processing circuits can be converted to Application Specific Integrated Circuit (ASIC) in a very miniaturized form suitable to Electronic Tongue and Electronic Nose applications. Multi-component sweat analysis [49] is also possible with interdigital sensors. The flexible printed interdigital sensors will play a great role in wearable electronics for vital sign monitoring. Now organic electronic components can be printed in-circuit

forms over the fabrics. Textile being the material of our garments, it means that electronic functions can be integrated with interdigital sensors directly on them.

The sensors and the electronics can be placed over the human skin-like patch, and the vital parameters like ISF Glucose, sweat alcohol, lactate, and pH can be monitored in real-time. A similar patch with modifications can measure Cl^- and Na^+ ions in sweat.

Wearable motion detection [50] is mostly based on sensors. The interdigital sensor will be very effective in this area of application. The application of motion detection using the interdigital sensor for prosthesis limbs, soft robots, and physically impaired or elderly person will have future prospects requiring continuous activity tracking remotely [51].

References

1. A.V. Mamishev, K. Sundara, A. Rajan, Y. DU, Interdigital sensors and transducers. *Proc. IEEE* **92**(5) (2004)
2. N. Tesla, Electric condenser. U.S. Patent 464 667 (1891)
3. N. Afsarimanesh, A. Nag, M.E.E. Alahi, T. Han, S.C. Mukhopadhyay, Interdigital sensors: biomedical, environmental and industrial applications. *Sens. Actuators A: Phys.* <https://doi.org/10.1016/j.sna.2020.111923>
4. A. Bourjilat, F. Sarry, D. Kourtiche, M. Nadi, Modelization of interdigitated electrode sensor for impedance spectroscopy measurement, in *Proceedings of the 2017 Eleventh International Conference on Sensing Technology (ICST)* (IEEE Xplore, 2017). <https://doi.org/10.1109/ICST.2017.8304461>
5. K.B. Oldham, A Gouy-Chapman-Stern model of the double layer at a (metal)/(ionic liquid) interface. *J. Electroanal. Chem.* **613**(2), 131–138 (2008)
6. E. Barsoukov, J.R. Macdonald, *Impedance Spectroscopy: Theory, Experiment, and Applications*, 2nd edn. (New Jersey, Wiley)
7. G. Instruments, Basics of electrochemical impedance spectroscopy. in *G. Instruments, Complex impedance in Corrosion*, pp. 1–30 (2007)
8. Hioki LCR meter. https://www.hioki.com/en/products/detail/?product_key=5824
9. N. Afsarimanesh, A. Nag, M.E.E. Alahi, T. Han, S.C. Mukhopadhyay, Interdigital sensors: biomedical, environmental and industrial applications. *Sens. Actuators A: Phys.*, Elsevier. <https://doi.org/10.1016/j.sna.2020.111923>
10. A. Nag, A.I. Zia, S.C. Mukhopadhyay, J. Kosel, Performance enhancement of electronic sensor through mask-less lithography, in *Proceedings of the 2015 9th International Conference on Sensing Technology (ICST)* (IEEE Xplore, 2015). <https://doi.org/10.1109/ICST.2015.7438426>
11. J.K. Roy, S. Das, Low cost non-contact capacitive gauge glass level transmitter suitable for remote measurement and control, in *Proceedings of the 2015 Ninth International Conference on Sensing Technology (ICST)* (IEEE Xplore, 2015). <https://doi.org/10.1109/ICST.2015.7438463>
12. S.F. Ali, N. Mandal, Design and development of an electronic level transmitter using inter digital capacitor. *IEEE Sens. J.* **19**(13) (2019)
13. A. Haeusler, J.-U. Meyar, A novel thick-film conductive type CO_2 sensor. *Sens. Actuators B, Chem.* **34**(1–3) (1996). [https://doi.org/10.1016/S0925-4005\(96\)01847-3](https://doi.org/10.1016/S0925-4005(96)01847-3)
14. T. Lang, D. Wiemh, W.G. Opel, Carbonate based CO sensors with high performance. *Sens. Actuators B, Chem.* **B34**(2), 382–387 (1996)

15. L.R. Hartinger, H. Roth, E. Endres, A new SO sensor system with SAW and IDC elements. *Sens. Actuators B, Chem.* **B34**(2), pp. 339–342 (1996)
16. K.D. Schierbaum, J. Geiger, U. Weimar, W.G. Opel, Specific palladium and platinum doping for SnO based thin film sensor arrays. *Sens. Actuators B, Chem.* **13–14**, 143–147 (1993)
17. K. Higaki, S. Kudo, H. Ohnishi, Highly selective NO detection using Bi₂O₃ based materials. *Electrochem. Solid-State Lett.* **1**(2), 107–109 (1998)
18. L.E. Diane, R.Z. Mitchell, L.S. Bernstein, F.R. Michael, Conductive polymer films as ultra-sensitive chemical sensors for hydrazine and monomethylhydrazine vapor. *Anal. Chem.* **68**(5), p. 817 (1996)
19. R. Zhou, A. Hiermann, K.D. Schierbaum, K.E. Geckeler, W. Gopel, Detection of organic solvents with reliable chemical sensors based on cellulose derivatives. *Sens. Actuators B, Chem.* **24–25**, 443–447 (1995)
20. E. Endres, S. Drost, Optimization of the geometry of gas-sensitive interdigital capacitors. *Sens. Actuators B, Chem.* **4**, 95–98 (1991)
21. C.-H. Chuang, H.-P. Wu, C.-H. Chen, P.-R. Wu, Flexible pH sensor with polyaniline layer based on impedance measurement, in *Proceedings of IEEE Fifth International Conference on Sensing Technology Nov 28, 2011–Dec 1, 2011* (Palmerston North, New Zealand, 2011), pp. 211–216
22. K. Hammarling, M. Engholm, H. Andersson, M. Sandberg, H.-E. Nilsson, Broad-range hydrogel-based pH sensor with capacitive readout manufactured on a flexible substrate. *Chemosensors, MDPI* **16**(30) (2018)
23. EP1471349A2—Potentiometric sensor device for pH measurement—Google Patents. <https://patents.google.com/patent/EP1471349A2/en>
24. C.-Y. Lee, S.-M. Chuang, S.-J. Lee, C.-Y. Chiu, Fabrication of flexible micro pH sensor for use in proton exchange membrane fuel cell. *Int. J. Electrochem. Sci.* **11**, 2263–2268 (2016)
25. B. Oram (2014) *Nitrates and Nitrites in Drinking Water and Surface Waters*. <https://www.waterrsearch.net/index.php/nitrate>
26. L. Xie, A.I. Zia, S. Mukhopadhyay, L. Burkitt, Electrochemical impedimetric sensing of nitrate contamination in water, in *Proceedings of the 2015 Ninth International Conference on Sensing Technology* (IEEE Xplore, 2015). <https://doi.org/10.1109/ICST.2015.7438403>
27. 2018 Edition of the Drinking Water Standards and Health Advisories, EPA 822-F-18-001, Office of Water US Environmental Protection Agency Washington, DC. <https://www.epa.gov/sites/production/files/2018-03/documents/dwtable2018.pdf>
28. M.E. Alahi, N. Afsarimanesh, S. Mukhopadhyay, L. Burkitt, P.-L. Yu, Highly selective ion imprinted polymer-based interdigital sensor for nitrite detection, in *Proceedings of the 2016 Tenth International Conference on Sensing Technology* (IEEE Xplore, 2016). <https://doi.org/10.1109/ICST.2016.7796221>
29. M.E. Alahi, N. Afsarimanesh, S.C. Mukhopadhyay, L. Burkitt, Development of the selectivity of nitrate sensors based on ion imprinted polymerization technique, in *Proceedings of the 2017 Eleventh International Conference on Sensing Technology (ICST)* (IEEE Xplore, 2017). <https://doi.org/10.1109/ICST.2017.8304437>
30. H. Luo, X. Lin, Z. Peng, Y. Zhou, S. Xu, M. Song, L. Jin, X. Zheng, A fast and highly selective nitrite sensor based on interdigital electrodes modified with nanogold film and chrome-black T. *Front. Chem.* **8**(366) (2020)
31. S.B. Oliu, Integrated electrode arrays (IDEA) impedimetric transducers for bacterial biosensing applications. Ph.D. dissertation, Universitat Autònoma de Barcelona, TP:175 (2018)
32. M. Varshney, Y. B. Li, Interdigitated array microelectrodes based impedance biosensors for detection of bacterial cells. *Biosens. Bioelectron.* **24**, 2951–2960 (2009)
33. A.R.M. Syaifudin, S.C. Mukhopadhyay, P.L. Yu, C.-H. Chuang, H.-P. Wu, C.P. Gooneratne, J. Kosel, Characterizations and performance evaluations of thin film interdigital sensors for gram-negative bacteria detection, in *Proceedings of the 2011 Fifth International Conference on Sensing Technology* (IEEE Xplore, 2011) <https://doi.org/10.1109/ICST.2011.6136959>
34. N. Afsarimanesh, M.E. Alahi, S.C. Mukhopadhyay, Development of IoT-based impedimetric biosensor for point of care monitoring of bone loss. *IEEE J. Emerg. Sel. Top. Circuits Syst.* **8**(2) (2018)

35. A. Nag, S. Mukhopadhyay, J. Kosel, Transparent biocompatible sensor patches for touch-sensitive prosthetic limbs, in *Proceedings of the 2016 IEEE Tenth International Conference on Sensing Technology* (IEEE Xplore, 2016). <https://doi.org/10.1109/ICSensT.2016.7796261>
36. A.I. Zia, S.C. Mukhopadhyay, P.L. Yu, I.H. Al-Bahadly, A. Yudhana, C. Gooneratne, J. Kosel, Ovarian hormone estrone glucuronide (E1G) quantification-impedimetric electrochemical spectroscopy approach, in *Proceedings of the 2013 Seventh International Conference on Sensing Technology (ICST)*. <https://doi.org/10.1109/ICSensT.2013.6727610>
37. R.M. Syaifudin, S.C. Mukhopadhyay, K.P. Jayasundera, Electromagnetic interaction of planar interdigital sensors with chemicals contaminated in seafood, in *Proceedings of the 3rd International Conference on Sensing Technology* (IEEE Xplore, 2008) <https://doi.org/10.1109/ICS ENST.2008.4757180>
38. M.S. Abdul Rahman, S.C. Mukhopadhyay, P.-L. Yu, J. Kosel, Detection of bacterial endotoxin in food: new planar interdigital sensors based approach. *J. Food Eng.* **114**(3), 346–360 (2013)
39. A.I. Zia, N. Afsarimanesh, L.X. Anindya Nag, I.H. Al-Bahadly, P.L. Yu, J. Kosel, Improved detection limits for phthalates by selective solid-phase micro-extraction, in *Proceedings of the 2015 Ninth International Conference on Sensing Technology (ICST)* (IEEE Xplore, 2015) <https://doi.org/10.1109/ICSensT.2015.7438493>
40. Z.S.C. Mukhopadhyay, P.-L. Yu, I. Al-Bahadly, C. P. Gooneratne, J. Kosel, Rapid and molecular selective electrochemical sensing of phthalates in aqueous solution. *Biosens. Bioelectron.* **67**, 342–349 (2015)
41. Z.A.M. Syaifudin, S. Mukhopadhyay, P. Yu, I. Al-Bahadly, C.P. Gooneratne, et al., Electrochemical impedance spectroscopy-based MEMS sensors for phthalates detection in water and juices. *J. Phys.: Conf. Ser.* **439**, 012026 (2013)
42. S.C. Mukhopadhyay, C. Gooneratne, G.S. Gupta, S. Demidenko, A low-cost sensing system for quality of dairy products. *IEEE Trans. Instrum. Meas.* **55**(4), 1331–1338 (2006)
43. S.C. Mukhopadhyay, C.P. Gooneratne, A novel planar-type biosensor for noninvasive meat inspection. *IEEE Sens. J.* **7**(9), 1340–1346 (2007)
44. M.A.M. Yunus, V. Kasturi, S.C. Mukhopadhyay, G.S. Gupta, Sheep skin property estimation using a low-cost planar sensor, in *2009 IEEE Instrumentation and Measurement Technology Conference* (Publisher, IEEE, 2009). <https://doi.org/10.1109/IMTC.2009.5168497>
45. V. Kasturi, S.C. Mukhopadhyay, Planar interdigital sensors based looseness estimation of leather, in *Proceedings of 2008 3rd International Conference on Sensing Technology* (IEEE Xplore, 2008). <https://doi.org/10.1109/ICS ENST.2008.4757148>
46. M.S. Thakur, K. V. Ragavan, Biosensors in food processing. *J. Food Sci. Technol.* **50**(4), 625–641 (2013)
47. N. Mehmood, A. Hariz, S. Templeton, N.H. Voelcker, An improved flexible telemetry system to autonomously monitor sub-bandage pressure and wound moisture. *Sensors (Basel)* **14**(15), 21770–21790 (2014)
48. <https://www.healthline.com/health/kidney-health>
49. P. Sumedha, G. Chinthaka, M. Subhas, IoT-associated impedimetric biosensing for point-of-care monitoring of kidney health. *IEEE Sens. J.* (Early Access) (2020). <https://doi.org/10.1109/JSEN.2020.3011848>
50. B. Piro, G. Mattana, V. Noël, Recent advances in skin chemical sensors. *Sensors*, MDPI, **19**. <https://doi.org/10.3390/s19204376>
51. S. Khan, S. Ali, A. Bermak, Recent developments in printing flexible and wearable sensing electronics for healthcare applications. *Sensors*, MDPI, **19** (2019). <https://doi.org/10.3390/s19051230>